DOC.20070907.0003

QA: QA

ANL-EBS-MD-000033 REV 06

August 2007

Engineered Barrier System: Physical and Chemical Environment

Prepared for:
U.S. Department of Energy
Office of Civilian Radioactive Waste Management
Office of Repository Development
1551 Hillshire Drive
Las Vegas, Nevada 89134-6321

Prepared by:
Sandia National Laboratories
OCRWM Lead Laboratory for Repository Systems
1180 Town Center Drive
Las Vegas, Nevada 89144

Under Contract Number
DE-AC04-94AL85000

DISCLAIMER

This report was prepared as an account of work sponsored by an agency of the United States Government. Neither the United States Government nor any agency thereof, nor any of their employees, nor any of their contractors, subcontractors or their employees, makes any warranty, express or implied, or assumes any legal liability or responsibility for the accuracy, completeness, or any third party's use or the results of such use of any information, apparatus, product, or process disclosed, or represents that its use would not infringe privately owned rights. Reference herein to any specific commercial product, process, or service by trade name, trademark, manufacturer, or otherwise, does not necessarily constitute or imply its endorsement, recommendation, or favoring by the United States Government or any agency thereof or its contractors or subcontractors. The views and opinions of authors expressed herein do not necessarily state or reflect those of the United States Government or any agency thereof.

QA: QA

Engineered Barrier System: Physical and Chemical Environment

ANL-EBS-MD-000033 REV 06

August 2007

Model Signature Page/Change History

Complete only applicable items.

2. Type of Mathematical Model

☒ Process Model ☐ Abstraction Model ☐ System Model

Describe Intended Use of Model

The principal intentions of this model and analysis activity are:

- Predict the composition of potential seepage waters through time, by evaluating water–rock interactions as percolating waters move through the thermal field above the drift and arrive at the drift wall
- Predict the potential evolution of the in-drift chemical environment for the important parameters that affect drip shield and waste package durability, and control solubility and colloidal stability of radionuclides in the invert
- Provide compositions of gas and water that evolve during seepage evaporation in the drift in the form of lookup tables to TSPA-LA; this involves quantification of ionic strength, chloride and nitrate concentration, and pH as functions of relative humidity (RH), carbon dioxide partial pressure (pCO_2), and temperature.

3. Title

Engineered Barrier System: Physical and Chemical Environment

4. DI (including Rev. No.):

ANL-EBS-MD-000033 REV 06

	Printed Name	Signature	Date
5. Originator	Katheryn Helean		8/30/2007
6. Independent Technical Reviewer	David Sassani		8/30/2007
7. Checker	William Downs for Ernest Hardin		8/30/07
8. QCS/Lead Lab QA Reviewer	Robert E. Spencer		8/30/07
9. Responsible Manager/Lead	Patrick Brady		8/30/2007
10. Responsible Manager	Geoff Freeze		8/31/07

11. Remarks

Change History

12. Revision No.	13. Description of Change
REV 00	Initial Issue.
REV 00 ICN 01	Editorial changes in Response to AP-7.5Q acceptance review. Also corrected DTN in Section 6.1.8. Replaced DTN: GS961108312771.002 with DTN: MO0005PORWATER.000 for composition of pore water sample in Section 4.1.2.2. Editorial changes throughout.

REV 01	Revised for no-backfill design, and to include FEPs and IRSR analyses, and to address data qualification issues in Sections 4 and 5. Thermal-hydrology calculations are taken from another AMR, and discussions were added for fungal observations from the ECRB and the prediction of minerals formed by drying waters from THC calculation. Water compositions were re-calculated using a Pitzer model.
REV 02	Revision to address removal or replacement of non-LA product input (i.e. historical TPO or other information).
REV 03	Revision to address Regulatory Integration Team comments to enhance transparency. The in-drift oxygen balance was re-calculated, and model validation was augmented by inclusion of additional pore water analyses.
REV 04	Revision due to issues from CRs: CR-4290, CR-4713, CR-4961, CR-5673; and from TMRB decisions: TMRB-2005-007, TMRB-2005-016, TMRB-2005-026 and TMRB-2005-033. All changes from REV03 ACN01 are incorporated. Changes are indicated by vertical lines.
REV 05	DOE Comment Incorporation. Revision addresses CR-6242.
REV 06	Develops and implements the Near Field Chemistry process model and addresses the following CRs: 6770, 7190, 7786, 7820, 8316, and 8959.

ACKNOWLEDGEMENTS

Revision 06 of this report had significant input from Charles Bryan and assistance from David Shields, Wendy Mitcheltree, and Patrick V. Brady. Revisions 03 and 04 had significant assistance from David Shields. Revision 02 was originated by Darren Jolley and technically supported by (alphabetically): Russell Jarek, Carlos Jove-Colon, Paul Mariner, and Richard Metcalf.

INTENTIONALLY LEFT BLANK

CONTENTS

Page

CONTENTS (Continued)

Page

CONTENTS (Continued)

Page

CONTENTS (Continued)

Page

FIGURES

Page

FIGURES (Continued)

Page

FIGURES (Continued)

Page

FIGURES (Continued)

Page

FIGURES (Continued)

Page

FIGURES (Continued)

Page

FIGURES (Continued)

Page

INTENTIONALLY LEFT BLANK

TABLES

Page

TABLES (Continued)

Page

TABLES (Continued)

Page

INTENTIONALLY LEFT BLANK

ACRONYMS AND ABBREVIATIONS

Acronyms

ACM	alternative conceptual model
AFM	active-fracture model
ASTM	American Society for the Testing of Materials
BSW	basic saturated water
CDF	cumulative distribution function
CR	condition report
DD	degree of dilution
DST	Drift Scale Test
DTN	data tracking number
EBS	Engineered Barrier System
ECRB	Enhanced Characterization of the Repository Block
ESF	Exploratory Studies Facility
FEHM	finite element heat and mass transfer (code)
FEPs	features, events, and processes
IDPS	in-drift precipitates/salts
IPC	in-package chemistry
LA	license application
MSTHM	multiscale thermohydrologic model
NBS	National Bureau of Standards
NFC	near-field chemistry
P&CE	physical and chemical environment
PCA	Principal Component Analysis
RH	relative humidity
RH	relative humidity (numerical representation)
RIT	Regulatory Integration Team
SAW	simulated acidified water
SCW	simulated concentrated well water
SDW	simulated dilute water
SI	saturation index
SSW	simulated saturated water

ACRONYMS AND ABBREVIATIONS (CONTINUED)

TH	thermal-hydrologic
THC	thermal-hydrologic-chemical
TM	thermal measure
TSPA	total system performance assessment
TST	Transition State Theory
TWP	technical work plan
USGS	U.S. Geological Survey
UZ	unsaturated zone
WPOB	waste package outer barrier
WRIP	water–rock interaction parameter
YMP	Yucca Mountain Project
2-D	two-dimensional
3-D	three-dimensional

Selected Abbreviations

atm	atmosphere
a_w	thermodynamic activity of water
Eh	redox potential
I	ionic strength
K	Kelvin
kg	kilograms
kg/L	kilograms per liter
kg/m	kilograms per meter
log Q/K	saturation index
mg/L	milligrams per liter
mg/m	milligrams per meter
mm	millimeter
pCO_2	partial pressure of CO_2
pe	electron activity
pH	negative $\log_{10}$ of hydrogen ion activity
ppm	parts per million
µm	micrometer

1. PURPOSE

The purpose of this model report is to describe the evolution of the physical and chemical environmental conditions within the waste emplacement drifts of the repository, including the drip shield and waste package surfaces. This report documents the development of a new process-level model, the near-field chemistry (NFC) model, and develops two abstraction models. The resulting seepage dilution/evaporation and integrated invert chemistry abstraction models are used in the total system performance assessment (TSPA) for the license application (LA) to assess the performance of the Engineered Barrier System (EBS) and the waste form.

This report develops one process model (the NFC model) and two abstraction-level models (the seepage dilution/evaporation and the integrated invert chemistry abstraction models) that describe the EBS physical and chemical environment (P&CE). The integrated invert chemistry abstraction utilizes the same lookup tables in the same manner as those developed by the seepage dilution/evaporation abstraction. Therefore, much of the discussion of the development of the TSPA feeds is limited to the seepage dilution/evaporation abstraction model. The implementation in the invert is unique, however, and is discussed in detail in Section 6.15.2. Where possible, these models use information directly from other reports as input, which promotes integration among process models used for TSPA-LA. Specific tasks and activities of modeling the physical and chemical environment are included in *Technical Work Plan for Revision of Model Reports for: Near-Field Environment and In-Drift Water Chemistry* (SNL 2007 [DIRS 179287], Section 1.2.2). As described in the technical work plan (TWP), the development of this report is coordinated with the development of other engineered barrier system reports.

The TWP is highly detailed, and much of the work presented in this report has never been documented before, and consequently there are several deviations from the TWP:

- **Use of Critical Review for Model Validation** – Instead of using critical review as an additional validation method for the NFC model, its use is restricted to the seepage evaporation abstraction and the integrated invert chemistry abstraction models. This is justified because only two validation methods are required, and sufficient additional post-development validation is provided for the NFC model (Section 7). For the in-drift abstractions, however, the post-development validation will consist of comparison with the in-drift precipitates/salts (IDPS) process model, plus critical review.

- **Comparison of NFC Feldspar Dissolution Rate to Published Rates** – A comparison of the NFC alkali feldspar dissolution rate to the published range of feldspar dissolution rates was not carried out. This comparison requires knowledge of the surface area of feldspar in the tuff, which is not available. In addition, published feldspar dissolution rates are poorly constrained with respect to the effective mineral surface area in the systems studied. Instead, the NFC feldspar dissolution rate is validated using a comparison to rates calculated from rock and pore-water strontium isotopic data from Yucca Mountain. The validity of the predicted alkali feldspar dissolution rate will be established if the rate calculated using the NFC model lies within an order of magnitude of the range of rates developed from the strontium isotope data.

- **NFC Model Comparisons with Drift-Scale Test (DST) Data** – Not all possible comparisons with measured gas, pore water, and mineralogical analyses from the DST were used because some are not meaningful. While DST data are evaluated in the NFC post-development model validation, the applicability of these data is limited because they do not address the time scale of water–rock interactions that will occur in the repository host rock.

- **Pore-Water Selection** – The selection of pore waters from the host rock units for use in the NFC model does not include fine-scale comparisons with models of mineralogic variability and percolation flux. The pore-water data were too sparse for useful comparisons. As discussed in Section 6.6, the mineralogy of the host rock units is essentially uniform for purposes of modeling water composition, although the selected waters span a range of stratigraphic units. Spatial variability of measured pore-water compositions occurs on a scale that is too fine for comparison to percolation flux output from hydrologic models.

- **Uncertainties in P&CE Lookup Tables** − No lookup tables were to be generated for use by TSPA until thermal-hydrologic-chemical (THC) seepage sensitivity tests were conducted and uncertainties evaluated to ensure that they were appropriately incorporated in downstream models such as the P&CE (SNL 2007 [DIRS 179287], Section 8.3). The THC seepage model no longer provides direct feeds to this report and has been replaced by the NFC model. The implementation of uncertainties associated with NFC model are documented and described in Section 6.12.

- **Included FEP List** − Two sets of changes were made to the list of included features, events, and processes (FEPs) in Table 6.14-1. First, FEPs 2.1.09.06.0B and 2.1.09.07.0B were shown with the wrong FEP number in the TWP. This has been corrected in Table 6-14-1. Second, 13 FEPs were added to Table 6-14-1. In the TWP, these 13 FEPs were identified as being included in the THC seepage model. As noted above, the THC seepage model has been replaced by the NFC model and those 13 FEPs are now included in this report.

- **Screening of FEP 2.2.08.04.0A** − FEP 2.2.08.04.0A, Redissolution of precipitates directs more corrosive fluids to waste packages, is no longer considered as included in TSPA-LA from this report. This process is not explicitly part of the NFC model, and therefore is not represented in the lookup tables provided to TSPA. The status of this FEP must be changed to "excluded."

- **CR-8959** − This condition report (CR) is addressed in Section 6.8 but was not documented in the TWP.

- **American Society for the Testing of Materials (ASTM) Standard** − The most current ASTM standard (ASTM A 588/A 588M – 05 [DIRS 176255]) was used instead of the older reference (ASTM A 588/A 588M – 01 [DIRS 162724]) cited in the TWP.

Finally, comments from the Regulatory Integration Team (RIT) are generally addressed in this report except for: (a) discussion of dust–condensate interactions, beyond that in Section 6.10, is deferred to *Analysis of Dust Deliquescence for FEP Screening* (SNL 2007 [DIRS 181267]) or related documents; (b) effects on water chemistry from sorption onto corrosion products in the EBS are insignificant and are not included in the sensitivity analyses; and (c) choice of FRONT waters is no longer relevant.

1.1 INTENDED MODEL USE

The principal intentions for the use of this model and analysis are to:

- Predict the composition of potential seepage waters through time, by evaluating water–rock interactions as percolating waters move through the thermal field above the drift and arrive at the drift wall.

- Predict the potential evolution of the in-drift chemical environment for the important parameters that affect drip shield and waste package durability, and control solubility and colloidal stability of radionuclides in the invert.

- Provide compositions of gas and water that evolve during seepage evaporation in the drift in the form of lookup tables to TSPA-LA; this involves quantification of ionic strength, chloride and nitrate concentration, and pH as functions of relative humidity (RH), carbon dioxide partial pressure (pCO_2), and temperature.

This is accomplished through use of the P&CE models that consist of the NFC process model and the seepage dilution/evaporation and integrated invert chemistry abstraction models, which are not affected significantly by the presence of dust (Section 6.10). The NFC model provides a range of in-drift pCO_2 and its evolution with time, for use in TSPA (see Sections 6.3 and 6.15.1). The NFC model provides a quantitative measure of the degree of water–rock interaction determined by the thermal field and flux-dependent flow velocities of percolating pore waters. Additionally, the corrosion of introduced materials and their interaction with seepage waters have been evaluated and found to have no significant impact on the in-drift environment.

1.2 SCOPE OF MODELS

This report uses seepage water compositions provided by the NFC model as input to the two P&CE abstraction models that describe the composition of seepage water contacting the drip shield, the waste package surface, and the invert. As seepage waters percolate into the drift, their chemical compositions change by dilution or evaporation and mineral precipitation. Evaporation causes dissolved aqueous species concentrations to increase, minerals to precipitate, and the most soluble components to become concentrated in the resulting solution, ultimately leading to formation of brine. Dilution generally has the opposite affect.

The IDPS model (SNL 2007 [DIRS 177411]) uses reaction-path modeling with EQ3/6, an equilibrium aqueous and gas-phase chemical speciation code, to simulate evaporation of seepage water into highly concentrated brines to determine the potential range of in-drift water compositions (Na-K-H-Mg-Ca-Al-Cl-F-NO_3-SO_4-Br-CO_3-SiO_2-CO_2-O_2-H_2O).

Model conditions are variable, with temperatures from ambient to approximately 100°C, total pressures near 1 atm, and relative humidity (RH) values from 0% to 100%. The P&CE suite of models uses the IDPS process model to calculate the evaporative evolution of seepage (and drift wall condensation) in the drift.

Seepage water and gas composition inputs for in-drift chemistry modeling are provided by the NFC model. An abstraction method is used to represent evolution of seepage water in the drifts, using lookup tables for key chemical constituents, and incorporating the effects of seepage evaporation as functions of temperature, RH, and pCO_2. Lookup tables are provided for use in TSPA, to enable selection of predicted water chemistry as a function of starting group water chemistry, water–rock interaction parameter (WRIP, based on thermal-hydrologic processes in the host rock), RH, pCO_2, and temperature.

In addition, the following ancillary analyses are included:

- Evaluation of the corrosion of low-alloy or carbon steel invert materials and its effects on oxygen to determine whether there is sufficient flux of oxygen into the drifts to maintain an oxidizing environment in the EBS

- Evaluation of the corrosion of emplaced steel and its effects on the composition of seepage waters.

In addition to these modeling objectives, and in accordance with criteria given in Section 4.2, the following relevant CRs are addressed:

- CR-6770: *Integrated effect of uncertainties on the implementation of localized corrosion in TSPA has not been evaluated.* Uncertainty estimates have been revised to include parameter co-variance (Cl, N) and appropriate distributions assigned for the key chemical parameters provided to TSPA: RH, [Cl], [N], pH and *I*. Uncertainties are provided as functions of RH and their implementation is discussed in Section 6.12. Additional integrated uncertainty sensitivity analyses will be documented by TSPA. Note that, prior to finalizing this report, CR-6770 was closed.

- CR-7190: *RIT action items associated with AMR ANL-EBS-MD-000033 Physical and Chemical Environment Model*. The RIT actions items addressed in this report are as follows:

  – *The effect of condensate-dust reactions needs to be addressed.* This topic is addressed in Section 6.10.

  – *Predicted invert water chemistries fail to take into account several processes*. This is addressed in the integrated invert chemistry abstraction model discussed in Sections 6.9 and 6.15.

  – *Confirm that the transport of gasses into the drift by diffusion and advection is not significantly different than the assumed advective fluxes in the P&CE model*. A discussion of the effects of axial transport was added to Section 6.7.

- *The potential effect of EBS materials on water chemistry is not sufficiently investigated; the importance of reaction rates and sorption onto corrosion products is not fully considered.* The development of a sorption model is beyond the scope of this report but is addressed in *EBS Radionuclide Transport Abstraction* (SNL 2007 [DIRS 177407]). Updated analyses in the present report evaluate the impact of degradation of EBS materials on invert water chemistry (Sections 6.7 and 6.8).

- *Some consideration of brine evolution and deliquescence in an open drift is needed to allow evaluation of the effects of gas fluxes*. Previous work on the production and fate of acid-gas species in the drift environment has shown that while degassing of acid-gas species from deliquescent brine is possible, it can occur only to a limited extent, and the resulting gas-phase concentrations for acid-gas species are very small (SNL 2007 [DIRS 181267], Section 6.2). Therefore, this aspect of brine evolution has no significant effect on the in-drift chemical environment and is not addressed further in this report.

- *Lack of treatment for kinetics of mineral precipitation and redissolution in the P&CE, especially with respect to Mg-silicates*. Justification for use of amorphous Mg-silicate, and suppression of crystalline sepiolite, in the validation cases for the IDPS model is provided in the accompanying report (SNL 2007 [DIRS 177411], Table 6-3). Justification for use of amorphous antigorite in the NFC process model, as well as other kinetically controlled phases, is provided in Sections 6.2 and 6.3.

- *The choice of FRONT waters may be incorrect and should be re-evaluated.* The NFC process model provides the starting water compositions to represent seepage for TSPA, and does not abstract water compositions from the saturation front, so this comment no longer applies to this report.

- *Difficulty following data analysis without recourse to special information*. This comment was addressed previously and the discussion has been updated to address the new NFC process model inputs (Section 6.3).

- *Lack of basis for using seepage water lookup table to represent condensation*. With the introduction of the NFC model, reference to "condensation tables" is no longer applicable. The argument for using the seepage lookup tables for waters formed by dilution of NFC waters is outlined in Section 6.9.

- CR-7786: *Potential errors in tables about corrosion test solutions repeated in various documents*. Errors in the corrosion test solution descriptions have been corrected in Table 6.13-6.

- CR-7820: *Incorrect NBS pH values in EQ3/6 outputs*. Incorrect National Bureau of Standards (NBS) pH values could be generated if the "Internal pH" option was selected in the EQ3/6 V8.0 input files, resulting in the code reporting an incorrect NBS *pH* value under these conditions (SPR001520060309). The affected data

tracking numbers (DTNs) have been superseded and the new DTNs correctly report the Pitzer pH because the correct options in the EQ3/6 simulations were selected.

- CR-8316: *Pore-water chemistry analyses lack charge balance*. Additional available measured pore-water data are evaluated and the likely cause of charge imbalance is discussed in Section 6.6.

- CR-8959: *Nitrate reduction by drift support materials – effect on in-drift water chemistry not considered.* The effect of nitrate reduction on steel is addressed in Section 6.8.

In addition, the following review comments from a previous validation exercise are addressed by this report.

- IDC-7: *Criteria for Chemical Binning – a statistical binning analysis should be developed and either implemented or presented as an alternative model*. Chemical binning is no longer used because the NFC model does not use a binning strategy.

- IDC-19: *Implementation of invert chemistry model – use of crown seepage evaporation abstraction may not be conservative with respect to representing invert water compositions*. A new integrated invert chemistry abstraction is developed and its implementation is documented in Sections 6.9 and 6.15.2.

Finally, other reports that either use the output of this report (directly or through its output DTNs) or are sources to this report are listed below.

Reports using this report include:

- *In-Package Chemistry Abstraction*
- *Total System Performance Assessment (TSPA) Model/Analysis for the License Application*
- *Igneous Intrusion Impacts on Waste Packages and Waste Forms*
- *Dike/Drift Interactions*
- *Engineered Barrier System Features, Events, and Processes*
- *Dissolved Concentration Limits of Radioactive Elements.*

Reports that are direct or indirect sources for this report include:

- *Multiscale Thermohydrologic Model*
- *Drift-Scale THC Seepage Model*
- *In-Drift Precipitates/Salts Model*
- *Aqueous Corrosion Rates for Waste Package Materials*
- *Analysis of Dust Deliquescence for FEP Screening*
- *In-Drift Natural Convection and Condensation.*

1.3 MODEL LIMITATIONS

The main limitations of the P&CE model involve the ranges of pCO_2 and temperature for which the model can be used in TSPA-LA. The TSPA-LA lookup tables quantify the chemical parameters of interest for evaporated NFC seepage waters for three sets of pCO_2 (10^{-2}, 10^{-3}, and 10^{-4} bar of pressure), multiple temperatures (30°C, 70°C, and 100°C), and as a function of relative humidity.

When determining the chemical parameters for evaporated seepage waters under environmental conditions that fall within lookup tables, the parameters are estimated using linear interpolation of temperature and log-linear interpolation of pCO_2. Chemistry values are extrapolated for pH, ionic strength, chloride, and nitrate if the pCO_2 exceeds the range of 1×10^{-4} to 1×10^{-2} bar established in the lookup tables. Justification for this extrapolation is provided within the pCO_2 limits up to 2×10^{-2} and down to 1×10^{-5} bar (Section 7.2).

When determining the chemical parameters of evaporated seepage waters for temperatures above 100°C and below 30°C, the limiting values of 100°C or 30°C lookup tables are used with no extrapolation.

If the *RH* is greater than the highest value in the lookup tables, the highest *RH* value is used. Explicit consideration of condensation under the drip shield is not addressed by the seepage evaporation abstraction, consistent with its exclusion on the basis of low consequence (see discussion in Section 6.15.2).

The lowest *RH* values at which chemistries are provided in the lookup tables for evaporated seepage water do not always correspond to the final eutectic point for the mixture of salt minerals present (i.e., to dryness). For this reason, if the relative humidity is lower than the lowest value in a lookup table, an aqueous system must be considered to persist, and that lowest *RH* information is used.

INTENTIONALLY LEFT BLANK

2. QUALITY ASSURANCE

This report and the supporting analyses are subject to the Office of Civilian Radioactive Waste Management quality assurance program (DOE 2007 [DIRS 182051]), and the applicable quality assurance requirements identified in TWP (SNL 2007 [DIRS 179287], Section 8). Quality assurance procedures identified in the TWP (SNL 2007 [DIRS 179287], Section 4), or the appropriate revised or superseding procedures, were used to conduct the activities described in this report. The TWP (SNL 2007 [DIRS 179287], Section 8.4) also identifies the methods used to control the electronic management of data during the analysis and documentation activities.

This report addresses the potential effects of the in-drift physical and chemical environment on the waste isolation capability of the following safety category barriers that are important to the demonstration of compliance with the postclosure performance objective prescribed in 10 CFR 63.113 [DIRS 173273]:

- Engineered barrier system: drip shield
- Engineered barrier system: waste package
- Engineered barrier system: drift invert (ballast).

The modeling activities of this report provide information that is important to demonstrating compliance with the performance objectives in 10 CFR 63.113 [DIRS 173273]. However, this report does not directly address either engineered or natural barriers as defined in *Q-List* (BSC 2005 [DIRS 175539]).

INTENTIONALLY LEFT BLANK

3. USE OF SOFTWARE

The controlled software that was used to conduct the work described in this report is listed in Table 3.1-1. All qualified software discussed in this document was obtained from Software Configuration Management in accordance with IM-PRO-003, *Software Management*. All qualified software was used in the operating environments for which it was baselined. Qualified software was selected for use in this report because either it is the best available software for the modeling applications or is the only available software for it specific use. All qualified software selected is appropriate for the application and was only used within the range of validation in accordance with IM-PRO-003. Only standard functions were utilized, i.e., no macros or special software routines were developed for, or used by, the software selected. Note that GetEQData Version 1.0.1 is, itself, an Excel macro (see Table 3.1-1).

Commercial off-the-shelf software, including Microsoft Word, Microsoft Excel, Mathcad Versions 13 and 14, IGPET2006, JMP5.1, and Aq·QA V.1.0, was also employed to carry out this work (Table 3.1-2). This software is exempt from qualification per Section 2.0 of IM-PRO-003. Microsoft Word and Microsoft Excel are standard software applications used widely throughout the Yucca Mountain Project. They provide standard word processing and spreadsheet functions. There are no limitations on the use of the commercial off-the-shelf software used in this report related to their specified functions. No macros (other than GetEQData version 1.0.1 listed in Table 3.1-1) or special software routines were used by, or developed for, this software. Hand calculations or visual inspection of software outputs confirm that this software produces correct results. Note that, because the normative analysis performed by the IGPET2006 requires knowledge of petrology or mineralogy in order to follow the calculation, a hand calculation is included for reference as part of the documentation of the IGPET2006 data in Output DTN: SN0705PAEBSPCE.009. The use of each of these exempt software packages is documented in sufficient detail to allow a qualified person to reproduce and verify results. The documentation of inputs and outputs related to the use of the exempt software is contained within the following DTNs: IGPET2006 as noted above; JMP5.1 and Aq. QA V.1.0 files are located in Output DTN: SN0705PAEBSPCE.015; Mathcad files are located in Output DTNs: SN0703PAEBSPCE.006 and SN0705PAEBSPCE.013; Excel files are located in all output and validation DTNs listed in Section 8.2. Consequently, the software listed in Table 3.1-2 is exempt in accordance with Section 2.0 of IM-PRO-003. The work was conducted using project standard desktop computers.

Table 3.1-1. Qualified Software Used

Software	Software Tracking Number	Platform / OS	Limitations/Range of Use	Brief Description	Functions Utilized
EQ3/6 Version 8.0 [DIRS 162228]	10813-8.0-00	PC/ WIN2000	Temperature, pressure, and composition range determined by the input thermodynamic database	Thermodynamic speciation (EQ3NR) and solubility code, with reaction path capabilities (EQ6)	Standard functions
GetEQData Version 1.0.1 [DIRS 173680]	10809-1.0.1-00	PC/ WIN2000	Requires EQ3/6 V.8.0 or V.7.2b output files	Excel macro used to extract data from EQ3/6 V.8.0 output files	Data extraction
FEHM Version 2.24 [DIRS 178965]	10086-2.24-00	PC/ WIN2000	Used to perform one-dimensional, unsaturated zone flow and particle tracking transport calculations.	Finite element heat and mass transfer (FEHM) code for thermal-hydrologic calculations	Standard functions
ppptrk Version 1.0 [DIRS 165753]	11030-1.0-00	PC/ WIN2000	For use with particle tracking simulations only	Post-processor used to produce breakthrough curves from output files from FEHM particle tracking simulations	Data extraction and graphing
EARTHVISION 5.0	10393-5.0-00	SGI/ IRIX 6.2	Used to produce three-dimensional images and for data extraction	A multiuse program for three-dimensional visualization of data and data extraction	Data extraction

Table 3.1-2. Exempt Software Used

Software	Platform / OS	Limitations/Range of Use	Brief Description	Functions Utilized
Microsoft Word	PC/ WIN2000 or XP	No limitations; a common word processing program	Word processing	Standard functions
Microsoft Excel	PC/ WIN2000 or XP	No limitations; a common spreadsheet program	Spreadsheet software used to tabulate, calculate, analyze and visually display results	Standard functions
Mathcad version 13	PC/ WIN2000 or XP	No limitations; a common mathematics program	A standard engineering calculation software capable of advanced mathematics and graphing functions	Standard functions
Mathcad version 14	PC/ WIN2000 or XP	No limitations; a common mathematics program	A standard engineering calculation software capable of advanced mathematics and graphing functions	Standard functions
IGPET2006	PC/ WIN2000 or XP	Used to compute normative analyses from bulk chemical data, requires oxide weight percent input	Applies the CIPW algorithm to whole rock analyses to compute a normative analysis	Algebraic functions standard to the program
JMP5.1	PC/ WIN2000 or XP	Used to conduct principal component analysis	A statistical analysis software package used to calculate principle component analysis	Standard statistical functions
Aq·QA V.1.0	PC/ WIN2000 or XP	Used to compute and render Piper diagrams	Calculates chemical ratios and plots results on quaternary and ternary diagrams	Standard algebraic functions

INTENTIONALLY LEFT BLANK

4. INPUTS

4.1 DIRECT INPUT

If not otherwise indicated, data and parameters used in this section are specifically selected for direct use in this model and these direct inputs are all presented in Table 4.1-1. None of the inputs used to develop the models in this report were used in the validation of those models.

Sections 4.1.1 through 4.1.21 contain further discussions of the direct inputs identified Table 4.1-1.

Table 4.1-1. Direct Inputs

DTN or Document	Data/Parameter Description	Location in DTN or Report
GS030408312272.002 [DIRS 165226]	Group 1 representative pore-water composition	File: S03203_001 (See sample name: SD-9/1184.7-1184.8/UC)
GS031008312272.008 [DIRS 166570]	Group 2 representative pore-water composition	Spreadsheet: *PW data package.xls* (See sample name: ESF-THERMALK-017/26.5-26.9/UC)
MO0005PORWATER.000 [DIRS 150930]	Group 3 representative pore-water composition	File: S00281_001 (See sample name: ESF-HD-PERM-3/34.8-35.1/Alcove 5)
GS060908312272.004 [DIRS 179065]	Group 4 representative pore-water composition	File: S06131_001 (See sample name: HD-PERM-3/56.7-57.1/UC)
GS020408312272.003 [DIRS 160899] GS020808312272.004 [DIRS 166569] GS031008312272.008 [DIRS 166570] GS041108312272.005 [DIRS 178057] GS060908312272.004 [DIRS 179065] MO0005PORWATER.000 [DIRS 150930] GS0703PA312272.001 [DIRS 182478]	Chloride and nitrate concentrations used to calculate the Cl:N for pore waters in Groups 1 to 4	See Table 4.1-4 for specific file and sample names
SN0609T0502404.012 [DIRS 179067]	Pitzer thermodynamic database used for modeling concentrated solutions in geochemical systems	File: *data0.ypf.R2* (Description of use of the database given in Section 6.2.6)
SN0612T0502404.014 [DIRS 178850]	Thermodynamic database for geochemical modeling of dilute systems used for atomic weight data, and updated thermodynamic data for Ni, Cr phases	File: *data0.ymp.R5* (Description of use of the database given in Section 6.2.6)
LB0208UZDSCPMI.002 [DIRS 161243]	Porosity data for repository host rock units	Spreadsheet: *drift-scale calibrated properties for mean infiltration2.xls*
BSC 2004 [DIRS 170003]	Matrix saturation and grain density	Table 6-8
LB0610UZDSCP30.001 [DIRS 179180]	Relative permeability data for TSw lithostratigraphic units	File: *Calibrated Parameter_R113_30%.doc*
MO0612MEANTHER.000 [DIRS 180552]	Mean dry and wet thermal conductivity values for the repository host unit Tptpll	Spreadsheet: *Repository_Unit_Mean_kthermal.xls*

Table 4.1-1. Direct Inputs (Continued)

DTN or Document	Data/Parameter Description	Location in DTN or Report
MO0702PAGLOBAL.000 [DIRS 179343]	10th and 90th percentile dry and wet thermal conductivity values for the repository host unit Tptpll	Spreadsheets: *Repository_Unit_10P_90P_wet Kthermal.xls* *Repository_Unit_10P_90P_dry Kthermal.xls*
SN0404T0503102.011 [DIRS 169129]	Matrix and lithophysal porosity, and bulk density of unit Tptpll	File: *ReadMe_Summary.doc*, Tables 7-10 and 7-11
SN0307T0510902.003 [DIRS 164196]	Specific rock grain heat capacity, unit Tptpll	Spreadsheet: *rock_grain_heat_capacity(edited).xls*, worksheet: "Cp grain 25-325," row 10, column y
MO0012MWDGFM02.002 [DIRS 153777]	Thickness of four major TSw units Distance from the base of PTn to the repository level	Geologic framework model; average values over entire repository footprint used
BSC 2004 [DIRS 170003]	Average mineral abundances in the mineralogic model, and composition of the smectite-illite group (10 to 20 wt % illite)	Table 6-2
LB0208ISODSTHP.001 [DIRS 161638]	Ambient repository pCO_2	Table S02230_001
GS000308313211.001 [DIRS 162015]	Average chemical composition of the phenocryst-poor rhyolite member of the TSw (units Tptpul, Tptpmn, Tptpll, Tptpln)	Data in entire DTN file S0224_001
LB0612PDPTNTSW.001 [DIRS 179150]	Percolation fluxes at the PTn/TSw boundary, for the present-day, monsoonal, glacial transition, and post-10,000-year climate states	Spreadsheets: *ptn_bot_flux_10%_pd.xls* *ptn_bot_flux_30%_pd.xls* *ptn_bot_flux_50%_pd.xls* *ptn_bot_flux_90%_pd.xls*
LB0701MOPTNTSW.001 [DIRS 179156]		Spreadsheets: *ptn_bot_flux_10%_mo.xls* *ptn_bot_flux_30%_mo.xls* *ptn_bot_flux_50%_mo.xls* *ptn_bot_flux_90%_mo.xls*
LB0701GTPTNTSW.001 [DIRS 179153]		Spreadsheets: *ptn_bot_flux_10%_gt.xls* *ptn_bot_flux_30%_gt.xls* *ptn_bot_flux_50%_gt.xls* *ptn_bot_flux_90%_gt.xls*
LB0702UZPTN10K.002 [DIRS 179332]		Spreadsheets: *ptn_bot_q_pd1_10k.xls* *ptn_bot_q_pd2_10k.xls* *ptn_bot_q_pd3_10k.xls* *ptn_bot_q_pd4_10k.xls*
GS031208312232.003 [DIRS 171287]	Borehole temperature data for borehole SD-12	File: *TEMPERATURE.txt*

Table 4.1-1. Direct Inputs (Continued)

DTN or Document	Data/Parameter Description	Location in DTN or Report
SNL 2007 [DIRS 179354]		Parameter numbers:
	Waste package decay heat generation curve	05-03
	Ground support Stainless Steel Type316L design specifications	02-03
	Invert materials and invert configuration	02-08, 02-10
	Repository design information, waste package end-point coordinates	02-01
LB990501233129.004 [DIRS 111475]	Geologic contacts used in FEHM simulations	File: *primary.mesh*, data corresponding to rock column "j34"
MO0701VENTCALC.000 [DIRS 179085]	Preclosure ventilation model	Spreadsheet: *Base Case Analysis Rev01.xls*, worksheet: "Ventilation Efficiency," case CSTR04
AISC 1991 [DIRS 127579]	135 lb/yd gantry rail specifications	p. 1-113
Sawyer et al. 1994 [DIRS 100075]	Age of the Topopah Spring Tuff, 12.8 Ma	Table 1 (See Section 4.1.12 for justification and/or qualification of this outside source)
LA0506BR831371.001 [DIRS 174331]	3.47×10^{-11} m^2 s^{-1} A representative effective diffusion coefficient for weakly sorbing chemical species	File: *fehm_amr_base.mptr*
Blum and Stillings 1995 [DIRS 126590]	Activation energy for feldspar dissolution	Table 2 (See Section 4.1.13 for justification and/or qualification of this outside source)
Lide 2000 [DIRS 162229]	Molar gas constant Arrhenius equation	p. 1-8 p. 5-106 (Considered to be Established Fact)
Haar et al. 1984 [DIRS 105175]	pSAT as a function of temperature	Table 1 (Considered to be Established Fact)
Incropera and DeWitt 2002 [DIRS 163337]	Density and specific heat capacity of water at 63°C	p. 924 (Considered to be Established Fact)
MO0701EQ36IDPS.000 [DIRS 179290]	Inputs for pH uncertainty analysis	See Table 6.12-3 for a list of files used.
LL000202905924.117 [DIRS 144913] LL991008004241.041 [DIRS 120487] LL991008104241.042 [DIRS 120489]	Inputs for pH uncertainty analysis	See Table 6.12-3 for a list of files used. (See Section 4.1.16 for justification and/or qualification of these sources)
SN0611T0509206.007 [DIRS 179335]	Estimated IDPS uncertainties	Spreadsheet: *Estimated IDPS uncertainties.xls*

Table 4.1-1. Direct Inputs (Continued)

DTN or Document	Data/Parameter Description	Location in DTN or Report
Southwell et al. 1976 [DIRS 100927], Bomberger et al. 1954 [DIRS 163699]	Conditions and Sources for Stainless Steel Type 316L Corrosion Rate Data	Tables 5 and 7 in Southwell et al. 1976 [DIRS 100927]; Table II in Bomberger et al. 1954 [DIRS 163699] (See Section 4.1.17 for justifications or qualifications of these outside sources)
Southwell and Bultman 1982 [DIRS 100928]		Tables 64.5 and 64.6 (Considered to be Established Fact)
SNL 2007 [DIRS 181648]	Mathematical model for evolution of the thermal field	Section 6.3.5.1.1
Weast and Astle 1981 [DIRS 100833]	Molecular Weight of O_2 and Fe	pp. B-126 and B-107 (Considered to be Established Fact)
DTN: LL980704605924.035 [DIRS 147298]	Conditions and sources for low-alloy or carbon steels corrosion rate data	File: S98217_016
Weast and Astle 1981 [DIRS 100833]	Volume fraction of O_2 in atmospheric air	p. F-172 (Considered to be Established Fact)
Incropera and DeWitt 1996 [108184]	O_2 in atmospheric air	Table inside back cover
Incropera and DeWitt 1996 [108184]	Density of steel	Table A.1 (plain carbon steel)
Incropera and DeWitt 1996 [108184]	Gas constant	Table inside back cover
Incropera and DeWitt 1996 [108184]	Binary diffusion coefficient of O_2 in air at 25°C	Table A.8
SN0612T0502404.014 [DIRS 178850] for molar volume data; formula weight of goethite from Weast and Astle 1981 [DIRS 100833]	Density of goethite (kg/m^3), calculated using molar volume and formula weight	Molar volume for goethite in the goethite data block in the *data0.ymp.R5* file in DTN: SN0612T0502404.014 [DIRS 178850]; atomic weights from Weast and Astle [DIRS 100833], pp. B-107 and B-126.
SNL 2007 [DIRS 177407]	Corrosion product porosity	Section 6.3.4.3.4
LB0704DSTHONLY.001 [DIRS 181164]	Thermal-hydrologic time-series boundary conditions at drift wall (81 and 162 m drift-spacing)	Spreadsheets: *th7_162.xls* and *th7_81.xls*
GS030108312242.001. [DIRS 163118]	Atmospheric pressure at repository elevation = 0.89 bar.	Files: S03226_001, *YMBarometricPressure.xls*
ASTM A 240/A 240M-02a 2002 [DIRS 162720]	Composition of Stainless Steel Type 316L steel sheets and rock bolts	Table 1
ASTM G 1-90 1999 [DIRS 103515]	Stainless Steel Type 316L density	Table X1.1
Incropera and DeWitt 1996 [DIRS 108184]	Low-Alloy Carbon Steel A588 density	Table A.1
ASTM A 588/A 588M – 05 [DIRS 176255]	Composition of Low-Alloy Carbon Steel A588	Table 1

4.1.1 Pore-Water Compositions

A review of Topopah Spring Tuff pore-water compositions was completed, and is documented in Section 6.6. In the review of over 90 pore-water analyses, many were determined to have been affected by microbial activity during core storage prior to collection of the water samples. A statistical analysis of the 34 samples determined to be minimally affected by microbial activity determined that they clustered into four groups; these samples are presented in Tables 4.1-2 and 4.1-3. A representative water composition was determined for each group, on the basis of proximity to the cluster centroid. These four representative waters (see Table 4.1-3) were used in the calculation of seepage and dilution/evaporation compositions. The representative pore waters for Groups 1 through 4 are identified in Table 4.1-3.

Table 4.1-2. Summary of Pore-Water Analyses That Are Direct Feeds to the P&CE Models

Pore-Water Designation	Source DTN
NRG-7/7A/839.3-839.8/UC	GS020408312272.003 [DIRS 160899]
SD-9/991.7-992.1/UC	
SD-9/669.1-669.2/UC	GS020808312272.004 [DIRS 166569]
SD-9/1184.8-1185.0/UC	
ESF-THERMALK-017/16.6-17.2/UC	GS031008312272.008 [DIRS 166570]
ESF-THERMALK-019/19.2-19.5/UC	
ESF-THERMALK-019/19.5-19.7/UC	
ESF-THERMALK-017/22.3-22.9/UC	
ESF-THERMALK-017/22.9-23.0/UC	
ESF-THERMALK-017/26.3-26.5/UC	
ESF-THERMALK-017/26.5-26.9/UC	
SD-9/1184.7-1184.8/UC	GS030408312272.002 [DIRS 165226]
SD-9/1060.1-1060.5/UC	GS041108312272.005 [DIRS 178057]
SD-9/1119.7-1119.9/UC	
SD-9/1234.9-1235.1/UC	
SD-9/1276.5-1276.8/UC	
SD-9/1276.8-1277.0/UC	
SD-9/1303.4-1303.9/UC	
SD-9/1185.0-1185.3/UC1	GS060908312272.004 [DIRS 179065]
HD-PERM-3/22.4-23.0/UC	
HD-PERM-3/56.7-57.1/UC	
ESF-HD-PERM-1	MO0005PORWATER.000 [DIRS 150930]
ESF-HD-PERM-2	
ESF-HD-PERM-3	

Table 4.1-2. Summary of Pore-Water Analyses That Are Direct Feeds to the P&CE Models (Continued)

Pore-Water Designation	Source DTN
ECRB-DS3-1616/10.1-10.4/UC	GS0703PA312272.001 [DIRS 182478]
ECRB-DS3-1616/10.6-11.0/UC	
ECRB-DS3-1616/12.5-12.7/UC	
ECRB-DS3-1616/12.7-13.3/UC	
ECRB-DS3-1616/7.5-7.7/UC	
ECRB-DS3-1616/7.7-7.9/UC	
ECRB-DS3-1616/7.9-8.0/UC	
ECRB-DS3-1616/8.0-8.1/UC	
ECRB-DS3-1616/9.6-9.8/UC	
ECRB-DS3-1616/9.8-10.1/UC	

Table 4.1-3. Chemical Compositions of the 34 Pore Waters and Group IDs with the Four Representative Waters Identified

Pore-Water ID	Group Number	pH	Na (mg/L)	K (mg/L)	Mg (mg/L)	Ca (mg/L)	Cl (mg/L)	SO_4 (mg/L)	HCO_3 (mg/L)	NO_3 (mg/L)	F (mg/L)	SiO_2 (mg/L)
NRG-7/7A/839.3-839.8/UC	1	7.9	67	6.9	1.6	19	31	24	151	25	2.8	41
SD-9/991.7-992.1/UC	1	7.9	61	5.4	0.60	27	26	13	—	20	3.30	55
SD-9/669.1-669.2/UC	4	—	61	6.3	6.9	66	76	75	136	29	1.20	49
SD-9/1184.8-1185.0/UC	1	7.9	62	5.4	<0.4	24	16	12	196	12	0.84	47
ESF-THERMALK-017/16.6-17.2/UC	2	—	51	14.2	9.8	73	82	105	104	45	1.3	63
ESF-THERMALK-019/19.2-19.5/UC	2	—	47	13.7	9.0	69	84	80	104	47	0.67	62
ESF-THERMALK-019/19.5-19.7/UC	2	—	44	13.2	9.1	71	82	82	124	50	0.60	59
ESF-THERMALK-017/22.3-22.9/UC	2	—	48	14.1	7.8	60	65	86	95	41	1.5	51
ESF-THERMALK-017/22.9-23.0/UC	2	7.9	37	14.5	9.9	72	69	94	116	46	1.1	55
ESF-THERMALK-017/26.3-26.5/UC	2	—	42	13.6	7.6	58	58	76	150	43	1.4	58
ESF-THERMALK-017/26.5-26.9/UC	2*	7.7	45	14.4	7.9	62	67	82	126	44	1.4	52
SD-9/1184.7-1184.8/UC	1*	8.2	59	4.8	0.70	19	23	16	142	16	2.20	42
SD-9/1060.1-1060.5/UC	1	7.6	68	8.8	<0.5	21	32	15	140	21	1.50	50
SD-9/1119.7-1119.9/UC	1	7.7	81	12.8	<0.6	34	32	24	193	19	1.20	45
SD-9/1234.9-1235.1/UC	1	7.9	67	8.0	0.50	18	17	16	156	11	1.10	42
SD-9/1276.5-1276.8/UC	1	7.9	67	6.4	0.60	23	29	17	136	10	1.90	59
SD-9/1276.8-1277.0/UC	1	7.6	69	6.9	0.60	23	35	17	165	10	2.00	67
SD-9/1303.4-1303.9/UC	1	—	95	11.3	2.30	37	65	28	194	19	4.80	54
SD-9/1185.0-1185.3/UC1	1	—	70	8.6	0.27	18.4	42.4	12	145	18.2	2.4	—
HD-PERM-3/22.4-23.0/UC	4	—	103	14.6	17.4	48.7	131	123	120	27.9	1.6	—
HD-PERM-3/56.7-57.1/UC	4*	—	123	13.8	16.7	59.9	146	126	149	57.4	1.3	—
ESF-HD-PERM-1	3	7.79	61	6	25.7	98	123	124	—	22	0.36	79

Table 4.1-3. Chemical Compositions of the 34 Pore Waters and Group IDs with the Four Representative Waters Identified (Continued)

Pore-Water ID	Group Number	pH	Na (mg/L)	K (mg/L)	Mg (mg/L)	Ca (mg/L)	Cl (mg/L)	SO_4 (mg/L)	HCO_3 (mg/L)	NO_3 (mg/L)	F (mg/L)	SiO_2 (mg/L)
ESF-HD-PERM-2/30.1-30.5/Alcove 5	3	8.32	61	7	16.6	106	110	111	—	3	0.96	66
ESF-HD-PERM-3/34.8-35.1/Alcove 5	3*	8.31	62	9	17.4	97	123	120	—	10	0.76	75
ECRB-DS3-1616/10.1-10.4/UC	1	—	39.8	6.03	0.91	20.1	7.2	9.48	128	14.5	1.51	39
ECRB-DS3-1616/10.6-11.0/UC	1	—	61	7.68	1.44	34.1	20.4	22.3	142	33.2	2.32	46
ECRB-DS3-1616/12.5-12.7/UC	1	—	32.5	4.21	0.91	23.5	8.99	13.2	123	18.9	1.15	38
ECRB-DS3-1616/12.7-13.3/UC	1	—	51.4	6.81	1.05	28.8	15	17.8	166	27	1.86	44
ECRB-DS3-1616/7.5-7.7/UC	1	—	52.9	5.9	0.81	28.7	15.7	25.3	107	34.3	1.66	55
ECRB-DS3-1616/7.7-7.9/UC	1	—	50.9	7.27	0.72	25.4	15.3	19.5	107	29.8	1.46	51
ECRB-DS3-1616/7.9-8.0/UC	1	—	36.5	4.1	0.35	16.7	7.79	10.5	82	17.4	1.16	52
ECRB-DS3-1616/8.0-8.1/UC	1	—	46.9	5.63	0.59	23.4	11.5	15.4	115	23.8	1.59	58
ECRB-DS3-1616/9.6-9.8/UC	1	—	36.8	6.06	0.73	16.5	6.89	5.29	113	8.07	1.38	42
ECRB-DS3-1616/9.8-10.1/UC	1	—	38	5.77	0.76	20.7	4.98	8.84	149	10.4	1.35	46

* Representative waters for each group.

NOTE: See Table 4.1-2 for DTN sources. A dash ("—") indicates no measurement.

4.1.2 $Cl:NO_3$ Ratios for Pore Waters in Groups 1 to 4

There are 34 TSw waters determined to be unaffected by microbial activity that provide feeds to the P&CE abstraction models. This is required to adequately represent the uncertainty associated with the distribution of $Cl:NO_3$ ratios among all the available waters. The $Cl:NO_3$ ratios are calculated from the chlorine and nitrate concentrations from the selected waters. These waters and their DTN sources are identified in Table 4.1-4 with a more detailed description in Section 6.6.

Table 4.1-4. Sources and Cl and N concentrations for the 34 Other Pore-Water Compositions Used in the P&CE Models

Pore-Water Designation	[Cl], [NO_3] (mg/L)	Source
NRG-7/7A/839.3-839.8/UC	31, 25	GS020408312272.003 [DIRS 160899]
SD-9/991.7-992.1/UC	26, 20	
SD-9/669.1-669.2/UC	76, 29	GS020808312272.004 [DIRS 166569]
SD-9/1184.8-1185.0/UC	16, 12	
ESF-THERMALK-017/16.6-17.2/UC	82, 45	GS031008312272.008 [DIRS 166570]
ESF-THERMALK-017/22.3-22.9/UC	65, 41	
ESF-THERMALK-017/22.9-23.0/UC	69, 46	
ESF-THERMALK-017/26.3-26.5/UC	58, 43	
ESF-THERMALK-019/19.2-19.5/UC	84, 47	
ESF-THERMALK-019/19.5-19.7/UC	82, 50	
ESF-THERMALK-017/26.5-26.9/UC	67, 44	
SD-9/1060.1-1060.5/UC	32, 21	GS041108312272.005 [DIRS 178057]
SD-9/1119.7-1119.9/UC	32, 19	
SD-9/1234.9-1235.1/UC	17, 11	
SD-9/1276.5-1276.8/UC	29, 10	
SD-9/1276.8-1277.0/UC	35, 10	
SD-9/1303.4-1303.9/UC	65, 19	
SD-9/1184.7-1184.8/UC	23, 16	GS030408312272.002 [DIRS 165226]
SD-9/1185.0-1185.3/UC1	42.4, 18.2	GS060908312272.004 [DIRS 179065]
HD-PERM-3/22.4-23.0/UC	131, 27.9	
HD-PERM-3/56.7-57.1/UC	146, 57.4	
ESF-HD-PERM-1	123, 22	MO0005PORWATER.000 [DIRS 150930]
ESF-HD-PERM-2	110, 3	
ESF-HD-PERM-3	123, 10	

Table 4.1-4. Sources and Cl and N concentrations for the 34 Other Pore-Water Compositions Used in the P&CE Models (Continued)

Pore-Water Designation	[Cl], [NO_3] (mg/L)	Source
ECRB-DS3-1616/10.1-10.4/UC	7.2, 14.5	GS0703PA312272.001 [DIRS 182478]
ECRB-DS3-1616/10.6-11.0/UC	20.4, 33.2	
ECRB-DS3-1616/12.5-12.7/UC	8.99, 18.9	
ECRB-DS3-1616/12.7-13.3/UC	15, 27	
ECRB-DS3-1616/7.5-7.7/UC	15.7, 34.3	
ECRB-DS3-1616/7.7-7.9/UC	15.3, 29.8	
ECRB-DS3-1616/7.9-8.0/UC	7.79, 17.4	
ECRB-DS3-1616/8.0-8.1/UC	11.5, 23.8	
ECRB-DS3-1616/9.6-9.8/UC	6.89, 8.07	
ECRB-DS3-1616/9.8-10.1/UC	4.98, 10.4	

4.1.3 Thermodynamic Databases

Two datasets have been developed by the Yucca Mountain Project (YMP) for geochemical modeling calculations using EQ3/6 (see Table 3.1-1). These two qualified YMP databases, the *data0.ypf.R2* database (DTN: SN0609T0502404.012 [DIRS 179067]) and the *data0.ymp.R5* database (DTN: SN0612T0502404.014 [DIRS 178850]), provide data for the P&CE models.

4.1.4 Hydrologic and Thermal Properties of the Repository Units

4.1.4.1 Matrix and Fracture Porosities for Repository Units

The estimated matrix and fracture porosities for the four repository host units are given in Table 4.1-5. These values are from DTN: LB0208UZDSCPMI.002 [DIRS 161243] (spreadsheet: *drift-scale calibrated properties for mean infiltration2.xls*).

Table 4.1-5. Matrix and Fracture Porosities for the Four Repository Host Units

Mineralogic Model Units	Material Name	Porosity	Sum
Tptpul	tswM3	0.155	0.1608
	tswF3	0.0058	
Tptpmn	tswM4	0.111	0.1195
	tswF4	0.0085	
Tptpll	tswM5	0.131	0.1406
	tswF5	0.0096	
Tptpln	tswM6	0.103	0.1160
	tswF6	0.013	

Source: DTN: LB0208UZDSCPMI.002 [DIRS 161243], spreadsheet: *drift-scale calibrated properties for mean infiltration2.xls*.

4.1.4.2 Matrix Saturation and Grain Density for Repository Units

Values for matrix saturation and grain density for the four repository units are given in Table 4.1-6. These values are taken from *Heat Capacity Analysis Report* (BSC 2004 [DIRS 170003], Table 6-8) and represent averages of hundreds of measured values. The original data are tabulated in DTNs: MO0109HYMXPROP.001 [DIRS 155989], GS980808312242.014 [DIRS 106748], and GS980708312242.010 [DIRS 106752].

Table 4.1-6. Matrix Saturation and Grain Density Values (%) for the Four Repository Host Units

Mineralogic Model Units	Matrix Saturation		Grain Density (g/cm^3)	
	Average	Std Dev.	Average	Std Dev.
Tptpul	0.744	0.142	2.5	0.03
Tptpmn	0.856	0.113	2.52	0.03
Tptpll	0.794	0.126	2.54	0.03
Tptpln	0.866	0.089	2.54	0.04

Source: BSC 2004 [DIRS 170003], Table 6-8.

4.1.4.3 Inputs for Modeling the Evolution of the Thermal Field

The mathematical method used to calculate the evolution of the thermal field through time is developed in *In-Drift Natural Convection and Condensation* (SNL 2007 [DIRS 181648], Section 6.3.5.1.1), and is justified and validated within that document.

For preclosure times, the analytical ventilation model used is archived in DTN: MO0701VENTCALC.000 [DIRS 179085] (spreadsheet: *Base Case Analysis Rev01.xls*, worksheet: "Ventilation Efficiency," case CSTR04).

Rock hydrologic and thermal properties are used for modeling the evolution of the thermal field. Properties for the Tptpll unit are used, including matrix and lithophysal porosity and bulk density taken from the qualified project DTN: SN0404T0503102.011 [DIRS 169129] (file: *ReadMe_Summary.doc*, Tables 7-10 and 7-11). The specific heat capacity is taken from DTN: SN0307T0510902.003 [DIRS 164196] (file: *rock_grain_heat_capacity (edited).xls*, worksheet: "Cp grain 25-325," row 10, column y). Mean, 10th percentile, and 90th percentile thermal conductivity values for the Tptpll unit are from DTNs: MO0612MEANTHER.000 [DIRS 180552] (mean values) and MO0702PAGLOBAL.000 [DIRS 179343] (10th and 90th percentile values). These values are shown in Table 4.1-7.

The rock heat capacity is modified for saturation by using the volume heat capacity of water, which is calculated for saturated water at elevated temperature at 63°C (as the nominal temperature between 25°C and 100°C) by multiplying the density of water (kg m^{-3}) by the specific heat of water (J kg^{-1} K^{-1}), where:

- Density of water = 982.3 kg m^{-3}
- Specific heat capacity = 4,186 J kg^{-1} K^{-1}.

These values are from Incropera and DeWitt (2002 [DIRS 163337], p. 924). Note that the density of water was calculated from the specific volume provided by this source. The widely used textbook from these authors is considered Established Fact; no further justification for use is required.

Table 4.1-7. Tptpll Thermal and Hydrologic Properties Used in Modeling the Evolution of the Thermal Envelope

Thermal Conductivity Range	Thermal Conductivity, Bulk Dry[a,b]	Thermal Conductivity, Bulk Wet[a,b]	Matrix Porosity[c]	Lithophysal Porosity[c]	Bulk Density[c]	Rock Grain Specific Heat Capacity[d]
Percentile	W/m°C	W/m°C	m^3 void/ m^3 rock	m^3 void/ m^3 rock	kg/m^3	J/g K
10th	1.071	1.69	0.15	0.09	1,980	0.93
Global mean	1.24	1.87				
90th	1.414	2.055				

[a] DTN: MO0612MEANTHER.000 [DIRS 180552] (mean values).
[b] DTN: MO0702PAGLOBAL.000 [DIRS 179343] (10th and 90th percentile values).
[c] DTN: SN0404T0503102.011 [DIRS 169129], file: *ReadMe_Summary.doc*, Tables 7-10 and 7-11. Porosity values rounded to two decimal places.
[d] DTN: SN0307T0510902.003 [DIRS 164196], spreadsheet: *rock_grain_heat_capacity (edited).xls*, worksheet: "Cp grain 25-325," row 10, column y.

4.1.5 Stratigraphy and Thickness of Geologic Units Used in Calculating the WRIP Value

Stratigraphic information is used in two ways in the WRIP calculations. The near-field model treats the TSw as a single unit, with hydrologic properties that are weighted averages of those for the four repository host units, the Tptpul, Tptpmn, Tptpll, and Tptpln. The weighting is done on the basis of unit thickness. Average unit thicknesses for the four lithostratigraphic units over the repository footprint were extracted from the geologic framework model (DTN: MO0012MWDGFM02.002 [DIRS 153777]), using EARTHVISION v5.1. The values used are given in Table 4.1-8 below.

Table 4.1-8. Average Thicknesses of the Four TSw Repository Host Units over the Repository Footprint

Mineralogic Model Units	Thickness (ft)
Tptpul	229.46
Tptpmn	113.41
Tptpll	338.61
Tptpln	133.41

Source: DTN: MO0012MWDGFM02.002 [DIRS 153777].

4.1.6 Mineral Abundances in the Repository Units

The abundances of feldspar and alteration minerals in the repository units are used to calculate the feldspar dissolution rate at ambient conditions (Section 6.3.4.2). Feldspar and alteration mineral abundances for the four TSw repository host units are given in Table 4.1-9. These values are taken from *Heat Capacity Analysis Report* (BSC 2004 [DIRS 170003], Table 6-2). They represent averaged values and standard deviations for mineral abundances for each unit, extracted from *Mineralogic Model (MM3.0) Report* (BSC 2004 [DIRS 170031]), which provide

a three-dimensional map of mineral abundances throughout Yucca Mountain. The mineralogic model itself is based on mineral abundances determined by X-ray diffraction analysis of borehole core samples (DTN: LA9908JC831321.001 [DIRS 113495]).

Table 4.1-9. Mineral Abundances in the Four Repository Host Units, in wt %

Stratigraphic Unit	Mineralogic Model Layer*	Smectite-Illite		Sorptive Zeolite		Feldspar	
		Average	Std Dev.	Average	Std Dev.	Average	Std Dev.
Tptpul	17	2.5	1.37	0.06	0.14	61.38	7.87
Tptpmn	16	2.03	0.62	0.01	0.02	62.35	3.61
Tptpll	15	2.48	2.13	0.23	0.28	59.36	6.76
Tptpln	14	1.13	1.07	0.59	0.6	61.87	4.09

Source: BSC 2004 [DIRS 170003], Table 6-2.

* BSC 2004 [DIRS 170031], Figure 6-4.

Other mineral phases present in these units are not quantitatively used in the NFC model, but provide the basis for some model implementation choices. These are the silica polymorphs, which comprise most of the remainder of each unit (approximately 35 wt%; BSC 2004 [DIRS 170003], Table 6-2), and consist of quartz and cristobalite-opal CT, with lesser amounts of tridymite. Also, trace amounts (less than 0.5 % total; BSC 2004 [DIRS 170003], Table 6-2) of calcite are present.

It is important to note that these units, as represented in the mineralogical model (DTN: LA9908JC831321.001 [DIRS 113495]) and summarized in *Heat Capacity Analysis Report* (BSC 2004 [DIRS 170003], Table 6-2), do not contain any vitric component. The upper vitrophyre in the Topopah Spring Tuff is not included in the Tptpul; neither is the devitrified latitic top of the tuff, between the vitrophyre and the rhyolitic body of the unit. In addition, the basal vitrophyre is not included in the Tptpln unit. The entire center of the TSw, between these two vitric zones, is completely devitrified (Vaniman et al. 1996 [DIRS 105946], v. 1, Section 3, p. 2; BSC 2004 [DIRS 170003], Table 6-2). Hence, glass is not a component in these units, and is not incorporated in the NFC model, which only models water–rock interactions in the rhyolitic part of the TSw. In addition, the Tptpln as defined in the mineralogic model does not include the heavily zeolitized zone, which occurs above the basal vitrophyre of the Topopah Spring Tuff at many locations (BSC 2004 [DIRS 170031], Section 6.1). This is appropriate for the NFC model, because the intent of the model is to evaluate water–rock reactions only in the TSw overlying or containing the repository.

4.1.7 Ambient Conditions at the Repository Level

Ambient pCO_2 at the repository level: The partial pressure at the repository level is taken to be 10^{-3} bar. This is based on CO_2 concentrations near 1,000 ppmv measured in repository units in the Exploratory Studies Facility (ESF) (DTN: LB0208ISODSTHP.001 [DIRS 161638]) and is corroborated by data from borehole UZ-1 (Yang et al. 1996 [DIRS 100194], p. 43). This value is also consistent with that used in all other repository chemistry models.

Ambient temperature at the repository level: The ambient temperature at the repository level is taken to be 23.4°C, based on analysis of borehole temperature data in DTN: GS031208312232.003 [DIRS 171287]. This analysis is discussed in Section 6.3.2.4.

4.1.8 Selected Composition of Alkali Feldspar

The choice of composition for the alkali feldspar phase used by the NFC model (and subsequently by the P&CE abstraction models) is based on the average normative composition for the four TSw repository host units, as calculated from compositional data in DTN: GS000308313211.001 [DIRS 162015], using the same method used by Peterman and Cloke (2002 [DIRS 162576], Table 5 in the erratum). The average normative composition contains close to equal amounts of albite and orthoclase and small quantities of anorthite and is discussed in Sections 6.3.2.2 and 6.3.2.4.2.

4.1.9 Percolation Fluxes

The percolation flux values used in the NFC model are taken from the following DTNs: LB0612PDPTNTSW.001 [DIRS 179150] (present day), LB0701MOPTNTSW.001 [DIRS 179156] (monsoonal), LB0701GTPTNTSW.001 [DIRS 179153] (glacial transition), and LB0702UZPTN10K.002 [DIRS 179332] (post-10,000-years). The data are summarized in Table 6.3-1.

4.1.10 Waste Package Decay Heat Curve and Repository Design Information

The waste package decay curve heat generation curves are taken from *Total System Performance Assessment Data Input Package for Requirements Analysis for EBS In-Drift Configuration* (SNL 2007 [DIRS 179354], parameter 05-03).

The end-point coordinates for waste packages within the drifts were used in modeling the thermal envelope around the drift. Waste package end-point locations are taken from *Total System Performance Assessment Data Input Package for Requirements Analysis for Subsurface Facilities* (SNL 2007 [DIRS 179354], parameter 02-01).

4.1.11 Stratigraphy and Hydrologic Properties Used in the FEHM Modeling

For the FEHM modeling, the geologic section at a specific location was used to model flow from the PTn/TSw boundary to the repository level, rather than the averaged values given in Table 4.1-7. Specific depths for stratigraphic contacts were taken from the model calibration grid for the three-dimensional (3-D) unsaturated zone (UZ) flow model, in qualified project DTN: LB990501233129.004 [DIRS 111475] (file: *primary.mesh*, rock column "j34"; note that the repository is in the Tptpll unit at this location). Relative permeability data (e.g., van Genuchten parameters) for the rock units intersected by the model were taken from qualified project DTN: LB0610UZDSCP30.001 [DIRS 179180]; matrix and fracture porosities for the units are from the source given in Section 4.1.4.2 and presented in Table 4.1-6.

4.1.12 Age of the Topopah Spring Tuff

The age of the Topopah Spring Tuff is used in calculating the ambient alkali feldspar dissolution rate (Section 6.3.2.4.2). The value used is 12.8 Ma, as given by Sawyer et al. (1994 [DIRS 100075], Table 1).

Sawyer et al. 1994 [DIRS 100075], Table 1—*Description of Data:* Age of the Topopah Spring Tuff. *Qualification Status*: This value is qualified here per the requirements of SCI-PRO-006, *Models*, and SCI-PRO-001, *Qualification of Unqualified Data*, and is considered qualified for the intended use in this document (Appendix B). The data is qualified in this report using Method 2 ("Corroborating Data") in accordance with Attachment 3 of SCI-PRO-001. *Rationale for selecting methodology*: Corroborating data are available for comparison with the unqualified data set and any inferences drawn to corroborate the unqualified data can be clearly identified, justified and documented. Table 1 of the article from Byers et al. (1989 [DIRS 102177]) reports an age for the Topopah Spring Member of the Paintbrush Tuff Formation as 13 Ma. This value corresponds to a K-Ar age date, and, as stated in the source table footer, these values are good to the nearest 0.5 Ma. The value of 12.8 Ma from Sawyer et al. (1994 [DIRS 100075]) falls within the uncertainty of the Byers et al. (1989 [DIRS 102177]) value and is therefore corroborated. These values are directly comparable because they both correspond to empirical measurements of the age of the Topopah Springs Member. The accuracy, precision, and representativeness of the corroborating data are documented in the article from Byers et al. (1989 [DIRS 102177]).

Within the scope of this criterion, added confidence in the data is given by their Qualification Process Attributes as discussed below and outlined in Attachment 4 of SCI-PRO-001 and include: the extent to which the data demonstrate the properties of interest; prior peer and other professional reviews of the data; and the extent and quality of corroborating data.

Extent to Which the Data Demonstrate the Properties of Interest: The reference from Sawyer et al. (1994 [DIRS 100075]) provides $^{40}Ar/^{39}Ar$ ages for volcanic units, including the Topopah Spring Tuff, occurring in the Nevada Test Site. The age of the Topopah Spring Tuff is used directly in the calculation of the ambient feldspar dissolution rate in Section 6.3.2.4.5. This datum is relevant to Yucca Mountain because the Topopah Spring Tuff is the repository host unit. *Prior peer and other professional reviews of the data:* These data were published in an article in the *Geological Society of America Bulletin*, the flagship publication for that organization and a peer-reviewed journal. Technical issues are raised during the review process and either resolved prior to publication or the article is rejected. The source article as published is thus vetted to the extent that the reader can have confidence that the data may be considered worthy of use in other research. The authors of the article are U.S. Geological Survey (USGS) personnel widely experienced in mapping and characterization of silicic volcanic rocks. *Extent and quality of corroborating data*: The article from Byers et al. (1989 [DIRS 102177]) was published in the *Journal of Geophysical Research*, a well respected journal with a long publication history. As such, the article was subject to peer review prior to publication. The work was conducted under the supervision of the authors who are associated with Los Alamos National Laboratory and the USGS.

4.1.13 Activation Energy for Feldspar Dissolution

The activation energy for feldspar dissolution is used to determine the temperature-dependence of the process. Experimental data for activation energies for Na- and K-feldspar dissolution vary widely, from approximately 30 kJ/mol to 90 kJ/mol from acidic to alkaline pH (Blum and Stillings 1995 [DIRS 126590], Table 2). The value used by the NFC model is calculated from the data provided by Blum and Stillings (1995 [DIRS 126590], Table 2), by adding the average value for albite at neutral pH to that for K-feldspar at neutral pH, and dividing by 2. The small contribution by anorthite is ignored because no reliable, relevant experimental data were found in the literature. The calculated average value for the activation energy used in this report is 49 kJ/mol. The values used in this calculation are presented in Table 4.1-10.

Blum and Stillings 1995 [DIRS 126590], Table 2—*Description of Data:* Activation energy for feldspar dissolution (Table 4.1-10). *Qualification Status:* These data are qualified using Method 2 ("Corroborating Data") in accordance with Attachment 3 of SCI-PRO-001 (see Appendix B). *Rationale for selecting methodology*: Corroborating data are available for comparison with the unqualified data set and any inferences drawn to corroborate the unqualified data can be clearly identified, justified and documented. Brady (1991 [DIRS 182475], p 18103) reports a range of activation energies for framework silicates, from 10 to 20 kcal/mol. This is equivalent to a range from approximately 42 to 84 kJ/mol. In addition, White et al. (1999 [DIRS 182474], abstract) report an activation energy for Si dissolution from a granitoid of 51 kJ/mol. The activation energy value for a mixed feldspar from Blum and Stillings (1995 [DIRS 126590], Table 2) is 49 kJ/mol, which is the value used in this report. This value is corroborated by the two articles cited above. The inference is that, because feldspar is a framework silicate and comprises the bulk of the granitoid mineralogy, the use of the values reported by Brady (1991 [DIRS 182475], p. 18103) and White et al. (1999 [DIRS 182474], abstract) as corroboration is valid. The accuracy, precision, and representativeness of the corroborating data are documented in the respective articles.

Qualification Process Attributes are documented below in accordance with Attachment 4 of SCI-PRO-001 and include: the extent to which the data demonstrate the properties of interest; prior peer or other professional reviews of the data and their results; and the extent and quality of corroborating data.

Extent to Which the Data Demonstrate the Properties of Interest: The Blum and Stillings (1995 [DIRS 126590]) reference provides activation energies for feldspar dissolution. These data are used directly (see Section 6.3.2.4.2) in the calculation of the rate of feldspar dissolution as a function of temperature. The authors present a summary of data for feldspar dissolution as a function of temperature and pH from multiple sources. The results of this compilation are data relevant to dissolution of feldspars at Yucca Mountain.

Prior Peer Review: These data were published in *Reviews in Mineralogy*, which is a respected monograph series published by the Mineralogical Society of America with a long record of publication. *Reviews in Mineralogy* chapters are typically authored by the most esteemed mineralogists in the topic area and are peer-reviewed, i.e., reviewed by other experts in the pertinent technical field(s), individuals with experience in the subject matter who typically use such information in the course of their work. Technical issues are raised during the review

process and either resolved prior to publication or the chapter is rejected. The source chapter as published is thus vetted to the extent that the reader can have confidence that the data may be considered worthy of use in other research.

Extent and Quality of Corroborating Data: Both articles used as corroboration were published in well respected journals. The White et al. (1999 [DIRS 182474]) article was published in *Geochimica et Cosmochimica Acta*, considered in professional circles as the preeminent geochemical journal with a long history of publication. The Brady (1991 [DIRS 182475]) article was published by the *Journal of Geophysical Research*, a well respected Earth science journal. Both articles were subject to peer review prior to publication.

Table 4.1-10. Reported Activation Energies for Feldspar Dissolution

Mineral	Ea, kJ/mol
Albite	54.4
	50.7
	68.8
	67.7
K-feldspar	38.0
	36.0

NOTE: Data taken from Blum and Stillings 1995 [DIRS 126590], Table 2, corresponding to values reported for neutral pH.

4.1.14 Value of Molar Gas Constant and Arrhenius Equation

The molar gas constant, R, is used in calculating the temperature dependence of the alkali feldspar dissolution rate, as described in Section 6.3.4.2. The value used in the work described here is $R = 8.314472$ J mol^{-1} K^{-1}. This value was obtained from *CRC Handbook of Chemistry and Physics* (Lide 2000 [DIRS 162229], p. 1-8). This handbook is considered Established Fact; no further justification for use is required.

The Arrhenius equation is also used in calculating the temperature dependence of the alkali feldspar dissolution rate (Section 6.3.4.2, Equation 6.3-10). This equation is also taken from *CRC Handbook of Chemistry and Physics* (Lide 2000 [DIRS 162229], p. 5-106), which is considered Established Fact and requires no further justification for use in this report.

4.1.15 Saturation Pressures at Temperatures from 23°C to 96°C

Saturation pressures at temperatures from 23°C to 96°C are used in calculating the in-drift pCO_2 range (Section 2.1). The values were taken from *NBS/NRC Steam Tables: Thermodynamic and Transport Properties and Computer Programs for Vapor and Liquid States of Water in SI Units* (Haar et al. 1984 [DIRS 105175], Table 1). This National Bureau of Standards (NBS) publication is considered Established Fact; no further justification for use is required.

4.1.16 Uncertainty Inputs

4.1.16.1 Estimated IDPS Uncertainty

IDPS uncertainty factors for the Cl, N, Cl:N, and *I* of in-drift water are used directly by the P&CE abstraction models and are given in Table 4.1-10. The uncertainty associated with the sum Cl+N is calculated assuming linear combinations of the uncertainties on Cl and N provided by the IDPS model (SNL 2007 [DIRS 177411]) (see Table 4.1-10). These uncertainties apply between 20°C and 140°C and are defined as triangular distributions with the most likely uncertainty equal to ±0.0 with the maximum and minimum uncertainties defined in Table 4.1-11.

The uncertainty in pH adopted by the P&CE abstraction models is treated differently than in the IDPS over a portion of the relevant RH range (from 100% to 75%; see Table 4.1-12). Details concerning the re-evaluation of pH uncertainty are provided in Section 6.12.3.1.

Table 4.1-11. IDPS Uncertainty Factors for the Cl, N, Cl+N, Cl:N, and *I* of In-Drift Water

Parameter	Units	RH Range 100% to 85%	RH Range 85% to 65%	RH Range 65% to 40%	RH Range 40% to 20%	RH Range 20%to 0%
Cl	log molal	±0.0	±0.1	±0.4	±0.5	±0.7
N	log molal	±0.0	±0.2	±0.4	±0.5	±0.9
Cl:N	log mole ratio	±0.0	±0.2	±0.5	±0.5	±1.4
Cl+N*	log molal	±0.0	±0.22	±0.57	N/A	N/A
Ionic Strength, *I*	log molal	±0.1	N/A	N/A	N/A	N/A

Source: DTN: SN0611T0509206.007 [DIRS 179335], spreadsheet: *Estimated IDPS Uncertainties.xls*.
* Uncertainties calculated for Cl+N in this table assume linear combinations of independent variables.
NOTE: N/A = not applicable.

Table 4.1-12. IDPS and NFC Uncertainty Factors for pH of In-Drift Water

Parameter	Units	RH Range 100% to 75%	RH Range 75% to 65%*	RH Range 65% to 40%*	RH Range 40% to 20%*	RH Range 20% to 0%*
pH	pH units	Discrete CDF	±1	±2	±2	±2

* DTN: SN0611T0509206.007 [DIRS 179335], spreadsheet: *Estimated IDPS Uncertainties.xls*.
NOTE: CDF = cumulative distribution function. The discrete CDF is output of this report and is included in this table for reference. The CDF is archived in Output DTN: SN0703PAEBSPCE.007, spreadsheet: *Re-evaluation of pH uncertainty.xls*, tab: "CDF of pH uncertainty."

4.1.16.2 Inputs for Evaluation of pH Uncertainty

Qualified inputs for the analysis of pH uncertainty presented in Section 6.12.3.1 are taken from the IDPS model report (SNL 2007 [DIRS 177411]) model validation test cases archived in DTN: MO0701EQ36IDPS.000 [DIRS 179290]. See Table 4.1-13 for a list of the files used and their locations within the DTN. Data qualified for intended use are derived from DTNs: LL000202905924.117 [DIRS 144913], LL991008004241.041 [DIRS 120487], and LL991008104241.042 [DIRS 120489], and are also listed in Table 4.1-13.

To evaluate the uncertainty in total carbon concentration, denoted throughout as $[C]_{total}$, the validation cases for the IDPS model were examined, and all cases for which measured data for

$[C]_{total}$ or alkalinity in solution were available were summarized. In all, data from 11 different studies were examined, and 10 were used (138 data points). These validation studies are summarized in Table 4.1-13, and a short description is provided below. Measured and calculated $[C]_{total}$ values were extracted from the IDPS validation simulations archived in DTNs: MO0701EQ36IDPS.000 [DIRS 179290] and the other three DTNs listed in Table 4.1-13. For a more complete description of these validation simulations, see the IDPS model report (SNL 2007 [DIRS 177411], Section 7).

Table 4.1-13. List of IDPS Validation Studies Used to Evaluate Uncertainty in $[C]_{total}$

IDPS Validation Study	Number of Samples	Location (folder*file*)
Qualified for intended use in this report		
Evaporation of J13 Water DTN: LL991008104241.042 [DIRS 120489]	3	J13\j*13n1pitpH.xls* (Qualified for intended use in this report)
Evaporation of 100x Conc. J13 Water DTN: LL000202905924.117 [DIRS 144913]	2	100XJ13\j*13b1 v3.xls* (Qualified for intended use in this report)
Evaporation of Topopah Spring Tuff water at 75°C DTN: LL991008004241.041 [DIRS 120487]	1	Topopah*tspw3pitpH.xls* (Qualified for intended use in this report)
IDPS DTN: MO0701EQ36IDPS.000 [DIRS 179290]		
Evaporation of Topopah Spring Tuff water at 95°C (SNL 2007 [DIRS 177411], Section 7.2.4)	16 (15 used)*	Topopah95*FEC[9/12/13/14]bsumPitpH r1.xls*
$CaCO_3$ solubility in Na-K-Ca-Mg-Cl-SO_4 solutions (SNL 2007 [DIRS 177411], Section 7.1.3.3.2)	15 (10 used)*	Ca-CO3-CO2\He&Morse*Calcite He and Morse r2.xls*
$CaCO_3$ solubility in KCl (SNL 2007 [DIRS 177411], Section 7.1.3.3.1)	18	Ca-CO3-CO2\Wolf*Calcite Wolf et al KCl r1.xls*
$CaCO_3$, $CaSO_4$ solubility in KCl (SNL 2007 [DIRS 177411], Section 7.1.3.3.1)	15	Ca-CO3-CO2\Wolf*Calcite Wolf et al KCl gyp r1.xls*
$CaCO_3$, $CaSO_4$ solubility in NaCl (SNL 2007 [DIRS 177411], Section 7.1.3.3.1)	18	Ca-CO3-CO2\Wolf*Calcite Wolf et al NaCl gyp r1.xls*
$CaCO_3$ solubility in $CaCl_2$ (SNL 2007 [DIRS 177411], Section 7.1.3.3.1)	31	Ca-CO3-CO2\Wolf*Calcite Wolf et al CaCl2 r1.xls*
$CaCO_3$ solubility in water (SNL 2007 [DIRS 177411], Section 7.1.3.2)	24	Ca-CO3-CO2\Linke*caco3-ev.xls*
CO_2 solubility in water at varying T, pCO_2 (SNL 2007 [DIRS 177411], Section 7.1.3.1)	42 (0 used)*	Ca-CO3-CO2\CO2*co2.xls*

* Some data were evaluated but not used in the final analysis. See text for discussion.

4.1.16.3 Inputs for Evaluation of pH Uncertainty Qualified for Intended Use in This Report

Three sources of direct input for the evaluation of pH uncertainty are qualified here per the requirements of SCI-PRO-006 and SCI-PRO-001, and are considered qualified for the intended use in this document (Appendix B). These data are qualified in this report using Method 2 ("Corroborating Data") in accordance with Attachment 3 of SCI-PRO-001. The rationale for selecting this methodology is that corroborating data are available for comparison with the unqualified data set and any inferences drawn to corroborate the unqualified data can be clearly

identified, justified, and documented. Within the scope of this criterion, added confidence in the data is given by their *specific attributes* as discussed below and outlined in Attachment 4 of SCI-PRO-001 and include: the extent to which the data demonstrate the properties of interest, and the extent and quality of corroborating data.

DTNs: LL991008104241.042 [DIRS 120489]; LL000202905924.117 [DIRS 144913]; and LL991008004241.041 [DIRS 120487]

Description of Data: These DTNs report water chemical analyses, specifically chlorine and carbon concentrations, used in this report to evaluate the uncertainty in pH. *Qualification Status:* Qualified for intended use in this report in accordance with SCI-PRO-006 and SCI-PRO-001. These data are qualified using Method 2 ("Corroborating Data") in accordance with Attachment 3 of SCI-PRO-001. *Rationale for selecting methodology*: Corroborating data are available for comparison with the unqualified data set and any inferences drawn to corroborate the unqualified data can be clearly identified, justified, and documented.

The corroborating data are from DTN: MO0701EQ36IDPS.000 [DIRS 179290], which contains numerous water analyses, several of which are used in this report to assess pH uncertainties (see Table 4.1-13 and Section 6.12.3.1 for details). Six calcite equilibrium solubility experiments and one evaporation study were selected for use in Section 6.12.3.1 and are listed in Table 4.1-13. These studies provide total measured chlorine and inorganic carbon concentrations, which are then used to calculate an uncertainty associated with the determination of pH (Section 6.12.3.1). The difference between the measured and the modeled log[C] is the error in the $\log[C]_{total}$, and by inference pH. The results were evaluated statistically and provide a direct feed to TSPA in the form of a discrete CDF of pH uncertainty (Figure 4.1-1). DTNs: LL991008104241.042 [DIRS 120489], LL000202905924.117 [DIRS 144913], and LL991008004241.041 [DIRS 120487] provide six water chemistries for evaporation experiments using J-13 and Topopah Springs Tuff used in Section 6.12.3.1 and listed in Table 4.1-13. The uncertainty values derived from these six analyses are shown in red on the discrete CDF in Figure 4.1-1. Each of the six data points is bounded by qualified data that are derived from DTN: MO0701EQ36IDPS.000 [DIRS 179290] in an identical manner. Thus, these six values are corroborated. The data from DTN: MO0701EQ36IDPS.000 [DIRS 179290] is directly comparable to the data provided by the three DTNs qualified here, because they report related water chemistries. In addition, at least one of the data sets in DTN: MO0701EQ36IDPS.000 [DIRS 179290] is derived from an evaporation study of Topopah Springs Tuff water, and therefore using DTN: MO0701EQ36IDPS.000 [DIRS 179290] as corroboration is valid. The accuracy, precision, and representativeness of the corroborating data are documented in the sources listed in Table 4.1-13.

Qualification Process Attributes are documented below in accordance with Attachment 4 of SCI-PRO-001 and include: the extent to which the data demonstrate the properties of interest, and the extent and quality of corroborating data. *Extent to Which the Data Demonstrate the Properties of Interest:* All three DTNs report test results from evaporation of waters collected at or near the Yucca Mountain site. Their associated pH uncertainties are directly relevant to the application of uncertainty in pH derived by the seepage dilution/evaporation abstraction model developed in this report. *Extent and Quality of Corroborating Data:*

DTN: MO0701EQ36IDPS.000 [DIRS 179290] is considered qualified project output. Therefore, no additional justification of its use as corroboration is required.

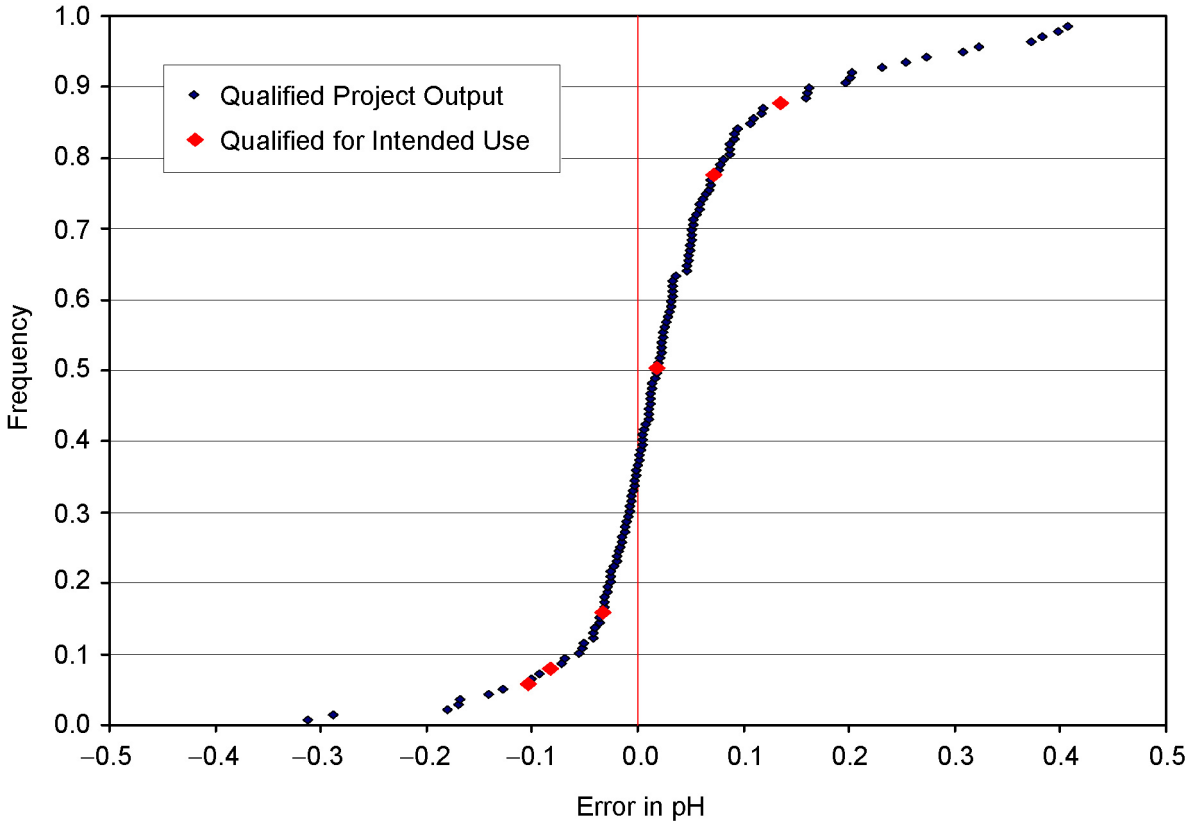

Source: Output DTN: SN0703PAEBSPCE.007, spreadsheet: *Re-evaluation of pH uncertainty.xls*, tab: "Summary charts."

NOTE: The error values form a distribution with a very narrow, high-probability peak, but with scattered higher and lower values. It is slightly offset towards positive values. The red diamonds correspond to the data qualified for intended use in this report. The blue diamonds correspond to qualified project output.

Figure 4.1-1. Modification of Figure 6.12-6 Showing the CDF of Error in $[C]_{total}$

4.1.17 Material Corrosion Rates

Corrosion rates for low-alloy or carbon steels are direct input required for the oxygen demand calculations (Section 6.7). The inclusion of Stainless Steel Type 316L and low-alloy A588 steel is for the direct use in the analysis of seepage water interactions (Section 6.8) along with inputs from Section 4.1. Committed materials deemed to have no significant impact to oxygen consumption are not included as direct input to these analyses. For example, the low corrosion and degradation activity of titanium and Alloy 22, and the small quantity of copper and aluminum are examples of why these materials will not significantly affect the demand for oxygen.

The sources for these data and brief descriptions are provided in Tables 4.1-14 and 4.1-15 for the atmospheric corrosion of Stainless Steel Type 316L and steam corrosion of carbon or low alloy steels, respectively. The mean aqueous corrosion rates for Stainless Steel Type 316L in

salt water are taken from DTN: MO0409SPAACRWP.000 [DIRS 172059] (spreadsheet: *aqueous-316L.xls*, tab: "saltwater") as 1.939 μm/yr. The mean aqueous corrosion rate for A588 steel is approximated by the mean aqueous corrosion rate reported for A516 steel from DTN: MO0409SPAACRWP.000 [DIRS 172059] (spreadsheet: *aqueous-A516.xls*, tab: "saltwater") as 10.61 μm/yr for the 60°C data for the 1.00-year tests. The data for the 60°C tests were used as they were faster than the data reported for the 90°C tests, archived in the same DTN. Low-alloy A588 contains small quantities of Cr and Ni, and thus utilizing the corrosion data for A516 is conservative.

Tables 4.1-14 and 4.1-15 list the sources used in the analysis of corrosion rates in this report. The report by Southwell and Bultman (1982 [DIRS 100928]) is considered Established Fact, as it is a professional society monograph published in *The Corrosion Monograph Series*. The specific corrosion values in DTN: LL980704605924.035 [DIRS 147298] (as listed in Table 4.1-15 and additionally documented in McCright 1998 [DIRS 114637], Section 2.2.6, Supplements 1 and 2) are qualified project data.

Table 4.1-14. Description of Conditions and Sources for Stainless Steel Type 316L Corrosion Rate Data

Temperature (°C)	Relative Humidity (*RH*)	Exposure Time (years)	Note	Measured Rate (various units)	Source
Approximately 27	Approximately 83%	1	1	<0.3 μm loss	Southwell and Bultman 1982 [DIRS 100928], Table 64.6
Approximately 27	Approximately 83%	2	1	<0.3 μm loss	
Approximately 27	Approximately 83%	4	1	<0.3 μm loss	
Approximately 27	Approximately 83%	8	1	<0.3 μm loss	
Approximately 27	Approximately 83%	16	1	<0.3 μm loss	
Approximately 27	Approximately 83%	1	2	0 g/m^2	Southwell and Bultman 1982 [DIRS 100928], Table 64.5
Approximately 27	Approximately 83%	2	2	0 g/m^2	
Approximately 27	Approximately 83%	4	2	0 g/m^2	
Approximately 27	Approximately 83%	8	2	0 g/m^2	
Approximately 27	Approximately 83%	16	2	0 g/m^2	
Approximately 27	Approximately 83%	1	3	1 g/m^2	Southwell et al. 1976 [DIRS 100927], Table 7
Approximately 27	Approximately 83%	4	3	7 g/m^2	
Approximately 27	Approximately 83%	16	3	54 g/m^2	
Approximately 27	Approximately 83%	1	3	1 g/m^2	
Approximately 27	Approximately 83%	4	3	4 g/m^2	
Approximately 27	Approximately 83%	16	3	66 g/m^2	
Approximately 27	Approximately 83%	1	2	0 g/m^2	
Approximately 27	Approximately 83%	4	2	0 g/m^2	
Approximately 27	Approximately 83%	16	2	35 g/m^2	
Approximately 27	Approximately 83%	1	2	0 g/m^2	
Approximately 27	Approximately 83%	4	2	0 g/m^2	
Approximately 27	Approximately 83%	16	2	50 g/m^2	

Table 4.1-14. Description of Conditions and Sources for Stainless Steel Type 316L Corrosion Rate Data (Continued)

Temperature (°C)	Relative Humidity (*RH*)	Exposure Time (years)	Note	Measured Rate (various units)	Source
15.78	—	5	4	0.0013 mils/yr	Bomberger et al. 1954 [DIRS 163699], Table II
15.31	—	5	5	0 mils/yr	
12.5	—	4.92	6	0.0003 mils/yr	

NOTES: 1. Panama Canal Zone, coastal exposure.
2. Panama Canal Zone, inland exposure.
3. Panama Canal Zone, coastal exposure (Stainless Steel Type 316/316 couple).
4. Kure Beach, NC, shore rack 80 ft from breakers.
5. Kure Beach, NC, main lot 800 ft from breakers.
6. Bridgeport, CT.

Temperatures listed as “approximately 27°C” and RH values listed as “approximately 83%” are approximated by taking the average value of January through December provided by Southwell and Bultman (1982 [DIRS 100928], Figure 64.1). The actual values of temperature and RH corresponding to each month are not given by these authors, but rather were estimated from the temperature and RH values at the beginning of each month, and then averaging these values.

Table 4.1-15. Description of Conditions and Sources for Low-Alloy or Carbon Steel Corrosion Rate Data

Temperature (°C)	Relative Humidity (*RH*)	Exposure Time (years)	Rate (μm/yr)
90	Near 100%	0.5	241.82
90	Near 100%	0.5	321.82
90	Near 100%	0.5	257.97
90	Near 100%	0.5	238.11
90	Near 100%	0.5	195.23
90	Near 100%	0.5	192.02
90	Near 100%	0.5	185.47
90	Near 100%	0.5	228.28
90	Near 100%	0.5	228.04
90	Near 100%	0.5	276.51
90	Near 100%	0.5	175.85
90	Near 100%	0.5	269.12
90	Near 100%	1	342.99
90	Near 100%	1	363.36
90	Near 100%	1	358.68
90	Near 100%	1	423.06
90	Near 100%	1	190.72
90	Near 100%	1	139.58
90	Near 100%	1	133.91
90	Near 100%	1	121.31
90	Near 100%	1	144.45
90	Near 100%	1	132
90	Near 100%	1	146.48

Table 4.1-15. Description of Conditions and Sources for Low-Alloy or Carbon Steel Corrosion Rate Data (Continued)

Temperature (°C)	Relative Humidity (*RH*)	Exposure Time (years)	Rate (μm/yr)
90	Near 100%	0.53	150.33
90	Near 100%	0.53	210.6
90	Near 100%	0.53	313.05
90	Near 100%	0.53	166.22
90	Near 100%	0.53	261.61
90	Near 100%	0.53	203.28
90	Near 100%	0.53	75.29
90	Near 100%	0.53	93.33
90	Near 100%	0.53	102.31
90	Near 100%	0.53	129.12
90	Near 100%	0.53	180.84
90	Near 100%	0.53	218.57
90	Near 100%	1.01	212.81
90	Near 100%	1.01	193.28
90	Near 100%	1.01	272.06
90	Near 100%	1.01	80.15
90	Near 100%	1.01	120.81
90	Near 100%	1.01	168.75
90	Near 100%	1.01	72.96
90	Near 100%	1.01	85.05
90	Near 100%	1.01	87.64
90	Near 100%	1.01	113.86
90	Near 100%	1.01	146.72
90	Near 100%	1.01	220.08
60	Aqueous SCW	1.00	7.93
60	Aqueous SCW	1.00	11.19
60	Aqueous SCW	1.00	8.03
60	Aqueous SCW	1.00	9.45
60	Aqueous SCW	1.00	11.05
60	Aqueous SCW	1.00	9.1
60	Aqueous SCW	1.00	6.77
60	Aqueous SCW	1.00	10.07
60	Aqueous SCW	1.00	11.72
60	Aqueous SCW	1.00	12.2
60	Aqueous SCW	1.00	12.9
60	Aqueous SCW	1.00	12.99
60	Aqueous SCW	1.00	10.67
60	Aqueous SCW	1.00	10.00
60	Aqueous SCW	1.00	7.42
60	Aqueous SCW	1.00	8.09
60	Aqueous SCW	1.00	10.32

Table 4.1-15. Description of Conditions and Sources for Low-Alloy or Carbon Steels Corrosion Rate Data (Continued)

Temperature (°C)	Relative Humidity (*RH*)	Exposure Time (years)	Rate (μm/yr)
60	Aqueous SCW	1.00	10.83
60	Aqueous SCW	1.00	12.09
60	Aqueous SCW	1.00	14.36
60	Aqueous SCW	1.00	12.21
60	Aqueous SCW	1.00	11.94
60	Aqueous SCW	1.00	12.62

Source: DTN: LL980704605924.035 [DIRS 147298]; aqueous corrosion rates for low-alloy steel from DTN: MO0409SPAACRWP.000 [DIRS 172059], spreadsheet: *aqueous-A516.xls*, tab: "saltwater" (data for 60°C, 1.00-year tests in SCW water).

NOTES: Materials tested in SCW. SCW = simulated concentrated well (water).
See Output DTN: MO0705OXYBALAN.000 (spreadsheet: *atmospheric May2007.xls*, tab: "Carbon Steel") for more details of input usage.
Representative low-alloy or carbon steel is considered similar to ASTM A 516/A516M-01 2001 [DIRS 162723], Table 1.

Two sources of direct input for corrosion rates are qualified here per the requirements of SCI-PRO-006 and SCI-PRO-001, and are considered qualified for the intended use in this document (Appendix B). These data are qualified in this report using Method 2 ("Corroborating Data") in accordance with Attachment 3 of SCI-PRO-001. The rationale for selecting this methodology is that corroborating data are available for comparison with the unqualified data set and any inferences drawn to corroborate the unqualified data can be clearly identified, justified, and documented. Within the scope of this criterion, added confidence in the data is given by their specific attributes as discussed below and outlined in Attachment 4 of SCI-PRO-001 and include: the extent to which the data demonstrate the properties of interest; prior peer and other professional reviews of the data; and the extent and quality of corroborating data.

Bomberger, H.B.; Cambourelis, P.J.; and Hutchinson, G.E. 1954 [DIRS 163699]; **Southwell, C.R.; Bultman, J.D.; and Alexander, A.L. 1976 [DIRS 100927]**

Description of Data: Corrosion rate data for 316 stainless steel as reported in Table 4.1-14. *Qualification Status:* Qualified for intended use in this report in accordance with SCI-PRO-006 and SCI-PRO-001. These data are qualified using Method 2 ("Corroborating Data") in accordance with Attachment 3 of SCI-PRO-001. *Rationale for selecting methodology*: Corroborating data are available for comparison with the unqualified data set and any inferences drawn to corroborate the unqualified data can be clearly identified, justified, and documented. Southwell and Bultman (1982 [DIRS 100928]) conducted studies of the corrosion of Stainless Steel Type 316 in the coastal region of the Panama Canal Zone at ambient temperatures and local relative humidities of approximately 83%. Their studies lasted from 1 to 16 years (see Table 4.1-14). Converting their reported values to units of micrometers per year (μm/yr) yields a corrosion rate range from 0.02 to 0.30 μm/yr, with an average of 0.12±0.04 μm/yr. The corrosion rate data reported by Bomberger et al. (1954 [DIRS 163699]) and Southwell et al. (1976 [DIRS 100927]) (see Table 4.1-14 for details), when converted to like units, yield an

average corrosion rate for Stainless Steel Type 316 of 0.15±0.02 μm/yr. Note that the uncertainty is calculated as two standard deviations of the mean. This value is corroborated by the Southwell and Bultman (1982 [DIRS 100928]) article cited above. These values are directly comparable, because all of these studies utilized weight loss as a measure for Stainless Steel Type 316 corrosion in coastal, or near coastal, environments at ambient temperatures at relative humidities close to 80%. Therefore, using the article from Southwell and Bultman (1982 [DIRS 100928]) as corroboration is valid. The accuracy, precision, and representativeness of the corroborating data are documented in the respective articles.

Qualification Process Attributes are documented below in accordance with Attachment 4 of SCI-PRO-001 and include: the extent to which the data demonstrate the properties of interest; prior peer or other professional reviews of the data and their results; and the extent and quality of corroborating data.

Extent to Which the Data Demonstrate the Properties of Interest: These articles report test results that were carried out on materials of specific interest in waste package corrosion (in particular Stainless Steel Type 316) in drift-relevant water types (dilute and salt/concentrated waters). These data are directly relevant to Stainless Steel Type 316 corrosion processes at Yucca Mountain.

Prior peer or other professional reviews of the data and their results: The article from Bomberger et al. (1954 [DIRS 163699]) was published in *Journal of the Electrochemical Society*, a peer-reviewed journal of a professional society whose area of expertise includes the corrosion of metals. The three Stainless Steel Type 316 values taken from Table II in this article are each the average of three specimens. The test durations were five years, and four years eleven months. The article by Southwell et al (1976 [DIRS 100927]) describes the results of 16-year tests on a wide variety of materials, including copper and Stainless Steel Type 316, in tropical seawater (total and intermittent submersion). The article was published in *Materials Performance*, an official publication of the Corrosion Society, the National Association of Corrosion Engineers. Authors from the Naval Research Laboratory performed the tests using established engineering practices. Coastal and inland corrosion values from Table 7 of this article were used to derive the mean value used in this report.

Extent and Quality of Corroborating Data: The report by Southwell and Bultman (1982 [DIRS 100928]) is considered Established Fact, as it is a professional society monograph published in *The Corrosion Monograph Series*. Therefore, no additional justification for its use as corroboration is required.

4.1.18 Committed Low-Alloy or Carbon Steel Materials

Section 6.7.1 estimates to what extent the partial pressure of oxygen might change because of the fast corrosion of low-alloy or carbon steels. This involves a quantitative description of the low-alloy or carbon steel materials that are emplaced within the drift.

The only significant source of low-alloy or carbon steel within the emplacement drift is found within the invert structure. These structural elements and their size specifications are listed in Table 4.1-16. Size specifications are used to calculate the surface areas of each component

to determine its oxygen demand from corrosion for both a baseline case and a bounding case. This is described in Section 6.7. The mass included in Table 4.1-16 is 2,460 kg/m for the bounding case.

Table 4.1-16. Low-Alloy or Carbon Emplacement Drift Steel Materials and Size Specifications for Invert Steel Inventory: Bounding Case

Committed Materials List	Size	Material	Weight[a] (lb/ft of drift)
Bounding Case (Source: SNL 2007 [DIRS 179354], parameters 02-08 and 02-10**)**			
Crane rails	171 lb/yd	A759[b]	114
Runway beams	W12x210	A588 Gr. 50[c]	420
Longitudinal beams	W12x72	A588 Gr. 50[c]	144
Transverse beam w/ angles	W12 × 210	A588 Gr. 50[c]	688
Stub columns	W10 × 100	A588 Gr. 50[c]	57
Stub column top plates	3/4" × 13" × 13"	A588 Gr. 50[c]	14
Stub column base plates	1-1/4" × 15" × 22"	A588 Gr. 50[c]	47
Side plates	1-1/4" × 18" × 24"	A588 Gr. 50[c]	61
Splice plates	5/8" × 8" × 24-1/2"	A588 Gr. 50[c]	7
Structural bolts	1-1/4" dia.	A325	57
Rock anchors	2" dia.	Stainless steel	41

[a] Weights are calculated in Output DTN: MO0705OXYBALAN.000, spreadsheet: *Invert steel worksheet June 2007.xls*, using the inputs listed in this table and are reported here for reference only.
[b] ASTM A 759-00 2001 [DIRS 159971], Table 1.
[c] ASTM A 588/A588M-01 2001 [DIRS 162724], Table 1.

Additional references are necessary to define components that are not plate structures. The 135-lb/yd gantry rails are defined in *Manual of Steel Construction, Allowable Stress Design* (AISC 1991 [DIRS 127579], p. 1-113); the "W" size specifications are defined in the same reference in the tables on pp. 1-28 and 1-32. This source is considered "Established Fact," as it comes from the American Institute of Steel Construction. The primary purpose of this organization is to standardize steel construction designs.

4.1.19 Oxygen Demand

In Section 6.7.1, the effects of corrosion of EBS committed materials on the concentration of oxygen in the drift atmosphere through time are evaluated in two ways. One uses a steady-state rate balance calculation to estimate oxygen fugacity. The second is a limitation on the degradation of steel analysis from the mass transfer of oxygen by diffusion through a layer of corrosion products. Table 4.1-17 lists the data inputs for the calculations in Section 6.7.1. For complete descriptions of the methodologies used to determine oxygen demand, see Section 6.7.1 (all calculation results in Output DTN: MO0705OXYBALAN.000).

Table 4.1-17. Data Inputs for Oxygen Demand Calculations from Section 6.7.1

Parameter	Values	Location in Output DTN: MO0705OXYBALAN.000	Source
Molecular weight of O_2	31.9988 g/mol	*th7_81_GasCalc_Invert June2007.xls*, *th7_162_GasCalc_Invert June2007.xls*	Weast and Astle 1981 [DIRS 100833], p. B-126
Molecular weight of Fe	0.055847 kg/mol	*th7_81_GasCalc_Invert June2007.xls*, *th7_162_GasCalc_Invert June2007.xls*	Weast and Astle 1981 [DIRS 100833], p. B-107
Volume fraction of O_2 in atmospheric air	0.20946	*th7_81_GasCalc_Invert June2007.xls*, *th7_162_GasCalc_Invert June2007.xls*	Weast and Astle 1981 [DIRS 100833], p. F-172
O_2 in atmospheric air	101,330 Pa	*th7_81_GasCalc_Invert June2007.xls*, *th7_162_GasCalc_Invert June2007.xls*	Incropera and DeWitt 1996 [DIRS 108184], table inside back cover
Density of steel	7,854 kg/m^3	*th7_81_GasCalc_Invert June2007.xls*, *th7_162_GasCalc_Invert June2007.xls*	Incropera and DeWitt 1996 [DIRS 108184], Table A.1 (plain carbon steel)
Gas constant	8.309 Pa-m^3/mol-K	*th7_81_GasCalc_Invert June2007.xls*, *th7_162_GasCalc_Invert June2007.xls*	Incropera and DeWitt 1996 [DIRS 108184], table inside back cover
Binary diffusion coefficient of O_2 in air at 25°C	2.10×10^{-4}	*Deff (RTA based) May2007.xls*	Incropera and DeWitt 1996 [DIRS 108184], Table A.8
Density of goethite (kg/m^3)	4.0×10^3 (kg/m^3) (calculated value using molecular weight and molar volume, rounded to one significant figure)	*th7_81_GasCalc_Invert June2007.xls*, *th7_162_GasCalc_Invert June2007.xls*	DTN: SN0612T0502404.014 [DIRS 178850] for molar volume data; formula weight of goethite from Weast and Astle 1981 [DIRS 100833]
Corrosion product porosity	0.4	*th7_81_GasCalc_Invert June2007.xls*, *th7_162_GasCalc_Invert June2007.xls*	SNL 2007 [DIRS 177407], Section 6.3.4.3.4
Thermal-hydrologic time-series boundary conditions at drift wall (81 and 162 m drift spacing)	Gas fluxes (see source spreadsheets for values in Output DTN: MO0705OXYBALAN.000)	*th7_81_GasCalc_Invert June2007.xls*, *th7_162_GasCalc_Invert June2007.xls*	DTN: LB0704DSTHONLY.001 [DIRS 181164]
Chosen specific surface areas of steel	1 m^2/g and 22 m^2/g	*Deff (RTA based) May2007.xls*	SNL 2007 [DIRS 177407], Section 6.3.4.3

4.1.20 Steel Interaction with Seepage Water

This section provides inputs to Section 6.8, which examines the chemical impact of both the steel ground support system and invert structure on seepage waters entering the drift. The current design for drift ground support calls for using Stainless Steel Type 316L sheets and rock bolts (SNL 2007 [DIRS 179354], parameter 02-03). Stainless Steel Type 316L is the specific material used for modeling the corrosion-seepage water interaction for the ground support system in Section 6.8.3. For the invert structure, the composition is primarily low-alloy carbon steel type A588 (>95% by weight). Low-alloy carbon steel type A588 is used to model the corrosion-seepage water interaction for the invert components in Section 6.8.3.

Design Specifications—The relevant input design specifications used to model corrosion seepage water interactions in Section 6.8 are given in Tables 4.1-15 and 4.1-17. Invert low-alloy carbon steel design components and specifications are listed in Table 4.1-15. Design information specifics used for the ground support SS316L sheets and rock bolts are presented in Table 4.1-18.

Table 4.1-18. Design Specifications Used for Modeling Stainless Steel Type 316L Sheets and Rock Bolts Seepage-Water Interactions

Parameter	Value
Sheet thickness	3 mm
Rock bolt component	10 bolts/row 3.0 m long
Rock bolt outer diameter	54 mm
Rock bolt thickness	3 mm
Rock bolt row spacing	1.25 m

Source: SNL 2007 [DIRS 179354], parameter 02-03.

The material compositions of both the perforated "Bernold" SS316L sheets and rock bolts and the low-alloy carbon steel A588 are contained within ASTM A 240/A 240M-02a 2002 [DIRS 162720], Table 1; and ASTM A 588/A 588M – 05 [DIRS 176255], Table 1. Section 6.8.3 provides further discussion on the material compositions used in the analysis.

Condition Parameters—The calculations for Stainless Steel Type 316L and carbon low-alloy steel A588 corrosion are performed in Sections 6.8.3 and 6.8.4. Table 4.1-19 summarizes the specific inputs utilized to analyze the degree of corrosion as a function of time.

Table 4.1-19. Parameters Used to Analyze Stainless Steel Type 316L Ground Support and A588 Low-Alloy Carbon Steel Corrosion

Input Parameter Used to Analyze Steel–Water Interactions	Value	Source
Stainless Steel Type 316L density	7.98 g/cm^3	ASTM G 1-90 1999 [DIRS 103515], Table X1.1
Composition of Stainless Steel Type 316L	See source Table 1	ASTM A 240/A 240M-02a 2002 [DIRS 162720], Table 1
Low-Alloy Carbon Steel A588 density	7.85 g/cm^3	Incropera and DeWitt 1996 [DIRS 108184], Table A.1
Composition of Low-Alloy Carbon Steel A588	See source Table 1	ASTM A 240/A 240M-02a 2002 [DIRS 162720], Table 1
Percolation fluxes; 50th percentiles[a]	Present-Day (0 to 600 years); 7.1 mm/yr Monsoon (600 to 2,000 years); 10.91 mm/yr[a] Glacial Transition (2,000 to 10,000 years); 10.54 mm/yr[a] Post-10,000-years; 20.62 mm/yr	DTNs: LB0612PDPTNTSW.001 [DIRS 179150] (present day), LB0701MOPTNTSW.001 [DIRS 179156] (monsoonal), LB0701GTPTNTSW.001 [DIRS 179153] (glacial transition), and LB0702UZPTN10K.002 [DIRS 179332] (post-10,000-years). The data are summarized in Table 6.3-1.

[a] Values used for percolation fluxes for the Monsoon and Glacial Transition periods are interpolated 50th percentiles calculated from these inputs (file: *Perc_Extraction_w_Post_10k_Rev02.xls*, tab: "Time History"). Interpolations were performed between the 47.5 and 52.5 percentiles (columns K and L of the "Time History" tab); these calculations are documented in Output DTN: SN0703PAEBSPCE.006.

NOTE: Corrosion rate inputs to model SS316L and A588 corrosion-seepage water interactions given in Tables 6.5-6 and 6.5-7. The atmospheric mean value of 0.113 µm/yr and aqueous mean value of 1.939 µm/yr are used for SS316L. The mean aqueous (SCW) corrosion rate of 10.61 µm/yr is used for A588.

4.2 CRITERIA

4.2.1 Acceptance Criteria Addressed

The TWP (SNL 2007 [DIRS 179287], Section 3.2) lists the following criteria from *Yucca Mountain Review Plan, Final Report* (NRC 2003 [DIRS 163274], Section 2.2.1.3.3.3) as applicable to this report. These criteria are based on meeting the requirements of 10 CFR 63.114(a)–(c) and (e)–(g).

Quantity and Chemistry of Water Contacting Waste Packages and Waste Forms (NRC 2003 [DIRS 163274], Section 2.2.1.3.3.3)—from 10 CFR 63.114(a)–(c) and (e)–(g):

- **Acceptance Criterion 1**—System Description and Model Integration Are Adequate:

  (1) Total system performance assessment adequately incorporates important design features, physical phenomena, and couplings, and uses consistent and appropriate assumptions throughout the quantity and chemistry of water contacting engineered barriers and waste forms abstraction process.

  (2) The abstraction of the quantity and chemistry of water contacting engineered barriers and waste forms uses assumptions, technical bases, data, and models,

that are appropriate and consistent with other related U.S. Department of Energy abstractions.

(3) Important design features, such as waste package design and material selection, backfill, drip shield, ground support, thermal loading strategy, and degradation processes, are adequate to determine the initial and boundary conditions for calculations of the quantity and chemistry of water contacting engineered barriers and waste forms.

(4) Spatial and temporal abstractions appropriately address physical couplings (thermal-hydrologic-mechanical-chemical).

(5) Sufficient technical bases and justification are provided for total system performance assessment assumptions and approximations for modeling coupled thermal-hydrologic-mechanical-chemical effects on seepage and flow, the waste package chemical environment, and the chemical environment for radionuclide release. The effects of distribution of flow on the amount of water contacting the engineered barriers and waste forms are consistently addressed, in all relevant abstractions.

(6) The expected ranges of environmental conditions within the waste package emplacement drifts, inside the breached waste packages, and contacting the waste forms and their evolution with time are identified.

(7) The model abstraction for quantity and chemistry of water contacting engineered barriers and waste forms is consistent with the detailed information on engineered barrier design and other engineered features.

(8) Adequate technical bases are provided, including activities such as independent modeling, laboratory or field data, or sensitivity studies, for inclusion of any thermal-hydrologic-mechanical-chemical couplings and features, events, and processes.

(9) Performance-affecting processes that have been observed in thermal-hydrologic tests and experiments are included into the performance assessment.

(10) Likely modes for container corrosion (Section 2.2.1.3.1 of the Yucca Mountain Review Plan) are identified and considered in determining the quantity and chemistry of water entering the engineered barriers and contacting waste forms. For example, the model abstractions consistently address the role of parameters, such as pH, carbonate concentration, and the effect of corrosion on the quantity and chemistry of water contacting engineered barriers and waste forms.

(12) Guidance in NUREG–1297 (Altman et al. 1988 [DIRS 103597]) and NUREG-1298 (Altman et al. 1988 [DIRS 103750]), or other acceptable approaches, is followed.

- **Acceptance Criterion 2**—Data Are Sufficient for Model Justification:

  (1) Geological, hydrological, and geochemical values used in the license application are adequately justified. Adequate description of how the data were used, interpreted, and appropriately synthesized into the parameters is provided.

  (2) Sufficient data were collected on the characteristics of the natural system and engineered materials to establish initial and boundary conditions for conceptual models of thermal-hydrological-mechanical-chemical coupled processes that affect seepage and flow and the engineered barrier chemical environment.

  (4) Sufficient information to formulate the conceptual approach(es) for analyzing water contact with the drip shield, engineered barriers, and waste forms is provided.

- **Acceptance Criterion 3**—Data Uncertainty Is Characterized and Propagated through the Model Abstraction:

  (1) Models use parameter values, assumed ranges, probability distributions, and bounding assumptions that are technically defensible, reasonably account for uncertainties and variabilities, and do not result in an under-representation of the risk estimate.

  (2) Parameter values, assumed ranges, probability distributions, and bounding assumptions used in the total system performance assessment calculations of quantity and chemistry of water contacting engineered barriers and waste forms are technically defensible and reasonable, based on data from the Yucca Mountain region (e.g., results from large block and drift-scale heater and niche tests), and a combination of techniques that may include laboratory experiments, field measurements, natural analog research, and process-level modeling studies.

  (3) Input values used in the total system performance assessment calculations of quantity and chemistry of water contacting engineered barriers (e.g., drip shield and waste package) are consistent with the initial and boundary conditions and the assumptions of the conceptual models and design concepts for the Yucca Mountain site. Correlations between input values are appropriately established in the U.S. Department of Energy total system performance assessment. Parameters used to define initial conditions, boundary conditions, and computational domain in sensitivity analyses involving coupled thermal-hydrologic-mechanical-chemical effects on seepage and flow, the waste package chemical environment, and the chemical environment for radionuclide release, are consistent with available data. Reasonable or conservative ranges of parameters or functional relations are established.

  (4) Adequate representation of uncertainties in the characteristics of the natural system and engineered materials is provided in parameter development for conceptual models, process-level models, and alternative conceptual models.

The U.S. Department of Energy may constrain these uncertainties using sensitivity analyses or conservative limits. For example, the U.S. Department of Energy demonstrates how parameters used to describe flow through the engineered barrier system bound the effects of backfill and excavation-induced changes.

- **Acceptance Criterion 4**—Model Uncertainty Is Characterized and Propagated through the Model Abstraction:

  (1) Alternative modeling approaches of features, events, and processes are considered and are consistent with available data and current scientific understanding, and the results and limitations are appropriately considered in the abstraction.

  (2) Alternative modeling approaches are considered and the selected modeling approach is consistent with available data and current scientific understanding. A description that includes a discussion of alternative modeling approaches not considered in the final analysis and the limitations and uncertainties of the chosen model is provided.

  (3) Consideration of conceptual-model uncertainty is consistent with available site characterization data, laboratory experiments, field measurements, natural analog information and process-level modeling studies; and the treatment of conceptual-model uncertainty does not result in an under-representation of the risk estimate.

  (4) Adequate consideration is given to effects of thermal-hydrologic-mechanical-chemical coupled processes in the assessment of alternative conceptual models.

- **Acceptance Criterion 5**—Model Abstraction Output Is Supported by Objective Comparisons:

  (1) The models implemented in this total system performance assessment abstraction provide results consistent with output from detailed process-level models and/or empirical observations (laboratory and field testings and/or natural analogs).

  (2) Abstracted models for coupled thermal-hydrologic-mechanical-chemical effects on seepage and flow and the engineered barrier chemical environment, as well as on the chemical environment for radionuclide release, are based on the same assumptions and approximations demonstrated to be appropriate for process-level models or closely analogous natural or experimental systems. For example, abstractions of processes, such as thermally induced changes in hydrological properties, or estimated diversion of percolation away from the drifts, are adequately justified by comparison to results of process-level modeling, that are consistent with direct observations and field studies.

  (3) Accepted and well-documented procedures are used to construct and test the numerical models that simulate coupled thermal-hydrologic-mechanical-

chemical effects on seepage and flow, engineered barrier chemical environment, and the chemical environment for radionuclide release. Analytical and numerical models are appropriately supported. Abstracted model results are compared with different mathematical models, to judge robustness of results.

4.3 CODES, STANDARDS, AND REGULATIONS

4.3.1 Codes

This model documentation was prepared to comply with the U.S. Nuclear Regulatory Commission high-level waste rule (10 CFR Part 63). Subparts of this rule applicable to data include Subpart B, Section 15 (Site Characterization), and Subpart E, Section 114 (Requirements for Performance Assessment). The Subpart applicable to models is also Subpart E, Section 114. The sections applicable to FEPs are 10 CFR 63.114(d), (e), and (f).

4.3.2 Standards

The following standards are applicable to this report. The specific use of each standard is listed below with that standard's reference.

- ASTM A 240/A240M-02a [DIRS 162720], *Standard Specification for Chromium and Chromium-Nickel Stainless Steel Plate, Sheet, and Strip for Pressure Vessels and for General Applications*
- ASTM A 276-03 [DIRS 165006], *Standard Specification for Stainless Steel Bars and Shapes*
- ASTM A 516/A516M-01 [DIRS 162723], *Standard Specification for Pressure Vessel Plates, Carbon Steel, for Moderate- and Lower-Temperature Service*
- ASTM A 588/A588M-05 [DIRS 176255], *Standard Specification for High-Strength Low-Alloy Structural Steel, up to 50ksi [345Mpa] Minimum Yield Point, with Atmospheric Corrosion Resistance*
- ASTM A 759-00 [DIRS 159971], *Standard Specification for Carbon Steel Crane Rails*
- ASTM G 1-90 (1999) [DIRS 103515], *Standard Practice for Preparing, Cleaning, and Evaluating Corrosion Test Specimens*.

4.3.3 Level of Accuracy, Precision, and Representativeness of Results

The accuracy, precision, and representativeness of results are provided for by justifying the selection of the input data used, expressing the range of uncertainty and variability of the model and analyses parameters, and indicating the range of applicability for which the results apply. The representativeness of direct inputs used by the models described in this report is discussed in Section 4.1. The level of accuracy for predictions of the chemical environment is addressed in Section 6: specifically, equilibrium versus kinetics (Section 6.2.2), mineral suppression

(Section 6.2.5), basis for selecting seepage water compositions (Section 6.6), effects from ground support materials (Section 6.8), evaluation of alternative conceptual models (Section 6.11), lookup table interpolation and extrapolation (Sections 6.9 and 7.2), and other validation issues that pertain to accuracy (Section 7). Numerical precision is not a significant concern for thermochemical modeling of the in-drift environment, although convergence of EQ3/6 simulations is addressed in Sections 6.2 and 6.15.1. Uncertainty in model output is addressed and represented explicitly in the feeds to TSPA-LA (Sections 6.12 and 6.15).

INTENTIONALLY LEFT BLANK

5. ASSUMPTIONS

This section addresses the assumptions built into the P&CE model and those passed into it from upstream documentation that may have significant impact on the results of this model.

5.1 DISCUSSION OF ASSUMPTIONS IN UPSTREAM DOCUMENTATION

The assumptions listed in *In-Drift Precipitates/Salts Model* (SNL 2007 [DIRS 177411], Section 5), the primary model report that feeds this model, were reviewed and evaluated for their potential consequences. Those assumptions having a potentially significant impact are addressed below.

5.1.1 Standard State of Liquid Phase (Assumption 5.1 of the IDPS Model)

Assumption: Liquid phase is at standard state.

Basis: As discussed in *In-Drift Precipitates/Salts Model* (SNL 2007 [DIRS 177411], Section 5.1), an aqueous solution at standard state has an equilibrium relative humidity equivalent to the activity of water in the aqueous solution. Standard state in this sense implies that the water–air interface is flat (i.e., that the boundary between water and air is a plane) and that the behavior of the water molecule (H_2O) is not influenced by solid surfaces in contact with the water. Adsorption and air–water interface curvature, such as the curvature of menisci caused by capillary forces, create nonstandard-state conditions with respect to vapor pressure and equilibrium relative humidity near the air–water interface (Walton 1994 [DIRS 127454]; Koorevaar et al. 1983 [DIRS 125329], pp. 67 to 68).

For the IDPS model, nonstandard-state aqueous solutions are not considered. Only dissolved salts and temperature are considered to affect liquid–vapor equilibrium. The small amounts of water held in double layers and adsorbed to solid surfaces have negligible roles in radionuclide transport and waste package corrosion due to their near immobility. Water held by the surface tension effects of capillarity is more mobile than water in double layers or adsorbed to solids; however, even capillary forces under very dry conditions (in the range of −500 meters water pressure head) have a limited effect on H_2O activity in solution (Walton 1994 [DIRS 127454], pp. 3,480 to 3,481).

Confirmation Status: No further confirmation is required. Because of this limited effect, uncertainties due to the assumption that the liquid phase in the IDPS model is at standard state are negligible compared to the more-sizable uncertainties in the IDPS model and model inputs.

Use in the Model: This assumption is used throughout.

5.1.2 Equilibrium Conditions (Assumption 5.2 of the IDPS Model)

Assumption: The system is in a state of local metastable equilibrium. All aqueous and gas constituents in the model achieve and maintain local equilibrium, and most mineral phases achieve and maintain local equilibrium upon saturation. Several slow-forming and unlikely minerals identified in *In-Drift Precipitates/Salts Model* (SNL 2007 [DIRS 177411], Section 5.2) will not precipitate upon saturation or supersaturation. The model can be used, however, to

make steady-state nonequilibrium predictions with respect to relative humidity, provided the appropriate inputs are used.

Basis: Most chemical reactions included in the model occur rapidly compared to the modeling timeframe. Redox reactions, which generally are not rapid, are not included in the model. Similarly, certain mineral precipitation reactions are not expected to be rapid enough to occur to a considerable degree for the anticipated applications of the model. Mineral precipitation reactions that fall into this category are suppressed, as explained in *In-Drift Precipitates/Salts Model* (SNL 2007 [DIRS 177411], Section 6.6.2.6), permitting the formation of metastable mineral phases in the model.

Highly soluble nitrate and chloride salts, which are direct inputs into TSPA-LA, rapidly deliquesce, dissolve, and precipitate, and are well approximated by equilibrium modeling. As seepage changes rather slowly with time, its most recent compositions will rapidly dominate and overcome any preexisting mineral formation influence. For this reason, kinetic properties of various mineral phases need not be explicitly included in the model during drying and rewetting cycles.

Confirmation Status: No further confirmation is required because mineral precipitation reactions that are expected to be kinetically limited are suppressed, as explained in *In-Drift Precipitates/Salts Model* (SNL 2007 [DIRS 177411]), permitting the formation of metastable mineral phases in the model.

Use in the Model: This assumption is used throughout.

5.2 ASSUMPTIONS INTERNAL TO THE PHYSICAL AND CHEMICAL ENVIRONMENT MODEL

5.2.1 Repository Location

Assumption: It is assumed that the NFC model results, calculated using averaged rock properties (mineralogy, porosity, saturation, grain density) for the four repository host units to evaluate the degree of water–rock interaction, and thermal properties for the Tptpll lithologic unit to model development and evolution of the thermal field, are applicable to all lithologies intersected by the repository drifts.

Basis: There are three bases for this assumption:

- Repository thermal conditions are evaluated using three sets of wet and dry thermal conductivities, representing the 10th, 50th, and 90th percentile values for the Tptpll unit. This range of values overlaps most of the range of thermal conductivity values observed for the other three units. These values are implemented parametrically in the NFC model; TSPA samples P&CE model results by matching the thermal history at the location of interest to a specific NFC model thermal history. Because the range of thermal conductivity values implemented comprises most of the range observed in all four repository host units, the range of thermal histories developed by the NFC model will sufficiently represent the total range expected.

- The repository horizon within the Topopah Spring Tuff (including the Tptpll, Tptpul, Tptpmn, and Tptpln units) is relatively uniform in composition. Peterman and Cloke (2002 [DIRS 162576]) analyzed twenty core samples, in duplicate, from the cross drift within the four lithologic units constituting the repository level. All samples were compositionally similar with respect to major oxides and trace elements (Peterman and Cloke 2002 [DIRS 162576], Table 4), and normative mineral compositions (Peterman and Cloke 2002 [DIRS 162576], Table 5, Figure 4, p. 692). Samples vary by only 2% in SiO_2 concentration, and plot as a tight cluster in the rhyolite field on the chemical rock classification diagram for igneous rocks (SiO_2 plotted against $Na_2O + K_2O$) (Peterman and Cloke 2002 [DIRS 162576], Figure 3, Table 4, p. 687). The tight clustering also indicates that the effect of localized mineral heterogeneity on large-scale rock compositions, due to the presence of minerals which precipitated from the vapor phase during cooling of the tuff, and low-temperature minerals, such as calcite and amorphous SiO_2 (opal), is insignificant (Peterman and Cloke 2002 [DIRS 162576], pp. 695 to 696). Because the four repository host units are compositionally very similar, use of averaged values to represent them is appropriate.

  In addition, the variability in both the mineralogic and hydrologic properties of the four repository units is explicitly propagated through the NFC model as uncertainty in the degree of water–rock interaction.

- The four starting waters used in the NFC seepage model simulations were chosen to represent the entire range of available pore-water compositions, and include pore waters from three of the four repository-level lithologic units (Tptpmn, Tptpll, and Tptpul) (Section 6.6).

Confirmation Status: No further confirmation is required because the thermal properties are implemented parametrically, variability in mineralogy and rock hydrologic properties is incorporated explicitly, and four starting waters from several of the repository host units are used. This assumption allows the TSPA-LA model to implement the lookup tables derived in Section 6.9.3 throughout the repository.

Use in the Model: This assumption is used throughout.

5.2.2 Representative Distribution of Seepage Water Compositions

Assumption: NFC/P&CE model simulations using the four starting waters adequately represent all possible seepage waters.

Basis: The four starting waters were chosen from available measured pore-water compositions for repository-level lithologic units. The TSw waters selected carry the chemical signature of the vitreous layer at the base of the PTn, and although they originate from throughout the TSw, they are envisioned to enter at the top of the unit. These waters cover the observed spread of in situ pore-water compositions (Section 6.6). However, pore-water samples are not available from all possible locations in the repository, and available data can only be assumed to be representative of all water chemistries actually present in the repository units. This assumption is supported by

the chemical similarity of the four TSw lithostratigraphic units that will host the repository, as described in the previous assumption. Reaction with these rocks should make large variations in the concentrations of nonconservative aqueous species from any single unit unlikely.

Confirmation Status: No further confirmation is required because the range of input waters is representative of the waters in the host rock.

Use in the Model: This assumption is used throughout but is explicitly referenced in Section 6.6

5.2.3 Pore-Water Transport Velocities through the NFC Model Domain

Assumption: Pore-water transport times through the NFC model domain can be calculated assuming plug flow through a single unit with averaged rock properties (porosity, saturation, grain density) for the four repository host units.

Basis: The plug flow assumption is based on a comparison with FEHM modeling results for the model domain (Section 6.3.2.4.4). The FEHM simulations were conducted using a one-dimensional column that depicted the separate TSw units individually, using the hydrologic parameters for each unit from the UZ calibrated properties set (DTN: LB0610UZDSCP30.001 [DIRS 179180]. The FEHM code explicitly models matrix–fracture interactions. At percolation flux rates of 1 mm yr^{-1} to 100 mm yr^{-1}, the predicted mean breakthrough times for the FEHM simulations varied from the plug flow breakthrough times calculated using a single combined unit with averaged rock properties, by no more than 15%. The small magnitude of this difference means that matrix–fracture interactions, estimated using the UZ calibrated properties set, are rapid relative to downward transport, and the plug flow approach is reasonable.

The difference between the two approaches was further reduced by calibrating the plug flow approach to match the FEHM rates for the five test cases run.

Additional support for the plug flow implementation is provided by Sr and U isotopic data from pore waters and fracture-lining minerals, which indicate that pore and fracture waters in the TSw are in equilibrium. These data are discussed in detail in Section 6.3.2.3.

Confirmation Status: No further confirmation is required because the plug flow approach is corroborated by the FEHM rates.

Use in the Model: This assumption is explicitly referenced in Section 6.3.2.4.4.

5.2.4 Feldspar Dissolution Rate

Assumption: When the degree of water–rock interaction is evaluated in the NFC model, feldspar dissolution rates are calculated assuming that the sole factor controlling the rate is temperature. This implicitly assumes that the alkali feldspar accessible surface area does not change with time.

Basis: The TSw is 12.8 Ma old, and underwent a prolonged period of elevated temperatures (several millions of years) in its early history (Section 6.3.3.2). During the entire history of the tuff, only a few percent of the feldspar dissolved. Since a significant thermal pulse around the

drift will only last a few thousands to tens of thousands of years, there is little chance that feldspar dissolution, or precipitation of secondary minerals, will significantly alter the bulk mineralogy of the tuff, or the available feldspar surface area.

Confirmation Status: No further confirmation is required because the mineralogy and past thermal history of the tuff indicates that mineral dissolution rates are too slow, even at elevated temperatures (up to 96°C), to significantly affect available mineral surface areas over the interval of the thermal pulse.

Use in the Model: This assumption is explicitly referenced in Section 6.3.2.4.2.

5.2.5 Rock Saturation Used for Calculating Rock Thermal Conductivity and Heat Capacity

Assumption: The initial water saturation of the stratigraphic layers is assumed to be approximately 90.5%, for the purpose of calculating host-rock specific heat and thermal conductivity only (Section 6.3.2.4.3).

Basis: This value is typical for the range of data from the densely welded host-rock units, and is evaluated in *Ventilation Model and Analysis Report* (BSC 2004 [DIRS 169862], Sections 6.9 and 6.11). The saturation of 90.5% is corroborated by *Characterization of Hydrogeologic Units Using Matrix Properties* (Flint 1998 [DIRS 100033], Figure 4). In addition to *Ventilation Model and Analysis Report* (BSC 2004 [DIRS 169862], Sections 6.9 and 6.11), this saturation value is also used in *Thermal Management Flexibility Analysis* (SNL 2007 [DIRS 179196], Section 5.3).

Confirmation Status: No further confirmation is required because the value is representative of the field data, and also because a range of thermal conductivity values (10th, mean, and 90th percentile of observed values) is implemented in the model.

Use in the Model: This assumption is explicitly referenced in Section 6.3.2.4.3.

5.2.6 Baseline Invert Design

Assumption: The baseline invert design contains 1,081 kg/m low alloy or carbon steel, and a total surface area of 15.78 m^2/m of drift.

Basis: The only significant source of low-alloy or carbon steel within the emplacement drift is found within the invert structure. The structural elements and the size specifications for the *bounding case* are listed in Table 4.1-16. Size specifications are used to calculate the surface areas of each component to determine its oxygen demand from corrosion for both a bounding case, and a baseline case assumed to be less than the bounding case. This is described in Section 6.7. Tables 4.1-16 and 6.7-1 report the mass and the surface area for the bounding case as 2,460 kg/m and 19.08 m^2/m of drift. The baseline case is assumed to be less than half the mass (1,081 kg/m of drift) and just over 80% of the surface area (15.78 m^2/m of drift) relative to the bounding case.

Confirmation Status: No further confirmation is required because the value is representative and is appropriately conservative with respect to in-drift oxygen consumption and steel–water interactions in the invert.

Use in the Model: This assumption is explicitly referenced in Sections 6.7 and 6.8.

6. MODEL DISCUSSION

6.1 MODELING OBJECTIVES

The main objective of the Engineered Barrier System (EBS) physical and chemical environment (P&CE) report is to predict the evolution of the environment in the disposal drifts in response to the chemical and physical processes shaping that environment following repository closure. The chemical conditions can affect drip shield and waste package corrosion, radionuclide solubility, and colloidal stability. The conceptual model (Section 6.3) for the evolution of water chemistry in the EBS includes the consideration of seepage dilution/evaporation effects, interactions with engineered materials, and reactions with in-drift gases.

The P&CE model report develops one process model, the near-field Chemistry (NFC) model, and two model abstractions, the seepage dilution/evaporation and the integrated invert chemistry abstractions. The NFC process model provides potential seepage water compositions at the drift wall, the water–rock interaction parameter (WRIP), and the range of in-drift pCO_2. The NFC process model is developed, described, and validated in this report (Section 6.3).

The NFC model outputs are used by the P&CE seepage dilution/evaporation and integrated invert chemistry abstractions to provide in-drift and invert water chemistries through application of the in-drift precipitates/salts (IDPS) process model (SNL 2007 [DIRS 177411]). The integrated invert chemistry abstraction utilizes the same lookup tables in the same manner as those developed by the seepage dilution/evaporation abstraction. Therefore, much of the discussion of the development of the TSPA feeds is limited to the seepage dilution/evaporation abstraction model. The implementation in the invert is unique, however, and is discussed in detail in Section 6.15.2. The NFC and IDPS model uncertainties are propagated into the P&CE abstraction models, which provide data to TSPA, in the form of lookup tables. The P&CE lookup tables describe the dilution and evaporative evolution of these waters. The tables containing the associated uncertainties with instructions for implementation by TSPA are described in Sections 6.12 and 6.15 and are archived in Output DTN: SN0703PAEBSPCE.007.

In general, Section 6 can be divided into three major areas of focus: (1) models developed and abstracted, with uncertainties, for use by the total system performance assessment (TSPA) for the license application (LA) in evaluating engineered barrier performance and radionuclide mobility; (2) a set of screening analyses conducted to evaluate the effects of introduced materials on the EBS geochemical environment; and (3) an alternative conceptual model.

One of the screening analyses provided in Section 6 consists of evaluating predominant engineered material types, compositions, and corrosion rates (Section 6.5). Section 6.5 presents corrosion rates for iron steel and alloy materials. Once the corrosion rates have been determined, most of the materials are screened out as having little potential to affect the chemical environment.

Of the introduced materials, the rock bolts and the perforated stainless steel sheets are the engineered items that could react with, and affect the chemical composition of, potential seepage before it makes contact with the drip shield or waste package outer barrier. These items are

made of Stainless Steel Type 316L, and their potential interactions with seepage water are evaluated in Section 6.8.

Low-alloy steels dominate the committed materials in the invert in the form of gantry rails, beams, and stiffeners. The primary material type is A588 structural steel. A new evaluation is added to this report that examines the interaction of corroding A588 steel with invert waters, that are compositionally identical to the seepage waters used in the dilution/evaporation abstractions (Section 6.8).

Also included in the screening analyses is an evaluation of the effect of the degradation of introduced materials on the in-drift gas composition (particularly O_2; see Section 6.7). This analysis investigates whether corrosion of the introduced low-alloy steel has the potential to affect one of the main boundary conditions established for the model calculations: that oxidizing conditions will be maintained in the drift.

Section 6.6 describes the evaluation of more than 100 pore-water analyses from which 34 pore waters were selected that met the criteria for being relatively complete and unaffected by microbial activity. These 34 pore waters were grouped based on the evolution of their chemical compositions along similar evaporation pathways. From each of the four resulting groups, a single representative water was selected and subsequently used by the NFC process model (Section 6.3) as the basis of the NFC potential seepage water compositions. In addition to the chemistry of potential seepage waters, the NFC provides a WRIP and a range of in-drift pCO_2 values.

In the remainder of Section 6, two abstraction models are developed:

- An abstraction model to represent the evolution of in-drift water compositions that result from dilution and evaporation of seepage (seepage dilution/evaporation abstraction, Sections 6.9 and 6.15.1)

- An integrated invert chemistry abstraction model (Sections 6.9 and 6.15.2).

The main software tool used in the development of the NFC process model and the P&CE abstraction models is EQ3/6 V8.0 (see Table 3.1-1). Section 6.2 discusses the mathematics used by the EQ3/6 calculations and some of the modeling constraints required to produce the model results used in developing the dilution/evaporation lookup tables for potential seepage waters.

Sections 6.12 and 6.13 summarize the results of the modeling calculations. Section 6.12 details the uncertainties associated with key chemical parameters as determined by the IDPS and NFC process models. Section 6.12 also documents additional sensitivity analyses and the justification of IDPS pH uncertainty reduction over a limited RH range.

Section 6.13 summarizes and discusses the model results in terms of the potential physical and chemical environmental conditions on waste packages, drip shields, and in the invert. That section also discusses the potential evolution of brines, the controlling mineral phases for each brine type, and the types of water that could impact the EBS environment. Finally, there are specific instructions important to the TSPA to ensure the lookup tables will be properly implemented in the TSPA-LA model. These instructions are located primarily in Section 6.15,

and describe the implementation of both the seepage dilution/evaporation abstraction model and the integrated invert chemistry abstraction model.

Instructions for implementing uncertainty for each of the TSPA parameters are given in Sections 6.12 and 6.15. Some discussion on the implementation of interpolation between the lookup tables and extrapolation of chemical parameters is provided in Section 6.13. An alternative conceptual model and features, events, and processes (FEPs) are discussed in Sections 6.11 and 6.14, respectively.

In addition to these modeling objectives the following condition reports (CRs) are addressed:

- CR-6770: *Integrated effect of uncertainties on the implementation of localized corrosion in TSPA has not been evaluated.* Uncertainty estimates have been revised to include parameter co-variance (Cl, N) and appropriate distributions assigned for the key chemical parameters provided to TSPA: RH, [Cl], [N], pH, and *I*. Uncertainties are provided as functions of RH and their implementation is discussed in Section 6.12. Additional integrated uncertainty sensitivity analyses will be documented by TSPA.

- CR-7190: *RIT action items associated with AMR ANL-EBS-MD-000033 Physical and Chemical Environment Model*. The RIT actions items addressed in this report are as follows:

  – *The effect of condensate-dust reactions needs to be addressed.* This topic is addressed in Section 6.10.

  – *Predicted invert water chemistries fail to take into account several processes*. This is addressed in the integrated invert chemistry abstraction model discussed in Sections 6.9 and 6.15.

  – *Confirm that the transport of gasses into the drift by diffusion and advection is not significantly different than the assumed advective fluxes in the P&CE model*. A discussion of the effects of axial transport was added to Section 6.7.

  – *The potential effect of EBS materials on water chemistry is not sufficiently investigated; the importance of reaction rates and sorption onto corrosion products is not fully considered.* The development of a sorption model is beyond the scope of this report but is addressed in *EBS Radionuclide Transport Abstraction* (SNL 2007 [DIRS 177407]). Updated analyses in the present report evaluate the impact of degradation of EBS materials on invert water chemistry (Sections 6.7 and 6.8).

  – *Some consideration of brine evolution and deliquescence in an open drift is needed to allow evaluation of the effects of gas fluxes*. Previous work on the production and fate of acid-gas species in the drift environment has shown that while degassing of acid-gas species from deliquescent brine is possible, it can occur only to a limited extent, and the resulting gas-phase concentrations for acid-gas species are very small (SNL 2007 [DIRS 181267], Section 6.2). Therefore, this aspect of brine evolution

has no significant effect on the in-drift chemical environment and is not addressed further in this report.

– *Lack of treatment for kinetics of mineral precipitation and redissolution in the P&CE, especially with respect to Mg-silicates*. Justification for use of amorphous Mg-silicate, and suppression of crystalline sepiolite, in the validation cases for the IDPS model is provided by the IDPS report (SNL 2007 [DIRS 177411], Table 6-3). Justification for use of crystalline sepiolite in the NFC process model, as well as other kinetically controlled phases, is provided in Section 6.3.

– *The choice of FRONT waters may be incorrect and should be re-evaluated.* The NFC process model provides the starting water compositions to represent seepage for TSPA, so this comment no longer applies to this report.

– *Difficulty following data analysis without recourse to special information*. This comment was addressed previously and the discussion has been updated to address the new NFC process model inputs (Section 6.3).

– *Lack of basis for using seepage water lookup table to represent condensation*. With the introduction of the NFC model, reference to "condensation tables" is no longer applicable. The argument for using the seepage lookup tables for waters formed by dilution of NFC waters is outlined in Section 6.9.

- CR-7786: *Potential errors in tables about corrosion test solutions repeated in various documents*. Errors in the corrosion test solution descriptions have been corrected in Table 6.13-6.

- CR-7820: *Incorrect NBS pH values in EQ3/6 outputs*. The affected DTNs have been superseded and the new DTNs correctly report the Pitzer pH.

- CR-8316: *Pore-water chemistry analyses lack charge balance*. Additional available measured pore-water data are evaluated and the likely cause of charge imbalance is discussed in Section 6.6.

- CR-8959: *Nitrate reduction by drift support materials – effect on in-drift water chemistry not considered.* The effect of nitrate reduction on steel is addressed in Section 6.8.

In addition, the following review comments from a previous validation exercise are addressed by this report:

- IDC-7: *Criteria for Chemical Binning – a statistical binning analysis should be developed and either implemented or presented as an alternative model*. Chemical binning is no longer used because the NFC model does not use a binning strategy.

- IDC-19: *Implementation of invert chemistry model – use of crown seepage evaporation abstraction may not be conservative with respect to representing invert water*

compositions. A new integrated invert chemistry abstraction is developed and its implementation is documented in Sections 6.9 and 6.15.2.

6.2 GEOCHEMICAL MODELING CONSTRAINTS

This section summarizes the main set of mathematical models used in this report and establishes a modeling framework for developing equilibrium-type geochemical models in systems under metastable or partial equilibrium. This section provides much of the basis for the conceptual model outlined in Section 6.3. It is also intended to demonstrate the importance of mineral and species suppression (i.e., the way equilibrium models are used to predict chemical conditions in metastable systems), which is a fundamental modeling concept of this report.

6.2.1 Mathematical Models Implemented by the Use of EQ3/6 V8.0 Geochemical Modeling Software

Geochemical modeling constraints are imposed by the primary geochemical modeling software used in this report, EQ3/6 V8.0 (see Table 3.1-1). This software is composed of two independent codes: EQ3NR and EQ6. Both of these are described in general terms in the following subsections, much of which is derived from *Software User's Manual EQ3/6 Version 8.0* (SNL 2003 [DIRS 162494], Appendices B and D). The reader is referred to the EQ3/6 user's manual for a more detailed explanation of the concepts discussed in the following paragraphs.

6.2.1.1 EQ3NR: Speciation-Solubility Modeling of Aqueous Systems

EQ3NR is an equilibrium speciation-solubility code for aqueous systems that is part of the EQ3/6 V8.0 code (Table 3.1-1). As such, given sufficient data for a chemical species to characterize a specific aqueous system, it computes a model of the solution that consists of two principal parts: the distribution of species in the solution and a set of saturation indices (SI = log Q/K) for various reactions of interest. The saturation indices measure the degree of disequilibrium of corresponding solution–mineral reactions. They provide a means for evaluating solubility controls on natural waters. For example, at equilibrium the SI = 0, but under close to equilibrium conditions where a series of related fluids all have a given mineral SI value close to zero, it is probable that this mineral is present and partial equilibrium with this mineral is maintained as the solutions evolve in composition.

EQ3NR is not a specific computerized geochemical model, but a software code that is useful in evaluating many different conceptual geochemical models, which are defined by the contents of a supporting thermodynamic data file (from which there are now several to choose, including *data0.ymp.R5* (DTN: SN0612T0502404.014 [DIRS 178850]) and *data0.ypf.R2* (DTN: SN0609T0502404.012 [DIRS 179067])) and by other user-defined inputs and constraints in the EQ3NR input file. The supporting thermodynamic data files differ not only in terms of data values but also, more importantly, in terms of the identities of the components and chemical species represented, and in terms of the general approaches used in the estimation of activity coefficients. Because of various limitations (such as the use of the Pitzer model for estimation of activity coefficients), some problems may require the use of only certain data files, while others can be treated using any of the available data files. For, the thermodynamic modeling simulations carried out for the P&CE models, a slightly modified version of the *data0.ypf.R2*

database (DTN: SN0609T0502404.012 [DIRS 179067]), called *data0.pce* and archived in Output DTN: SN0703PAEBSPCE.006, was used. This database, and its modifications relative to *data0.ypf.R2*, are described in Section 6.2.6.

6.2.1.1.1 Input Constraints, Governing Equations, and Outputs

Aqueous speciation models can be constructed to satisfy a variety of combinations of possible input constraints and governing equations. The input constraints may include:

- Total (analytical) concentrations
- An electrical balance requirement
- Mass balance
- Free ion concentrations
- Aqueous species activities
- pH
- Eh
- pe
- Oxygen pressure
- Phase equilibrium requirements
- Homogeneous equilibria
- Run-specific values for equilibrium constants.

The governing equations are the corresponding mathematical expressions, such as the mass-balance equation and the charge-balance equation.

The choice of governing equations in large part depends on which parameters are to be inputs to the model, and which are to be outputs. This, in turn, is a function of what data on a given water are available, what form they are in, and what constraints the modeler would like to use.

Chemical analysis mainly provides a set of values for the so-called total concentrations of dissolved components. The analytical value for an ion such as calcium is an example. It does not discriminate between the various calcium species in solution, but rather estimates the dissolved calcium contributed by all of them. This leads to a mass-balance equation of the form:

$$m_{T,Ca} = m_{Ca^{2+}} + m_{CaOH^{-}} + m_{CaCO_3(aq)} + m_{CaHCO_3^{+}} + \ldots \qquad \text{(Eq. 6.2-1)}$$

where $m_{T,Ca}$ is the total or analytical concentration (on the molal scale) and m_i is the molality of any individual chemical species contributing to the mass balance. The summations must be weighted by the appropriate stoichiometric equivalences; for example, in the case of F^-:

$$m_{T,F} = m_{F^-} + m_{HF(aq)} + 2m_{H_2F_2(aq)} + 2m_{HF_2^-} + 3m_{AlF_3(aq)} + \ldots \qquad \text{(Eq. 6.2-2)}$$

The total concentration is the most common type of input parameter to an aqueous speciation model. Therefore, the most common governing equation is the mass balance constraint. As will be seen, there are situations in which a total concentration is replaced by another type of input

such as the use of the input flag "heterogeneous equilibrium," where an aqueous concentration can be calculated from a gas pressure. In these cases, the mass-balance constraint is replaced by a different governing equation, and the total concentration becomes something to be calculated (an output parameter). Charge balance is also a common governing concept that will either calculate the apparent charge imbalance or force the aqueous solution to maintain electrical balance. Large charge imbalance errors indicate there may be incomplete or erroneous chemical analysis or a misinterpretation of reported analytical results.

Mathematically, there is no reason to discriminate among ion pairs (and ion triplets, etc.) and complexes. For some investigators, the term "ion pair" implies a species in which an anion is separated from a cation by an unbroken hydration sheath about the latter, whereas the term "complex" implies direct contact and perhaps some degree of covalent bonding. Other investigators use these terms interchangeably. It is a general presumption in cases of geochemical interest that the concentrations of ion pairs and complexes are governed by thermodynamic equilibrium.

Each case of this equilibrium can be represented by a mass-action equation for the dissociation of the ion pair or complex. As an example, the calcium sulfate ion pair dissociates according to the reaction:

$$CaSO_4(aq) = Ca^{2+} + SO_4^{2-} \qquad \text{(Eq. 6.2-3)}$$

where "=" is used as the sign for a reversible chemical reaction. The corresponding mass-action equation is:

$$K_{CaSO_4(aq)} = \frac{a_{Ca^{2+}} a_{SO_4^{2-}}}{a_{CaSO_4(aq)}} \qquad \text{(Eq. 6.2-4)}$$

where K is the equilibrium constant and a_i represents the thermodynamic activity of each species. This may also be written in logarithmic form:

$$\log K_{CaSO_4(aq)} = \log a_{Ca^{2+}} + \log a_{SO_4^{2-}} - \log a_{CaSO_4(aq)} \qquad \text{(Eq. 6.2-5)}$$

The thermodynamic activity is related to the molal concentration by the relation:

$$a_i = m_i \gamma_i \qquad \text{(Eq. 6.2-6)}$$

where γ_i is the activity coefficient, a function of the composition of the aqueous solution. As the solution approaches infinite dilution, the value of γ_i for each species approaches unity. The user, in the EQ3/6 input calculation file, chooses the set of equations for computing the activity coefficients of aqueous species. The requisite supporting data are in the EQ3/6 database file. The activity of pure mineral phases is specified to be at unity.

6.2.1.1.2 Activity Coefficient Models of Aqueous Species

The thermodynamic activities (a_i) of aqueous solute species are usually defined on the basis of molalities. Thus, they can be described by the product of their molal concentrations (m_i) and molal activity coefficients ($\gamma_{i,}$), as shown in Equation 6.2-6.

The thermodynamic activity of the water (a_w) is always defined on a mole-fraction basis. Thus, it can be described analogously by the product of the mole fraction of water (x_w) and its mole-fraction activity coefficient (λ_w):

$$a_w = x_w \lambda_w \qquad \text{(Eq. 6.2-7)}$$

The activity coefficients, in reality, are complex functions of the composition of the aqueous solution. In electrolyte solutions, the activity coefficients are influenced mainly by electrical interactions. Much of their behavior can be correlated in terms of the ionic strength, defined by:

$$I = \frac{1}{2}\sum_i m_i z_i^2 \qquad \text{(Eq. 6.2-8)}$$

where the summation is over all aqueous solute species and z_i is the electrical charge. However, the use of the ionic strength as a means of correlating and predicting activity coefficients has a very limited range of usefulness (e.g., in the mean-salt method used by Garrels and Christ 1965 [DIRS 144877], pp. 58 to 60). A comparison between the mean-salt method of Garrels and Christ and the classical Debye-Hückel activity model (Garrels and Christ 1965 [DIRS 144877], Figure 2.15, p. 63) shows a reasonable agreement up to an ionic strength of 0.05 to 0.1 depending on the ion. In general, model equations that express the dependence of activity coefficients on solution composition only in terms of the ionic strength are restricted in applicability to dilute solutions.

The three basic options for computing the activity coefficients of aqueous species in EQ3/6 calculations are models based on the Davies (1962 [DIRS 162482]) equation, the Hückel equation, also known as the "B-dot" equation (Helgeson 1969 [DIRS 137246]), and Pitzer's equations (1973 [DIRS 152738]; 1975 [DIRS 152740]; 1979 [DIRS 119530]; 1987 [DIRS 162481]). The first two models, owing to limitations on accuracy, are only useful in dilute solutions (generally up to ionic strengths of 1 molal, although extension for specific application is possible). The third basic model is useful in highly concentrated as well as dilute solutions, but is limited in terms of the components that can be accurately treated, as defined by the input database. Calculations of relevance to this report were performed with both the Pitzer and the B-dot activity model.

All EQ3/6 calculations in this report, with the exception of some comparative sensitivity analyses performed in Section 6.8, use the Pitzer activity model. Therefore, the EQ3/6 modeling results in are presented in terms of the "Pitzer" pH scale.

6.2.1.2 EQ6: Reaction-Path and Single-Point Modeling

EQ6 computations can first be broken down into "single-point" thermodynamic equilibrium calculations and irreversible mass transfer reaction-path calculations. A single-point thermodynamic calculation is essentially just the special case of a reaction path with no steps (e.g., used when precipitating supersaturated phases or making a temperature jump). Reaction paths may be calculated for titrations, irreversible reaction in closed systems, and irreversible reaction in certain well-defined types of open systems (e.g., a fluid-centered flow-through open system). Such calculations may be in reaction progress mode (time independent) or time mode (explicit kinetic or time dependent), depending on the rate law being implemented.

EQ6 is a part of the EQ3/6 V8.0 code (Table 3.1-1) and uses separate methodologies for treating intrinsically algebraic equations and intrinsically differential equations. The former govern the thermodynamic calculations, and the latter consist of rate laws for irreversible processes. This numerical decoupling makes it possible to perform thermodynamic calculations, given the necessary inputs of total number of moles of components, the temperature, and the pressure, independently of the integration of rate equations. This decoupling permits making "single-point" thermodynamic equilibrium calculations, such as temperature jump problems, in which rate equations do not appear.

In EQ6 reaction-path models, the two types of equations are coupled in the mathematically formal sense, but the solution of each is performed semi-independently. Each calculation type is performed alternately, the output of one becoming the input to the next execution of the other. For example, in moving a step forward in reaction progress (ξ), rate equations are integrated. This defines new values for the temperature, pressure, and total number of moles of the components, which are inputs to the following thermodynamic calculation. This, in turn, gives a new distribution of species from which values may be calculated for the rates of the irreversible processes at the new point. If accuracy tests on the ordinary differential equation integration are satisfied, these rate values are used in making the next integration step. Otherwise, the step size may be cut until those tests are satisfied.

When the rate chosen to constrain an irreversible process is a relative rate ($d\xi_j/d\xi$), the rate function is either a constant or a simple function of the overall reaction progress variable (ξ). When EQ6 operates in the mode of arbitrary kinetics (all irreversible processes constrained by relative rate expressions; no time variable in the model), these rates can be integrated by simple closed-form expressions. It is, therefore, possible to take arbitrarily large step sizes, subject only to the following conditions.

In the case of closed and open system calculations, the rate of an irreversible reaction is set to zero when the corresponding thermodynamic driving force, the affinity, is no longer positive. Affinities are outputs of the thermodynamic calculations. EQ6 locates the point of reaction progress where the affinity goes to zero. If the corresponding reactant is a mineral, this means that the aqueous solution has reached saturation. The code then changes the status of the reactant to inactive (meaning it is effectively removed from the set of reactants) and any remaining mass of the reactant is moved into the *equilibrium system*. Titration calculations are very similar to closed-system calculations, but the rate of an irreversible reaction is not set to zero when

saturation is reached, and the remaining reactant mass continues to be added to the equilibrium system according to the rate law.

The rate of an irreversible reaction also becomes zero when the associated "reactant" becomes exhausted, no matter what kind of system model the code is dealing with. The user specifies how much of a reactant is available at the start of the calculation run. The code then finds the point of reaction progress at which exhaustion occurs.

6.2.1.2.1 Constraints on Thermodynamic Calculations

The following thermodynamic constraints are enforced in EQ6 calculations:

- Mass balance
- Charge balance
- Law of mass action
- Activity coefficients of aqueous species
- Activity coefficients of solid solution components
- Saturation indices and affinities.

Details on each of these can be found in *Software User's Manual EQ3/6 Version 8.0* (SNL 2003 [DIRS 162494], Appendix D1.2).

6.2.1.2.2 Constraints on Reaction Path Calculations

The following reaction path constraints are enforced in EQ6 calculations:

- Reaction progress variable (ξ), which is a measure of the extent to which a reaction has proceeded

- Reaction rates and time for each irreversible reaction as a function for either the relative rate or the absolute rate

- Rate laws programmed into EQ6: relative rate, partial equilibrium, transition-state theory, and linear rate.

Details on each of these can be found in *Software User's Manual EQ3/6 Version 8.0* (SNL 2003 [DIRS 162494], Appendix D1.3).

6.2.2 Geochemical Modeling Methodology

Generally, a reaction path geochemical equilibrium model is constructed using the steps outlined in Figure 6.2-1. First, a conceptual model is defined where the chemical system and state are defined. This system and state are tested and investigated to produce results. Those results are compared with independent experimental, natural analogue, or other modeling data to ensure that the model is representative of the system and state to be analyzed.

Decisions about mineral suppression or inclusion require:

- A reasonable understanding of mineralogy and petrology
- A well-researched conceptual model
- An understanding of how to develop a reaction-path model using software codes like EQ3/6 (Wolery 1992 [DIRS 100836]; Wolery and Daveler 1992 [DIRS 100097]), PHREEQC (Parkhurst 1995 [DIRS 142177]), or MINTEQA2 (HydroGeoLogic and Allison Geoscience Consultants 1999 [DIRS 158974])
- An understanding of how to ensure that confidence exists in the model and that model uncertainty has been appropriately addressed.

The following subsection contains a brief summary of the kinetics versus equilibrium relations rationale that must be considered in the selection of mineral phases for the model. Bethke (1996 [DIRS 162270]), Smith and Missen (1991 [DIRS 161602]), and Van Zeggeren and Storey (1970 [DIRS 161603]) provide more-detailed discussions concerning modeling methodology aspects.

6.2.3 Equilibrium versus Kinetics

Bethke (1996 [DIRS 162270], Chapter 2) reports two main types of equilibrium end states that are important to recognize in reaction path modeling: complete and metastable equilibrium. In complete equilibrium, the chemical state of the system attains stable equilibrium such that there is no chemical potential to drive any net chemical reaction. Usually, when an equilibrium model is first constructed, the first-order model (Figure 6.2-1) is allowed to go to complete equilibrium. When the initial system is constrained based on the end equilibrium state by determining variables such as the temperature, dissolved aqueous concentrations, quantity of given minerals in the system, or the fugacities of any gases, the calculation results in a fluid saturated with respect to the stable equilibrium mineral assemblage for the system.

Once this first-order model is constructed, the boundary conditions and the conceptual model are evaluated to determine whether various states of metastable equilibrium should be taken into account (Section 6.2.5). The first-order model is then refined to account for these effects. For example, if the model predicts the complete equilibrium state to include minerals that do not occur in the actual system, this may imply that a metastable equilibrium situation exists in the actual system.

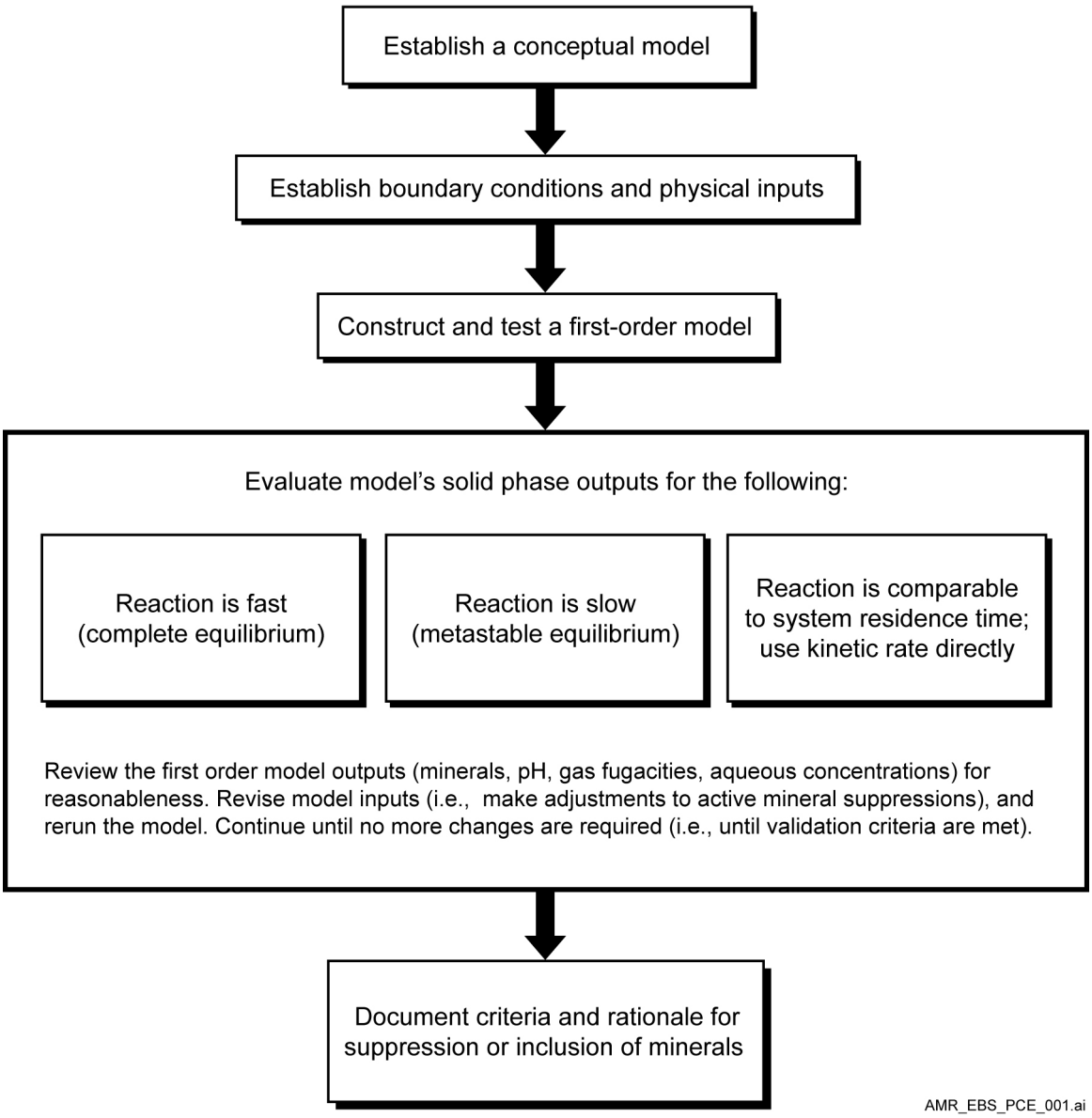

NOTE: A first-order model is a model that accounts for complete equilibrium (i.e., no metastable equilibrium or kinetic controls) with no active mineral suppressions.

Figure 6.2-1. Simplified Roadmap of the Process Required to Construct a Valid Technical Basis for Mineral Suppression or Inclusion in Geochemical Equilibrium Modeling

Metastable equilibrium occurs when one or more chemical reactions proceed toward equilibrium at a rate that is so small relative to the time scale of interest that the system does not reflect the consequences of reaction with that phase. In this case, the system can be considered not to include the reaction(s) involving that mineral. Such reactions are commonly heterogeneous reactions involving mineral precipitation. That is, the nucleation or growth of the mineral is subject to kinetic barriers that are large enough to preclude, or allow only negligible progress of, the reaction. In such a case, the mineral that should exert an equilibrium compositional

constraint is supplanted by another, less stable phase that is not kinetically constrained from forming and growing.

In other words, mineral suppression is used in equilibrium calculations to represent, in a simple manner, the fact that some solid phases are kinetically inhibited from precipitating or dissolving under equilibrium conditions in certain environments (e.g., quartz precipitation at low temperature). Because of the kinetic constraints, the chemical constituents commonly controlled by the inhibited solid phase are controlled instead, if at all, by a somewhat less-stable phase that reaches its metastable equilibrium rapidly compared to the inhibited phase. Inclusion of the explicit kinetic approaches would handle mineral dissolution or precipitation directly, but for simpler equilibrium calculations this is commonly handled by suppressing the occurrence of a mineral phase in the model to represent the kinetic barrier and to achieve the same result found in real systems. Suppression of minerals, therefore, is a practical tool in being able to define the end-state equilibrium of a modeled system or to use an equilibrium-type model to mimic the effect of kinetic processes without having to know actual details about the kinetic rates of dissolution or precipitation.

Partial equilibrium and local equilibrium are specific cases or subsets of metastable equilibrium that can have relevance to a given geochemical problem. Partial equilibrium (also known as heterogeneous equilibrium) is defined by Wolery and Daveler (1992 [DIRS 100097]) such that some (usually most) reactions are in a state of equilibrium, while others, usually few in number and representing heterogeneous processes such as mineral dissolution or precipitation, are not. For example, the fluid in sandstone might be in equilibrium itself but may not be in equilibrium with the mineral grains in the sandstone or with just some of the grains. Local equilibrium, which is sometimes called mosaic equilibrium (i.e., temperature, mineralogy, or fluid chemistry vary across the system of interest), can be thought of as a system that is open to groundwater flow (Bethke 1996 [DIRS 162270], p. 12). In this idealized flow-through system, the aqueous phase moves over or through several different mineral assemblages and the water reacts with each of these and achieves some degree of equilibrium on the local scale with each assemblage, even though each location is at a different equilibrium state comparatively. All of these various types of equilibrium conditions can be combined into a single model, depending on the conceptual model.

Kinetics can be combined into reaction path modeling because the equilibrium point of a reaction is the point at which dissolution and precipitation rates balance. Bethke (1996 [DIRS 162270], Chapter 2) indicates that kinetic reactions fall into three groups:

- Those in which reaction rates are so slow relative to the period of interest that the reaction can be ignored (i.e., accounting for metastable equilibrium). This slow reaction rate group commonly corresponds to what mineral suppression is used to represent.
- Those fast enough to maintain equilibrium (accounting for complete equilibrium).
- All other reactions that do not fall into the first two groups. These “other reactions” are the only reactions that require a kinetic description.

6.2.4 Engineered Barrier System Geochemical Equilibrium Modeling

The equilibrium reaction path models used by the P&CE model are designed to predict long-term chemical processes within a potential repository drift. Although short-term occurrences (such as seepage water falling onto the drip shield) can cause transitory divergence from the conceptualized state of metastable equilibrium, an equilibrium approach is adopted because it provides valuable insight into long-term processes. This modeling provides the exposure conditions needed by *General Corrosion and Localized Corrosion of Waste Package Outer Barrier* (SNL 2007 [DIRS 178519], Section 6.4.4); specifically, these are pH, and chloride and nitrate concentrations.

An equilibrium reaction-path model, such as that implemented using EQ6, relies on a thermodynamic database that contains standard-state thermochemical parameters of the different chemical species in a system to determine the chemical reaction equilibria as functions of the changing conditions. In addition to the homogeneous reactions that occur within each phase (e.g., water, gas, solid), there are heterogeneous reactions that involve more than one phase, such as mineral precipitation and degassing of volatile constituents from the aqueous phase. Most of the reactions in the equilibrium models employed by the P&CE model are rapid relative to the timeframe of the modeling period; therefore, most reactions are allowed to reach equilibrium. However, there are many minerals in the thermodynamic database that will not form under the expected conditions of the repository. Minerals that could be excluded from consideration are those that form during the oxidation of pyrite or other sulfide minerals, because sulfides are not expected to form. Sulfate minerals, not sulfides, form under the redox conditions that will likely occur in the repository (Section 6.7.1).

The pressure in the repository is expected to remain near atmospheric (Figure 6.7-5), and the temperature at the drift wall is not expected to rise above 200°C (SNL 2007 [DIRS 181383]). These conditions limit those minerals in the database that can realistically be expected to form at a significant rate. As discussed previously, an equilibrium model ignores the use of kinetic rates; it predicts the most stable mineral phases at equilibrium, except when the user suppresses (i.e., rules out) those minerals. When precipitation is suppressed for a mineral, the equilibrium model does not allow the mineral to precipitate, resulting in a condition of supersaturation with respect to that phase. In this way, the equilibrium model can incorporate simplified kinetic constraints as metastable equilibrium conditions. Current conceptualization of postclosure drift conditions allows for conditions in the repository to be essentially dry. Any seepage entering the drift would be subject to conditions in which the relative humidity or activity of water would fall below one. Therefore, evaporative processes are expected to dominate during the evolution of in-drift seepage.

6.2.4.1 Modeling of Mineral Precipitation

The Pitzer thermodynamic database (*data0.ypf.R2* in DTN: SN0609T052404.012 [DIRS 179067]) currently includes more than 220 minerals, but only a small fraction of these have been suppressed in the modeling run calculations evaluated to date. It is unnecessary to identify *a priori* which of the more than 220 minerals should be suppressed for these calculations. The limited range of chemical compositions of the waters likely to occur within the drift dictates that a majority of the more than 220 minerals will never achieve a chemical

potential favoring precipitation. This point is demonstrated by the results to date. The predicted starting water compositions at Yucca Mountain were evaporated to dryness, at varying temperatures, pCO_2 values, and WRIP quantities, using EQ3/6 V8.0 (see Table 3.1-1) and the Pitzer database in the development of the dilution/evaporation abstraction (Section 6.9). In all the evaporation simulations, fewer than 40 minerals became saturated or supersaturated with respect to the aqueous composition. Thus, it is not necessary to categorize the remaining 180-plus minerals according to their potential for precipitating under drift conditions.

Having some sort of simple criteria to appropriately suppress or include the approximately 40 minerals that have become saturated in the engineered barrier system models developed for TSPA-LA facilitates determining the end equilibrium state in a model and provides consistency between the P&CE abstraction models and the IDPS report (SNL 2007 [DIRS 177411]). Six criteria have been developed to assist in determining the rationale for suppression or inclusion in the models to account for the kinetic or metastable equilibrium arguments stated previously. These six criteria are listed in the following paragraphs.

Criterion 1—*Is the mineral of interest beyond or outside the defined chemical system of the model?*

If the mineral lies outside or beyond the defined chemical system of the model, there is no reason to include the mineral. For example, while modeling mineral formation at low temperatures and pressures (near ambient), any mineral could be excluded that was known to form only at high temperatures or pressures.

Individuals trained in mineralogy or petrology can readily make these determinations. Example reference sources, used to make these decisions when combined with expert judgment, are Klein and Hurlbut's *Manual of Mineralogy* (1999 [DIRS 124293]), Kerr's *Optical Mineralogy* (1977 [DIRS 161606]), and Roberts et al.'s *Encyclopedia of Minerals, 2nd Ed.* (1990 [DIRS 107105]), or any similar reference source that discusses the petrology or mineralogy of a given system or analogue system.

If a mineral is not included in the database, it is, in effect, suppressed. The formation conditions applicable to the great majority of the over 3,000 minerals listed by Roberts et al. (1990 [DIRS 107105]) lie outside the physiochemical boundaries of the repository system. Most of these can be excluded because they contain trace or minor elements of no interest to repository operations, or have been addressed through studies of corrosion and radionuclide solubility.

Criterion 2—*Is the mineral of interest likely or unlikely to precipitate because of kinetic controls?*

Langmuir (1997 [DIRS 100051]) provides a general rule of thumb for determining the need for a kinetic description of mineral dissolution or precipitation. When a reaction is irreversible or its rate is comparable to, or slower than, the system residence time (i.e., the half-life is greater than or equal to the residence time), a kinetic rate is needed to describe the state of reaction. When this rule of thumb is met and kinetic data are available, the data are used directly. Often, however, rate data are not available for the system being modeled, or it is much simpler to invoke a state of metastable equilibrium and use a mineral suppression to simplify the model.

Therefore, a modeler will make a mineral suppression that mimics the conceptualized state of metastable or localized equilibrium. As an example, one of the most common mineral suppressions used in geochemical modeling is that of considering the kinetic rates of reaction for amorphous silica, quartz, or one of its polymorphs (tridymite and chalcedony). In general, amorphous precipitates will tend to form first, and then a process of mineral recrystallization will take place (Langmuir 1997 [DIRS 100051], p. 55). Therefore, the metastable phase that would generally be used in a reaction path model for quartz would be amorphous silica. If the conceptual model were to account for a longer system residence time or higher temperatures, the modeler would allow quartz or one of its polymorphs to precipitate. For iron oxides, it would be expected that either goethite or ferrihydrite would form first, depending on temperature and relative humidity. Ferrihydrite recrystallizes relatively quickly to form goethite or hematite, which may persist for eons.

Criterion 3—*Is analytical or natural analogue information available that warrants the inclusion or exclusion of the mineral?*

Commonly, when performing geochemical modeling, information or data are found by researching the relevant literature used to develop the conceptual model. This information often comes from analytical data or natural analogue information, and warrants the suppression or inclusion of minerals that could be handled differently based on Criteria 1 and 2. This allows for inclusion of minerals that could form due to some unknown kinetic constraint that has not been accounted for directly in the model.

Although care is taken in constructing and attempting to "validate" a model as it is developed, conceptual model or thermodynamic database uncertainty must still be addressed. Therefore, three additional criteria are included to allow evaluation of the effect of mineral suppressions on model results.

Criterion 4—*Do minerals need to be suppressed or included to test overall model uncertainty or sensitivity due to reported uncertainty in the supporting literature, database, or conceptual model?*

Criterion 5—*Does the suppression or inclusion of minerals that are highly uncertain drive the resulting chemical output to a more or less conservative modeling result?*

Criterion 6—*Do other minerals that are in a database provide an adequate surrogate or proxy for the mineral?*

Certainly, Criteria 4 through 6 are not applicable to the normal types of mineral dispositions in models. However, they are of great use when conducting sensitivity studies or handling modeling uncertainties.

Although the six criteria are written to address mineral suppressions, they can and should be used to document the suppression of any aqueous species of concern (Table 6.2-2).

6.2.4.2 Modeling of Trace Elements

The term "trace" used in reference to solutes in natural water cannot be precisely defined. Commonly, the term is used for substances that occur in concentrations less than 1.0 mg/L (Hem 1985 [DIRS 115670], pp. 129 to 130). Trace elements from the natural system that are potentially present in the in-drift seepage waters that have been identified and considered for affects on the waste package and drip shield environments are lead (Pb), arsenic (As), and mercury (Hg). The potential impacts of fluoride on corrosion processes have also been evaluated and found to not significantly enhance the general corrosion of the drip shield under repository conditions (SNL 2007 [DIRS 180778], Section 8.3). The chemical composition of the rhyolite tuff that makes up the repository horizon is well characterized and essentially uniform (Peterman and Cloke 2002 [DIRS 162576]). Compositions of pore waters extracted from the tuff at the repository horizon have been characterized for trace element concentration. Table 6.6-1 shows the composition of analyzed minor and trace elements in the pore waters extracted from cores collected in the TSw. As can be seen from Table 6.6-1, Pb and Hg concentrations and more than one-third of the arsenic concentrations are below the detection limits or not reported.

Elements in introduced materials that are normally considered as trace species in natural waters may be important to certain in-drift processes, yet not be significant contributors to the major ion geochemistry. Most analyses presented to date have focused on the chemical reactions among major constituents because these are considered to be the primary system drivers controlling the in-drift environmental conditions. Bruno et al. (1998 [DIRS 110969]) also conclude in their studies of trace metals in natural systems that good characterization of the site mineralogy and a sound understanding of the main geochemical driving forces (i.e., bulk chemistry) are needed to further investigate the reactions of trace species; that is, the trace species will only have a small effect upon the bulk chemistry (e.g., pH, ionic strength, or major cation–anion concentrations).

Iron, chromium, nickel, and manganese, considered important constituents of introduced materials in the drift, are specifically considered in Section 6.8.

6.2.5 Rationale for Including or Excluding Precipitating Minerals

Table 6.2-2 provides a listing of the minerals that have been suppressed in the IDPS (SNL 2007 [DIRS 177411]) and P&CE models; Table 6.2-3 provides a listing of the minerals that precipitated during modeling run calculations. In each case, a rationale for the decision to suppress or include each mineral is provided. In addition to the rationales listed in Tables 6.2-2 and 6.2-3, which are used to strengthen model confidence, each engineered barrier system model is independently validated against natural analogue data or experimental results, to ensure that the model is an appropriate representation. Minerals that are present in the thermodynamic database but did not precipitate during model development were not included in Table 6.2-3.

It is important to acknowledge some key limitations of the thermodynamic database developed for use in this report and that apply to thermodynamic databases in general with respect to mineral precipitation. First, empirical data are not always available for the mineral of interest. If there are no thermodynamic data available and no reasonable modeling approach is possible, then that phase can not be modeled. Second, there may be reasonable thermodynamic data available for a mineral but not for the specific composition of interest. An example of this is

clinoptilolite, nominally $(Na,K,Ca)_{2-3}Al_3(Al,Si)_2Si_{13}O_{36}\cdot 12(H_2O)$, which commonly contains a wide range of minor element substitutions. The general clinoptilolite phase included in the *data0.ymp.R5* database (DTN: SN0612T0502404.014 [DIRS 178850]) has the chemical formula $Na_{0.954}K_{0.543}Ca_{0.761}Mg_{0.124}Sr_{0.036}Ba_{0.062}Mn_{0.002}Al_{3.45}Fe_{0.017}Si_{14.533}O_{46.922}H_{21.844}$. In addition to this heavily substituted phase, there are eight other discrete compositions in *data0.ymp.R5* that correspond to Ca, Cs, K, NH_4, Na, and Sr-rich end members, as well as a dehydrated phase and a solid solution phase. Even with extensive thermodynamic data for so many variations of composition, this particular zeolite would never precipitate in the NFC model domain owing to the trace quantities of Fe in each of these compositions. The NFC model does not include trace Fe as a component in its waters. Fortunately in this case, because the quantities of Fe were small (<0.02 moles per formula unit), a correction could be applied to "remove" the Fe from these phases, thus allowing them to precipitate if modeling conditions warranted (Output DTN: SN0703PAEBSPCE.006). In the case of heulandite, a zeolite mineral observed to form at Yucca Mountain, no similar correction was possible because of the large quantities of Ba and Sr in the heulandite included in the *data0.ymp.R5* database ($Ba_{0.065}Sr_{0.175}Ca_{0.585}K_{0.132}Na_{0.383}Al_{2.165}Si_{6.835}O_{18}\bullet 10.33H_2O$). However, as described in Sections 6.3.2.6 and 7.1.2.3, because appropriate sinks for the major cations are present in the model as representative clays or zeolites, the NFC model captures the general observed mineral behavior and the resultant water chemistry is little affected by the specific mineral precipitate.

Table 6.2-2. Mineral Suppressions Used in P&CE Geochemical Modeling

Mineral	Formula	Criteria Selected	Rationale	References
Cristobalite (alpha)	SiO_2	Criterion 2	Cristobalite is thermodynamically stable at temperatures greater than 1,470°C. At standard temperatures and pressures, cristobalite will slowly convert to quartz.	Krauskopf 1979 [DIRS 105909], Figure 14-1
Dolomite	$CaMg(CO_3)_2$	Criterion 2	Although dolomite is a common mineral in evaporite deposits from springs derived from carbonate and tuffaceous waters in southern Nevada at Yucca Mountain, its growth mechanism is slow when compared to the precipitation calcite, opal, and Mg-bearing minerals such as sepiolite.	Vaniman et al. 1992 [DIRS 107066]
Glaserite	$NaK_3(SO_4)_2$	Criterion 4	Although glaserite is a mineral that is expected to form in evaporitic type deposits, at the time modeling runs for this report were initiated, the thermodynamic data for glaserite being considered for inclusion in the Pitzer database was in question.	suppressed, subject to sensitivity analysis
Magnesite	$MgCO_3$	Criterion 2	Magnesite is commonly associated with metamorphic mineral assemblages, such as serpentine. There are instances where magnesite is associated with salt deposits, yet it is uncertain that it can form under standard temperatures and pressures as magnesite could be associated with the diagenesis of buried salt deposits.	Kerr 1977 [DIRS 161606] Eugster and Hardie 1978 [DIRS 100743]
K-Feldspar	$KAlSi_3O_8$	Criterion 1	K-Feldspar, or orthoclase, is generally associated with the formation of granite, syenite, and gneiss. Although it is often found as a common mineral in sandstone or arkose, the occurrence in these instances is detrital.	Kerr 1977 [DIRS 161606], p. 306
Cryolite	Na_3AlF_6	Criterion 2	The only important cryolite deposit is located on the west coast of Greenland as a massive bed in granite. It is commonly associated with sulfide minerals, galena, sphalerite and chalcopyrite.	Klein and Hurlbut 1999 [DIRS 124293], p. 400.

Table 6.2-2. Mineral Suppressions Used in P&CE Geochemical Modeling (Continued)

Mineral	Formula	Criteria Selected	Rationale	References
Quartz	SiO_2	Criterion 2	Literature evidence suggests that amorphous silica is at metastable equilibrium with respect to quartz at low temperatures and pressures. This is also evidenced by the precipitation of opal-A (an amorphous silica phase) as opposed to quartz in evaporated carbonate and tuffaceous waters of southern Nevada.	Langmuir 1997 [DIRS 100051] Vaniman et al. 1992 [DIRS 107066]
Sepiolite	$Mg_4Si_6O_{15}(OH)_2 \bullet 6H_2O$	Criterion 3	The precipitation of sepiolite is common in conjunction with calcite precipitation in calcrete deposits. However, it is typically the amorphous phase that is a common fracture-lining mineral above the basal vitrophyre of the Topopah Spring Member at Yucca Mountain. Amorphous Sepiolite (or the chemically related antigorite) is also known to commonly form on evaporation of either carbonate-source or tuff-source waters in southern Nevada. The crystalline phase is therefore suppressed so that the amorphous Mg-silicate may precipitate.	Hay and Wiggens 1980 [DIRS 162281] Carlos et al. 1995 [DIRS 105213] Vaniman et al. 1992 [DIRS 107066]
Talc	$Mg_3Si_4O_{10}(OH)_2$	Criterion 1	Talc is characteristically associated with low-grade metamorphic rock and hydrothermal alteration of ultramafic rocks.	Kerr 1977 [DIRS 161606]
Ca-saponite Mg-saponite Na-saponite H-saponite K-saponite	$Ca_{0.165}Mg_3Al_{0.33}Si_{3.67}O_{10}(OH)_2$ $Mg_{3.165}Al_{0.33}Si_{3.67}O_{10}(OH)_2$ $Na_{0.33}Mg_3Al_{0.33}Si_{3.67}O_{10}(OH)_2$ $H_{0.33}Mg_3Al_{0.33}Si_{3.67}O_{10}(OH)_2$ $K_{0.33}Mg_3Al_{0.33}Si_{3.67}O_{10}(OH)_2$	Criterion 1	Saponite is a montmorillonite or smectite clay. Smectite clays are commonly associated with fracture linings at Yucca Mountain. However, saponitic clays are associated with the weathering of basalt and not rhyolitic tuffs. Saponite does not generally form independently from its associated parent material, nor does it precipitate independently in soil environments.	Krauskopf 1979 [DIRS 105909] Carlos et al. 1995 [DIRS 105213] Deer et al. 1966 [DIRS 162338] Borchardt 1989 [DIRS 156639]

Table 6.2-3. Minerals Allowed to Precipitate in P&CE Geochemical Modeling

Mineral	Formula	Criteria Selected	Rationale	References
Calcite	$CaCO_3$	Criterion 3	Calcite is a common evaporite mineral formed from evaporated waters of southern Nevada.	Vaniman et al. 1992 [DIRS 107066]
SiO_2(am)	SiO_2	Criterion 2	Literature evidence suggests that amorphous silica is at metastable equilibrium with respect to quartz at low temperatures and pressures. This is also evidenced by precipitation of opal-A as opposed to quartz in evaporated carbonate and tuffaceous waters of southern Nevada.	Langmuir 1997 [DIRS 100051] Vaniman et al. 1992 [DIRS 107066]
Fluorite	CaF_2	Criterion 3	Fluorite is associated with evaporite deposits in Nevada playas.	Papke 1976 [DIRS 162274], Tables 1
Celadonite	$KMgAlSi_4O_{10}(OH)_2$	Criterion 3	Although its occurrence is generally associated with hydrothermally altered mafic volcanic rocks and with illite-chlorite minerals, celadonite is also found as an authigenic silicate mineral in saline, alkaline, and nonmarine environments such as playa deposits.	Li et al. 1997 [DIRS 159034] Hay et al. 1966 [DIRS 105965]
Thenardite	Na_2SO_4	Criterion 3	Thenardite is associated with evaporite deposits in Nevada playas.	Papke 1976 [DIRS 162274], Table 1
Halite	NaCl	Criterion 3	Halite is associated with evaporite deposits in Nevada playas.	Papke 1976 [DIRS 162274], Table 1 Kerr 1979 [DIRS 161606], p. 221
Huntite	$CaMg_3(CO_3)_4$	Criterion 3	Huntite is a Mg carbonate mineral associated with cave and evaporite deposits as well as with meteoric (low-temperature) dissolution, and re-precipitation of calcite, dolomite, or magnesite. Huntite will precipitate instead of calcite when Mg^{2+} is concentrated in solutions with respect to Ca^{2+} due to evaporative processes.	Faust 1953 [DIRS 162282] Walling et al. 1995 [DIRS 162283], p. 360
Sellaite	MgF_2	Criterion 3	Sellaite is the Mg analogue to fluorite that forms in evaporite deposits.	Palache et al. 1951 [DIRS 162280], pp. 37 to 39
Gypsum	$CaSO_4 \bullet 2H_2O$	Criterion 3	Gypsum is associated with evaporite deposits in Nevada playas.	Papke 1976 [DIRS 162274], Table 1 Kerr 1979 [DIRS 161606], p. 221
Glauberite	$Na_2Ca(SO_4)_2$	Criterion 3	Glauberite is associated with evaporite deposits in Nevada playas.	Papke 1976 [DIRS 162274], Table 1

Table 6.2-3. Minerals Allowed to Precipitate in P&CE Geochemical Modeling (Continued)

Mineral	Formula	Criteria Selected	Rationale	References
Niter	KNO_3	Criterion 3	Niter is associated with evaporite deposits in Nevada playas.	Papke 1976 [DIRS 162274], Table 1
Sylvite	KCl	Criterion 3	Sylvite is associated with evaporite deposits in Nevada playas.	Papke 1976 [DIRS 162274], Table 1 Kerr 1979 [DIRS 161606], p. 221
Arcanite	K_2SO_4	Criterion 3	Arcanite is a very soluble mineral belonging to the Mascagnite group and can be precipitated in the laboratory from the slow evaporation of water solutions. This mineral is related to thenardite and should have similar properties.	Palache et al. 1951 [DIRS 162280], pp. 398 to 400
Antigorite (am)	$Mg_3Si_2O_5(OH)_4$	Criterion 2	Amorphous antigorite is a serpentine mineral that commonly forms from the alteration of magnesium silicates. In addition, poorly crystalline antigorite has been shown to rapidly precipitate from Mg, Si-bearing solutions in the temperature range of 39°C to 150°C.	Klein and Hurlbut 1999 [DIRS 124293], p. 507. Gunnarsson et al. 2005 [DIRS 176844], abstract.
Soda Niter	$NaNO_3$	Criterion 3	Soda Niter is associated with evaporite deposits in Nevada playas.	Papke 1976 [DIRS 162274], Table 1
Carnallite	$KMgCl_3 \bullet 6H_2O$	Criterion 3	Carnallite is associated with evaporite deposits in Nevada playas.	Papke 1976 [DIRS 162274], Table 1 Kerr 1979 [DIRS 161606], p. 221
Pentasalt (Gorgeyite)	$K_2Ca_5(SO_4)_6 \bullet H_2O$	Criterion 3	Gorgeyite occurs in association with glauberite, halite, and polyhalite in salt deposits.	Fleischer and Efremov 1954 [DIRS 162312]
Syngenite	$K_2Ca(SO_4)_2 \bullet H_2O$	Criterion 3	Syngenite is associated with salt deposits (especially halite) and precipitates in cavities created by volcanic action. It precipitates at room temperatures from solutions that contain K_2SO_4.	Palache et al. 1951 [DIRS 162280], pp. 442 to 444
Anhydrite	$CaSO_4$	Criterion 3	Anhydrite is associated with evaporite deposits in Nevada playas.	Papke 1976 [DIRS 162274], Table 1 Kerr 1979 [DIRS 161606], p. 221
Natrite	Na_2CO_3	Criterion 3	Natrite is a highly soluble carbonate mineral associated with shortite, pirssonite, and gaylussite. These three minerals are also associated with the precipitation of trona, calcite, and montmorillonite and are found in clay beds that have deposited in borax lakes.	Fleischer and Pabst 1983 [DIRS 162284] Palache et al. 1951 [DIRS 162280]

Table 6.2-3. Minerals Allowed to Precipitate in P&CE Geochemical Modeling (Continued)

Mineral	Formula	Criteria Selected	Rationale	References
Trona	$Na_3H(CO_3)_2 \bullet 2H_2O$	Criterion 3	Trona is associated with evaporite deposits in Nevada playas.	Papke 1976 [DIRS 162274], Table 1
Burkeite	$Na_6CO_3(SO_4)_2$	Criterion 3	Burkeite is a saline mineral associated with Na-CO_3-SO_4-Cl brines.	Eugster and Hardie 1978 [DIRS 100743], Table 3
Clinoptilolite-K Clinoptilolite-NA	$(Na,K)_6[Al_6Si_{30}O_{72}] \bullet 24H_2O$	Criterion 3	A family of zeolites that are commonly major constituents of volcanic tuffs and ancient saline lake deposits.	Deer et al. 1966 [DIRS 162338]
Erionite	$NaK_2MgCa_{1.5}[Al_8Si_{28}O_{72}] \bullet 28H_2O$	Criterion 3	A zeolite that is commonly a major constituent of volcanic tuffs and ancient saline lake deposits.	Deer et al. 1966 [DIRS 162338]
Kalicinite	$KHCO_3$	Criterion 3	Kalicinite is a saline mineral associated with K-CO_3-Cl brines, by analogy with nahcolite.	Eugster and Hardie 1978 [DIRS 100743], Table 3.
Kogarkoite	Na_2SO_4F	Criterion 3	Kogarkoite has been shown to form in water upon mixing Na_2SO_4 with NaF at temperatures ranging from 17°C to 35°C.	Linke 1965 [DIRS 166191], p. 1033.
Nahcolite	$NaHCO_3$	Criterion 3	Nahcolite is a saline mineral associated with Na-CO_3-Cl brines.	Eugster and Hardie 1978 [DIRS 100743], Table 3.
Pirssonite	$Na_2Ca(CO_3)_2 \bullet 2H_2O$	Criterion 3	Pirssonite forms as an authegenic precipitate in saline lakes deposits such as the Green River formation.	Eugster and Hardie 1978 [DIRS 100743], Table 11.
Polyhalite	$K_2Ca_2Mg(SO_4)_2 \bullet 2H_2O$	Criterion 3	A highly soluble evaporite salt.	Klein and Hurlbut 1999 [DIRS 124293], p. 577.
Villiaumite	NaF	Criterion 3	Villiaumite is so soluble that it rarely forms in evaporate deposits and only forms in evaporative simulations near the dryout RH.	Sonnenfeld 1984 [DIRS 156721], p. 226.
Stellerite	$Ca_2Al_4Si_{14}O_{36} \bullet 14H_2O$	Criterion 3	Stellerite is a zeolite mineral commonly associated with fracture linings at Yucca Mountain.	Carlos et al. 1995 [DIRS 105213]
Phillipsite	$K_{0.7}Na_{0.7}Ca_{1.1}Al_{3.6}Si_{12.4}O_{32} \bullet 12.6H_2O$	Criterion 3	Phillipsite is a zeolite mineral commonly associated with evaporite deposits.	Hay et al. 1966 [DIRS 105965]
Kieserite	$MgSO_4 \bullet H_2O$	Criterion 3	Kieserite is an evaporite mineral commonly found in salt deposits. Often it is associated with halite or carnallite.	Palache et al. 1951 [DIRS 162280], pp. 477 to 479

6.2.6 Thermodynamic Database Used by the NFC and P&CE Models

Thermodynamic calculations performed for the NFC and the two seepage abstraction models use the *data0.pce* database (Output DTN: SN0703PAEBSPCE.006). This database represents a slightly modified version of the Pitzer database, *data0.ypf.R2* (DTN: SN0609T0502404.012 [DIRS 179067]), which is qualified in the IDPS report (SNL 2007 [DIRS 177411], Appendix I). Many of these modifications involve inserting data blocks for solid phases or aqueous species from the qualified project database for dilute solutions, *data0.ymp.R5* (DTN: SN0612T0502404.014 [DIRS 178850]), or modifying data blocks to be consistent with that database. The modifications made to the Pitzer database *data0.ypf.R2* (DTN: SN0609T0502404.012 [DIRS 179067]) to produce the *data0.pce* database are documented and justified for one-time use in the P&CE models in this section. Those modifications are as follows:

(1) $NiNO_3^+$ data block removed, as this species is already counted in the interaction parameters.

(2) $NiBr^+$ data block removed to avoid double counting this species, as it is already counted in the interaction parameters.

(3) Added a data block for $NiCO_3$:5.5H_2O taken from the *data0.ymp.R5* database (DTN: SN0612T0502404.014 [DIRS 178850]).

(4) Modified data block for eskolaite to make similar to the *data0.ymp.R5* database (DTN: SN0612T0502404.014 [DIRS 178850]). The new values are consistent with the SUPCRT values for Cr^{+++}. Note that between the time that *data0.ymp.R5* was submitted and finalized, a slight change in the eskolaite data block was made. The differences never exceed 0.06 log(K) units and are, therefore, well within the experimental error and no adjustment is required to the *data0.pce* database (Output DTN: SN0703PAEBSPCE.006).

(5) Modified the $CrOH^{++}$ data block to be consistent with the *data0.ymp.R5* database (DTN: SN0612T0502404.014 [DIRS 178850]).

(6) Added a data block for a fictive solid (titled SS316L) calculated assuming that the three most abundant components of Stainless Steel Type 316L (Fe, Cr, and Ni) adequately define the chemical interactions between seepage water and the corroding metal. This data block has an arbitrarily large log(K) at 25°C assigned to ensure that the solid never saturates in solution.

(7) Modified the clinoptilolite-Ca, clinoptilolite-K, clinoptilolite-Na data blocks by removing Fe and adding the corresponding amount of Al to maintain charge balance. This change allows these phases to precipitate in the absence of Fe in the P&CE model.

(8) Added a data block for a mixed feldspar called Alkali_Feldspar calculated as a mechanical mixture of anorthite, sanidine_high and albite_high for use in P&CE titrations.

The first six changes above were made to facilitate sensitivity analyses of stainless steel interactions with seepage water but do not otherwise impact the geochemical modeling calculations documented in this report. The stainless steel sensitivity analyses are documented in Section 6.8. The remaining two changes, the addition of recalculated clinoptilolite and alkali feldspar, were required to implement the NFC process model and generate potential seepage water compositions and range of in-drift pCO_2, as described in Section 6.6. Note that the quantity of alkali feldspar to be titrated into the seepage waters (the WRIP) is calculated, not from EQ3/6 simulations utilizing the thermodynamic data associated with the alkali feldspar phase added to the database, but rather is calculated by estimation of a temperature-dependent dissolution rate from observations of mineral assemblages in the rock and activation energies from empirical study. By calculating a thermal field and assuming a percolation flux, a range of potential WRIP values was generated (see discussion in Section 6.3.2.4.2). The goal of the thermodynamic treatment of the alkali feldspar phase was twofold: first, the appropriate ratios of the major cations, Na, K, and Ca, measured in the rock should be maintained when titrating the feldspar into the seepage waters; and second, the mixed volcanic feldspar should never saturate in the model domain (Section 6.3.2.4.2). This is accomplished by assigning a composition to the mixed feldspar phase from the tuff mineralogy and assuming an ideal mixing model in calculating the log(K) grid in the database. The log (Q/K) for the alkali feldspar phase in all of the evaporation simulations is typically less than −4 and never exceeds −2 units; thus, no affinity effects are expected (Output DTN: SN0705PAEBSPCE.009, spreadsheet: *AF_saturation.xls*). As the choice of mixing model is irrelevant to the stated goals of this treatment, an ideal mixing model was chosen, as it was less arbitrary than assuming a degree of exsolution and then applying a regular mixing model to the exsolved phases. The application of Raoult's Law is commonly used in the absence of phase-specific site mixing information and is adequate for the purposes of this report (Stumm and Morgan 1981 [DIRS 100829], p.41).

In order to utilize the *data0.pce* database (Output DTN: SN0703PAEBSPCE.006), a well known translation error of the α-parameter by the execution code owing to an ill-defined matrix in the compiled binary file was fixed according to the instructions found in the readme file associated with the DTN that contains the Pitzer database (DTN: SN0609T0502404.012 [DIRS 179067]). In addition to the ill-defined matrix in the binary file, the compiled database, *data1.pce* (Output DTN: SN0703PAEBSPCE.006), must be used with EQ3/6 v8.0 or higher. The earlier versions of the software are more sensitive to variations in formatting and may not read the compiled database correctly.

As outlined above, three modifications to the Ni model in the Pitzer database were adopted in the modified *data0.pce* database (Output DTN: SN0703PAEBSPCE.006). Both the $NiNO_3^+$ and the $NiBr^+$ data blocks were removed as these species are already accounted for in the Pitzer interaction parameters. A hydrous nickel carbonate phase, $NiCO_3{:}5.5H_2O$, was added for consistency with *data0.ymp.R5* (DTN: SN0612T0502404.014 [DIRS 178850]).

As a demonstration of the adequacy of the changes to the Ni-system, several comparisons were made between experimental and calculated data utilizing the *data0.ymp.R5* database (DTN: SN0612T0502404.014 [DIRS 178850]) and the modified Pitzer database, *data0.pce* (Output DTN: SN0703PAEBSPCE.006). The EQ3 simulations used to calculate the aqueous nickel concentrations in equilibrium with $Ni(OH)_2$ and $NiCO_3$ at various pH are archived in Output DTN: SN0705PAEBSPCE.010. The solubility curve for $Ni(OH)_2$ is shown in

Figure 6.2-2. The Ni system utilized in both *data0.pce* (Output DTN: SN0703PAEBSPCE.006) and *data0.ymp.R5* (DTN: SN0612T0502404.014 [DIRS 178850]) is compared to data originated by Plyasunova et al. (1998 [DIRS 168289]) and presented by Hummel and Curti (2003 [DIRS 181199], Fig. 1, mean Ni quantities as a function of pH). Figure 6.2-2 confirms that both databases provide an accurate model of the experimental data. The mononuclear hydrolysis species that dominate the solubility above approximately pH of 9 and the aqueous Ni^{2+} species that dominates solubility below approximately pH of 9 are adequately represented in *data0.pce* (Output DTN: SN0703PAEBSPCE.006) and will provide an accurate assessment of nickel solubility in the sensitivity studies presented in Section 6.8. In addition to the Ni^{2+} and the mononuclear hydrolysis species, for some of the sensitivity simulations in Section 6.8, Ni-carbonate species dominate the aqueous equilibrium. Therefore, a comparison between *data0.pce* (Output DTN: SN0703PAEBSPCE.006) and *data0.ymp.R5* (DTN: SN0612T0502404.014 [DIRS 178850]) solubility calculations for $NiCO_3$ solid was also made as a check on the aqueous nickel carbonate species. The results are shown in Figure 6.2-3 and they verify that the *data0.pce* database (Output DTN: SN0703PAEBSPCE.006) accurately predicts the solubility limit as compared to the B-dot database. The pH range of relevance to the sensitivity studies is approximately 6.5 to 9.5 pH units (see discussion in Section 6.8).

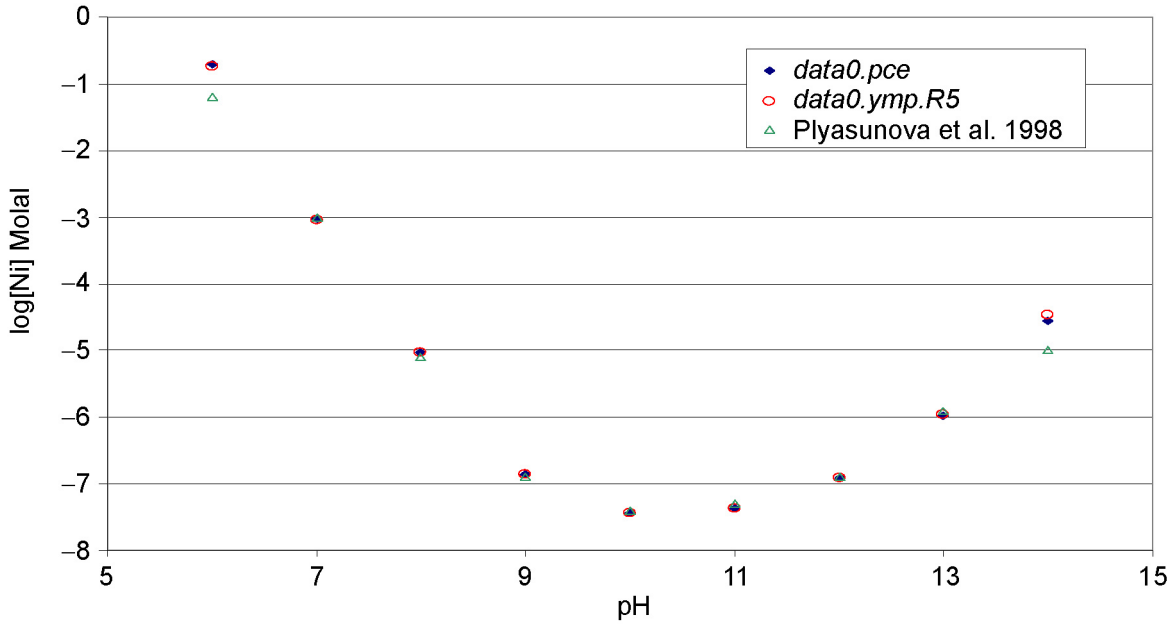

Source: Output DTN: SN0705PAEBSPCE.010.

Figure 6.2-2. Modeled vs. Measured Aqueous Equilibrium Nickel Solubility over $Ni(OH)_2$ Solid

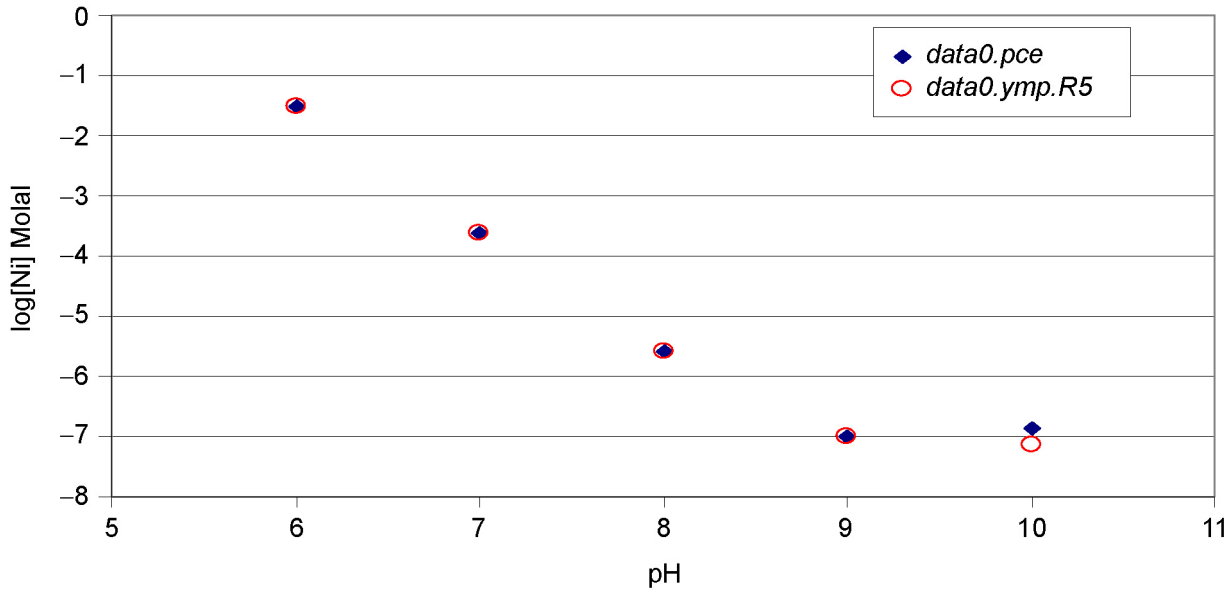

Source: Output DTN: SN0705PAEBSPCE.010.

Figure 6.2-3. Comparison of Aqueous Equilibrium Nickel Solubility over $NiCO_3$ Solid Calculated Using Two Different Thermodynamic Databases

The Cr-system updates in the *data0.pce* (Output DTN: SN0703PAEBSPCE.006) were similarly investigated. Solubility of aqueous equilibrium Cr-species over $Cr(OH)_3$(am) were calculated using EQ3 simulations and compared to measured data reported by Rai et al. (2004 [DIRS 179582]). There is excellent agreement among the compared data, which was generated using the *data0.pce* (Output DTN: SN0703PAEBSPCE.006), *data0.ymp.R5* (DTN: SN0612T0502404.014 [DIRS 178850]), and the literature values for pH above approximately 6 (Figure 6.2-4). The mononuclear hydrolysis species that dominate the solubility above approximately pH of 6 match well. The calculated aqueous Cr^{3+} species that dominates solubility below approximately pH of 6 are less adequately representative of the experimental data. This may be due to experimental limitations in that pH range (Rai et al. 2004 [DIRS 179582]). However, the updated Cr-system in the *data0.pce* database (Output DTN: SN0703PAEBSPCE.006) provide an accurate assessment of chromium solubility in the sensitivity studies presented in Section 6.8 over the relevant pH range of 6.5 to 9.5.

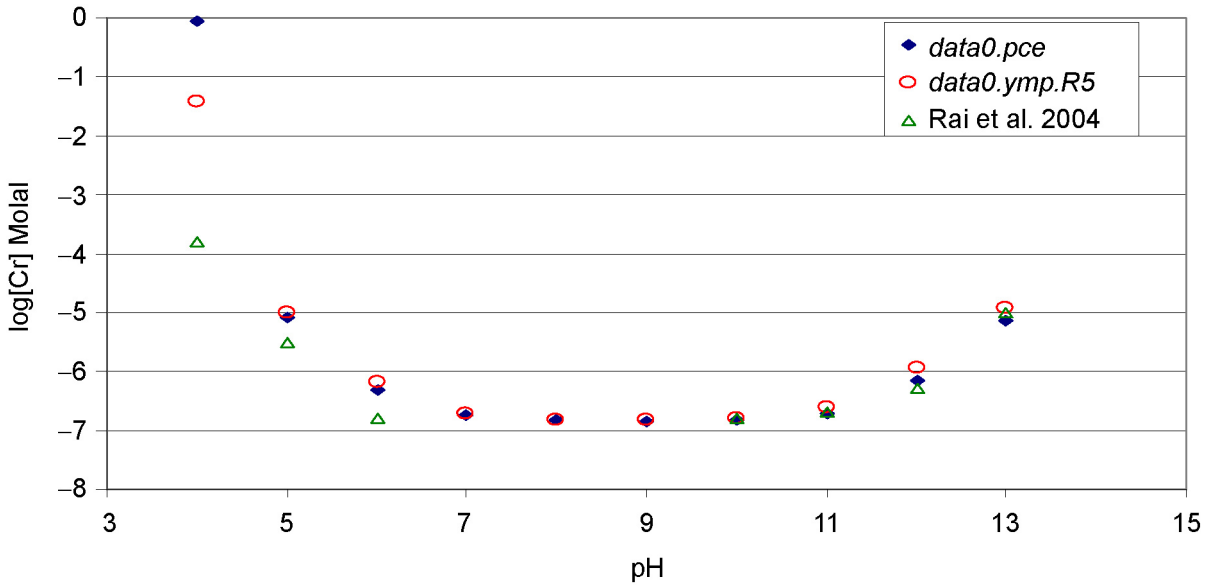

Source: Output DTN: SN0705PAEBSPCE.010.

Figure 6.2-4. Modeled vs. Measured Aqueous Equilibrium Chromium Solubility over $Cr(OH)_3$ Amorphous Solid

The *data0.ymp.R5* database (DTN: SN0612T0502404.014 [DIRS 178850]) is the source of the thermodynamic data for "sanidine_high," "albite_high," and "anorthite" used to calculate the log(K) values for the "Alkali_Feldspar" ($Na_{0.51}K_{0.46}Ca_{0.03}Al_{1.03}$ $Si_{2.97}O_8$) used by the NFC process model and the P&CE abstraction models (see discussion in Section 6.3.2 for justification of this alkali feldspar composition). There are several polymorphs of K- and Na-feldspar in the database; the high-temperature polymorphs were chosen as the source of the thermodynamic data because the alkali feldspar phase present initially most likely formed as the "high" phase, and while exsolution has occurred, the actual feldspar phases present have considerable solid solution, and exist as unmixed micron-to-nanometer-scale lamellae (e.g., "X-ray perthites") that are considerably more soluble than bulk phases of equivalent chemistry. The "high" phases of the feldspars have the highest solubility. The calculation of the log(K) grid for the alkali feldspar is archived in Output DTN: SN0703PAEBSPCE.006.

The *data0.ymp.R5* database (DTN: SN0612T0502404.014 [DIRS 178850]) is the source of the thermodynamic data for clinoptilolite-Ca, clinoptilolite-K, and clinoptilolite-Na used to calculate new log(K) values for these phases used by the NFC process model and the P&CE abstraction models. In order to allow the precipitation of clinoptilolite in these models, the trace quantities of iron in the original clinoptilolite data blocks had to be removed. These calculations are archived in Output DTN: SN0703PAEBSPCE.006.

6.3 ENGINEERED BARRIER SYSTEM PHYSICAL AND CHEMICAL ENVIRONMENT CONCEPTUAL MODEL

The suite of submodels comprising the P&CE model provides information on the chemical environment in the drift through time. They evaluate changes in water chemistry as pore waters percolate downwards through the rock above the drift and provide potential seepage

compositions at the drift wall and ranges of in-drift gas compositions. The effects of in-drift processes of dilution and evaporation are then evaluated, and the compositions of solutions potentially contacting the waste package and drip shield, and solutions in the invert, are predicted.

6.3.1 Integrated Perspective on the Evolution of the Engineered Barrier System Physical and Chemical Environments

The EBS environments are important to repository performance to the extent that they help determine introduced materials degradation rates, the source term and transport rates for radionuclides, and the flux of fluids through the drift into the unsaturated zone (UZ). The drip shield and the waste package outer barrier are the principal performance-related engineered barrier components that initially prevent water contact with waste forms and determine fluid transport paths. The EBS chemical environment affects radionuclide solubility and colloid stability in the invert, which affect the mobile radionuclide source term for transport. Fluid transport paths and rates, coupled with the source term, determine radionuclide transport rates to the UZ.

The main purpose of this report is to evaluate the potential evolution of water chemistry in the near field and of the in-drift physical and chemical environment with respect to the important parameters that affect drip shield and waste package durability, and that control solubility and colloidal stability of radionuclides in the invert by:

1. Providing TSPA-LA the lookup tables for potential geochemical conditions on the waste package and drip shield, where concentrated brines could potentially form through the evaporation of seepage waters.

2. Providing TSPA-LA the means to evaluate the potential geochemical conditions that determine radionuclide solubility and colloidal stability in the invert.

Three models are used to evaluate the evolution of the EBS environment. The first is the NFC model, which evaluates the effect of the thermal pulse and of water–rock interactions on the evolution of percolating waters above the drift. It provides potential seepage water compositions at the drift wall, and also the in-drift CO_2 concentration, to the seepage dilution/evaporation and integrated invert chemistry abstraction models. The two abstraction models evaluate the evolution of the in-drift chemical environment, as a function of the potential seepage composition, the in-drift CO_2 concentration, and the degree of evaporation of dilution due to thermal-hydrologic and relative humidity changes over time. The effect of dust deposition on the waste packages is also evaluated. The IDPS report (SNL 2007 [DIRS 177411]) also discusses many of these same concepts and processes.

6.3.2 Near-Field Chemistry Model

The NFC process-level model utilized by the P&CE suite of models is developed and justified in this section. The NFC model evaluates the effect of water-rock interactions on the composition of water percolating downwards through the TSw above the drift. The NFC model provides (1) potential seepage water compositions at the drift wall, (2) the WRIP value, and (3) the range of in-drift pCO_2 values as a function of time. This information is provided for a suite of waste

package locations across the repository footprint, and a range percolation fluxes. Major feeds for the model are the *data0.pce* thermodynamic database (Output DTN: SN0703PAEBSPCE.006), ambient TSw pore-water and gas phase compositions, and mineralogy and rock properties for the repository host rock units.

6.3.2.1 General Conceptual Model

The overall conceptual model for near-field chemistry is depicted in Figure 6.3-1. As percolating water moves downward towards the repository it moves up a thermal gradient. The water interacts with minerals in the rock, maintaining equilibrium with calcite and amorphous silica, present in excess, and dissolving alkali feldspar, while precipitating out one or more secondary phases. The degree of feldspar dissolution is a function of the temperature at any location along the percolation path, and is calculated using a temperature-dependent dissolution rate. The dissolution rate was estimated for ambient conditions from the degree of alteration that the tuff has undergone since it erupted, 12.8 million years ago, and adjusted for temperature using literature data for the activation energy for feldspar dissolution. The general chemical effects of feldspar dissolution are an increase in Na^+ and K^+ in solution, while divalent ions such as Ca and Mg are sequestered into secondary minerals—clays and zeolites. Little evaporation or degassing occurs as the water moves up the thermal gradient, until it reaches a lower-saturation zone from which steam and gas can readily escape into the drift. Steam is transported axially to cooler zones and condenses. The "low saturation zone" is the drift and areas in the surrounding rock, including fractures connecting to the drift that are readily accessed by the in-drift atmosphere. Evaporation occurs at the boundary between the higher saturation area surrounding the drift and the lower saturation area, which will hereafter be referred to as the evaporation front. During the boiling period, this boundary corresponds to the boiling zone around the drift. At later times, it corresponds to the drift wall and fractures extending outward from the drift, close enough to be in gas-phase equilibrium with the drift. The pCO_2 in the drift is controlled by equilibrium with the water at the evaporation front. In addition, the pCO_2 may be diluted by water vapor during evaporation in the drift.

In the following sections, each of the major inputs and components of the NFC model are described, an example calculation is performed, and the results are evaluated within the context of the chemical reactions and mineralogical changes that the NFC model predicts.

6.3.2.2 Thermodynamic Database used by the NFC model

The NFC model uses the *data0.pce* database (Output DTN: SN0703PAEBSPCE.006), a modified version of the project database for concentrated solutions, the Pitzer database *data0.ypf.R2* (DTN: SN0609T0502404.012 [DIRS 179067]). Although the NFC model does not predict the existence of concentrated solutions, the Pitzer model is implemented to maintain consistency with the P&CE seepage dilution/evaporation abstraction model, to which the NFC model provides initial water compositions. As discussed in Section 6.2.6, the *data0.ypf.R2* database was modified for use by the NFC model by addition of a data block for a mixed Na-K-Ca alkali feldspar phase, and by modification of several zeolite phases to allow them to precipitate in the absence of Fe, which is not included in the NFC model. Additional modifications to the *data0.pce* database (Output DTN: SN0703PAEBSPCE.006) are discussed in Section 6.2.6.

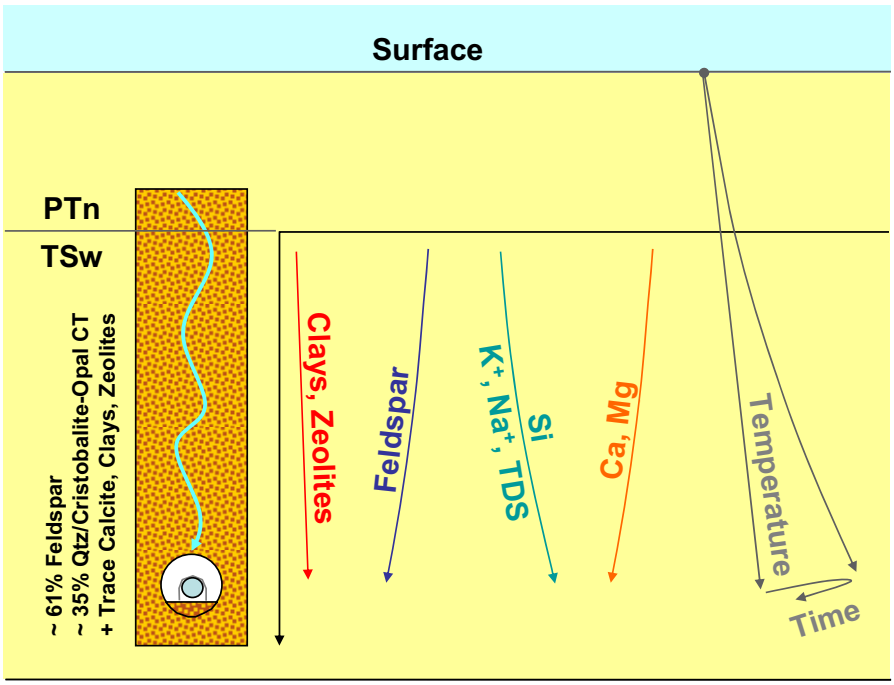

Figure 6.3-1. General Conceptual Model for Near Field Chemistry

The choice of composition for the alkali feldspar phase used by the NFC model (and subsequently by the P&CE abstraction models) is based on the average normative composition for the four TSw repository host units, as calculated from compositional data in DTN: GS000308313211.001 [DIRS 162015], using the same method used by Peterman and Cloke (2002 [DIRS 162576], Table 5 in the erratum). These calculations are documented and corroborated by a hand calculation, and are archived in Output DTN: SN0705PAEBSPCE.009. The average normative composition contains close to equal amounts by weight of albite (28.6 %) and orthoclase (29.7%) with small quantities of anorthite (1.9%) (Output DTN: SN0705PAEBSPCE.009). This average normative composition is consistent with the total feldspar present in the TSw, as determined by X-ray diffraction analyses, which averages approximately 60% feldspar (Table 4.1-9). Alkali feldspars form a complex solid solution at elevated temperatures, but not at low temperatures; exsolution occurs by spinodal decomposition when the coherent solvus is intersected, at about 570°C for alkali feldspar with nearly equal amounts of Na and K (Yund 1983 [DIRS 179304], Figure 1). Hence, alkali feldspar phenocrysts that form within a magma chamber, or form in the tuff matrix at elevated temperatures, may be present initially as a single phase, but will unmix as the tuff cools, with K-rich (>Or_{37}, sanidine) and Na-rich (<Or_{37} anorthoclase) cryptoperthitic layers segregating out. The degree of unmixing and the composition of the K- and Na-rich lamellae that form are a function of the cooling rate. X-ray diffraction studies (Bish and Vaniman 1985 [DIRS 101196]) have determined that alkali feldspars in the Topopah Spring Tuff have unmixed; however, the degree of unmixing and the composition of the unmixed lamellae have not been determined. The following two quotes summarize the state of knowledge:

> In many tuff samples, there are at least four separate feldspar species, present: groundmass and phenocryst feldspar, both of which have exsolved an additional feldspar. The resultant diffraction pattern is so complex that it is usually

> difficult to determine the exact nature of the individual feldspar phases. (Bish and Vaniman 1985 [DIRS 101196], p. 5)

and

> Our new peak-decomposition technique allows greater precision to be obtained in feldspar, cristobalite and tridymite analyses, although feldspars exhibit exceptionally large amounts of crystalline solution and sample-to-standard variability. (Bish and Vaniman 1985 [DIRS 101196], p. 6)

Even if the exact composition of the exsolved phases were known, the lamellae are so fine they are not visible with an optical microscope (e.g., the feldspars are "X-ray perthites"). Because of strain associated with structural mismatches between the two finely interlayered phases, neither would exhibit the thermodynamic properties of bulk mineral phases. Therefore, the NFC model adopts a single alkali feldspar composition, $Na_{0.51}K_{0.46}Ca_{0.03}Al_{1.03}Si_{2.97}O_8$, based on the normative analysis documented in Output DTN: SN0705PAEBSPCE.009, and on the abundances determined by X-ray diffraction analysis (Table 4.1-8), and calculates thermodynamic properties assuming mechanical (physical) mixing of end-member phases as a modeling simplification.

6.3.2.3 Starting Pore-Water Compositions

The starting point for evaluating potential water compositions in the near field is the composition of ambient pore waters in the TSw. The available pore-water data from the four repository host units (Tptpul, Tptpmn, Tptpll, Tptpln) were evaluated and grouped into four compositional groups. This analysis is documented in Section 6.6. Representative waters for the four groups were selected statistically, by choosing the sample closest to the centroid of the group. The representative waters and their compositions are listed in Tables 4.1-2 and 4.1-3.

It is likely that the majority of downward flow through the TSw represents fracture flow, because fracture permeabilities are much higher than the matrix permeability. The use of matrix pore water compositions as starting waters for the NFC model is justified, however, because multiple lines of evidence show that fracture waters equilibrate rapidly with the matrix pore waters (relative to downward transport rates), even though no fracture water compositions have been measured directly. This evidence comes from modeling of UZ flow and transport processes using the finite element heat and mass transfer code FEHM, which explicitly models matrix-fracture transport and matrix diffusion, and from water and mineral isotopic data collected at Yucca Mountain.

The FEHM code is used to calibrate the plug flow implementation of the NFC model, as described in Section 6.3.2.4.4. The FEHM model domain included the four TSw repository host rock units, each with the hydraulic and capillary properties taken from the calibrated rock properties set developed by the UZ flow model (SNL 2007 [DIRS 180016], Section 2.3.2), which are derived from field-based measurements of rock porosities and ambient rock saturations. The FEHM simulations were performed at percolation fluxes ranging from 1 mm yr^{-1} to 100 mm yr^{-1}. Prior to calibration of the plug flow results to the FEHM results, median breakthrough times for the two methods varied by no more than 15%. Also, regardless

of whether the particles were initially injected into the fractures or the matrix in the FEHM simulations, the predicted breakthrough curves were virtually identical. Both of these results indicate that, for the parameter values in the UZ calibrated rock properties set, matrix-fracture interactions are rapid relative to downward transport, and assuming that fracture and matrix pore waters are in equilibrium is reasonable.

The Sr isotopic compositions of fracture-lining calcite from the TSw also support rapid matrix-fracture equilibration. The calcite displays a microstratigraphy, with $^{87}Sr/^{86}Sr$ ratios that systematically increase from the earliest-deposited to the outermost layers (Paces et al. 2001 [DIRS 156507]), with the outermost layers of the calcite having $^{87}Sr/^{86}Sr$ values similar to those of the present-day matrix pore waters. This trend reflects precipitation from water in isotopic equilibrium with matrix pore waters (Marshall and Futa 2001 [DIRS 156503]). The isotopic signature of the matrix pore waters reflects incorporation of Sr released by dissolution of the rhyolitic tuff matrix, the $^{87}Sr/^{86}Sr$ ratio of which changed significantly through time, because of the relatively Rb-rich, Sr-poor composition of the unit. Thus, the calcite Sr-isotopic data indicate that matrix and fracture waters in the TSw are in isotopic, and therefore chemical, equilibrium.

Uranium-series isotopic data also indicate fracture-matrix water equilibrium. Gascoyne et al. (2002 [DIRS 154800]) examined fractured tuff samples from the Sundance and Drill Hole Wash fault zones intersected in the ESF and unfractured tuff samples from the Enhanced Characterization of the Repository Block (ECRB). They found that both exhibited equivalent whole-rock deficiencies of ^{234}U relative to ^{238}U, indicating that fracture rock does not represent a "fast path" with respect to transport. Fractures could still represent preferred flow pathways, however, if equilibration between matrix and fracture waters is rapid relative to downward flow.

Uranium isotopic data from fracture minerals provide more evidence of extensive matrix-fracture interactions (Paces et al. 2001 [DIRS 156507]). $^{234}U/^{238}U$ isotopic data indicate that deposition of opal and calcite in UZ fractures was a continuous rather than an intermittent process, with a long-term, stable source of ^{234}U being provided to the fracture waters. The fracture minerals exhibited no pedogenic signature with respect to uranium isotopes, suggesting that complete equilibration between matrix and fracture waters had occurred prior to reaching the depths from which the mineral samples were collected. Paces and Neymark (2004 [DIRS 174513]) note that deep UZ pore waters exhibit the same degree of uranium isotopic disequilibrium as that measured for fracture minerals (and presumed fracture waters) and for the perched waters at the base of the TSw. Because matrix waters percolate very slowly though the rock, and are exposed to large mineral surface areas relative to fracture waters, which only contact the fracture surface, the matching U isotopic signatures indicate rapid diffusive/advective equilibration of matrix and fracture waters.

Thus, both FEHM modeling of flow and transport using the UZ calibrated properties set (Section 6.3.2.4.4), and field measurements of water and mineral isotopic data, indicate rapid equilibration of matrix and fracture waters relative to downward transport, and support the use of matrix pore water compositions as starting waters for the NFC model.

Prior to using these pore-water compositions, they were modified; missing component concentrations in Table 4.1-3 were estimated using the EQ3/6 thermodynamic speciation and solubility software code and the *data0.pce* database (Output DTN: SN0703PAEBSPCE.006).

This database is a slightly modified version of the *data0.ypf.R2* database (DTN: SN0609T0502404.012 [DIRS 179067]), as described in Section 6.2.6. The general approach is to charge balance the waters with H^+, while fixing the bicarbonate concentration to be in equilibrium with a pCO_2 of 10^{-3} bars, a value representative of the in situ pCO_2 at the repository level. This value is based on CO_2 concentrations near 1,000 ppmv measured in repository units in the ESF (DTN: LB0208ISODSTHP.001 [DIRS 161638]) and in borehole UZ-1 (Yang et al. 1996 [DIRS 100194], p. 43). The temperature of equilibration was 23°C, rounded to two significant digits from 23.4°C (Section 4.1.7). Aluminum concentrations were estimated by fixing the Al concentration to be in equilibrium with alkali feldspar ($Na_{0.51}K_{0.46}Ca_{0.03}Al_{1.03}Si_{2.97}O_8$), the most abundant aluminosilicate in the tuff. For the Group 4 representative water, the aqueous silica concentration was calculated assuming equilibrium with SiO_2(am). These EQ3 simulations are archived in Output DTN: SN0701PAEBSPCE.002.

The resulting water compositions are slightly supersaturated with respect to calcite, as well as with several different aluminosilicates. Supersaturation with respect to calcite when the pCO_2 is fixed to 10^{-3} bars is characteristic of the waters affected by microbial activity (this is a conclusion of the pore-water screening analysis, which is described in Section 6.6 and may be an artifact of that process, even though these waters were selected to be minimally affected by microbial processes). Prior to using the calculated water concentrations, the pickup files generated by the EQ3 simulations were attached to EQ6 input files, and supersaturated phases were allowed to precipitate, while holding the pCO_2 constant at 10^{-3} bars. Calcite and very small amounts of stellerite (10^{-9} to 10^{-11} moles), the solubility-limiting phase with respect to aluminum, precipitated in all four cases, and SiO_2(am) precipitated from the four group waters. It was recognized that equilibrating with alkali feldspar would result in supersaturation with respect to another aluminosilicate (see the discussion in Section 6.3.2.2), but, because precipitation of a few nanomoles of aluminosilicate has no effect on the concentration of any component except for Al, this approach was considered less arbitrary than initially assuming equilibrium with any given secondary mineral phase. Hence, the assumption of equilibrium with alkali feldspar is sufficient for the intended purpose of setting an initial concentration for Al in solution, even though it results in a slight degree of supersaturation. The EQ6 pickup files produced represent the starting waters for all further simulations. The EQ6 input/output files are archived in Output DTN: SN0701PAEBSPCE.002.

6.3.2.4 Water–Rock Interactions

A major process affecting pore water as it percolates through the rock is interaction with the minerals in the tuff. Primary silicate minerals such as silica polymorphs and alkali feldspar dissolve, releasing components into solution, which in turn affects whether secondary minerals such as calcite, opal, clays, and zeolites, dissolve and precipitate. These water–rock interactions modify the water composition as it percolates downward. Because heating within the PTn is limited, any change in the degree of water–rock interaction relative to the ambient case in the Paintbrush Tuff non-welded unit (PTn) is minimal and only water–rock interactions in the TSw unit will be considered. By far the most abundant minerals in this unit are silica polymorphs (quartz, tridymite, cristobalite/opal-CT), accounting for 30% to 40% of the total, and alkali feldspar, accounting for approximately 60% of the total (Section 6.3.2.2). Alteration phases, zeolites, clays, opal and calcite are minor constituents.

6.3.2.4.1 Treatment of Calcite and Silica Polymorphs

Modeling water–rock interactions requires deciding how to treat each of these minerals. Calcite is a widely distributed phase in the fractures, comprising between 0.01% and 0.41% of the total rock mass in the four repository units (BSC 2004 [DIRS 170003], Table 6-2). Also, it precipitates as pore waters percolate downwards towards the drift and heat up, because of the inverse solubility of the mineral (Langmuir 1997 [DIRS 100051], p. 205). Hence, it is likely to be present throughout the system to be modeled. Although some components in solution can inhibit calcite precipitation if present in high concentrations, in general, calcite precipitates and dissolves readily. Hence, because it is present throughout the system, and its precipitation/dissolution is not usually kinetically controlled, calcite is treated as being present, and at equilibrium, with the waters at all times. This is consistent with the general observation that calcite is at saturation in geothermal systems (Figure 6.3-2).

The appropriate treatment of silica is less clear. Several silica phases are present in the Topopah Spring Tuff, including quartz, tridymite/cristobalite, and opal. Ambient pore waters in the repository host rock units contain about 50 μg/ml SiO_2(aq) (Table 4.1-3), but EQ3 thermodynamic simulations show that this concentration is too high to be in equilibrium with quartz or cristobalite, and less than that required to be in equilibrium with amorphous silica (see EQ3 simulations for Group 1, 2, and 3 representative pore waters in Output DTN: SN0701PAEBSPCE.002; Group 4 water had no measured silica value). General trends in low-temperature (<100°C) geothermal waters indicate that this is a typical condition (Figure 6.3-3). In the NFC model, percolating waters are treated as being in equilibrium with SiO_2(am). While this treatment potentially results in slightly high aqueous silica concentrations, it is justified because dissolution of amorphous silica has little effect on pH, in the likely range of pH values encountered in this system, and dissolved silica does not interact significantly with most other species in solution. Clay and zeolite precipitation is limited by Al concentrations in solution, which are many orders of magnitude lower than silica. Only aqueous Mg concentrations are significantly affected by aqueous silica concentrations, through precipitation of amorphous/crystalline sepiolite or amorphous antigorite. Even ambient silica concentrations are sufficient to limit Mg concentrations by precipitation of Mg-silicates, and silica concentrations can only rise with increasing temperature (silica phases do not exhibit inverse solubility). While silica concentrations could potentially affect the dissolution rate of alkali feldspar by driving up the saturation index with respect to this species, this effect is negligible because precipitation of zeolites, clays, and/or end-member feldspars limits the concentration of other alkali feldspar components in solution, preventing the alkali feldspar from approaching saturation.

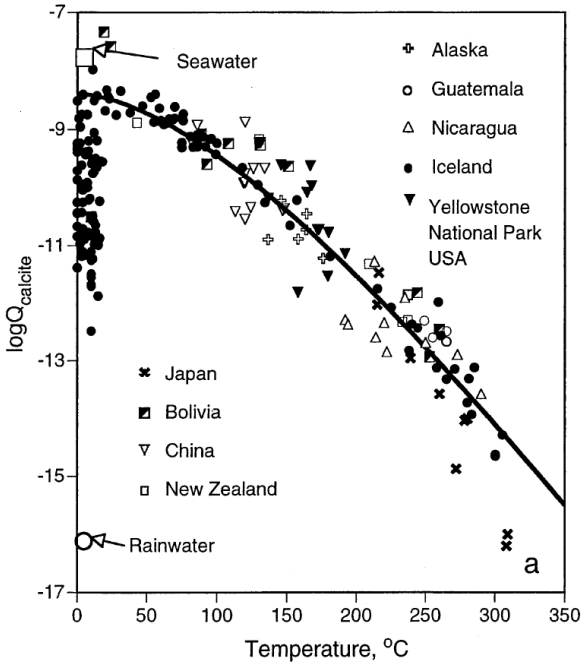

Source: Stefansson and Arnorsson 2000 [DIRS 153578], Figure 4a.

Figure 6.3-2. Comparison of Predicted Calcite Solubility Curve with Water Compositional Data from Several Geothermal Fields

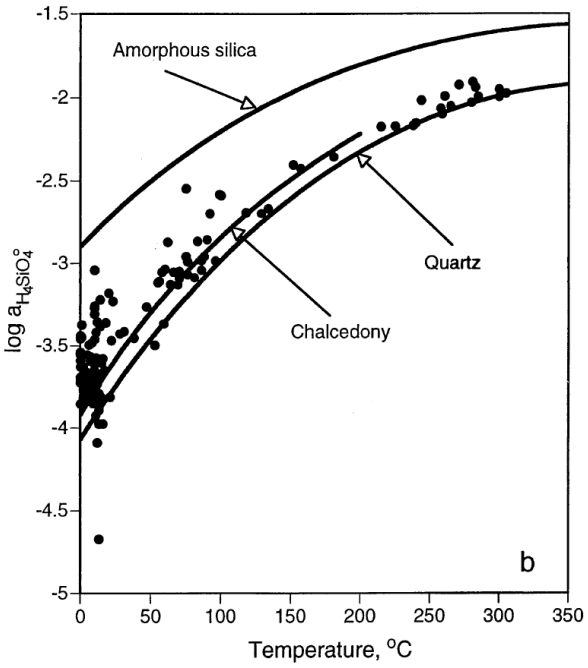

Source: Stefansson and Arnorsson 2000 [DIRS 153578], Figure 4b.

Figure 6.3-3. Comparison of Predicted Silica Polymorph Solubility Curves with Water Compositional Data from Several Geothermal Fields

6.3.2.4.2 Treatment of Alkali Feldspar

Alkali feldspars are the most abundant phases in the tuff. A single feldspar composition ($Na_{0.51}K_{0.46}Ca_{0.03}Al_{1.03}Si_{2.97}O_8$) is used in this model, for reasons described in Section 6.3.2.2. The thermodynamic data for this solid solution phase was derived from that for "sanidine_high" and "albite_high" in *data0.ymp.R5* (DTN: SN0612T0502404.014 [DIRS 178850]), assuming the two phases form a mechanical mixture of end-member phases (Section 6.2.6) (i.e., no entropy of mixing was included). These calculations are documented in spreadsheet *Solids_j_Alkali_Feldspar_KBH.xls* in Output DTN: SN0703PAEBSPCE.006.

As discussed in Section 6.3.2.2, alkali feldspars in the TSw are solid solutions (Bish and Vaniman 1985 [DIRS 101196], p. 6). Volcanic alkali feldspars are undersaturated in groundwaters and geothermal waters (Stefansson and Arnorsson 2000 [DIRS 153578], p. 2575) for two reasons. First the high-temperature disordered forms are more soluble than the lower temperature polymorphs. Second, volcanic feldspars exhibit considerable solid solution, and the mixed phases have higher solubilities than the pure feldspar end-members. In EQ3 simulations with Yucca Mountain groundwaters and the *data0.pce* database (Output DTN: SN0703PAEBSPCE.006), setting Al concentrations to be in equilibrium with an alkali feldspar solid solution results in supersaturation with respect to several zeolite and clay phases, and with respect to K-feldspar and albite. Hence, pore waters can never be saturated with respect to alkali feldspar, and dissolution of this phase must be treated as a kinetically limited process, as opposed to an equilibrium process.

In order to do this, a dissolution rate for the feldspar must be assigned. The common approach for quantifying mineral dissolution rates generally requires using pure mineral dissolution rates developed in laboratory experiments, and then estimating available mineral reactive surface areas. However, laboratory-derived mineral dissolution rates have been shown to be up to several orders of magnitude higher than field-measured dissolution rates (White 1995 [DIRS 179312], Table 7). In addition, estimating mineral reactive surface areas is difficult. Two commonly used approaches are to estimate the surface area geometrically, and to use measured gas adsorption (Brunauer-Emmett-Teller, or BET) surface area data. However, no measurements of gas adsorption surface areas are available for the tuff, and mineral grain surface areas estimated through geometric calculations are generally one to three orders of magnitude lower than measured gas adsorption surface areas (White 1995 [DIRS 179312], Figure 8), due to surface roughness and internal porosity. Rather than using laboratory-derived mineral dissolution rates which may not be relevant to the in situ system, and attempting to quantify mineral surface areas, for this model, a feldspar dissolution rate was estimated for ambient conditions from Yucca Mountain-specific mineralogic data. This rate is calculated from the observed abundances of Al-containing alteration products—clays and zeolites—in the repository units. Because these units are entirely devitrified (Vaniman et al. 1996 [DIRS 105946], v. 1, Section 3, p. 2), feldspar dissolution is the only possible source for the Al in these phases, and the very low solubility of Al in neutral groundwaters ensures that Al is conserved in the solid phases, and is not significantly removed in aqueous form. Hence, the Al mass balance allows the calculation of an average ambient feldspar dissolution rate, over the age of the Topopah Spring Tuff, from the alteration phases. This value is a maximum because, as discussed in Section 6.12.2.1, much of the alteration occurred at elevated temperatures (Levy and O'Neil

1989 [DIRS 133364]). The steps used to calculate the ambient dissolution rate for alkali feldspar are described below.

The average abundance of smectite clays and zeolites in each of the four repository units is tabulated in Table 6-2 of *Heat Capacity Analysis Report* (BSC 2004 [DIRS 170003]) and are shown in Table 4.1-9 of this report. Converting these to mole fractions and using Al as a conserved species, the observed alteration assemblage requires that 7.6×10^{-2} moles of alkali feldspar per kilogram of tuff have dissolved. Given that the age of the Topopah Spring Tuff is 12.8 Ma (Sawyer et al. 1994 [DIRS 100075]), this yields a dissolution rate of 5.94×10^{-9} mol yr^{-1} kg $tuff^{-1}$. These calculations are documented in Output DTN: SN0703PAEBSPCE.006 (spreadsheet: *feldspar dissolution rate calculations.xls*, worksheet: "diss. rate from mineralogy").

The water:rock ratio (the mass of rock in contact with 1 kg of water, the default mass of water present in an EQ3/6 simulation) is based on estimates of fracture and matrix porosity for the four repository units (Table 4.1-5), and the grain density and saturation for these units, listed in Table 4.1-6. Weighted averages of these parameters were used (see Section 6.12.2.2.1 for a discussion of the averaging method used for each parameter). Assuming an average unit porosity of 0.139 and an average total saturation of 0.798 (Output DTN: SN0703PAEBSPCE.006, spreadsheet: *Feldspar dissolution rate calculations.xls*, tab: "Water:rock ratio"), then:

$$\text{Volume water per liter substrate} = \text{Sat.} \times \theta = 0.798 \times 0.139 = 0.111 \text{ liters} \quad \text{(Eq. 6.3-1)}$$

where Sat. is the average total saturation and θ is the average unit porosity, and

$$\text{Volume of rock containing one liter of water} = 1 / 0.111 = 9.00 \text{ liters.} \quad \text{(Eq. 6.3-2)}$$

The grain volume present per liter water is:

$$\text{Grain volume} = 9.00 \times (1 - 0.139) = 7.75 \text{ liters} \quad \text{(Eq. 6.3-3)}$$

The mass of rock in contact with one liter of water as it percolates downward can be calculated from the grain density (2.526 kg $liter^{-1}$, from Output DTN: SN0703PAEBSPCE.006, spreadsheet: *feldspar dissolution rate calculations.xls*, tab: "diss. rate from mineralogy") as:

$$\text{Mass of rock in contact with one liter water} = 7.75 \times 2.526 = 19.6 \text{ kg liter}^{-1} \quad \text{(Eq. 6.3-4)}$$

Using these inputs, under the ambient case, each liter of water in the rock is in contact with 19.6 kg of rock. Assuming that all secondary minerals formed under ambient conditions, the ambient alkali feldspar dissolution rate would be 3.68×10^{-15} moles $liter^{-1}$ sec^{-1}. This value is derived by multiplying the dissolution rate determined from mineralogy by the water:rock ratio and then converting from years to seconds:

$$5.94 \times 10^{-9} \text{ mol yr}^{-1} \text{ kg tuff}^{-1} \times 19.6 \text{ kg liter}^{-1} \div (365 \text{ d/yr} \times 24 \text{ hr/d} \times 60 \text{ min/hr} \times 60 \text{ s/min}) = 3.68 \times 10^{-15} \text{ moles liter}^{-1} \text{ sec}^{-1} \quad \text{(Eq. 6.3-5)}$$

Thus, the alkali dissolution rate utilized by the NFC model to calculate the WRIP does not rely on estimates of rock surface areas.

As discussed in Section 6.12.2.1, this value is not actually the ambient rate, as much of the alteration occurred under elevated temperature conditions early in the history of the tuff. However, as documented in Section 6.12.2.1, given knowledge of the thermal history of the tuff, it is possible to constrain the ambient feldspar dissolution rate to a range of values, the median value for which is 1.14×10^{-15} moles liter^{-1} sec^{-1}. This is the value that is used in the NFC model calculations of the WRIP (Output DTN: SN0703PAEBSPCE.006, Mathcad files located in folder: \WRIP calculations\Mathcad calculations of WRIP values).

Temperature-Dependence of the Alkali Feldspar Dissolution Rate—The dissolution of silicate minerals, including feldspars, in disequilibrium systems typically follow a zero-order (linear) kinetic rate law (Claassen and White 1979 [DIRS 105735]). Linear rate laws are observed when the specific wetted surface area, A_w (m^2/m^3), is assumed to be constant with time (Rimstidt and Barnes 1980 [DIRS 101708]). The empirical rate law is:

$$R = dC/dt = A_w k \quad \text{(Eq. 6.3-6)}$$

where C is the aqueous concentration of a mineral representative species and k is the rate constant in mol m^{-2} s^{-1}. Thus, assuming a constant surface area:

$$R=k[H^+]n[1 - EXP(\Delta G_{rxn}/\sigma RT)] \quad \text{(Eq. 6.3-7)}$$

where σ = average stoichimetric number of the reaction (1 for a first-order reaction), $[H^+]$ = proton activity, n = zero at neutral pH (approximately 1 at low pH), ΔG_{rxn} is the Gibbs energy of the dissolution reaction, R is the molar gas constant, and T is temperature in Kelvin (Rimstidt and Barnes 1980 [DIRS 101708]).

ΔG may also be expressed in terms of the saturation index (Rimstidt and Barnes 1980 [DIRS 101708]):

$$\Delta G_{rxn} = -RT\ln(K_{eq}/Q) \quad \text{(Eq. 6.3-8)}$$

where K_{eq} is the equilibrium constant and Q is the reaction quotient. Substituting for ΔG_{rxn} in Equation 6.3-7 yields:

$$R = k[H^+]n(1 - Q/K_{eq}) \quad \text{(Eq. 6.3-9)}$$

If $Q/K_{eq} \leq 0.05$ then Equation 6.3-9 reduces to $R = k[H^+]n$; if $Q/K_{eq} \geq 0.8$, then it reduces to $R = k[H^+]n(-\ln(Q/K_{eq}))$.

However, the effect of pH is minor across a wide range of conditions, from approximately pH 3 to 9, and can be ignored (see Lasaga et al. 1994 [DIRS 106466], abstract; Helgeson et al. 1984 [DIRS 140382], Figure 24), yielding:

$$R = k[1 - Q/K_{eq}] \quad \text{(Eq. 6.3-10)}$$

Far from equilibrium, R = k, while at saturation, R = 0. Therefore, in this system where alkali feldspar will be far from equilibrium, no impact of changing saturation index on alkali feldspar dissolution rate is expected.

Temperature dependence of the rate constant for feldspar dissolution may be expressed as an Arrhenius relationship (Lide 2000 [DIRS 162229], p. 5-106):

$$k = k_1 \, EXP[-E_a/R(1/T - 1/296.55 \, K)] \quad \text{(Eq. 6.3-11)}$$

where k_1 is the ambient rate, E_a is the activation energy, R is the molar gas constant and T is temperature expressed in K, and 296.55 K is the ambient case. The temperature effect on feldspar dissolution is discussed in detail below.

The reaction rate constant can be related to T(K) by the Arrhenius equation:

$$k = A \, EXP(-E_a/RT) \quad \text{(Eq. 6.3-12)}$$

where A is a T-independent constant. This expression can also be written:

$$\ln(k) = \ln(A) - E_a/RT \quad \text{(Eq. 6.3-13)}$$

Thus, if the Arrhenius relation is obeyed then a plot of ln(k) vs. 1/T is a straight line with the slope = $-E_a/2.303R$ (Figure 6.3-4).

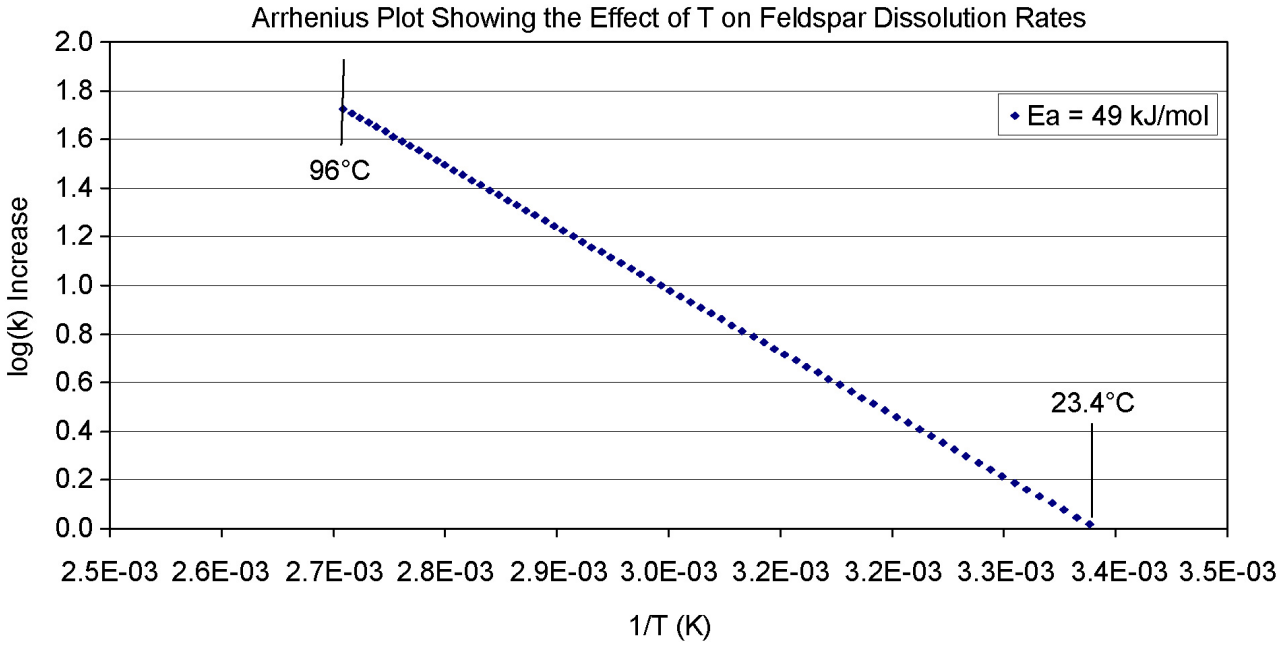

Source: Output DTN: SN0703PAEBSPCE.006.

NOTE: The slope is equivalent to $-E_a/2.303R$.

Figure 6.3-4. Change in the log of the Rate Constant (k) as a Function of the Inverse of the Reaction Temperature (K)

For a T increase from T_1 to T_2, and taking the natural log of the Arrhenius expression:

$$\ln(k_1) = \ln(A) - E_a/(RT_1) \text{ and } \ln(k_2) = \ln(A) - E_a/(RT_2) \quad \text{(Eq. 6.3-14)}$$

Taking the difference and combining to get the typical expression for the T dependence:

$$\ln(k_1/k_2) = E_a/R\,[1/T_2 - 1/T_1] \quad \text{(Eq. 6.3-15)}$$

One may then calculate the increased dissolution rate as follows:

$$k_2 = k_1\,\mathrm{EXP}(-E_a/8.31441 \times ((1/T_2) - (1/296.55))) \quad \text{(Eq. 6.3-16)}$$

where k_1 is the ambient rate, and the ambient temperature is assumed to be 23.4°C (296.55 K). The ambient alkali feldspar dissolution rate was determined, as described previously in this section, to be 1.14×10^{-15} moles liter^{-1} sec^{-1} (expressed in terms of liters water, instead of mass tuff or feldspar surface area).

The activation energy for dissolution was derived from published values in the following manner: (AVE Albite E_a + AVE K-feldspar E_a)/2 at neutral pH, rounded to two significant digits, is 49,000 J/mol (Blum and Stillings 1995 [DIRS 126590], pp. 291 to 351, Table 2). The tiny contribution of anorthite to this calculation is ignored because no relevant activation energies for anorthite dissolution were found in the literature.

The modeling choice of a single, averaged activation energy was made to maintain consistency with the use of a single-phase feldspar by the NFC model. If separate E_a values were assigned to the component end-members, then as temperature increases, the ratio of Na-K-Ca would change because the end member Ea values range widely (Blum and Stillings 1995 [DIRS 126590], Table 2). Instead, an averaged value is adopted for use in this report calculated from the end-member data as described above and qualified for intended use by corroboration with other published data in Section 4.1.13.

It is important to note that the slope of the line in the Arrhenius plot (Figure 6.3-4) is not a function of the ambient rate, but only of the activation energy. An E_a value of 49 kJ/mol is used here for alkali feldspar dissolution, calculated from published data for albite and orthoclase. Using this value, the alkali feldspar dissolution rate will increase by approximately 1.7 log units as the temperature increases from approximately 23°C to the boiling point at the repository level (96°C) (see Figure 6.3-4). A rate at any temperature can be calculated by the Arrhenius relationship. These rates are not insignificant, especially the higher temperature rate, because of the long contact times, and the low water:rock ratios.

The actual amount of alkali feldspar that will dissolve is a function of the transport time and the temperature profile the water experiences along the flow path to the drift. To determine this, it is necessary to model the thermal gradient above the drift through time, and to determine the temperature profile encountered by water as it percolates slowly downward to the drift crown.

6.3.2.4.3 Modeling the Evolution of the Thermal Field

Because of the time required for percolation to occur, the instantaneous thermal gradient above the drift is not representative of the temperature profile that a packet of water would experience as it percolates downward to the drift. However, if thermal profiles from the drift to the surface can be calculated for several points in time during the repository history, then the temperature along the flow path through time can be estimated.

The evolution of the thermal field through time was calculated using the method developed in *In-Drift Natural Convection and Condensation* (SNL 2007 [DIRS 181648], Section 6.3.5.1.1). The method uses a conductive-only heat loss solution, implementing a line source solution derived from the transient solution for a continuous point source in an infinite medium, as described by Carslaw and Jaeger (1959 [DIRS 100968], p. 261). The waste package heat decay curves are taken from *Total System Performance Assessment Data Input Package for Requirements Analysis for EBS In-Drift Configuration* (SNL 2007 [DIRS 179354], parameter 05-03). The solution for an infinite medium was modified by utilizing the method of images to hold the land surface, 300 m above the drift center, isothermal. The lower boundary condition remains an infinite extension of the homogeneous medium. Using the principle of superposition, the contribution from all 108 drifts, plus the natural geothermal gradient, is summed in calculating the thermal profile above the drift at each location evaluated. For the preclosure ventilation period, the analytical ventilation model used is from DTN: MO0701VENTCALC.000 [DIRS 179085] (spreadsheet: *Base Case Analysis Rev01.xls*, worksheet: "Ventilation Efficiency," case CSTR04). The contribution of the geothermal gradient is based on analysis of borehole temperature data from borehole SD-12 (DTN: GS031208312232.003 [DIRS 171287], file: *TEMPERATURE.txt*), as evaluated in Mathcad file *Geothermal gradient SD-12.xmcd* in Output DTN: SN0703PAEBSPCE.006. The NFC model assumes a repository depth of 300 m; the predicted geothermal gradient ranges from 17°C at the land surface to 23.4°C at the repository level. Note that, within the Mathcad files used to evaluate the geothermal gradient, the incorrect DTN for the temperature data is referenced (the referenced DTN is GS031208312232.008 [DIRS 178750]).

The model treats the stratigraphy from the repository as a single unit, with the thermal properties of the Tptpll rock unit. Rock properties—matrix and lithophysal porosity, and bulk density—are from DTN: SN0404T0503102.011 [DIRS 169129] (file: *ReadMe_Summary.doc*, Tables 7-10 and 7-11). The rock grain specific heat capacity is from DTN: SN0307T0510902.003 [DIRS 164196] (spreadsheet: *rock_grain_heat_capacity.xls*, worksheet: "Cp grain 25-325," Row 10, Column y, data for Layer 8, "Tptpll"). Wet and dry thermal conductivities are from DTNs: MO0612MEANTHER.000 [DIRS 180552] (mean values) and MO0702PAGLOBAL.000 [DIRS 179343] (10th and 90th percentile values). Thermal conductivities were calculated from wet and dry conductivities using rock saturation. Matrix saturation conditions can vary from a minimum value of 10% and 20% saturation (DTN: LB0207REVUZPRP.002 [DIRS 159672], workbook: *DATAfix_satsum.xls*, worksheet: "Summary"), up to fully saturated conditions. A value of 90.5% was chosen, to be consistent with the value used in *Thermal Management Flexibility Analysis* (SNL 2007 [DIRS 179196], Section 5.3) and in *Ventilation Model and Analysis Report* (BSC 2004 [DIRS 169862], Sections 6.9 and 6.11). The calculations were repeated three times, using sets of thermal conductivities corresponding to the 10th, 50th, and 90th percentile values.

The calculations were done in seven drifts located throughout the repository, at 16 locations through each drift. The locations of the drifts considered are shown in Figure 6.3-5. Thermal gradient profiles were generated at 41 points in time, from repository closure (50 years) to one-million years.

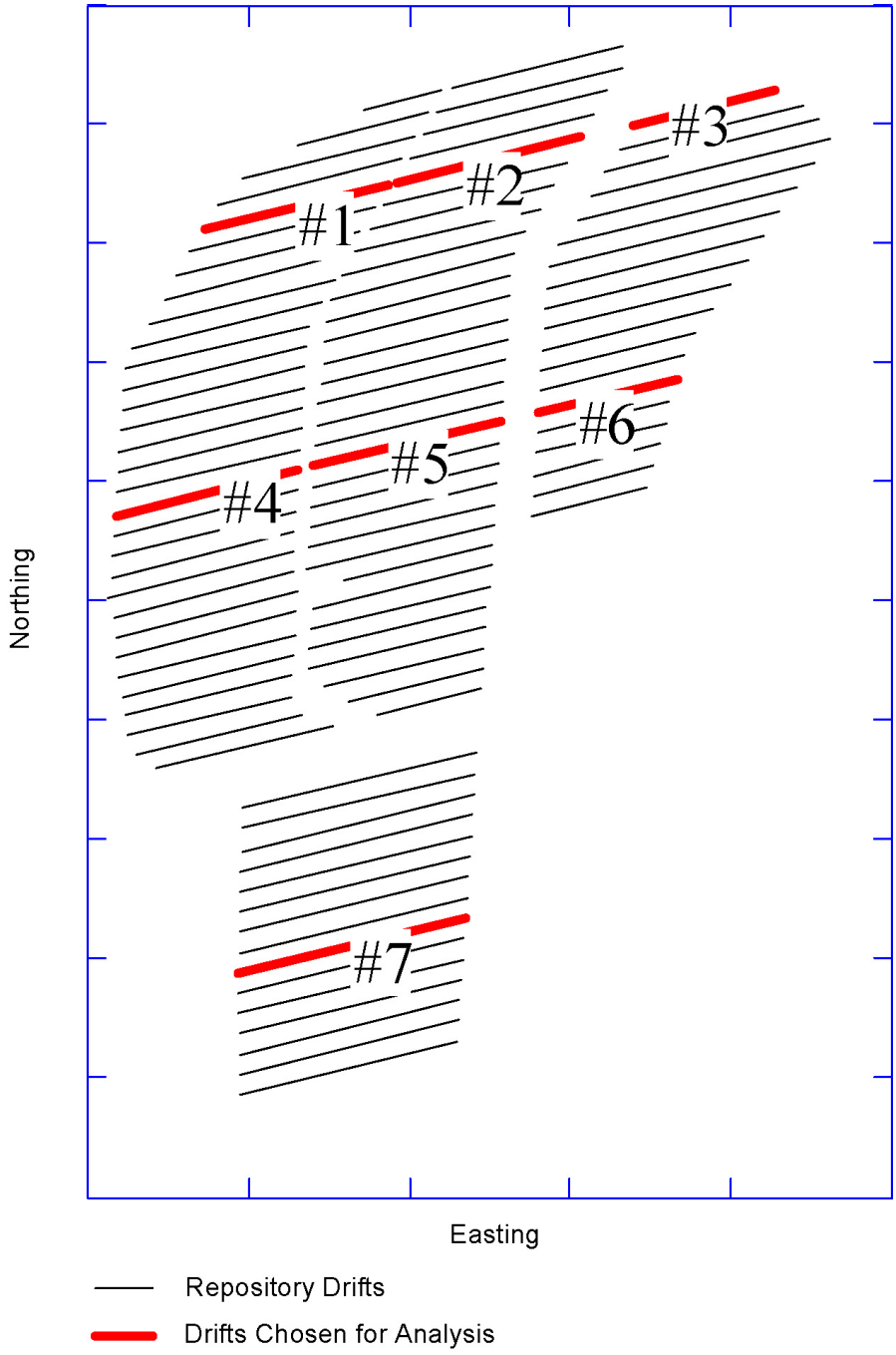

NOTE: Drifts defined on the basis of waste package end-point coordinates in SNL 2007 [DIRS 179354], parameter 02-01.

Figure 6.3-5. Representative Repository Drift Locations Selected for the NFC Model

An example of the results for one location and one set of rock thermal conductivity values is given in Figure 6.3-6. The thermal profiles initially exhibit a strong thermal gradient near the drift; over time as heat is conducted upwards, the gradient becomes more linear, with only a slight steepening near the repository wall. If the drift wall remains above the boiling temperature for several hundred years, as in this example, then a nearly stable gradient will evolve and persist until the end of the boiling period. Once the drift wall drops below boiling, the temperature gradient begins to decrease, while still being largely linear except for very close to the drift. Given sufficient time, the temperature gradient would evolve to the geothermal gradient at the repository, from approximately 17°C at the surface to 23.4°C at the repository level.

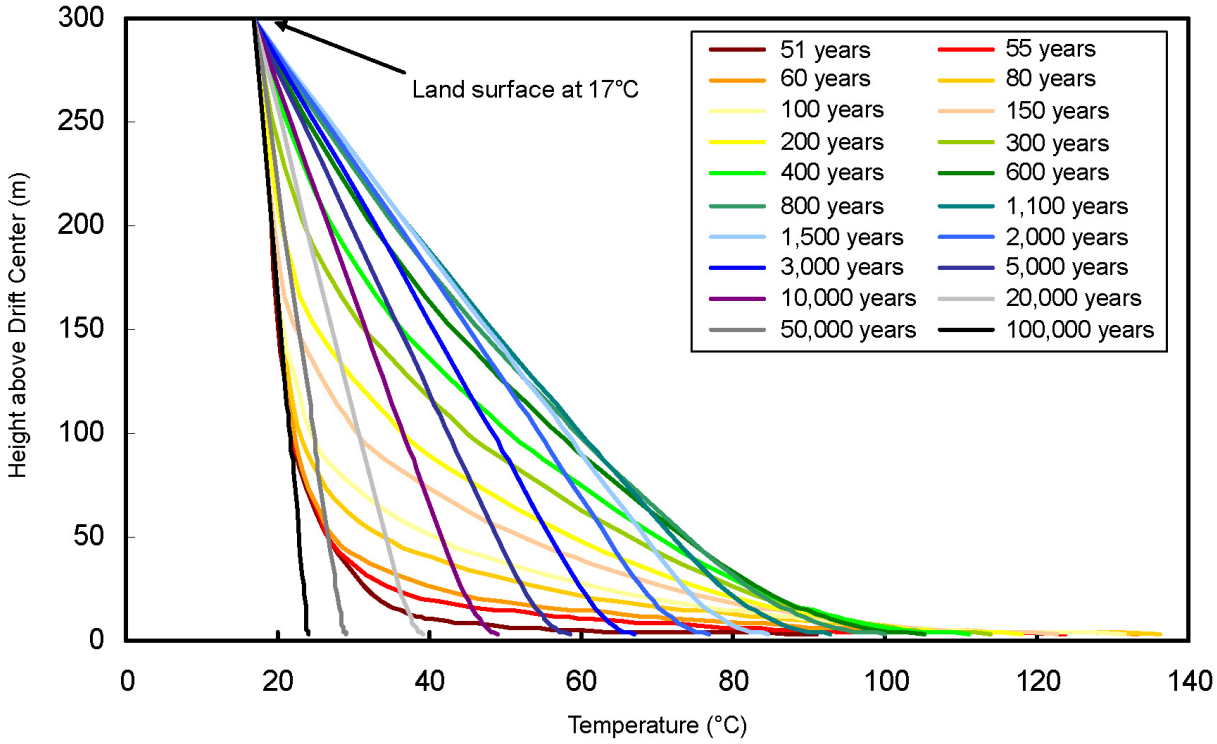

Source: Output DTN: SN0703PAEBSPCE.006, folder: \Figures, spreadsheet: *Figure, thermal profiles, mean, Drift 4, loc. 8.xls*.

NOTE: Values in legend are "years since loading and beginning of ventilation" (i.e., repository closure is at 50 years). In this simulation, the maximum drift wall temperature was 137°C at 70 years after loading (20 years after cessation of ventilation and closure), and the drift wall remained above boiling for 900 to 1,000 years. The land surface is 17°C at a distance of 300 m above the drift. These thermal profiles are for a location near the center of drift choice #4 (Figure 6.3-5), using the mean rock thermal conductivities.

Figure 6.3-6. Thermal Profiles above the Drift, through Time

The temperature profile encountered by a packet of water moving downwards to the drift does not resemble these thermal gradients, which represent the gradient at any single point in time, as the water takes a relatively long time to reach the drift, and the thermal gradient evolves. Hence, the water will follow a time-temperature path that crosses these instantaneous thermal profiles. However, that path can be calculated from the thermal profiles, by interpolating between the different profiles as a function of time and depth, with the two parameters being correlated by the percolation flux rate. The thermal profiles in Figure 6.3-6 extend to the land surface because they are calculated assuming that the temperature at the land surface is isothermal

(i.e., T = 17°C). Only that part of the profiles from 0 to 200 m above the drift are used in the NFC model. Figure 6.3-6 shows the complete thermal profiles for illustrative purposes only.

6.3.2.4.4 Modeling Flow through the Topopah Springs Welded Tuff (TSw)

Defining the flow path also requires modeling the flow velocity through the TSw. The NFC model determines flow velocities at any given flux by using an assumption of plug flow, and assuming a wetted porosity equal to the ambient condition. In this case, the transport time is equal to:

$$\text{Plug flow transport time, yr} = \text{Dist. traveled, m} \div \text{Velocity, m yr}^{-1} \qquad \text{(Eq. 6.3-17)}$$

where

$$\text{Velocity m yr}^{-1} = (\text{Perc. flux, mm yr}^{-1} \div 1{,}000) \times (1 \div (\text{Sat.} \times \theta)). \qquad \text{(Eq. 6.3-18)}$$

where saturation (Sat.) and porosity values (θ) are averages of ambient values for the four repository units (Tptpul, Tptpmn, Tptpll, and Tptpln; see Tables 4.1-5 and 4.1-6), weighted by the average thickness of each unit over the repository footprint from the geologic framework model (DTN: MO0012MWDGFM02.002 [DIRS 153777]) (see Section 6.12.2.1 for details).

The percolation flux values used in the NFC model range from less than 1 mm/yr to more than 100 mm/yr, and are based on fluxes at the PTn/TSw boundary predicted by the UZ transport model calibrated flow fields, archived in DTNs: LB0612PDPTNTSW.001 [DIRS 179150], LB0701MOPTNTSW.001 [DIRS 179156], LB0701GTPTNTSW.001 [DIRS 179153], and LB0702UZPTN10K.002 [DIRS 179332].

The NFC model incorporates the effects of varying percolation fluxes by evaluating the WRIP value using 20 different sets of percolation fluxes. Each set contains four climate-state-dependent fluxes, representing the present day (0 to 600 years), monsoonal (600 to 2,000 years), glacial transition (2,000 to 10,000 years), and post-10,000-year infiltration rates. The 20 sets of percolation fluxes represent values for each climate state, at 5% intervals of probability of occurrence, from 2.5 % to 97.5%.

The representative values were derived from UZ flow model maps of PTn/TSw percolation flux rates (mm yr^{-1}), which calculate fluxes at 2,042 locations for each of four infiltration maps (10th, 30th, 50th, 90th percentiles) and the four climate states. DTN sources for these data are listed in Section 4.1, Table 4.1-1. The calculation is archived in Output DTN: SN0703PAEBSPCE.006 (folder: \WRIP calculations\Percolation fluxes, spreadsheet: *Perc_Extraction_w_Post_10k_Rev02.xls*). First, the raw data from the DTN sources were imported into the spreadsheet (tab: "Raw Data"), then the percolation fluxes were extracted (tab: "Raw Data w Percentiles," columns A through P), and the Microsoft Excel PERCENTILE function was used to extract representative values for each climate state at intervals of 5% probability of occurrence, from 2.5% to 97.5% (tab "Raw Data w Percentiles," columns AH through AK). The results are tabulated for convenience, and a number (1 through 20) assigned to each flux set on tab "Results." The resulting percolation fluxes are given in Table 6.3-1.

Table 6.3-1. Summary of Percolation Fluxes, as a Function of Climate State and Probability of Occurrence

Percentile	All Present-Day	All Monsoon	All Glacial Transition	Post-10,000-Years
2.5	0.05	0.28	0.05	0.19
7.5	0.37	1.14	0.50	1.22
12.5	0.86	2.11	1.06	2.66
17.5	1.41	3.35	1.67	4.34
22.5	2.10	4.50	2.39	5.93
27.5	2.79	5.62	3.37	7.79
32.5	3.58	6.74	4.55	10.41
37.5	4.49	7.78	5.85	13.25
42.5	5.47	8.94	7.44	16.20
47.5	6.47	10.15	9.35	19.15
52.5	7.73	11.68	11.73	22.08
57.5	9.22	13.47	14.76	25.33
62.5	10.88	16.23	18.71	29.37
67.5	12.61	19.21	22.99	35.63
72.5	14.74	23.13	28.63	44.03
77.5	17.38	29.03	36.06	52.09
82.5	21.82	46.13	44.73	59.73
87.5	28.09	73.59	58.00	66.88
92.5	35.14	94.73	75.60	76.10
97.5	44.19	119.94	102.33	93.46

Source: Output DTN: SN0703PAEBSPCE.006.

NOTE: All values in mm/yr.

The use of a plug-flow model with averaged rock properties, assuming ambient saturation levels, is a simplification that does not consider that the different units in the TSw have different hydrologic properties, and that actual matrix and fracture saturations (and hence the rock capacity and water flow velocities) will be a function of the percolation flux. To evaluate the accuracy of this assumption with respect to flow rates and residence times, hydrologic simulations were performed using FEHM. The simulations were run for a location near the repository center, using the stratigraphic contacts from column "j34" of the primary calibration mesh of the 3-D UZ flow model (DTN: LB990501233129.004 [DIRS 111475], file: *primary.mesh*); the total distance from the PTn boundary to the repository is approximately 210 m at this location. Hydrologic properties for the TSw units (e.g., capillary properties) are from qualified project DTN: LB0610UZDSCP30.001 [DIRS 179180]. The simulations were run in particle-tracking mode, for five different percolation fluxes: 1, 3, 10, 30, and 100 mm/yr.

The results of the FEHM modeling are shown in Figure 6.3-7. The breakthrough curves are given in terms of concentration/initial concentration, C/C_o, versus time. As shown in the graph, transport times based upon the plug flow implementation are slightly faster than those predicted by the FEHM modeling, with the relative difference being greater at higher percolation fluxes. This is primarily due to the increase in matrix saturation in the FEHM model with increasing flux. Higher saturations mean that the rock capacity is higher, and transport times

correspondingly slower. The plug flow model uses the ambient saturation value at all fluxes and therefore produces slightly faster transport times.

The mean breakthrough times predicted by the FEHM model are compared to those calculated using the plug-flow approximation in Table 6.3-2. The mean breakthrough times were determined by fitting a normal distribution to the log-transformed breakthrough times and determining the mean and standard deviation on the data (Output DTN: SN0703PAEBSPCE.007, spreadsheet: *Transport time uncertainty.xls*). The resulting mean values vary only slightly from interpolated values for $C/C_0 = 0.5$. Although the differences between the FEHM mean values and the values calculated assuming plug flow are relatively minor, they have a significant effect on the calculated WRIP value under some conditions (see spreadsheet *Transport time uncertainty.xls* in Output DTN: SN0703PAEBSPCE.007).

Because the difference between the two models is significant with respect to the value of the WRIP, a correction was implemented. The percolation fluxes in Table 6.3-1 were adjusted to result in plug flow travel times that matched the FEHM results. This was done in the following manner: Equations 6.3-17 and 6.3-18 were rearranged to solve for percolation flux, and "equivalent" percolation fluxes were calculated for the five cases in Table 6.3-2—flux values that yield plug flow transport times equal to the FEHM mean transport values. The "equivalent" percolation fluxes are shown in Table 6.3-3. The five pairs of data points in Table 6.3-3 are nearly perfectly linear, but were fitted with a second-order polynomial fit to improve prediction of the lower flux values. Then the polynomial was used to adjust the percolation fluxes in Table 6.3-1 to produce flow velocities and transport times consistent with the FEHM results. Values below 1 mm/yr were not adjusted. These "adjusted" percolation fluxes are shown in Table 6.3-4, and are used only internally to the NFC model.

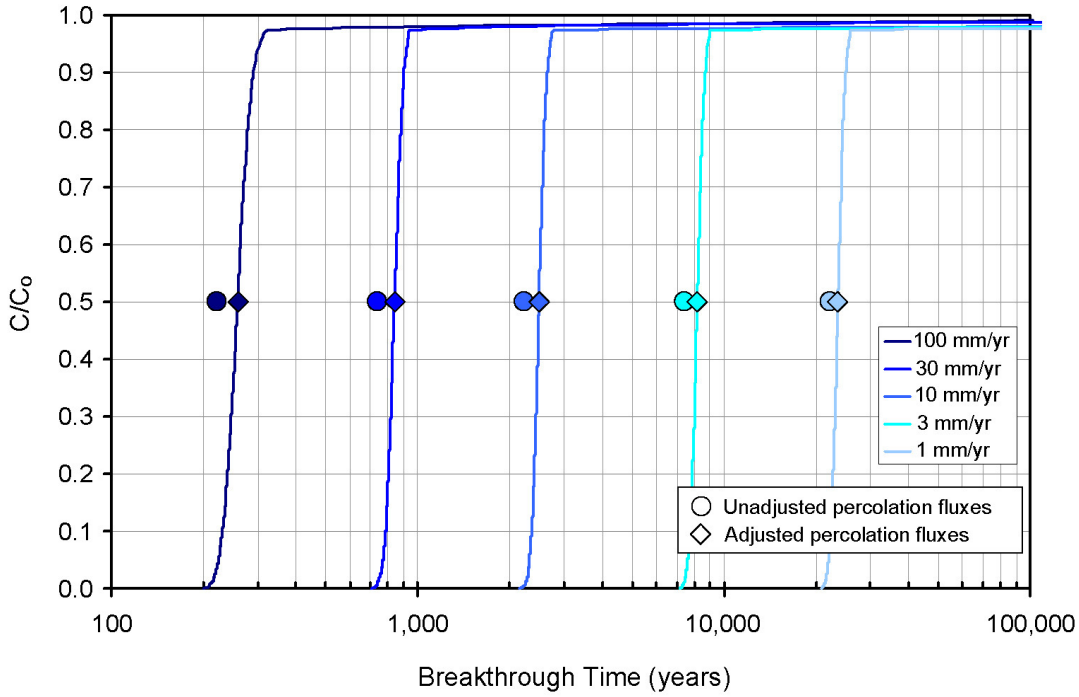

Source: Output DTN: SN0703PAEBSPCE.007, spreadsheet: *Transport time uncertainty.xls*.

NOTE: Also shown are the predicted transport times for the same percolation fluxes using a plug flow assumption (filled circles), and also transport times for "adjusted" percolation fluxes (filled diamonds).

Figure 6.3-7. Breakthrough Curves Generated by FEHM Modeling of Transport through the TSw at Five Different Percolation Fluxes, Using the Particle Tracking Option

Table 6.3-2. Transport Times, Plug-Flow versus FEHM Mean Values

Percolation Flux (mm/yr)	FEHM Mean Transport Times (years)	Plug-Flow Transport Times (years)
1	23,484	22,224
3	8,170	7,408
10	2,494	2,222
30	840	741
100	258	222

Source: Output DTN: SN0703PAEBSPCE.007, spreadsheet: *Transport time uncertainty.xls*.

Table 6.3-3. "Equivalent" Percolation Fluxes, Which Result in Plug-Flow Transport Times That Match FEHM Mean Values

Percolation Flux Used in FEHM Models (mm/yr)	Equivalent Percolation Flux (mm/yr)
1	0.95
3	2.72
10	8.91
30	26.45
100	86.05

Source: Output DTN: SN0703PAEBSPCE.007, spreadsheet: *Transport time uncertainty.xls*.

Table 6.3-4. "Adjusted" Percolation Fluxes (mm/yr), Generated by Modifying Those in Table 6.3-1 to Match Mean Flow Velocities Predicted by FEHM Modeling

Percentile	All Present-Day	All Monsoon	All Glacial Transition	Post-10,000 Years
0.025	0.048	0.28	0.052	0.19
0.075	0.37	1.1	0.50	1.1
0.125	0.86	1.9	1.0	2.4
0.175	1.3	3.0	1.5	3.9
0.225	1.9	4.1	2.2	5.3
0.275	2.5	5.0	3.0	7.0
0.325	3.2	6.0	4.1	9.3
0.375	4.0	7.0	5.2	11.8
0.425	4.9	8.0	6.6	14.4
0.475	5.8	9.0	8.3	17.0
0.525	6.9	10.4	10.4	19.5
0.575	8.2	12.0	13.1	22.4
0.625	9.7	14.4	16.6	25.9
0.675	11.2	17.0	20.3	31.3
0.725	13.1	20.5	25.3	38.6
0.775	15.4	25.6	31.7	45.6
0.825	19.3	40.4	39.2	52.1
0.875	24.8	63.9	50.6	58.2
0.925	30.9	81.7	65.6	66.0
0.975	38.8	102.5	88.0	80.6

Source: Output DTN: SN0703PAEBSPCE.007, spreadsheet: *Transport time uncertainty.xls*.

The above calculations were performed using FEHM results generated by injecting particles into the fracture continuum at the top of the model. In additional simulations, also archived in Output DTN: SN0703PAEBSPCE.007, the particles were injected into the matrix. The breakthrough times for each of the five percolation fluxes were nearly identical in the two cases, varying by only a few percent. The breakthrough curves for both sets of FEHM calculations, varying by a maximum of 15% from the unadjusted plug-flow values, provide an important conclusion with respect to fracture–matrix interactions. Because the FEHM calculations so closely match the plug flow approximation, and because of the reciprocity exhibited when the particles are injected into the fracture or the matrix, fracture–matrix exchange must be rapid relative to downward transport through the TSw.

Evaluation of an Error in the FEHM Modeling Used to Calibrate the Percolation Flux Values—Following TSPA implementation of the model presented here, using the "adjusted" percolation flux values shown in Table 6.3-4, it was discovered that the FEHM simulations had been run without implementing the active-fracture model (AFM). The AFM utilizes a parameter, gamma, to modify the effective fracture surface area over which matrix-fracture equilibration can occur, as a function of saturation. The UZ calibrated properties set used in the FEHM modeling was derived by fitting measured rock saturation data, and the AFM was implemented during the fitting process. Thus, the rock hydrologic properties in the calibrated properties set should be used with the AFM implemented.

This is relevant to the NFC model because failure to implement the AFM might affect the predicted FEHM transport times that were used to calibrate the plug flow approach in the NFC model. To evaluate this, FEHM simulations at 10 mm/yr and 100 mm/yr were rerun with the AFM, using the gamma parameters for each unit from the UZ calibrated properties set. Tracer injection into both matrix and fracture continuums was evaluated. A diffusion coefficient consistent with weakly sorbing ions was utilized in this analysis (DTN: LA0506BR831371.001 [DIRS 174331], file: *fehm_amr_base.mptr*). These simulations are archived in Output DTN: SN0705PAEBSPCE.009 (folder: \FEHM runs with AFM) and are summarized and compared to the baseline results in spreadsheet *Comparison, AFM-no AFM results.xls*. The differences in the median breakthrough times between the simulations with and without the AFM were insignificant. For the four simulations compared (two with fracture injection, and two with matrix injection), the largest deviation was less than 1.1%. Breakthrough curves were slightly wider with the AFM, but the differences were minor; for instance, 95th percentile breakthrough times for the simulations varied by less than 4% in all four cases.

These differences in predicted transport times are small, and the effect of not implementing the AFM is insignificant relative to other uncertainties that are propagated through the NFC model (Section 6.12). Thus, this error has no impact on the output of the NFC model or the seepage dilution/evaporation model to which it provides feeds.

6.3.2.4.5 Calculating the Amount of Feldspar Dissolved as Water Percolates through the Thermal Field (WRIP)

In this section, the ambient feldspar dissolution rate, the dissolution rate temperature dependence, the model for the thermal field, and the plug flow model for transport through the TSw are combined to evaluate the amount of feldspar that dissolves as the water percolates downward through the unit to the repository. This value is passed to TSPA in a lookup table, as the WRIP. The total amount of feldspar that dissolves along the flow path is determined using a calculation that takes as input the location-specific thermal field data generated in Section 6.3.2.4.3, and the percolation flux values in Table 6.3-4. This calculation and supporting documentation are archived in Output DTN: SN0703PAEBSPCE.006. Because the TSw is represented as a single unit with averaged rock properties and the feldspar dissolution rate is calculated from average alteration mineral abundances, the results of this calculation represent an average flow path through the unit.

The general procedure for determining the amount of feldspar dissolved involves discretizing the flow path into 20 or more sections, and determining an average temperature and residence time for each discrete section. Then the amount of feldspar dissolved is calculated using a temperature-dependent feldspar dissolution rate, based on the activation energy relationship described in Section 6.3.2.4.2 and the average temperature for the interval. This is done for each interval, and then the total feldspar dissolved is summed up over the entire flow path. A complicating factor is that the percolation flux rate changes in steps as the climate states change (Table 6.3-1).

The WRIP calculation is carried out in three Mathcad 14 files, one each for the mean, 10th percentile, and 90th percentile thermal conductivity values (Output DTN: SN0703PAEBSPCE.006, files: *Model for water-rock interactions*, ***.xmcd*, where ** is

equal to "mean," "10th percentile," or "90th percentile), which calculate the amount of feldspar dissolved as the water percolates downward from a starting location to the drift, for any given seepage time, and for any given set of climate-dependent percolation fluxes. As the starting location within the stratigraphic column for water that reaches the drift at any given time is not known *a priori,* the calculation is done in reverse, from the drift, backwards in time and up the section, to the starting location. Thus, the first step in the calculation is to choose a time of seepage, and identify an end point—the distance from drift center at which seepage is assumed to occur. After the boiling period, this corresponds to the drift wall (2.75 m from the drift center); prior to that, it is taken to correspond to the 96°C isotherm (representing boiling at the repository level). The justification for this is that fracture capillarity is too small to significantly elevate the boiling temperature, so the 96°C isotherm should correspond closely to the boundary of the dryout zone. During the boiling period, seepage penetration of the dryout zone around the drift would require rapid flow, locally quenching the region to temperatures below boiling. This is required because although brines may persist at above-boiling temperatures, the necessary degree of water concentration is so high that there would be insufficient water to saturate the dryout zone. Hence, the point of seepage during the boiling period is taken to be the boundary of the dryout zone. The location of this at any given point in time is determined by interpolation between the thermal profiles described in Section 6.3.2.4.3, using 96°C as the point of boiling.

Once the starting point is identified, the Mathcad calculation back-calculates the flow path and temperatures as a function of the thermal field and the percolation rates used, checking whether climate state boundaries are crossed and adjusting the percolation fluxes accordingly. First, it determines which climate-state-dependent percolation flux is relevant at the time of seepage. Then it calculates a provisional starting time at the relevant percolation flux. The provisional starting time represents either (1) the time at which the water would have been at the top of the model domain (200 m above the drift center), or (2) the model start time of 50 years (corresponding to the time of repository closure). If the provisional starting time falls within the same climate state, then the WRIP value is generated by integrating along the entire flow path at the flux rate for that climate state. This is done by discretizing the flow path into twenty intervals, calculating a flux-dependent residence time and temperature-dependent feldspar dissolution rate (calculated using the activation energy relationship described in Section 6.3.2.4.2 and the average temperature for the interval) for each interval, and summing the results. If the provisional start time falls within the previous climate interval (or earlier), then only that fraction of the flow path that corresponds to the time interval from the seep time to the climate state boundary is evaluated. Then, the end-point and end-time are changed to the values at the climate state boundary, the percolation flux rate is changed, and a new provisional start time is calculated. The calculation is repeated for the interval of the flow path that falls within the new climate state, and the result is added to the previous value. This process is repeated each time a climate state boundary is crossed, until one of two conditions is met. Either the water packet is tracked backward to the top of the model, 200 m above the drift center, or the model start time of 50 years (repository closure) is reached.

For example, assume that the WRIP value (amount of feldspar dissolved) for seepage at 12,000 years is being evaluated. First, a provisional start time (the time that percolation was at a height of 200 m above the drift center) is calculated using the post-10,000-year flux rate (*Start-time-P4*). If *Start-time-P4* is greater than 10,000 years, then the WRIP is calculated over the flow path using the single post-10,000-year flux rate. However, if *Start-time-P4* is less

than 10,000 years, then the WRIP is calculated over that portion of the flow path extending from 10,000 to 12,000 years. The flux rate is changed to the glacial transition flux rate, the end location of the "seepage" is updated from the drift wall to the predicted stratigraphic location at 10,000 years, and a new provisional start time (*Start-time-P3*) is calculated using the glacial transition rate. If *Start-time-P3* is greater than 2,000 years, then the WRIP is integrated over the remainder of the flow path (the part less than 10,000 years) using the glacial transition flux rate and added to the previous value to produce the WRIP value for the entire flow path. If *Start-time-P3* is less than 2,000 years, then the WRIP is calculated over that portion of the flow path extending from 2,000 to 10,000 years. The flux rate is changed to the monsoonal flux rate, the end location of the "seepage" is updated to the predicted stratigraphic location at 2,000 years, and a new provisional start time (*Start-time-P2*) is calculated using the monsoonal flux rate. This process is continued until the entire flow path has been evaluated, from 200 m above the repository to the drift level, or until the start time of 50 years (repository closure) has been reached.

The results of this calculation are shown in Figure 6.3-8 for three locations in the repository; that corresponding to the lowest thermal measure (TM) (the sum of the time when the drift wall drops below boiling and the maximum drift wall temperature achieved), a location with a median thermal measure, and the location with the highest thermal measure. The TM is utilized here to provide an interface with the outputs from *Multiscale Thermohydrologic Model* (SNL 2007 [DIRS 181383]) where the TM concept is developed and used. The amount of feldspar dissolved rises sharply after closure, as the thermal field expands outward around the drift, and then falls slowly as the thermal field collapses. The amount of feldspar dissolved varies with the percolation flux and is larger for lower percolation fluxes (e.g., longer residence times), and the peak in the amount dissolved shifts to higher times as percolation flux rate decreases. In locations where a boiling front develops (Figures 6.3-8b and 6.3-8c), the feldspar dissolution rates nearly match during the boiling period; however, in the long term, feldspar dissolution rates decrease more slowly in the hotter case. Below a value of approximately 10^{-5} moles/L, the mass of added feldspar is too small to significantly affect water chemistry.

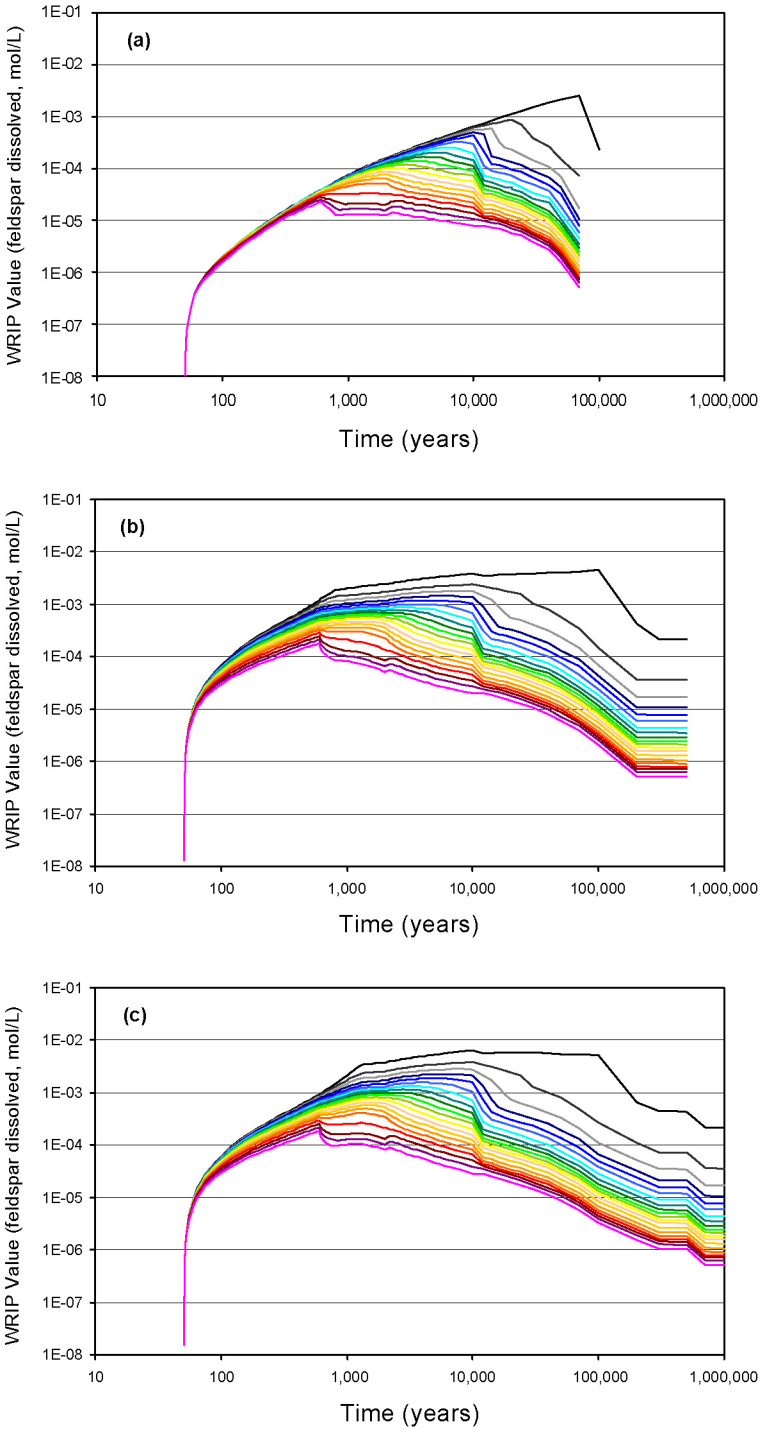

Source: Output DTN: SN0703PAEBSPCE.006, folder: \Figures, spreadsheet: *Figure, WRIP values at three TMs.xls*.

NOTE: The twenty profiles in each case represent the adjusted percolation flux sets given in Table 6.3-4, with the flux rates increasing towards the bottom of each graph, from black (row 1 in Table 6.3-9), to red (row 20 in Table 6.3-9).

Figure 6.3-8. Calculated WRIP Values (moles feldspar dissolved) for Three Different Locations within the Drift: (a) the Coolest Location Evaluated (TM = 37.8); (b) a Median TM Value (TM = 859); and (c) the Hottest Location Evaluated (TM = 1,546)

To determine possible seepage water compositions, the calculated amount of feldspar is titrated into a starting water composition, and brought to the temperature of interest. This is described in detail in Section 6.3.2.4.2. One limitation of the NFC model is that the starting water compositions are based on pore waters collected throughout the TSw. Hence, they have already reacted to a greater or lesser degree with the tuff. If the NFC water–rock interaction model is run at ambient conditions, a measurable amount of feldspar would dissolve, meaning that the starting composition would be modified, and the current TSw pore waters would not be predicted to occur. There are two possible ways of addressing this. First, the change at ambient conditions can be ignored, meaning that, as the repository returns to ambient temperatures, the pore-water compositions do not return to those observed today. Or, a temperature cutoff can be implemented, such that feldspar dissolution is not allowed to occur once the temperatures return to the ambient value at the repository level (estimated to be 23.4°C; rounded up to 24°C). Hence, as the 24°C isotherm collapses in towards the drift, the length of the flow path along which feldspar dissolution occurs decreases, and once the drift wall returns to ambient temperatures, no feldspar dissolution occurs and the observed starting water compositions are once again predicted. Because the desire was to return to ambient pore-water compositions with time, the latter method was chosen. This has two limitations; it results in a step function at 24°C in the amount of feldspar dissolved, which can be significant at very low percolation fluxes, where the very long transport times result in significant feldspar dissolution at temperatures just above 24°C. This is evident in Figure 6.3-8; the curves truncate when the 24°C isotherm intersects the drift, and at the lowest flux rates, this is significantly above the value corresponding to no significant reaction (approximately 10^{-5} moles). Second, it results in ambient pore-water compositions once the temperature has returned to ambient for all percolation rates, when the actual measured pore-water compositions are specific to the actual percolation rates under which they formed. This last limitation is moderated by using four chemically distinct starting waters, which likely represent different local percolation fluxes.

To summarize this section, water–rock interactions in the thermal zone above the drift are modeled by considering three minerals. Calcite is a common fracture mineral in the TSw, and waters passing through the rock are treated as being in equilibrium with this phase, based on the observation that geothermal waters are always at saturation with respect to this phase. The tuff itself consists almost entirely of silica polymorphs and alkali feldspars, and in addition, opal is a common fracture mineral. In the NFC model, water percolating through the thermal envelope above the drift is treated as being at equilibrium with amorphous silica. This slightly overestimates aqueous silica concentrations at ambient conditions; however, assuming equilibrium with tridymite, cristobalite, or quartz would underestimate aqueous silica concentrations. Alkali feldspar initially present in the tuff has exsolved to varying degrees to alternating potassium- and sodium-rich lamellae. Because the degree of exsolution is variable, and because the two phases formed are not pure end-members, but vary widely in composition, the alkali feldspars are treated as a single phase, with a kinetically limited dissolution rate, in the NFC model.

The amount of feldspar dissolved is a primary parameter in determining the composition of potential seepage waters, and it is implemented in the NFC model as the WRIP value. For use in TSPA, WRIP values are summarized in the WRIP lookup table (Output DTN: SN0703PAEBSPCE.006, folder: \WRIP calculations\Mathcad calculations of WRIP values, spreadsheet: *WRIP lookup table.xls*), which tabulates the WRIP values through time as a

function of two location-specific parameters, the thermal measure (the sum of the time when the drift wall drops below boiling in years and the maximum drift wall temperature in °C), and the percolation fluxes. The first step in determining the WRIP value for any given location and time in the repository is to choose a set of thermal profiles from those calculated in Section 6.3.2.4.3 that best matches the location of interest with respect to the thermal measure. This narrows the WRIP value to twenty sets of time histories, one for each percolation flux set in Table 6.3-1 (note that the *unadjusted* percolation fluxes are used to enter in the WRIP table). The two sets of percolation fluxes from Table 6.3-1 that bound the actual value at the location of interest are identified, each providing a time history of WRIP values at 102 points in time from 50.1 to 1,000,000 years. The WRIP value at the time of interest is interpolated as necessary between points in time and the two bounding percolation flux values. Finally, an uncertainty is added to the value, using the procedure described in Section 6.12.2.2.5.

For use in TSPA evaporation/dilution lookup tables, the range of WRIP values is discretized into 11 values. These values were chosen to capture the range of the calculated WRIP values on the WRIP map. There are thousands of WRIP values calculated in the NFC model and it is not possible to provide lookup tables associated with each WRIP. Therefore, eleven values were selected that provide alkali feldspar quantities in steps from 10^{-4} to 10^{-3} moles, to provide adequate coverage of the anticipated chemical effects while minimizing the total number of lookup tables provided to TSPA. The last lookup table "L" is 10^{-2} moles larger than the previous value "J" and was included as the maximum value from the WRIP map even though such large WRIP values are unlikely in the NFC model. The values range from 0 to 1.47×10^{-2} moles feldspar, and are not evenly distributed across this range, but are rather spaced more densely in the more probable parts of the range. These values and their alphanumeric designations in the lookup tables are given in Table 6.3-5.

Table 6.3-5. Discrete WRIP Values (mol) and Their Alphanumeric Designations in TSPA Lookup Tables

WRIP Lookup Table Designation	WRIP Value
0	0.00E+00
B	6.81E-05
C	1.47E-04
D	3.16E-04
E	4.64E-04
F	6.81E-04
G	1.00E-03
H	1.47E-03
I	2.15E-03
J	3.16E-03
L	1.47E-02

Source: Output DTN: SN0703PAEBSPCE.006, folder: \WRIP calculations\Mathcad calculations of WRIP values, spreadsheet: *WRIP lookup table.xls*.

6.3.2.4.6 Example Calculation of the WRIP and Water Chemistry along the Flow Path and at the Drift Wall

To illustrate the WRIP calculation, a simplified example is given here. This example is documented in Output DTN: SN0705PAEBSPCE.009 (spreadsheet: *Flow paths.xls*) and is calculated using a thermal history based on the mean thermal conductivity value, at the location corresponding to Drift 1, Location 8. For this example, a single percolation flux of 4 mm/yr is assumed to apply for all climate periods. The calculation of the WRIP value is performed for potential seepage waters intersecting the drift wall at five different times in the repository history: 2,000, 4,000, 6,000, 10,000, and 20,000 years.

First, the starting elevation above the drift and a starting time are calculated for each case using the percolation flux and the plug flow assumption. For the shorter two seepage times, the percolating water starts at about 73 and 145 m above the drift, because the time since closure is less than the length of time required to travel 200 meters at the given percolation flux (about 5,500 years); the starting time is 50 years (corresponding to the end of the ventilation period). For the later three seepage times, the percolating waters start at the top of the modeled section, 200 m above drift center, at starting times corresponding to the seepage time minus the travel time of 5,500 years. The total distance traveled is discretized into 19 locations (in this example) through time, and the temperature is determined by interpolation between the point-in-time thermal profiles (Figure 6.3-6), as a function of time and elevation above the drift. The resulting temperature-flow pathways are shown in Figure 6.3-9.

Once a discretized set of temperatures along the flow path has been determined, each pair of adjacent temperatures is averaged, and the average value is used to calculate a temperature-dependent feldspar dissolution rate applicable to the interval between the two points. This rate is used to calculate the amount of feldspar that dissolves as the water percolates through the interval, and total dissolution along the flow path is calculated by summing cumulatively along the flow path. This is shown in Figure 6.3-10 for the same five flow pathways shown in Figure 6.3-9. The cumulative amount of feldspar dissolved is the WRIP value, and is used to calculate the composition of potential seepage at the drift wall, as discussed in the previous section.

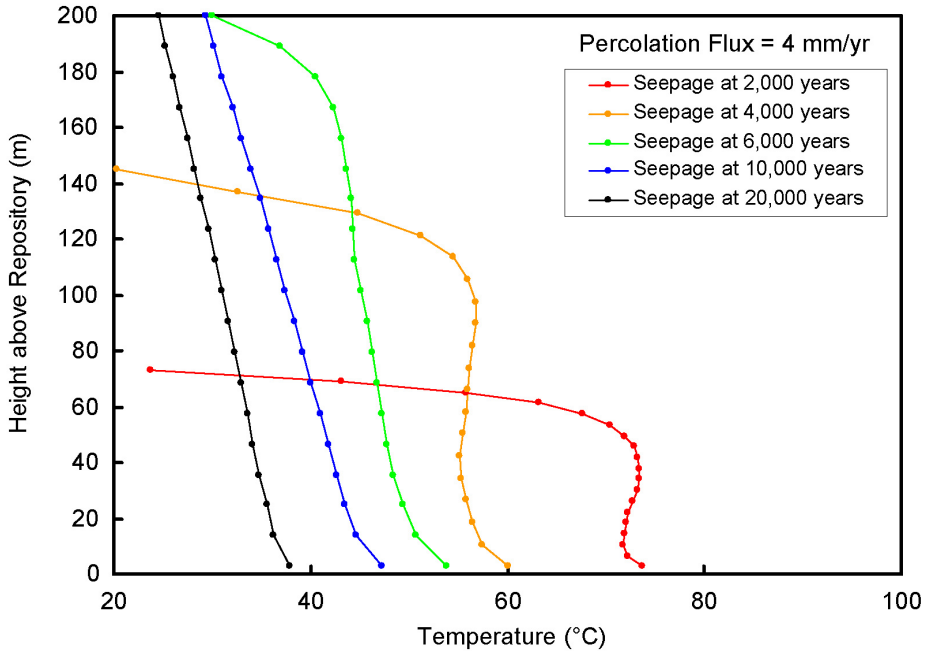

Source: Output DTN: SN0705PAEBSPCE.009, spreadsheet: *Flow paths.xls.*

NOTE: For a 4 mm/yr flux rate, the water reaching the repository at 2,000 and 4,000 years starts at an elevation below the top of the NFC model section (200 m).

Figure 6.3-9. Temperature-Flow Paths Followed by Percolating Waters Representing Five Different Seepage Times

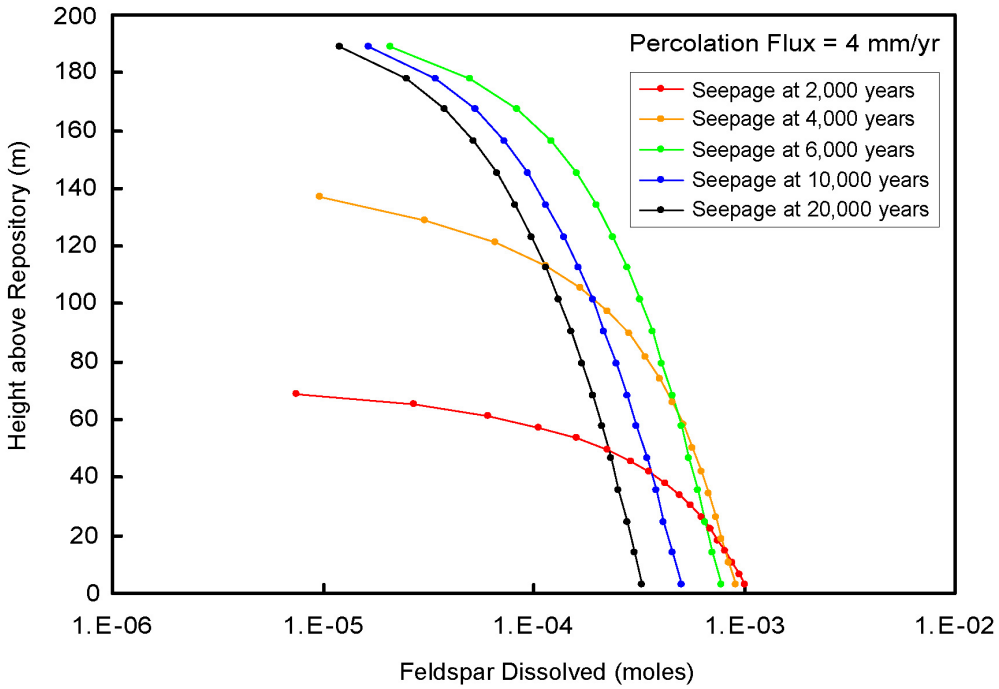

Source: Output DTN: SN0705PAEBSPCE.009, spreadsheet: *Flow paths.xls.*

Figure 6.3-10. Cumulative Amount of Feldspar Dissolved as Water Percolates along the Temperature-Flow Paths Shown in Figure 6.3-9

Although not explicitly calculated by the NFC model, the predicted chemistry along the flow pathway can be extracted from the NFC model outputs. Specifically, the EQ3/6 files used to calculate potential seepage waters as starting waters for the P&CE dilution/evaporation modeling can be queried to determine the chemistry along the flow paths. These "seepage" files are archived in Output DTN: SN0701PAEBSPCE.002, and tabulate potential pore-water compositions as a function of two parameters—the temperature and the amount of feldspar dissolved. These EQ6 simulations terminate at temperatures of 30°C, 70°C, and 96°C, and generate EQ6 pickup files that are used as the starting water compositions for the P&CE seepage evaporation calculations at those temperatures. The results of the 96°C simulations contain the results of the lower-temperature calculations. The simulations were carried out for the four starting waters, for 11 discrete amounts of feldspar dissolved (WRIP values), and each provides water compositions and pCO_2 values at one-degree temperature steps over the interval from 23°C to 96°C. To evaluate water chemistry along the calculated flow paths in Figures 6.3-9 and 6.3-10, the amount of feldspar dissolved for each location along the pathways is used to select a pair of EQ6 "seepage" output files representing bounding WRIP values. Representative water compositions from the bounding files are chosen corresponding to the temperature at that point along the flow path. The actual concentration of each chemical species of interest, and of the pCO_2, is then calculated by interpolation, as a function of the amount of feldspar dissolved, from the two bounding water compositions. These calculations were performed for Group 1 and Group 3 waters using the data in Figures 6.3-9 and 6.3-10, and are archived in Output DTN: SN0705PAEBSPCE.009 (spreadsheets: *PCE_GRP1_profiles.xls* and *PCE_GRP1_profiles.xls*). Chemical data were only extracted for three of the profiles, corresponding to seepage intersecting the drift wall at 2,000, 6,000, and 20,000 years.

The results for Group 1 waters are shown in Figures 6.3-11 and 6.3-12. In Figure 6.3-11, the observed changes in pH and pCO_2 are due to the offsetting effects of the temperature increase and the increase if the alkalinity due to feldspar dissolution. For the two early time cases, the initial increase in temperature results in degassing of CO_2, and the pH drops and ${}_pCO_2$ rises. As the water percolates downward, dissolution of feldspar results in an increase in the pH and alkalinity of the pore water, and the CO_2 is re-absorbed. The pH rises again, and the pCO_2 drops. In the 20,000-year case, the temperature has cooled to the point that feldspar dissolution rates are slow; the effect of the temperature gradient is greater than that of feldspar dissolution, and the pH drops and pCO_2 rises more or less monotonically as the water percolates downwards. In Figure 6.3-12, other chemical parameters are shown. Ca decreases with depth, as feldspar dissolves and stellerite and celadonite precipitate, and K and Na show the opposite behavior. Aqueous silica concentrations are entirely a function of the change in amorphous silica solubility with temperature, because equilibrium with that phase is always assumed to exist (Section 6.3.2.4.1).

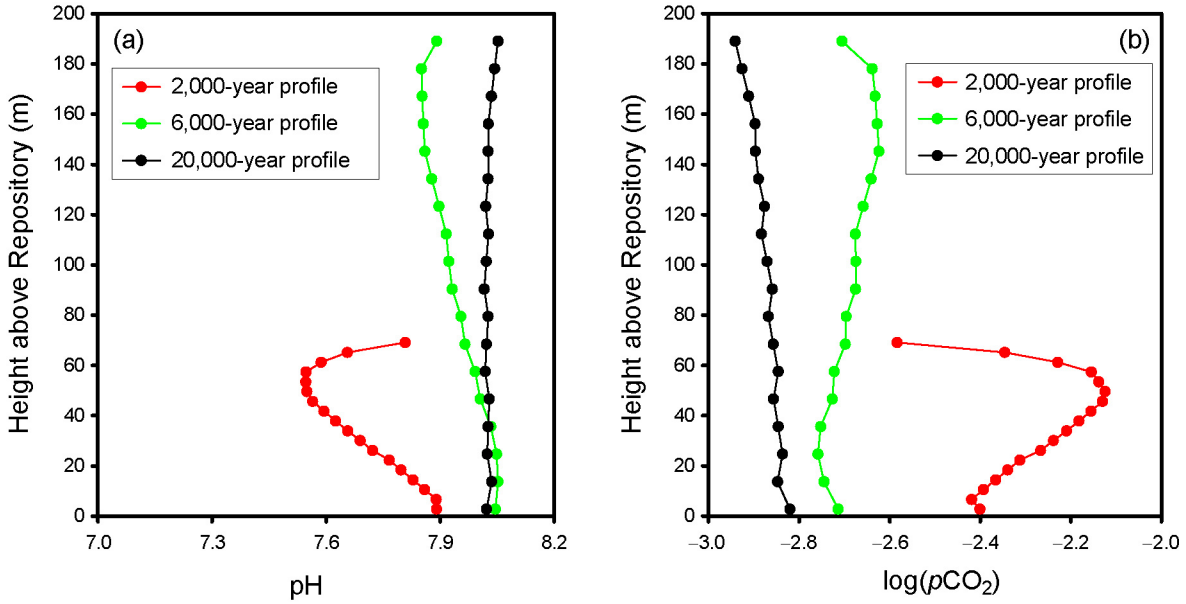

Source: Output DTN: SN0705PAEBSPCE.009, spreadsheet: *PCE_GRP1_profiles.xls*.

NOTE: The profiles correspond to water reaching the drift wall at 2,000, 6,000, and 20,000 years. The graphs are for (a) pH, and (b) pCO_2.

Figure 6.3-11. Predicted Chemical Evolution of Group 1 Representative Pore Water (pH and log(pCO_2)) as It Migrates Downwards through the TSw to the Drift

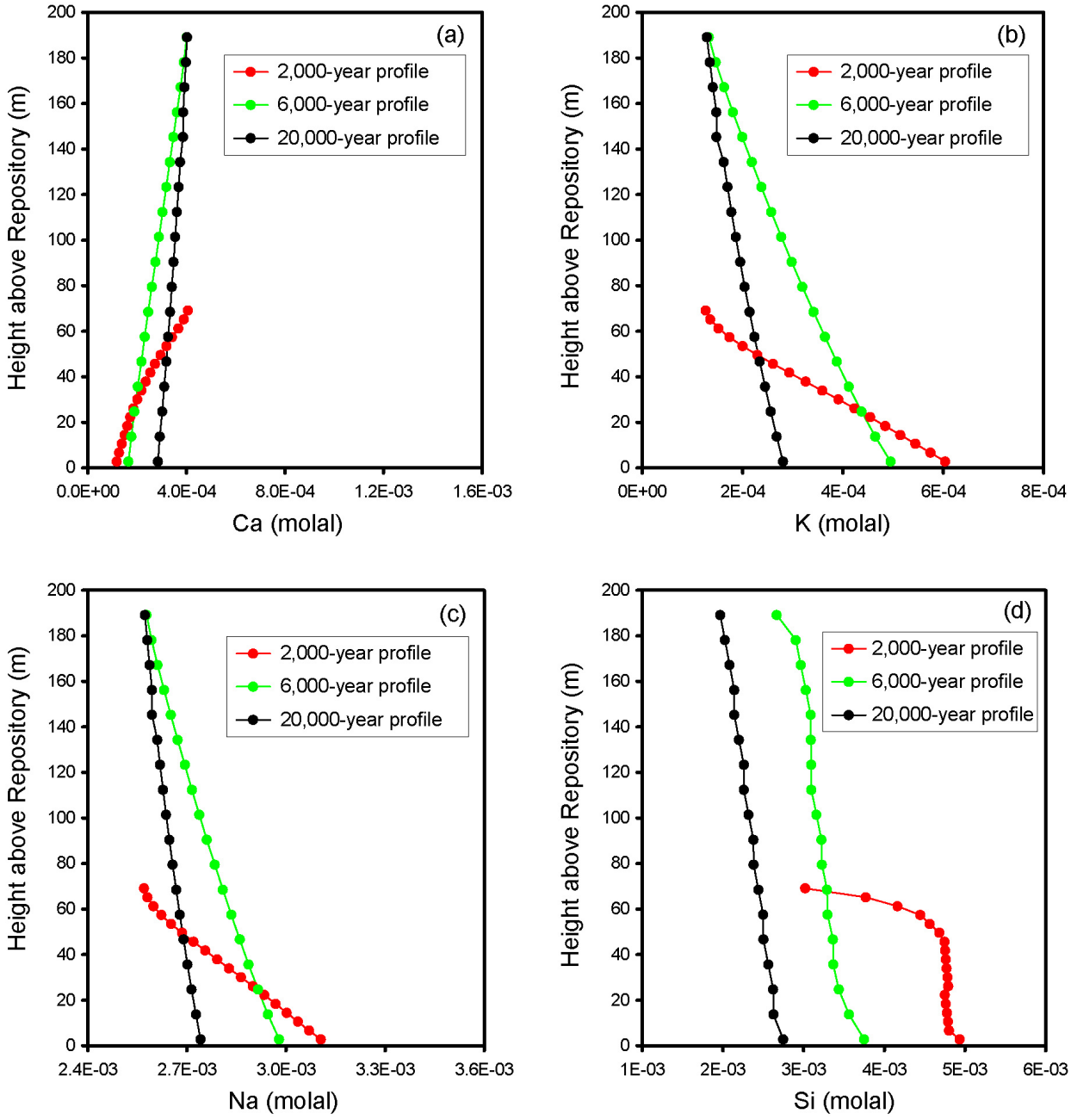

Source: Output DTN: SN0705PAEBSPCE.009, spreadsheet: *PCE_GRP1_profiles.xls*.

NOTE: The profiles correspond to water reaching the drift wall at 2,000, 6,000, and 20,000 years. The graphs are for (a) Ca, (b) K, (c) Na, and (d) Si.

Figure 6.3-12. Predicted Chemical Evolution of Group 1 Representative Pore Water (major cations) as It Migrates Downwards through the TSw to the Drift

The results for the more Ca-rich Group 3 waters are shown in Figures 6.3-13 and 6.3-14, using axes scales that match those for the Group 1 results for ease of comparison. The trends in pH and pCO_2 are similar to those for the Group 1 representative water, although the pH range is somewhat lower for the Group 3 waters; pCO_2 values are shifted correspondingly higher. Ca, K, Na, and Si all show very similar trends to the Group 1 results, although there is a considerable difference in the total Ca concentrations. It is clear that, although the effect of the elevated thermal field and of feldspar dissolution is much larger than the effect of variations in the composition of the initial waters, the chemical variation in the starting waters is still an important parameter.

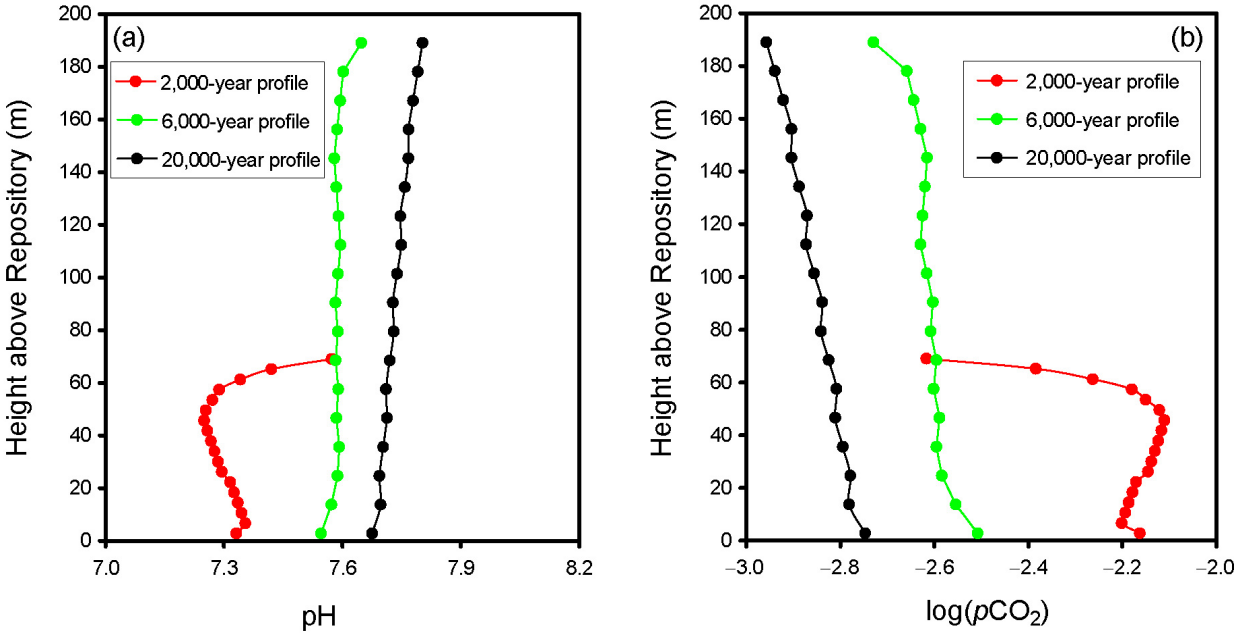

Source: Output DTN: SN0705PAEBSPCE.009, spreadsheet: *PCE_GRP3_profiles.xls*.

NOTE: The profiles correspond to water reaching the drift wall at 2,000, 6,000, and 20,000 years. The graphs are for (a) pH, and (b) pCO_2. Compare with Figure 6.3-11 to evaluate the importance of different starting waters.

Figure 6.3-13. Predicted Chemical Evolution of Group 3 Representative Pore Water (pH and log(pCO_2)) as It Migrates Downwards through the TSw to the Drift

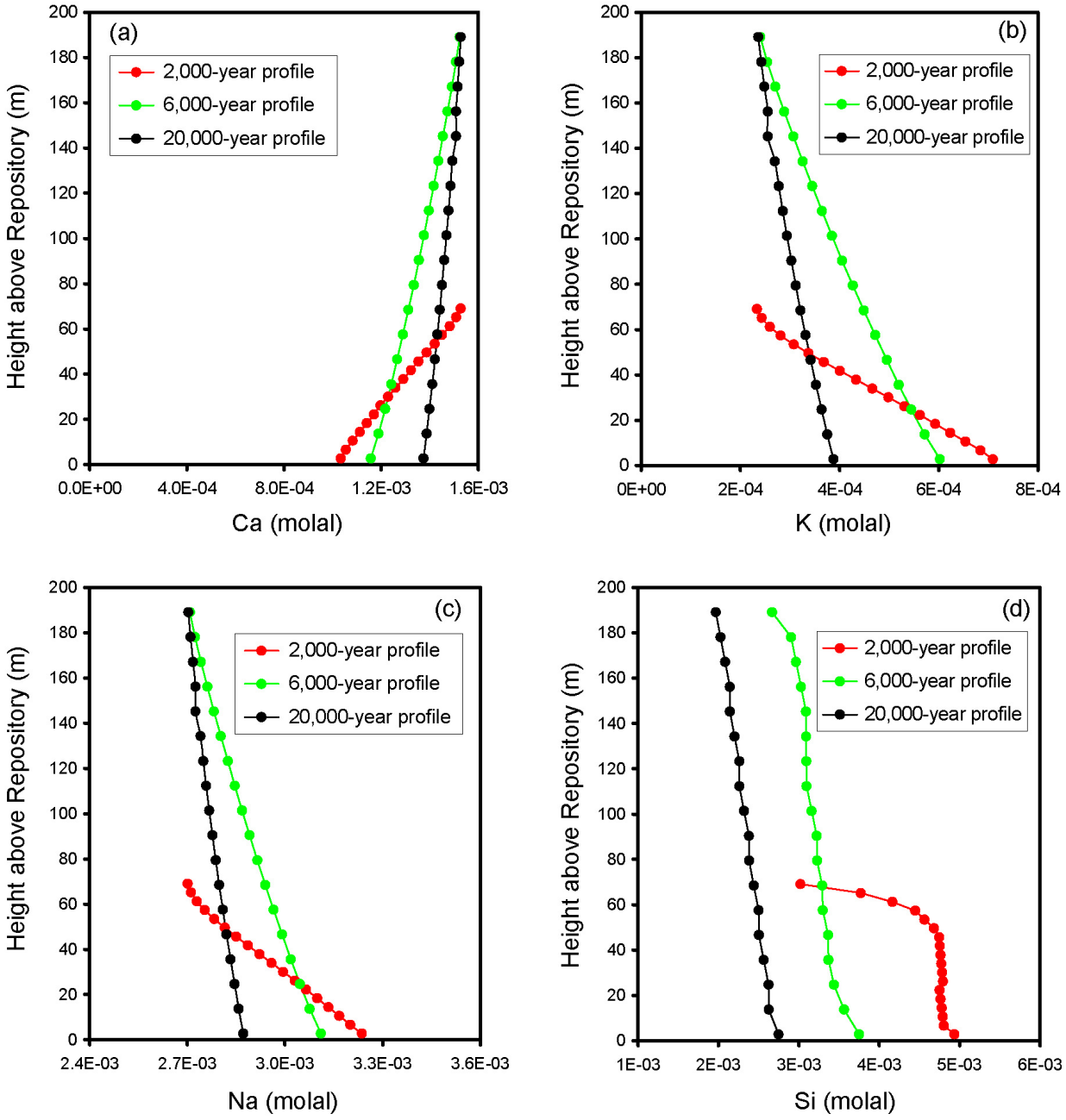

Source: Output DTN: SN0705PAEBSPCE.009, spreadsheet: *PCE_GRP3_profiles.xls*.

NOTE: The profiles correspond to water reaching the drift wall at 2,000, 6,000, and 20,000 years. The graphs are for (a) Ca, (b) K, (c) Na, and (d) Si. Compare with Figure 6.3-12 to evaluate the importance of different starting waters.

Figure 6.3-14. Predicted Chemical Evolution of Group 3 Representative Pore Water (major cations) as It Migrates Downwards through the TSw to the Drift

6.3.2.5 Liquid-Gas Exchange along the Flow Path

Liquid-gas phase exchange as percolating water moves downward towards the heated repository could have an effect on the composition of the water. Two potentially important processes to consider are evaporation (loss of water vapor) and CO_2 exchange.

Evaporation cannot be an important process as water percolates downward through the thermal gradient, until the drift, or the dryout zone around the drift, is reached. The reason for this is because the ambient saturation levels in the rock are high (approximately 80%; Table 4.1-6), and would increase as the temperature gradient is established and hot saturated air from zones closer to the repository moves upward along fractures and cools, condensing out water. Saturation would also increase at the higher percolation fluxes expected in future climate states. High saturations leave little room for a gas phase, and because of the large volume change associated with the transition from water to water vapor, significant vapor loss is impossible. For example, under boiling conditions at the repository level (assumed 96°C), one liter of water evaporates to become approximately 1,400 liters of steam. Hence, to dry out one cubic meter of saturated tuff (porosity approximately 0.13) requires removal of 180,000 liters of steam. Vapor transport is orders of magnitude more effective in fractures than in the matrix, but the fracture porosity is only approximately 0.01 (Table 4.1-5). At lower temperatures, where the capacity of air to hold water is lower, an even larger volume of atmosphere would be required; at 79°C, one liter of water would saturate over 2,700 liters of air. In addition, once a temperature gradient is established, the RH at any point will be 100%. This is because the vapor pressure at higher temperatures is greater than at lower temperatures. Water vapor diffusing down the temperature gradient to lower temperatures will keep the whole system on the temperature–water vapor saturation curve. At 100% RH, with a limited volume of gas, little evaporation or degassing can occur, and water will not significantly concentrate or degas until it hits the low saturation zone around the drift and vapor can be lost into the drift.

The location of the evaporation front, the boundary between the area in equilibrium with the drift atmosphere, and the area further out which is in local equilibrium with the pore water, is a function of the vapor pressure in the drift, which indicates the temperature at which evaporation occurs. This requires some explanation. During the boiling period, the vapor pressure of water in the drift corresponds to 0.89 bars (DTN: GS030108312242.001 [DIRS 163118], files: *S03226_001*, *YMBarrometricpressures.xls*), the vapor pressure of boiling water at the repository elevation. It is controlled by boiling in the boiling zone around the drift. After the boiling period, the vapor pressure of water in the drift drops, corresponding to the saturation pressure, *p*SAT at a lower temperature. This eventually becomes coincident with the drift wall temperature. Because of the steepness of the water vapor saturation curve with respect to temperature, it is at the temperature for which the vapor pressure in the drift represents the saturation pressure that most evaporation occurs. For a given vapor pressure, an increase in temperature of even a single degree above the corresponding saturation temperature corresponds to a change in RH of 4% to 6% (Haar et al. 1984 [DIRS 105175], Table 1). This corresponds to a concentration factor of several hundred, since the pore waters are very dilute and have an activity near unity. This is more or less independent of the actual vapor pressure and saturation temperature. Hence, the boundary between the area in which the in-drift transport processes (e.g., evaporation, advection, and condensation) dominate the gas phase composition, and that in

which local equilibrium with pore water dominates, must be very close to the isotherm representing the temperature at which the in-drift vapor pressure represents saturation.

Relevant CO_2 concentrations in the gas phase within the rock are difficult to determine. As water percolates downward through the thermal field and heats up, CO_2 is partitioned into the gas phase. This is offset by the effects of feldspar dissolution, which raises the alkalinity and reduces the degree of partitioning into the gas phase. The relative rates of these two processes are important because the degree to which the gas phase acts as an open system—the amount of CO_2 that would be lost or gained by gas phase advection and mixing—is unknown. Given that matrix saturations are high and fracture porosity is low, it is assumed for the NFC model that gas phase transport is limited, except for the area immediately around the drift, where loss into the drift can occur; therefore, the gas-phase composition at any location in the rock column is determined by assuming equilibrium with the aqueous composition, rather than being controlled by gas-phase advection and mixing. Note that this assumption has no effect on the rate of feldspar dissolution because the rate of feldspar dissolution is a function of temperature, but is not sensitive to water chemistry (Section 6.3.2.4.2).

6.3.2.6 General Processes Occurring in the Near-Field Chemistry Model

In the NFC model, most mineral precipitation and dissolution reactions are modeled by assuming thermodynamic equilibrium between the solid and aqueous phases. Alkali feldspar dissolution, which has the strongest effect on water composition, is modeled as being kinetically limited, with a rate that is a function of temperature. Hence, species concentrations in solution at any given time and location are largely controlled by the amount of feldspar dissolved along the flow pathway to that point. The strongest controls on this parameter are the temperature profile along the flow path (the temperature at any point controls the feldspar dissolution rate), and the percolation flux, which determines the water–rock contact time.

As pore waters percolate downwards through the TSw, the most important processes affecting pore-water chemistry are feldspar dissolution, dissolution/precipitation of calcite, and the increase in temperature with depth. The types of secondary minerals that form depends on the amount of feldspar that dissolves. At low amounts of feldspar dissolved, the following reaction occurs:

$$\underset{\text{(alkali feldspar)}}{2Na_{0.5}K_{0.5}AlSi_3O_8} + Ca^{2+} + SiO_2(aq) + 7H_2O \rightarrow \underset{\text{(stellerite)}}{\tfrac{1}{2}Ca_2Al_4Si_{14}O_{36}{:}14H_2O} + K^+ + Na^+$$

(Eq. 6.3-19)

As this reaction occurs, Ca^{2+} is depleted from solution, and K^+ and Na^+ increase. The solution becomes undersaturated with respect to calcite, and it begins to dissolve. The total reaction becomes:

$$2Na_{0.5}K_{0.5}AlSi_3O_8 + CaCO_3 + H^+ + SiO_2(aq) + 7H_2O \rightarrow$$
(alkali feldspar) (calcite)

$$\rightarrow \tfrac{1}{2}Ca_2Al_4Si_{14}O_{36}{:}14H_2O + K^+ + Na^+ + HCO_3^-$$
(stellerite)

(Eq. 6.3-20)

This reaction results in an increase in pH and solution alkalinity with increasing feldspar dissolution; Ca^{2+} concentrations continue to drop as bicarbonate concentrations increase.

Eventually, as greater amounts of feldspar dissolve, K^+ builds up in solution and a potassium-bearing clay phase saturates. In the NFC model, the K-phase is the mineral celadonite, and the reaction becomes:

$$6Na_{0.5}K_{0.5}AlSi_3O_8 + 2CaCO_3 + 2Mg^{2+} + 4SiO_2(aq) + 16H_2O \rightarrow$$
(alkali feldspar) (calcite)

$$\rightarrow Ca_2Al_4Si_{14}O_{36}{:}14H_2O + 2KMgAlSi_4O_{10}(OH)_2 + K^+ + 3Na^+ + 2CO_2$$
(stellerite) (celadonite)

(Eq. 6.3-21)

Once celadonite begins to precipitate, further dissolution of feldspar results in a drop in the pH. However, the amount of magnesium in solution is limited. With continued feldspar dissolution, this reaction rapidly becomes inhibited by lack of Mg^{2+}, and the reaction shown in Equation 6.3-20 once again becomes dominant.

The above reactions are observed in the EQ6 simulations performed for the ambient condition validation case described in Section 7.1.2 (Validation DTN: SN0705PAEBSPCE.014, folder: \Ambient pore waters\PTn waters\d-TST runs). In the NFC model simulations that support TSPA (DTN: SN0701PAEBSPCE.002, folder: \EQ3_6 seepage), greater amounts of feldspar can dissolve because of the elevated temperature conditions due to the thermal pulse. Under those conditions, other Na- and K-bearing zeolites such as phillipsite can saturate and begin to precipitate.

With respect to the secondary minerals that are predicted to form by the NFC model, it should be remembered that clays and zeolites are compositionally complex minerals that are represented in the *data0.pce* thermodynamic database (Output DTN: SN0703PAEBSPCE.006) as single, compositionally fixed phases. In the reactions described above, it is appropriate to consider the secondary minerals as representing, progressively, sinks for Al and Ca (stellerite); Al, K, and Mg (celadonite); or Al, Na, K, and Ca (phillipsite) in the NFC model. While the actual minerals that form may not be chemically identical to the species in the database, the general trends described above are expected to be maintained (Section 7.1.2.3).

In addition to the reaction of feldspar to form secondary minerals, other processes occur due to the increase in temperature as the water percolates downwards. The effect of the increase in temperature is to cause calcite to precipitate, while feldspar dissolution consumes calcite (Equations 6.3-20 and 6.3-21 above). The relative rate of these two reactions determines whether calcite is predicted to precipitate or dissolve. In the ambient validation case, a very small amount of calcite either precipitates or dissolves, depending on the starting water. In the simulations for TSPA, calcite is generally predicted to dissolve, because of the increase in feldspar dissolution rate at elevated temperatures.

Specific effects of thermal-hydrologic processes on water chemistry depend on the intrinsic characteristics of the dissolved species and the types of chemical reactions in which they are involved. The expected behaviors of the major species are as follows:

- Cl^-, NO_3^-, and SO_4^{2-} are conservative species, the relative concentrations of which are not affected during downwards transport to the drift because mineral phases containing these species are highly soluble and do not precipitate.

- Ca^{2+} concentrations are affected primarily by calcite dissolution and precipitation, by feldspar dissolution (which affects the pH), and by precipitation of Ca-bearing secondary phases such as clays and zeolites.

- Mg^{2+} concentrations are affected by dissolution of feldspar and subsequent precipitation of secondary Mg-bearing clay minerals (e.g., celadonite). The thermodynamic database used in the NFC model does not contain a magnesium zeolite, but such phases are scarce at and above the drift horizon, and are not expected to form.

- Na^+ and K^+ are more conserved in solution than the divalent ions as the pore waters percolate downwards, and concentrations are mainly controlled by feldspar dissolution reactions and precipitation of K-bearing clays. At the highest degrees of feldspar dissolution, Na- and K-bearing zeolites precipitate.

- SiO_2(aq) concentrations are controlled by precipitation and dissolution of amorphous silica. Silica solubilities increase with temperature, and SiO_2(aq) concentrations increase as pore waters percolate downwards through the thermal zone above the drift.

- CO_2 concentrations in the gas phase through the rock column above the drift are controlled by equilibrium with the local aqueous phase. CO_2 gas concentrations are strongly dependent upon the temperature profile above the drift, because CO_2 partitions more strongly into the gas phase at higher temperatures. Also important is feldspar dissolution, which increases the solution alkalinity and pH, offsetting the effects of increasing temperature with respect to gas-phase CO_2. Calcite, through dissolution and precipitation, provides the source/sink for aqueous carbonate and gas-phase CO_2.

6.3.2.7 Predicting the Composition of Potential Seepage Waters

To summarize the NFC model, percolating pore water moves up a temperature gradient as it approaches the drift, but does not evaporate or degas significantly until water hits the isotherm representing the saturation temperature for the in-drift vapor pressure; even if that temperature is below boiling, the seepage water evaporates and becomes concentrated at that point. The water just behind the evaporation front is represented by pore water at the temperature of the interface, in equilibrium with a gas phase pCO_2 predicted by ramping the water up to temperature in a closed system (e.g., no degassing), while maintaining equilibrium with calcite and amorphous silica, and titrating in an amount of feldspar determined by the thermal field and flux-dependent flow velocities. In EQ3/6 modeling, this is implemented by taking the starting pore-water compositions, titrating in a fixed amount of alkali feldspar (see Table 6.3-5), and an excess of amorphous silica and calcite, and then increasing the temperature from ambient (23°C) to 96°C. The water vapor pressure is maintained at pSAT as the temperature increases, so no evaporation occurs. This is done by setting the partial pressure of water vapor, pH_2O, at 0.89 bars in the EQ6 files. At temperatures below 96°C where that pH_2O is impossible to reach, EQ6 automatically uses the highest achievable pH_2O, which corresponds to pSAT (the saturation vapor pressure of water) at that temperature.

The composition of seepage at the evaporation front is not provided to TSPA. The simulations were done three times, ending at 30°C, 70°C, and 96°C, to provide EQ6 pickup files for the P&CE evaporation/dilution EQ6 simulations to determine in-drift chemistry. The EQ3/6 files for this calculation are archived in Output DTN: SN0701PAEBSPCE.002.

The choice of mineral suppressions for both the seepage and the dilution/evaporation simulations is documented in Sections 6.2 and 6.9. In addition to the justification of the mineral suppressions used, a discussion of the mineral precipitates observed is also documented in Section 6.13. EQ6 output files were scrutinized to ensure that only expected and reasonable minerals precipitated.

6.3.2.8 Predicting the In-Drift Gas Composition

In the NFC model, the composition of potential seepage water entering the drift is simply that of water behind the evaporation front after accounting for processes that might have affected water composition during transport to that location. Equilibrium is assumed with calcite and amorphous silica, while alkali feldspar dissolution is kinetically limited, with a dissolution rate dependent upon temperature but not on water chemistry. It is assumed that no evaporation or CO_2 degassing occurs as the water moves towards the drift and increases in temperature. The composition of potential seepage at the dryout zone is calculated in the NFC model, at temperatures of 30°C, 70°C, and 96°C, to generate EQ6 pickup files for the in-drift seepage dilution/evaporation model described in Section 6.3.3.

The in-drift atmosphere consists of air that has diffused or advected into the drift from the surrounding rocks, diluted by water vapor generated by evaporation at the dryout zone interface. The amount of dilution can be readily determined from the vapor pressure of water in the drift, which can be obtained from the output of the multiscale thermohydrologic model (MSTHM) (SNL 2007 [DIRS 181383]). Carbon dioxide in the drift atmosphere comes from two sources.

The first is CO_2 that is released from pore water as it evaporates at the dryout zone boundary. The amount of CO_2 that is released can be calculated from the molar ratio of carbon to pore water at the evaporating water interface. This value is on the order of 1×10^{-5} to 5×10^{-5} moles C per mole water, and is summarized for potential seepage at 30°C, 70°C, and 96°C in Output DTN: SN0701PAEBSPCE.002 (folder: \C_total). About half of the inorganic carbon in the water will be released during evaporation; the rest will precipitate as carbonate minerals.

The second source of CO_2 is in the gas phase that diffuses or advects into the drift. This is more difficult to constrain. Two bounding cases are considered:

- *Minimum CO_2 concentration in the drift*. In this bounding case, gas movement into and out of the drift, and through the mountain, is assumed to occur readily through fractures. The CO_2 concentration in the air fraction entering the drift is equal to the ambient CO_2 concentration in the mountain at the repository level (10^{-3} bars). The contribution of this to the total CO_2 in the drift atmosphere is equal to this concentration times the mole fraction of air in the drift.

  Assuming ambient CO_2 concentrations and summing the CO_2 entering the drift in air with that released as water evaporates at the dryout front yields a minimum concentration for CO_2 in the drift. This calculation is described in detail in Section 6.15.1.

- *Maximum CO_2 concentration in the drift*. Behind the evaporation front, the gas phase is assumed to be in equilibrium with the aqueous phase at the temperature of the evaporation interface, assuming that the water moved up the temperature gradient to the interface without degassing. Treating the drift as a closed system, the in-drift pCO_2 would equal this value, which can be taken as a maximum for the in-drift atmosphere. This calculation is documented in Section 6.15.1, and the maximum pCO_2 values thus generated are tabulated in Output DTN: SN0701PAEBSPCE.002 (folder: \pCO2 max). If the model predicts large amounts of feldspar dissolution, but relatively low temperatures (e.g., for extremely slow percolation flux rates, water percolated through hot rocks, but did not reach the drift wall until it had cooled), then it is possible for the predicted maximum pCO_2 to actually be below 10^{-3} bars. This is because the alkalinity increases as feldspar dissolves, increasing the amount of CO_2 dissolved into the water. If this occurs, it is assumed that the maximum pCO_2 value is 10^{-3} bars.

Thus, combining the lower and upper bounds for the in-drift pCO_2 yields the possible range of CO_2 concentrations in the drift. TSPA samples within this range once per realization, as described in Section 6.15.1.

6.3.3 Seepage Dilution/Evaporation Model

The seepage dilution/evaporation abstraction model takes potential seepage water compositions and in-drift pCO_2 values provided by the NFC model, and evaluates the effects of in-drift processes on water chemistry. The integrated invert chemistry abstraction utilizes the same lookup tables in the same manner as those developed by the seepage dilution/evaporation abstraction. Therefore, the remainder of the discussion of the development of the TSPA feeds is

limited to the seepage dilution/evaporation abstraction model. Although the NFC model predicts potential seepage water compositions at any postclosure time, seepage into the drift cannot always occur. During the initial heat pulse, or boiling period, due to the radioactive decay of waste package components, areas near the drift rise in temperature above 96°C, the boiling point of water at repository elevation. During this period, water is driven away as steam, resulting in some areas of the drift that do not have liquid water available for chemical reactions. This process is important because it limits aqueous corrosion on the waste package and drip shield. The process also limits the water available to transport soluble and colloidal radionuclides from the waste form.

Once the radiogenic heat begins to abate and the drift wall temperature falls below 96°C, water can potentially seep into the drift and onto the engineered barriers from the host rock. One result is that evaporation and concentration of potential seepage waters may occur on the drip shield or waste package surface. Minerals may precipitate onto the surface of the waste package and drip shield during seepage evaporation. This can also cause a separation of components from the aqueous phase during transport to the invert—a phenomenon known as salt separation that is discussed in detail in Section 6.15.1.

6.3.3.1 Chemical Divides

As seepage waters make their way into the drift, their chemical composition changes by evaporation and mineral precipitation. When minerals (including salts) precipitate, the relative concentrations of remaining dissolved components change. Drever (1988 [DIRS 118564], p. 235) explains the chemical divide:

> Whenever a binary salt is precipitated during evaporation, and the effective ratio of the two ions in the salt is different from the ratio of these ions in solution, further evaporation will result in an increase in the concentration of the ion present in greater relative concentration in solution and a decrease in the concentration of the ion present in lower relative concentration.

The major geochemical divides for natural lakes are shown in Figure 6.3-15. These geochemical divides largely control the types of waters that can develop by evaporation. In general, natural waters fall into three groups, on the basis of the chemical divides encountered as they evaporate. At relatively low degrees of evaporation, saturation with respect to calcite is achieved, and depending upon the relative concentrations of bicarbonate and Ca^{2+}, the waters can evolve towards Ca-poor, carbonate-rich brines, or Ca-rich, carbonate-poor brines. The carbonate-rich brines are one of the three common natural brine types. Na and K bicarbonates/carbonates are generally lower solubility than Na and K chlorides/nitrates. Hence, at high degrees of evaporation, carbonate waters that are chloride or nitrate-rich, although still containing a significant component of carbonate.

Waters that evolve towards Ca-rich compositions intersect the calcium sulfate (gypsum or anhydrite) chemical divide. Depending upon the relative concentrations of sulfate and Ca^{2+}, the waters can evolve towards Ca-poor, sulfate-rich brines, or Ca-rich, sulfate-poor brines. The Ca-rich brines are the second common natural brine type; the dominant anions are chloride and/or nitrate. The sulfate-rich brines are the third common brine type. As with the carbonate

waters, because Na and K sulfates are lower solubility than Na and K chlorides/nitrates, high degrees of evaporation result in waters that are chloride or nitrate-rich, although still containing a significant component of sulfate.

As shown in Figure 6.3-15, it is also possible for sulfate-rich brines to develop from Mg-rich solutions, although this is relatively rare in nature because the abundance of silica generally limits Mg concentrations through precipitation of sepiolite.

In the P&CE model, potential seepage waters are grouped based on the composition of the concentrated brines that form upon evaporation after they have passed through these chemical divides (Section 6.6). In accordance with geochemical divide theory, the water composition changes due to the sequence of minerals that precipitate from solution. That sequence is a function of the initial water composition, the thermal conditions, and the gas composition. Evaporation to concentrated brines is simulated using geochemical speciation calculations (Section 6.9). These modeling results provide the suite of concentrated brine compositions that could potentially form on the waste package and drip shield.

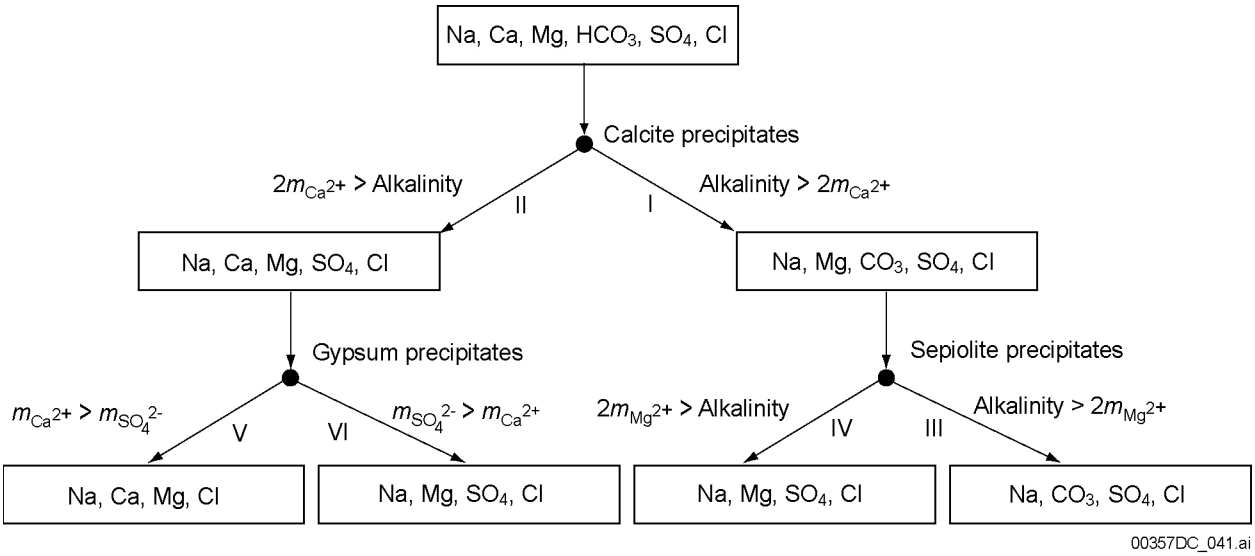

Source: Drever 1988 [DIRS 118564], p. 236. Note that Drever identifies dolomite or another Mg-bearing carbonate as a possible alternative to sepiolite in this diagram.

Figure 6.3-15. Simplified Chemical Divides Diagram Based on Evaporative Concentration of Dilute Starting Waters to Form a Suite of Naturally Occurring Lake Waters

As with previous revisions of the P&CE model, the in-drift water composition is predicted by taking potential seepage water compositions and evaporating or diluting them to equilibrium with the in-drift relative humidity. Water compositions are provided to TSPA in the form of dilution/evaporation lookup tables for each of the four starting waters at eleven different values of the WRIP (Table 6.3-5), and at nine different combinations of temperature (30°C, 70°C, and 100°C) and pCO_2 (10^{-2}, 10^{-3}, and 10^{-4} bars). The appropriate lookup tables for a given time and location are identified using the WRIP, the in-drift pCO_2, and the waste package surface temperature supplied by the MSTHM (SNL 2007 [DIRS 181383]). Once the bounding lookup tables have been identified, the RH at the waste package surface, also supplied by the MSTHM

(SNL 2007 [DIRS 181383]), is used to obtain a water composition in each table. Finally, the in-drift water composition is determined by interpolation between the values from the bounding tables.

6.3.3.2 Determining the Range of Temperature for the Seepage Dilution/Evaporation Abstraction

The temperature range of applicability of the P&CE seepage/dilution evaporation model is determined by the conditions when seepage can occur. Seepage within the drift is not anticipated to occur at drift wall temperatures of over 96ºC, the boiling point of water at the repository elevation. At higher temperatures, a vaporization barrier exists in the rock, a zone of lower liquid saturation, where macroscale liquid flow is unlikely. The presence of a vaporization barrier and a low-saturation zone at temperatures much above 100ºC is corroborated by results of the Drift Scale Test (DST) (Figure 6.3-16). Figure 6.3-16 shows the observed relationship of *in situ* moisture content with temperature, based on neutron logging of DST borehole 79 (February 1998 to December 2001).

Literature data and measured laboratory core-sample saturations (Flint 1998 [DIRS 100033], pp. 32 to 33) are in close agreement with observations from the DST (Figure 6.3-16), and show that at 60°C and 65% relative humidity, rock saturation becomes low enough that liquid flow essentially stops and vapor transport predominates. In measuring volumetric water content, Flint (1998 [DIRS 100033], pp. 32 to 38) used the standard drying heat of 105°C, which is normally considered to remove most pore waters, but noted that "some, but not all, water was removed from the zeolites, clays, and pore spaces." The literature surveyed by Flint (1998 [DIRS 100033], p. 38) suggests that most of the water released from 105°C to 180°C is from thermal dehydration of zeolites, clays, and interstitial waters.

These constraints indicate that seepage is not likely at drift wall temperatures much above boiling, or 96ºC. The waste package surface temperature can be as much as a few degrees higher than the drift wall temperature, so the seepage dilution/evaporation abstraction is designed to provide water chemistries over the temperature range from ambient (approximately 23°C) to around 100°C.

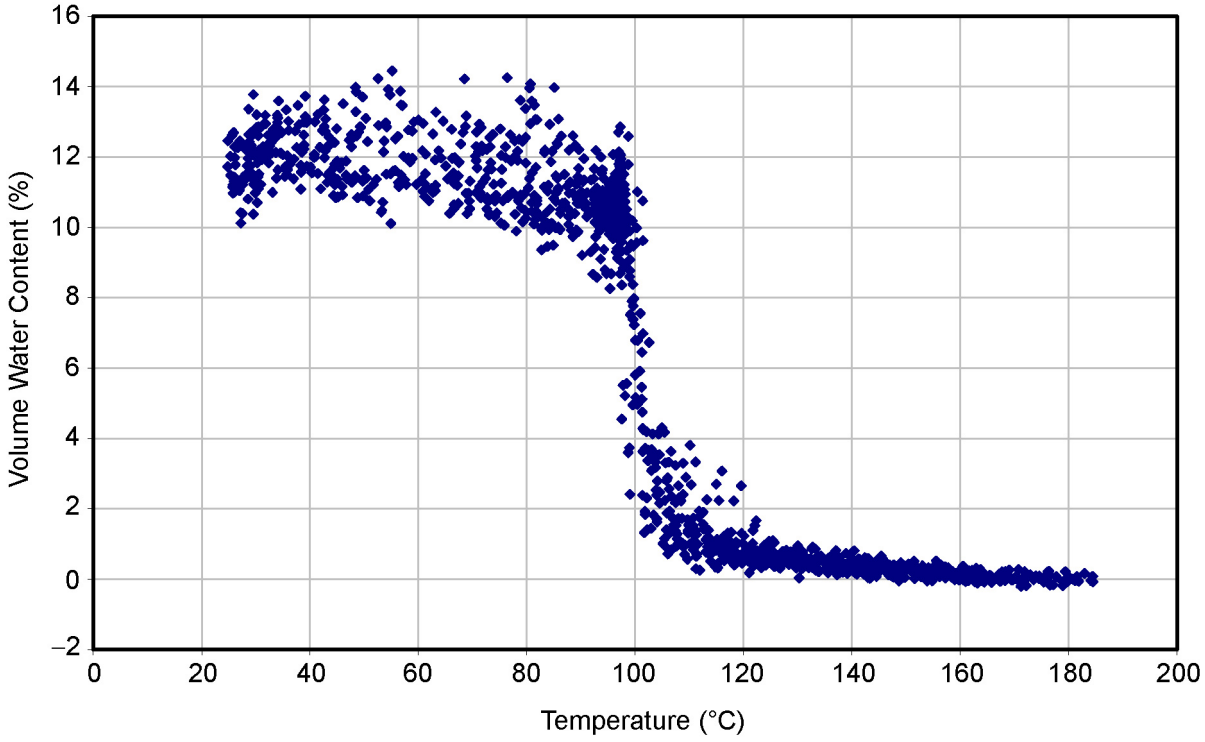

Source: DTN: MO0406SEPTVDST.000 [DIRS 170616], spreadsheet: *79_complete.xls*.

Figure 6.3-16. Rock Moisture Content as a Function of Temperature as Measured from Neutron Logging of Borehole 79 during the DST Heating Phase

6.3.3.3 Dust Deposition

During construction, ventilation, and waste package emplacement, and after sealing the primary entrances to the repository, dust will accumulate in the drift. Dust on the drip shields and waste packages is of concern for its potential influence on corrosion.

Dust is deposited initially from the tuff bedrock during excavation and construction of the repository. In addition, ventilation will carry surface dust into the drifts. Surface dust may contain natural evaporite minerals, blown in from the surrounding countryside and playas, possibly from up to hundreds of kilometers away (Reheis et al. 2002 [DIRS 163132]). Some excavation dust may contain small amounts of bromide, which has been used as a tracer in construction waters at Yucca Mountain.

Information on the general characteristics of atmospheric dust, on relevant atmospheric processes, and on dust from desert playas in Nevada, has been summarized in *Analysis of Dust Deliquescence for FEP Screening* (SNL 2007 [DIRS 181267], Sections 4.1.2 and 6.1.4). In general, nitrate and ammonia are important components of atmospheric dust, primarily due to their production in the upper atmosphere. Nitrate salts are recognized as an important component of atmospheric dusts and aerosols, and their properties (including deliquescence) are considered important to the understanding of certain weather and climatic phenomena. Anthropogenic sources add to the nitrate burden of atmospheric dust. The extent to which playa dusts are incorporated within atmospheric dust is uncertain. Nitrate minerals are not commonly

described as components of surface playa salts, so playas are not considered a significant source of nitrate in atmospheric dust.

6.4 COUPLED PROCESSES

Coupled processes are those in which two or more physical and chemical processes simultaneously interact to produce a result, or in which a process is affected by physical and chemical variables at the same time. The coupled processes considered in TSPA are those that have been found to have a potentially significant effect on dose calculations.

The relative importance of different coupled processes, formally classified as FEPs, is discussed briefly in Section 6.14 and documented in more detail in DTN: MO0706SPAFEPLA.001 [DIRS 181613]. These FEPs contain straightforward screening justifications if the FEP is excluded from further consideration, or a description of the TSPA disposition if it is included. The rationale for exclusion may be based upon regulatory requirements, low probability of occurrence, or low consequence in terms of impact on calculated dose.

Coupled processes are incorporated into the P&CE model implicitly through inputs from process-level models (e.g., the IDPS developed in SNL 2007 [DIRS 177411], or the NFC model discussed in Section 6.3). This report describes an abstraction methodology that produces a chemical environment dependent upon drip shield and waste package surface temperature and humidity; and reaction with gas-phase CO_2 and precipitation, and possible deliquescence, of soluble salts. Explicit consideration was given to the chemical interactions of potential crown seepage and ground support materials (Section 6.8).

Onsager Coupled Processes—Coupled processes involving diffusion and diffusion-like processes (e.g., heat conduction) can be described in terms of the Onsager processes, which are represented by a matrix of first-order relationships (Table 6.4-1). These are fundamental processes that can occur even if the associated physical or chemical properties of the medium are temporally or spatially invariant. Onsager couplings are driven indirectly by gradients of thermodynamic state variables (e.g., temperature, pressure, chemical potential, and electrical potential) that affect chemical transport in aqueous solution. Direct transport processes are driven by the same thermodynamic-state variables in well-known relations such as Fourier's Law, Darcy's Law, Fick's Laws, and Ohm's Law. Diffusive processes dominate in Onsager-coupled processes.

Direct processes lie along the main diagonal of the table, and indirect coupled processes are off-diagonal. The existence of indirect processes is generally known from controlled experiments. Phenomenological coefficients relating gradients and fluxes for indirect coupled processes are not generally known for geologic media. Nevertheless, the indirect coupled processes shown in Table 6.4-1 are not significant to performance of the repository because the magnitudes of the associated potential gradients or fluxes in the host rock are too small. The direct processes including Darcy flow and Fickian diffusion overwhelm the indirect processes. These direct processes are included in the models used for TSPA-LA. Some of the indirect Onsager-coupled processes listed in Table 6.4-1, such as chemical osmosis (observed in clays or zeolites) or the sedimentation current in response to heating the host rock (static potentials in the host rock), have been observed at Yucca Mountain. However, the effects of these processes are

relatively small, and not important to various aspects of repository performance, including the environment in which metal barriers might corrode and the possible migration of radionuclides from breached packages.

The possible effect of coupled processes (relevant to the Onsager process) on radionuclide migration has been discussed and evaluated (DTN: MO0706SPAFEPLA.001 [DIRS 179476]). The conclusion was reached that the off-diagonal processes are unimportant. The on-diagonal processes are either accounted for in current modeling for TSPA or are excluded. That determination is applicable to the effect of such processes acting on the chemical environment to which metal barriers are exposed. For example, no significant pressure gradients (sufficient to support significant off-diagonal type fluxes as included in Table 6.4-1) are expected between the drift wall and the waste package outer barrier, either radially or along the length of the drift (see the treatment of pressure in SNL 2007 [DIRS 177404]). Similarly, electrical potentials affecting the chemical environment are minimal and insufficient to drive associated off-diagonal fluxes. Temperature- and chemical-potential gradients are principal drivers for the in-drift chemical environment. Existing models incorporate the relevant effects, which are more often dominated by vapor–liquid equilibrium than condensed-phase transport effects. Osmotic equilibrium in particular is dominated by vapor–liquid equilibrium, as represented by deliquescence of salts. The same effect is controlling when a drop of seepage water falls from the drift wall onto a metal barrier surface (drip shield or waste package outer barrier). The drop re-equilibrates to new conditions of temperature (higher) and relative humidity (lower). Salt separation effects may occur on a metal barrier surface owing to several factors, including temperature and RH gradients on that surface and even in the absence of such gradients due to the flow of aqueous solution down a sloping surface while precipitated solids remain behind at the point of precipitation. However, vapor–liquid equilibrium at any point along such gradients or flow paths is a strong determinant of what results at any such point.

Lastly, it is worth pointing out that the Onsager framework of addressing coupled processes is nothing more than that, a framework. Other equivalent approaches can be taken that include the relevant effects. Consider, for example, diffusion of solutes in aqueous solution in the case in which the system of interest includes a temperature gradient. Instead of referring to the “Soret” effect, a treatment that explicitly expresses the diffusion coefficients as temperature-dependent quantities could be used. Furthermore, Table 6.4-1 could be expanded to include the effects of analogous potential gradients, such as a gravitational potential gradient.

Table 6.4-1. Onsager Couplings and Direct Transport Process Fluxes Driven by Temperature, Pressure, Chemical Potential, and Electrical Potential Gradients

	Gradient			
	Temperature	**Pressure**	**Chemical Potential**	**Electrical Potential**
Heat Flux	**Fourier's Law: heat flow in a temperature gradient**	Thermal filtration: heat flow in a pressure gradient	Dufour effect: heat flow in a density gradient	Peltier effect: heat flow in a voltage gradient
Volume Flux	Thermal osmosis: volume flow in a temperature gradient	**Darcy's Law: volume flow in a pressure gradient**	Chemical osmosis: volume flow in a concentration gradient	Electro-osmosis: volume flow in a voltage gradient
Mass Flux	Soret effect: particle flow in a temperature gradient	Reverse osmosis: mass flow in a pressure gradient	**Fick's Law: mass flow in a concentration gradient**	Electrophoresis: mass flow in a voltage gradient
Electrical Flux	Seebeck effect: electrical current in a temperature gradient	Streaming current: electrical current in a pressure gradient	Sedimentation current: electrical current in a density gradient	**Ohm's Law: current flow in a voltage gradient**

Source: Carnahan 1987 [DIRS 138706], p. 2.

NOTE: Onsager couplings and direct transport processes are along the diagonal in bold type. The Onsager couplings are important only when aqueous, liquid, or solid diffusion dominates over advection.

6.5 INTRODUCED MATERIALS

Figure 6.5-1 illustrates the general configuration of materials introduced into a repository drift. As the figure shows, the current emplacement drift configuration contains no cementitious materials. The materials that are emplaced are expected to undergo chemical and physical changes, and they may affect the in-drift chemical environment.

This section analyzes the corrosion rates and relative lifetimes of the primary introduced materials in the current repository design. This information is used later to establish boundary conditions, modeling constraints, and potential effects on the in-drift environment. Evolution of the in-package materials is evaluated in the in-package chemistry (IPC) report (SNL 2007 [DIRS 180506]).

The chemical effects and corrosion rates of other introduced materials are evaluated within this document. The low-alloy or carbon steels are found to be the only significant contributor to the oxygen mass balance calculations associated with the evolution of the in-drift gaseous environment (Section 6.7). Alloy 22 and titanium material corrosion rates are only presented here to demonstrate their insignificant effect upon the in-drift environment. The analyses in this section are also used to determine the extent of effect on seepage chemistry as it pertains to the interaction with the ground support (e.g., Stainless Steel Type 316L corrosion in Section 6.8).

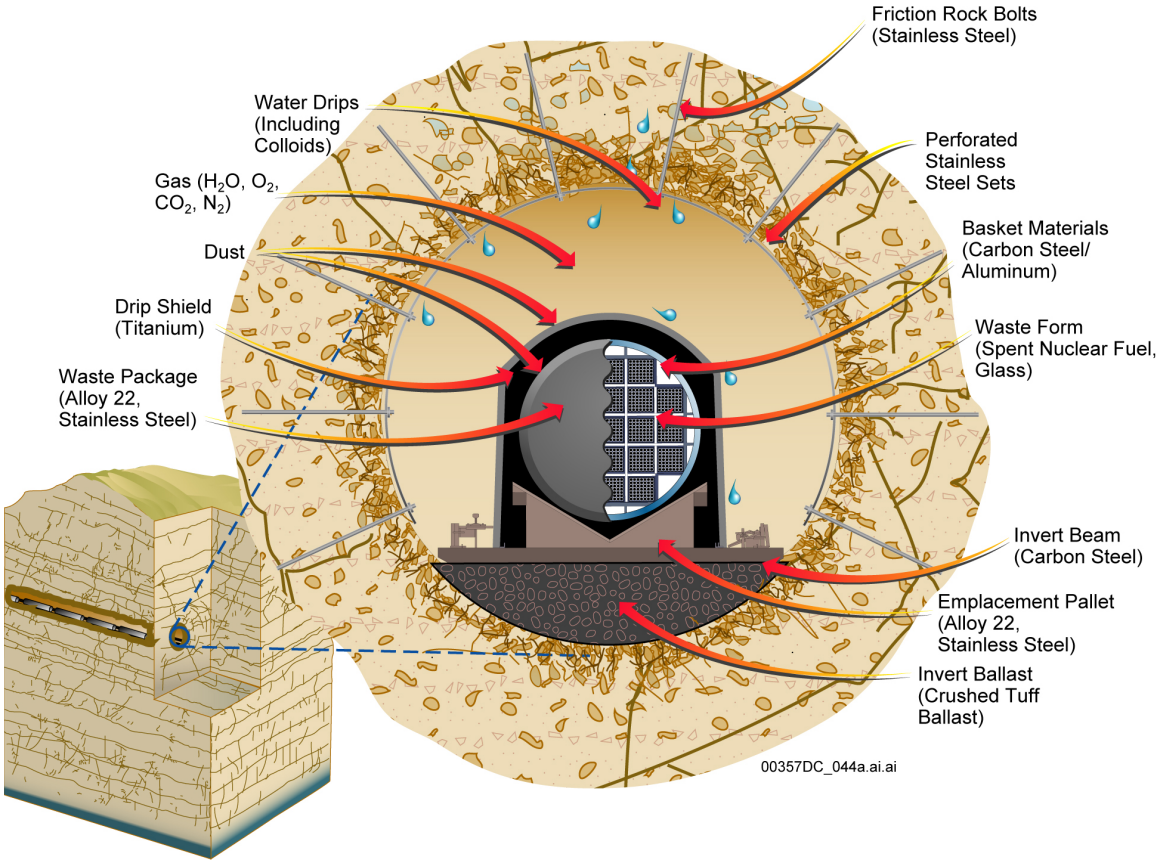

Figure 6.5-1. General Location of Engineered Barrier System Components and Materials

6.5.1 Material Corrosion Rates

In the following sections and tables, general corrosion rates under a variety of environmental conditions are discussed. These include corrosion rates determined under humid air and immersed conditions. Titanium and Alloy 22 corrosion rates are taken directly as those used by other project documents.

For other materials, a set of experimental work for the project was carried out using three waters, referred to as simulated dilute water (SDW), simulated concentrated water (SCW), and simulated acidified water (SAW), respectively (McCright 1998 [DIRS 114637]). The SDW simulates J-13 well water at concentrated by a factor of ten to account for minor effects of water evaporation and boiling. SCW simulates J-13 well water concentrated by a factor of 1,000 to account for long-term water evaporation and boiling in the repository environment. SAW represents J-13 well water that has been acidified and concentrated, which is intended to simulate the effect of possible microbial metabolic products. Corrosion tests were run on samples immersed in these waters, and in the humid air generated above these waters upon heating. Further information on these simulated solutions is provided by McCright (1998 [DIRS 114637]).

The corrosion of metals in the atmosphere is primarily controlled by temperature, relative humidity, and chemistry. Many other parameters can affect corrosion rates, including time of wetness, rainfall, fog, and hours of sunlight, but these are not discussed here as such parameters are not available to describe the in-drift environment. Temperatures and relative humidity values are presented in the tables below. However, details of chemistry are not available in many cases. Note that the tables in this document capture the data as it exists within each data source as opposed to providing a consistent number of significant figures. In the case of reporting values from EQ3/6 calculated data, rounding is usually done to three significant figures.

The most corrosive environments are typically the marine and industrial atmospheres, which represent corrosion under conditions of high humidity, of metal covered with a salt crust, or in the presence of high concentrations of atmospheric contaminants.

In the case of pooled water in or on materials, those values indicated by "freshwater" and "saltwater" are used for the corrosion rate. The freshwater rates are representative of those solutions that are dilute, such as lake water and J-13 well water. The saltwater rates are for ocean water with an average chloride content of approximately 17,000 ppm (Forgeson et al. 1958 [DIRS 159343]), and are used when the natural waters have been concentrated due to evaporation or contact with engineered materials. Modifications to these definitions will be discussed for each individual material in the following sections.

6.5.1.1 Titanium

Because a stable oxide film (TiO_2) forms quickly upon exposure to oxygen, titanium is generally resistant to corrosion. This is shown in Table 6.5-1, which lists the corrosion rates of titanium (Grade 16) determined for the dripping water case in *General Corrosion and Localized Corrosion of the Drip Shield* (SNL 2007 [DIRS 180778], Table 17). These general corrosion rates of the outer surface of the drip shield are represented by a cumulative distribution function (CDF) generated by combining the Long Term Corrosion Test Facility one-year weight-loss samples and the crevice samples from experimental results (SNL 2007 [DIRS 180778], Section 6.5.5). The minimum corrosion rate is taken as the lowest corrosion rate that is greater than zero from the CDF. The maximum corrosion rate is given as the corrosion rate that is closest to the 95th percentile from the CDF. The minimum, maximum, and 50th percentile of the CDF are shown in Tables 6.5-1 (in bold) and 6.5-8.

Table 6.5-1. Titanium Grade 16 Corrosion Rates

Sample	Corrosion Rate (µm/yr)	CDF
1	0.00E+00	0.00E+00
2	**4.18E-03** (minimum)	1.43E-01
3	7.91E-03	1.79E-01
4	7.91E-03	2.14E-01
5	7.92E-03	2.50E-01
6	7.99E-03	2.86E-01
7	1.60E-02	3.21E-01
8	1.61E-02	3.57E-01
9	1.65E-02	3.93E-01
10	2.10E-02	4.29E-01
11	2.36E-02	4.64E-01
12	**2.37E-02** (50th percentile)	5.00E-01
13	2.40E-02	5.36E-01
14	2.53E-02	5.71E-01
15	4.00E-02	6.07E-01
16	4.26E-02	6.43E-01
17	4.29E-02	6.79E-01
18	5.15E-02	7.14E-01
19	6.34E-02	7.50E-01
20	6.50E-02	7.86E-01
21	7.15E-02	8.21E-01
22	7.92E-02	8.57E-01
23	8.22E-02	8.93E-01
24	1.12E-01	9.29E-01
25	**1.13E-01** (maximum)	9.64E-01
26	3.19E-01	1.00E+00

Source: SNL 2007 [DIRS 180778], Table 17.

NOTE: Corrosion rates converted to µm/yr from mm/yr.

6.5.1.2 Alloy 22

Corrosion rates for Alloy 22 given here are consistent with those determined in *General Corrosion and Localized Corrosion of Waste Package Outer Barrier* (SNL 2007 [DIRS 178519], Section 6.4.3.4), which presents a base-case temperature-dependent general corrosion model that determines general corrosion rates of Alloy 22 based on an Arrhenius relation in logarithmic form (SNL 2007 [DIRS 178519], Equation 6-25). This does not account for any microbial activity, which can only increase the corrosion rate on a localized scale. The effect on mass corroded by microbial activity is small, and implemented in TSPA by increasing the general corrosion rate by up to a factor of two (SNL 2007 [DIRS 178519], Section 6.4.5). The calculated model output is presented as a general corrosion rate CDF at different temperatures (SNL 2007 [DIRS 178519], Figure 6-26; DTN: MO0409MWDUGCMW.000 [DIRS 171714]). Table 6.5-2 provides the 5th, 50th, and 95th percentile results of the corrosion rate CDF for Alloy 22 at 25°C, 50°C, 75°C, 100°C, 125°C, and 150°C. Table 6.5-8 provides

these same results but for 25°C, 100°C, and 150°C only. The corrosion rate results in Tables 6.5-2 and 6.5-8 have been converted from nm/yr to µm/yr.

Table 6.5-2. Corrosion Rates of Alloy 22

Temperature (°C)	5th Percentile (µm/yr)	50th Percentile (µm/yr)	95th Percentile (µm/yr)
25	0.0005	0.0024	0.0058
50	0.0011	0.0053	0.0131
75	0.0021	0.0106	0.0262
100	0.0039	0.0193	0.0477
125	0.0065	0.0326	0.0805
150	0.0104	0.0518	0.1278

Source: DTN: MO0409MWDUGCMW.000 [DIRS 171714], spreadsheet: *Base Case GC Rate CDF.xls*, tab: "Base Case GC Rate."

6.5.1.3 Copper Alloy

The summary of corrosion rates for copper under different environmental conditions is presented in Table 6.5-3. Copper may be emplaced in the drift as the bus (third) rail as part of the gantry system. Under outdoor conditions, the main factors influencing corrosion of copper are relative humidity and concentration of aerosol particles (Sequeira 2000 [DIRS 162970]).

Table 6.5-3. Corrosion Rates of Copper under Various Environmental Conditions

Environment	Maximum (µm/yr)	Mean (µm/yr)	Minimum (µm/yr)
90°C, J-13 steam, near 100% relative humidity	4.15	2.86	1.67
95°C to 100°C, J-13 steam, near 100% relative humidity	6.60	4.79	3.15
150°C, J-13 steam, near 100% relative humidity	1.78	1.09	0.46
90°C, Soln 7 steam, near 100% relative humidity (1,000 ppm Cl)	5.90	1.60	0.39
Marine atmosphere (70% to 83% relative humidity)	4.14	1.68	0.43
Marine atmosphere (60% to 70% relative humidity)	1.38	1.33	1.27
Rural atmosphere (wet: 69.5% to 83% relative humidity)	2.01	0.94	0.42
Rural atmosphere (dry: 39% relative humidity)	0.13	0.13	0.13
Industrial atmosphere (65% to 68% relative humidity)	1.90	1.50	1.30
Urban atmosphere (74% relative humidity)	1.40	1.22	1.04

NOTE: Calculations in Output DTN: MO0705OXYBALAN.000, spreadsheet: *atmospheric May2007.xls*, tab: "copper."

6.5.1.4 Aluminum Alloy

Measured aqueous corrosion rates for aluminum alloy are presented in Table 6.5-4. Aluminum differs from other metals in that the main corrosion behavior is a form of localized corrosion called pitting. Because pitting does not allow for easy determination of material lifetimes, pitting weight loss data for aluminum are converted to general rates for use in this report.

Table 6.5-4. Corrosion Rates of Aluminum Alloys in Aqueous Environments

Environment	Maximum (μm/yr)	Mean (μm/yr)	Minimum (μm/yr)
Freshwater	36.93	12.95	0.40
Saltwater	110.91	9.69	0.12

Source: DTN: MO0409SPAACRWP.000 [DIRS 172059], spreadsheet: *aluminum2.xls*, tab: "range."

Atmospheric data on the corrosion of aluminum alloy come from *Corrosion* (ASM International 1987 [DIRS 103753], Tables 8 and 11) and can be found in Table 6.5-5. The minimum value comes from 20-year atmospheric corrosion data, the median value from 10-year atmospheric corrosion data, and the maximum from the highest value of atmospheric corrosion.

Table 6.5-5. Atmospheric Corrosion Rates of Aluminum Alloy 6061

Maximum Rate (μm/yr)	Median Rate (μm/yr)	Minimum Rate (μm/yr)
0.422	0.35	0.076

Source: ASM International 1987 [DIRS 103753], Tables 8 and 11.

6.5.1.5 Stainless Steel Type 316L

In relatively uncontaminated but open environments, such as rural atmospheres or steam produced from dilute solutions such as J-13 well water, the corrosion rate for Stainless Steel Type 316L is slow. The data, mostly originating from non-sterile and open environments, inherently includes any increased corrosion rate due to microbial influences. However, when the atmosphere contains contaminants, such as chlorides, the corrosion rate rises significantly (Table 6.5-6). Chloride contamination can come from exposure to marine environments or concentrated underground waters. The amount of corrosion depends on the distance of the test specimen from the chloride source (i.e., the tide line), showing that an increase in chloride concentration results in a more corrosive environment (Bomberger et al. 1964 [DIRS 163699], and Southwell et al. 1976 [DIRS 100927]).

The two values in bold type in Table 6.5-6 below are used in the calculations to determine the effect of Stainless Steel Type 316L ground support degradation upon crown seepage water (Section 6.8).

Table 6.5-6. Corrosion Rates of Stainless Steel Type 316L under Various Environmental Conditions

Environment	Maximum (μm/yr)	Mean (μm/yr)	Minimum (μm/yr)
Marine atmosphere[a]	0.517	**0.113**	0.000
29.5°C freshwater[b]	0.0475	0.0083	0.0007
50°C freshwater[b]	0.2286	0.1614	0.1016
70°C freshwater[b]	0.2540	0.2413	0.2286
80°C freshwater[b]	0.2794	0.2141	0.1090
90°C freshwater[b]	0.2540	0.2032	0.1524
100°C freshwater[b]	0.5100	0.3247	0.0370
26.7°C saltwater[b]	14.787	**1.939**	0.0014

[a] Calculated in Output DTN: MO0705OXYBALAN.000, spreadsheet: *atmospheric May2007.xls*, tab: "316."
[b] DTN: MO0409SPAACRWP.000 [DIRS 172059], spreadsheet: *aqueous-316L.xls*.

6.5.1.6 Carbon and Low-Alloy Steels

The corrosion rates for carbon and low-alloy steels in different environments are shown in Table 6.5-7. Thus far, no specific data have been located for corrosion at 25°C of Carbon Steel Type A516, but in terms of composition it is a carbon or low-alloy steel (>98% iron; Table 4.1-14) and is considered equivalent to any other carbon or low-alloy steel for corrosion purposes. Under sub-aerial exposure, the highest corrosion rate of approximately 1,057 μm/yr comes from a steel sample sitting directly on the beach at Cape Canaveral, Florida. This sample was fully exposed to constant sea spray and is an indication of how salt buildup may affect the corrosion of metals. The lowest rate (0.40 μm/yr) comes from a rural atmosphere at a relative humidity below 60%. These two values show how the corrosion rate for these steels can greatly differ depending on the atmospheric environment. Both of these examples originate from non-sterile and open environments, and therefore inherently include any increased corrosion rate due to microbial influences.

Aqueous corrosion rates of carbon and mild steels are much lower than marine or industrial atmospheric corrosion rates (Table 6.5-7). Temperature effects are also different. In atmospheric corrosion, there is generally a direct correlation between temperature and corrosion rate. However, in aqueous environments, corrosion at 60°C is greater than that at 90°C. This is corroborated by Brasher and Mercer (1968 [DIRS 100883]), who measured the relationship between corrosion and temperature (Figure 6.5-2). As shown in the worksheet titled "rate vs. temperature" in DTN: MO0409SPAACRWP.000 [DIRS 172059], the highest corrosion rates occur at 60°C. The corrosion rate decreases with either increasing or decreasing temperature from this value (i.e., corrosion rates for 25°C and 90°C will be lower than the 60°C rates). As can be seen from Figure 6.5-2, the rates for the mild steel are within the same range as those for Carbon Steel Type A516 as provided by McCright (1998 [DIRS 114637]). The data plotted in Figure 6.5-2 show that in corrosion for mild steel, the rates at 25°C are slightly lower than those at 90°C. The rates for A516 corrosion are used in Section 6.8 to approximate the corrosion rates for the A759 and A588 steels in the invert (ASTM A 759-00 2001 [DIRS 159971]; ASTM A 588/A 588M – 05 [DIRS 176255]; and Table 6.7-1).

Table 6.5-7. Corrosion Rates of Carbon and Low-Alloy Steels in Various Environmental Conditions

Environment	Maximum (μm/yr)	Mean (μm/yr)	Minimum (μm/yr)
60°C-SDW near 100% RH[a]	74.25	41.97	18.60
90°C-SDW near 100% RH[a]	135.26	63.60	22.69
60°C-SCW near 100% RH[a]	360.78	177.16	76.38
90°C-SCW near 100% RH[a]	423.06	195.43	72.96
Marine atmosphere (80% relative humidity and over)[a]	851.09	153.33	9.87
Marine atmosphere (70% to 80% relative humidity)[a]	1,057.18	101.94	6.39
Industrial atmosphere (Over 80% relative humidity)[a]	123.00	102.5	85.50
Industrial atmosphere (70% to 80% relative humidity)[a]	137.80	46.28	12.55
Industrial atmosphere (60% to 70% relative humidity)[a]	164.54	20.58	3.77
Semi-industrial atmosphere (over 80% relative humidity)[a]	171.70	119.93	75.3
Semi-industrial atmosphere (60% to 70% relative humidity)[a]	60.88	35.23	17.33
Rural atmosphere (over 80% relative humidity)[a]	60.10	39.19	21.60
Rural atmosphere (70% to 79% relative humidity)[a]	59.00	26.63	10.68
Rural atmosphere (60% to 69% relative humidity)[a]	75.50	19.37	3.93
Rural atmosphere (less than 60% relative humidity)[a]	38.67	13.86	0.40
Urban atmosphere (70% to 80% relative humidity)[a]	68.70	34.81	10.76
Urban atmosphere (60% to 70% relative humidity)[a]	93.70	38.71	7.12
Urban atmosphere (below 60% relative humidity)[a]	29.16	11.09	0.70
60°C-SDW[b]	106.93	77.43	65.77
90°C-SDW[b]	88.68	51.80	29.53
60°C-SCW[b]	14.36	10.61	6.77
90°C-SCW[b]	9.35	6.84	3.69

[a] Calculated in Output DTN: MO0705OXYBALAN.000, spreadsheet: *atmospheric May2007.xls,* tabs: "A516-lab results (≈ 100%RH)," "Steel-marine," "Steel-industrial & semi.," "Steel-rural," and "Steel-urban."
[b] DTN: MO0409SPAACRWP.000 [DIRS 172059], spreadsheet: *aqueous-A516.xls*.

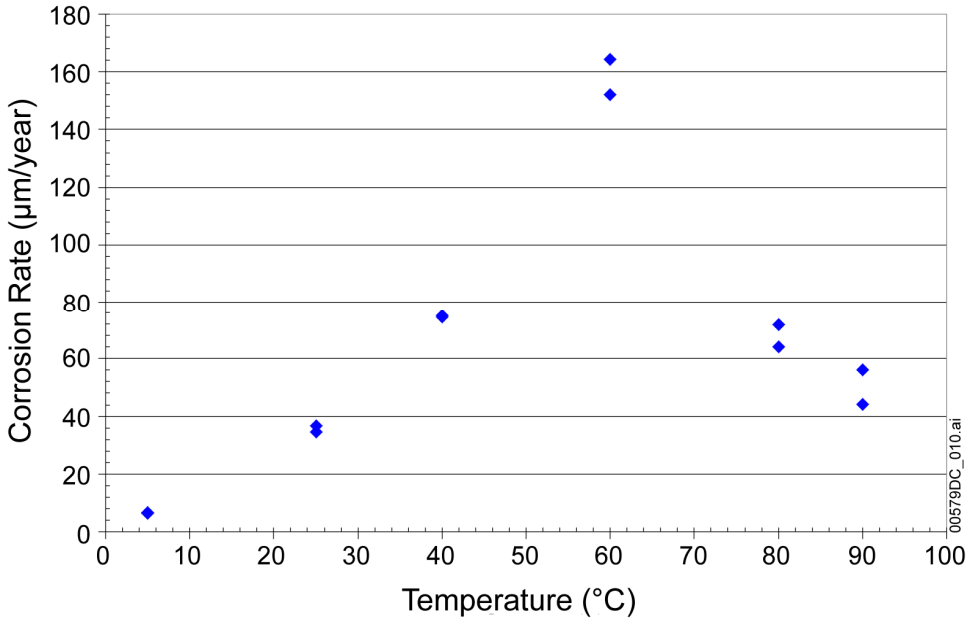

Source: DTN: MO0409SPAACRWP.000 [DIRS 172059], spreadsheet: *aqueous – A516.xls*.

Figure 6.5-2. Corrosion Rates for Mild Steel in Water, Plotted as a Function of Temperature (°C)

6.5.2 Material Lifetimes

The expected lifetime of introduced materials in the repository will be influenced by environmental parameters such as temperature, relative humidity, and available oxygen. Due to the variability of the in-drift environment, the corrosion rates are compiled into Table 6.5-8 by finding the maximum corrosion rate to represent each of the rate categories (maximum or 95%, mean or 50%, and minimum or 5%) for aqueous and atmospheric conditions. The "Comments" column in Table 6.5-8 indicates the conditions under which the corrosion occurred.

The materials that corrode away within a few hundred years (the low-alloy carbon steel) will consume oxygen at the greatest rate and form oxides that will settle in the drift. It is anticipated that the remaining materials will last long enough to potentially interact with crown seepage water entering the drift and possibly influence the chemistry of those waters.

The long-lasting component most likely to interact with crown seepage is the stainless steel ground support along the crown of the drift, and this interaction is explicitly analyzed in Section 6.8 and found to have an insignificant impact on water chemistry.

The analysis in Section 6.8 uses the Stainless Steel Type 316L mean corrosion rates of 0.113 µm/yr (steam and atmospheric) and 1.939 µm/yr (fresh or salt water) from Table 6.5-8 as direct input for the analysis of Stainless Steel Type 316L in Section 6.8.3. The availability of oxygen, as decreased by corrosion in the drift, is addressed in Section 6.7. The mean aqueous corrosion rate of 10.61 µm/yr for carbon or low alloy steels from the one year tests (Table 6.5-8) is used as direct input for calculating the steel interaction with invert waters in Section 6.8.

Table 6.5-8. Selected Corrosion Rates of Metallic and Alloy Materials for Use in Engineered Barrier System Chemical Environment Calculations

Material	Environmental Conditions	Maximum Corrosion μm/yr	Mean or 50th Percentile Corrosion μm/yr	Minimum Corrosion μm/yr	Reference	Comments
Titanium (Grade 16)	Water dripping case (seepage environment)	0.113	0.0237	0.00418	Table 6.5-1	50th percentile corrosion used, not the mean
Alloy 22	25°C	0.0058	0.0024	0.0005	Table 6.5-2	50th percentile corrosion used, not the mean
Alloy 22	100°C	0.0477	0.0193	0.0039	Table 6.5-2	50th percentile corrosion used, not the mean
Alloy 22	150°C	0.1278	0.0518	0.0104	Table 6.5-2	50th percentile corrosion used, not the mean
Copper alloy	Steam and atmospheric	6.60	4.79	3.15	Table 6.5-3	J-13 steam, 95°C to 100°C, near 100% RH
Aluminum alloy	Fresh/salt water	110.91	12.95	0.4	Table 6.5-4	Saltwater for maximum, freshwater for mean and minimum
Stainless Steel Type 316L	Steam and atmospheric	0.517	**0.113**[a]	0.099	Table 6.5-6	Marine atm for maximum and mean and 100°C J13 steam for minimum (data for 207°C brine steam not included)
Stainless Steel Type 316L	Fresh/salt water	14.787	**1.939**[b]	0.2286	Table 6.5-6	26.7°C saltwater for maximum and mean and 70°C freshwater for minimum
Carbon or low-alloy steels	Steam and atmospheric	1,057.18	**195.43**[a]	85.5	Table 6.5-7	Maximum marine atm 70 to 80% RH, mean SCW 90°C steam, and minimum industrial atm. Over 80% RH
Carbon or low-alloy steels	Simulated concentrated water, i.e. "saltwater"	14.36	**10.61**[c]	6.77	Table 6.5-7	60°C SCW for all data from one year tests[d]

Sources: DTN: MO0312SPAPCEML.003 [DIRS 167409] (indirect only) and MO0409SPAACRWP.000 [DIRS 172059]; only bolded items are use d further as direct input. Source for titanium corrosion rates is SNL 2007 [DIRS 180778], Table 17. Source for Alloy 22 corrosion rates is DTN: MO0409MWDUGCMW.000; [DIRS 171714], spreadsheet: *Base Case GC Rate CDF.xls*, tab: "Base Case GC Rate."

[a] Calculated in Output DTN: MO0705OXYBALAN.000, spreadsheet: *atmospheric May2007.xls*, tabs: "316" and "A516-lab results (≈ 100%RH)."

[b] DTN: MO0409SPAACRWP.000 [DIRS 172059], spreadsheet: *aqueous-316L.xls*, tab: "saltwater."

[c] DTN: MO0409SPAACRWP.000 [DIRS 172059], spreadsheet: *aqueous-A516.xls*, tab: "saltwater."

[d] For data reported for cities in which the temperature and RH are unknown or not given in the reference cited, values from another city in the same state are used as an approximate value.

Figure 6.5-3 shows the mean (or 50th percentile), minimum, and maximum lifetimes of materials listed in Table 6.5-8. These material lifetimes are presented on a per centimeter basis as that distance is an excellent proxy for general material thickness, within an order of magnitude. Specifically, material lifetimes were hand calculated by dividing the 10,000 µm/cm conversion by the mean or 50th percentile, minimum, and maximum corrosion rates (µm/yr) for each material given in Table 6.5-8. For example, the minimum corrosion rate for titanium (Grade 16) given in Table 6.5-8 is 0.00418 µm/yr; thus, by dividing 10,000 µm/cm by 0.00418 µm/yr, the maximum lifetime for titanium is calculated to be approximately 2.392×10^6 yr/cm of material.

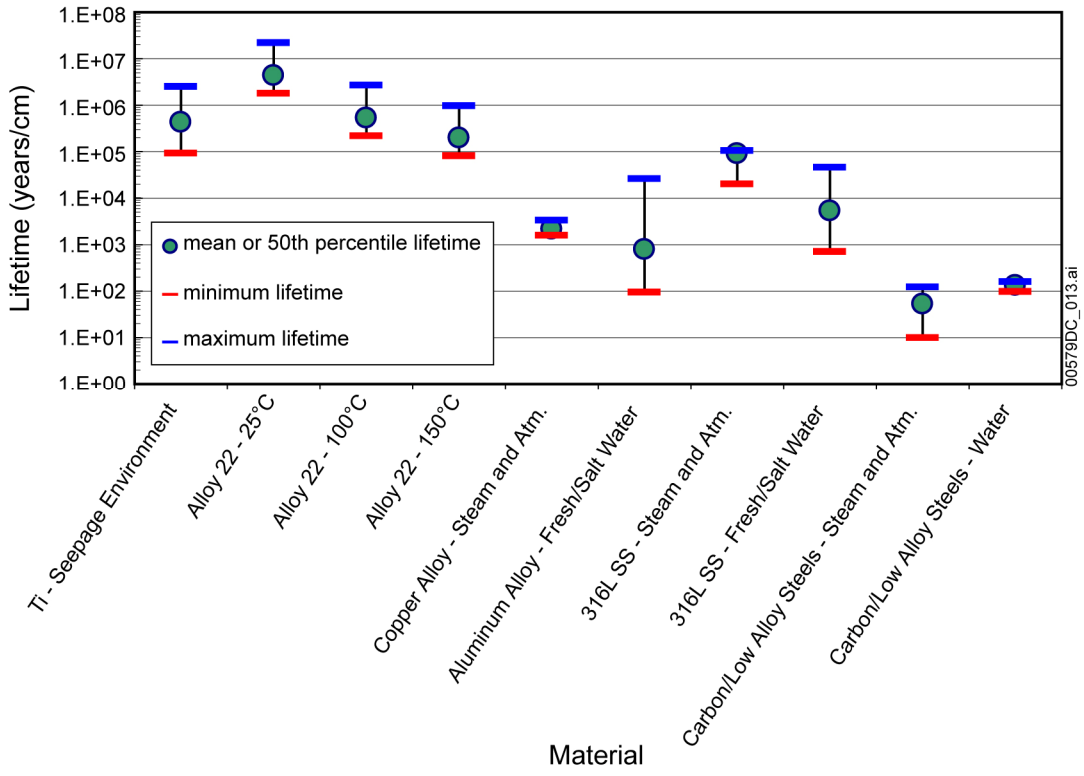

Figure 6.5-3. Relative Material Lifetimes Using the Mean or 50th Percentile, Minimum, and Maximum Corrosion Rates from Table 6.5-8.

As can be seen by Figure 6.5-3, the mean lifetime values for carbon or low-alloy steels in a steam and atmospheric environment is over one order of magnitude less than any other material. This comparison leads to the conclusion that for modeling of oxygen consumption, due to and proportional to corrosion, the most significant consumption from low-alloy or carbon steels will lead to a reasonable approximation of the total oxygen demand. The oxygen balance calculation based upon this is performed in Section 6.7.1 and utilizes the mean low-alloy steel corrosion rate for atmospheric conditions reported in Table 6.5-8.

6.6 SELECTION OF TSW PORE WATERS

6.6.1 Overview

Previously, the chemistry of the near field was evaluated using five starting waters, selected as being representative of the available pore-water analyses at the time. However, in recent years, additional analyses have become available, and, to ensure that the range of pore-water compositions was being adequately represented, all currently available TSw pore-water analyses (125) have been compiled and re-evaluated. This process is graphically depicted in Figure 6.6-1.

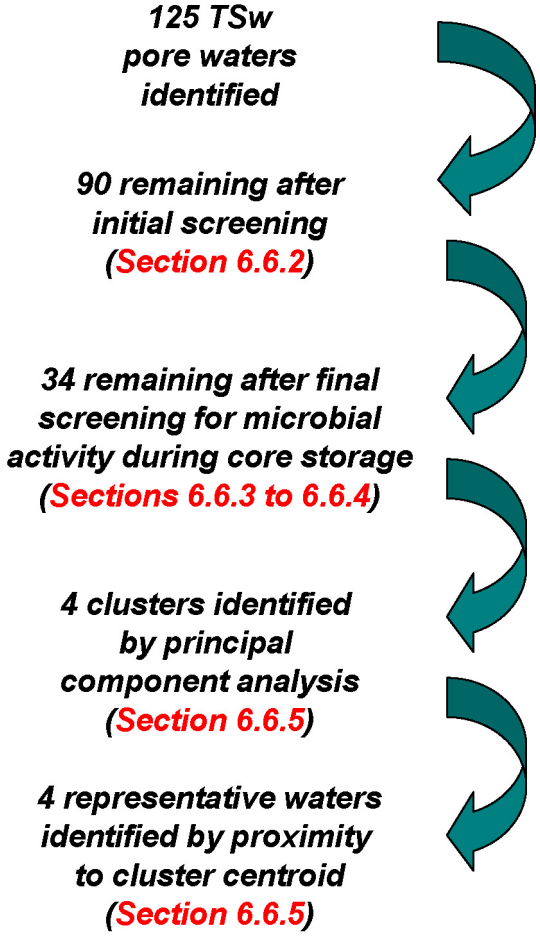

Figure 6.6-1. Diagram Showing the Flow of the Pore-Water Down-Selection Process

First, an initial screening of incomplete pore-water analyses and those not considered representative of current ambient conditions was carried out, reducing the total to 90 analyses. When the remaining analyses were examined, discrepancies in the data were identified and ultimately linked to biological processes occurring in the cores during core storage. Criteria for evaluating the degree of modification by microbial processes were developed and used to screen out affected waters, reducing the total to 34. The statistical method of principle component analysis was then used to determine the number of chemically distinct clusters represented by the remaining water analyses (4), and representative waters from each group were chosen by selecting those nearest to the cluster centroid. All waters identified as being minimally affected

by microbial activity provide feeds to the P&CE models in the form of chloride:nitrate ratios sampled by TSPA; the four representative water compositions are used as starting water compositions for EQ3/6 calculations of diluted and evaporated seepage water compositions within the drift, which are provided to TSPA by the P&CE abstraction models.

6.6.2 Initial Screening

A large number of pore-water compositions (125) are available from the TSw. These pore waters are summarized in Output DTN: SN0705PAEBSPCE.015 (spreadsheet: *TSw_Porewater_Data.xls*). From that group, a suite of starting water compositions for the P&CE models must be selected. These waters should capture the observed natural variability in the pore waters. An initial screening was performed to eliminate any analyses that were either incomplete or not representative of TSw pore waters expected to intersect the drift:

- Eight perched water analyses from the base of the TSw were eliminated because they are Pleistocene in age (Yang, 2002 [DIRS 160839]) and do not represent current percolating water compositions.

- Seventeen pore waters collected from areas that had been thermally perturbed during underground testing were eliminated. Specifically, these are TSw water analyses with sample identification prefixes of "ESF-HD-ChemSamp."

- Six analyses were excluded because they were incomplete. These waters are missing data for one or more major ions (other than bicarbonate).

- Three water analyses were not considered because the samples were collected prior to the development of procedures for pore-water sample collection and compositional analysis.

Of the remaining 90 waters, 70 are complete, while an additional 10 lack only SiO_2, and 10 more lack only bicarbonate. Samples lacking only SiO_2 measurements are included for consideration because water chemistry is insensitive to the exact SiO_2 concentration and a reasonable estimate could be made from other, more complete analyses. Samples lacking bicarbonate are retained because the bicarbonate concentration can be calculated by assuming equilibrium with a given pCO_2.

The 90 water analyses and their DTN sources are listed in Table 6.6-1. All core samples were wrapped in plastic and stored for up to 14 months prior to sample analysis. Water samples were collected using either uniaxial compression or centrifugation. Standard wet chemical and analytical methods were employed including inductively coupled plasma mass spectrometry and ion chromotography. Additional details of the analyses can be found in the records package associated with the DTNs listed in Table 6.6-1 (e.g. DTN: GS041108312272.005 [DIRS 178057], records package item #3). Also provided are the file names used for each of the pore waters in the EQ3/6 simulations described in the following sections. Actual pore-water compositions are not given here, but are compiled in Output DTN: SN0705PAEBSPCE.015 (spreadsheet: *TSw_Porewater_Data.xls*). Note that only the 34 analyses listed in Table 4.1-2

are direct feeds to the P&CE models; the remaining waters will be screened from consideration in the following sections.

Table 6.6-1. List of 90 TSw Pore-Water Analyses Used in the TSw Pore Water Evaluation

Pore-Water Identification	EQ3/6 Filename	Source DTN
***Samples with Complete Analyses**		
ECRB-SYS-CS400/5.6-6.2	ECRB1	GS020408312272.003
ECRB-SYS-CS450/5.3-6.0	ECRB2	GS020408312272.003
ECRB-SYS-CS500/12.0-16.7	ECRB3	GS020408312272.003
ECRB-SYS-CS600/3.6-4.0	ECRB4	GS020408312272.003
ECRB-SYS-CS750/6.2-6.5	ECRB5	GS020408312272.003
ECRB-SYS-CS800/4.9-5.6	ECRB6	GS020408312272.003
ECRB-SYS-CS850 5.1-5.6	ECRB7	GS020408312272.003
ECRB-SYS-CS900/3.5-4.1	ECRB8	GS020408312272.003
ECRB-SYS-CS900/5.4-5.9	ECRB9	GS020408312272.003
ECRB-SYS-CS950/4.8-5.5	ECRB10	GS020408312272.003
ECRB-SYS-CS950/5.2-5.3	ECRB11	GS020408312272.003
ECRB-SYS-CS1000/12.9-14.0	ECRB13	GS020408312272.003
ECRB-SYS-CS1000/7.3-7.7	ECRB15	GS020408312272.003
ECRB-SYS-CS1250/3.4-4.0	ECRB17	GS020408312272.003
ECRB-SYS-CS2000/16.3-16.5	ECRB19	GS020408312272.003
ECRB-SYS-CS2000/16.5-21.1	ECRB20	GS020408312272.003
ECRB-SYS-CS2150/5.5-6.1	ECRB22	GS020408312272.003
ECRB-SYS-CS2300/4.3-4.9	ECRB24	GS020408312272.003
NRG-7/7A/839.3-839.8	NRG1	GS020408312272.003
SD-9/990.4-991.7	SD9-1	GS020408312272.003
ECRB-SYS-CS2250/5.2-5.6	ECRB23	GS020808312272.004
ECRB-SYS-CS2300/6.1-6.7	ECRB25	GS020808312272.004
ECRB-SYS-CS1500/10.0-12.1	ECRB37	GS020808312272.004
ESF-SAD-GTB#1/194.2-195.2	ESFSAD1	GS020808312272.004
ESF-SAD-GTB#1/195.4-196.7	ESFSAD2	GS020808312272.004
ESF-SAD-GTB#1/119.4-120.0	ESFSAD3	GS020808312272.004
ESF-SAD-GTB#1/126.1-126.4	ESFSAD4	GS020808312272.004
SD-9/1184.0-1184.2	SD9-2	GS020808312272.004
SD-9/1184.8-1185.0	SD9-4	GS020808312272.004
SD-9/1236.4-1236.8	SD9-5	GS020808312272.004
SD-9/1275.6-1276.0	SD9-6	GS020808312272.004
SD-9/1330.4-1330.7	SD9-7	GS020808312272.004
SD-9/669.1-669.2	SD9-20	GS020808312272.004
ECRB-SYS-CS1100/3.7-3.8	ECRB16	GS030408312272.002
ECRB-SYS-CS1150/3.2-3.8	ECRB29	GS030408312272.002
ECRB-SYS-CS1000/15.6-15.8	ECRB30	GS030408312272.002
SD-9/1184.7-1184.8	SD9-3	GS030408312272.002

Table 6.6-1. List of 90 TSw Pore-Water Analyses Used in the TSw Pore Water Evaluation (Continued)

Pore-Water Identification	EQ3/6 Filename	Source DTN
***Samples with Complete Analyses (continued)**		
ECRB-SYS-CS1000/11.1-11.6	ECRB12	GS031008312272.008
ECRB-SYS-CS1000/5.4-6.1	ECRB14	GS031008312272.008
ECRB-SYS-CS2000/3.3-3.8	ECRB28	GS031008312272.008
ECRB-SYS-CS1000/10.9-11.1	ECRB33	GS031008312272.008
ECRB-SYS-CS900/2.8-3.0	ECRB35	GS031008312272.008
ECRB-SYS-CS2000/3.8-4.1	ECRB41	GS031008312272.008
ESF-THERMALK-017/26.5-26.9	ESFTHER1	GS031008312272.008
ESF-THERMALK-017/22.9-23.0	ESFTHER2	GS031008312272.008
ESF-THERMALK-017/22.3-22.9	ESFTHER3	GS031008312272.008
ESF-THERMALK-019/19.5-19.7	ESFTHER5	GS031008312272.008
ESF-THERMALK-017/26.3-26.5	ESFTHER6	GS031008312272.008
ESF-THERMALK-017/16.6-17.2	ESFTHER7	GS031008312272.008
ESF-THERMALK-019/19.2-19.5	ESFTHER8	GS031008312272.008
SD-9/1060.1-1060.5	SD9-9	GS041108312272.005
SD-9/1276.8-1277.0	SD9-8	GS041108312272.005
SD-9/1119.7-1119.9	SD9-10	GS041108312272.005
SD-9/1234.9-1235.1	SD9-11	GS041108312272.005
SD-9/1276.5-1276.8	SD9-16	GS041108312272.005
SD-9/1303.4-1303.9	SD9-19	GS041108312272.005
SD-12/1053.7-1054.1 UC-1	SD12-1	GS041108312272.005
ECRB-DS3-1616/12.5-12.7	DS3-1	GS0703PA312272.001
ECRB-DS3-1616/12.7-13.3	DS3-2	GS0703PA312272.001
ECRB-DS3-1616/10.6-11.0	DS3-3	GS0703PA312272.001
ECRB-DS3-1616/9.8-10.1	DS3-4	GS0703PA312272.001
ECRB-DS3-1616/9.6-9.8	DS3-5	GS0703PA312272.001
ECRB-DS3-1616/10.1-10.4	DS3-6	GS0703PA312272.001
ECRB-DS3-1616/10.4-10.6	DS3-8	GS0703PA312272.001
ECRB-DS3-1616/11.5-12.5	DS3-9	GS0703PA312272.001
ECRB-DS3-1616/7.1-7.5	DS3-11	GS0703PA312272.001
ECRB-DS3-1616/7.5-7.7	DS3-12	GS0703PA312272.001
ECRB-DS3-1616/7.7-7.9	DS3-13	GS0703PA312272.001
ECRB-DS3-1616/7.9-8.0	DS3-14	GS0703PA312272.001
ECRB-DS3-1616/8.0-8.1	DS3-15	GS0703PA312272.001
Samples without Measured Bicarbonate		
ECRB-SYS-CS400/3.8-4.3	ECRB26	GS020408312272.003
ECRB-SYS-CS700/5.5-5.8	ECRB32	GS020408312272.003
ECRB-SYS-CS1250/5.0-5.7	ECRB34	GS020408312272.003
SD-9/670.5-670.6	SD9-13	GS020408312272.003
SD-9/991.7-992.1	SD9-14	GS020408312272.003
ECRB-SYS-CS2350/5.0-5.7	ECRB42	GS020808312272.004

Table 6.6-1. List of 90 TSw Pore-Water Analyses Used in the TSw Pore Water Evaluation (Continued)

Pore-Water Identification	EQ3/6 Filename	Source DTN
Samples without Measured Bicarbonate (continued)		
ECRB-SYS-CS900/3.0-3.2	ECRB36	GS031008312272.008
ESF-HD-PERM-1	ESFPERM1	MO0005PORWATER.000
ESF-HD-PERM-2	ESFPERM2	MO0005PORWATER.000
ESF-HD-PERM-3	ESFPERM3	MO0005PORWATER.000
Samples without Measured SiO_2		
HD-PERM-3/56.7-57.1	ESFPERM4	GS060908312272.004
HD-PERM-2/34.5-34.9	ESFPERM5	GS060908312272.004
HD-PERM-3/22.4-23.0	ESFPERM6	GS060908312272.004
HD-PERM-2/61.7-62.3	ESFPERM7	GS060908312272.004
HD-PERM-2/19.3-19.7	ESFPERM8	GS060908312272.004
ESF-SAD-GTB#1/199.0-199.3	ESFSAD5	GS060908312272.004
SD-9/1185.0-1185.3	SD9-21	GS060908312272.004
ECRB-DS2-1613/18.6-18.9	DS2-16	GS0703PA312272.001
ECRB-DS2-1613/13.2-13.4	DS2-17	GS0703PA312272.001
ECRB-DS3-1616/8.7-8.9	DS3-10	GS0703PA312272.001

* Complete analysis is defined here as having measured Na, K, Mg, Ca, Cl, SO_4, and NO_3.

6.6.3 Pore-Water Evaluation and Trends in Pore-Water Chemistry

As an initial screening of the remaining 90 pore-water analyses, the anion-cation charge balance was calculated. There are different methods for calculating charge balance; to be consistent with the charge balances reported in some of the source DTNs, the following equation was used:

$$\text{Charge balance} = (\text{Equiv}_{\text{cations}} - \text{Equiv}_{\text{anions}})/(\text{Equiv}_{\text{cations}} + \text{Equiv}_{\text{anions}})$$

The charge balance is positive if the analysis has excess cations (that is, if the sum of the equivalents of the cations is greater than the sum of the equivalents of the anions), and negative if the analysis has excess anions. These calculations are documented in Output DTN: SN0705PAEBSPCE.015 (spreadsheet: *TSw_Porewater_Data.xls*). The results of these calculations are shown in Figure 6.6-2, for the 80 samples for which a charge balance can be calculated (the 10 samples lacking bicarbonate analyses are not included, but those missing SiO_2(aq) are, as this species has no charge and does not contribute to the charge balance). In general, an acceptable charge balance is ±5% to ±10%; many of the TSw pore waters fall outside of this range. In addition, virtually all the samples display a positive charge balance, indicating that there is a consistent deficiency in anions. This suggests that there may be a systematic error that occurred during sample storage, processing, or analysis. Alternatively, there may be an anionic component in the pore water that was not included in the analysis. It is important to determine the cause of the observed charge balance errors. If, for instance, the anion deficiency is due to CO_2 degassing after sample collection, then the use of a single value (10^{-3} bars) to represent ambient repository CO_2 pressures might have to be revisited. In the worst case, the presence of an unrecognized component could require a major modification of the geochemical system used in the P&CE models. Because of the systematic nature of the charge balance error,

even waters with less than a 10% error in the charge balance might be affected. To investigate this, the suite of pore-water compositions was evaluated for trends that might correlate with charge balance.

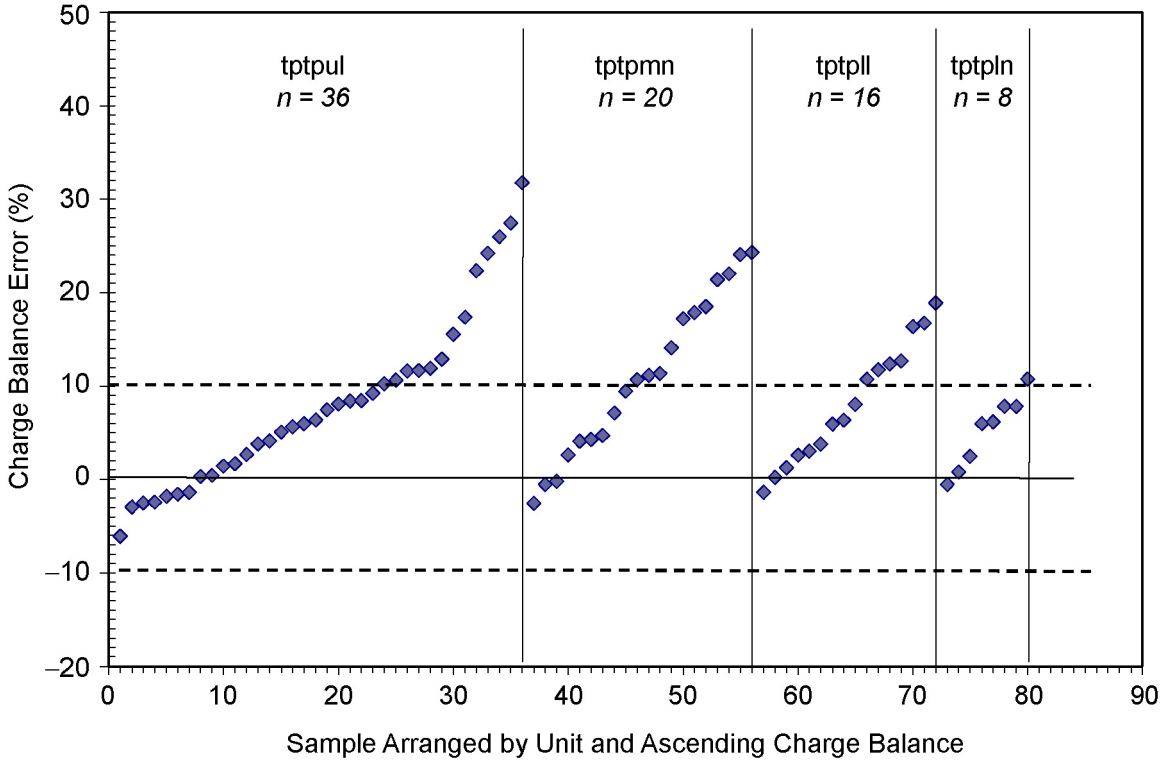

Source: Output DTN: SN0705PAEBSPCE.015, spreadsheet: *TSw_Porewater_Data.xls*.

NOTE: Dotted lines indicate ±10% error in charge balance, corresponding to the acceptable range.

Figure 6.6-2. Charge Balance Error, Calculated for 80 TSw Pore-Water Samples

In Figure 6.6-3, the pore-water compositional data are plotted on a Piper diagram; data points are color-coded according to the charge balance error. It is evident that the waters with poor charge balance are not randomly distributed, but generally cluster towards the carbonate/bicarbonate-rich corner of the diagram. A similar pattern is observed when nitrate:chloride ratio is used as the discriminator in the diagram (Figure 6.6-4). Comparing these two figures shows that larger charge balance errors do correlate with the concentrations of major element components in the waters, including chloride and nitrate, which are direct feeds to the localized corrosion model for the waste package outer barrier (SNL 2007 [DIRS 178519]) used in site performance assessment.

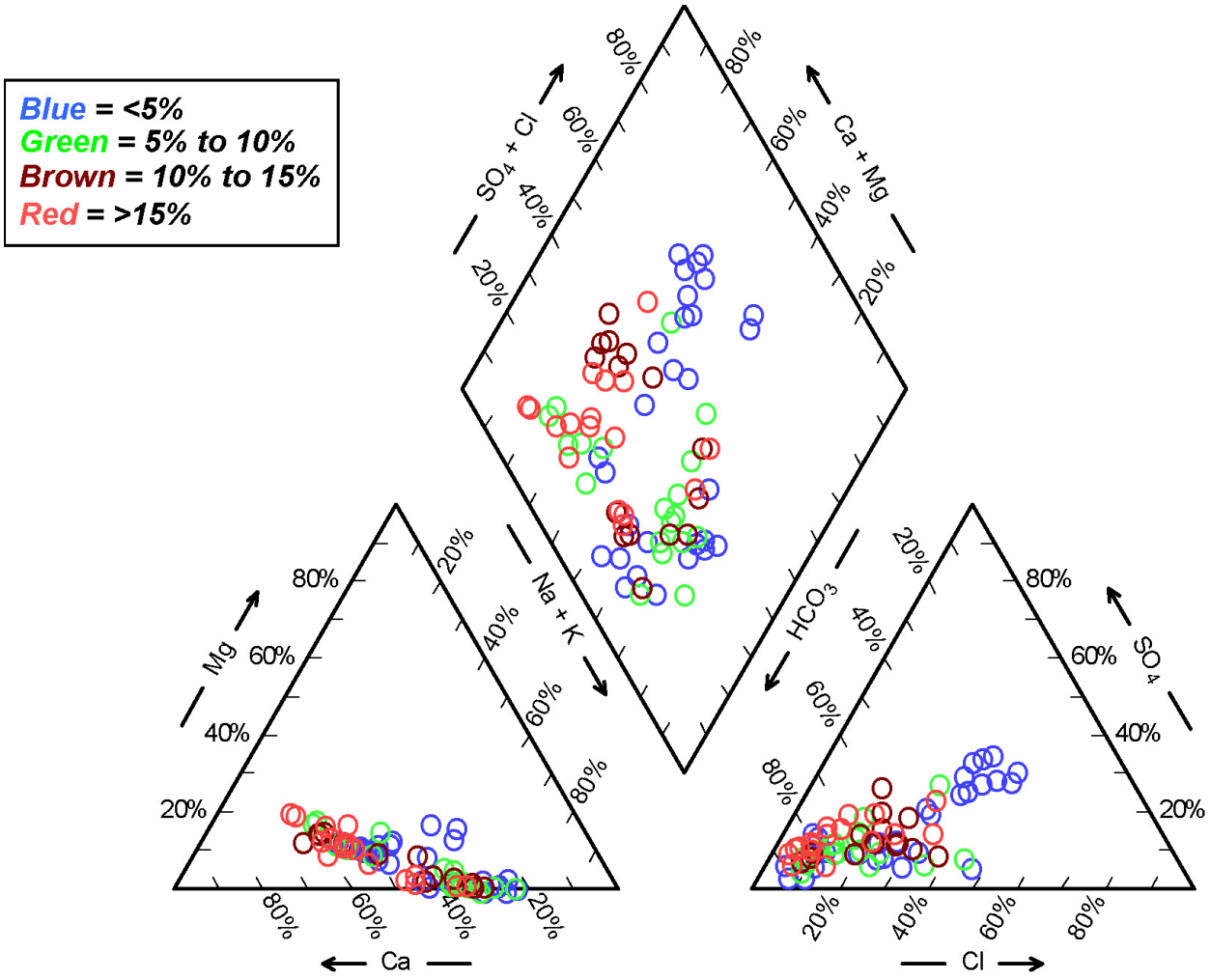

Source: Output DTN: SN0705PAEBSPCE.015, spreadsheet: *Piper_plots.xls*.

NOTE: Plotted data are measured pore-water compositions. Piper plots generated using the software program Rockware Aq·QA V.1.0 (see Section 3).

Figure 6.6-3. Piper Plot of 80 TSw Pore Waters, Color-Coded to Show the Magnitude of the Charge Balance Error

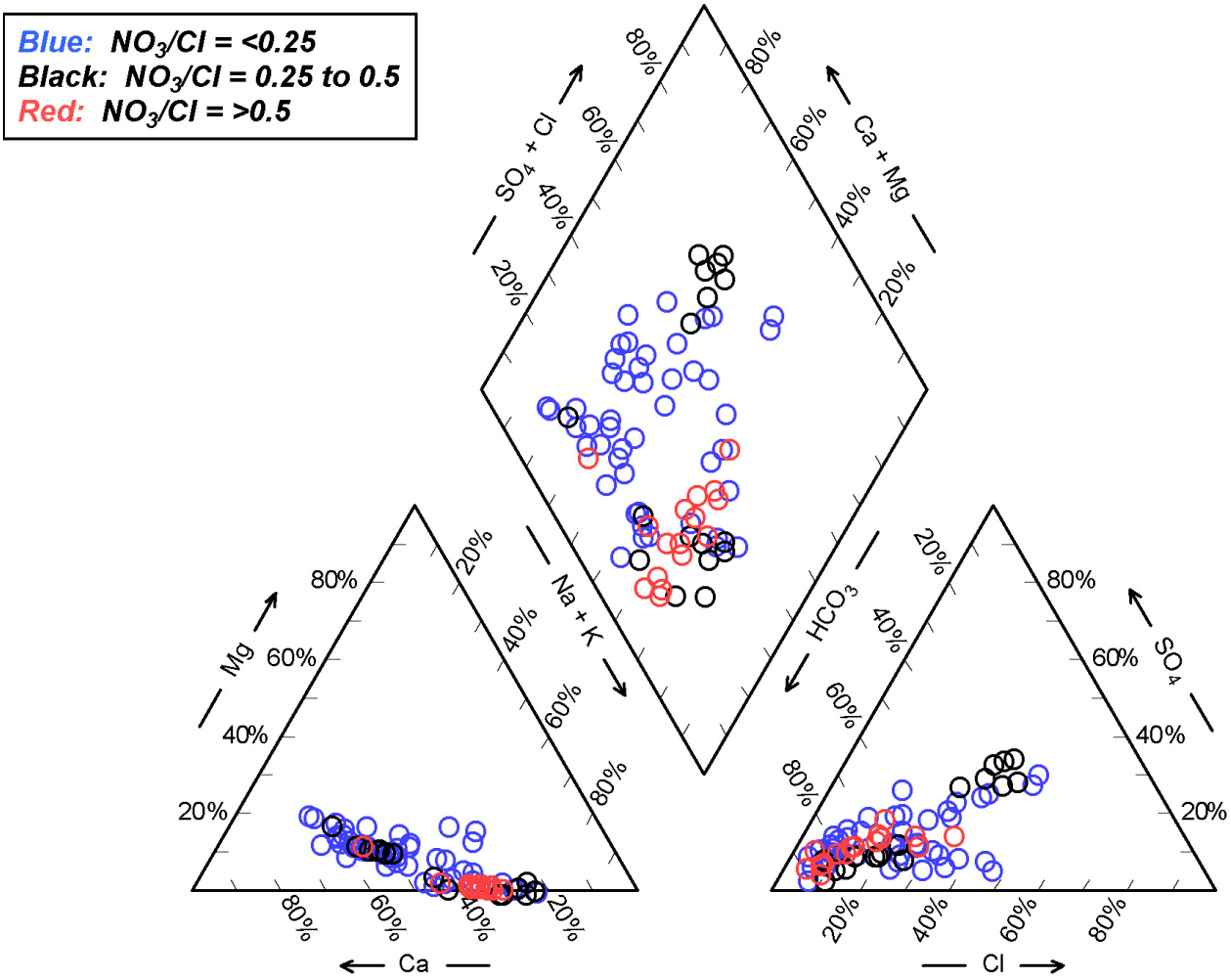

Source: Output DTN: SN0705PAEBSPCE.015, spreadsheet: *Piper_plots.xls*.

NOTE: Plotted data are measured pore -water compositions. Piper plots generated using the software program Rockware Aq·QA V.1.0 (see Section 3).

Figure 6.6-4. Piper Plot of 80 TSw Pore Waters, Color-Coded to Show the Magnitude of the NO_3/Cl Ratio

Several other chemical trends also correlate with charge balance. Waters with good charge balance are generally nitrate-rich and calcium-poor, while waters with a poor charge balance are calcium-rich and nitrate-poor. This is apparent when the calcium and nitrate concentrations are plotted against each other (Figure 6.6-5). There are two clear clusters or trends in the data—a well-defined cluster at low Ca concentrations, comprising mostly waters with a good charge balance, and scatter of points to lower Ca and higher nitrate concentrations, which mostly have poor charge balances. These two trends suggest that two or more processes may be responsible for the observed variation in the pore waters.

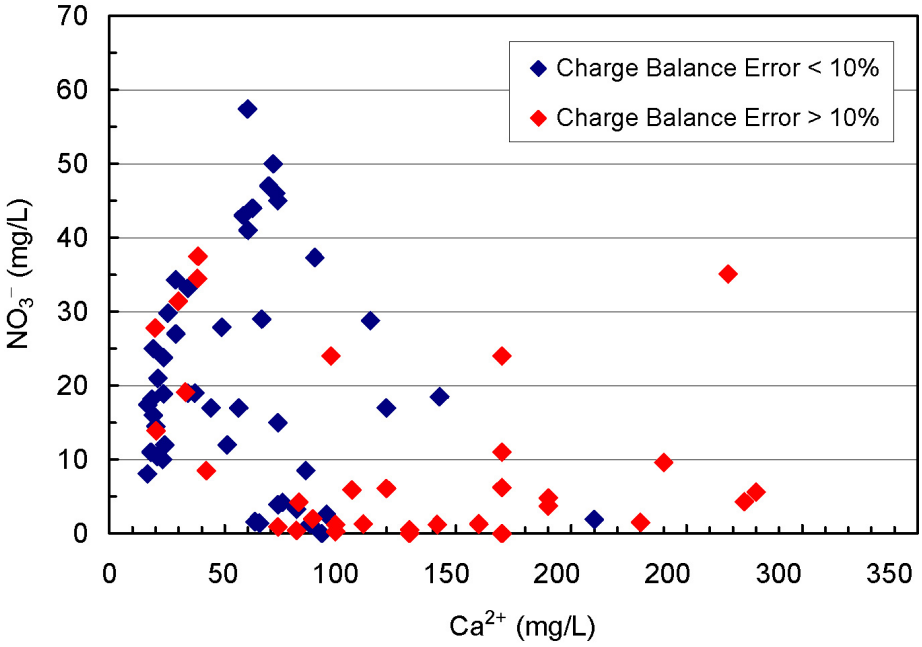

Source: Output DTN: SN0705PAEBSPCE.015, spreadsheet: *TSw_Porewater_Data.xls*.

NOTE: These two components show considerable correlation with charge balance, and with each other.

Figure 6.6-5. Plot of Ca^{2+} vs. NO_3^- for TSw Pore Waters

Other important observations can be made when the pore waters are evaluated for mineral- and gas-phase equilibrium using the thermodynamic speciation and solubility code EQ3NR. Two types of evaluations were performed. First, those pore-water analyses that included both bicarbonate and pH (43 samples, or about half the total) were equilibrated using EQ3, without using any charge balancing, and without imposing any fixed partial pressure of CO_2. This calculation can only be done with complete analyses, including pH. In the second evaluation, all of the pore-water analyses were brought to equilibrium with a pCO_2 of 10^{-3} bars, while allowing the pH to vary (e.g., charge balancing with H^+). This second process reflects that used to calculate initial pore-water compositions for the NFC model. However, this process can introduce artifacts into the water compositions. For samples with a poor charge balance—a large anion deficiency in the case of the TSw pore waters—a large shift in the pH (and concomitant shift in carbonate/bicarbonate concentration) is required to achieve charge balance. The anion deficiency requires a large amount of carbonate/bicarbonate be added to the water composition, resulting in a large shift in the predicted pH and water compositions that are highly supersaturated with respect to calcite. The pH shift and removal of Ca as calcite can affect how waters will evolve in the P&CE seepage evaporation model. The EQ3 input and output files for these two evaluations are archived in Output DTN: SN0705PAEBSPCE.015, and are summarized in spreadsheet *Results.xls*.

Pore waters were equilibrated at a pCO_2 of 10^{-3} bars because that is the accepted value in the repository units under ambient conditions. The pCO_2 in the devitrified rhyolitic center of the TSw is relatively well constrained by six years of gas analyses from borehole UZ-1, collected from packed-off intervals within that unit (Figure 6.6-6). The pCO_2 concentrations in the gas samples from this borehole vary from a little less than 1,000 ppm (10^{-3} bars) to about 2,500 ppm

($10^{-2.6}$ bars) over the interval of interest; most samples fall around 10^{-3} bars, and that value is commonly assumed to be characteristic of the gas phase at the repository level (see figure caption for the DTNs supporting this assumption).

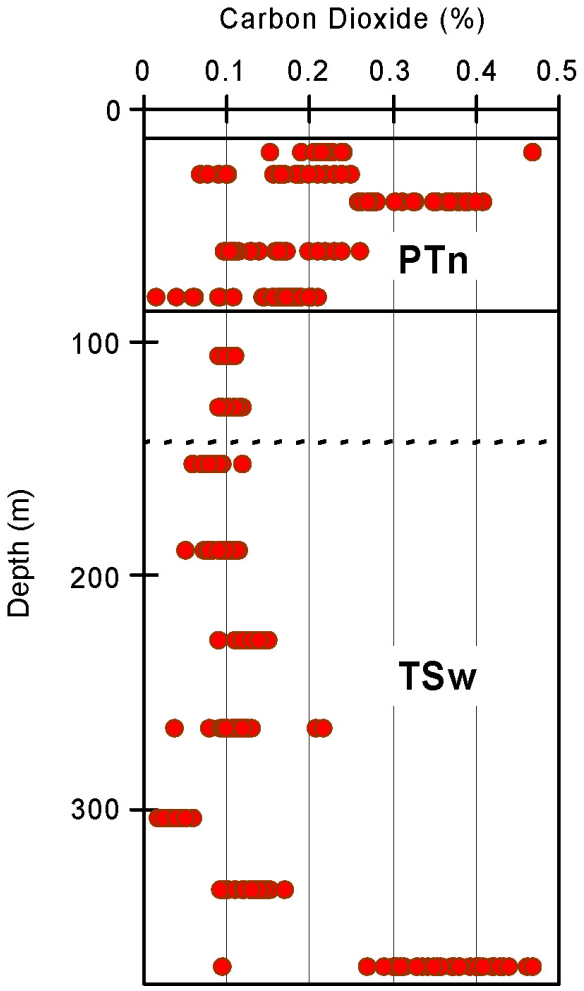

Source: DTNs: GS930408312271.014 [DIRS 145 533], GS911208312271.011 [DIRS 182482], GS930108312271.004 [DIRS 166448], GS940408312271.006 [DIRS 166451], GS940408312271.001 [DIRS 166450].

NOTE: Dashed line represents the top of the repository host horizon (Tptpul). A CO_2 of 0.1% is equivalent to a pCO_2 of 10^{-3} bar.

Figure 6.6-6. Measured Gas-Phase CO_2 Concentrations from Packed-off Intervals in Borehole UZ-1

However, when equilibrium gas compositions are calculated using EQ3, without charge balancing, predicted equilibrium pCO_2 values are much higher than 10^{-3} bars. Predicted pCO_2 values are plotted against the measured pH in Figure 6.6-7; they are nearly all above the observed range in the repository host rock, with several values exceeding 10^{-2} bars (1% CO_2), and a few as high as $10^{-1.5}$ bars. The pCO_2 values correlate strongly with the measured pH values, and form a linear trend that falls close to the trend predicted for the calcite-CO_2-H_2O system. These results suggest that the pore waters were in equilibrium with elevated pCO_2 values in systems containing calcite (calcite is a common trace mineral throughout the TSw).

An alternative way of evaluating this is shown in Figure 6.6-8. This figure is derived from the study by Stumm and Morgan (1996 [DIRS 125332], Figure 4.15), and plots HCO_3^- concentrations against Ca^{2+} concentrations, in mg L^{-1}. The diagonal blue lines represent calcite saturation at the listed pCO_2. The green line represents equal normalities of Ca^{2+} and HCO_3^-, and a closer proximity to this line suggests that these species contribute more to the total ionic strength of the solution. The plotted data indicate that the solutions would be highly supersaturated with calcite at a pCO_2 of 10^{-3} bars. In addition, the points fall closer to the equal normality line for Ca^{2+} and HCO_3^- at the higher pCO_2 values, indicating that the increase in bicarbonate concentrations is being balanced by Ca, and suggesting that calcite dissolution is occurring. This is consistent with data plotting in proximity to the calcite equilibrium line in Figure 6.6-7. It is important to note that the calcite saturation lines at given pCO_2 values are calculated for the Ca-CO_2-H_2O system using EQ3 and the *data0.pce* database (Output DTN: SN0703PAEBSPCE.006), and are not directly applicable to the pore waters; they suggest higher pCO_2 values than the actual equilibrated pore waters plotted in Figure 6.6-7.

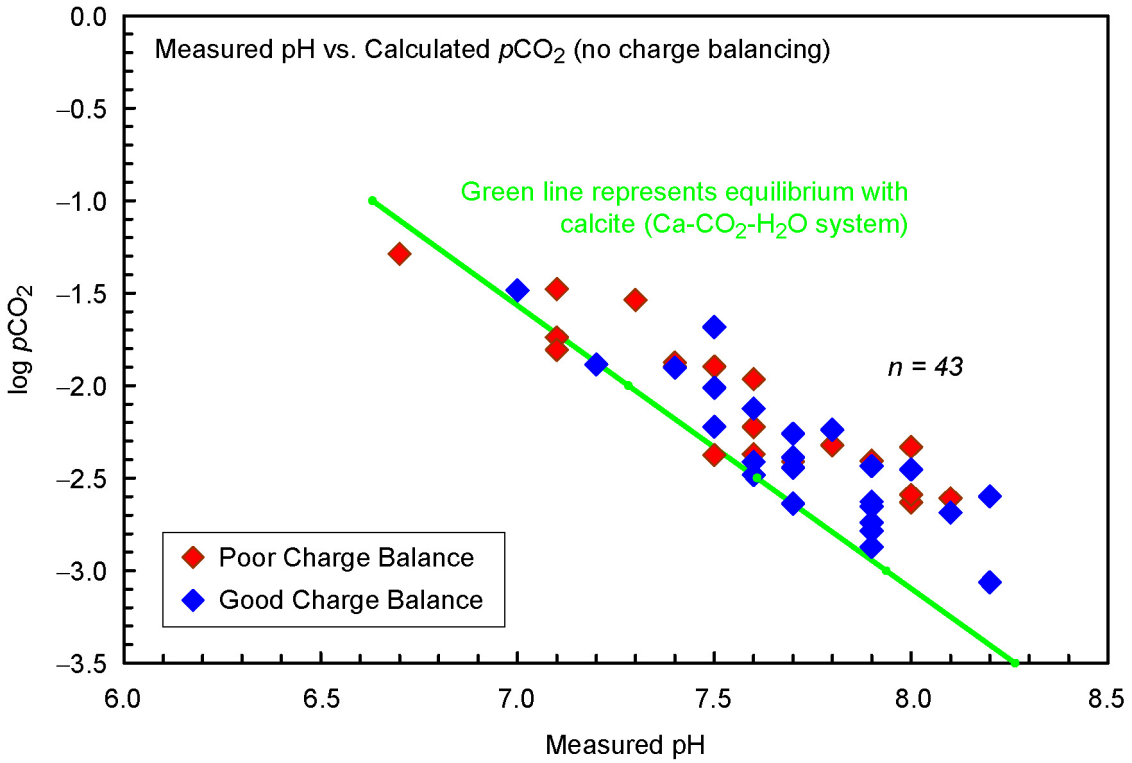

Source: Output DTN: SN0705PAEBSPCE.015, spreadsheet: *Results.xls*; tab: "Meas. pH vs PCO2."

NOTE: Samples without measured pH are not included because a water composition cannot be calculated without assuming a pH value.

Figure 6.6-7. Plot of Predicted log pCO_2 versus Measured pH

The source figure from Stumm and Morgan (1996 [DIRS 125332], Figure 4.15) is presented as an insert in Figure 6.6-8 and shows world surface water compositions. Some of these also indicate equilibrium with elevated pCO_2 values, a condition that the authors attribute to microbial degradation of organic materials in the river water.

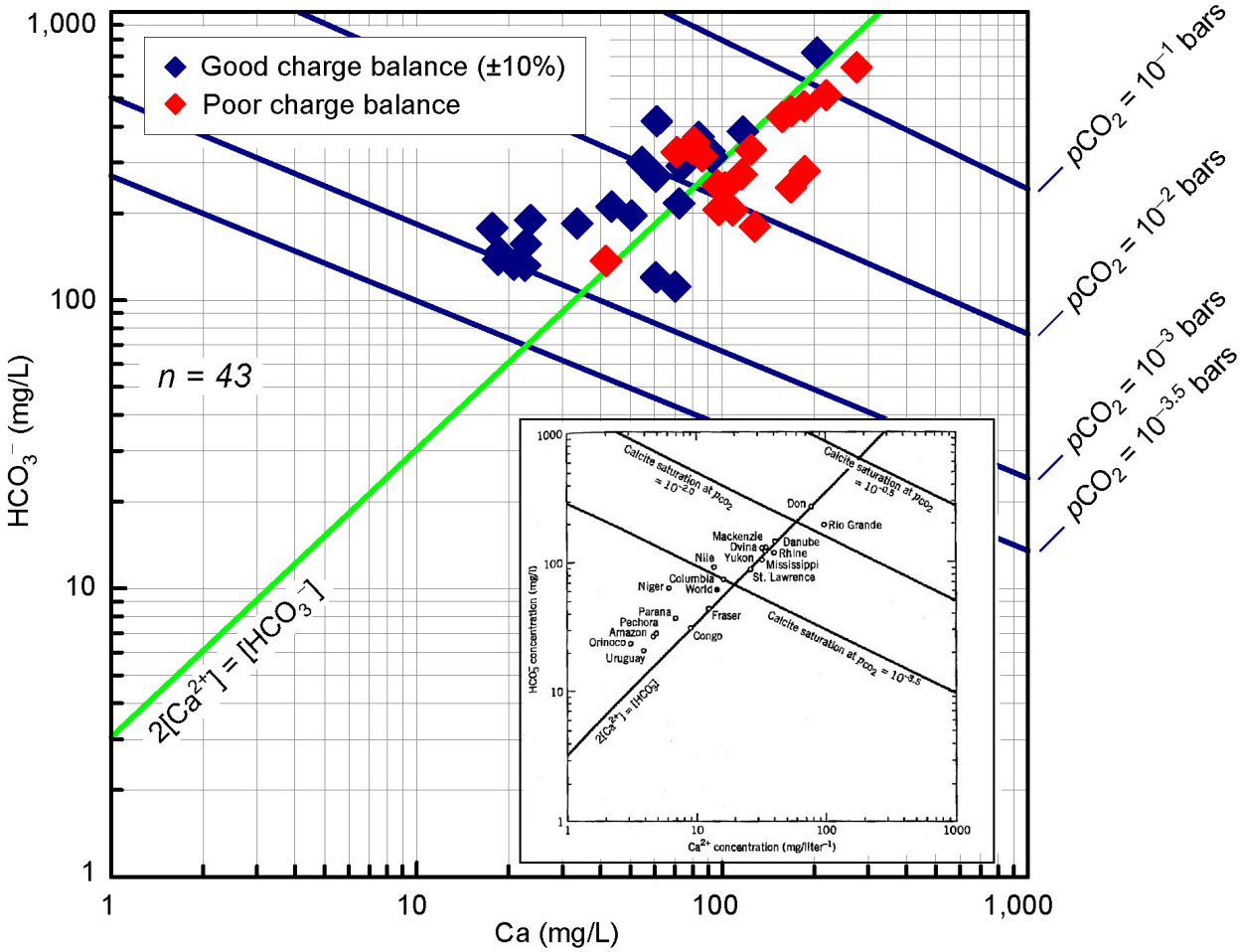

Source: Output DTN: SN0705PAEBSPCE.015, spreadsheet: *Results.xls*, tab: "Ca vs HCO3."

NOTE: Blue lines represent calcite saturation at the stated pCO_2 for the Ca-CO_2-H_2O system, calculated using EQ3 and *data0.pce* (Output DTN: SN0703PAEBSPCE.006). Insert from Stumm and Morgan 1996 [DIRS 125332], Figure 4.15.

Figure 6.6-8. TSw Pore Waters Supersaturated with Respect to Calcite at a pCO_2 of 10^{-3} bars

To summarize the observed trends, the pore waters evaluated here have relatively poor charge balances and exhibit a consistent anion deficiency which correlates with other compositional parameters, most notably Ca^{2+} and NO_3^- concentrations. Many of the pore-water analyses, including many with good charge balances, indicate equilibrium with calcite at pCO_2 values far in excess of that observed in the rock. Hence, they are supersaturated (in some cases, highly supersaturated) with calcite at the nominal repository pCO_2 of 10^{-3} bars. Pre-processing these water compositions for use in the P&CE models by charge balancing on H^+ while maintaining equilibrium with a pCO_2 of 10^{-3} bars would result in: (1) large shifts to higher pH with a concomitant increase in bicarbonate concentrations, and (2) precipitation of calcite, modifying the divalent/monovalent ion ratio in the pore water, and affecting how that water would evolve if evaporated. It is important to determine if the elevated pCO_2 values are realistic in situ values, or whether the values are indicative of analytical errors, or processes that occurred after sample collection. In the latter case, a screening criterion must be developed and used to distinguish affected waters from unaffected or minimally affected waters. Because waters with both good

and poor charge balances predict elevated pCO_2 values, and also because it cannot be applied to the significant number of pore-water analyses missing bicarbonate, the charge balance criterion is insufficient as a screening argument.

As discussed earlier, poor charge balances can result from several sources, including errors or uncertainty in the analytical methods or data, missing analytes, or degassing of CO_2 after sample collection and prior to analysis. The consistent deficiency in anions in pore-water samples collected over several years argues against analytical uncertainty, as this would produce charge balance errors symmetrically distributed around zero. In addition, the charge balance errors show no correlation with the method used to extract the pore water, which was either centrifugation or uniaxial compression (Output DTN: SN0705PAEBSPCE.015, spreadsheet: *TSw_Porewater_Data.xls*). The apparently elevated pCO_2 values might increase the probability of degassing, but the fact that the pore waters are close to equilibrium with calcite (Figure 6.6-7), and plot along the equivalent normality line for Ca^{2+} and HCO_3^- in Figure 6.6-8, indicates that degassing prior to analysis was insignificant.

Evidence from the more recent pore-water analyses carried out by the USGS suggests that missing analytes—specifically, organic acids—may be responsible for the charge balance errors. This is a common problem in sedimentary formation waters (Palandri and Reed 2001 [DIRS 181103], Section 1). The recent USGS analyses contain data for organic acids such as propionate, formate, and acetate, and in some samples (one third of those analyzed), the concentrations of these compounds, specifically propionic acid (CH_3CH_2COOH), were as high as 150 to 620 mg L^{-1} (DTN: GS070708312272.002 [DIRS 182307]). These organic acids would be present in the deprotonated, anionic forms at the pH values measured. Assuming a formula weight of 74 g/mol (calculated using data from DTN: SN0612T0502404.014 [DIRS 178850]), this is equal to 2 to 8 milliequivalents (meq), more than enough to account for the observed charge imbalances as the equilibrium concentrations in the pore waters average about 5 to 10 meq (Output DTN: SN0705PAEBSPCE.015).

Organic acids are byproducts of microbial fermentative processes, and are only produced under reducing conditions (for instance, the enzyme involved in the first step of production of propionic acid is inhibited by the presence of molecular oxygen. In situ conditions in the TSw are oxic, but microbial activity could have produced reducing conditions in the borehole cores because they were tightly sealed after collection. After collection, each core was wrapped in plastic wrap and then placed in a core tube with packing to minimize head space at each end of the tube, and finally, the core tube was wrapped in core wrap.

Direct evidence of high organic acids is limited to a few analyses, but these show that microbial activity under anoxic conditions has affected at least some pore-water samples. Other chemical trends observed in the pore waters provide additional, indirect support for microbial activity under anoxic conditions. Such conditions cannot have occurred in situ; all unsaturated zone gas phase analyses have yielded atmospheric levels of oxygen (Thorstenson et al. 1990 [DIRS 100831]).

The chemical trends observed in the pore-water compositions are consistent with microbial activity, probably in the tightly wrapped cores after collection and prior to sample extraction and analysis. The correlation of charge balance error (e.g., buildup of organic acids) with lower

nitrate concentrations is one line of evidence (Figures 6.6-3 and 6.6-4); under anoxic conditions, microbial communities will use nitrate as an electron acceptor in place of oxygen (denitrification) (Stumm and Morgan 1996 [DIRS 125332], p. 458). As will be shown later, a similar condition exists for sulfate, which can also function as an electron acceptor under anoxic conditions. However, the clearest evidence for microbial activity comes from the pCO_2 values that are predicted by the measured pore-water concentrations, which are much higher than the 10^{-3} bar observed in the UZ-1 gas samples. As shown in Figure 6.6-7, these waters plot along a line representing equilibrium with calcite (in a $Ca\text{-}CO_2\text{-}H_2O$ system), and the predicted pCO_2 values correlate nicely with pH, with higher partial pressures corresponding to lower pH. This is entirely consistent with microbial activity in the core, resulting in a build-up of CO_2 in the sealed, plastic-wrapped core tube. As the CO_2 built up in the gas phase, the pore water absorbed CO_2 and became more acidic; this occurred slowly enough for calcite, present in the rock in small amounts, to maintain equilibrium or near-equilibrium with the solution.

Figures 6.6-7 and 6.6-8 may also provide support for the theory that organic acids, as opposed to CO_2 degassing, are responsible for the poor charge balance in many of the samples. The well charge-balanced waters and poor charge-balanced waters overlap in Figure 6.6-7, indicating that the large errors in charge balance are not due to degassing. In Figure 6.6-8, the poor charge-balance waters are significantly enriched in calcium relative to the waters with smaller charge balance errors. Thus, at any given pH, there is more Ca in solution in the poorly balanced waters relative to the well-balanced waters, but both exhibit the same degree of saturation with respect to calcite. This suggests that some of the Ca is complexed, probably with organic acids.

Figures 6.6-7 and 6.6-8 indicate that charge balance is not a good discriminator with respect to screening samples for the effects of microbial activity. Apparently, while nearly all samples were in equilibrium with elevated CO_2 partial pressures, not all samples contain organic acids. However, even if the only effect of the elevated CO_2 concentrations is an increase in Ca and bicarbonate, subsequently re-equilibrating the waters at a pCO_2 of 10^{-3} bars, while allowing the pH to vary to accomplish charge balance, has large effects on water chemistry. This is illustrated in Figure 6.6-9 in which the calcite saturation index (log(Q/K)) is plotted against pH, for the pore waters with (a) no charge balancing, and (b) after charge balancing with H^+, at a fixed pCO_2 of 10^{-3} bars. The measured water compositions are saturated or slightly supersaturated with respect to calcite; after charge balancing, the pore waters are highly supersaturated, and the pH values are considerably elevated. The change in pH upon charge balancing is quite large (up to 2 pH units), and correlates well with the measured pH (Figure 6.6-10).

Clearly, waters that were affected by elevated CO_2 concentrations due to microbial activity are poor choices for NFC starting waters, regardless of the charge balance. First, re-equilibrating these waters at a pCO_2 of 10^{-3} bars will result in precipitation of calcite, changing the water composition; second, it is not clear if other components in the water (nitrate, sulfate) were affected by the microbial activity; and third, the adjusted pH for the starting water will be too high, affecting the predicted partitioning of CO_2 between the gas phase and aqueous phase, and potentially, mineral precipitation/dissolution reactions.

If measured pH and bicarbonate data were available for all waters, then the equilibrium pCO_2 without charge balancing, the measured pH, or the change in pH upon charge balancing, would all be reasonable metrics for evaluating the potential degree of microbial activity. The higher the

original pCO_2, the more acidic the original solution (Figure 6.6-7), and the greater the adjustment in pH upon charge balancing (Figure 6.6-10). However, fully half of the analyses lack pH data, and ten lack bicarbonate data, so another metric must be considered.

One useful metric that can be calculated for all waters is pH_{calc}, determined by charge balancing on H^+ while holding the HCO_3^- in equilibrium with a pCO_2 of 10^{-3} bars. One reasonable maximum pH cutoff for waters that have been affected by elevated CO_2 concentrations (microbial activity) would be a pH_{calc} of 7.95, corresponding to the pH in a Ca-CO_2-H_2O system in equilibrium with calcite at a pCO_2 of 10^{-3} bars. A slightly more conservative cutoff would be a pH_{calc} of 8.26, corresponding to pH in a Ca-CO_2-H_2O system in equilibrium with calcite at a pCO_2 of $10^{-3.5}$ bars. A best-fit line of the data in Figure 6.6-10 intersects zero on the y-axis at a pH of 8.30, corresponding to the value at which no pH adjustment occurred during charge balancing, indicating equilibrium with a pCO_2 of 10^{-3} bars. The actual measured pH values vary up to 8.32, possibly because the pore waters are more complex than a simple Ca-CO_2-H_2O system. All of these values are very similar, and suggest that, unless the pore waters were affected by elevated CO_2 pressures due to microbial activity, pH_{calc} values should not exceed a value of around 8.3. To avoid excluding any samples that actually had measured values above this, a pH cutoff of 8.35 was chosen.

The proposed pH criterion is shown in Figure 6.6-9(b). Many waters that meet the pH_{calc} cutoff still exhibit some degree of calcite supersaturation, up to one order of magnitude in some cases. Using a lower pH_{calc} criterion might be more accurate with respect to eliminating waters affected by microbial activity, but would significantly reduce the number of water samples that would pass the criterion. The cutoff value implemented, $pH_{calc} = 8.35$, is thus conservative.

Figure 6.6-11(a) and (b) illustrates that this simple metric is very effective at discriminating between different processes that have affected the pore-water compositions—in fact, much more effective than the charge balance criterion. In these plots, the poorly charge-balanced waters (>10%), well charge-balanced waters (< ±10%), waters missing SiO_2, and waters missing bicarbonate are all shown, with those having a $pH_{calc} < 8.35$ (the proposed pH cutoff) shown as filled symbols, and those having a higher pH_{calc} as open symbols. On both plots, the waters which pass the pH criterion form clearly defined trends, while those with pH values above the cutoff scatter to higher values of Ca and lower values of N and S, probably due to microbial denitrification and sulfate reduction once conditions in the stored core become anoxic.

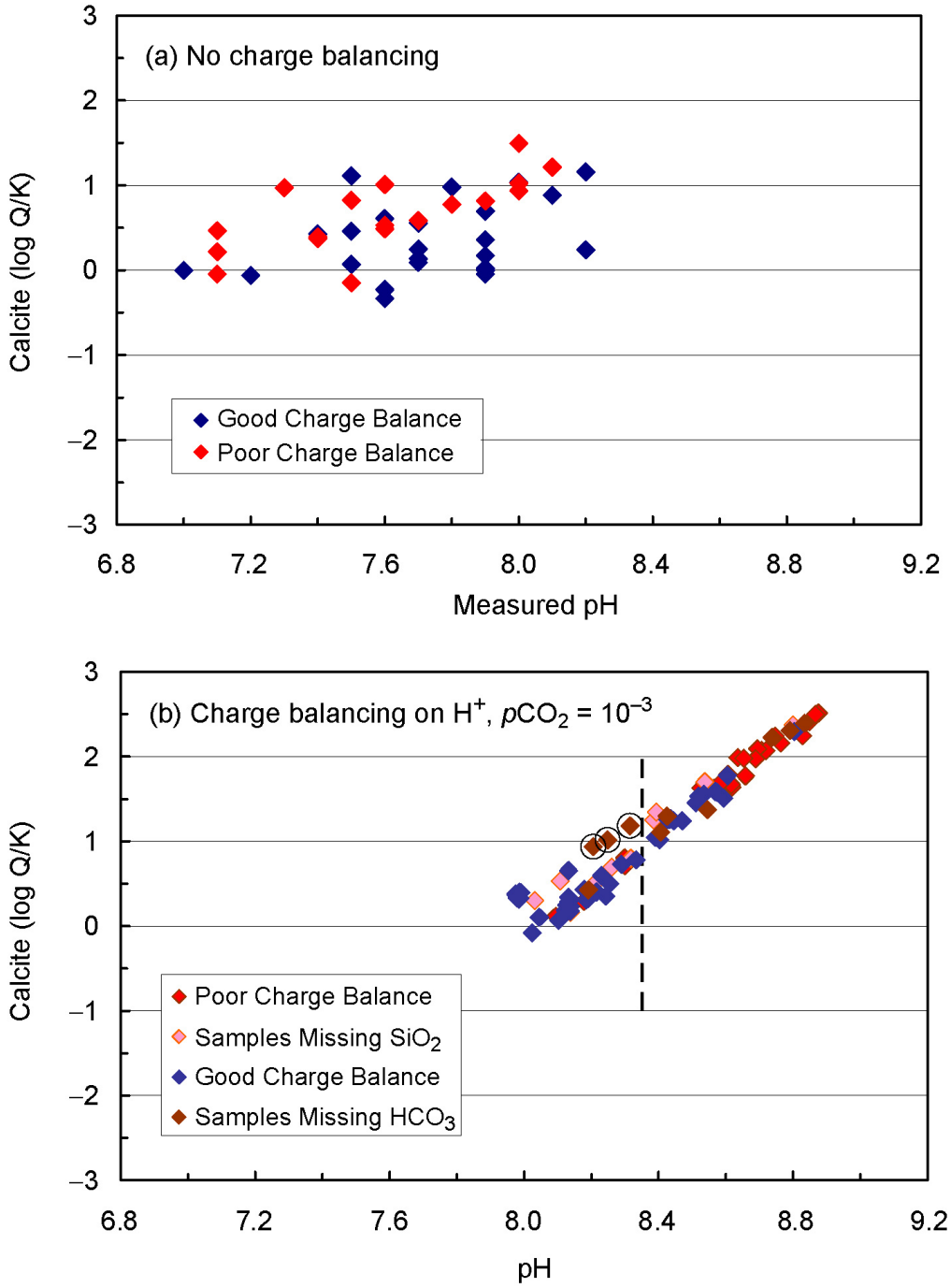

Source: Output DTN: SN0705PAEBSPCE.015, spreadsheet: *Results.xls*, tab: "No Bal Calcite Saturation and Bal Calcite Saturation."

NOTE: Dotted line corresponds to pH = 8.35. HD-PERM waters enclosed by circles. Only samples with measured pH are plotted in panel (a). A pH of 8.26 is the equilibrium value for the Ca-CO_2-H_2O system at a pCO_2 of $10^{-3.5}$ bars.

Figure 6.6-9. Calcite Saturation Index for TSw Pore Waters: (a) No Charge Balancing, (b) Charge Balancing with H^+, with $pCO_2 = 10^{-3}$ bars

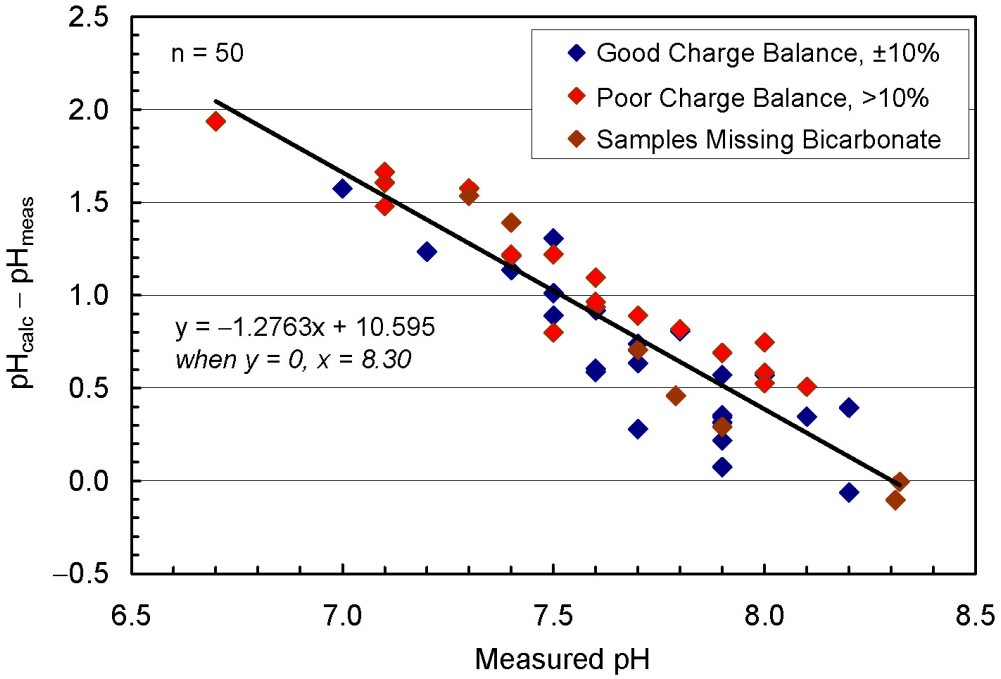

Source: Output DTN: SN0705PAEBSPCE.015, spreadsheet: *Results.xls*, tab: "change in pH vs initial pH."

NOTE: Only samples with measured pH values are plotted.

Figure 6.6-10. Change in pH Caused by Charge Balancing with H^+ at a pCO_2 of 10^{-3} bars (pH_{meas} – pH_{calc}) Decreasing Systematically with Increasing pH_{meas}

In addition to selecting a suite of pore waters, several observations about the causes of the trends in the data can be made:

(1) *Many, or even most, TSw pore waters reflect equilibrium with elevated concentrations of CO_2.* This statement is well supported by the data, which show that the pore-water compositions are in equilibrium with pCO_2 values much higher than the 10^{-3} bars observed in the repository host rocks. In addition, higher predicted pCO_2 values correspond to decreasing measured pH, consistent with acidification due to carbonic acid formation.

(2) *The elevated concentrations of CO_2 observed are due to microbial activity.* Samples most strongly affected by elevated CO_2 concentrations also show proportionally lower nitrate and sulfate concentrations, consistent with the development of anoxic conditions and microbial denitrification/sulfate reduction processes. The presence of significant levels of organic acids in samples that have been analyzed also indicates that reducing conditions must have developed (at least locally). Unless the organic acids were directly introduced to the core (for example, as a preservative or an antifungal agent), there is no explanation for its presence in these samples other than microbial activity.

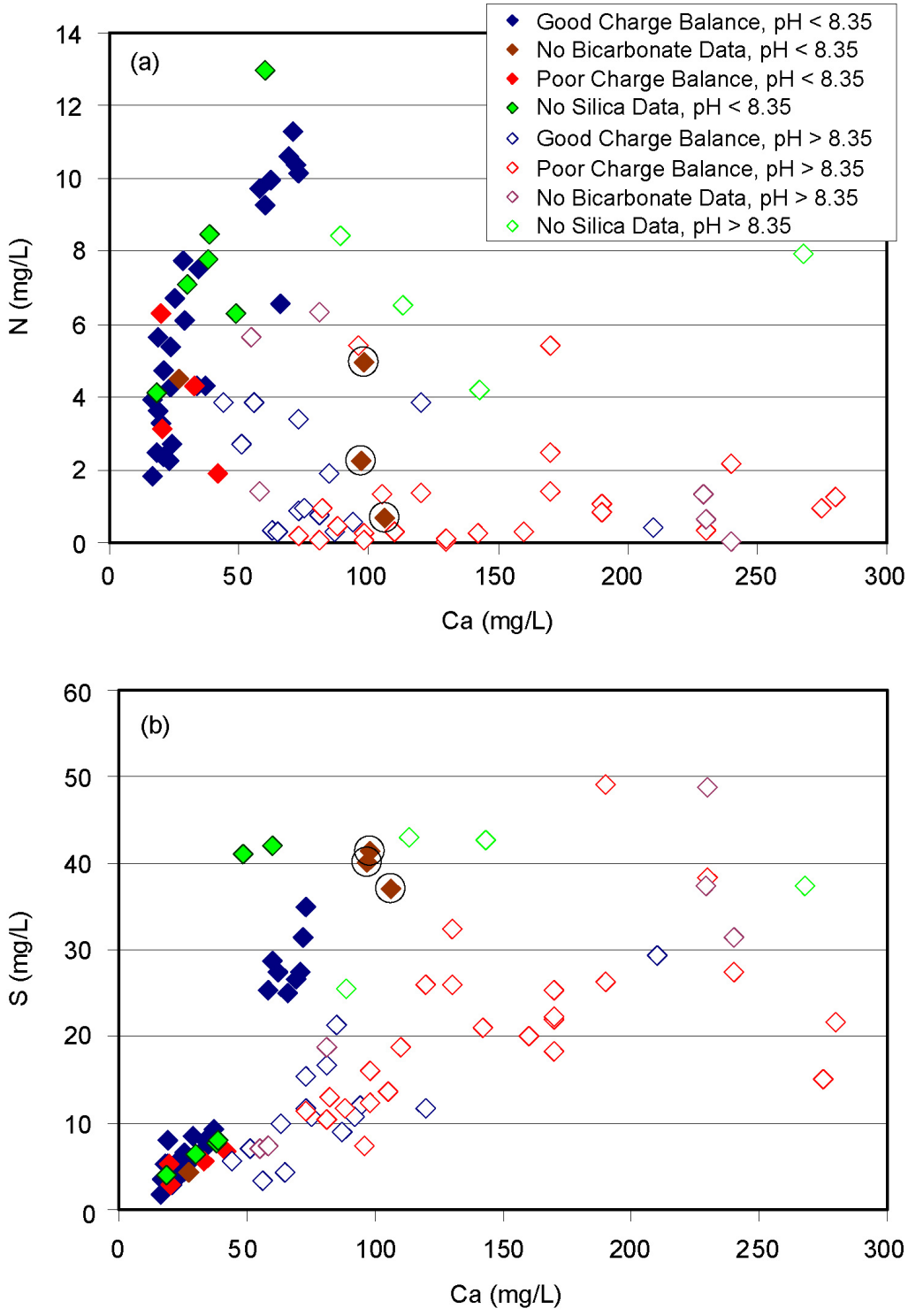

Source: Output DTN: SN0705PAEBSPCE.015, spreadsheet: *Results.xls*, tab: "Chemistry plots."

NOTE: Waters with a calculated pH of <8.35, after charge balancing at $pCO_2 = 10^{-3}$ bars, form a well-defined trend on both (a) Ca-N and (b) Ca-S plots. HD-PERM waters are enclosed by circles.

Figure 6.6-11. Element-Element Plots for the 90 TSw Pore Waters

(3) *The microbial activity did not occur in situ, but rather occurred in the core samples after collection.* The borehole UZ-1 gas-phase CO_2 data clearly show that repository horizon CO_2 levels are not high enough to account for the elevated levels in the pore waters. In addition, TSw gas sampling indicates that oxygen levels are similar to atmospheric levels in the gas phase. Denitrification, sulfate reduction, and organic acid generation all require anoxic conditions. Also, organic acids are rapidly metabolized by microbes under oxidizing conditions, and could not persist long in the oxidizing environment of the unsaturated zone (e.g., it could not represent organic material percolating down from surface soils). All of these factors suggest that microbial activity occurred in the tightly sealed cores, rather than in situ.

(4) *The charge balance errors observed in the pore-water samples are due to an unanalyzed anionic component—organic acids—and not due to CO_2 degassing.* This conclusion is supported by the presence of significant levels of organic acids (formate, acetate, and propionate) in some samples. Also, the measured water compositions are in equilibrium or near-equilibrium with calcite, indicating that significant degassing did not occur. Finally, the waters with both good and poor charge balance are both saturated with respect to calcite, but the waters with poor charge balance have higher Ca^{2+} concentrations, indicating that some of the Ca^{2+} formed complexes in solution, possibly with organic acids.

6.6.4 Screening Results and Trace Element Confirmation

Figure 6.6-11 illustrates that using a pH_{calc} cutoff of 8.35 (*screening criterion 1; corresponding to a slightly higher value than pH in a Ca-CO_2-H_2O system in equilibrium with calcite at a pCO_2 of $10^{-3.5}$ bars)* for waters affected by microbial activity is effective in discriminating between two sets of compositionally related waters. These waters are commonly, but not always, the same as those exhibiting a poor charge balance. However, the charge balance error criterion of ±10% is still retained (*screening criteria 2*), because other processes, such as analytical error, may affect the charge balance, and any sample that has a poor charge balance is sufficiently questionable to be excluded from consideration. Of the 90 pore-water analyses that passed the initial screening (Section 6.6.2), 56 failed the pH_{calc} and charge balance criteria, and 34 passed, and are considered to have been minimally affected by microbial activity. These 34 pore waters are direct feeds to the P&CE suite of models; they are identified in Table 4.1-1, and their compositions are in Table 4.2-2. Waters missing SiO_2 are included in the analysis because they are otherwise complete and a SiO_2 concentration can easily be estimated, because there is very little variation in TSw pore-water SiO_2 concentrations. Water analyses missing bicarbonate are included because a bicarbonate value is calculated in any case, when the water is charge balanced and equilibrated at a pCO_2 of 10^{-3} bars for use in the P&CE models.

The results of applying these two criteria to the pore-water analyses are shown in on a Piper diagram in Figure 6.6-12. The excluded waters tend to be rich in Ca^{2+} and HCO_3^- (because of equilibration with calcite at an elevated pCO_2) and, more importantly for performance assessment, nitrate-poor (compare Figure 6.6-12 to Figure 6.6-4).

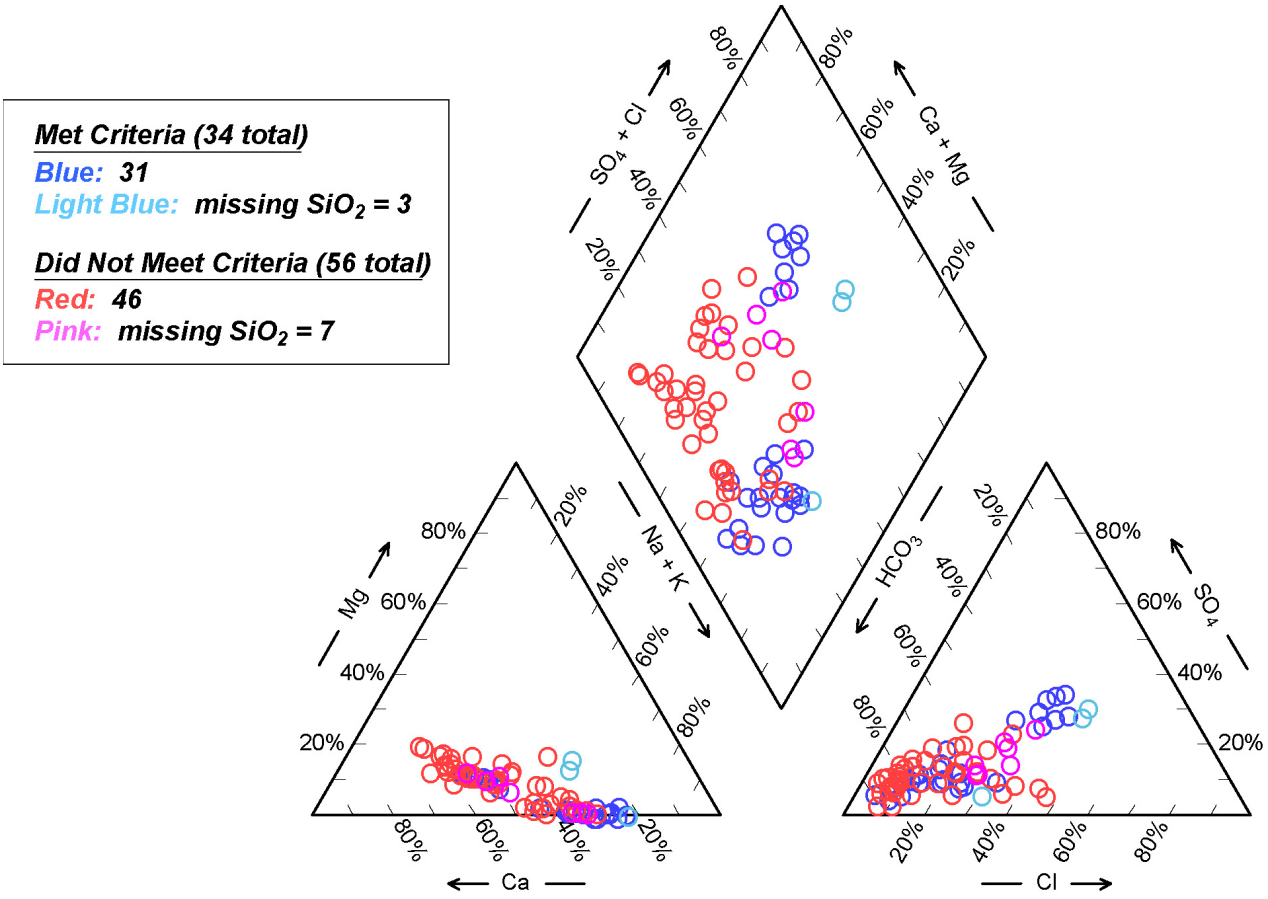

Source: Output DTN: SN0705PAEBSPCE.015.

NOTE: Plotted using Rockware Aq ·QA V.1.0 (see Section 3). Samples missing bicarbonate are not plotted, but are included in the totals.

Figure 6.6-12. Piper Diagram Showing Pore Waters That Meet the Two Criteria for Selection, Having a Charge Balance Error of Less Than 10%, and a $pH_{calc.}$< 8.35

Trace element data for the pore waters provide confidence in the screening criteria developed in the previous two sections. The trace elements Sr and Mn, in particular, are useful in discriminating between pore waters that pass and fail the screening criteria. Box and whisker plots for Sr and Mn concentrations in the pore waters are shown in Figure 6.6-13, and the pore-water Sr and Mn concentrations are plotted against each other in Figure 6.6-14, which emphasizes how strongly these two trace elements co-vary in the pore waters. The pore waters that are screened in by the two screening criteria consistently have much lower concentrations for Mn and Sr than the pore waters that are screened out. Possible causes for this are: (1) dissolution of calcite and release of crystallographically bound Mn and Sr as the pCO_2 increases due to microbial activity in the stored core, and the pH drops; (2) pH-induced dissolution of Mn oxides in the core; or (3) stabilization of desorbed or ion-exchanged Sr and Mn in solution by complexation with organic acids. The first process is supported by the evidence for calcite dissolution during core storage (Figures 6.6-7 and 6.6-8), although this does not preclude the occurrence of the other two processes. Note that, although most of the strontium in the tuff is in feldspars, dissolution of feldspar during core storage cannot contribute significantly to the Sr

content of the pore waters, because the feldspar dissolution rate is far too slow (Sections 6.3.2.4.2 and 6.12.2.1).

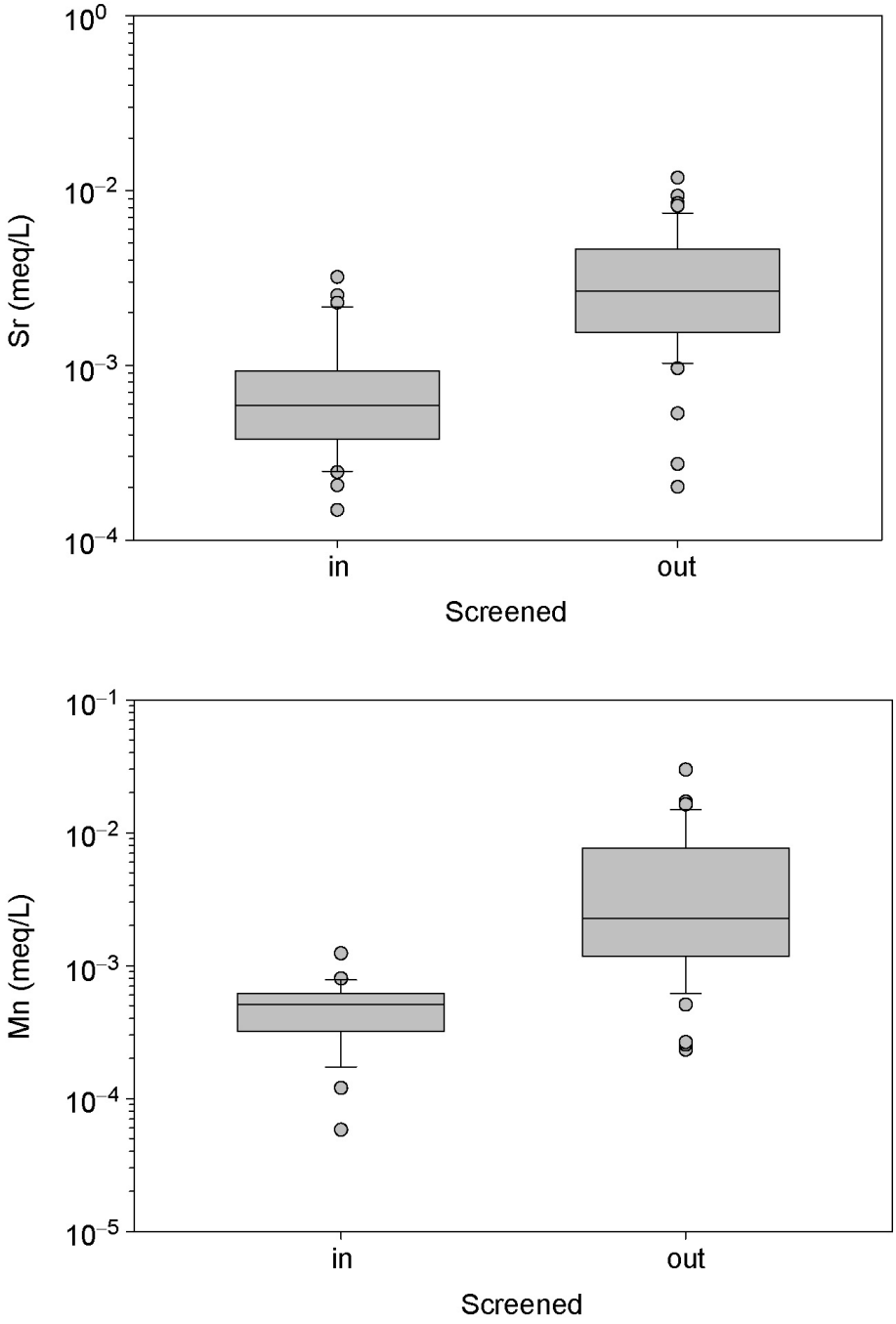

Source: Output DTN: SN0705PAEBSPCE.015, spreadsheet: *Sr_Mn_Plot.xls*.

NOTE: Sr and Mn data are not available for all samples: Mn, n =29 (in) and 49 (out); Sr, n = 30 (in) and 49 (out).

Figure 6.6-13. Box and Whisker Plots of Pore-Water Mn and Sr Concentrations Showing That Screened in and Screened out Pore Waters Form Different Populations

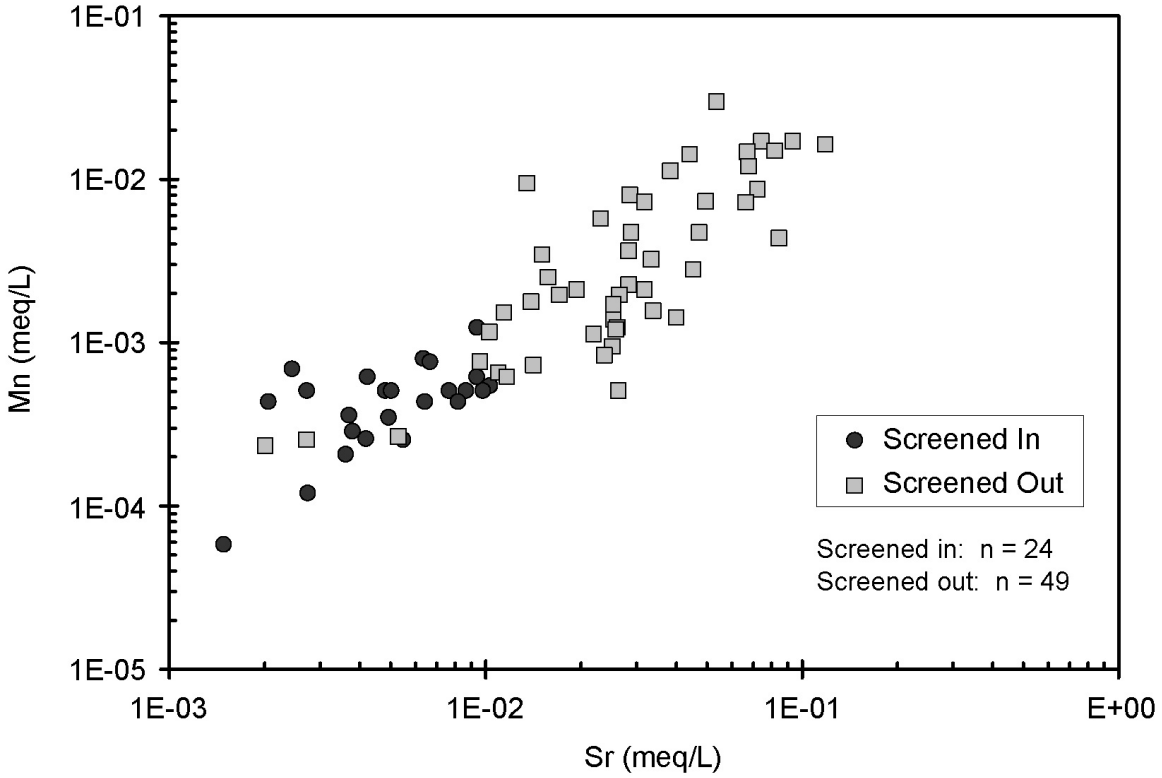

Source: Output DTN: SN0705PAEBSPCE.015, spreadsheet: *Sr_Mn_Plot.xls*.

NOTE: 16 of the 90 evaluated TSw waters lack either Sr or Mn and therefore are not plotted.

Figure 6.6-14. Sr versus Mn Pore-Water Concentrations

Sr and Mn concentrations discriminate well between the screened-in and screened-out pore waters, but do not match the screening results exactly. Most important would be the few pore waters that are screened out, but appear to match the characteristics of the screened-in waters. However, it must be remembered that, while the main effect of the two screening criteria is to screen out waters affected by microbial activity, the charge balance criterion is more general. Pore waters might fail this criterion for a variety of reasons; hence, it is not surprising that a few pore waters might be screened out for other discrepancies, rather than microbial activity. The three screened-out pore waters that plot within the screened-in field in Figure 6.6-14 were screened out on the basis of charge balance; all three passed the pH_{calc} screening criterion.

Despite the minor differences between the screening and trace element evaluations, the Sr and Mn data clearly show that the two screening criteria developed in Section 6.6.3 are effective in discriminating between two compositionally distinct clusters of water compositions. Several processes associated with microbial activity could explain the observed enrichment in Sr and Mn, including calcite or Mn-oxide dissolution due to the pH decrease as CO_2 builds up in the sealed cores, and stabilization of desorbed or ion-exchanged Sr and Mn in solution by complexation with organic acids.

6.6.5 Selection of NFC Model Starting Waters

In the previous sections, the available TSw pore-water analyses were screened, and a set of 34 analyses believed to be representative of in situ pore-water compositions was identified. However, using 34 water compositions in the P&CE suite of models is unwieldy, as it would require many thousands of EQ3/6 simulations and lookup tables, and unnecessary, as many of these pore waters are chemically similar, and could be adequately represented by a single water composition. In this section, the set of 34 pore waters is statistically evaluated in order to determine how many chemically distinct groups, or clusters, are present, and then, a representative water is chosen for each group. The representative waters are used as the starting water compositions in the P&CE suite of models.

Specifically, the following steps are performed:

- First, the number of chemically distinct "groups" of waters among the 34, and the members of each group, are identified using the statistical method of principal component analysis. This analysis was conducted first using the starting water compositions (after charge balancing and equilibrating at a pCO_2 of 10^{-3} bars using EQ3/6) and second using the predicted water compositions after simulated evaporation to an activity of water of 0.74 (an RH of 74%), just above the activity of water at which halite precipitates, for these samples. These two data sets are utilized to constrain the total variability in the pore waters at two points as they evaporate to salt saturation.

- The parameters used in the analysis are the Pitzer pH and the log-transformed molal concentrations of the following analytes: K, Na, Ca, Mg, S, C, Cl, F, and N. The SiO_2(aq) is not used in the analysis, because it shows little variation among samples, either before or after evaporation. Input values for the analysis are archived in Output DTN: SN0705PAEBSPCE.015 (spreadsheet: *Princ_Comp_ Results.xls*).

- Second, a representative pore water for each "group" is chosen by selecting that sample closest to the centroid of the group. These "representative Group waters" are used as starting waters for the P&CE models.

Principal Component Analysis (PCA) Overview—A PCA is a mathematical technique applied to matrices of data, in which the goal is to represent the variation in a suite of variables using the smallest number of factors (components) possible. Samples can be viewed by redefining the axes of the matrix on a plot as *components* rather than using original measured values. The new component axes (called principal components or "PCs") allow one to evaluate data sets with multiple variables, but to view the multivariant characteristics of the data set in as limited a number of dimensions as possible. For a more detailed description of PCA, its uses, and properties, see the work of Miller and Miller (2000 [DIRS 181601], pp. 217 to 221).

In this analysis, the data set consists of the suite of 34 equilibrated initial pore-water compositions and 34 evaporated pore-water compositions. In this PCA, these data describe a matrix with 34 rows and numerous column variables representing the analyte concentrations at

74% RH and initial equilibrium. The goal of the analysis is to reduce the number of variables needed to describe the overall variation in the samples.

The mathematics used to construct a PCA are such that the first principle component (PC1) describes the maximum variation possible in one direction, in the 20-dimensional space represented by the 10 analytes under initial and 74% RH conditions. The second principle component (PC2) describes the second most variation possible; the third principle component (PC3) describes the third most variation possible, and so on. The goal is to attain dimension reduction from the 20 variables. Additionally, percent of the total variation captured by each principle component is calculated by the PCA, so the cumulative percent variation captured by a given number of principle components can be determined. Furthermore, PCA can be used to evaluate the distances of the 34 pore waters from the chosen principle component axes and to define groups or clusters of waters based on similar distances from the axes, which correspond to compositional similarities.

PCA Results and Group Assignment—Using the commercial software JMP5.1, a PCA was carried out using the initial equilibrium compositions and the 74% evaporated compositions of the 34 waters. Water samples were defined as rows (34 total) and concentrations of analytes were defined as columns (20 total components). For a discussion of the options selected and steps taken in using the JMP5.1 software to create the PCA results see the spreadsheet *Princ_Comp_Results.xls* in Output DTN: SN0705PAEBSPCE.015 (tab: "Inputs to Princ Comp Analysis").

The results of the PCA are as follows:

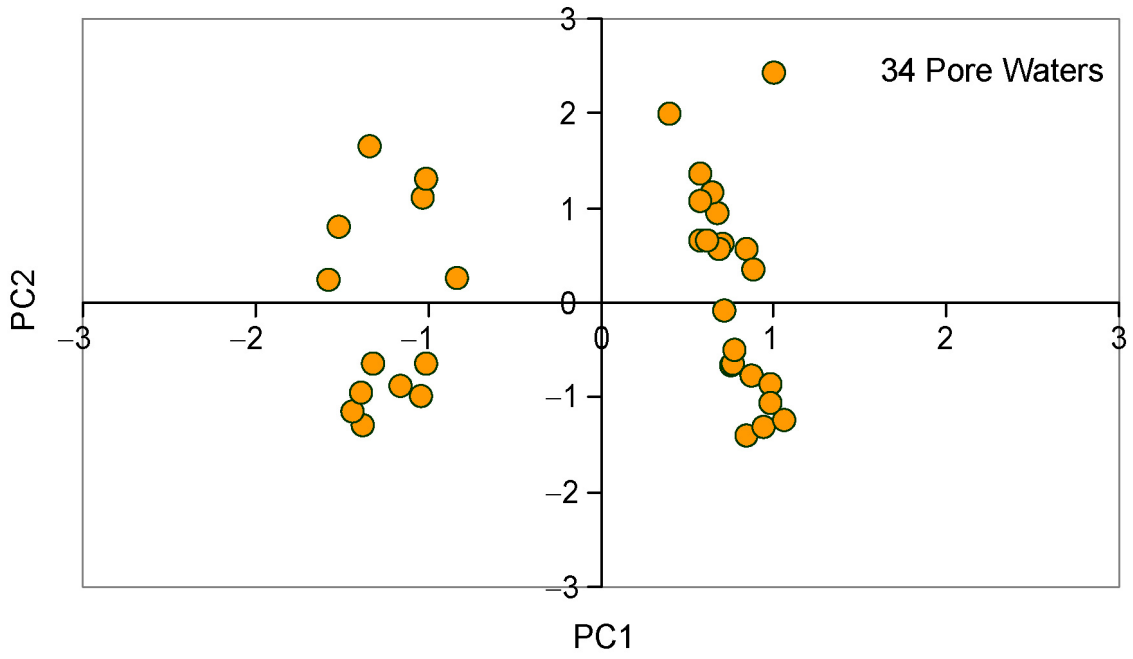

Source: Output DTN: SN0705PAEBSPCE.015, spreadsheet: *Princ_Comp_Results.xls*, tab: "4 Assigned Groups."

Figure 6.6-15. Two-Dimensional Plot Showing the 34 Pore-Water Compositions in PC1–PC2 Space

- Analyses using two PCs show that the 34 water samples cluster into two general groups based on representation from PC1 and PC2 (Figure 6.6-15). Analyses using three axes, PC1, PC2, and PC3, show that the water samples cluster into four groups (Figure 6.6-16).

- Table 6.6-2 provides the Eigen values, percent variation, and cumulative percentage for the described PCA. Eigen values are similar to the percent variation as they describe the partitioning of the total variation in the multivariant sample. The cumulative percent variation captured by the first two PCs is 82.5%, whereas that captured by the first three PCs is 90.4% (Table 6.6-2). Simply put, 90.4% of the variation of the data set is captured by PC1, PC2, and PC3 (three variables). PC4 through PC6 account for just 8.1% of the total variation, while PC7 through PC20 account for only approximately 1.5% of the total variation of the data set (Table 6.6-2). Thus, three PCs are adequate to describe the majority of variation in the pore-water data set. All results of the PCA are given in Output DTN: SN0705PAEBSPCE.015 (spreadsheet: *Princ_Comp_Results.xls*, tab: "Princ_Comp_Results").

Identified Groups

Group 1 = 21; Red

Group 2 = 7; Pink

Group 3 = 3; Blue

Group 4 = 3; Green

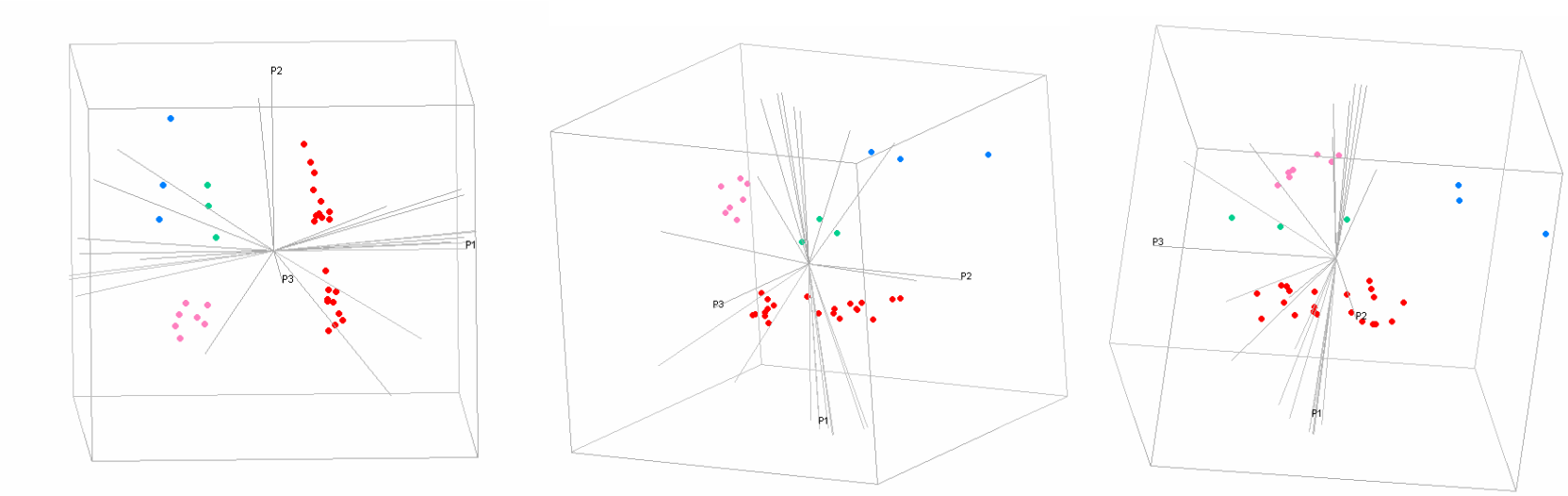

Source: Output DTN: SN0705PAEBSPCE.015, spreadsheet: *Princ_Comp_Results.xls*, tab: "4 Assigned Groups."

NOTE: Plots generated using the software program JMP5.1. PC1, PC2, and PC3 named P1, P2, and P3 on the plot.

Figure 6.6-16. Three Different Views of a 3-D Plot Showing the Clustering of the Pore-Water Analyses Based on Representation along PC1, PC2, and PC3

Table 6.6-2. Principal Component Analysis for the First Six Principal Components

Data parameter	PC1	PC2	PC3	PC4	PC5	PC6
Eigenvalue	13.92	2.57	1.59	0.77	0.51	0.34
% Variation	69.60	12.87	7.93	3.84	2.57	1.69
Cumulative % Variation	69.60	82.47	90.40	94.24	96.81	98.50

Source: Output DTN: SN0705PAEBSPCE.015, spreadsheet: *Princ_Comp_Results.xls*, tab: "Princ_Comp_Results."

Table 6.6-2 shows that PC1 and PC2 account for ~82.5% total variation. However, the plots using three PCs, accounting for 90.4% of the total variation in the data, clearly show that four clusters can be discriminated (Figure 6.6-16), especially when the plot is viewed from different directions. Since the purpose on this analysis is to identify individual clusters, the 3-D space offers better resolution. Each of the clusters on the plot is a "Group," and each of the 34 waters is assigned to one of four groups. The assigned group for each of the 34 waters is shown in Table 4.1-3.

The efficacy of the PCA grouping analysis is illustrated in Figures 6.6-17 and 6.6-18. In Figure 6.6-17, the change in the Ca concentration (a) and the pH (b) with evaporation is plotted for each of the 34 pore waters. Three groups are readily discriminated, but there is significant overlap in Groups 2 and 3. However, these two groups are readily distinguished in Figure 6.6-18, where the change in the chloride:nitrate ratio during evaporation is plotted.

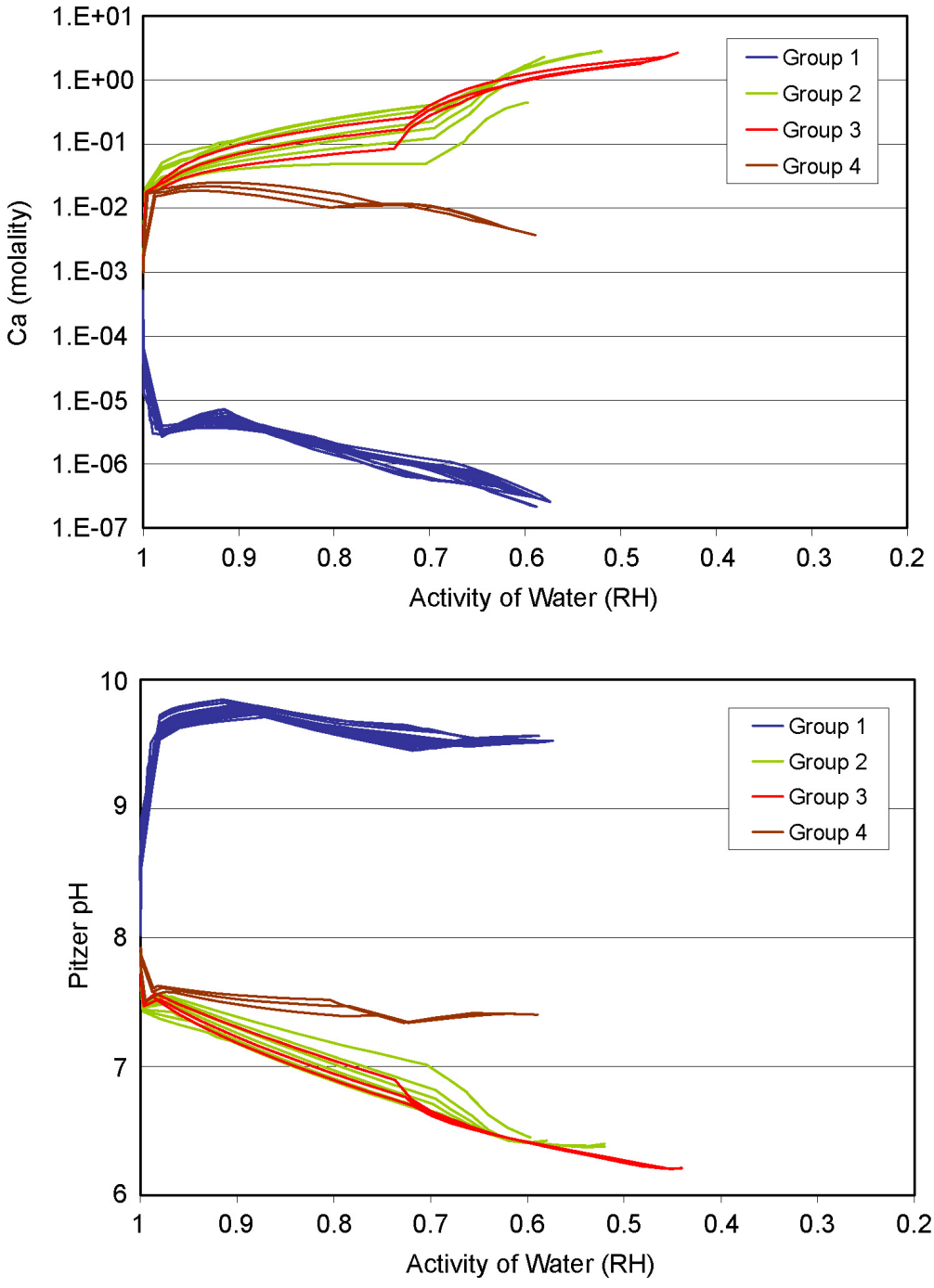

Source: Output DTN: SN0705PAEBSPCE.015, spreadsheet: *Results.xls*, tab: "Sel Waters; Ca vs RH, No N_Cl."

NOTE: The colors indicate the four groups determined by principal component analysis.

Figure 6.6-17. Evaporative Evolution of the 34 TSw Pore Waters That Meet the Screening Criteria

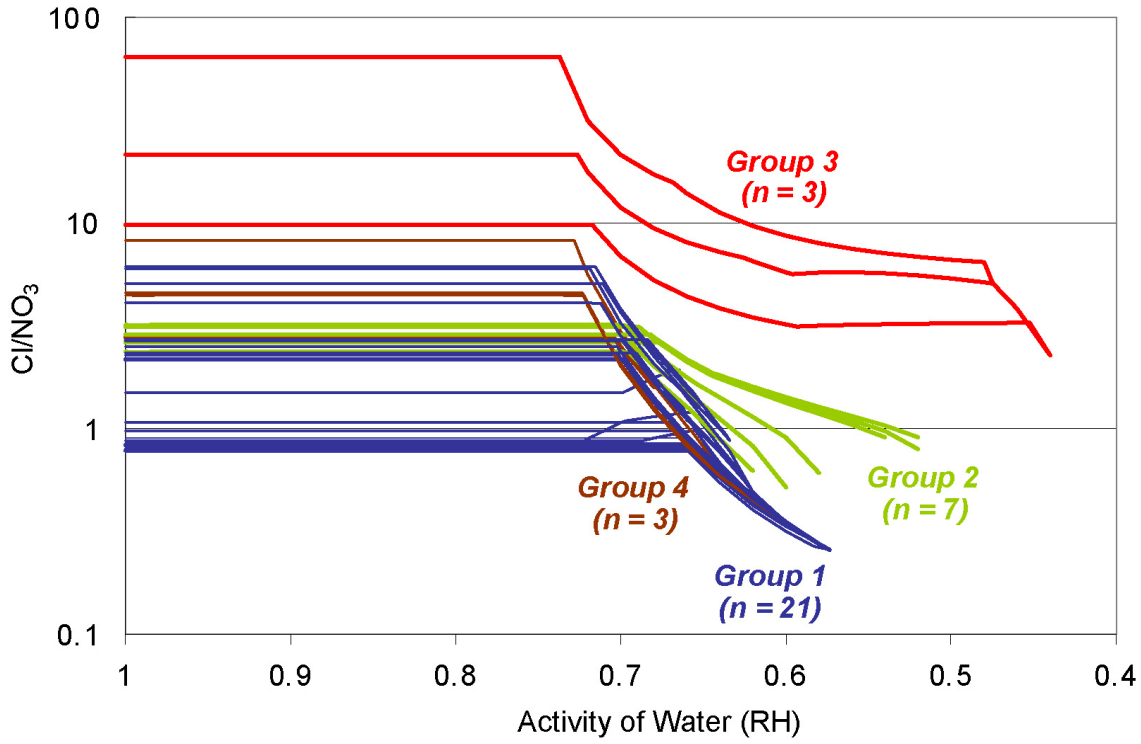

Source: Output DTN: SN0705PAEBSPCE.015, spreadsheet: *Results.xls*, tab: "Selected Waters; Cl-NO3 vs RH."

NOTE: The colors indicate the four groups determined by principal component analysis.

Figure 6.6-18. Change in Chloride:Nitrate Mass Ratio with Evaporation

Selection of Near-Field Seepage Waters—In order to select the representative water for each group, mean values for each of the 20 parameters used in the PCA were calculated. For each water in a group, each parameter value was subtracted from the cluster mean and the square root of the sum of the squares of the differences, which represents the distance from the group center, was calculated. The pore-water composition with the minimum square root of the sum of the squares is the composition closest to the cluster centroid, and is selected as the representative water for that group. These calculations are documented in Output DTN: SN0705PAEBSPCE.015 (spreadsheet: *Princ_Comp_Results.xls*, tab: "Choose Repr Group Waters").

The results of these calculations are summarized in Table 6.6-3. Representative waters for Groups 2, 3, and 4 are the waters closest to the group centroid: ESFTHER1, ESFPERM3, and ESFPERM4, respectively. For Group 1, the water closest to the group centroid is DS3-2 (distance = 0.524), but SD9-3 is nearly as close (distance = 0.528). Given that the distances are so similar, pore water SD9-3 was chosen as the Group 1 representative water, on the basis of the better charge balance for the original measured composition (+0.22 versus –1.38, from Output DTN: SN0705PAEBSPCE.015, spreadsheet: *TSw_Porewater_Data.xls*, tab: "All_Tsw").

Table 6.6-3. Representative Waters for Each of the Four Water Groups

Group	# Waters	Representative Water	EQ3/6 filename
1	21	SD-9/1184.7-1184.8/UC	SD9-3
2	7	ESF-THERMALK-017/26.5-26.9/UC	ESFTHER1
3	3	ESF-HD-PERM-3/34.8-35.1/Alcove 5	ESFPERM3
4	3	HD-PERM-3/56.7-57.1/UC	ESFPERM4

Source: Output DTN: SN0705PAEBSPCE.015, spreadsheet: *Princ_Comp_Results.xls*, tab: "Princ_Comp_Results."

6.7 EVOLUTION OF IN-DRIFT OXYGEN AND CARBON DIOXIDE

The purposes of this section are:

- To analyze oxygen demand in the drift. This determines the potential (given the large masses of introduced materials in the drift) for the development of oxygen-deficient conditions.
- To describe how the NFC model derives the expected range of pCO_2 in the drift.
- To establish the expected range of in-drift temperatures, for use in developing lookup tables.

6.7.1 Oxygen Evaluation

Of all materials present in the EBS, carbon- or low-alloy steel in the emplacement drift invert has the greatest potential to deplete the oxygen fugacity as it degrades. This is jointly due to the abundance of steel in the invert and the rails (together described as "invert steel") and its rapid degradation rate compared to the other major materials present including stainless steel, titanium, and Alloy 22. Corrosion rates for comparison may be found in *Aqueous Corrosion Rates for Waste Package Materials* (BSC 2004 [DIRS 169982]).

This section shows that corrosion of invert steel will decrease oxygen fugacity, but as a transient phenomenon, and with insufficient magnitude to qualitatively change any important chemical reactions in the EBS. The rates of reactions that depend on oxygen will be affected, generally slowing degradation processes. The results presented here are reasonable lower bounds on the oxygen fugacity, primarily because there will be transport of oxygen into the repository by processes not considered here.

Spent fuel (i.e., UO_2) waste forms have total oxygen demand that is comparable to that from invert steel; however, the waste forms cannot degrade until waste packages are breached. For oxygen fugacity to decrease as it does from degradation of invert steel, many waste packages would need to breach in the first few thousand years after closure. As will be shown in the following sections, the greatest impact on oxygen fugacity is from the combined effects of oxygen demand and displacement of air by steam. After the drift wall cools below 96°C, the predicted influx of oxygen to the drift increases. The likelihood of a seismic event of sufficient magnitude to breach many waste packages during the boiling period is small, and the effect

would be comparable to that which will be caused by invert steel, hence the oxygen demand from waste forms is not considered in this analysis.

Two evaluations of in-drift oxygen fugacity are described here: (1) a steady-state rate balance calculation that estimates oxygen fugacity by balancing the oxygen flux into the drift opening with the intrinsic, fugacity-dependent rate of oxygen consumption by corrosion of steel; and (2) analysis of limitation on the degradation of steel from mass transfer of oxygen by diffusion through a layer of corrosion products, combined with the intrinsic kinetics. The sections below present information on the quantity of steel in the invert, and on the temperature, gas flux, and air mass-fraction boundary conditions that are common to both approaches. The rate balance estimation approach is then presented, followed by evaluation of the importance of mass transfer through corrosion products on the in-drift O_2 fugacity.

6.7.1.1 Quantity of Steel in the Invert

Low-alloy weathering steel (primarily A588; SNL 2007 [DIRS 179354], parameters 02-08 and 02-10) is used for the invert. Steel quantity is needed to develop surface area and effective corrosion thickness for the oxygen balance analyses. Two different design descriptions are used in an effort to define a baseline case and a bounding case. The baseline case is described in Table 6.7-1. The bounding case is taken from a design change proposal that included significantly more steel, but was rejected because it included too much (SNL 2007 [DIRS 179354], which cites the original source: TMRB-2007-014).

The surface area per unit length of drift is based on the design elements, neglecting stainless steel items, and neglecting beam ends, which add little to the overall surface area (Output DTN: MO0705OXYBALAN.000, spreadsheet: *Invert steel worksheet June2007.xls*) (see Table 6.7-1). Rock bolts and splice plates used to join rail sections are also neglected as simplifications with small impact. The rail sections are approximated by several trapezoids for purposes of calculating perimeter and cross-sectional area.

The corrosion thickness is a composite value wherein the thickness of each element is weighted by the ratio of its mass to the total mass of steel in the invert, and the weighted thickness values for all elements are summed (Output DTN: MO0705OXYBALAN.000, spreadsheet: *Invert steel worksheet June2007.xls*) (see Table 6.7-1). This thickness value is intermediate between the thickest and thinnest design elements, and is used to represent the duration of significant corrosion effects on oxygen fugacity. For thickness calculations, corrosion is assumed to attack the major sides of plates, the largest external surfaces of rails and bolts, and the webs and flanges of beams. Ends, edges, and threads are not included since they are small and will be increasingly less important as corrosion progresses. Corrosion is assumed to attack both major sides of all elements, so corrosion-thickness values are half of dimensional values.

Table 6.7-1. Invert Steel Inventory, Mass, Surface Area, and Corrosion Thickness

Committed Materials List	Size	Material	Weight (lb./ft. of drift)	Surface Area (m^2/m of drift)	Estimated Corrosion Thickness (mm)	Mass-Weighted Thickness (mm)
Baseline Design						
Gantry rails	135 lb/yd	A759	90	1.22	6.82	0.85
Rail runway beams with stiffeners	W8 × 67	A588 Gr. 50	146	2.77	5.01	1.01
Runway beam cap plates	PL 1" × 12"	A588 Gr. 50	82	1.22	12.70	1.44
Longitudinal support beams	W12 × 35	A588 Gr. 50	105	3.86	2.58	0.37
Transverse beams with stiffeners	W12 × 72	A588 Gr. 50	173	4.38	3.73	0.89
Stub column top plate	3/4" × 10" × 12"	A588 Gr. 50	10	0.23	9.53	0.31
Stub column	W8 × 67	A588 Gr. 50	31	0.59	5.01	0.21
Base plates	1" × 12" × 24"	A588 Gr. 50	34	0.55	12.70	0.60
Rock bolts	(2) × 1-3/4" dia.	SS A276	14			
Stuctural bolts	7/8" dia.	A325	20	0.67	11.18	0.31
Misc. stiffener plates	Varies	A588 Gr. 50	20	0.29	12.70	0.35
Summary: Total mass: 1,081 kg/m of drift; total surface area: 15.78 m^2/m of drift; and total mass-weighted corrosion thickness: 6.16 mm.						
Proposed Design						
Crane rails	171 lb/yd	A759	114	1.41	7.50	0.52
Runway beams	W12 × 210	A588 Gr. 50	420	3.97	10.03	2.55
Longitudinal beams	W12 × 72	A588 Gr. 50	144	3.65	3.73	0.33
Transverse beam with angles	W12 × 210	A588 Gr. 50	688	6.51	10.03	4.18
Stub columns	W10 × 100	A588 Gr. 50	57	0.90	6.00	0.21
Stub column top plates	3/4" × 13" × 13"	A588 Gr. 50	14	0.32	9.53	0.08
Stub column base plates	1-1/4" × 15" × 22"	A588 Gr. 50	47	0.64	15.88	0.45
Side plates	1-1/4" × 18" × 24"	A588 Gr. 50	61	0.82	15.88	0.59
Splice plates	5/8" × 8" × 24-1/2"	A588 Gr. 50	7			
Structural bolts	1-1/4" dia.	A325	57	0.86	15.88	0.55
Rock anchors	2" dia.	Stainless steel	41			
Summary: Total mass: 2,460 kg/m of drift; total surface area: 19.08 m^2/m of drift; total mass-weighted corrosion thickness: 9.46 mm.						

Source: SNL 2007 [DIRS 179354], parameters 02-08 and 02-10. Data archived in Output DTN: MO0705OXYBALAN.000.

NOTE: Gantry rail specifications taken from AISC 1991 [DIRS 127579], p. 1-113.

6.7.1.2 Corrosion Rates for Invert Steel

The corrosion rate data described in Section 4.1.1 are used to develop minimum, mean, and maximum penetration rate values for low-alloy steels under aggressive conditions (Output DTN: MO0705OXYBALAN.000, spreadsheet: *atmospheric May2007.xls*) (see Table 6.7-2). These values are conservative for several reasons: (1) the environments represented among the literature data include extreme environments (e.g., marine); and (2) type A588 is a weathering steel that builds up a surface layer that slows corrosion, whereas some of the literature data represent faster corroding types. The values shown in Table 6.7-2 are generally consistent in magnitude, or greater than the rates recommended in ASTM G101-97 (ASTM 1997 [DIRS 151442]) for A588, and are conservative. Note that the mean rate from Table 6.7-2 is based on laboratory testing at 90°C (Output DTN: MO0705OXYBALAN.000, spreadsheet: *Invert steel worksheet June2007.xls*).

Table 6.7-2. Corrosion Rates for Invert Steel Used in Oxygen Balance Analysis

Minimum	85.50 μm/yr	Steel-industrial environment
Mean	195.43 μm /yr	Lab testing of A516 at near-100% relative humidity
Maximum	1057.18 μm /yr	Steel-marine

Source: Output DTN: MO0705OXYBALAN.000, spreadsheet: *atmospheric May2007.xls*. Inputs described in Section 4.1.1.

6.7.1.3 Thermal-Hydrologic Boundary Conditions

Thermal-hydrologic (TH) boundary conditions were taken from the output of the thermal-hydrologic-chemical (THC) model (DTN: LB0704DSTHONLY.001 [DIRS 181164]). These data are appropriate for evaluating O_2 fugacity because they can be compared directly with other data such as the CO_2 fugacity (SNL 2007 [DIRS 177404]). The two TH cases from the THC runs use 81-m and 162-m drift spacings to represent repository center and edge conditions, respectively. Use of a wider drift spacing with a two-dimensional (2-D) TH simulation has been shown to represent 3-D repository-edge effects on temperature (SNL 2007 [DIRS 181383]). The 2-D simulations used in this analysis do not include axial mass transport, and therefore underestimate the influx of air from the unheated ends of the drift, and underestimate the O_2 fugacity.

The temperature, pressure, and air mass-fraction for locations in the THC model grid at the drift crown, side, and base are plotted in Figure 6.7-1 for the 81-m and 162-m drift spacing cases. The 162-m repository-edge case (referred to below as the repository-edge case) cools more quickly, with boiling duration limited to approximately 150 years, compared to 1,000 years for the 81-m (repository-center) case. Only the TH data for the fracture continuum are used in this analysis because: (1) temperatures are very similar in the matrix and fractures; and (2) the preponderance of gas flux moves in or out of the drift through fractures.

The inflow of air from the host rock is a key input for estimating O_2 fugacity. Air inflow is estimated from total gas inflow and air mass-fraction. Gas inflow rate varies with changes in thermal convection in the host rock, and with volume changes that occur with evaporation and condensation in the host rock. Both inflow and outflow are calculated by the THC model; only

the inflow information is used to represent O_2 availability, but cumulative inflow and outflow are compared to confirm that the inflow and outflow are appropriately estimated.

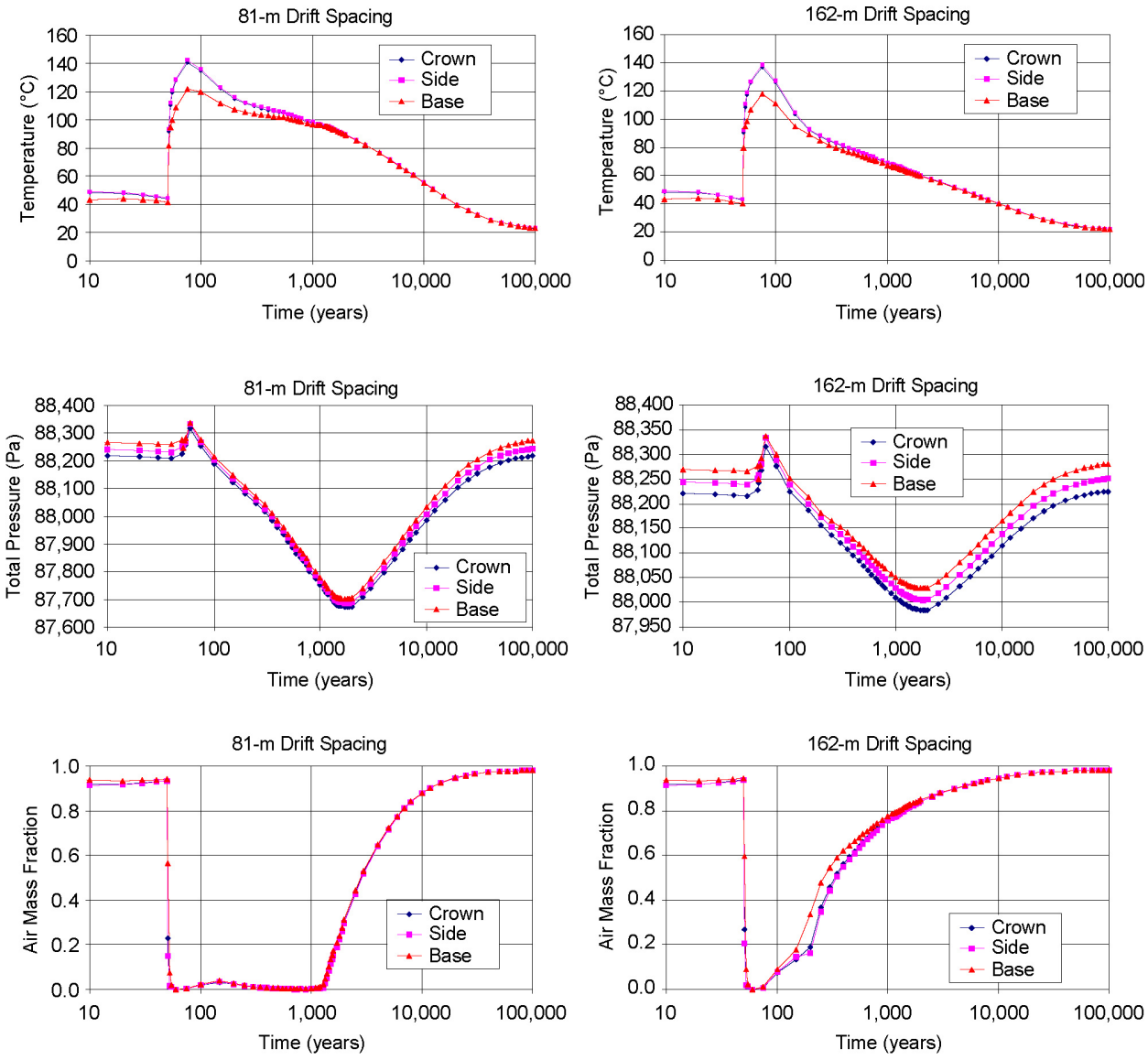

Source: Output DTN: MO0705OXYBALAN.000.

Figure 6.7-1. Thermal-Hydrologic Description of Conditions in the EBS, from THC Simulations with Drift Spacings of 81 and 162 m

The available inflow and outflow information from the THC model consists of gas mass transfer rates between three pairs of grid elements straddling the drift wall. The pairs are located at the crown, side, and base of the drift opening. The wall-flux results are denoted "CrownW," "SideW," and "BaseW," respectively (Output DTN: MO0705OXYBALAN.000, spreadsheets: *th7_81_GasCalc_Invert June2007.xls* and *th7_162_GasCalc_Invert June2007.xl*s, worksheets entitled "fractures-th"). The locations of the element pairs, and the flow area (i.e., drift-wall area) for each, are also noted (worksheets entitled "notes"). There are many element connections

defining the drift wall in the THC model, and the three reported pairs need to be combined in a weighted sum to approximate total gas inflow and outflow.

The weighted sum is approached by assuming that the crown connection represents 25% of the drift wall area, then choosing the percentage represented by the side connection to achieve balance between cumulative air inflow and outflow. (The base percentage is the complement of the crown plus side percentages.) Air inflow is simply the gas influx multiplied by the air mass-fraction. Several trial values for the crown fraction were used to evaluate the robustness of the estimation scheme, and the results were found to vary over approximately a factor of 2 (Output DTN: MO0705OXYBALAN.000, spreadsheets: *th7_81_GasCalc_Invert June2007.xls* and *th7_162_GasCalc_Invert June2007.xl*s, worksheets entitled "fractures-th," range BG19:BJ24). This factor of 2 is discussed further in relation to the resulting calculations of O_2 fugacity.

The cumulative air mass inflow for both the repository-center and -edge cases is plotted in Figure 6.7-2. The cumulative O_2 inflow is also plotted on the figure, with the assumption that the air fraction has the same O_2 composition as atmospheric air (20.946% O_2). The amount of O_2 inflow approaches the mass of steel discussed above (e.g., 1,081 kg/m of drift) after approximately 500 to 2,500 years for the edge and center cases, respectively.

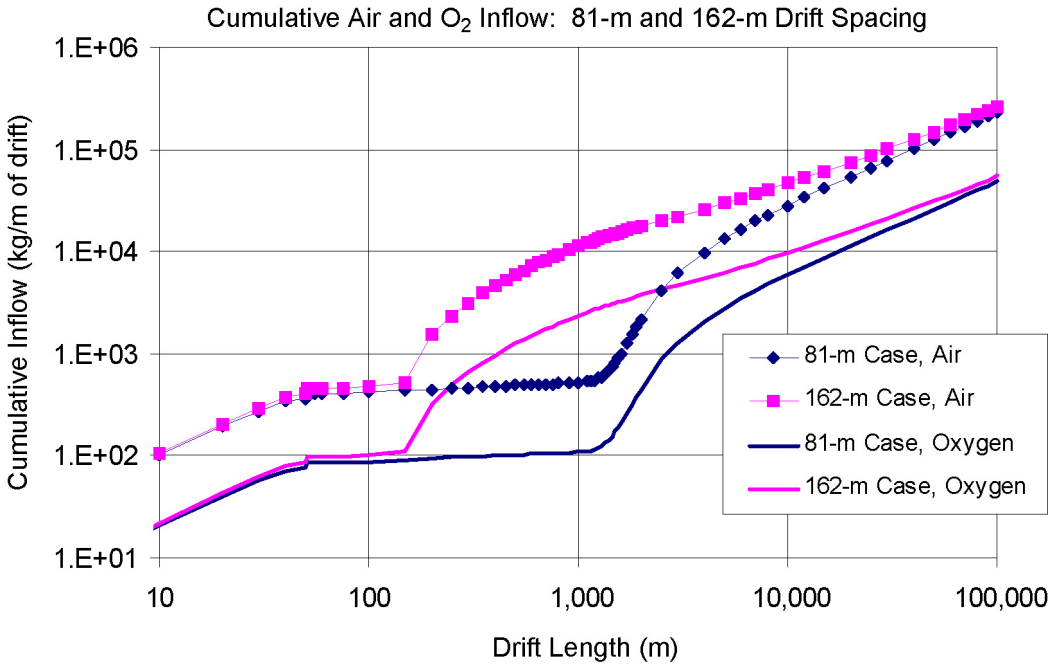

Source: Output DTN: MO0705OXYBALAN.000.

Figure 6.7-2. Cumulative Gas Inflow (mass flux) into the Drift Opening, per Meter of Drift Length, Developed from Output of THC Simulations with Drift Spacings of 81 and 162 m

The parameters needed for O_2 balance calculations are the mass flow rate for total gas inflow, temperature, total pressure, and air mass-fraction. From these variables the following are calculated: relative humidity, mass flow rate for O_2 inflow, and influent oxygen concentration. The "Base" output from the THC output is used because this location is closest to the invert,

except for total gas inflow which is integrated around the circumference of the drift. This is justified because gaseous constituents are readily dispersed in the EBS by diffusion and convective mixing.

6.7.1.4 Rate Balance for Oxygen Inflow vs. Corrosion Consumption by Invert Steel

As described above, a steady-state rate balance is calculated to evaluate oxygen fugacity conditions. The calculation involves: (1) estimating the inflow rate for gaseous O_2 through the drift walls, and (2) equating this to the rate of oxygen consumption by corrosion. The analysis is parametric with respect to the amount of steel present, center vs. edge location, and corrosion rates.

Although the effects of microbial activity on corrosion rates are not included, they are probably encompassed by the wide range of conditions considered. Discussion in *Evaluation of Potential Impacts of Microbial Activities on Drift Chemistry* (BSC 2004 [DIRS 169991], Section 6.5.1 and Equation 6-4) shows that the impact of microbial activity on CO_2 fugacity in the EBS environment is negligible. By analogy, the impact on O_2 consumption (the same essential reaction that generates CO_2) will be much less than the oxygen inflow and therefore negligible.

The instantaneous rate of change in moles of gaseous O_2 per length of drift is written as:

$$\frac{\partial M}{\partial t} = \frac{1}{V}\frac{\partial C}{\partial t} = C_{in}\, Q_{in} - C\, Q_{out} - \dot{m} \qquad \text{(Eq. 6.7-1)}$$

where

M = Moles gaseous O_2/meter of drift
V = Drift volume (m^3/m)
C_{in} = Molar concentration of O_2 in gas inflow (mol/m^3)
Q_{in} = Volumetric gas inflow rate (m^3/sec/m of drift)
C = Molar concentration of O_2 in the drift and in outflow (mol/m^3)
Q_{out} = Volumetric gas outflow rate (m^3/sec/m of drift)
$\dot{m}$ = Rate of O_2 fixing by corrosion (mol O_2/sec/m of drift).

Assuming a quasi-steady state because M can change rapidly compared to the lifetime of steel in the repository, then:

$$\frac{\partial C}{\partial t} = C_{in}\, Q_{in} - C\, Q_{out} - \dot{m} = 0 \qquad \text{(Eq. 6.7-2)}$$

and rearranging:

$$C = \frac{C_{in}\, Q_{in} - \dot{m}}{Q_{out}} \qquad \text{(Eq. 6.7-3)}$$

The effect of oxygen consumption in the drift is to decrease C_{out} compared with C_{in}, especially when the rate of consumption is highest (i.e., just before or after the boiling period). By setting

$Q_{out} \approx Q_{in}$, the expression is greatly simplified (avoiding solution of a higher order equation) and the predicted concentration is somewhat lower, which is conservative for the intended use of this analysis. The difference between Q_{in} and Q_{out} is depletion of oxygen, which is at most approximately:

$$X_{O2} \frac{MW_{O2}}{MW_{air}} \approx .21 \frac{32}{28.9} = 23\% \qquad \text{(Eq. 6.7-4)}$$

where X_{O2} is the inflow mole fraction of O_2, MW_{O2} is the molecular weight of O_2, and MW_{air} is the average molecular weight of air (Weast and Astle 1981 [DIRS 100833], pp. B-126, F-12, and F-172). The depletion percentage is much less during boiling period when the minimum O_2 fugacity occurs, because X_{O2} is smaller from displacement of air by water vapor. Finally, using the ideal gas law to relate concentration and pressure, the rate balance equation for the partial pressure of O_2 is:

$$P_{O2} = \frac{MRT}{V} = C \cdot RT \approx \frac{(C_{in} Q_{in} - \dot{m})RT}{Q_{in}} \qquad \text{(Eq. 6.7-5)}$$

where

T = Absolute temperature (K)
R = Gas constant (Pa m3/mol-K).

To evaluate $\dot{m}$, it is assumed that iron is the dominant constituent of steel, and that a ratio of 1.5 moles of atomic oxygen per mole of iron (or 0.75 moles O_2 per mole of Fe) is based on the formation of ferric iron according to the reaction:

$$\frac{4}{3}\mathrm{Fe(s)} + \mathrm{O_2} + 2\mathrm{H_2O} \rightarrow \frac{4}{3}\mathrm{Fe^{3+}} + 4\mathrm{OH^-} \rightarrow \frac{4}{3}\mathrm{FeOOH} + \frac{4}{3}\mathrm{H_2O} \qquad \text{(Eq. 6.7-6)}$$

The choice of goethite (FeOOH) or its polymorphs maximizes consumption of O_2(g). The so-called higher oxides such as hematite (Fe_2O_3) have the same maximum ratio of O_2(g) to Fe, but they are less likely to form than goethite. This ratio is also a maximum for iron oxidation, and therefore consumes the most oxygen.

The rate of O_2 consumption by steel corrosion is first order in the O_2 fugacity, or pO_2, according to a study by Jovancicevic and Bockris (1986 [DIRS 168509]) that explicitly investigated the dependence of corrosion rate on oxygen pressure. Their conclusions state that "In respect to O_2, the reaction order on both surfaces [bare and passive iron] is 1" (Jovancicevic and Bockris 1986 [DIRS 168509], p. 1805). A reaction order of one in this case means that consumption of oxygen by corrosion of steel is linearly dependent on the partial pressure. The partial pressures investigated ranged from 1 atmosphere down to 10^{-2} atmospheres. In this analysis, the dependence is treated as an intrinsic kinetic effect, since it was observed for both bare and passive surfaces. The possible effect of O_2 diffusion through a layer of corrosion products is discussed further below.

Accordingly, the rate of O_2 consumption (moles O_2/sec/m of drift) is written:

$$\dot{m} = S\frac{\rho_{steel}}{MW_{Fe}} A r_0 \frac{C\,RT}{P^*_{O2}} = B \cdot C, \qquad where \;\; B = \frac{S\rho_{steel} A r_0 RT}{MW_{Fe} P^*_{O2}} \qquad \text{(Eq. 6.7-7)}$$

where

S = Stoichiometric constant (O_2:Fe = 0.75)

ρ_{steel} = Density of steel (=7.850 kg/m^3; Incropera and DeWitt 1996 [DIRS 108184], Table A.1)

A = Surface area of steel (m^2/m of drift)

r_0 = Corrosion rate at 1 atm of air (m/sec; Table 6.7-2)

MW_{Fe} = Molecular weight of iron (0.055847 kg/mol; Weast and Astle 1981 [DIRS 100833], B-107)

P^*_{O2} = O_2(g) pressure at 1 atm of air (0.20946 atm; Weast and Astle 1981 [DIRS 100833], F-172).

Substituting gives the rate balance equation:

$$C \approx \frac{C_{in} Q_{in}}{Q_{in} + B} \qquad \text{(Eq. 6.7-8)}$$

This equation is implemented using the range of corrosion rates (Table 6.7-2) for the repository-center and -edge cases (Output DTN: MO0705OXYBALAN.000, spreadsheets: *th7_81_GasCalc_Invert June2007.xls* and *th7_162_GasCalc_Invert June2007.xls*, worksheets entitled "O2 Calc. Intrinsic Kinetics"). In the implementation, steel corrosion cannot occur unless the RH is at least 70% (Phipps and Rice 1979 [DIRS 100923]; CRWMS M&O 1998 [DIRS 100359], Section 5.5.3.1). The results (Figure 6.7-3) show that O_2 fugacity is greater than 10^{-9} atm, except for brief episodes at the start and end of boiling when gas inflow to the drift is minimal and the O_2 fugacity approaches 10^{-9} atm. For the repository-edge simulation (drift spacing of 162 m), there is more gas flux through the drift, so the steel is consumed sooner and with much less impact on the O_2 fugacity. Note that these are reasonable lower bound estimates for the reasons discussed in Section 6.7.1.7.

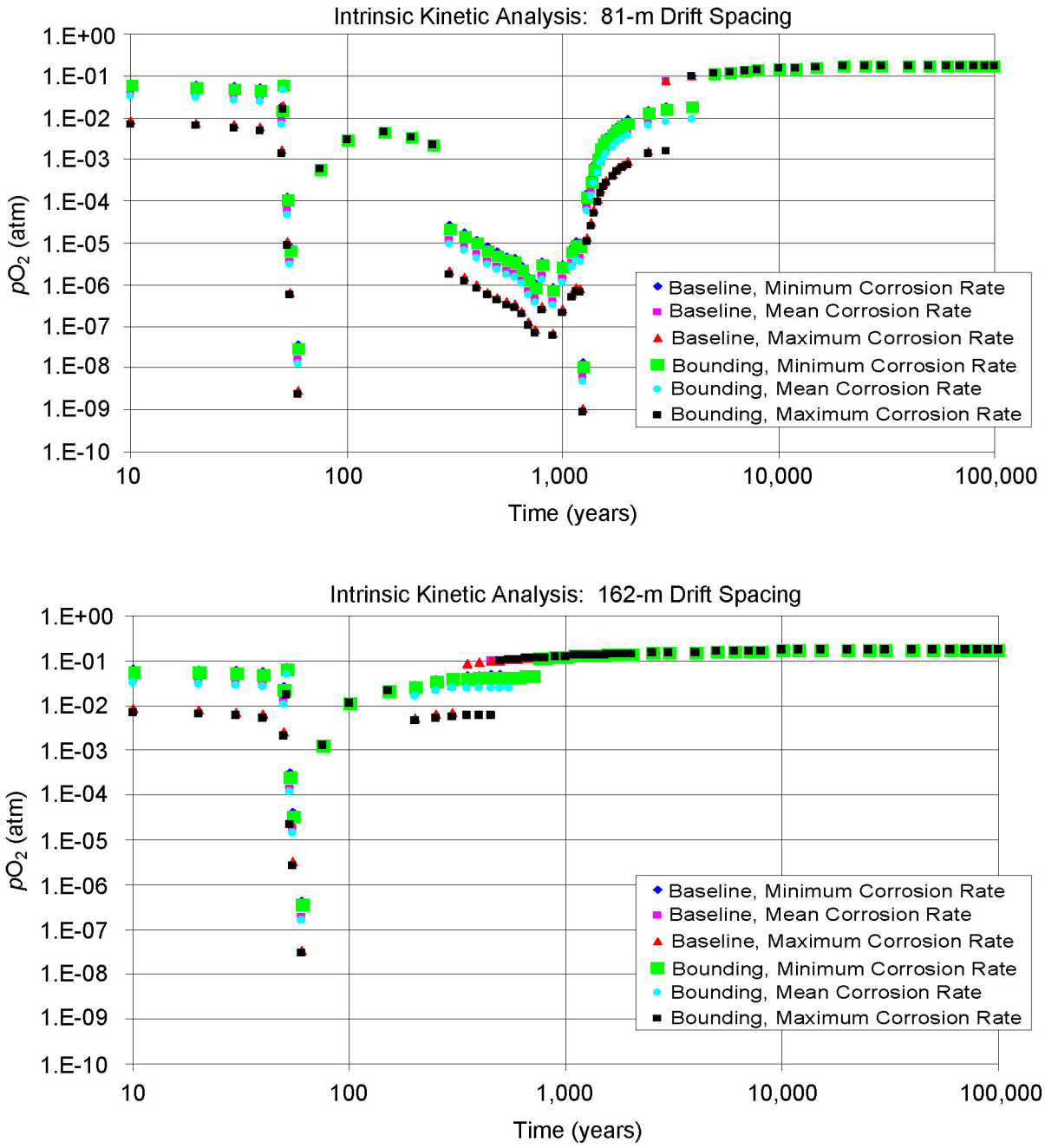

Source: Output DTN: MO0705OXYBALAN.000.

NOTE: Results cover a range of corrosion rates, baseline and bounding cases for quantity of invert steel, and drift spacing of 81 m (upper) and 162 m (lower), representing repository-center and -edge conditions.

Figure 6.7-3. Calculated Parametric Time Histories of In-Drift O_2 Fugacity Intrinsic Kinetic Analysis for a Drift Spacing of 81 m (upper) and 162 m (lower)

6.7.1.5 Mass Transfer Effect on Oxygen Consumption and Fugacity

As the invert steel corrodes, corrosion products will accumulate against the corroding surfaces. This is analogous to a moving-boundary reaction problem (for example, that derived in Doilnitsyna 2002 [DIRS 181153]). The corrosion product layer (Figure 6.7-4) thickens with time and hinders migration of O_2 to the metal surface, where the corrosion rate is subject to intrinsic kinetic limitation.

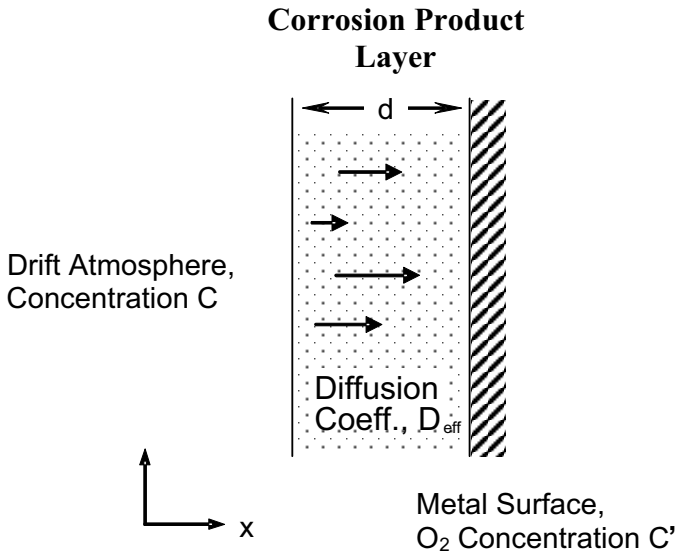

Figure 6.7-4. Schematic of Mass Transfer Mechanism for Limiting Corrosion Rates for Invert Steel

The equation of one-dimensional, steady diffusive transport within the corrosion product layer is:

$$\dot{m} = -\frac{\partial C}{\partial x} D_{eff} \qquad \text{(Eq. 6.7-9)}$$

Approximating the derivative by a difference, and imposing the quasi-steady state continuity condition that O_2 mass transport through the layer is equal to that consumed by corrosion at the metal surface, yields:

$$\dot{m} = -\frac{\partial C}{\partial x} D_{eff} = \frac{C - C'}{d} D_{eff} = B \cdot C \qquad \text{(Eq. 6.7-10)}$$

Simplifying, applying $Q_{out} \approx Q_{in}$, and $P_{O2} = CRT$ from Equation 6.7-5, gives:

$$P_{O2} \approx \frac{C_{in} Q_{in} RT}{Q_{in} + \dfrac{B}{1 + \dfrac{dB}{AD_{eff}}}} \qquad \text{(Eq. 6.7-11)}$$

where B is defined by Equation 6.7-7. If thickness d is small or zero, this expression is the same as Equation 6.7-3. Thickness d increases with time according to:

$$d = \left(\frac{\rho_{steel}}{\rho_{goethite}} \cdot \frac{1}{(1-\phi_{CP})}\right) \cdot \int_0^t \frac{\dot{m} MW_{Fe}}{SA \rho_{steel}} dt \qquad \text{(Eq. 6.7-12)}$$

where

$\rho_{goethite}$ = Approximate grain density of secondary goethite (kg/m^3)

ϕ_{CP} = Corrosion product porosity (40%; see SNL 2007 [DIRS 177407], Section 6.3.4.3.4).

Goethite is a common product of steel corrosion and is consistent with the oxidation reaction of Equation 6.7-6. The description of corrosion products by *EBS Radionuclide Transport Abstraction* (SNL 2007 [DIRS 177407]) is applied to degradation of A516 steel inside waste packages, but is applicable here because the invert steel has similar bulk composition and corrodes under similar conditions.

The integral on the right hand side of Equation 6.7-12 is the accumulated loss of steel from the surface, which is then modified to account for secondary changes in grain density and porosity. The effect of O_2 storage in the corrosion products is very small compared to the cumulative inflow of O_2 into the drift, and is neglected.

For in-package transport of radionuclides by diffusion through corrosion products, a set of moisture characteristic curves (liquid saturation vs. RH) and effective liquid-phase diffusion coefficients (D_{eff} vs. liquid saturation) was developed (SNL 2007 [DIRS 177407], Table 6.3-10). Several curves were developed depending on the specific surface area (m^2/unit mass) assumed. As specific surface area increases, the water content increases for a given RH, so the effective liquid-phase diffusion coefficient also increases. The two smallest values of specific surface area (1 m^2/g and 22 m^2/g) from *EBS Radionuclide Transport Abstraction* (SNL 2007 [DIRS 177407]) are used in this analysis. This is conservative with respect to estimating the impact on O_2 fugacity in the EBS, while the larger value (22 m^2/g) is sufficient to cause significant reduction in the rate of O_2 consumption by invert steel as discussed below. Considerably larger values of specific surface area are possible, as indicated in *EBS Radionuclide Transport Abstraction* (SNL 2007 [DIRS 177407], Section 6.3.4.3) and measured by Ishikawa et al. (2007 [DIRS 181136]).

The liquid saturation and liquid-phase diffusion coefficient data for 1 m^2/g and 22 m^2/g were regressed against $\log_{10}$(1-RH) using exponential functions for use in this analysis (Output DTN: MO0705OXYBALAN.000, spreadsheet: *D_{eff} (RTA based) May2007.xls*). For the postclosure analysis, RH was calculated from total pressure, temperature, and air mass-fraction obtained from the THC simulations discussed above (Output DTN: MO0705OXYBALAN.000, spreadsheets: *th7_81_GasCalc_Invert June2007.xls* and *th7_162_GasCalc_Invert June2007.xls*, worksheets entitled "fractures-th").

Oxygen may be transported through the corrosion product layer by diffusion through the gas phase as well as the liquid phase, depending on the state of liquid saturation and whether a connected gas phase exists. For this analysis, a simple dependence on gas-filled porosity is used:

$$D_{eff,gas} = D_{gas}\phi_{CP}\left(1 - S_{liq}\right) \quad \text{(Eq. 6.7-13)}$$

where

D_{gas} = Binary diffusion coefficient for O_2 in air (m^2/sec)
S_{liq} = Liquid saturation of corrosion products.

This dependence is conservative ($D_{eff,gas}$ is large) because it corresponds to a formation factor of unity (De Marsily 1986 [DIRS 100439], p. 233), which is large for granular geologic media. In other words, Equation 6.7-13 is based on straight volume-averaging and does not include the effect of phase tortuosity that occurs at partial saturation. This relationship is implemented in this analysis, using S_{liq} expressed by its regression on RH (Output DTN: MO0705OXYBALAN.000, workbooks: *th7_81_GasCalc_Invert June2007.xls* and *th7_162_GasCalc_Invert June2007.xl*s, worksheets entitled "O2 Calc. with Mass Transfer").

The results for in-drift O_2 fugacity from implementing Equations 6.7-11 through 6.7-13 are shown in Figures 6.7-5 and 6.7-6. These figures include the parametric sensitivities for repository center vs. edge locations, baseline vs. bounding invert steel design, corrosion rate, and specific area of corrosion products. The results indicate that for corrosion products with open, large-grained structure (1 m^2/g), oxygen consumption is controlled by the intrinsic kinetics (Section 6.7.1.4). For the larger specific surface area, liquid saturation impedes transport through the corrosion product layer, moderating the corrosion rate and the effect on O_2 fugacity.

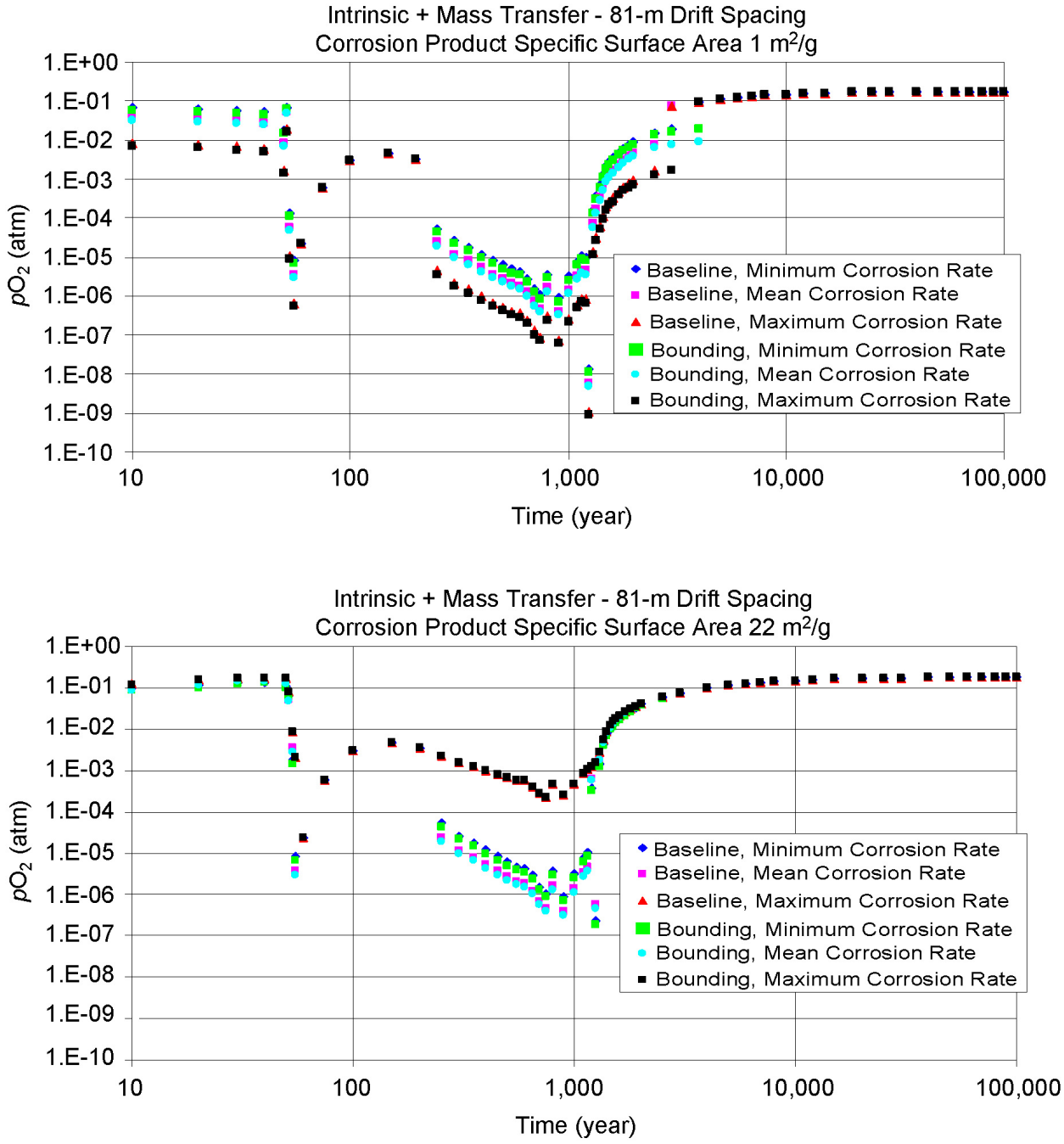

Source: Output DTN: MO0705OXYBALAN.000.

NOTE: Results cover a range of corrosion rates, baseline and bounding cases for quantity of invert steel, and drift spacing of 81 m (representing repository-center conditions).

Figure 6.7-5. Calculated Parametric Time Histories of In-Drift O_2 Fugacity for Specific Surface Areas of 1 m^2/g (upper) and 22 m^2/g (lower) for 81 m Drift Spacing

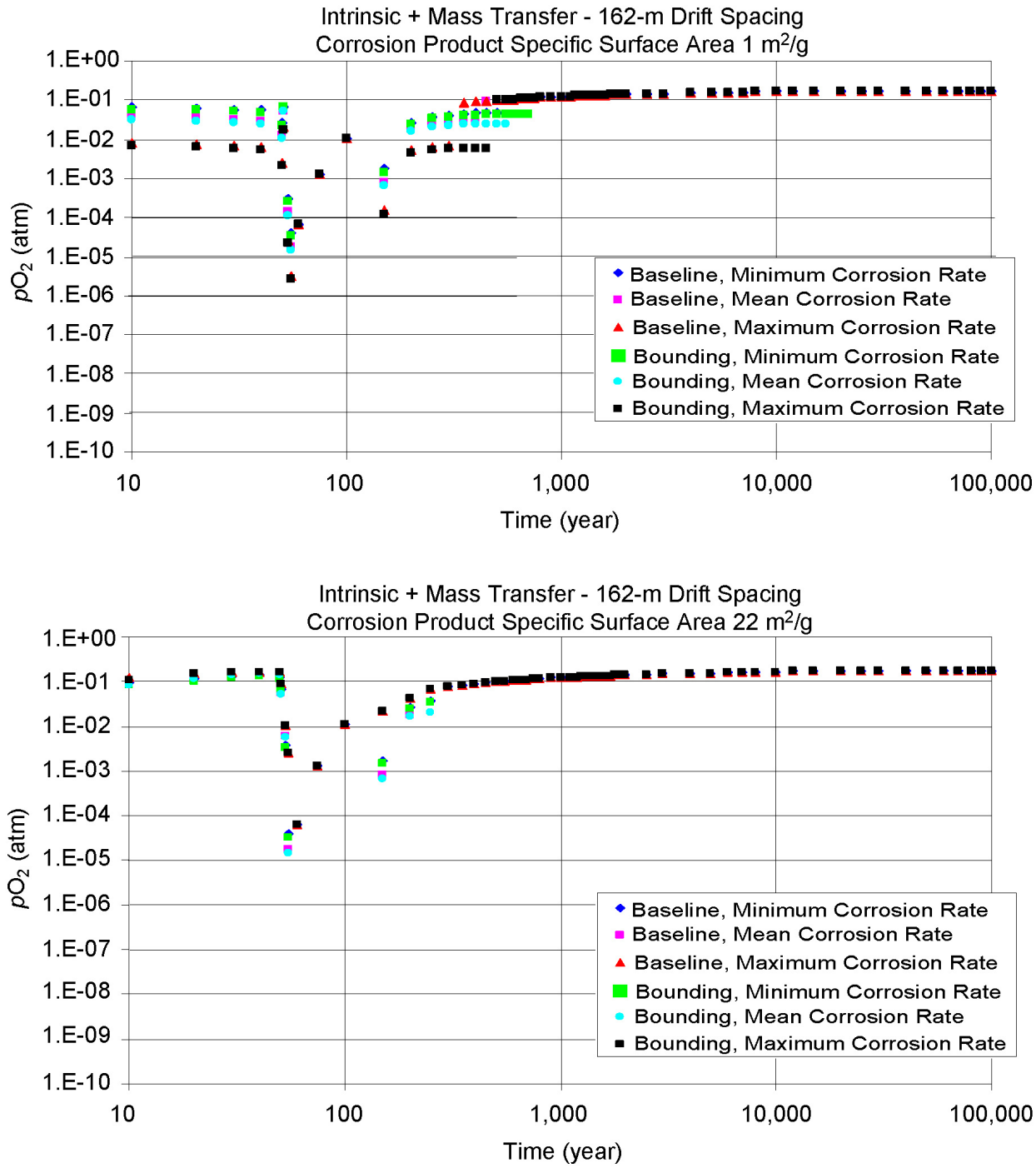

Source: Output DTN: MO0705OXYBALAN.000.

NOTE: Results cover a range of corrosion rates, baseline and bounding cases for quantity of invert steel, and drift spacing of 162 m (representing repository-edge conditions).

Figure 6.7-6. Calculated Parametric Time Histories of In-Drift O_2 Fugacity for Specific Surface Areas of 1 m^2/g (upper) and 22 m^2/g (lower) for 162 m Drift Spacing

6.7.1.6 Comparison to Important Redox Couples

All of the oxygen levels from the discussion above are still significantly above those required to produce anoxic conditions. To demonstrate this, EQ3/6 calculations are performed to determine the following:

- Nitrate/nitrite equivalence-point oxygen pressure
- Approximate goethite/magnetite equivalence-point oxygen pressure.

These calculations are contained in Output DTN: MO0705OXYBALAN.000 in the input/output files, corresponding to the list above (*no2no3_7.3i/.3o, no2no3_9.3i/.3o, fe2fe3.3i_7/.3o, fe2fe3.3i_9/.3o*), where the first set in each series corresponds to an evaluation at pH = 7 and the second to a pH = 9.

The nitrate–nitrite couple was calculated using the *data0.pce* thermodynamic database (Output DTN: SN0703PAEBSPCE.006). Setting both nitrate and nitrite equal to molality of 0.01, charge balanced by sodium, the equilibrium oxygen pressure is determined to be at 2.7×10^{-28} bar at both pH = 7 and 9, indicating no impact of the changing pH in the seepage waters on this redox couple, as expected.

The goethite–magnetite couple was calculated using the same database described above. The concentration of ferrous iron was set by heterogeneous equilibrium with magnetite and the ferric iron by goethite. For a pH = 7, the resulting oxygen pressure is 1.4×10^{-62} bar. For pH = 9, the resulting oxygen pressure is 1.4×10^{-54} bar.

These comparisons all indicate that the minimum oxygen pressures expected within the in-drift environment are sufficient to prevent anoxic conditions from occurring and generating reduced aqueous species.

6.7.1.7 Summary of Oxygen Balance Analysis

Oxygen will be depleted in the emplacement drifts as the invert steel corrodes, and replaced continuously by convective gas flux from the host rock. The reduction in oxygen fugacity, or partial pressure, depends on the flux of incoming air, and on the environmental conditions favoring rapid corrosion of the steel. Because steel corrosion rates tend to be first-order with respect to oxygen pressure, a rate-balance equation can be used to estimate fugacity if the incoming flux and corrosion parameters are known. This rate balance is implemented parametrically, using ranges of corrosion rates, and a bounding case for the quantity and surface area of invert steel. The flux of incoming air is estimated using output from two-dimensional THC simulations, one representing the repository center (81-m drift spacing), and one for repository-edge conditions (162 m) and does not take into account axial transport. The results show that oxygen fugacity may decrease by several orders of magnitude compared to atmospheric air, as low as 10^{-9} atm. This is jointly caused by steel corrosion and displacement of air from the drifts by steam during the boiling period. Importantly, these results represent lower-bound estimates of oxygen fugacity, primarily because the THC simulations do not include gas-phase axial transport in the drifts. Axial transport effects such as barometric

pumping (BSC 2004 [DIRS 164327], Section 6.3.7) can potentially greatly increase the availability of oxygen in the emplacement drifts.

To evaluate the effect on consumption of oxygen of an accumulated layer of corrosion products (rust) on the invert steel, an additional parametric analysis was performed. The transport properties of corrosion products were taken from *EBS Radionuclide Transport Abstraction* (SNL 2007 [DIRS 177407]), choosing a conservative range of specific surface area. The results show that a layer of corrosion products will hinder corrosion, and decrease the impact on in-drift oxygen fugacity while extending the duration of the effect. This is further support that the estimates described above are lower bounds on O_2 fugacity, and that actual fugacity is likely to be much greater than 10^{-9} atm.

6.7.2 In-Drift pCO_2 and Temperature Range for Seepage Dilution/Evaporation Abstraction

The intent of the in-drift seepage dilution/evaporation abstraction (Section 6.9) is to use the four representative pore waters that have seeped through the TSw to the repository horizon (Section 6.6) and analyze the resulting water compositions after evaporation or dilution by adopting the IDPS model (SNL 2007 [DIRS 177411]) to generate lookup tables for use in the TSPA-LA. For the evaporation calculations, ranges of temperature and carbon dioxide pressure are needed to capture the effects of these parameters on the evaporative evolution.

The NFC model provides potential seepage water compositions as a function of maximum drift wall temperature and WRIP assuming the seepage waters are saturated with respect to amorphous silica and calcite (see Section 6.3). The EQ6 code was used to add the appropriate amount of alkali feldspar (WRIP) and excess calcite and amorphous silica up to a drift wall temperature of 96°C. The resulting equilibrium pCO_2 of all 44 seepage simulations (4 starting waters × 11 WRIP values; archived in Output DTN: SN0701PAEBSPCE.002) and the minimum pCO_2 calculated by TSPA in the manner described in Section 6.15 provide the range of possible in-drift values.

The overall pressure ranges from a maximum of approximately 2×10^{-2} bar to a minimum of approximately 10^{-5} bar as read from the spreadsheets archived in Output DTN: SN0701PAEBSPCE.002 (folders: \C_total and \pCO2_max). The maximum pCO_2 values are read directly from the spreadsheets entitled *PCE_pCO2_C_max_Gp(1-4).xls*, and the minimum pCO_2 is approximately half of the total carbon values reported in the spreadsheets entitled *Gp(1-4)_C_total.xls* (see Section 6.3.3.2.9 for details). In order to maximize coverage of the potential pCO_2 range while minimizing extrapolation errors, three values were selected for the dilution/evaporation abstraction simulations. The three values selected for use are 1.0×10^{-2}, 1.0×10^{-3}, and 1.0×10^{-4} bar of carbon dioxide. A validation of the extended extrapolation range is presented in Section 7.2.

Accurate modeling is also limited to temperatures of approximately 100°C or less because of the limits imposed by the boiling point at the elevation of the drift, uncertainties in the boiling point elevation due to concentration of pore-water salts, and temperature limitations on the applicability of some thermodynamic data in the *data0.pce* database (Output DTN: SN0703PAEBSPCE.006). Therefore, an upper calculation limit of 100°C is within

an acceptable range limit to consider evaporated seepage water chemistries of calculated uncertainty.

For the infrequent and brief events where seepage onto surfaces occurs slightly above 100°C, the results at 100°C are used as an extrapolation. Likewise, for temperatures below 30°C, the values provided at 30°C are used as an extrapolation. The effect of this higher temperature extrapolation on the equilibrium seepage modeling will be upon the log(K) values. The solubilities of the most soluble minerals of relevance at such temperatures typically increase and thereby nullify any net effect upon the relative seepage composition. Therefore, extrapolation above 100°C to the temperature of the waste package is reasonable.

With the upper and lower (ambient) bounds, the approximate midpoint between these two bounding points is selected (70°C). The three temperatures (30°C, 70°C, and 100°C) are used to construct the lookup tables for use by TSPA-LA.

6.8 STEEL INTERACTIONS WITH SEEPAGE WATER

This section evaluates the impact on seepage water chemistry from interactions with key chemical components of the ground support system and the committed materials in the invert and their corrosion products. The materials and their properties of interest have been tabulated in Tables 4.1-13, 4.1-14, and 4.1-15, and are composed of low-alloy steels, primarily A588, and Stainless Steel Type 316L (referred to as SS316L herein) (also see in-drift schematic Figure 6.4-1). Based upon the lifetime estimates of the invert low-alloy steels in humid environments, like those expected in the repository after closure, on the order of 50 yr/cm minimum relative lifetime (Figure 6.4-3), effects of low-alloy steel on seepage chemistry will likely be short-lived but are considered in this analysis with respect to potential impact on invert water chemistry. In contrast, SS316L has a significantly longer lifetime (relative per-cm lifetime on the order of 5,000 years; see Figure 6.4-3) and is located over the crown of the drift, where it may affect seepage water compositions on the drip shield and/or waste package surface.

Current design specifications for the drift configuration ground support system indicate that SS316L is to be used for the perforated sheets and the friction-type rock bolts (SNL 2007 [DIRS 179354], parameter 02-03). A review of the design specifications for the invert structure indicates that a significant quantity of steel, 1,123 kg/linear meter of drift (≈ 2,475 lbs/m) (SNL 2007 [DIRS 179354], parameters 02-08 and 02-10) may be emplaced. The vast majority (>95% by weight) of the invert steels are low-alloy A588 (ASTM A 588/A 588M – 05 [DIRS 176255]) or the chemically similar A759 (ASTM A 759-00 [DIRS 176423]). Therefore, the major elemental components of these steels are discussed, and the materials are examined in detail with respect to their corrosion/precipitation and subsequent effect upon seepage water chemistry. The results presented here show that the corrosion of steel—the release of aqueous species and formation of corrosion products—has only negligible effect on the composition of seepage waters.

6.8.1 Corrosion Product Concepts

Corrosion of the ground support materials is modeled as occurring by direct oxygen and proton consumption and can be generalized in Equation 6.8-1:

$$M_{(s)} + \frac{n}{4} O_{2(g)} + n\, H^+ \rightarrow M^{n+}{}_{(aq)} + \frac{n}{2} H_2O \qquad \text{(Eq. 6.8-1)}$$

If this process alone occurs, the pH in the aqueous phase must increase. However, the magnitude of this effect is dependent upon the disposition of the metal ion released. If the ion is highly soluble, then the oxidation reaction shown in Equation 6.8-1 will dominate, and the pH of the seepage water will rise. However, if it is of low solubility, then the resulting precipitation reaction must be accounted for. Typically, this reaction involves the formation of a hydroxide or oxide (or combined oxyhydroxide). A general metal-hydroxide formation reaction can be represented as shown in Equation 6.8-2:

$$M^{n+}{}_{(aq)} + n\, H_2O \rightarrow M(OH)_{n(s)} + n\, H^+ \qquad \text{(Eq. 6.8-2)}$$

This has the effect of releasing as many hydrogen ions as were consumed during corrosion, thereby negating any effect upon the water chemistry pH. This is also the general case for oxide formation, shown by Equation 6.8-3:

$$M^{n+}{}_{(aq)} + \frac{n}{2} H_2O \rightarrow MO_{n/2(s)} + n\, H^+ \qquad \text{(Eq. 6.8-3)}$$

The following subsections will discuss the four primary metals comprising the steels destined for use in the emplacement drifts; Stainless Steel Type 316L is composed of Fe, Cr, and Ni, which account for greater than 90% of this alloy by weight; A588 (here used to represent the low-alloy steels used in the invert) is composed almost entirely (>99% by weight) of Fe and Mn.

6.8.1.1 Iron (Fe)

Iron in the natural environment exists in two oxidation states. Fe(II) is the soluble form, but is not stable under the redox conditions in the drift (i.e., consistently oxic pO_2, Section 6.7). Fe(III) primarily forms sparingly soluble oxides and oxyhydroxides (e.g., Fe_2O_3 and FeOOH, respectively); its solubility product ranges from 10^{-36} to 10^{-42} at 25°C and pH > 3, based on the Pitzer thermodynamic database (DTN: SN0609T0502404.012 [DIRS 179067]), and it is increasingly soluble with lower pH values (Pankow 1991 [DIRS 105952], p. 231).

Table 6.8-1 shows the typical oxidation–reduction reactions for iron aqueous species and minerals. The Eh-pH diagram for iron plotted in Figure 6.8-1 shows that Fe(III) oxyhydroxides are the stable phase at the relatively high oxidation potentials expected at Yucca Mountain. The stability of the various forms of iron hydroxides and oxyhydroxides increases from amorphous $Fe(OH)_3$ to goethite to hematite (Fe_2O_3) at 25°C (Stumm and Morgan 1981 [DIRS 100829], p. 434). However, predicting if goethite or hematite will be present in a given system is difficult, because geochemical conditions may favor nucleation and growth of one or the other phase, and

because goethite may persist in a metastable state for millions of years, as the conversion of goethite to hematite can be very slow (Krauskopf 1979 [DIRS 105909], p. 208). However, in soils, goethite tends to form at low temperatures (in cool or temperate climate zones), at high H_2O activity, and with higher organic matter contents. The hematite-to-goethite ratio usually increases with increasing soil temperature (Schwertmann and Taylor 1995 [DIRS 105959], pp. 398 to 400). The pH also plays a role in the preferred formation of the two phases. Goethite is favored in soils with low pH (3 to 7), whereas hematite is favored above pH 7 (Schwertmann and Taylor 1995 [DIRS 105959], pp. 401 to 402). However, if a small amount of titanium is present (< 0.05 mol fraction) in the solution, it inhibits hematite formation and favors the formation of goethite (Fitzpatrick et al. 1978 [DIRS 105795]).

Table 6.8-1. Typical Oxidation–Reduction Reactions and Potential Fe Minerals

Reaction	Oxidation State	Minerals Formed
$2Fe^{2+} + ½O_2 + 2H_2O = Fe_2O_3 + 4H^+$ $Fe_3O_4 + 2H^+ = Fe_2O_3 + Fe^{2+} + H_2O$ $2FeOOH + 2H^+ + ½O_2 = Fe_2O_3 + Fe^{2+} + 2H_2O$	3	*Hematite* (α-Fe_2O_3)
$Fe^{2+} + ¼O_2 + {}^3/_2H_2O = FeOOH + 2H^+$ $Fe_3O_4 + H^+ + ½O_2 = Fe_2O_3 + FeOOH$	3	*Goethite* (α-FeOOH)
$3Fe^{2+} + ½O_2 + 3H_2O = Fe_3O_4 + 6H^+$	2.67	*Magnetite* (Fe_3O_4)

Source: Designed for Fe minerals using Tebo et al. 1997 [DIRS 105960], Table 2, as an example.

Given the slow rate of hematite formation, its suppression by high humidity conditions, and the presence of large quantities of titanium, goethite is expected to be the prevalent iron corrosion species for the period of regulatory interest. However, it is important to note that there is only a difference of < 0.5 log units between the solubility of goethite and hematite, so, for modeling purposes, the choice of mineral has little impact.

Other minerals that could potentially form, based on the geochemical system at Yucca Mountain, are Fe carbonates, Fe-rich silicates, or any of the Fe-bearing spinel-type phases. Given the low-temperature conditions, the iron would most likely be incorporated into a solid solution of smectite clay (nontronite). Several studies of the corrosion of steels report that spinel phases form at or near the surfaces of the corroding metal within the rust layer abutting the corroding surface enriched in Cr and Ni forming mixed cation spinels, e.g., $NiFe_2O_4$ (Kimimura et al. 2006 [DIRS 181151]; Smith 1982 [DIRS 181150], p. 860; Pieraggi et al 2005 [DIRS 181149], p. 249; Ostwald and Grabke 2004 [DIRS 181153], p. 1114 to 1116).

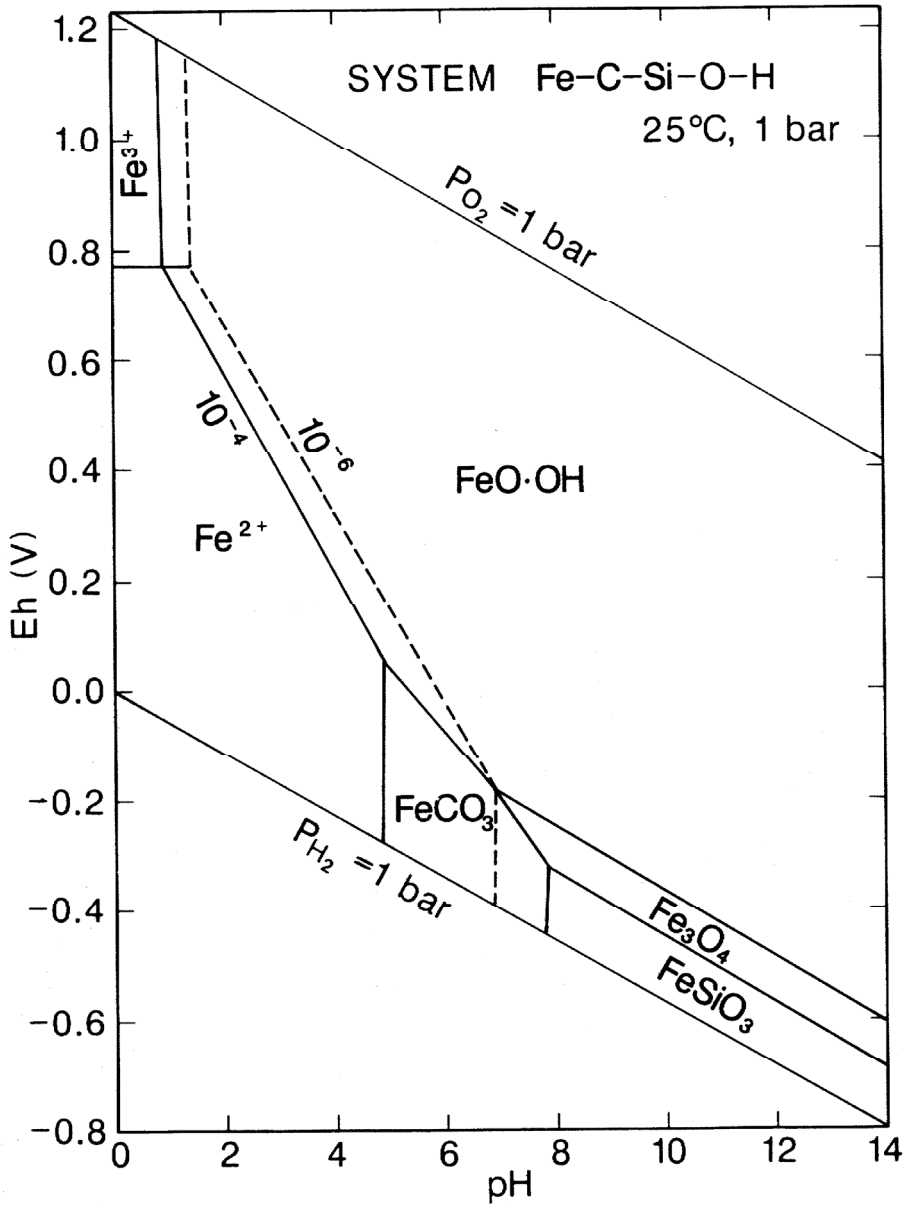

Source: Brookins 1988 [DIRS 105092].

NOTE: Approximated activities for dissolved species are: Fe = 10^{-6}, Si = 10^{-3}, C = 10^{-3}. Goethite and magnetite are considered Fe(III) solid phases.

Figure 6.8-1. Eh-pH Diagram for Part of the System Fe-C-Si-O-H at 25°C

6.8.1.2 Chromium (Cr)

Unless otherwise indicated, the source of the following summary is *Natural Attenuation of Hexavalent Chromium in Ground Water and Soils* (Palmer and Puls 1994 [DIRS 108991]).

Chromium exists in oxidation states ranging from +6 to −2; however, only the +6 and the +3 oxidation states are commonly encountered in the environment (refer to Eh/pH diagram in Figure 6.8-4). Cr(VI) exists in solution as the monomeric ions $H_2CrO_4^o$, $HCrO_4^-$ (bichromate),

and CrO_4^{2-} (chromate), or as the dimeric ion $Cr_2O_7^{2-}$ (dichromate). The relative concentration of each of these species depends on both the pH of the chromium-laden water and the total concentration of Cr(VI).

Significant concentrations of $H_2CrO_4^o$ only occur at pH ≤ 1. Above pH 6.5, CrO_4^{2-} generally dominates. Below pH 6.5, $HCrO_4^-$ dominates when Cr(VI) concentrations are low (<30 mM), but $Cr_2O_7^{2-}$ becomes significant when concentrations are greater than 1 mM, and may even dominate when the total Cr(VI) concentrations are greater than 30 mM.

In the Cr(III)-H_2O system, Cr(III) exists predominantly as Cr^{3+} below a pH of 3.5. With increasing pH, hydrolysis of Cr^{3+} yields $Cr(OH)^{2+}$, $Cr(OH)_2^+$, $Cr(OH)_3^0$, and $Cr(OH)_4^-$. From slightly acidic through alkaline conditions, Cr(III) can precipitate as an amorphous chromium hydroxide. Amorphous $Cr(OH)_3$ can crystallize to $Cr(OH)_3 \cdot 3H_2O$ or Cr_2O_3 (eskolaite) depending upon conditions. In the presence of Fe(III), trivalent chromium can precipitate as a solid solution, $Fe_xCr_{1-x}(OH)_3$, with a lower solubility (Sass and Rai 1987 [DIRS 105957], Figure 1). If the pH of the system is between 6 and 12, the aqueous solubility of Cr(III) should be less than 1 μmole/L. In addition, when the pH of the groundwater is greater than 4, Cr(III) coprecipitates with the Fe(III) in a solid solution with the general composition $Cr_xFe_{1-x}(OH)_3$ (Sass and Rai 1987 [DIRS 105957], pp. 2228 to 2229; Amonette and Rai 1990 [DIRS 105701]). This should limit the concentration of Cr(III) to less than 10^{-6} molar, in the pH range from 6 through 12. Cr(III) may also be incorporated into spinel phases depending upon the available cations in solution (e.g., $NiCr_2O_4$). The precipitation of Cr in a spinel phase would limit the solubility of Cr(III) in solution to approximately 10^{-9} molal (see Tables 6.8-3 and 6.8-4).

Cr(VI) is a strong oxidant and is reduced in the presence of electron donors. A common electron donor that could be present in the repository is ferrous iron. This reaction is very fast on the time scales of interest for most environmental problems, with the reaction going to completion in about five minutes even in the presence of dissolved oxygen (Eary and Rai 1988 [DIRS 105784]). When the pH is greater than 10, the rate of oxidation for Fe(II) by dissolved oxygen will exceed the rate of oxidation by Cr(VI) (Eary and Rai 1988 [DIRS 105784]).

Efficient Cr(VI) reduction in the presence of stainless steel, iron oxides, iron-containing silicates, and organic matter has been observed in several experiments. The reduction of Cr(VI) in the presence of hematite (Fe_2O_3) was demonstrated by Eary and Rai (1989 [DIRS 105788]). They attribute the reduction to the presence of a small amount of an FeO component in the hematite. They also suggest that the reaction occurs in solution after the FeO component has been solubilized. Reduction by biotite occurs when potassium ions are released to solution and Fe^{3+} ions are adsorbed onto the surface of the biotite. Potassium ions are released to maintain charge balance in the biotite structure. Reduction seems to occur even in oxygenated solutions. Lastly, experiments by Smith and Purdy (1995 [DIRS 162976], Abstract) addressing corrosion of SS316L and chromium speciation show that "Oxidation of chromium(III) to chromium(VI) was negligible at room temperature and only became significant in hot concentrated nitric acid. The rate of reduction of chromium(VI) back to chromium(III) by reaction with stainless steel or oxalic acid was found to be much greater than the rate of the reverse oxidation reaction."

Humic and fulvic acids are often associated with reduction by organic matter. The rate of reduction of Cr(VI) by the humic and fulvic acids will decrease with increasing pH. It increases with increasing initial Cr(VI) concentration and increases as the concentration of soil humic substances increases. At neutral pH, complete reduction of Cr(VI) may take many weeks. Sedlak and Chan (1997 [DIRS 105964]) studied the reaction of Cr(VI) with Fe(II) with respect to temperature and pH and determined that the reduction of Cr(VI) occurred on the time scale of minutes to months in sediments, soils, and waters that contained ferrous iron. Similar experiments conducted in NaCl, $NaClO_4$, and seawater solutions showed a parabolic dependence on pH, and the influences of temperature, ionic strength, and reductant concentration showed various linearly dependent effects on reduction (Pettine et al. 1998 [DIRS 105955]). In low-temperature soil environments that have been contaminated with chromate-laden solutions, $KFe_3(CrO_4)_2(OH)_6$ has been shown to precipitate and can reduce the amount of Cr(VI) in groundwater (Baron and Palmer 1996 [DIRS 105730]). This mineral, analogous to the sulfate mineral jarosite, is stable in oxidizing environments between a pH of 2 and 6.

Oxidation of Cr(III) to Cr(VI) is achieved in three ways. The first requires dissolved oxygen, the second requires either manganese dioxide (MnO_2) (Eary and Rai 1987 [DIRS 105780]) or manganite (MnOOH) (Johnson and Xyla 1991 [DIRS 105878]), and the third requires using hot concentrated nitric acid (Smith and Purdy 1995 [DIRS 162976]). Eary and Rai (1987 [DIRS 105780], p. 1188) found that dissolved oxygen is not an especially effective or likely way to oxidize Cr(III). However, interaction with manganese dioxide has been demonstrated to increase as pH decreases and the ratio of surface area to solution volume increases. Eary and Rai (1987 [DIRS 105780]) developed an empirical rate law for the oxidation of Cr(III) by β-MnO_2 (pyrolusite). For manganite, the rate law has been determined to be independent of pH and ionic strength; however, it proceeds slower in the presence of organic ligands (Johnson and Xyla 1991 [DIRS 105878]).

Sorption of Cr(VI) onto goethite has been demonstrated to be a surface complexation mechanism dependent on pH. However, on magnetite, the mechanism has been determined to be reductive precipitation onto Fe(II) surface sites (Deng et al. 1996 [DIRS 105778]). Competition between common anionic groundwater ions (CO_2(g), H_4SiO_4, and SO_4^{2-}) and the CrO_4^{2-} ion is known to occur, where the adsorption of CrO_4^{2-} onto amorphous iron oxides was suppressed between 50 to 80% (Zachara et al. 1987 [DIRS 105963]).

6.8.1.3 Nickel (Ni)

Only Ni(II) occurs at ambient environmental conditions. The higher oxidation states occur rarely and, even in those cases, it is not clear whether it is the ligand rather than the metal atom that is oxidized (Cotton and Wilkinson 1988 [DIRS 105732], p. 741). No other oxidation state would be expected under repository environmental conditions once Ni is released by oxidation of the metal alloys.

Once the Ni is released into an aqueous environment under oxidizing conditions, nickel hydroxides [$Ni(OH)_2$] are stable in a pH range between 8 and 12 (Figure 6.8-2). Otherwise, either the Ni^{2+} ion or the $HNiO_2^-$ ions are in solution, indicating that nickel is relatively soluble under neutral-acidic conditions and under relatively alkaline conditions (Garrels and Christ 1990 [DIRS 144877], pp. 244 to 245).

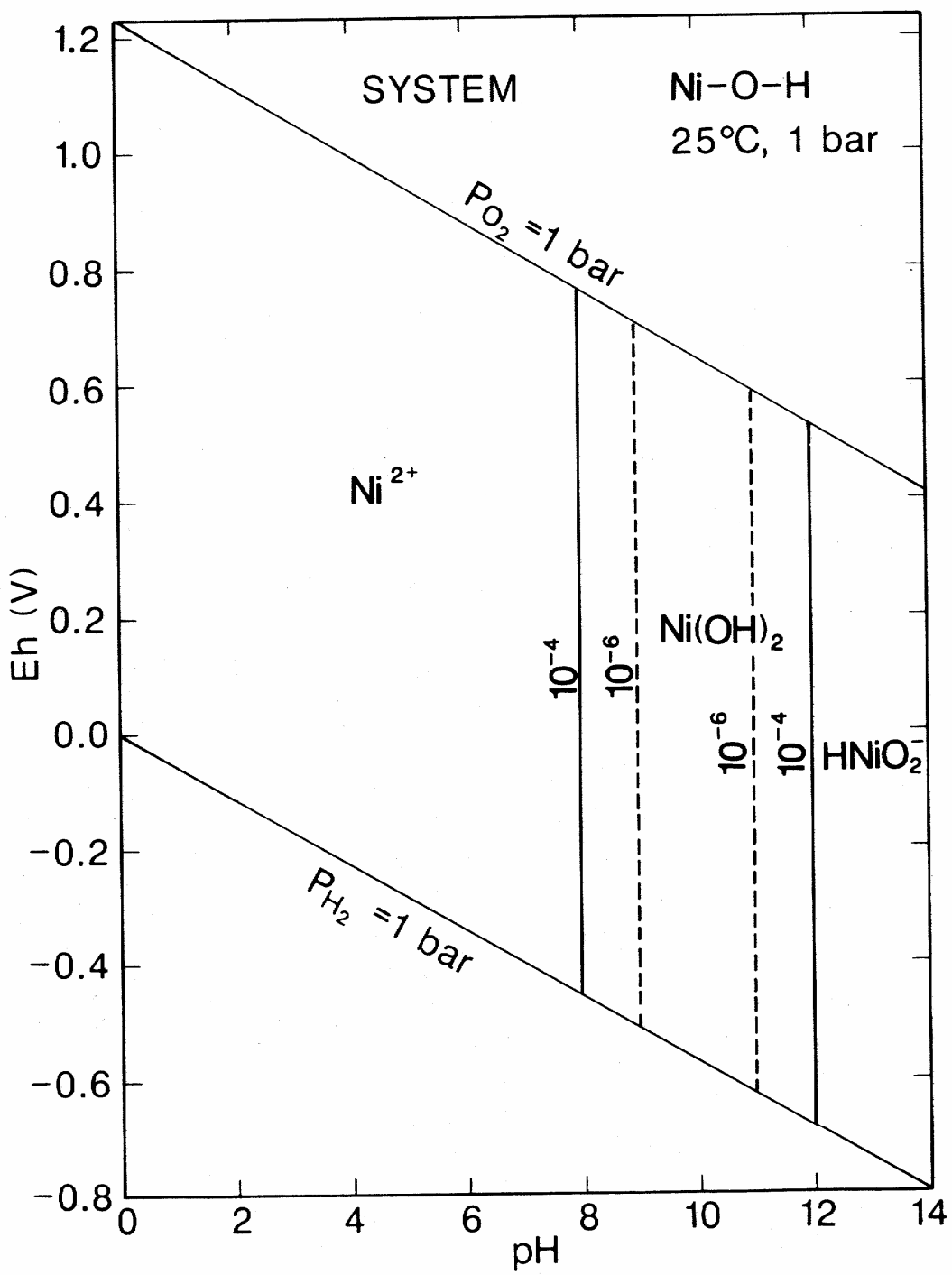

Source: Brookins 1988 [DIRS 105092].

NOTE: Estimated activity for Ni = 10^{-4}, 10^{-6}.

Figure 6.8-2. Eh-pH Diagram for Part of the System Ni-O-H at 25°C

Nickel tends to substitute for iron and manganese in solid phases, and tends to be coprecipitated as $Ni(OH)_2$ with both iron oxides as Ni-ferrite, $NiFe_2O_4$, and manganese oxides (Hem 1985 [DIRS 115670]; Hem et al. 1989 [DIRS 105854]). Nickel will also adsorb to clays, iron and manganese oxides, and organic matter (McLean and Bledsoe 1992 [DIRS 108954]).

6.8.1.4 Manganese (Mn)

In the presence of dissolved oxygen, manganese is stable only as solid "oxidized" oxides (Stumm and Morgan 1981 [DIRS 100829], p.456). The oxygenation reactions involving Mn(II) in solution are apparently autocatalytic in nature and proceed according to the following pattern:

$$Mn(II) + \tfrac{1}{2} O_2 \rightarrow MnO_2\,(s) \quad \text{slow} \qquad \text{(Eq. 6.8-4)}$$

$$Mn(II) + MnO_2(s) \rightarrow Mn(II)\bullet MnO_2\,(s) \quad \text{fast} \qquad \text{(Eq. 6.8-5)}$$

$$Mn(II)\bullet MnO_2\,(s) + \tfrac{1}{2} O_2 \rightarrow 2MnO_2 \quad \text{slow} \qquad \text{(Eq. 6.8-6)}$$

Note that these reactions are not balanced with respect to water and protons and are used to illustrate the self-catalyzing properties of MnO_2 (Stumm and Morgan 1981 [DIRS 100829], p. 467). Non-stoichiometry in the Mn(II)-oxides is commonly observed and the higher-valence Mn-oxides have a strong affinity for the adsorption of Mn(II) from slightly alkaline solutions.

An examination of the Eh-pH diagram for the Mn-CO_2-H_2O system (Figure 6.8-3), indicates that MnO_2 is a likely solubility controlling phase for intermediate pH and slightly positive Eh (≈0.4 to 0.8), likely repository conditions. As was noted in Section 6.8.1.3, one of the pathways for the oxidation of Cr(III), the presumed predominant Cr form in the seepage waters, is by catalysis on the surface of pyrolusite, MnO_2. Several factors mitigate the oxidation by MnO_2 of Cr(III) to Cr(VI) in groundwater.

First, there is experimental evidence that the catalytic oxidation of Cr(III) to chromate by pyrolusite in solution is strongly dependent on pH and becomes rapid only at pH less than approximately 4 (Eary and Rai 1987 [DIRS 105780], Figure 2). Investigators also noted that the available Cr(III) in solution was limited by the solubility control of the Cr-hydroxides to approximately 10^{-5} molar (≈ 10^{-8} molar with respect to Cr-bearing spinels). At pH > 6.3, the rate of Cr(III) oxidation is exceedingly slow as indicated by the near zero slope of the Cr(VI) concentration vs. time curve (Eary and Rai 1987 [DIRS 105780], Figure 4). The pH of the potential seepage waters predicted by the NFC model range from 6.9 to 9.7 for all starting waters (Output DTN: SN0701PAEBSPCE.002; read from the EQ3 output files). Upon evaporation, the pH range is broadened from a minimum of approximately 5 to a maximum of just over 11 (Output DTN: SN0701PAEBSPCE.001; from an examination of the lookup tables archived in this DTN). This covers the entire range of potential in-drift environmental conditions as defined by the dilution/evaporation abstraction model that could effect seepage water compositions. Thus, the oxidation of Cr(III) to Cr(VI) is limited by the low availability of aqueous Cr(III) in solution and will be kinetically hindered in the pH range of concern.

Second, ferrous iron has been shown to rapidly reduce Cr(VI) from typical groundwater solutions (i.e., small quantities of dissolved salts) at pH less than approximately 10 (Eary and Rai 1988 [DIRS 105784], abstract). Even though Cr comprises 17 wt % of the SS316L used in the

ground support, it is absent in the low-alloy steels of the invert. More than 99% of the invert steels are iron and current plans would emplace approximately 2,500 lbs/m (SNL 2007 [DIRS 179354], parameters 02-08 and 02-10). The result would be large quantities of ferrous iron available to reduce any oxidized chromium.

Third, the precipitation of MnO_2 would be strictly limited to the invert as this is where the low-alloy steels are located in the drift (see Figure 6.4-1). In this event, even if Cr(III) could be oxidized to Cr(VI), no impact is possible with respect to drip shield or waste package corrosion and any impact with respect to invert water chemistry is mitigated by the mixing that must occur with waters emanating from the waste package, the only possible source for radionuclides in the invert.

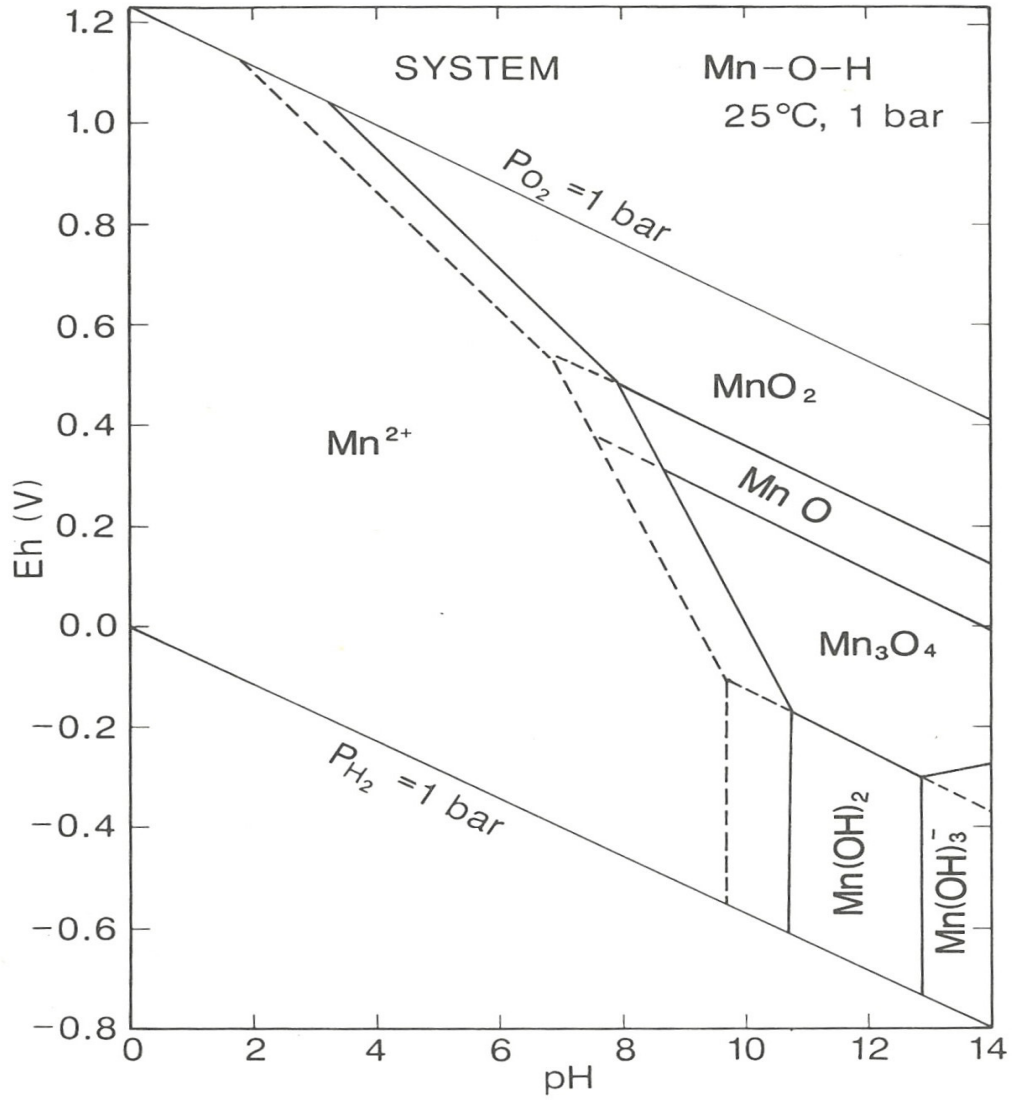

Source: Brookins 1988 [DIRS 105092].

NOTE: Estimated activity for Mn = 10^{-4}, 10^{-6}.

Figure 6.8-3. Eh-pH Diagram for Part of the System Mn-O-H at 25°C

6.8.2 Definition of the SS316L and A588 Modeling Choices

Base case for SS316L and A588/seepage water interactions:

- Materials and dimensions of SS316L and A588 as defined by the engineered drawings referenced in (SNL 2007 [DIRS 179354], parameters 02-03, 02-08, and 02-10). (See Section 4.1 and Tables 4.1-13, 4.1-14, and 4.1-15 for details; see also Section 6.7.1.1 for a discussion and derivation of the surface area for invert steel reported in Table 6.7-1.)

- Potential seepage water impacts evaluated using Group 1 and Group 3 as these are most chemically distinct (see description in Section 6.6) (seepage compositions archived in Output DTN: SN0701PAEBSPCE.002) with a zero and moderate water–rock interaction parameter (WRIP = 0 and G) defined in Table 6.3-5.

- Oxidation corrosion products that include Fe(III), Cr(III), and Ni(II) for SS316L and Fe(III) and Mn(IV) for A588.

- Solubility limiting phases for SS316L corrosion products: goethite (FeOOH), Ni-ferrite ($NiFe_2O_4$), Ni-chromite ($NiCr_2O_4$), Ni-carbonate ($NiCO_3$), and nontronite clays. Solubility limiting phases for A588 corrosion include goethite (FeOOH) and MnO_2.

- Temperature of 25°C and pressure of CO_2 and O_2 at 10^{-3} and $10^{-0.7}$ bar, respectively.

- Corrosion rates for SS316L and A588 (approximated by A516) taken from *Aqueous Corrosion Rates for Waste Package Materials* (BSC 2004 [DIRS 169982]). Both atmospheric and aqueous mean corrosion rates were used and are discussed below (see Tables 4.1-13 and 4.1-14).

Solubility Controlling Solids and Observed Aqueous Species

Only Fe(III) phases were observed during EQ3/6 simulations involving both the SS316L and the A588 steels as corrosion products that may influence seepage water chemistry because Fe(III), as opposed to Fe(II), is the oxidation state that would form under the relatively oxidizing conditions presumed to dominate and mild pH ranges of the selected seepage waters. This is consistent with the plotted diagram of Figure 6.8-1, which shows that in the pH range of 6 through approximately 9.5, with an O_2-fixed Eh range of ~0.8 through ~0.6 volts, the Fe(III) species are dominant. The Fe(III) solid phases observed to form were goethite, Ni-ferrite, and some nontronite clays.

Selection of Cr(III) over the more soluble Cr(VI) species is based on experimentally observed corrosion products, and on the kinetics and conditions required to obtain the fully oxidized Cr(VI) state (Smith and Purdy 1995 [DIRS 162976]). Smith and Purdy's (1995 [DIRS 162976], Figure 6) examination of the actual chromium speciation as a result of corrosion of SS316L demonstrated a predominance of the less soluble Cr(III) species, except under the conditions of

hot concentrated nitric acid (111°C and >7 molar HNO_3). Other groups performing oxidation experiments, conducted under more ambient conditions, examined the oxidation of Cr(III) to Cr(VI) by dissolved oxygen. The experiments of Eary and Rai (1987 [DIRS 105780], p. 1188) were performed from pH 4.0 to 12.5 without the detection of Cr(VI) formation in 24 days. Additionally, observed disequilibrium of dissolved oxygen in water corresponds to the much more rapidly reacting O_2–H_2O_2 couple (Langmuir 1997 [DIRS 100051], Figure 11.5). The Eh values for this couple in the pH range from 6 to approximately 9.5 are in the range of ~0.6 down to ~0.4 volts, corresponding to the Cr(III) field of Figure 6.8-4. The Cr-bearing solids phase was Ni-chromite.

Only Ni(II) species formed during the EQ6 simulations. This is entirely consistent with the discussion in Section 6.8.1.3. Both Ni-ferrite and Ni-chromite formed during the EQ6 modeling simulations. Manganese precipitated from the modeling simulations as MnO_2, pyrolusite. This is also consistent with the predominance diagram and the discussion in Section 6.8.1.4.

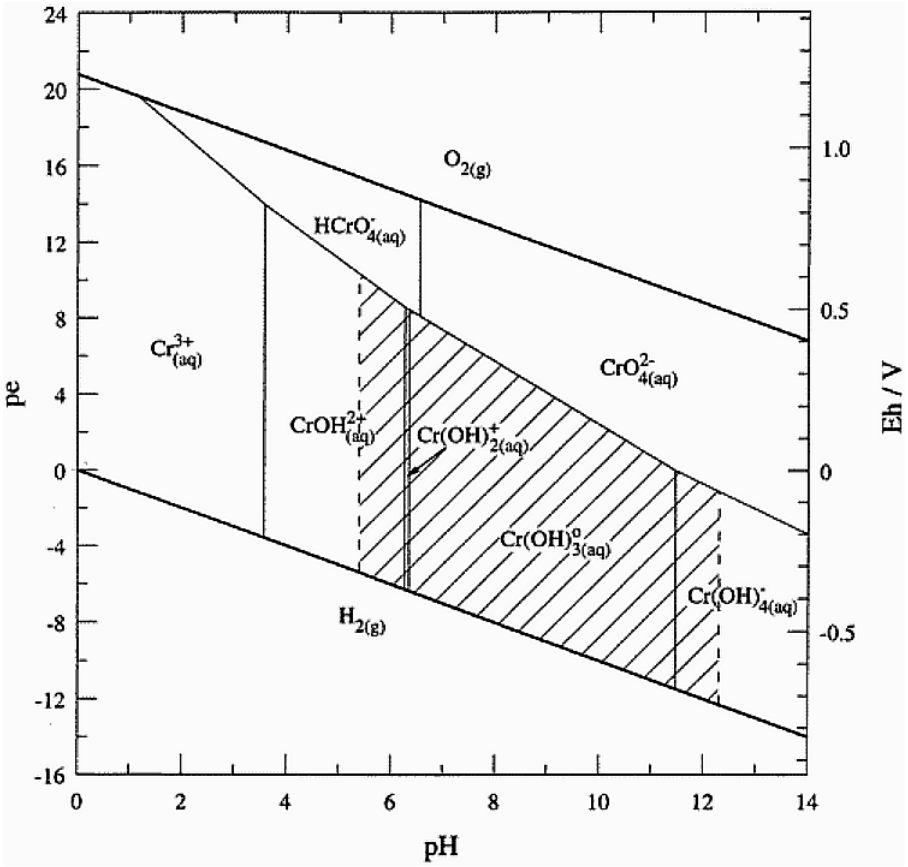

Source: Ball and Nordstrom 1998 [DIRS 163015].

NOTE: Eh units in volts (V), not Eh/V as shown on the figure. Hatched area indicates predominance region for $Cr(OH)_3(s)$.

Figure 6.8-4. pe-pH Diagram for Aqueous Inorganic Chromium Hydrolysis Species

6.8.2.1 Mineral and Aqueous Suppressions

The mineral suppressions utilized by these sensitivity analyses include those identified by the IDPS report (SNL 2007 [DIRS 177411]; also see Table 6.2-2 of the present report) and the two additional minerals identified for suppression in the evaporation simulations in Section 6.9 (albite and maximum microcline). Other mineral suppressions and the bases for their suppression are listed in Table 6.8-2 and are described below.

Table 6.8-2. Additional EQ3/6 Mineral Suppressions Included for Seepage Ground Support Interactions

Mineral/ Aqueous Species	Formula	Criterion Selected	Rationale	References
Hematite	Fe_2O_3	Criterion 3	Over long time frames, hematite is more stable than goethite, and the temperatures in the drift are elevated enough to warrant the precipitation of hematite; however, if small amounts of Ti are present in solution, hematite is inhibited and goethite forms. Therefore, due to the large amount of titanium being emplaced in the repository drift, hematite will be suppressed (see discussion in Section 6.8.1.1).	Stumm and Morgan 1981 [DIRS 100829], p. 434 Fitzpatrick et al. 1978 [DIRS 105795]
Eskolaite	Cr_2O_3	Criterion 2	Eskolaite is a common chromium mineral that may precipitate from a cooling magma. Although details of its liquid precipitation curves are still emerging, present data shows that 0.5 to 1.0% by mass of eskolaite precipitates in the range from 1,000°C to 1,150°C, and it is likely to begin precipitation above 920°C at atmospheric pressures.	Perez et al. 2001 [DIRS 163030], p. 4-31 Hrma et al. 2001 [DIRS 163031], Table 3.14, p. 3.27
Chromate	CrO_4^{2-}	Criterion 3	Oxidation of the initial Cr(III) corrosion species to this Cr(VI) basis species is very slow in the absence of a strong oxidizing agent or extreme temperature and pH conditions.	Eary and Rai 1987 [DIRS 105780], p. 1188 Smith and Purdy 1995 [DIRS 162976], Abstract

NOTE: The criteria used to include suppression of a mineral are defined in Section 6.2.4.1.

Iron Solid and Aqueous Species

No adjustments to the thermodynamic database were required to accurately model the Fe-system. The only suppression associated with these sensitivity calculations was hematite for the reasons stated in Table 6.8-2.

Chromium Solid and Aqueous Species

After determining that the most common aqueous chromium oxidation state will be Cr(III) (and not Cr(VI); see Section 6.8.1.3), Cr(VI)-related species were suppressed in the EQ3/6 geochemical modeling calculations. A review of the Cr-system as implemented by the Pitzer database (DTN: SN0609T0502404.012 [DIRS 179067]) was conducted and the appropriate updates were made and incorporated into the modified Pitzer database, *data0.pce* (Output DTN: SN0703PAEBSPCE.006). The details of the updates incorporated for use in the P&CE model are documented in Section 6.2.6. The hexavalent chromium system was suppressed

simply by suppressing the dominant chromate aqueous species, CrO_4^{2-}, for the reasons stated in Table 6.8-2.

The sensitivity of the EQ3/6 modeling simulations to the suppression/precipitation of eskolaite was tested. No difference was observed with respect to the aqueous phase chemistry. Eskolaite was suppressed in the modeling of SS316L interactions with seepage water for the reason stated in Table 6.8-2 and the simulations where eskolaite was allowed to precipitate showing no difference in aqueous chemistry are archived in Output DTN: SN0705PAEBSPCE.010. The remaining observed solid Cr-bearing precipitates were calculated by the modeling code and were not pre-selected to be the solubility limiting phases. The solids that formed were determined to be consistent with Cr-limiting phases observed during the corrosion of steel and are described in the results section below.

Nickel Solid and Aqueous Species

In addition to the modifications made to the Pitzer database for the chromium system, updates to the Ni-system were also made and justified in Section 6.2.6 (Output DTN: SN0705PAEBSPCE.010). A summary of these updates and a comparison of modeled and experimental data for equilibrium Ni-species are documented in Section 6.2.6. With the updated data, no suppressions of Ni-species, either aqueous or solid, was necessary for the steel interaction assessment.

Manganese Solid and Aqueous Species

No adjustments to the thermodynamic database were required with respect to the Mn system.

6.8.2.2 Modeling Limitations

The base case is limited to supporting calculations at 25°C, because the primary solid and aqueous phases that control Cr and Ni solubility are defined only at that temperature (see *data0.pce* in Output DTN: SN0703PAEBSPCE.006). A CO_2 pressure of 10^{-3} bar was chosen to be consistent with the median value from the ranges used for the in-drift seepage dilution/evaporation abstraction model (Section 6.9). In order to assess the impact of steel corrosion on seepage waters, two starting waters (Group 1 and Group 3) and two WRIP values (0 and G) were selected.

6.8.3 Modeling the Corrosion of SS316L and A588

The development of this analysis begins with a review of the standard specifications for SS316L and A588, as determined by the ASTM standard (ASTM A 240/A 240M-02a 2002 [DIRS 162720], Table 1; A588/A 588M-05 [DIRS 176255]). These specifications establish weight-percentage values or limits or ranges for the various compositional elements that comprise these steels. The maximum of the impurity ranges were selected for this sensitivity analysis. It is assumed that utilizing the elements that account for approximately 95 wt % or greater of these steels will adequately capture the chemical impacts of the corrosion process on the water compositions. The calculated compositions using Fe, Cr, and Ni for the SS316L simulations, and Fe and Mn for the A588 simulations, are documented in Output DTN: SN0705PAEBSPCE.011 (spreadsheets: *DegradationMolality_PCEREV06.xls* and

A588_corrosion_calcs.xls, worksheets entitled "Composition"). The result is two fictive metal species called "SS316L" and "A588." EQ3/6 data blocks were created for each of these fictive species and utilized in the geochemical modeling of the steel interactions. The data block for the SS316L was incorporated into the *data0.pce* database (Output DTN: SN0703PAEBSPCE.006). The data block for the A588 steel is archived in Output DTN: SN0705PAEBSPCE.011.

The fictive stainless steel species, with molecular formula $Fe_{3.6}CrNi_{0.06}$, is defined by the dissociation reaction:

$$Fe_{3.6}CrNi_{0.6} + 15H^+ + 3.75O_2\,(g) \rightarrow 3.6Fe^{3+} + Cr^{3+} + 7.5\,H_2O + 0.6\,Ni^{2+} \quad \text{(Eq. 6.8-7)}$$

The fictive low-alloy steel species, with molecular formula $FeMn_{0.0136}$, is defined by the dissociation reaction:

$$FeMn_{0.0136} + 3.0272H^+ + 0.7568O_2\,(g) \rightarrow Fe^{3+} + 0.0136Mn^{2+} + 1.5136H_2O \quad \text{(Eq. 6.8-8)}$$

These reactions are not shown as being reversible because steel will never precipitate. This is achieved operationally by providing an arbitrarily large solubility log(K) value of 266 in the data blocks.

The next step in the analysis of the impact of corroding steels on potential seepage waters is an assessment of the expected amount of corrosion. These calculations determine a mole quantity of metal available for interactions with the infiltrating waters by multiplying the estimated surface areas of the metals by their corrosion rates, which are converted from a linear dimension per year to a mole quantity by scaling with density (ASTM G 1-90 1999 [DIRS 103515]) and the molecular weight. Once the moles of metal are determined the quantity is converted to molar, by dividing by the expected volume of infiltrating water as determined by the percolation fluxes for the time frame of interest (see Table 6.3-1 and Output DTN: SN0703PAEBSPCE.006; Output DTN: SN0705PAEBSPCE.011, spreadsheet: *DegradationMolality_PCEREV06.xls*, tab: "degradation"; spreadsheet: *A588_corrosion_calcs.xls*, tab: "A588 moles").

It is assumed in this analysis that SS316L will survive in the drift environment for significant periods of time (see Section 6.5.3 and Figure 6.5-3). As a starting point for the assessment of SS316L degradation, a step-function for transition from steam and atmospheric to immersed or aqueous conditions, along with percolation fluxes associated with the monsoonal and the glacial transition periods, were utilized. For the much shorter-lived A588, and because it is emplaced in the invert, only an aqueous rate was used and a percolation flux associated with the monsoonal period. The calculations are archived in Output DTN: SN0705PAEBSPCE.011 (spreadsheet: *DegradationMolality_PCEREV06.xls*, tab: "degradation"; spreadsheet: *A588_corrosion_calcs.xls*, tab: "A588 moles"). Drift wall surface temperature may fall below 96°C at variable times through out the repository, and thus seepage may begin any time from 0 to approximately 1,500 years after closure. Because there is uncertainty in the selection of the time of seepage as well as the corrosion rates, the calculated amount of SS316L and A588 corrosion were parametrically increased to capture the effect of increasing these parameters.

The corrosion rates adopted for use in this study were taken from *Aqueous Corrosion Rates for Waste Package Materials* (BSC 2004 [DIRS 169982]) and its associated DTN (MO0409SPAACRWP.000 [DIRS 172059]). For the analysis of the corrosion of SS316L, both

an atmospheric and an aqueous corrosion rate were used (Output DTN: SN0705PAEBSPCE.011, spreadsheet: *DegradationMolality_PCEREV06.xls*, tab: "degradation"). For the invert steel analysis only an aqueous rate was used (Output DTN: SN0705PAEBSPCE.011, spreadsheet: *A588_corrosion_calcs.xls*, tab: "degradation") for the reasons discussed above.

As an example, the A588 is modeled assuming that A516 provides an adequate proxy for the corrosion rate of A588. This is conservative for the reasons outlined in Section 6.7.1.2. An aqueous corrosion rate was selected from *Aqueous Corrosion Rates for Waste Package Materials* (BSC 2004 [DIRS 169982], Table 6-9). The average corrosion rate selected corresponds to data collected over one year in saltwater. The selected mean rate for aqueous corrosion is 10.61 μm/yr. This is a reasonable selection because the invert steels may be exposed to concentrated brines that form by evaporation on the hot waste package surface and then advect off the waste package into the invert. The density of A588 is given as 7.85 g/cc (Incropera and DeWitt 1996 [DIRS 108184], Table A-1), and the mass of A588 in a volume 1 cm^2 per 1 μm deep is converted by dividing by 10,000 to get 7.85×10^{-4} g/(cm^2 μm). Now multiplying the mean corrosion rate by this value gives 0.008 g/(cm^2 yr). Grams are converted to moles by dividing by the molecular weight of A588, 56.6048 g/mol (Output DTN: SN0705PAEBSPCE.011, calculated in spreadsheet *A588_corrosion_calcs*, tab: "composition"). This yields 1.47×10^{-4} moles/(cm^2 yr). The surface area of invert low-alloy steel is reported in Table 6.7-1 and is 157,000 cm^2 per linear meter of drift for the baseline case and 190,800 cm^2/m for the bounding case. The final moles of A588 to interact with the infiltrating water are then:

$$1.47 \times 10^{-4} \text{ moles/(cm}^2 \text{ yr)} \times 157{,}000 \text{ cm}^2 \div 10.92 \text{ L/yr} = 2 \text{ mol/L A588} \qquad \text{(Eq. 6.8-9)}$$

and

$$1.47 \times 10^{-4} \text{ moles/(cm}^2 \text{ yr)} \times 190{,}800 \text{ cm}^2 \div 10.92 \text{ L/yr} = 3 \text{ mol/L A588} \qquad \text{(Eq. 6.8-10)}$$

where 10.92 L/yr is the interpolated value for the 50th percentile percolation flux for the monsoon period (Output DTN: SN0705PAEBSPCE.011, file: *A588_corrosion_calcs.xls*, tab: "A588 moles").

These calculations provide a useful point of reference for the analyses that follow. However, because the design of the subsurface facilities at Yucca Mountain is still in progress and there may be considerable uncertainty in the parameters used to calculate the moles of steel to interact with the water, it is useful to parametrically increase the amount of steel interactions so that this assessment and its conclusions are independent of any particular data set. To that end, a value equal to 100 g A588 (1.77 moles) was selected for the first set of simulations. This value was multiplied by a factor of five (500 g A588 per liter of seepage) for the bounding simulations that demonstrate, quantitatively, no impact on seepage water chemistry. This upper limit drastically exceeds the quantity calculated in Equation 6.8-10 and provides an extreme upper limit on A588 interactions with seepage water.

The corrosion rate of SS316L controls the quantity of corrosion product and the extent to which corrosion affects the seepage water chemistry that may impact the drip shield and the waste package. The corrosion rate was estimated by determining the mean quantity of SS316L ground

support over a one-square-meter section of drift wall. This quantity includes the stainless steel sheets and rock bolts (SNL 2007 [DIRS 179354], parameter 02-03). A step-function for the corrosion rate was used to approximate the transition from dry to wet drift-wall conditions, which is estimated to occur any time after the drift wall temperature falls below approximately 96°C. The molar quantity of SS316L was determined in a similar manner as described above for A588. The amount of SS316L used in these sensitivity calculations is 1.3×10^{-2} mol/L seepage (Output DTN: SN0705PAEBSPCE.011, spreadsheet: *DegradationMolality_PCEREV06.xls*).

A parametric sensitivity to this corrosion rate, with an increase in corrosion by a factor of 10, is also examined (1.3×10^{-1} moles/L). This increased corrosion rate more than accounts for any uncertainty in the corrosion rate (mostly due to the uniqueness of the in-drift environment). The results support the conclusions of this analysis in Section 6.8.4.3 that there is no significant impact to the aqueous geochemistry of the seepage waters due to steel interactions.

6.8.4 EQ3/6 Modeling Simulations

The analysis of steel interaction with seepage water consists of the following sequential EQ3/6 simulations:

1. Initial EQ3NR speciation of Group 1 (WRIP = 0 and G) and Group 3 (WRIP = 0 and G) seepage water (Output DTN: SN0705PAEBSPCE.011) with trace quantities of "Fe^{2+}" (10^{-16} molal), "Cr^{3+}" (10^{-16} molal) and Ni^{2+} (10^{-16} molal) added; EQ3 pickup files from these simulations were used in Step 2 below.

2. EQ6 simulations precipitated solids from the equilibrated fluids; EQ6 pickup file used in Step 3 below.

3. EQ6 "seepage" simulations titrate SiO_2 (am), Calcite, and alkali feldspar (two quantities, WRIP = 0, G). The temperature is increased from ambient, 23°C, to 25°C. The pCO_2 is allowed to vary. The EQ6 seepage pickup files are used in Step 4 below.

4. EQ6 simulations to introduce varying amounts of SS316L and A588 steels into the seepage waters; the EQ6 pickup files are used in Step 5 below.

5. EQ6 evaporation simulations take the waters equilibrated with SS316L and A588 to dryout. The output files generated by the evaporation simulations provide the basis for comparing water chemistries with and without steel interactions.

Note that these simulations were conducted assuming unlimited available oxygen (see the discussion of in-drift oxygen in Section 6.7). This is consistent with the presumption that oxidizing conditions are maintained in the drift. This is reasonable because the corrosion rates used to estimate the amount of steel interaction is based on data collected in oxidizing environments (BSC 2004 [DIRS 169982]). For the EQ6 simulations, when titrating in the largest quantities of steel, up to 8 moles of oxygen were used. If conditions in the drift go sub-oxic, the corrosion rates for steel would be substantially reduced; thus, the analyses documented in this section represent a maximum steel interaction and provide a conservative assessment of the impact on water chemistry for that case.

6.8.4.1 Results

A588 low alloy steel interactions with seepage waters

Titrating large quantities (100 g and 500 g) of A588 low-alloy steel into Group 1 and Group 3 seepage water with both WRIP = 0 (no alkali feldspar added) and WRIP = G (10^{-3} moles alkali feldspar added) resulted in no significant change in the aqueous phase chemistry (Figures 6.8-5 through 6.8-8 and Tables 6.8-3 and 6.8-4).

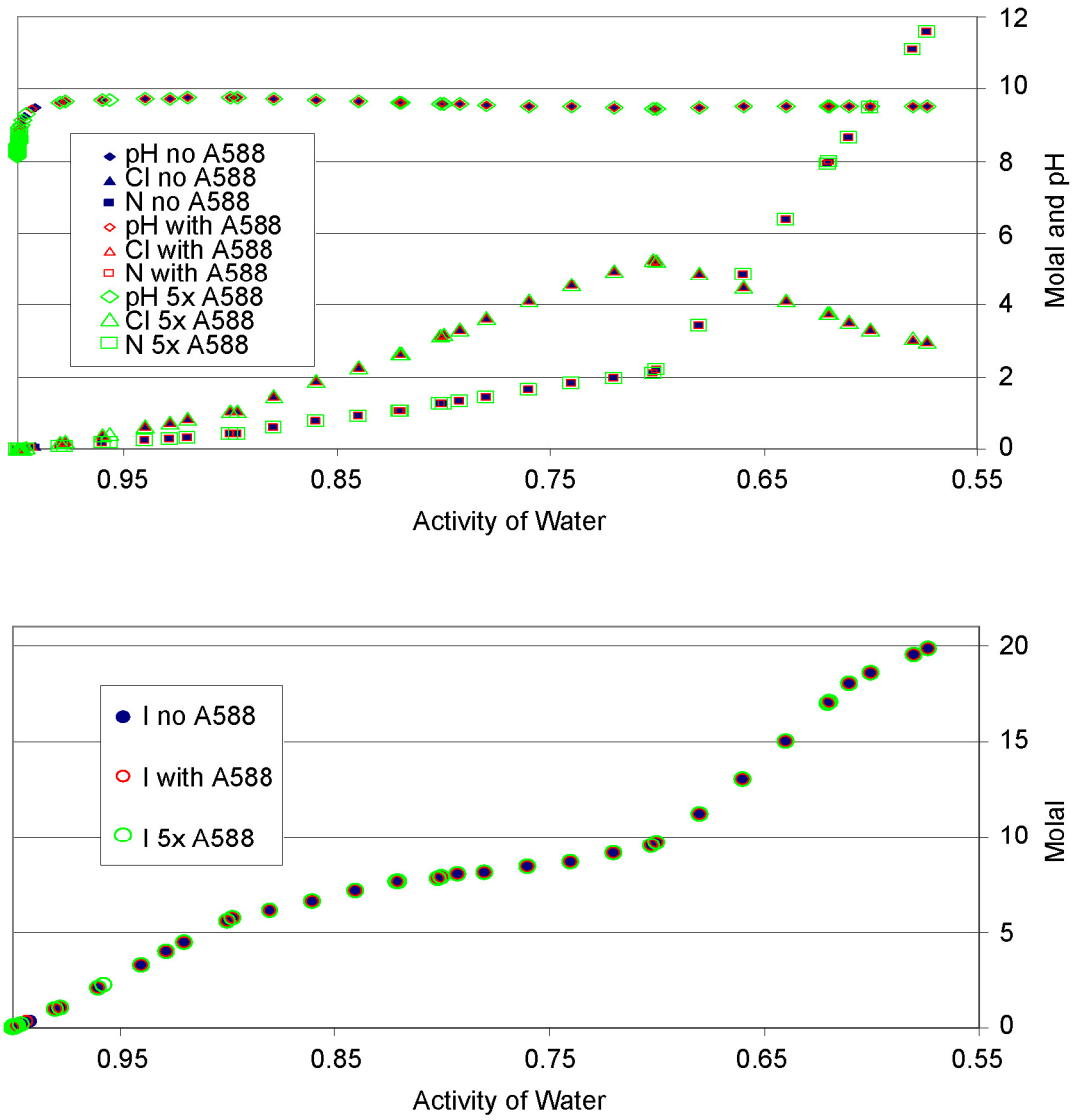

Source: Output DTN: SN0705PAEBSPCE.011, spreadsheet: *Steel_evaluation.xls*, tab: "Gp1 A588 comparison plots."

Figure 6.8-5. Evaporative Evolution of Group 1 Water with WRIP = 0, with Trace Fe and Mn (blue symbols), with 100 g A588 Added (red symbols), and with 500 g A588 Added (green symbols) for the Key Chemical Parameter Provided to TSPA-LA (top: pH, [Cl], and [N]; bottom: ionic strength, *I*)

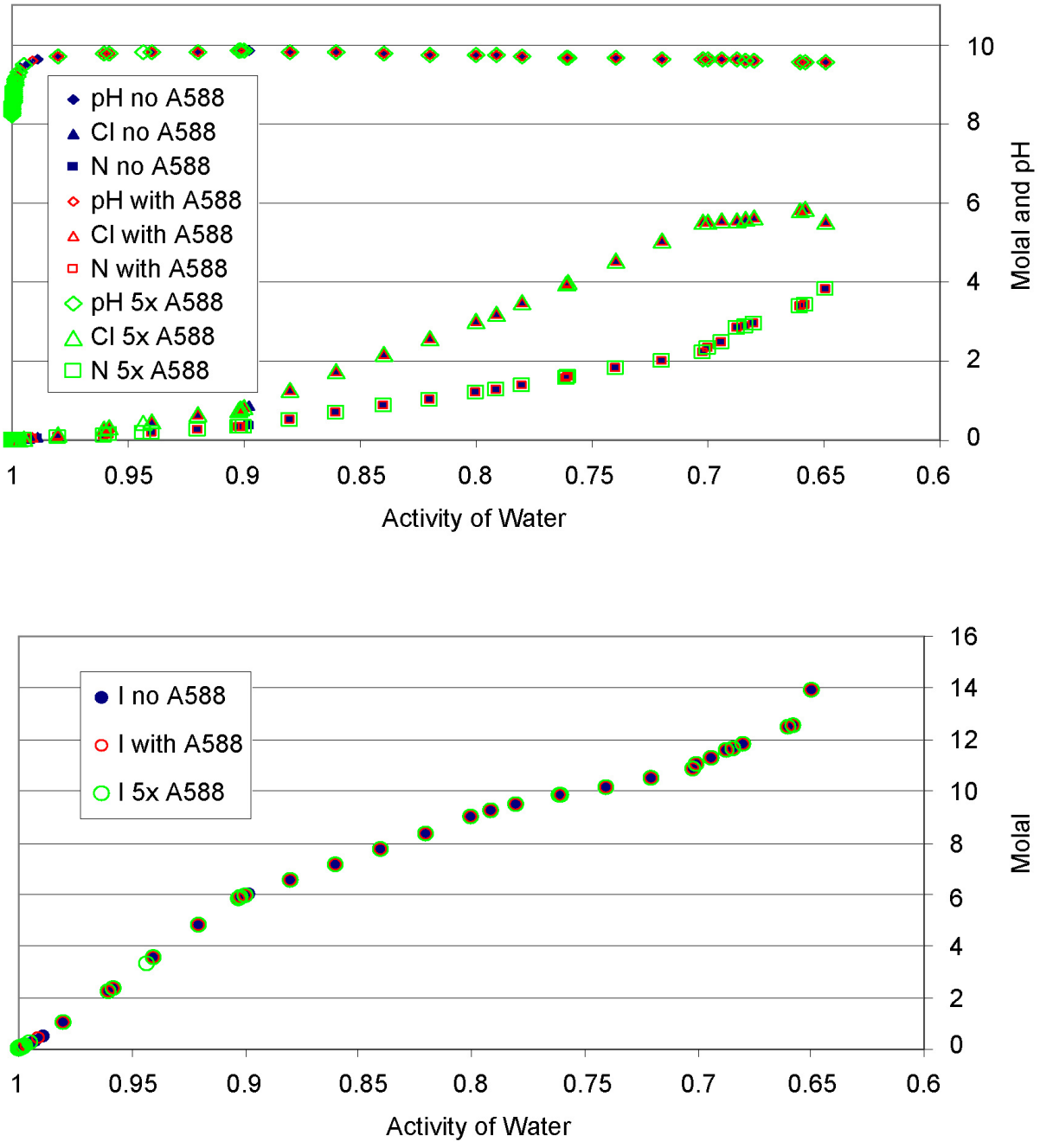

Source: Output DTN: SN0705PAEBSPCE.011, spreadsheet: *Steel_evaluation.xls*, tab: "Gp1 A588 comparison plots."

Figure 6.8-6. Evaporative Evolution of Group 1 Water with WRIP = G, with Trace Fe and Mn (blue symbols), with 100 g A588 Added (red symbols), and with 500 g A588 Added (green symbols) for the Key Chemical Parameter Provided to TSPA-LA (top: pH, [Cl], and [N]; bottom: ionic strength, *I*)

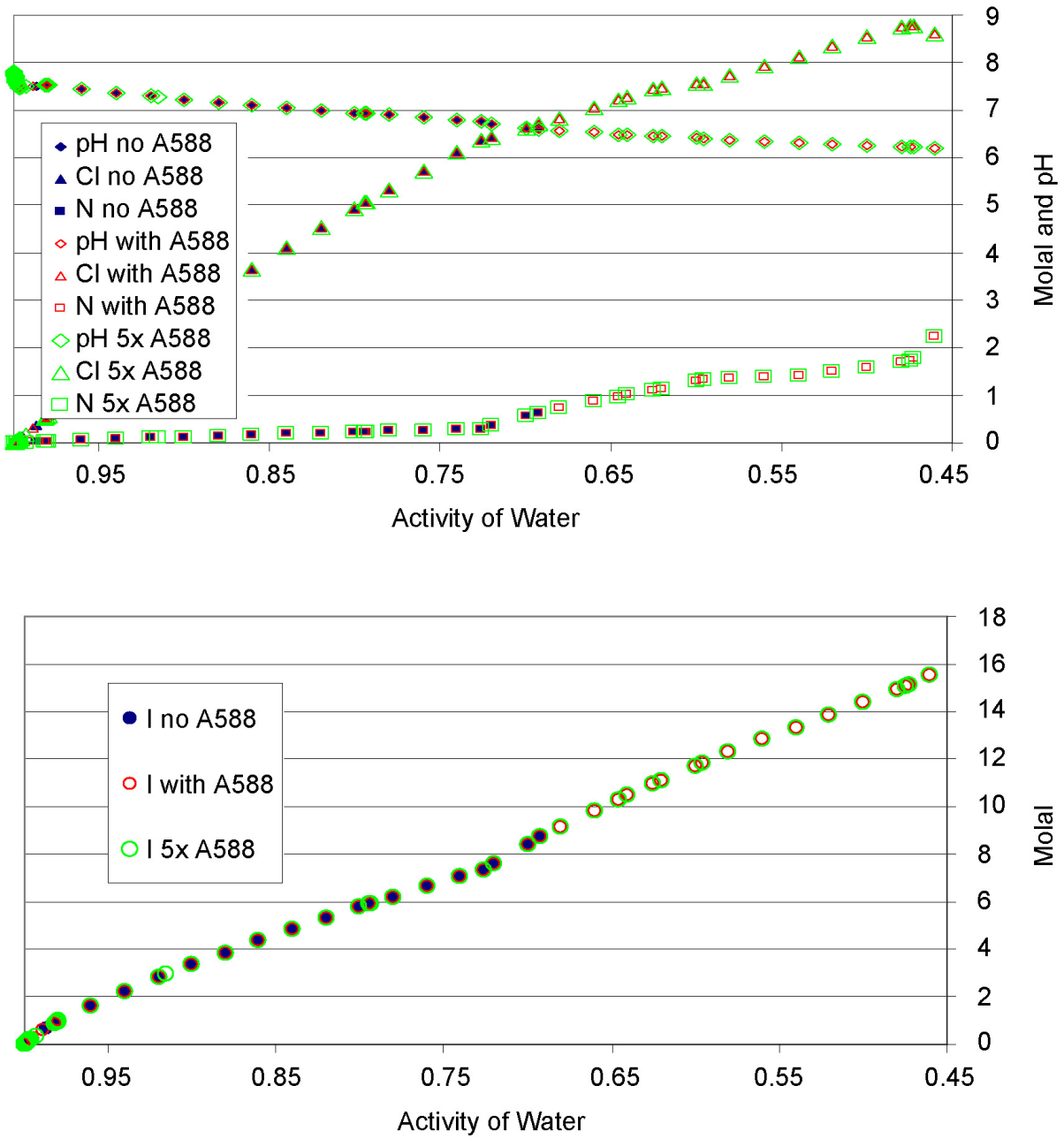

Source: Output DTN: SN0705PAEBSPCE.011, spreadsheet: *Steel_evaluation.xls*, tab: "Gp3 A588 comparison plots."

Figure 6.8-7. Evaporative Evolution of Group 3 Water with WRIP = 0, with Trace Fe and Mn (blue symbols), with 100 g A588 Added (red symbols), and with 500 g A588 Added (green symbols) for the Key Chemical Parameter Provided to TSPA-LA (top: pH, [Cl], and [N]; bottom: ionic strength, *I*)

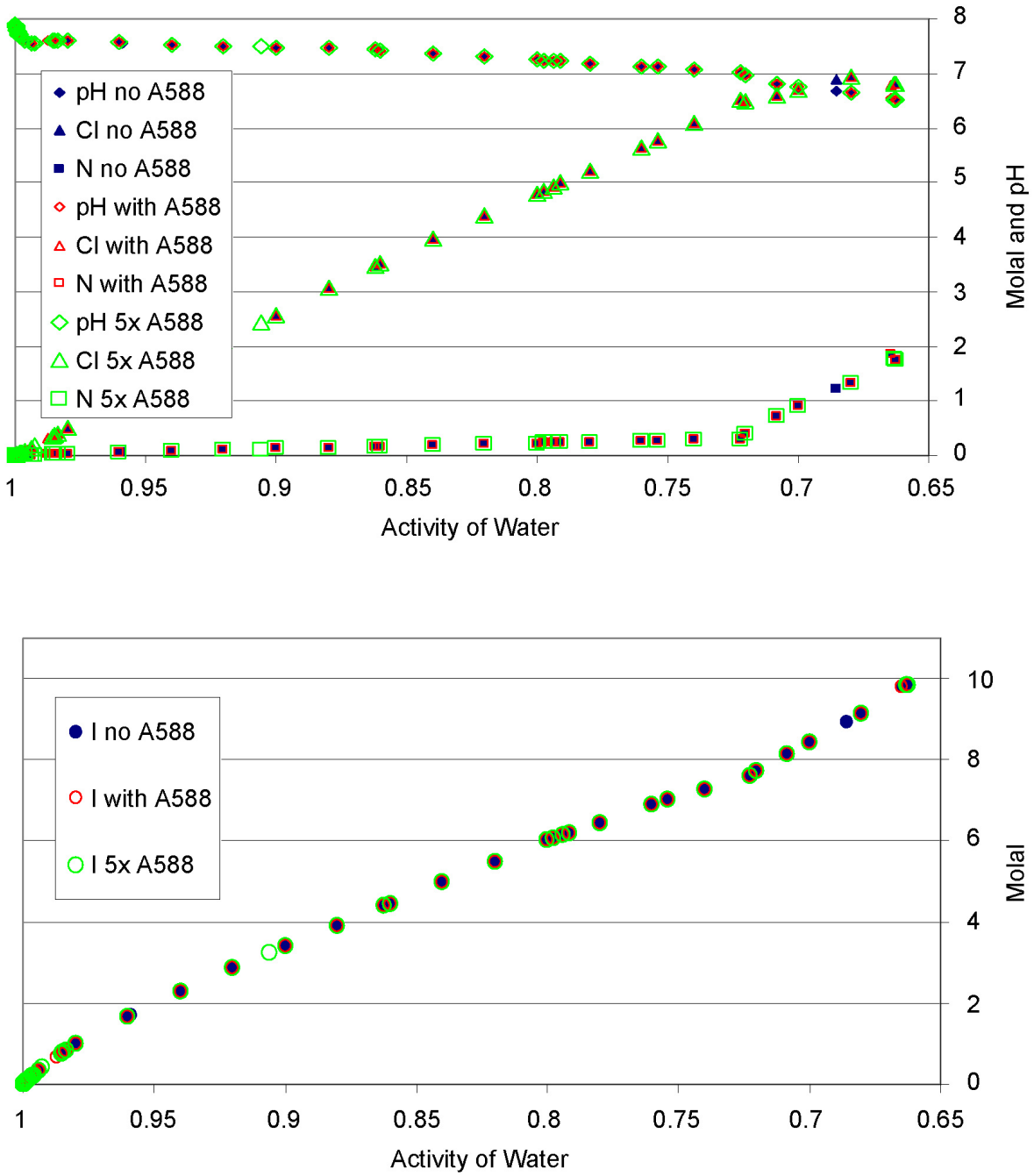

Source: Output DTN: SN0705PAEBSPCE.011, spreadsheet: *Steel_evaluation.xls*, tab: "Gp3 A588 comparison plots."

Figure 6.8-8. Evaporative Evolution of Group 3 Water with WRIP = G, with Trace Fe and Mn (blue symbols), with 100 g A588 Added (red symbols), and with 500 g A588 Added (green symbols) for the Key Chemical Parameter Provided to TSPA-LA (top: pH, [Cl], and [N]; bottom: ionic strength, *I*)

The key chemical parameters provided to TSPA-LA by the P&CE dilution/evaporation abstraction model are pH, ionic strength, Cl^- (as total chlorine), and NO_3^- (as total nitrogen) as a function of RH. These parameters are plotted for three evaporation simulations: trace quantities

of the steel components, 100 g (1.77 moles) A588 added, and 500 g (8.85 moles) A588 added. For all three evaporation simulations for two starting waters with two WRIP quantities, there are no significant differences in aqueous concentrations owing to the steel interactions. The lone exception is the Group 3 water with WRIP = 0. This water has no added buffering capacity from added alkali feldspar; once the steel components are added to this water the EQ6 Pitzer code was able to calculate equilibrium aqueous concentrations to the eutectic or "dry out" composition. The un-buffered simulation did not converge, resulting in no data for comparison below approximately RH = 69%. However, it is clear from Figure 6.8-7 that the Group 3 water with and without A588 added is evolving along the same evaporative pathway. (See Section 6.15.1.1 for a discussion of non-convergence.)

Table 6.8-3 provides the calculated equilibrium aqueous concentrations at the dryout RH for all the elements and the precipitated solid phases for Group 1 water with and without A588 steel. There is little or no difference in the values for most of the elements in solution. The exception is Al which is decreased from a scant 10^{-18} molal to a negligible 10^{-31} molal owing to the precipitation of a tiny quantity (10^{-13} moles for Group 1, WRIP = G) of nontronite clays. The Fe in solution allowed the precipitation of these clays, which contain a small fraction of Al.

Table 6.8-4 provides the calculated equilibrium aqueous concentrations for all the elements and the precipitated solid phases for Group 3 water with and without A588 steel. This comparison is provided at the dryout RH, except for the Group 3, WRIP = 0 water where the comparison is made at the lowest RH from the water with only trace components of the A588 steel (i.e., the non-convergent simulation). Only negligible differences are observed among the aqueous chemistry of these waters, regardless of the quantity of A588 steel interacted. The exception, as noted above, is Al. An examination of the solids that precipitated indicate that the effect of more A588 titrated into these waters is simply the precipitation of more corrosion products. The Fe and Mn-bearing solid phases serve to limit their aqueous components to very low ($<10^{-12}$ molal) quantities (Table 6.8-4).

316L Stainless Steel Interactions with Seepage Waters

Titrating large quantities of 316L stainless steel into Group 1 and Group 3 seepage water with both WRIP = 0 (no alkali feldspar added) and WRIP = G (1.0×10^{-3} moles alkali feldspar added), yielded results analogous to those described above for A588 steel; no significant change in the aqueous phase chemistry was observed (Tables 6.8-5 and 6.8-6 and Figures 6.8-9 through 6.8-12).

The key chemical parameters are plotted for three evaporation simulations: trace quantities of the steel components, 1.3×10^{-2} moles SS316L added, and 1.3×10^{-1} moles SS316L added. For all three evaporation simulations for two starting waters with two WRIP quantities, there are no significant differences in aqueous concentrations owing to the steel interactions. The lone exception is the Group 3 water with WRIP = 0, as described above for A588. However, it is clear from Figure 6.8-11 that the Group 3 water with and without SS316L added is evolving along the same evaporative pathway. (See Section 6.15.1.1 for a discussion of non-convergance.)

Table 6.8-3. Group 1 A588 Comparison among Evaporated Quantities of Aqueous and Solid Components

Comparison of Gp1 WRIP=G evaporated water chemistry with and without A588 and with 5x the A588																
Filename	a(w)	O mol/kg H2O	Al mol/kg H2O	C mol/kg H2O	Ca mol/kg H2O	Cl mol/kg H2O	F mol/kg H2O	Fe mol/kg H2O	H mol/kg H2O	K mol/kg H2O	Mg mol/kg H2O	Mn mol/kg H2O	N mol/kg H2O	Na mol/kg H2O	S mol/kg H2O	Si mol/kg H2O
1ge.6o	0.649495	7.31E+01	3.97E-18	3.62E-01	7.34E-06	5.52E+00	6.68E-03	9.26E-15	1.11E+02	4.58E+00	2.47E-05	4.95E-14	3.80E+00	7.84E+00	1.26E+00	3.61E-03
cs1ge.6o	0.6495	7.31E+01	3.97E-31	3.62E-01	7.34E-06	5.52E+00	6.68E-03	1.29E-12	1.11E+02	4.58E+00	2.47E-05	4.95E-14	3.80E+00	7.84E+00	1.26E+00	3.60E-03
cs1gex5.6o	0.649497	7.31E+01	3.97E-31	3.62E-01	7.34E-06	5.52E+00	6.68E-03	1.29E-12	1.11E+02	4.58E+00	2.47E-05	4.95E-14	3.80E+00	7.84E+00	1.26E+00	3.60E-03

Comparison of Gp1 WRIP=G evaporated equilibrium solids with and without A588 and with 5x the A588														
Filename	a(w)	Antigorite(am) mol	Arcanite mol	Calcite mol	Celadonite mol	Goethite mol	Halite mol	Kogarkoite mol	Nahcolite mol	Niter mol	Nontronite-K mol	Pyrolusite mol	SiO2(am) mol	Sylvite mol
1ge.6o	0.649495	8.10E-06	5.08E-05	9.72E-05	3.49E-14		4.30E-04	1.16E-04	2.30E-03	2.58E-04	5.00E-17	4.40E-17	2.06E-03	2.19E-04
cs1ge.6o	0.6495	8.10E-06	5.08E-05	9.72E-05		1.77E+00	4.30E-04	1.16E-04	2.30E-03	2.58E-04	1.06E-13	2.41E-02	2.06E-03	2.19E-04
cs1gex5.6o	0.649497	8.10E-06	5.08E-05	9.72E-05		8.85E+00	4.30E-04	1.16E-04	2.30E-03	2.58E-04	1.06E-13	1.20E-01	2.06E-03	2.19E-04

Comparison of Gp1 WRIP=0 evaporated water chemistry with and without A588 and with 5x the A588																
Filename	a(w)	O mol/kg H2O	Al mol/kg H2O	C mol/kg H2O	Ca mol/kg H2O	Cl mol/kg H2O	F mol/kg H2O	Fe mol/kg H2O	H mol/kg H2O	K mol/kg H2O	Mg mol/kg H2O	Mn mol/kg H2O	N mol/kg H2O	Na mol/kg H2O	S mol/kg H2O	Si mol/kg H2O
10e.6o	0.57354	9.73E+01	2.04E-18	2.18E-01	7.38E-06	2.98E+00	3.39E-03	6.61E-15	1.11E+02	3.65E+00	2.76E-05	7.25E-14	1.16E+01	1.45E+01	1.61E+00	3.19E-03
cs10e.6o	0.573537	9.73E+01	9.82E-32	2.18E-01	7.38E-06	2.98E+00	3.39E-03	1.04E-12	1.11E+02	3.65E+00	2.76E-05	7.25E-14	1.16E+01	1.45E+01	1.61E+00	3.19E-03
cs10ex5.6o	0.573537	9.73E+01	9.82E-32	2.18E-01	7.38E-06	2.98E+00	3.39E-03	1.04E-12	1.11E+02	3.65E+00	2.76E-05	7.25E-14	1.16E+01	1.45E+01	1.61E+00	3.19E-03

Comparison of Gp1 WRIP=0 evaporated equilibrium solids with and without A588 and with 5x the A588														
Filename	a(w)	Antigorite (am) mol	Calcite mol	Celadonite mol	Goethite mol	Halite mol	Kogarkoite mol	Nahcolite mol	Niter mol	Nontronite-Na mol	Pyrolusite mol	SiO2 (am) mol	Soda Niter mol	Thenardite mol
10e.6o	0.57354	9.60E-06	3.89E-04	1.72E-14		6.49E-04	1.16E-04	1.33E-03	1.23E-04	5.00E-17	1.00E-16	1.95E-03	1.35E-04	5.08E-05
cs10e.6o	0.573537	9.60E-06	3.89E-04		1.77E+00	6.49E-04	1.16E-04	1.33E-03	1.23E-04	5.21E-14	2.41E-02	1.95E-03	1.35E-04	5.08E-05
cs10ex5.6o	0.573537	9.60E-06	3.89E-04		8.85E+00	6.49E-04	1.16E-04	1.33E-03	1.23E-04	5.21E-14	1.20E-01	1.95E-03	1.35E-04	5.08E-05

Source: Output DTN: SN0705PAEBSPCE.011, spreadsheet: *Steel_evaluation.xls*, tab: "Gp1 A588 comparison plots."

Table 6.8-4. Group 3 A588 Comparison among Evaporated Quantities of Aqueous and Solid Components

Comparison of Gp3 WRIP=0 evaporated water chemistry with and without A588 and with 5x the A588

Filename	a(w)	O mol/kg H2O	Al mol/kg H2O	C mol/kg H2O	Ca mol/kg H2O	Cl mol/kg H2O	F mol/kg H2O	Fe mol/kg H2O	H mol/kg H2O	K mol/kg H2O	Mg mol/kg H2O	Mn mol/kg H2O	N mol/kg H2O	Na mol/kg H2O	S mol/kg H2O	Si mol/kg H2O
30e.6o	0.691961	5.74E+01	5.29E-16	5.05E-03	3.95E-01	6.70E+00	3.48E-05	2.56E-14	1.11E+02	8.96E-01	9.83E-01	3.89E-13	6.28E-01	3.69E+00	5.71E-03	5.22E-04
cs30e.6o	0.691965	5.74E+01	5.39E-29	5.05E-03	3.94E-01	6.70E+00	3.48E-05	3.56E-12	1.11E+02	8.96E-01	9.83E-01	1.13E-12	6.27E-01	3.69E+00	5.71E-03	5.22E-04
cs30ex5.6o	0.691967	5.74E+01	5.39E-29	5.05E-03	3.94E-01	6.70E+00	3.48E-05	3.56E-12	1.11E+02	8.96E-01	9.83E-01	1.13E-12	6.27E-01	3.69E+00	5.71E-03	5.22E-04

Comparison of Gp3 WRIP=0 evaporated equilibrium solids with and without A588 and with 5x the A588

Filename	a(w)	Anhydrite mol	Antigorite (am) mol	Calcite mol	Celadonite mol	Goethite mol	Halite mol	Nontronite-K mol	Nontronite-Mg mol	Pyrolusite mol	Sellaite mol	SiO2(am) mol
30e.6o	0.691961	1.25E-03	1.48E-04	1.63E-04	9.94E-15		1.75E-03	4.67E-17			2.00E-05	1.66E-03
cs30e.6o	0.691965	1.25E-03	1.48E-04	1.63E-04		1.77E+00	1.75E-03			2.41E-02	2.00E-05	1.66E-03
cs30ex5.6o	0.691967	1.25E-03	1.48E-04	1.63E-04		8.85E+00	1.75E-03		3.02E-14	1.20E-01	2.00E-05	1.66E-03

Comparison of Gp3 WRIP=G evaporated water chemistry with and without A588 and with 5x the A588

Filename	a(w)	O mol/kg H2O	Al mol/kg H2O	C mol/kg H2O	Ca mol/kg H2O	Cl mol/kg H2O	F mol/kg H2O	Fe mol/kg H2O	H mol/kg H2O	K mol/kg H2O	Mg mol/kg H2O	Mn mol/kg H2O	N mol/kg H2O	Na mol/kg H2O	S mol/kg H2O	Si mol/kg H2O
3ge.6o	0.662399	6.12E+01	4.97E-16	6.13E-03	1.68E-02	6.81E+00	2.04E-05	5.97E-14	1.11E+02	2.53E+00	9.49E-01	2.28E-12	1.74E+00	4.33E+00	1.16E-01	4.08E-04
cs3ge.6o	0.662399	6.12E+01	4.99E-29	6.13E-03	1.68E-02	6.81E+00	2.04E-05	8.33E-12	1.11E+02	2.53E+00	9.49E-01	2.28E-12	1.74E+00	4.33E+00	1.16E-01	4.08E-04
cs3gex5.6o	0.662399	6.12E+01	4.99E-29	6.13E-03	1.68E-02	6.81E+00	2.04E-05	8.33E-12	1.11E+02	2.53E+00	9.49E-01	2.28E-12	1.74E+00	4.33E+00	1.16E-01	4.08E-04

Comparison of Gp3 WRIP=G evaporated equilibrium solids with and without A588 and with 5x the A588

Filename	a(w)	Anhydrite mol	Antigorite (am) mol	Celadonite mol	Goethite mol	Halite mol	Niter mol	Nontronite-K mol	Pentasalt mol	Polyhalite mol	Pyrolusite mol	Sellaite mol	SiO2(am) mol	Sylvite mol
3ge.6o	0.662399	5.87E-04	2.09E-04	1.18E-14		3.21E-03	1.61E-04	5.00E-17	6.45E-05	6.87E-05	1.00E-16	2.00E-05	1.54E-03	2.63E-04
cs3ge.6o	0.662399	5.87E-04	2.09E-04		1.77E+00	3.21E-03	1.61E-04	3.57E-14	6.45E-05	6.87E-05	2.41E-02	2.00E-05	1.54E-03	2.63E-04
cs3gex5.6o	0.662399	5.87E-04	2.09E-04		8.85E+00	3.21E-03	1.61E-04	3.57E-14	6.45E-05	6.87E-05	1.20E-01	2.00E-05	1.54E-03	2.63E-04

Source: Output DTN: SN0705PAEBSPCE.011, spreadsheet: *Steel_evaluation.xls*, tab: "Gp3 A588 comparison plots."

Table 6.8-5. Group 1 SS316L Comparison among Evaporated Quantities of Aqueous and Solid Components

Comparison of Gp1 WRIP=G evaporated water chemistry with and without SS316L and with 10x the SS316L

Filename	a(w)	O mol/kg H2O	Al mol/kg H2O	C mol/kg H2O	Ca mol/kg H2O	Cl mol/kg H2O	Cr mol/kg H2O	F mol/kg H2O	Fe mol/kg H2O	H mol/kg H2O	K mol/kg H2O	Mg mol/kg H2O	N mol/kg H2O	Na mol/kg H2O	S mol/kg H2O	Si mol/kg H2O	Ni mol/kg H2O
1ge.6o	0.649495	7.31E+01	3.97E-18	3.62E-01	7.34E-06	5.52E+00	2.52E-10	6.68E-03	9.26E-15	1.11E+02	4.58E+00	2.47E-05	3.80E+00	7.84E+00	1.26E+00	3.61E-03	7.52E-08
ss1ge.6o	0.649499	7.31E+01	3.97E-31	3.62E-01	7.34E-06	5.52E+00	1.27E-09	6.68E-03	1.29E-12	1.11E+02	4.58E+00	2.47E-05	3.80E+00	7.84E+00	1.26E+00	3.60E-03	2.97E-09
ss1gex10.6o	0.649495	7.31E+01	3.96E-31	3.62E-01	7.34E-06	5.52E+00	1.27E-09	6.68E-03	1.29E-12	1.11E+02	4.58E+00	2.47E-05	3.80E+00	7.85E+00	1.26E+00	3.61E-03	2.97E-09

Comparison of Gp1 WRIP=G evaporated equilibrium solids with and without SS316L and with 10x SS316L

Filename	a(w)	Antigorite (am) mol	Arcanite mol	Calcite mol	Celadonite mol	Ferrite-Ni mol	Goethite mol	Halite mol	Kogarkoite mol	Nahcolite mol	NiCO3 mol	NiCr2O4 mol	Niter mol	Nontronite-K mol	SiO2 (am) mol	Sylvite mol
1ge.6o	0.649495	8.10E-06	5.08E-05	9.72E-05	3.49E-14			4.30E-04	1.16E-04	2.30E-03	4.53E-17	5.00E-17	2.58E-04	5.00E-17	2.06E-03	2.19E-04
ss1ge.6o	0.649499	8.10E-06	5.08E-05	9.72E-05		1.30E-03	4.42E-02	4.30E-04	1.16E-04	2.30E-03		6.50E-03	2.58E-04	1.06E-13	2.06E-03	2.19E-04
ss1gex10.6o	0.649495	8.10E-06	5.08E-05	9.72E-05		5.33E-03	1.81E-01	4.30E-04	1.16E-04	2.30E-03		2.67E-02	2.58E-04	1.06E-13	2.06E-03	2.19E-04

Comparison of Gp1 WRIP=0 evaporated water chemistry with and without SS316L and with 10x SS316L

Filename	a(w)	O mol/kg H2O	Al mol/kg H2O	C mol/kg H2O	Ca mol/kg H2O	Cl mol/kg H2O	Cr mol/kg H2O	F mol/kg H2O	Fe mol/kg H2O	H mol/kg H2O	K mol/kg H2O	Mg mol/kg H2O	N mol/kg H2O	Na mol/kg H2O	S mol/kg H2O	Si mol/kg H2O	Ni mol/kg H2O
10e.6o	0.573539	9.73E+01	2.04E-18	2.18E-01	7.38E-06	2.98E+00	2.08E-10	3.39E-03	6.61E-15	1.11E+02	3.65E+00	2.76E-05	1.16E+01	1.45E+01	1.61E+00	3.19E-03	7.44E-08
ss10e.6o	0.57353	9.74E+01	9.82E-32	2.18E-01	7.38E-06	2.98E+00	1.11E-09	3.39E-03	1.04E-12	1.11E+02	3.65E+00	2.76E-05	1.16E+01	1.45E+01	1.61E+00	3.19E-03	2.60E-09
ss10ex10.6o	0.573538	9.73E+01	9.82E-32	2.18E-01	7.38E-06	2.98E+00	1.11E-09	3.39E-03	1.04E-12	1.11E+02	3.65E+00	2.76E-05	1.16E+01	1.45E+01	1.61E+00	3.19E-03	2.60E-09

Comparison of Gp1 WRIP=0 evaporated equilibrium solids with and without SS316L and with 10x SS316L

Filename	a(w)	Antigorite(am) mol	Calcite mol	Celadonite mol	Ferrite-Ni mol	Goethite mol	Halite mol	Kogarkoite mol	Nahcolite mol	NiCO3 mol	NiCr2O4 mol	Niter mol	Nontronite-Na mol	SiO2(am) mol	Soda Niter mol	Thenardite mol
10e.6o	0.573539	9.60E-06	3.89E-04	1.72E-14			6.49E-04	1.16E-04	1.33E-03	4.49E-17	5.00E-17	1.23E-04	5.00E-17	1.95E-03	1.35E-04	5.08E-05
ss10e.6o	0.57353	9.60E-06	3.89E-04		1.30E-03	4.42E-02	6.49E-04	1.16E-04	1.33E-03		6.50E-03	1.23E-04	5.21E-14	1.95E-03	1.35E-04	5.08E-05
ss10ex10.6o	0.573538	9.60E-06	3.89E-04		5.33E-03	1.81E-01	6.49E-04	1.16E-04	1.33E-03		2.67E-02	1.23E-04	5.21E-14	1.95E-03	1.35E-04	5.08E-05

Source: Output DTN: SN0705PAEBSPCE.011, spreadsheet: *Steel_evaluation.xls*, tab: "Gp1 SS316L comparison plots."

Table 6.8-6. Group 3 SS316L Comparison among Evaporated Quantities of Aqueous and Solid Components

Comparison of Gp3 WRIP=G evaporated water chemistry with and without SS316L and with 10x SS316L

Filename	a(w)	O mol/kg H2O	Al mol/kg H2O	C mol/kg H2O	Ca mol/kg H2O	Cl mol/kg H2O	Cr mol/kg H2O	F mol/kg H2O	Fe mol/kg H2O	H mol/kg H2O	K mol/kg H2O	Mg mol/kg H2O	N mol/kg H2O	Na mol/kg H2O	S mol/kg H2O	Si mol/kg H2O	Ni mol/kg H2O
3ge.6o	0.662398	6.12E+01	4.96E-16	6.13E-03	1.68E-02	6.81E+00	1.12E-07	2.04E-05	5.97E-14	1.11E+02	2.53E+00	9.50E-01	1.74E+00	4.33E+00	1.16E-01	4.08E-04	8.99E-07
ss3ge.6o	0.662398	6.12E+01	4.99E-29	6.13E-03	1.68E-02	6.81E+00	1.86E-08	2.04E-05	8.33E-12	1.11E+02	2.53E+00	9.49E-01	1.74E+00	4.33E+00	1.16E-01	4.08E-04	3.24E-05
ss3gex10.6o	0.662398	6.12E+01	4.99E-29	6.13E-03	1.68E-02	6.81E+00	1.86E-08	2.04E-05	8.33E-12	1.11E+02	2.53E+00	9.49E-01	1.74E+00	4.33E+00	1.16E-01	4.08E-04	3.24E-05

Comparison of Gp3 WRIP=G evaporated equilibrium solids with and without SS316L and with 10x SS316L

Filename	a(w)	Anhydrite mol	Antigorite (am) mol	Celadonite mol	Ferrite-Ni mol	Goethite mol	Halite mol	NiCr2O4 mol	Niter mol	Nontronite-K mol	Pentasalt mol	Polyhalite mol	Sellaite mol	SiO2(am) mol	Sylvite mol
3ge.6o	0.662398	5.87E-04	2.09E-04	1.18E-14			3.21E-03	4.67E-17	1.61E-04	5.00E-17	6.45E-05	6.87E-05	2.00E-05	1.54E-03	2.63E-04
ss3ge.6o	0.662398	5.87E-04	2.09E-04		1.30E-03	4.42E-02	3.21E-03	6.50E-03	1.61E-04	3.57E-14	6.45E-05	6.87E-05	2.00E-05	1.54E-03	2.63E-04
ss3gex10.6o	0.662398	5.87E-04	2.09E-04		5.33E-03	1.81E-01	3.21E-03	2.67E-02	1.61E-04	3.57E-14	6.45E-05	6.87E-05	2.00E-05	1.54E-03	2.63E-04

Comparison of Gp3 WRIP=0 evaporated water chemistry with and without SS316L and with 10x SS316L

Filename	a(w)	O mol/kg H2O	Al mol/kg H2O	C mol/kg H2O	Ca mol/kg H2O	Cl mol/kg H2O	Cr mol/kg H2O	F mol/kg H2O	Fe mol/kg H2O	H mol/kg H2O	K mol/kg H2O	Mg mol/kg H2O	N mol/kg H2O	Na mol/kg H2O	S mol/kg H2O	Si mol/kg H2O	Ni mol/kg H2O
30e.6o	0.691961	5.74E+01	5.29E-16	5.05E-03	3.95E-01	6.70E+00	3.89E-13	3.48E-05	2.56E-14	1.11E+02	8.96E-01	9.83E-01	6.28E-01	3.69E+00	5.71E-03	5.22E-04	3.89E-13
ss30e.6o	0.69196	5.74E+01	5.39E-29	5.05E-03	3.94E-01	6.70E+00	1.19E-08	3.48E-05	3.56E-12	1.11E+02	8.96E-01	9.83E-01	6.28E-01	3.69E+00	5.71E-03	5.22E-04	2.90E-05
ss30ex10.6o	0.691871	5.74E+01	5.40E-29	5.06E-03	3.95E-01	6.70E+00	1.19E-08	3.48E-05	3.56E-12	1.11E+02	8.97E-01	9.84E-01	6.28E-01	3.69E+00	5.70E-03	5.21E-04	2.90E-05

Comparison of Gp3 WRIP=0 evaporated equilibrium solids with and without SS316L and with 10x SS316L

Filename	a(w)	Anhydrite mol	Antigorite (am) mol	Calcite mol	Celadonite mol	Ferrite-Ni mol	Goethite mol	Halite mol	NiCr2O4 mol	Nontronite-K mol	Sellaite mol	SiO2(am) mol
30e.6o	0.691961	1.25E-03	1.48E-04	1.63E-04	9.94E-15			1.75E-03		4.67E-17	2.00E-05	1.66E-03
ss30e.6o	0.69196	1.25E-03	1.48E-04	1.63E-04		1.30E-03	4.42E-02	1.75E-03	6.50E-03		2.00E-05	1.66E-03
ss30ex10.6o	0.691871	1.70E-01	1.48E-04	1.63E-04		5.00E-03	1.70E-01	1.75E-03	2.50E-02		2.00E-05	1.66E-03

Source: Output DTN: SN0705PAEBSPCE.011, spreadsheet: *Steel_evaluation.xls*, tab: "Gp3 SS316L comparison plots."

Tables 6.8-5 and 6.8-6 provide the calculated equilibrium aqueous concentrations for all the elements and the precipitated solid phases. This comparison is provided at the dryout RH, except for the Group 3, WRIP = 0 water where the comparison is made at the lowest RH from the water with only trace components of the SS316L steel (i.e., the non-convergent simulation). Only negligible differences are observed among the aqueous chemistry of these waters, regardless of how much SS316L steel is interacted. (See the discussion above for A588 regarding aqueous Al.) An examination of the solids that precipitated indicates that the effect of adding more SS316L into these waters is simply the precipitation of more corrosion products. The Fe, Cr, and Ni-bearing solid phases serve to limit their aqueous components to low quantities. The majority of the Fe was precipitated as goethite; the remaining Fe solid phase was $NiFe_2O_4$; the Cr-phase was $NiCr_2O_4$. The equilibrium aqueous concentrations reflect the variable solubility of these phases. The aqueous Fe was $<10^{-12}$ molal; the aqueous Cr was $<10^{-9}$ molal; the aqueous Ni was $<10^{-5}$ molal for the largest quantity of SS316L interaction. The major elements are identical to several significant digits among the evaporation simulations (see Output DTN: SN0705PAEBSPCE.011, spreadsheet: *Steel_evaluation.xls*) and there is negligible impact on the key chemical parameters provided to TSPA-LA.

6.8.4.2 Summary of Steel/Water Interactions

Not all of the components in the steels were used in these analyses. However, approximately 95% by weight of the components of SS316L were used and approximately 99% by weight of the components of A588 were used (see Section 6.8.3 and Output DTN: SN0705PAEBSPCE.011, spreadsheet: *DegradationMolality_PCEREV06.xls*, tab: "degradation"; and spreadsheet: *A588_corrosion_calcs.xls*, tab: "A588 moles"). This is a reasonable approach and captures the range of steel–water interactions adequately.

By increasing the amount of steel corrosion well beyond the calculated values, which must assume a specific corrosion rate and surface area of the steels, the conclusions of this analysis are not tied directly to a particular design specification or set of corrosion data. In general, these conclusions reinforce that if there is no limit to the oxygen supply, the result of adding more steel to the water is simply the formation of more corrosion product precipitates.

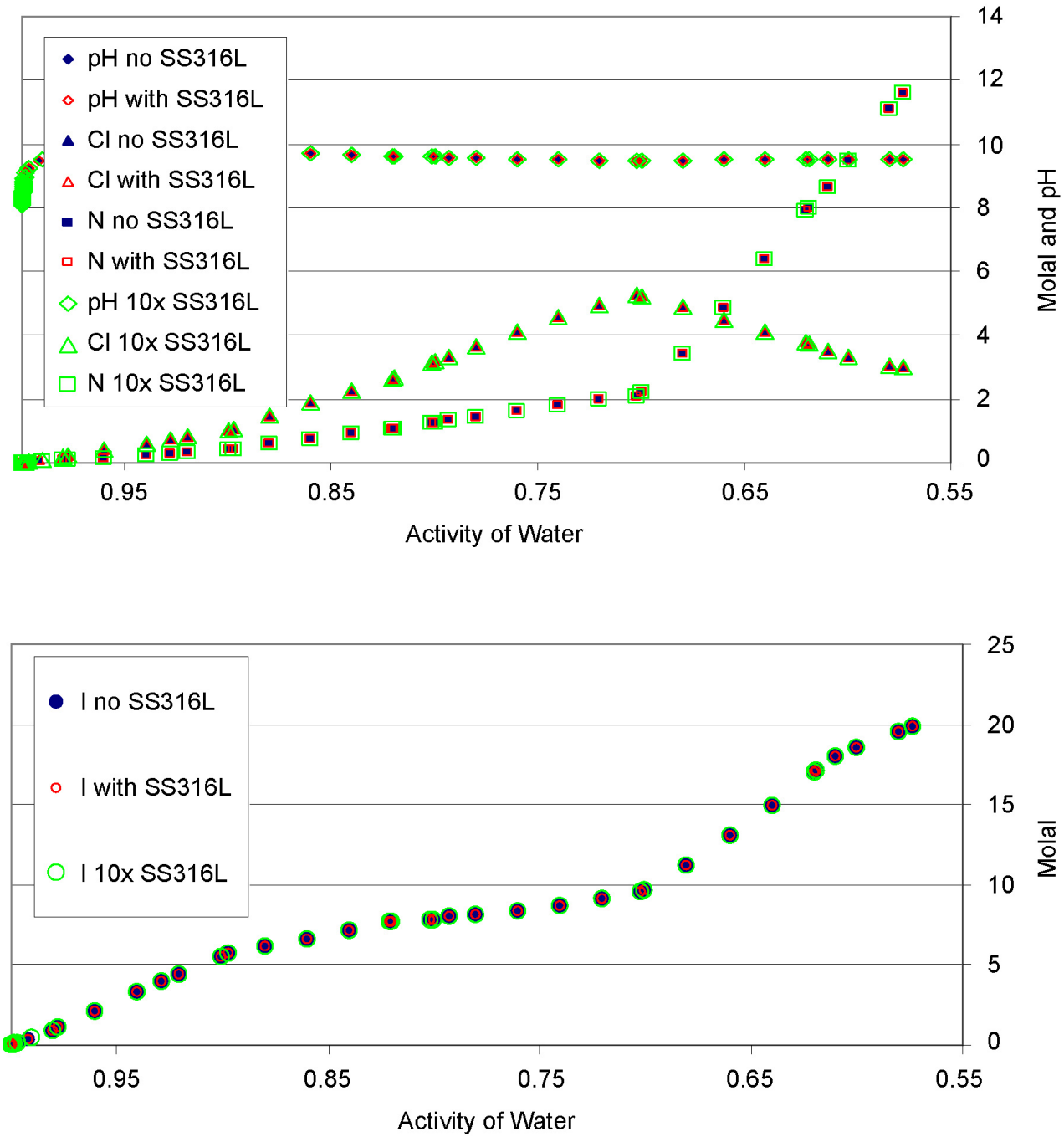

Source: Output DTN: SN0705PAEBSPCE.011, spreadsheet: *Steel_evaluation.xls*, tab: "Gp1 SS316L comparison plots."

Figure 6.8-9. Evaporative Evolution of Group 1 Water with WRIP = 0, with Trace Fe, Cr, Ni (blue symbols), with 1.3×10^{-2} moles SS316L Added (red symbols), and with 1.3×10^{-1} moles SS316L Added (green symbols) for the Key Chemical Parameter Provided to TSPA-LA (top: pH, [Cl], and [N]; bottom: ionic strength, *I*)

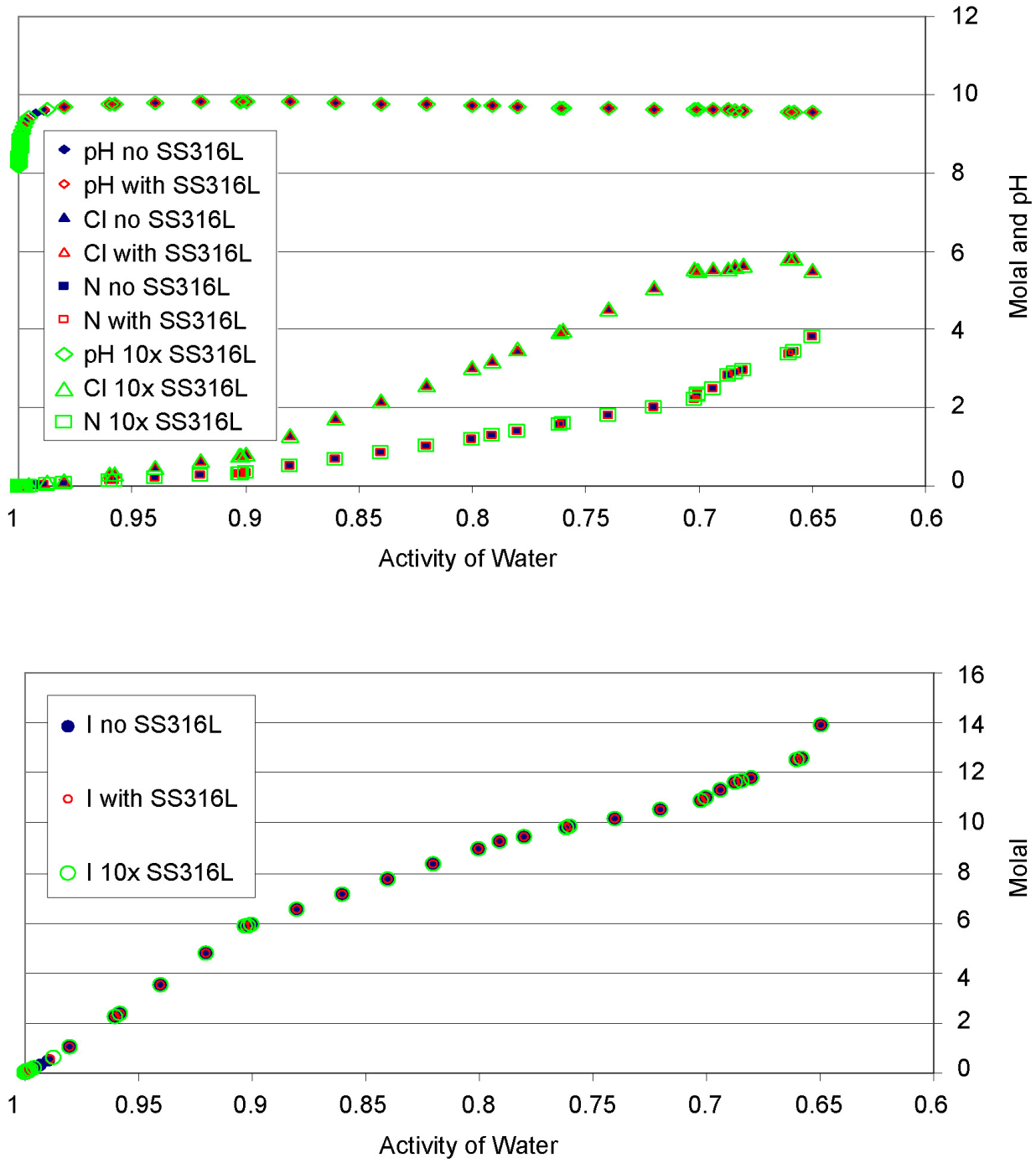

Source: Output DTN: SN0705PAEBSPCE.011, spreadsheet: *Steel_evaluation.xls*, tab: "Gp1 SS316L comparison plots."

Figure 6.8-10. Evaporative Evolution of Group 1 Water with WRIP = G, with Trace Fe, Cr, Ni (blue symbols), with 1.3×10^{-2} moles SS316L Added (red symbols), and with 1.3×10^{-1} moles SS316L Added (green symbols) for the Key Chemical Parameter Provided to TSPA-LA (top: pH, [Cl], and [N]; bottom: ionic strength, *I*)

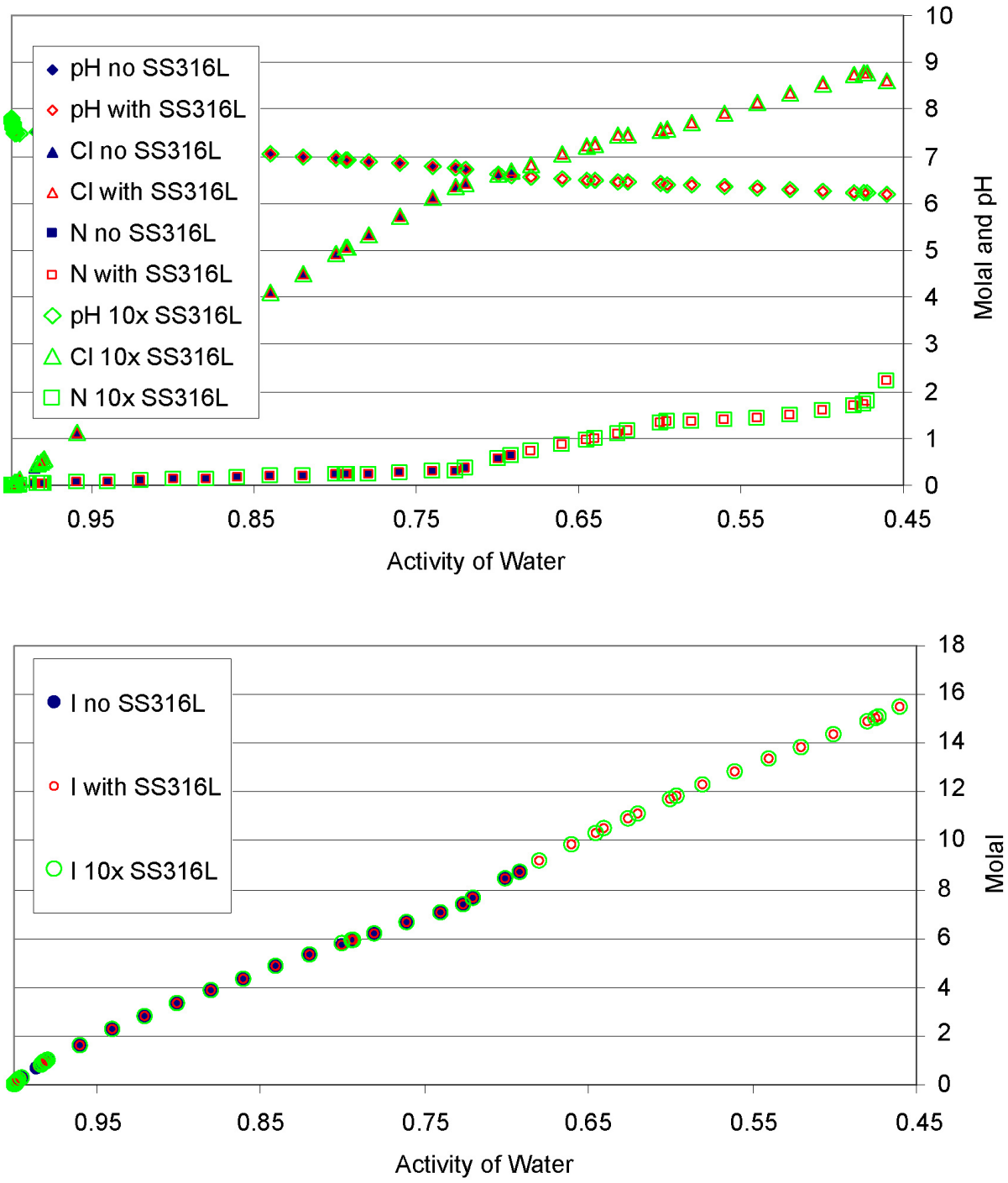

Source: Output DTN: SN0705PAEBSPCE.011, spreadsheet: *Steel_evaluation.xls*, tab: "Gp3 SS316L comparison plots."

Figure 6.8-11. Evaporative Evolution of Group 3 Water with WRIP = 0, with Trace Fe, Cr, Ni (blue symbols), with 1.3×10^{-2} moles SS316L Added (red symbols), and with 1.3×10^{-1} moles SS316L Added (green symbols) for the Key Chemical Parameter Provided to TSPA-LA (top: pH, [Cl], and [N]; bottom: ionic strength, *I*)

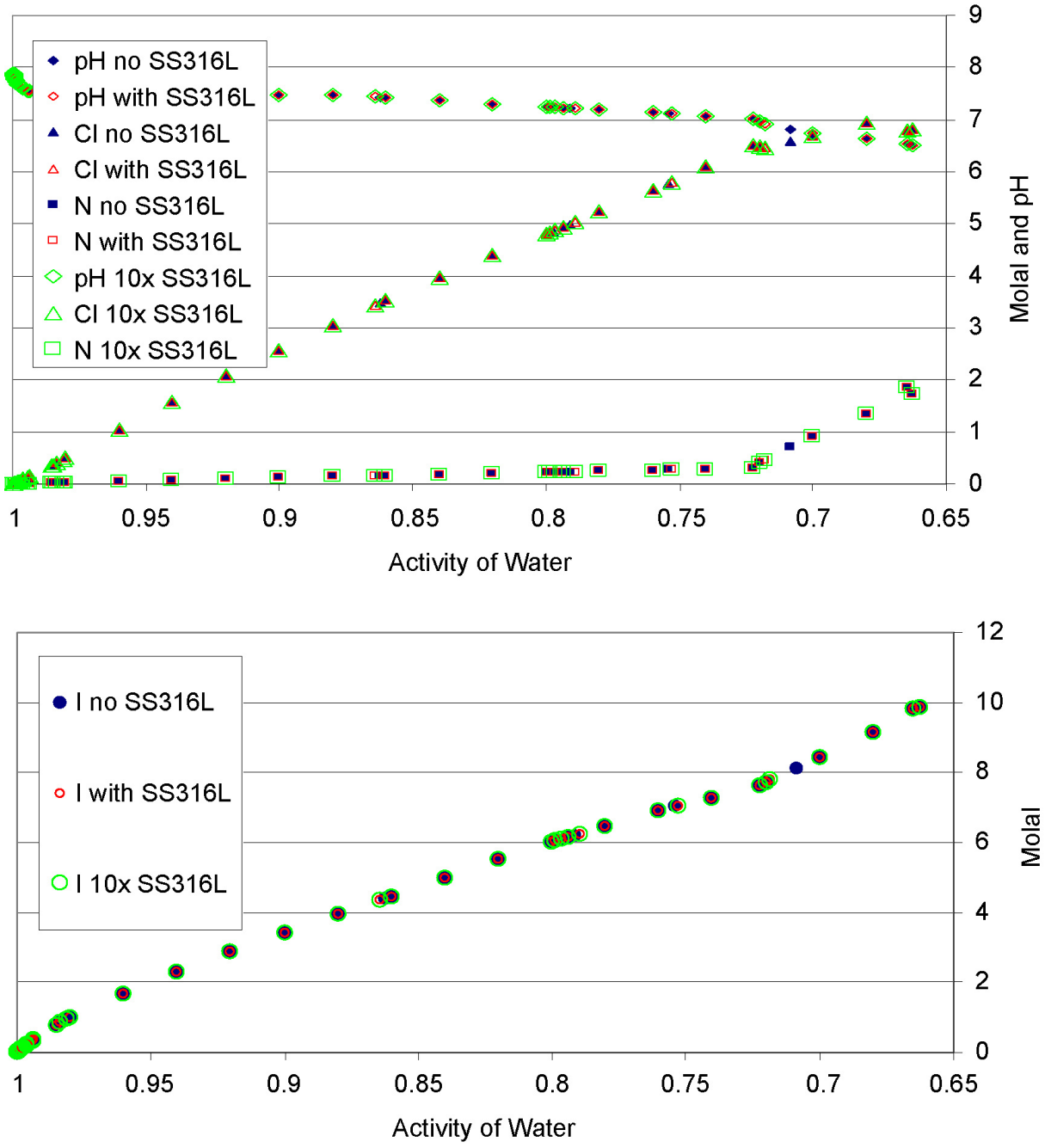

Source: Output DTN: SN0705PAEBSPCE.011, spreadsheet: *Steel_evaluation.xls*, tab: "Gp3 SS316L comparison plots."

Figure 6.8-12. Evaporative Evolution of Group 3 Water with WRIP = G, with Trace Fe, Cr, Ni (blue symbols), with 1.3×10^{-2} moles SS316L Added (red symbols), and with 1.3×10^{-1} moles SS316L Added (green symbols) for the Key Chemical Parameter Provided to TSPA-LA (top: pH, [Cl], and [N]; bottom: ionic strength, *I*)

6.8.5 Evaluation of the Impact of Nitrate Reduction by Steel

Reduction of nitrate in drift seepage requires the presence of reduced chemical species, the most abundant being steels and adventitious organic matter. Nitrate can, in theory, be reduced to N_2 or NH_3, by the addition of electrons acquired in the corrosion of steel, e.g.:

$$3NO_3^- + 5Fe_{(steel)} + 3H^+ + H_2O \rightarrow 5FeOOH_{(goethite)} + 3/2N_2 \qquad \text{(Eq. 6.8-11)}$$

or

$$3NO_3^- + 8Fe_{(steel)} + 3H^+ + 7H_2O \rightarrow 8FeOOH_{(goethite)} + 3NH_3 \qquad \text{(Eq. 6.8-12)}$$

Other reductants produced in the corrosion of steel that are able to reduce nitrate include H_2 and Fe^{2+}. Their production might lead indirectly to the reduction of nitrate in the invert. However, both reduced intermediates are rapidly oxidized to, respectively, water and Fe(III)-solids, when free oxygen is present. Microorganisms often facilitate the relevant electron transfer reactions. Nitrate reduction by microorganisms tends to occur under reducing conditions, i.e., only after free oxygen has become depleted (Stumm and Morgan 1981 [DIRS 100829], p. 454).

Steel corrosion is a surface-controlled process and nitrate reduction by steel is favored by surface exposure of reduced Fe (and Cr and Ni) sites. When free oxygen is present, exposed Fe sites tend to be rapidly oxidized to Fe(III)-hydroxide solids, a process that inhibits the reactions above. Subsequent corrosion beneath this oxide coating occurs by the diffusion of water and electron acceptors through, and electron donors out of, this layer. For nitrate to be reduced during corrosion beneath a passive surface layer it must encounter reactive intermediates (e.g., H_2 and/or Fe^{2+}) in or on the layer before free oxygen does. And it must do so repeatedly: denitrification ($NO_3^- \rightarrow N_2$) requires 5 electrons, meaning 5 encounters with Fe^{2+} or 2.5 encounters with H_2. Conversion of nitrate to ammonia involves a net transfer of eight electrons, hence greater interaction. Because O_2 is a more powerful oxidant than NO_3^-, and because it will be more abundant under ambient conditions, reduction of O_2—not nitrate—should prevail (Stumm and Morgan 1981 [DIRS 100829], p. 461).

Low alloy steel in the drift corrodes rapidly (see Section 6.5.1) and within a few thousand years may be completely oxidized given O_2 levels near ambient. Stainless steels corrode roughly an order of magnitude slower than low alloy steels under oxidizing conditions and will therefore certainly be present in abundance once seepage re-enters the drift (Section 6.5.2). Note that relatively slow corrosion of stainless steels is a direct result of the oxidation inhibiting characteristics of the oxide coating that passivates and protects their surface. Under oxidizing conditions, the presence of the passive surface layer, and the much greater abundance and selectivity of oxygen relative to nitrate in the drift environment, will work against a reduction of seepage water nitrate values.

6.9 IN-DRIFT SEEPAGE DILUTION/EVAPORATION ABSTRACTION

In-drift water compositions resulting from heating and evaporation of seepage are calculated by applying the IDPS process model (SNL 2007 [DIRS 177411]) to the NFC seepage water compositions (see Section 6.6). This model includes the chemical influence of the in-drift

atmosphere and provides a set of mineral suppressions to accurately capture evaporative and precipitation processes. Calculated outputs from the P&CE dilution/evaporation abstraction are presented in the form of lookup tables for use as inputs to TSPA-LA calculations (Output DTN: SN0701PAEBSPCE.001). Section 6.15.2 describes the TSPA implementation instructions for the integrated invert chemistry abstraction, which utilizes the same lookup tables developed for the dilution/evaporation abstraction discussed below. Additional instructions are provided to TSPA to integrate the invert chemistries provided by this report with those provided by the IPC report (SNL 2007 [DIRS 180506]) (see Table 6.15-2). The description below is therefore germane to the integrated invert chemistry abstraction as well.

6.9.1 Diluted and Evaporated Seepage Water Inputs

Section 6.6 describes the pore-water selection process that examined more than 100 pore-water analyses and distilled from these 34 TSw waters for use by the NFC model. Four representative group waters were selected from among these 34, and are called Groups 1, 2, 3, and 4. This section proceeds from those four group waters and creates the abstraction based upon them at various environmental relative humidity, temperature, and pCO_2 conditions.

The four EQ3 input files with NFC model starting water compositions were equilibrated using EQ3NR (Output DTN: SN0701PAEBSPCE.002). EQ3NR calculates (see Section 6.2.1) an equilibrium aqueous speciation. It does not equilibrate the solutions with respect to solids and gases. The Al concentrations for each of the starting group waters were set by heterogeneous equilibration with alkali feldspar. The selection of an appropriate alkali feldspar composition and thermodynamic properties is discussed in Section 4.1.8. Subsequent EQ6 calculations were used to precipitate the solids from the equilibrated fluids. The EQ6 pickup files, thus produced, were then appended to a series of seepage simulations. The NFC model assumes that the potential seepage waters are in equilibrium with calcite and amorphous silica with varying degrees of water–rock interactions. This is executed computationally by titrating into each seepage fluid excess calcite, amorphous silica, and varying quantities of alkali feldspar. The temperature was increased from ambient, 23°C, to three different maximum drift wall temperatures, 30°C, 70°C, and 96°C. Seepage simulations were conducted as a function of starting group water (Groups 1 through 4), eleven discrete WRIP values (see Table 6.3-5), and maximum drift wall temperature for seepage. Each of the pickup files from the seepage calculations were appended to both a dilution and an evaporation EQ6 simulation. The outputs from these dilution/evaporation calculations were extracted using GETEQDATA (see Table 3.1-1) to construct the lookup tables provided to TSPA-LA. The details of the dilution/evaporation simulations are described below. All of the files supporting the development of the NFC seepage water chemistries and the P&CE seepage dilution/evaporation abstraction are archived in Output DTNs: SN0701PAEBSPCE.001 and SN0701PAEBSPCE.002.

The P&CE seepage dilution/evaporation abstraction is designed to cover a range of environmental conditions that the infiltrating seepage waters will encounter. Once the drift wall temperature cools to 96°C, the boiling point of water at repository elevation, seepage may enter the drift. Temperature and pCO_2 were varied to capture their effects on the compositional evolution of the seepage waters during dilution and evaporation. Three values are chosen for each parameter, such that the expected ranges are covered while minimizing uncertainties associated with interpolation and extrapolation. For temperature, the values were 30°C, 70°C,

and 100°C. Note that the temperatures used in the dilution/evaporation abstraction correspond to the waste package surface and hence the upper limit is slightly higher than the maximum drift wall temperature used in the seepage simulations, 96°C. The pCO_2 values were 10^{-2}, 10^{-3}, and 10^{-4} bar. Each temperature is combined with each CO_2 pressure, resulting in nine combinations for each group water, and each of these cases is combined with the eleven discrete WRIP values (Table 6.3-5). The result is 396 EQ6 simulations each for the dilution and the evaporation calculations. The dilution simulations are combined with their corresponding evaporation simulations to construct a single, continuous lookup table that contains the data from both files. The lookup tables are archived in Output DTN: SN0701PAEBSPCE.001 (folder: \Lookup Tables).

To cover the range of expected in-drift relative humidity values for seepage, the waters were evaporated to dry out and also diluted by a factor of 100. The starting group waters are sufficiently dilute that they represent solutions in equilibrium with relative humidity between 99.9 and 99.99%. Dilution by water vapor is simulated for potential relative humidity values higher than the equilibrium relative humidity values of the starting group waters. Thus, for each temperature and pCO_2 combination, two EQ6 input files were generated, one for evaporation and one for dilution. The resulting EQ6 input and output data files for the group waters are archived in Output DTN: SN0701PAEBSPCE.001. The file nomenclature is described in Section 6.15.1 and also in the readme file associated with that DTN.

In addition to the environmental variables, two additional mineral suppressions were added to the IDPS mineral suppressions (SNL 2007 [DIRS 177411]) for the dilution/evaporation simulations; the end-member feldspars albite and maximum microcline. Both of these minerals are structurally complex and typically form at elevated temperatures (Deer et al. 1966 [DIRS 162338]). Their precipitation during the relatively rapid evaporation of seepage waters on the surface of a hot waste package would be kinetically hindered. These mineral suppressions are irrelevant to the dilution calculations, but are included to simplify the construction of the EQ6 input files.

Initially, a third mineral suppression was entered into the EQ6 input files: huntite. The P&CE seepage dilution/evaporation abstraction generally takes its mineral suppressions from the IDPS model report (SNL 2007 [DIRS 177411]). Between the times the P&CE EQ6 simulations were conducted and the IDPS model was finalized, huntite was removed from the IDPS model's suppressed minerals list except for one sensitivity study. Huntite is a calcium, magnesium carbonate mineral with chemical formula $CaMg_3(CO_3)_4$. Huntite is structurally similar to calcite and has been observed to precipitate from cool groundwaters that are magnesium-rich (Deer et al. 1966 [DIRS 162338], p. 652). In order to account for the effect of the erroneous suppression of this mineral, all of the evaporation simulations were scrutinized for huntite saturation indices near unity. If the saturation index was found to be positive at any point along the evaporative pathway, then the simulation was corrected and huntite was allowed to precipitate. In all, 77 EQ6 evaporation simulations were affected and 77 revised lookup tables were produced. Output DTN: SN0701PAEBSPCE.001 was revised to include the new EQ6 input/output files and the new lookup tables. The revision is documented in the DTN, the readme file associated with the DTN, and in the Technical Data Management System.

6.9.2 Lookup Tables

The abstracted results of the dilution and evaporation calculations provided as direct input to TSPA-LA calculations are summarized in a set of combined dilution/evaporation lookup tables documented in Output DTN: SN0701PAEBSPCE.001. These lookup tables include stated boundary conditions, abstracted output, and results of supplemental calculations. Each dilution/evaporation lookup table corresponds to two of the EQ6 output files (one each for dilution and evaporation) also archived in Output DTN: SN0701PAEBSPCE.001. Each row in these tables provides output parameter values as the water incrementally evolves due to evaporation or dilution, given the defined boundary conditions. Each value is defined by a unique equilibrium relative humidity, concentration factor, and relative evaporation rate. Because the lookup tables contain combined dilution/evaporation data, the ambient case is highlighted yellow in each table. Above the ambient line is the dilution data and below is the evaporation data.

The general lookup table format and the calculations placed in the lookup tables are developed and described in the IDPS model report (SNL 2007 [DIRS 177411], Sections 6.6.3.5 and 6.7.3). The first three columns of these tables are supplemental spreadsheet calculations for concentration factor (*CF*), relative evaporation rate (*Qe*/*Qs*), and dilution factor (*DF*). The next column is the equilibrium *RH*, calculated by multiplying the activity of water (in column L) by 100%. The rest of the columns are filled with selected output data extracted from the EQ6 output files using GETEQDATA (see Table 3.1-1). Columns E through H show reaction progress and the boundary conditions for the starting water (i.e., the temperature and the partial pressures of oxygen and carbon dioxide). Columns I through Y show reaction progress, pH, ionic strength, mass of H_2O in the system, and the total concentrations of the aqueous elemental components. Columns Z through AA present reaction progress, and the mass of H_2O. Finally, columns AB through BE show the amounts of minerals accumulated.

The values in the lookup tables may be used to define equilibrium chemical response surfaces so that interpolations and extrapolations (pCO_2 parameter only; see Section 6.15.1) may be obtained for more precise input values not provided in the tables.

6.9.3 Illustration of Results

Figures 6.9-1 through 6.9-4 graphically illustrate the dilution/evaporation results from two lookup tables: *10P3T70.xls* and *1JP3T70.xls* (Output DTN: SN0701PAEBSPCE.001). These are Group 1 dilution/evaporation results at a temperature of 70°C and a pCO_2 of 10^{-3} bar. The first file represents the ambient case, or no water–rock interaction (WRIP = 0) and is illustrative of high percolation flux rates, cooler temperatures and/or shorter water–rock contact times. The second case represents a high level of water–rock interaction (WRIP = J) illustrative of median to lower percolation fluxes at higher temperatures with longer contact times. Group 1 water is chosen as an illustration. The same plots have been generated for each of the water types over the range of potential WRIP and environmental values and are archived in Output DTN: SN0701PAEBSPCE.001. Figures 6.9-1 and 6.9-2 plot the total elemental aqueous concentrations and pH as a function of relative humidity and concentration factor. Figures 6.9-3 and 6.9-4 plot pH, the fixed CO_2 and O_2 pressures, and the moles of minerals precipitated from one kilogram of incoming water as a function of relative humidity and concentration factor.

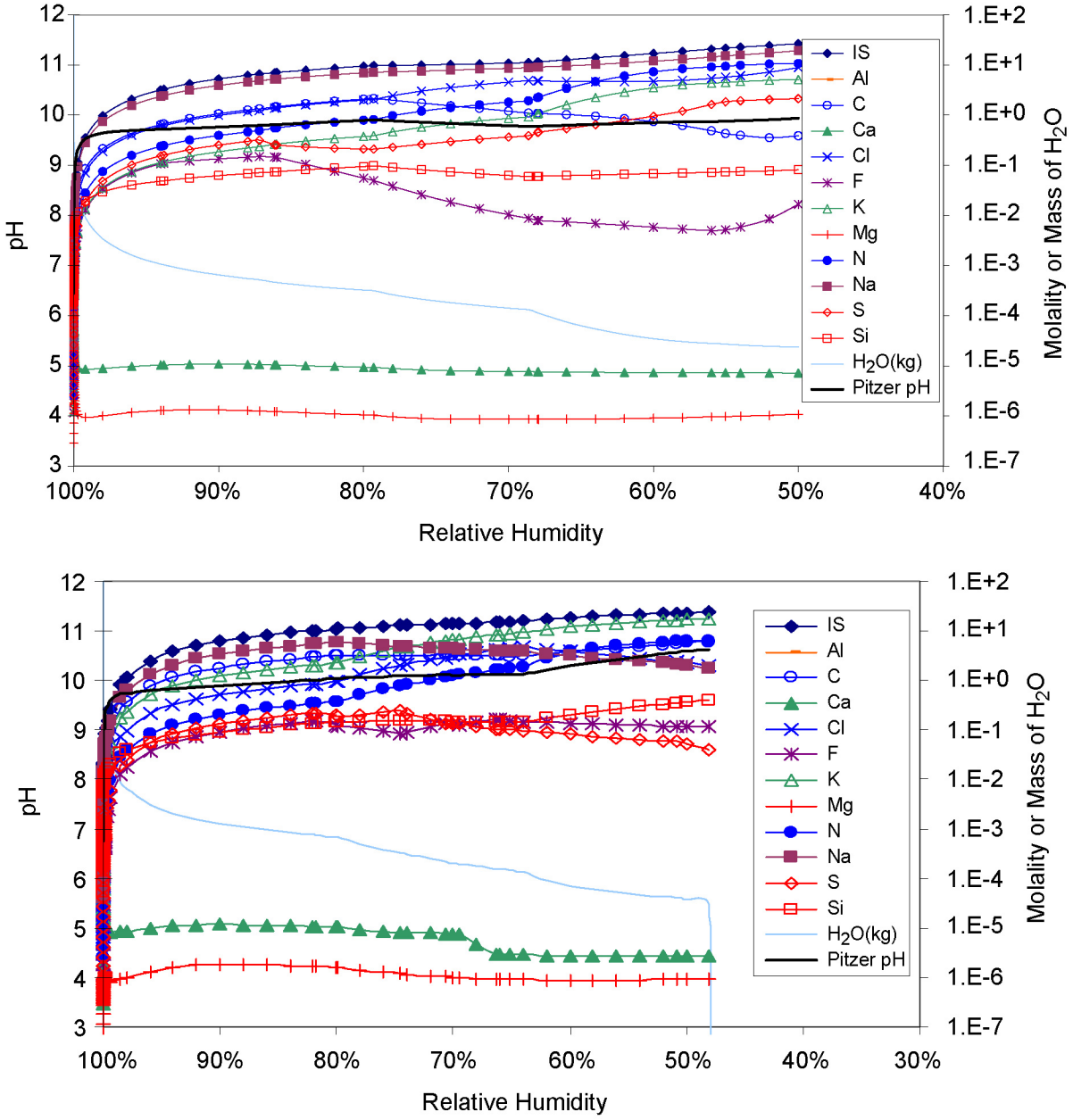

Source: Output DTN: SN0701PAEBSPCE.001.

NOTE: IS = ionic strength.

Figure 6.9-1. Predicted Compositional Evolution during Dilution/Evaporation of Group 1 Waters at 70°C, No Water–Rock Interaction and pCO_2 10^{-3} bar, versus Relative Humidity (upper) from Lookup Table *10p3t70.xls*; Predicted Compositional Evolution during Dilution/Evaporation of Group 1 Waters at 70°C, High Water–Rock Interaction and pCO_2 10^{-3} bar, versus Relative Humidity (lower) from Lookup Table *1jp3t70.xls*

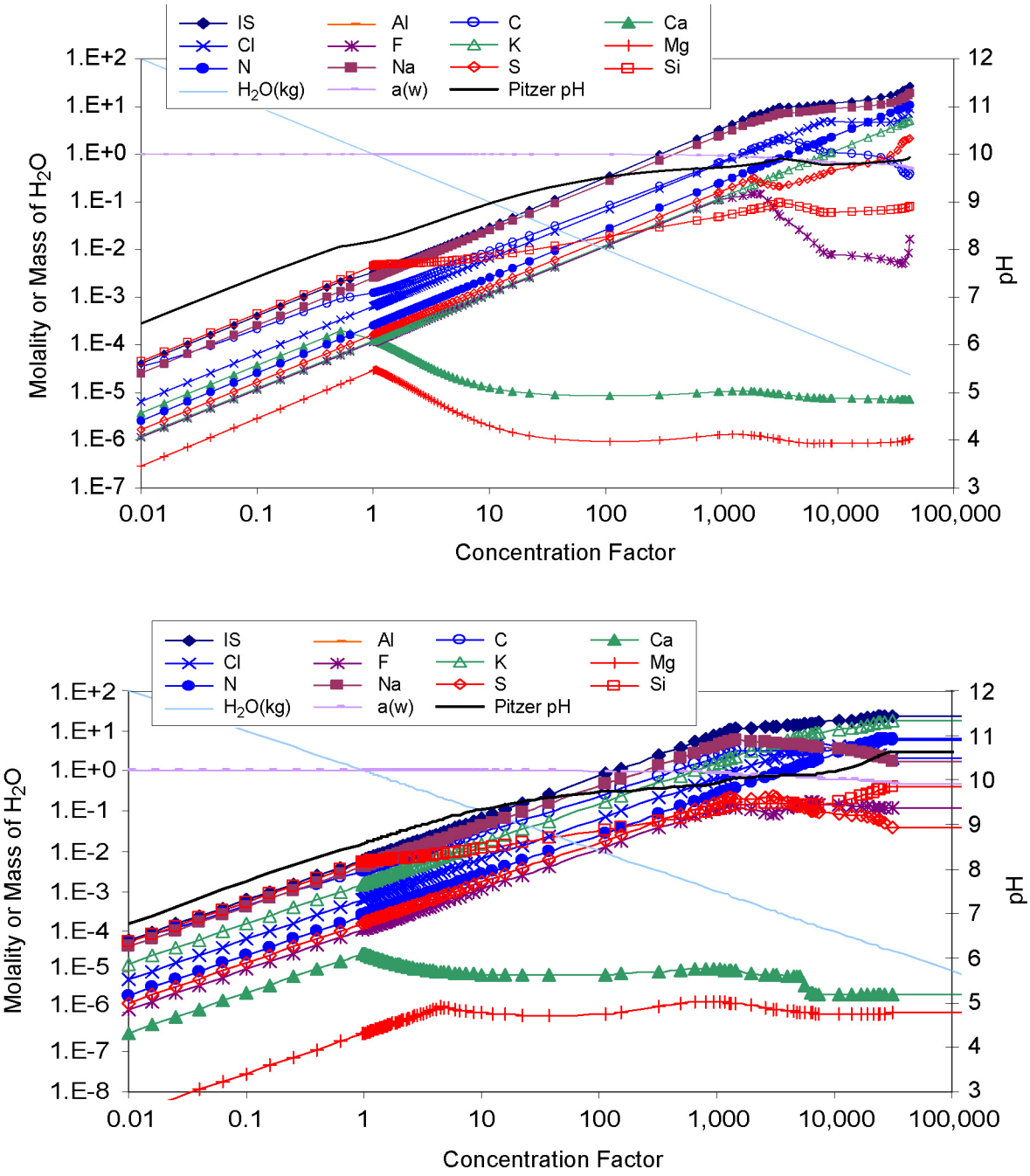

Source: Output DTN: SN0701PAEBSPCE.001.

Figure 6.9-2. Predicted Compositional Evolution during Dilution/Evaporation of Group 1 Waters at 70°C, No Water–Rock Interaction and pCO_2 10^{-3} bar, versus Concentration Factor (upper) from Lookup Table *10p3t70.xls*; Predicted Compositional Evolution during Dilution/Evaporation of Group 1 Waters at 70°C, High Water–Rock Interaction and pCO_2 10^{-3} bar, versus Concentration Factor (lower) from Lookup Table *1jp3t70.xls*

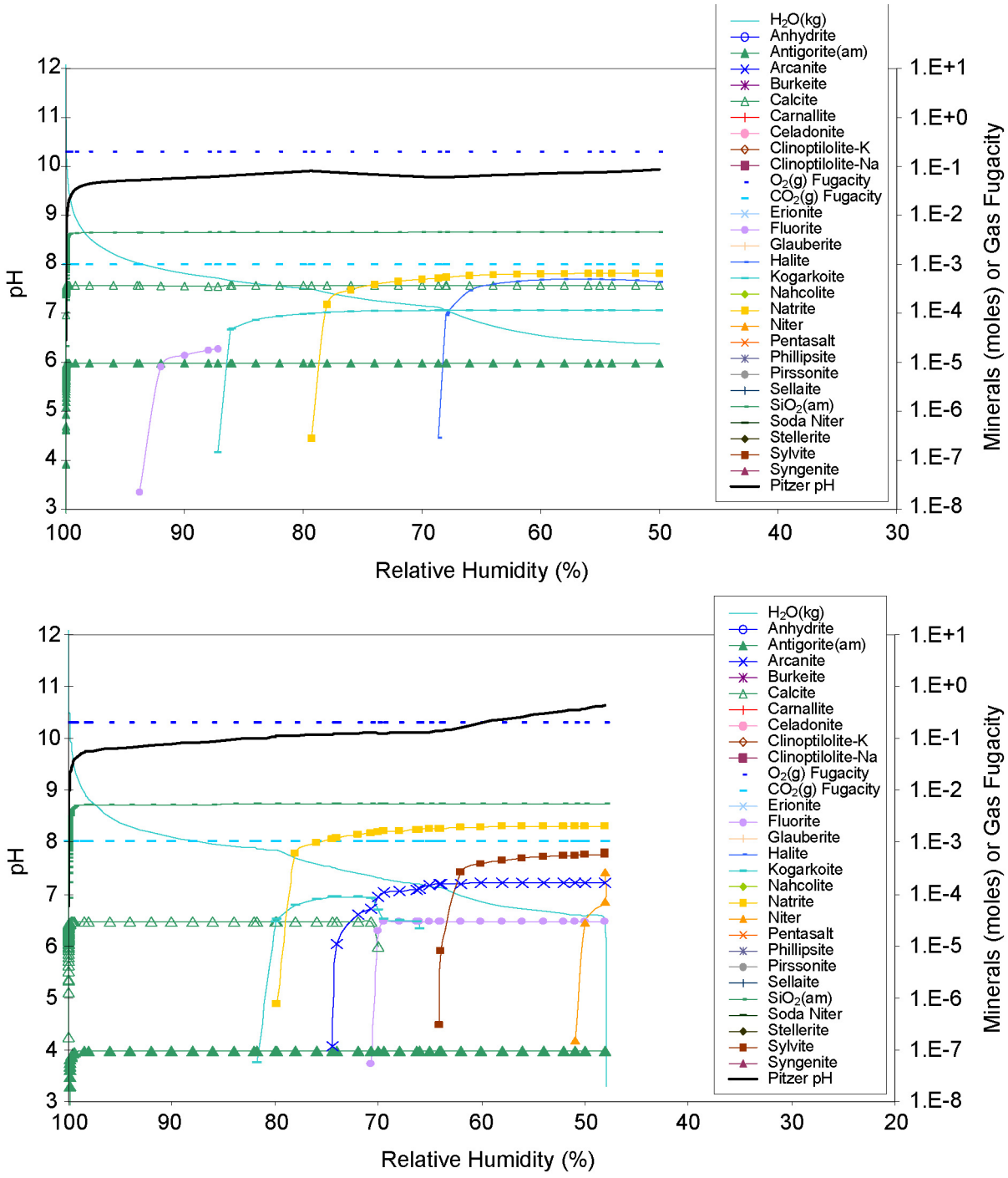

Source: Output DTN: SN0701PAEBSPCE.001.

NOTE: The legend contains all the potential mineral precipitates while the graph contains only those minerals that precipitate at the parameters listed above.

Figure 6.9-3. Predicted Mineral Precipitation as Group 1 Waters Evaporate at 70°C, No Water–Rock Interaction and pCO_2 10^{-3} bar, versus Relative Humidity from Lookup Table *10p3t70.xls* (upper); Mineral Precipitation as Group 1 Waters Dilute/Evaporate at 70°C, WRIP = J and pCO_2 10^{-3} bar, versus Relative Humidity from Lookup Table *1Jp3t70.xls* (lower)

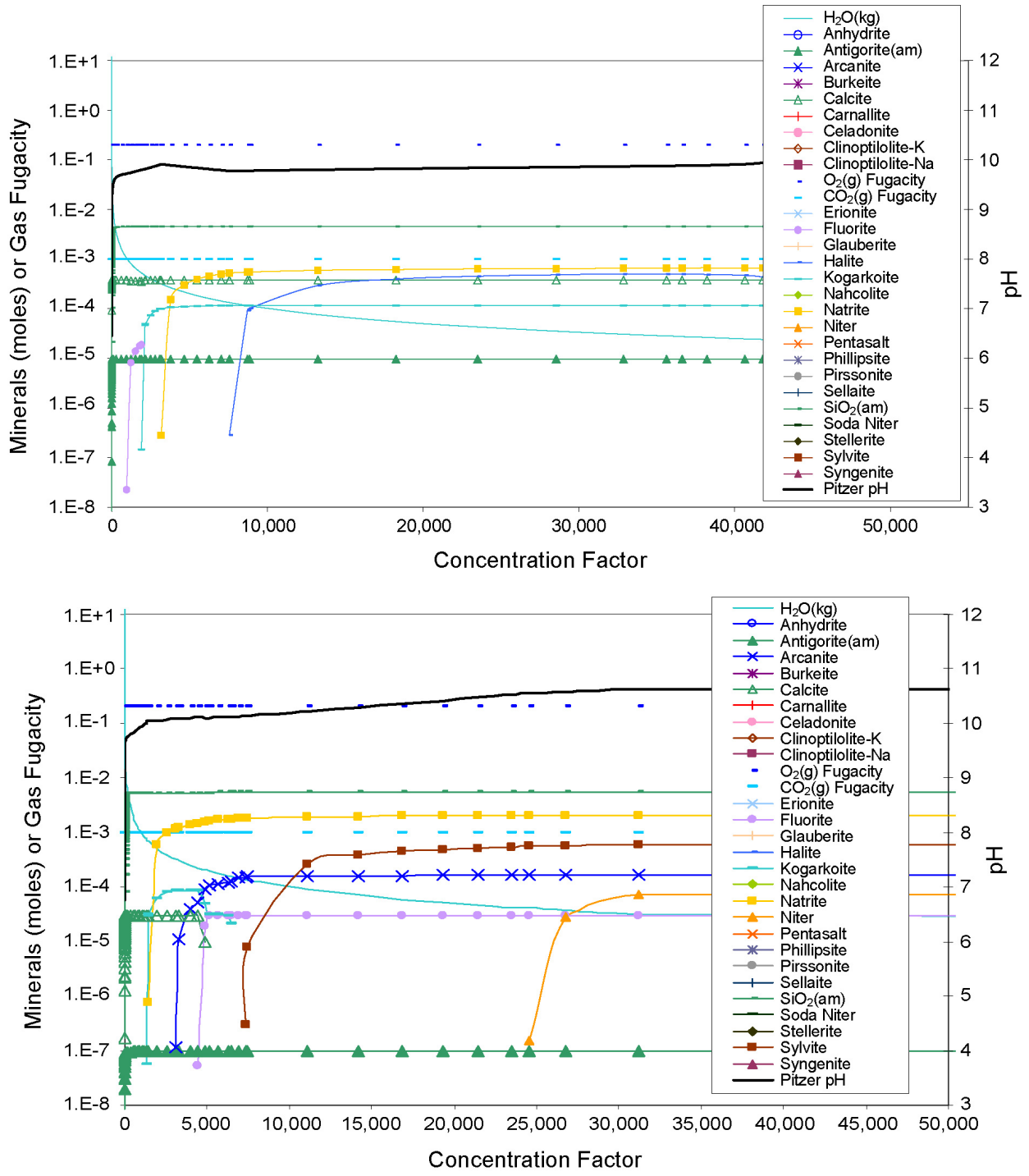

Source: Output DTN: SN0701PAEBSPCE.001.

Figure 6.9-4. Predicted Mineral Precipitation as Group 1 Waters Dilute/Evaporate at 70°C, No Water–Rock Interaction and pCO_2 10^{-3} bar, versus Concentration Factor from Lookup Table *10p3t70.xls* (upper); Predicted Mineral Precipitation as Group 1 Waters Dilute/Evaporate at 70°C, WRIP = J and pCO_2 10^{-3} bar, versus Concentration Factor from Lookup Table *1Jp3t70.xls* (lower)

The figures presented in this section allow a visual assessment of the evolutionary pathways for the seepage waters represented here. It is immediately apparent that with an increasing WRIP there is an increase in K in the end-point brine (Figures 6.9-1 and 6.9-2). The end-point brine is Na-Cl-N-rich for the WRIP = 0 case with a pH of approximately 10. The WRIP = J case evolves to a K-Cl-N-rich brine and gained a full unit of pH at dryout, a direct effect of increased alkali feldspar to the solution. Both waters have relatively low Mg, limited by the precipitation of amorphous antigorite (Figures 6.9-3 and 6.9-4). For both waters, amorphous silica and calcite are saturated. The sequence of mineral precipitation changes as WRIP increases. For WRIP = 0, the sequence is fluorite, CaF_2, kogarkoite, Na_3SO_4F, natrite, Na_2CO_3, and finally halite, NaCl. The difference in the sequence of mineral precipitates due to evaporation for WRIP = J is indicative of the increase in Na and K due to the added feldspar. The sequence is kogarkoite, Na_3SO_4F, natrite, Na_2CO_3, arcanite, K_2SO_4, fluorite, CaF_2, sylvite, KCl, and just before dryout, niter, KNO_3. (For additional discussion of mineral precipitation sequence as a function of starting group water and increasing WRIP, see Section 6.13.)

Similar figures were generated for each of the 396 discrete dilution/evaporation simulations and are archived in Output DTN: SN0701PAEBSPCE.001. The lookup tables archived in that DTN contain the calculated molal quantities of precipitating minerals (see tab "lookup table" in each spreadsheet). The figures attached to these lookup tables may or may not contain all of the precipitated phases and should be used for illustrative purposes only. Additional discussion of the EBS physical and chemical environment can be found in Section 6.13.

6.9.4 Limited Dilution in the Invert

Dilution of seepage waters in the invert is not likely because seepage represents a source for evaporation, rather than condensation. Seepage water enters the drift at the temperature of the drift wall, then warms on contact with the EBS, including the invert. The drift wall is cooler and acts as a sink for condensing vapor. Cooler waste package locations act as additional sinks, with the result that seepage will not typically become more dilute for most locations. However, for those rare cases where drift wall condensation is significant, a degree of dilution for invert seepage may be possible. Drift wall condensation as represented in TSPA originates above the drip shield and follows the same path as seepage through the engineered barrier system. Drift wall condensation may occur separately or in conjunction with seepage. The composition of drift wall condensation can range between very dilute (e.g., dilute solution of silica and bicarbonate) and more concentrated (i.e., like seepage). For conditions when drift wall condensation occurs with seepage, a reasonable upper bound approximation is used to represent the maximum attainable state of dilution. To calculate this dilution maximum, solutions were equilibrated with calcite, amorphous silica, for three temperatures (30°C, 70°C, and 100°C) and three pCO_2 values (10^{-4}, 10^{-3}, and 10^{-2}). These EQ3/6 simulations are archived in Output DTN: SN0706PAEBSPCE.016. Both calcite and amorphous silica are ubiquitous in the repository rock (see Section 6.3.2) and are expected to equilibrate, or nearly equilibrate, with waters upon contact at times of a few days to a few years. Thus, assuming equilibrium with these two phases is reasonable for assessing invert dilution. The dilution simulation results are plotted for each of the three temperatures and pCO_2 values in Figure 6.9-5. For comparison, all 396 P&CE seepage water are plotted as well. The P&CE seepage water data represent the equilibrium activities of water, as extracted from the first reaction step of the evaporation files archived in Output DTN: SN0701PAEBSPCE.001. The full range of data is shown and covers

not only the nine combinations of three temperatures and three pCO_2 values but also all 11 WRIP values. The maximum equilibrium relative humidity for all examined conditions was 99.994% for the T = 30°C, $pCO_2 = 10^{-4}$ bar maximum dilution case (see Table 6.9-1). Equilibrium RH limits are provided on the basis of this analysis to TSPA for each of the nine combinations of T and pCO_2 used by the P&CE dilution/evaporation abstraction model (Table 6.9-1) and implementation instructions are provided in Section 6.15.2.

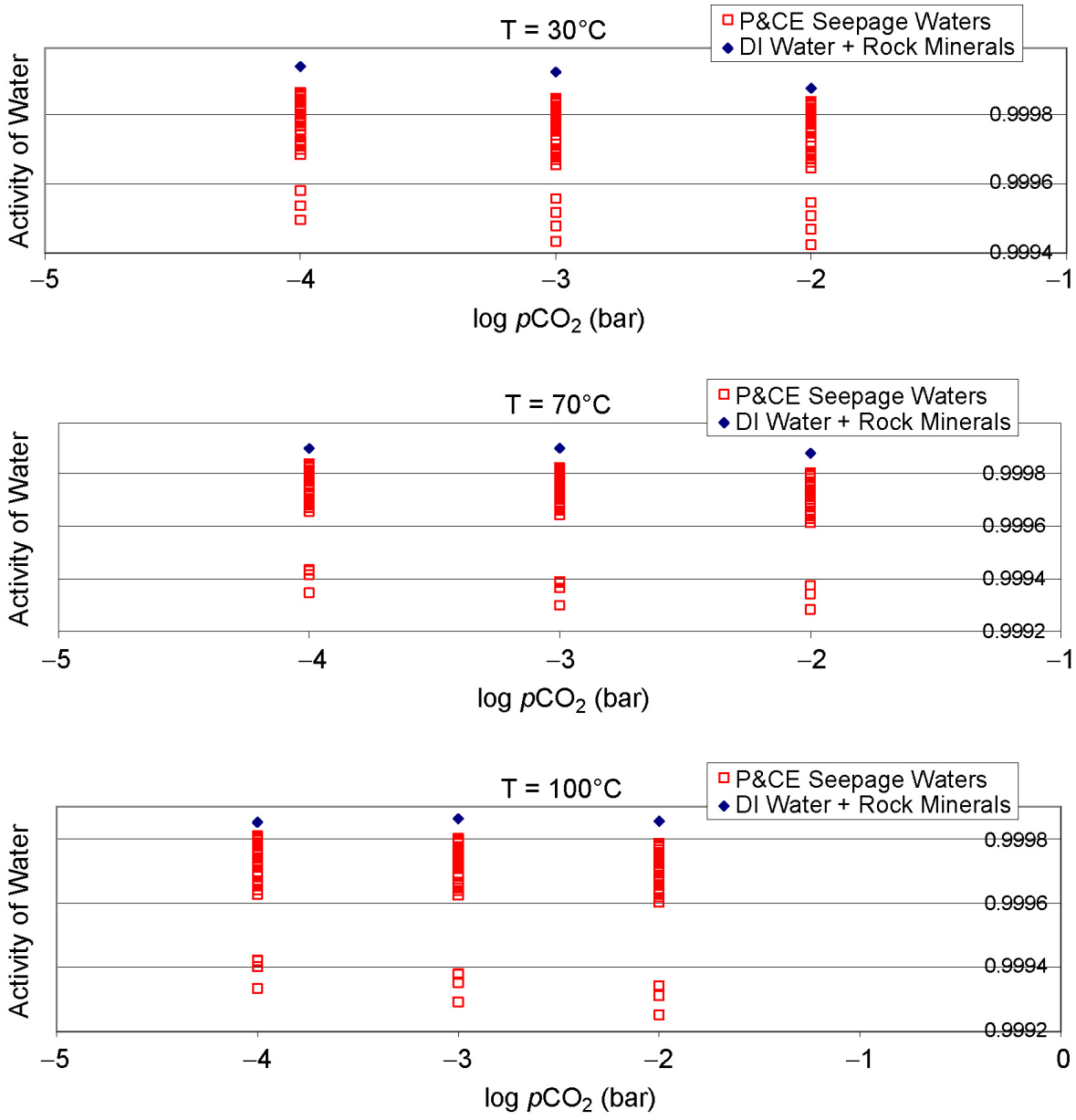

Source: Output DTN: SN0706PAEBSPCE.016.

NOTE: The dilution maximums were calculated assuming deionized water in equilibrium with calcite and amorphous silica over the range of T and pCO_2 utilized by the P&CE dilution/evaporation abstraction model.

Figure 6.9-5. RH Boundaries for Invert Dilution as a Function of Temperature and log pCO_2

Table 6.9-1. Upper RH Boundaries for Seepage Dilution in the Invert

Temperature (°C)	CO_2(g) Log Fugacity	a(w)	RH Boundary (%)
30	−2	0.999875	99.9875
30	−3	0.999921	99.9921
30	−4	0.999937	99.9937
70	−2	0.999875	99.9875
70	−3	0.999895	99.9895
70	−4	0.999894	99.9894
100	−2	0.999855	99.9855
100	−3	0.999862	99.9862
100	−4	0.999851	99.9851

Source: Output DTN: SN0706PAEBSPCE.016.

6.10 EVALUATION OF DUST DEPOSITED ON WASTE PACKAGES

The following is a summary of the report *Analysis of Dust Deliquescence for FEP Screening* (SNL 2007 [DIRS 181267]). This brief summary describes the general conclusions of the dust screening analysis that has led to the decision to screen out localized corrosion caused by deliquescence of dust (SNL 2007 [DIRS 181267], Section 7.1.5). The reader is referred to the source document for additional information.

Small amounts of dust will be deposited on the surfaces of waste packages in drifts at Yucca Mountain during the operational and the preclosure ventilation periods. Salts present in the dust will deliquesce as the waste packages cool and relative humidity in the drifts increases. The source report (SNL 2007 [DIRS 181267], Sections 6.4 and 6.5) evaluates the potential for brines formed by dust deliquescence to initiate and sustain localized corrosion that results in failure of the waste package outer barrier and early failure of the waste package. These arguments have been used to show that dust deliquescence-induced localized or crevice corrosion of the waste package outer barrier (Alloy 22) is of low consequence with respect to repository performance (SNL 2007 [DIRS 181267], Section 1.1).

Measured atmospheric and underground dust compositions are the basis of thermodynamic modeling and experimental studies to evaluate the likelihood of brine formation and persistence, the volume of brines that may form, and the relative corrosivity of the initial deliquescent brines and of brines modified by processes on the waste package surface (SNL 2007 [DIRS 181267], Sections 6.1 and 6.2). In addition, the source report (SNL 2007 [DIRS 181267], Section 6.5) evaluates several mechanisms that could inhibit or stifle localized corrosion should it initiate.

The dust compositions considered include tunnel and atmospheric dust samples from Yucca Mountain, National Airfall Deposition Program rainout data, and other literature information on atmospheric aerosols (SNL 2007 [DIRS 181267], Sections 6.1.1 through 6.1.3). Included for consideration is the decomposition of ammonium salts, a process that could affect dust composition prior to deliquescence. Ammonium chlorides, nitrates, and even sulfates decompose readily into ammonia and acid gasses, and will be lost from the surface of the waste package prior to deliquescence (SNL 2007 [DIRS 181267], Section 6.1.2.3).

Arguments are developed using a logic-tree approach, based upon that presented by Apted et al. (2005 [DIRS 172858]) evaluating the potential importance of localized corrosion by high-temperature deliquescent brines. Expanding on this approach, *Analysis of Dust Deliquescence for FEP Screening* (SNL 2007 [DIRS 181267]) considers a wider range of dust and brine compositions, conditions, and arguments. In order for dust deliquescence to cause failure of the waste package, each of the following propositions must be affirmative (SNL 2007 [DIRS 181267], Section 7.1):

1) *Can multiple-salt deliquescent brines form at elevated temperature?* **Yes.** Some important salt phases in the dust (e.g., ammonium salts) will decompose into gaseous components prior to deliquescence. However, other salts in the dust are stable, and form eutectic assemblages that can deliquesce at temperatures much higher than the individual salt components. For most single-salt phases (nitrates, chlorides, and carbonates), boiling points at one atmosphere are limited to temperatures below 120°C; boiling points of saturated salt solutions represent the maximum temperature of deliquescence at a given pressure. Multi-salt mixtures always boil at higher temperatures than the individual salt components. The boiling points for important salt assemblages predicted to occur on the waste package surface have been investigated experimentally. The two-salt mixture $NaCl + KNO_3$ boils at a maximum temperature of 134°C and the three-salt mixture, $NaCl + KNO_3 + NaNO_3$, and four-salt mixture, $NaCl + KNO_3 + NaNO_3 + Ca(NO_3)_2$, transition from an aqueous solution to a molten salt mixture without ever drying out.

2) *If brines form at elevated temperature, will they persist?* **Sometimes**. Brines on the waste package surface will degas acid phases—HCl and HNO_3—which can result in precipitation of less deliquescent salts and dryout. High-temperature calcium and magnesium chloride brines degas rapidly and dry out, precipitating non-deliquescent hydroxide-chloride or carbonate phases. All predicted deliquescent brine compositions are unstable in the drift environment and will degas acid phases, leading to an increase in pH, increases in the NO_3^-/Cl^- ratio, precipitation of less deliquescent salts, and, if sufficient degassing occurs, dryout. Reactions with low-solubility minerals in the dust (silicates, sulfates) may also lead to dryout, by modifying cation concentrations in the brine (specifically, divalent cations are removed) and changing the deliquescent salt assemblage. However, for most brines, kinetics of acid degassing and mineral reactions are slow, and dryout is unlikely.

3) *If deliquescent brines persist, are they corrosive?* **Unlikely.** Brines that form at elevated temperature by dust deliquescence are near-neutral to alkaline pH, nitrate-rich and chloride-poor, and are therefore benign with respect to initiation of localized corrosion. Based on thermodynamic principles, brines that form beyond the temperature limits of available thermodynamic models are constrained to be even more nitrate-rich. However, high temperature (≥180°C) data are equivocal with respect to whether nitrate inhibition continues to operate at such high temperatures. Processes occurring after deliquescence, including acid degassing and reactions with silicate minerals, do not result in corrosive brines. Acid degassing has beneficial effects, increasing the NO_3^-/Cl^- ratio of the remaining solution, and even small degrees of degassing will result in increases in the brine pH, to values ranging from near-neutral to alkaline. Brine interactions with silicate

minerals may also buffer the pH to near-neutral or slightly alkaline values, and may lead to dryout by precipitation of a less deliquescent salt assemblage.

4) *If deliquescent brines are potentially corrosive, will they initiate localized corrosion?* **No.** Potential dust deposition on waste packages in the drift has been quantified, and brines generated by dust deliquescence will be limited in volume. Physical isolation of salt minerals in the dust may inhibit formation of eutectic brines, further decreasing deliquescent brine volumes. Capillary and surface tension effects in the dust are likely to reduce surface contact or inhibit brine flow into pores or crevices. Characterization of dust porosity indicates that a typical dimension of about one micron characterizes the capillary response of the dust. This dimension suggests that brine flow through the dust will be inhibited and that pores or crevices on the metal surface would need to have similar dimension in order to compete successfully for the brine. Also, predicted deliquescent brine volumes, represented as layer thicknesses or droplets on the waste package, are too small to support differences in O_2 concentration required to develop the separate anodic and cathodic zones required for initiation of localized corrosion.

5) *Once initiated, will localized corrosion penetrate the waste package outer barrier?* **No.** The process of crevice corrosion requires that water be consumed by redox reactions in both the anodic and cathodic regions of the corrosion cell. As corrosion products accumulate in the cell, cathodic limitation will occur from decreased availability of reaction sites where secondary products precipitate, and potentially from decreased availability of oxygen and water if the required transport pathways are restricted. As with many other materials, localized or crevice corrosion penetration of Alloy 22 is best described by a power rate law. Laboratory data clearly show that stifling of crevice corrosion in Alloy 22 occurs. In addition, physical sequestration of brine in the porous corrosion products will inhibit further corrosion. Given the small volumes of brine involved, corrosion products would have to be nearly nonporous not to volumetrically deplete the brine by capillary retention. Finally, the consumption of brine components, especially chloride, by incorporation into corrosion products, may decrease brine corrosivity or lead to brine dryout.

The arguments presented in *Analysis of Dust Deliquescence for FEP Screening* (SNL 2007 [DIRS 181267]) show that brines formed by deliquescence of tunnel and atmospheric dust compositions are probably benign with respect to corrosion. Processes that act to modify them on the waste package surface are beneficial with respect to corrosivity. Should corrosive brines form, scale factors related to brine volume will inhibit initiation of localized corrosion. Finally, should corrosion initiate, several processes will act to limit or stifle it before waste package breach.

The effect of condensate-dust interactions is anticipated to be minor relative to the deliquescence scenario described above. Condensate on the drip shield is excluded in TSPA-LA (see discussion in Section 6.15.2).

Drift wall condensation as represented in TSPA originates above the drip shield and follows the same path as seepage through the engineered barrier system. Drift wall condensation may occur separately or in conjunction with seepage, but will contain at least a small component of pore

water. The composition of drift wall condensation can range between very dilute and more concentrated (i.e., like seepage). In other words, drift wall condensate will interact with and take on the chemical characteristics of the seepage waters at the drift wall.

Condensation on the waste package surface will serve to dilute the deliquescent brines discussed above, thus potentially reducing their relative corrosivity. For a more detailed discussion see *Analysis of Dust Deliquescence for FEP Screening* (SNL 2007 [DIRS 181267]).

6.11 ALTERNATIVE CONCEPTUAL MODEL

The NFC model provides potential seepage water compositions as a function of water:rock interactions and also provides a range of pCO_2 values for the gas phase within the drift. The primary chemical inputs for the model are ambient pore-water compositions and rock properties for the repository host rock units.

The NFC conceptual model is simple (see Section 6.3.3). As infiltrating water moves downward towards the repository it moves up a thermal gradient. The thermal gradient extends from the land surface to the repository level, and is assumed to vary linearly with depth. The water interacts with minerals in the rock, maintaining equilibrium with calcite and amorphous silica, present in excess, and dissolving alkali feldspar, while precipitating out one or more secondary phases.

The alternative conceptual model (ACM) developed in this section examines the impact on seepage water chemistry of selecting a different starting water composition as well as an alternate treatment of the alkali feldspar. The focus is on the starting waters and on the treatment of the alkali feldspar phase and not the thermal and hydrologic aspects of the model. The implementation of a conductive-heat-transfer-only model is consistent with use in other project models. *Multiscale Thermohydrologic Model* (SNL 2007 [DIRS 181383], Section 6.2.5) implements a conduction-only model and provides justification that heat flow is conduction-dominated. The method is also implemented, and validated, in *In-Drift Natural Convection and Condensation* (SNL 2007 [DIRS 181648]). Because this approach is validated and alternative approaches investigated in other project documents, these aspects of the NFC model are not addressed here.

6.11.1 Use of PTn versus TSw Starting Water by the NFC Model

The NFC model selects from among the ambient pore-water compositions available from the TSw to determine the four starting waters (Section 6.6). The starting waters are then assumed to travel from the top of the devitrified TSw unit downward towards the repository, dissolving alkali feldspar along the way (Section 7.1.2). The ACM selects ambient pore water from the overlying unit, the PTn, and then allows this water to seep up the geothermal gradient (from 23°C to 96°C) downward through the TSw to the repository horizon. The range of potential seepage water chemistry is evaluated by titrating varying amounts of alkali feldspar, assuming saturation with calcite and amorphous silica and increasing the temperature up to a maximum of 96°C. This mimics the approach utilized by the NFC and allows a direct comparison of water chemistry and an evaluation of the sensitivity of the NFC model to starting water composition.

The water chosen for this exercise was the PTn pore water, SD6-3345, (composition as listed in Table 6.11-1) along with the NFC representative TSw pore waters, Groups 1 and 3, compositions for comparison. The SD6-3345 composition was chosen because it falls in the middle of the available PTn pore-water compositions and will serve as representative water for this assessment (see Section 7.2).

The files that support this analysis are archived in Output DTN: SN0705PAEBSPCE.012. The EQ6 input files used to calculate potential seepage waters for the NFC model were adjusted for the ACM by replacing the original starting water composition (EQ3 pick up file) with the SD6-3345 composition. EQ6 was then executed for each of the eleven discrete WRIP values and the outputs were post-processed to generate three profiles at 2,000, 6,000 and 20,000 years postclosure as described in Section 6.3.3.2.6. Six parameters were plotted as a function of height above of the repository: pH and pCO_2, as well as the concentrations of Ca, Na, K, and Si. The results are tabulated in spreadsheet *ACM_profiles.xls* in Output DTN: SN0705PAEBSPCE.012.

Table 6.11-1. Water Compositions Utilized by the ACM

	SD6-3345	Group 1	Group 3
pH	7.4	8.2	8.3
Na (mg/L)	65.5	59	62
K (mg/L)	4	4.8	9
Mg (mg/L)	11.7	0.7	17.4
Ca (mg/L)	48.2	19	97
Cl (mg/L)	47.3	23	123
SO_4 (mg/L)	98	16	120
HCO_3 (mg/L)	101	CO_2 equilibrium (10^{-3} bars)	
NO_3 (mg/L)	86	16	10
F (mg/L)	6.3	2.2	0.76
SiO_2 (mg/L)	84.4	42	75
Al	Alkali feldspar equilibrium		

Source: Output DTN: SN0705PAEBSPCE.012.

The results for all three waters are shown in Figures 6.11-1 through 6.11-6. In Figures 6.11-1 and 6.11-2, the observed changes in pH and pCO_2 illustrate the effects of the temperature gradient and increasing feldspar dissolution. For the two early time cases, the initial increase in temperature results in degassing of CO_2, and the pH drops and pCO_2 rises. As the water percolates downward, the water–rock interaction increases, resulting in an increase in the pH and alkalinity of the pore waters, and the CO_2 is re-absorbed. The pH rises again, and the pCO_2 drops. For the 20,000-year case, the temperature has cooled and feldspar dissolution rates are slow; the effect of the temperature gradient is greater than that of feldspar dissolution, and the pH drops and pCO_2 rises in a linear fashion downward through the section. The modeled trends for both pH and pCO_2 for the PTn pore water fall between the trends for the Group 1 and Group 3 waters.

In Figures 6.11-2 through 6.11-6, other chemical parameters are shown. Ca decreases with depth, as feldspar dissolves and stellerite and celadonite precipitate, and K and Na show the

opposite behavior. These trends are identical for all three waters compared. There is a wide range of Ca concentrations among the waters, with the representative PTn seepage water between the Group 1 and Group 3 values. The K concentration for the PTn water is somewhat depleted. However, the K-trend for the PTn water follows a similar trend as Group 1. The only significant chemical difference observed between the PTn water and the two TSw waters is the Na concentration. The PTn seepage water has significantly more Na. This can be partially explained by the starting water composition and the increase in Na content due to feldspar dissolution. Aqueous silica concentrations are entirely a function of the change in amorphous silica solubility with temperature, as equilibrium with that phase is assumed and the variation observed among the three waters is minor.

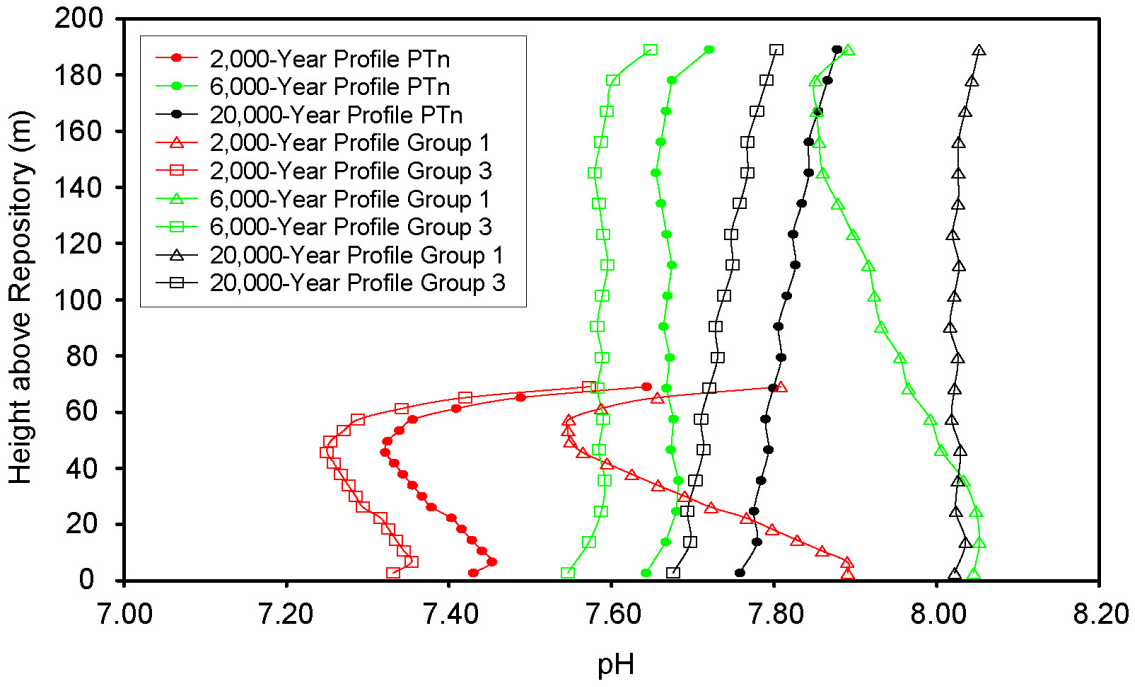

Source: Output DTN: SN0705PAEBSPCE.012.

NOTE: Groups 1 and 3 are TSw waters selected by the NFC model (open symbols); the PTn pore water is SD6-3345 used by the ACM (closed symbols).

Figure 6.11-1. pH Trends as a Function of Height above the Repository for Three Starting Pore-Water Types

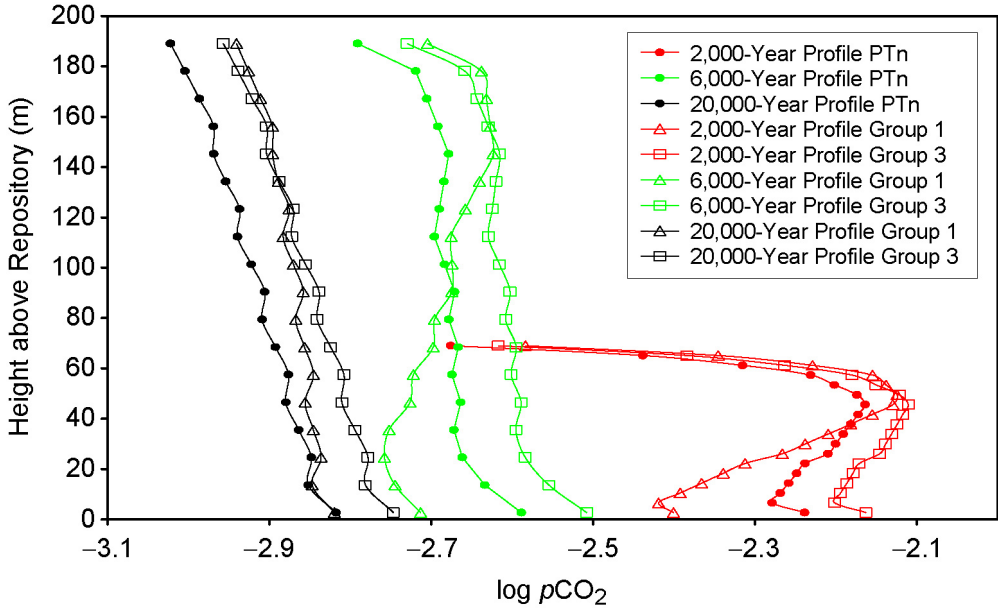

Source: Output DTN: SN0705PAEBSPCE.012.

NOTE: Groups 1 and 3 are TSw waters selected by the NFC model (open symbols); the PTn pore water is SD6-3345 used by the ACM (closed symbols).

Figure 6.11-2. pCO_2 Trends as a Function of Height above the Repository for Three Starting Pore-Water Types

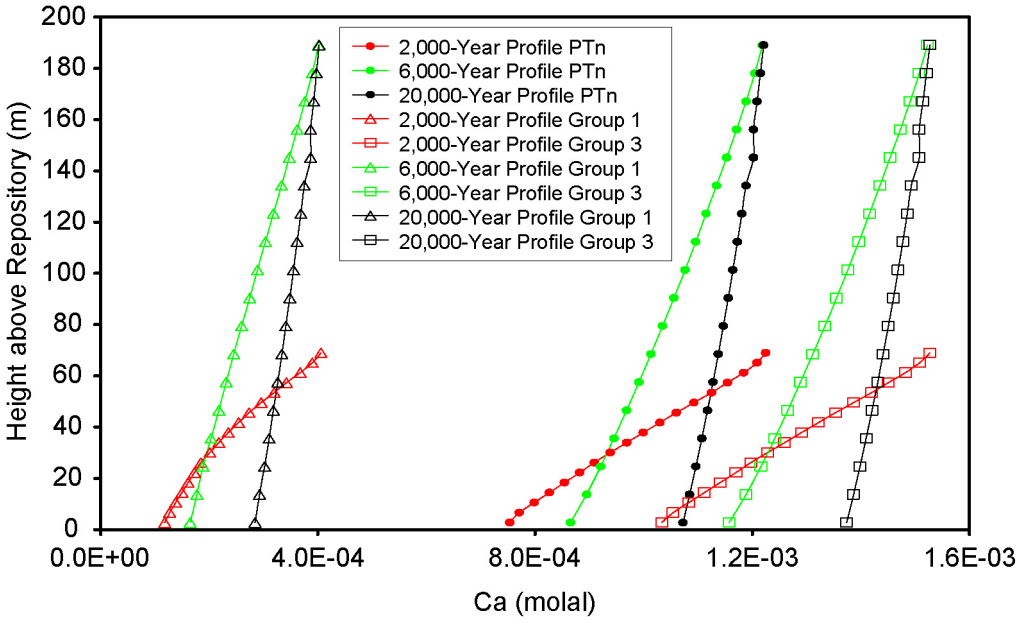

Source: Output DTN: SN0705PAEBSPCE.012.

NOTE: Groups 1 and 3 are TSw waters selected by the NFC model (open symbols); the PTn pore water is SD6-3345 used by the ACM (closed symbols).

Figure 6.11-3. Ca Trends as a Function of Height above the Repository for Three Starting Pore-Water Types

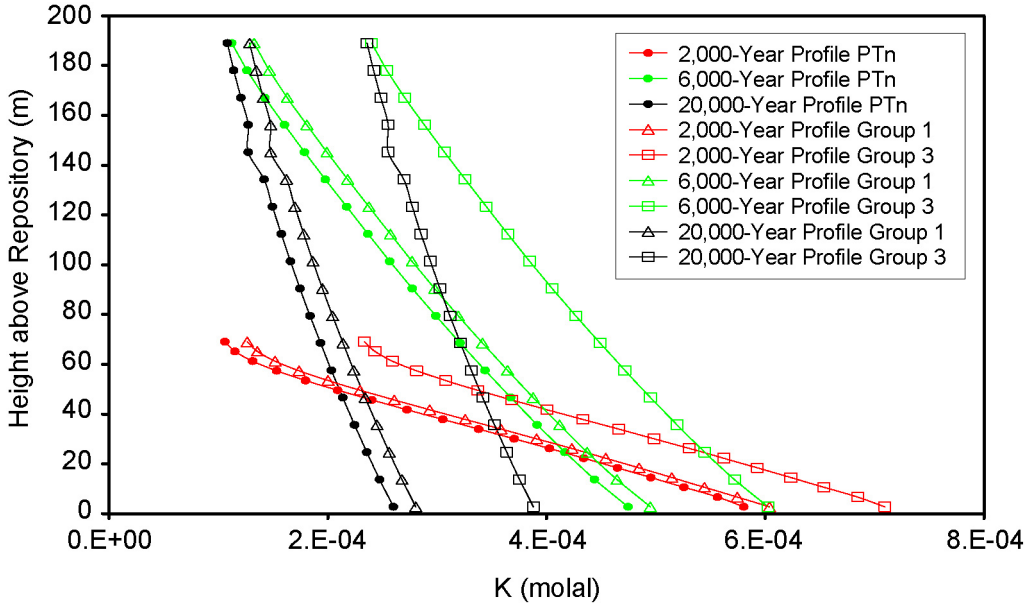

Source: Output DTN: SN0705PAEBSPCE.012.

NOTE: Groups 1 and 3 are TSw waters selected by the NFC model (open symbols); the PTn pore water is SD6-3345 used by the ACM (closed symbols).

Figure 6.11-4. K Trends as a Function of Height above the Repository for Three Starting Pore-Water Types

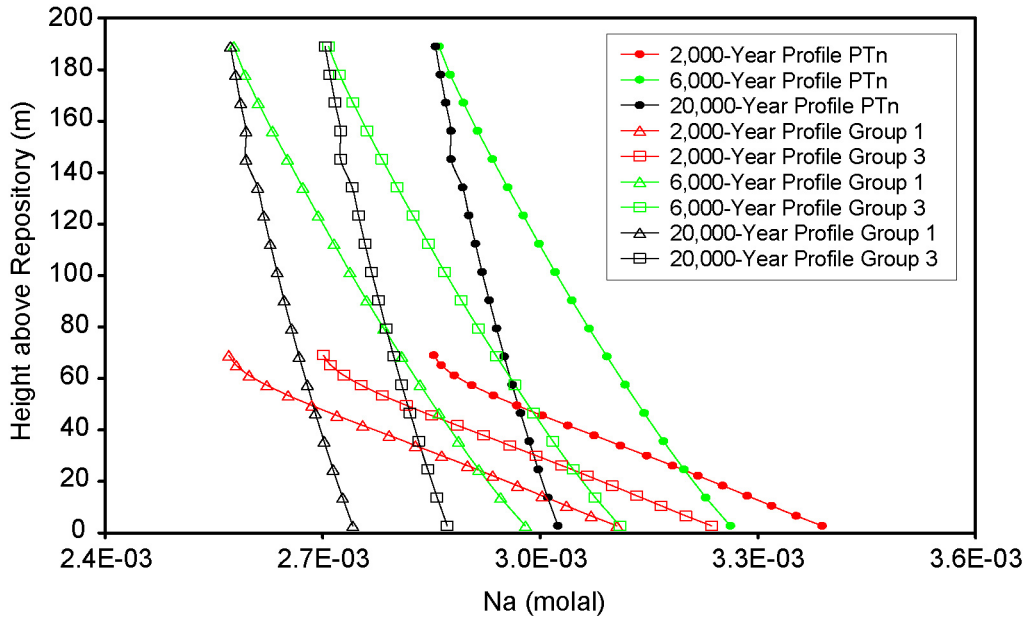

Source: Output DTN: SN0705PAEBSPCE.012.

NOTE: Groups 1 and 3 are TSw waters selected by the NFC model (open symbols); the PTn pore water is SD6-3345 used by the ACM (closed symbols).

Figure 6.11-5. Na Trends as a Function of Height above the Repository for Three Starting Pore-Water Types

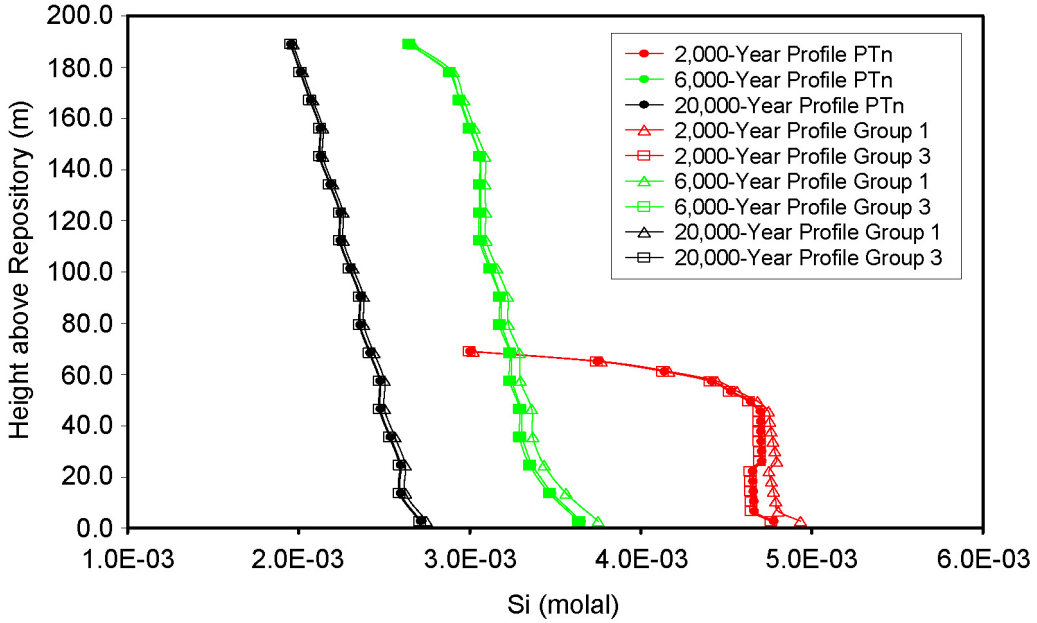

Source: Output DTN: SN0705PAEBSPCE.012.

NOTE: Groups 1 and 3 are TSw waters selected by the NFC model (open symbols); the PTn pore water is SD6-3345 used by the ACM (closed symbols).

Figure 6.11-6. Si Trends as a Function of Height above the Repository for Three Starting Pore-Water Types

One reason the NFC model utilizes TSw pore water compositions is that selecting waters from below the glassy base of the PTn ensures that the chemical signature of this unit is captured in the representative waters. Developing a quantitative thermodynamic and kinetic modeling scheme to address water–rock interactions including this vitreous layer would involve numerous assumptions including unit permeability, reactive surface area, and dissolution rate of the glass. Little experimental data is available to constrain such a model. Selecting from among the available TSw data circumvents these issues. The analysis presented in this section demonstrates that there may be little impact from the water–glass interactions for the ambient case at least for the representative case examined here. The impact of the glassy unit on water chemistry may be more pronounced if the vertical proximity of this unit to the repository horizon is considered because in some locations the latitic glass at the base of the PTn is not 200 m above but much closer to the repository unit. Close proximity of the glass to the repository would result in significantly elevated temperatures after waste emplacement and the temperature effects on the glass dissolution rate would be large, resulting in a high degree of interaction and concomitant chemical changes in the potential seepage waters.

The analysis presented here for the ACM leads to the conclusion that the use of pore waters from the TSw by the NFC model adequately captures the chemical characteristics of a representative PTn pore water even without the specific treatment of the latitic glass layer at the base of the PTn. The use of PTn starting compositions does not significantly impact the key chemical components (pH, pCO_2, Ca, K, Si) of seepage.

6.11.2 Treatment of Alkali Feldspar by the NFC Model: Kinetics versus Equilibrium

Throughout this report, the mixed feldspar phase adopted to represent the volcanic feldspar observed in the Topopah Spring Tuff is treated kinetically, i.e., this phase is always undersaturated with respect to clays, zeolites, and its own end-members. Hence, the degree of water–rock interaction determined for the potential seepage waters in the NFC model is determined by calculating a residence time (largely dependent on the percolation flux), a temperature profile (calculated as a thermal field assuming conduction dominates the thermal process), and a dissolution rate for the alkali feldspar that is calculated from the observed mineral assemblage as a kinetically limited process. These concepts are described and developed in great detail in Section 6.3.2. In particular, this modeling choice is supported by the fact that the alkali feldspar initially present in the tuff has exsolved to varying degrees to alternating potassium- and sodium-rich lamellae. Because the degree of exsolution is variable, and because the two phases formed are not pure end-members, but vary widely in composition, the alkali feldspars are treated as a single phase, with a kinetically limited dissolution rate, by the NFC model (Section 6.3.2.4.5).

An alternate approach would be to assume that the volcanic feldspar has reached equilibrium or near equilibrium, and thus thermodynamic controls of feldspar dissolution (e.g. saturation indices) must be considered when calculating seepage water compositions. In order to implement an equilibrium approach, several assumptions must be made. First, the degree of exsolution of the feldspar must be assumed, as they are so fine grained (X-ray perthites) that no quantitative chemical analysis or structural evaluation has been done. Second, thermodynamic properties must be estimated by assuming a mixing model. This is problematic because, even though ideal or regular mixing may provide a reasonable approach at elevated temperatures, once the tuff began to cool and exsolution occurred significant site-ordering is likely. The application of a regular mixing model is inherently contradictory to the structural reality that most intermediate to slowly cooled feldspars are “un-mixed” to a degree, because while this mixing model assumes a non-zero enthalpy of mixing (a likely state due to the size-mismatch between K and Na), it also assumes a configurational entropy associated with random, ideal mixing. The enthalpy of mixing and the configurational entropy are the two parameters that determine the excess Gibbs energy of mixing. Thus, the Al-Si order/disorder has a significant impact on feldspar solubility. The feldspar structural state, generally determined by the state of Al-Si order/disorder, is a function of not only the initial crystallization temperature, but also the cooling history. In general, if rapid cooling occurred, then Al-Si tends toward more disorder, if cooling was relatively slow, then Al-Si may tend toward a greater degree of order. If a small amount of Ca is present, as is indicated by the empirical studies (Sections 4.1.8, 6.3.2.2, and 6.3.2.4.2), then a coupled substitution mechanism is required to maintain charge balance and oxygen deficient phases may form. This detailed structural information is not available for the volcanic tuff of the TSw. Nonetheless, even with these difficulties, estimates of the thermodynamic properties of mixed feldspars have been applied to the study of natural systems (Stefansson and Arnorsson 2000 [DIRS 153578]).

Even if there were good structural and chemical information as to the state of the mixed feldspar, there are several geochemical arguments for why equilibrium with the alkali feldspar would never be approached in the ambient system. The study by Stefansson and Arnorsson (2000 [DIRS 153578]) is germane to the discussion of kinetic versus equilibrium control of the

volcanic feldspar in the TSw. The authors examined the saturation sate of 217 natural waters with respect to feldspars over a wide range of temperatures and geochemical conditions. They found that secondary, ordered end-member feldspars such as low-albite and microcline (the stable low temperature form of K-feldspar) may exert solubility control on geochemical systems above 200°C, but not at ambient temperatures. From their concluding remarks, however, it is clear that a kinetic treatment of the alkali feldspar by the NFC model is the appropriate approach (Stefansson and Arnorsson 2000 [DIRS 153578], p. 2582):

> Primary disordered plagioclase and alkali-feldspars of compositions typically found in volcanic rocks ranging from basaltic to silicic composition are predicted to be undersaturated and dissolving.

and

> Cold waters are usually undersaturated with respect to feldspars regardless of composition and Al-Si ordering. All types of feldspars are, therefore, generally unstable under weathering conditions.

In the geochemical system utilized by the NFC model, it is important to note that end-member feldspars remain undersaturated in all seepage simulations, instead zeolite and clay phases form (Section 6.3.2). This is consistent with the observations of secondary zeolites and clays in the tuff and the absence of secondary feldspars.

6.12 EVALUATION OF PARAMETER VALUE UNCERTAINTIES

6.12.1 Statement and Justification of Uncertainty Treatment

Justifications for parameter uncertainties are presented in this section. The choice of uncertainty distributions and their quantification are also discussed here. The P&CE uncertainties are archived in Output DTN: SN0703PAEBSPCE.007.

6.12.2 Quantification of Uncertainty

The quantification of uncertainty for all parameters treated with uncertainty in the two process models—the NFC model and the IDPS model (SNL 2007 [DIRS 177411])—and the P&CE abstraction models is documented in this section.

6.12.2.1 Overview of Uncertainty Treatment in Process Level and Abstraction Models

The NFC process model provides potential seepage water compositions, the WRIP, and the range of potential pCO_2 values in the drift. Uncertainties in the NFC inputs are treated as follows. The four input waters (Groups 1 through 4) were chosen statistically to represent the variability in 34 Topopah Spring Tuff (TSw) waters upon evaporation. The water selection process is documented in Section 6.6. The uncertainty in the starting water composition is sampled by TSPA when it randomly selects one of the water types (see Figure 6.15-1). Because representative waters are used, it is also necessary to sample the range of Cl:N in the 34 TSw waters from a discrete CDF as described in Sections 6.15.1 and 6.12.3 to capture the uncertainty associated with these key chemical parameters. The uncertainties associated with the rock

properties that are inputs to the NFC for the WRIP evaluation are described and discussed in Sections 6.12.2.2 and 4.1.1. In addition to NFC model input uncertainties, there are three conceptual uncertainties. First, the NFC model approximates water transport by plug-flow. This model choice is evaluated by comparison to Finite Element Heat and Mass Transfer (FEHM) code simulations (see Section 4.1.12) and is discussed in Sections 6.12.2.2. Second, the NFC model develops and uses an alkali feldspar dissolution rate based on field observations as discussed in Sections 6.12.2.2 and 4.1.8. Third, the NFC model uses a model for the evolution of the thermal field based on conductive heat transfer only, an approach that has been evaluated and justified in *In-Drift Natural Convection and Condensation* (SNL 2007 [DIRS 181648]) and is discussed further in Section 4.1.4. NFC model output uncertainties are, therefore, passed to TSPA by (1) randomly selecting the starting water type, (2) by an integrated uncertainty in the WRIP, which is sampled over a beta distribution as described in Section 6.12.2.2, and (3) pCO_2 uncertainties sampled over the range provided by the NFC model by application of an offset (ΔpCO_2), as described in Section 6.15.1.

There are two abstraction models developed in this report: the seepage dilution/evaporation abstraction model and the integrated invert chemistry abstraction model. Uncertainties in the seepage water chemistries are sampled when TSPA randomly selects the starting water type, and the entire range of seepage dilution/evaporation chemistries are sampled when TSPA generates the WRIP value. The P&CE seepage dilution/evaporation abstraction also instructs TSPA to apply IDPS uncertainties on key chemical parameters. The chemical uncertainties are described and their application discussed in Section 6.12.2.3. IDPS uncertainties are used directly from the accompanying report (SNL 2007 [DIRS 177411]), with the exception of pH uncertainties over a portion of the relevant RH range (see discussion in Section 6.12.2.3). Uncertainties in the integrated invert chemistry abstraction model are the same as for the seepage dilution/evaporation abstraction model. The integrated invert chemistry abstraction model also requires TSPA to make comparisons to IPC chemistries (DTN: SN0702PAIPC1CA.001 [DIRS 180451]) to ensure that they are conservative with respect to total radionuclide release and transport through the invert (see Section 6.15.2 and Table 6.15-1).

6.12.2.2 Water–Rock Interaction Parameter Uncertainties

There are several sources of uncertainty in the WRIP value generated by the NFC process model. These include the uncertainty in the field study-based ambient feldspar dissolution rate due to uncertainty in: (a) the average mineral abundances for the four repository units; (b) the water:rock ratio due to uncertainty in rock properties such as porosity, ambient saturation (including the use of ambient saturation for the thermal case), and grain density; and (c) the timing of alteration because much of the alteration may have happened when the tuff was still hot and, thus, may not represent feldspar dissolution under ambient conditions. Another source of uncertainty in the WRIP lies in the estimation of activation energy (E_a) for feldspar dissolution. Also, the NFC process model uses a plug flow assumption for transport time, as opposed to explicitly calculating fracture and matrix flow and fracture–matrix interactions as a function of permeability and capillary properties. This may lead to significant under- or over-estimation of the WRIP. Uncertainty related to the percolation flux and the extent and shape of the thermal field is handled explicitly by TSPA and is not evaluated here. Each of these sources of uncertainty in the WRIP is evaluated in turn below.

6.12.2.2.1 Evaluating Uncertainty in the Dissolution Rate of Alkali Feldspar

The process for calculating the ambient dissolution rate of alkali feldspar, based on field observations of secondary mineral abundance, is described in Section 4.1.6. Parameters used in this calculation include mineral abundances in the TSw lithologic unit, porosity, matrix saturation, grain density, and most importantly, timing and temperature of secondary mineral formation. A single value for each of these parameters has been estimated by averaging data from four repository host units comprising the bulk of the TSw: the TSw upper lithophysal unit (Tptpul), TSw middle non-lithophysal unit (Tptpmn), TSw lower lithophysal unit (Tptpll), and TSw lower non-lithophysal unit (Tptpln). The actual inputs used are discussed in Section 4.1. The uncertainties in these parameters are discussed below, and are propagated into the uncertainty in the ambient dissolution rate for alkali feldspar.

Calculating Average Mineral Abundances—The reported standard deviations on the average mineral abundances for each of the four repository host units are relatively large (two σ would result in values below zero in many cases), so assuming a lognormal distribution is justified. The mean value is calculated by taking the mean and standard deviation values for each unit and calculating the lognormal distribution, adding the weighted distributions together, and calculating the mean of the new distribution. The weighting for each unit is based on the average thickness of the unit over the area of the repository footprint. These calculations are discussed and documented in three Mathcad files, *Feldspar* [*Smectite*] [*Zeolite*] *Abundances in repository units, combination_4_lognormals.xmcd*, and in the spreadsheet *Feldspar Dissolution Rate Calculations.xls,* archived in Output DTN: SN0703PAEBSPCE.006.

Calculating an Average Porosity—The average porosity for the four repository units is weighted according to the thickness of each unit. No standard deviations are given on the data for the original units. The standard deviation is calculated from the four values without weighting. These calculations are discussed and documented in *Feldspar Dissolution Rate Calculations.xls* in Output DTN: SN0703PAEBSPCE.006.

Calculating an Average Matrix Saturation—As with the mineral abundances, the standard deviations of the estimated matrix saturations are large relative to the mean values (two σ would result in saturation values above unity), so assuming a lognormal distribution is justified. The mean value is calculated by taking the mean and standard deviation values for each unit and calculating the lognormal distribution, adding the weighted distributions together, and calculating the mean of the new distribution. The weighting for each unit is based on the average thickness of the unit over the area of the repository footprint. These calculations are documented in the Mathcad file *Matrix saturations in repository units, combination_4_lognormals.xmcd*, and in the spreadsheet *Feldspar Dissolution Rate Calculations.xls*, archived in Output DTN: SN0703PAEBSPCE.006.

Calculating an Average Grain Density—There is little variation in the average grain density values for the four repository host units. The standard deviations are very small; assuming a normal distribution is therefore justified. The mean value is calculated by taking the mean and standard deviation values for each unit and calculating the normal distribution, adding the weighted distributions together, and calculating the mean of the new distribution. The weighting for each unit is based on the average thickness of the unit over the area of the

repository footprint. These calculations are documented in Mathcad file *Grain densities in repository units, combination_4_normals.xmcd*, and in the spreadsheet *Feldspar Dissolution Rate Calculations.xls*, archived in Output DTN: SN0703PAEBSPCE.006.

Evaluating Uncertainty in the Timing of Alteration—Most studies of the timing and conditions of zeolitization at Yucca Mountain have concentrated on the zeolite-rich zones that occur in the stratigraphic section. Specifically, heavily zeolitized rocks have been associated with the following conditions:

- Heavily zeolitized rocks occur below or just above the water table, through alteration of volcanic glass in poorly welded or non-welded vitric units. The following text from Section 3.3.5.1.2 of *Yucca Mountain Site Description* (BSC 2004 [DIRS 169734]) applies:

  > The most extensive post-cooling mineralogic and geochemical change affecting the rocks at Yucca Mountain has been the diagenetic zeolitization of nonwelded glassy tuffs. Diagenetic alteration involved dissolution of glass pyroclasts by groundwater at ambient temperatures (e.g., 50°C or lower) and precipitation of clinoptilolite with or without lesser amounts of mordenite, smectite, silica, iron-manganese oxides and hydroxides, and other minor phases.
  >
  > The working hypothesis is that most zeolitization occurred around or below the static water level present at the time of alteration, and that glass in nonwelded tuffs is preserved only where the rocks have not been subjected to prolonged saturation. This concept forms one basis for estimating the highest static water level ever reached at Yucca Mountain.

  Also from *Yucca Mountain Site Description* (BSC 2004 [DIRS 169734], Section 5.2.1.1):

  > Correlation of fracture-lining zeolites just above and below the water table with degree and type of zeolitization of the high-porosity host tuff suggests that the fracture coatings may have formed at the same time as the tuff alteration. The similarity of chemical compositions of matrix and fracture-lining clinoptilolite supports this hypothesis. An increase in degree of alteration from clinoptilolite/mordenite to analcime in both fractures and matrix toward the north of Yucca Mountain suggests that this alteration may have been a result of hydrothermal activity related to the Timber Mountain volcanism, constraining the age of the zeolites to >9 Ma or older (Bish and Aronson 1993 [DIRS 100006], pp. 154 to 156). The net evidence, from both matrix and fracture minerals in high-porosity tuffs, is thus indicative of early pervasive alteration, overprinted at critical boundaries (particularly within the glass-to-zeolite transition in the unsaturated zone) by subsequent cation exchange. Although zeolites might still be forming at Yucca Mountain, the evidence shows that rates of

> formation are presently very low, and the principal impact of zeolites on site processes is through ion exchange.

- Levy and O'Neil (1989 [DIRS 133364], p. 322) noted that smectites and zeolites in the Topopah Spring Tuff, and within the unsaturated zone, were dominantly concentrated in the transition zone between the densely welded devitrified tuff and the underlying vitrophyre, and conclude on the basis of oxygen isotopes that they formed dominantly at temperatures somewhat elevated relative to the ambient, 40°C to 100°C or higher, probably due to downward percolation of heated waters from the central, hottest parts of the cooling tuff. Although this zone is not part of the zone of interest for this study, it still suggests that the rate of zeolitization was higher in the past, when the tuff was above ambient temperatures, and slowed as the tuff cooled to ambient temperatures. The authors state that temperature range of 40°C to 100°C is based on the oxygen isotope data, and might represent minimum zeolite formation temperatures, but note that the maximum possible temperature, on the basis of clinoptilolite stability, is ~180°C.

However, conditions within the densely welded, rhyolitic center of the Topopah Spring Tuff within the repository block differ from those in the underlying vitrophyre. At this location, these units have never been below the water table. Also, the four units forming the densely welded center of the Topopah Spring Tuff between the upper and lower vitric zones, comprising the Tptpul, Tptpmn, Tptpll, and Tptpln, are completely devitrified (Vaniman et al. 1996 [DIRS 105946], v. 1, Section 3, p. 2; also DTN: LA9908JC831321.001 [DIRS 113495]). There is no glass in these units, and the secondary minerals that are present must have formed by alteration of feldspars within the devitrified tuff. It is these units, extending to about 200 m above the repository, which are considered in the NFC model.

The following observation about zeolites and clays in the fracture coatings pertains to the timing of zeolite and clay formation in the densely welded devitrified center of the Topopah Spring Tuff (BSC 2004 [DIRS 169734], Section 7.7.1):

> Secondary mineral deposits consist of ~1 to ~40 mm (~0.05 to ~1.5 in.) thick irregular coatings of predominantly calcite, interlayered with lesser amounts of silica phases, including opal, chalcedony, and quartz. Other phases may also be present in minor amounts, including fluorite, clay minerals, zeolites, and manganese oxides. However, these phases are mostly present in older parts of the coatings.

To summarize, it is generally believed that most secondary mineral (e.g., clays, zeolites) formation occurred early in the history of the Topopah Spring Tuff, at temperatures above ambient. Hence, most of the alteration products did not form under ambient conditions, and the ambient feldspar dissolution rate is significantly slower than that estimated assuming all the secondary minerals formed at ambient temperatures.

While the amount of secondary minerals that formed at elevated temperatures versus diagenetically (e.g., under ambient conditions) cannot be determined with accuracy, the possible range of ambient alteration rates can be estimated from the available information.

The time required for the Topopah Spring Tuff to cool to ambient is not known. However, it is known that the tuff has been at ambient temperatures for many millions of years. The following information allows an estimate of the cooling history of the tuff:

- In the absence of an external source of added heat, cooling of an ash-flow tuff outflow sheet may take thousands to tens thousands of years. For instance, cooling rates for a 50 m thick ash-flow unit in the Bishop Tuff were estimated to be as low as 10^{-8}°C/sec (~0.3°C/yr) (Wallace et al. 2003 [DIRS 178837], p. 109). For an emplacement temperature of ~600°C, this would require about 1,800 years to cool to ambient temperatures. Even allowing for the greater thickness of the Topopah Spring Tuff, the initial cooling of the tuff to temperatures below boiling (100°C) was unlikely to have taken more than several thousand years.

- Additional heat input when the overlying Timber Mountain Group was erupted (11.4 Ma), and circulation of heated fluids from deeper heated rocks, appears to have resulted in elevated temperatures (50°C to 100°C) persisting, perhaps periodically, for up to several million years after eruption of the initial eruption of the tuff. Evans et al. (2005 [DIRS 178836], p. 1103) performed (U-Th)/He dating of fluorite in the Topopah Spring Tuff, and obtained ages of 9.7 Ma. They estimated the He closure temperature for fluorite to be about 90°C, but noted that partial loss could have occurred at lower temperatures, and estimated deposition temperatures of the fluorite are 65°C to 80°C. The authors interpreted this to mean that the last period of elevated temperature fluid circulation at Yucca Mountain occurred at that time.

- Wilson et al. (2003 [DIRS 163589], p. 1171) determined ages (U-Pb dating) and temperatures (fluid inclusion homogenization temperatures) of calcite/silica mineral formation in the unsaturated zone at Yucca Mountain. They determined that mineral deposition temperatures above 50°C are associated with mineral ages of 6.3 Ma or greater, while mineral deposition at temperatures between 35°C to 45°C last occurred about 5.3 Ma. There is no evidence of trapping of fluids above ambient temperatures in the last 5.3 Ma.

- Whelan et al. (2007 [DIRS 179305], Figure 8) examined the available data on ages and temperatures of mineral formation, and developed a probable thermal history for the Topopah Spring Tuff, which proposes that tuff cooled rapidly, but was reheated to temperatures just below 100°C by magmatic heat related to Timber Mountain group volcanism at 11.4 Ma. Temperatures above 80°C persisted until about 10 Ma, and then dropped over the next several Ma to ambient values, by perhaps 4 Ma.

The possible range of ambient feldspar dissolution rates can be evaluated by taking advantage of the knowledge that most of the alteration occurred at temperatures between 40°C and 100°C, with a maximum temperature of 180°C (Levy and O'Neil 1989 [DIRS 133364], p. 324), and also that there is a relationship between the ambient rate and the elevated temperature rate defined by the Arrhenius relationship (e.g., the 96°C rate is ~59 times the 23°C rate) (see the spreadsheet *Feldspar Dissolution Rate Calculations.xls* in Output DTN: SN0703PAEBSPCE.006). The total feldspar dissolved (and the amount of secondary minerals formed) is the sum of that dissolved at elevated temperatures (e.g., syngenetic alteration) and that dissolved at ambient

conditions (e.g., diagenetic alteration). The ambient rate can be calculated as a function of how long elevated temperatures might have persisted. The maximum bound for the ambient feldspar dissolution rate is calculated by assuming that the tuff was never at elevated temperature and all secondary minerals formed at ambient conditions. The minimum bound is calculated by assuming that the tuff has always been at elevated temperature; in this case, all feldspar dissolved at elevated temperature, and the dissolution rate calculated using the entire abundance of secondary minerals is the high temperature dissolution rate. The Arrhenius relationship can then be used to calculate the relevant ambient rate. For instance, if 100°C conditions persisted over the entire history of the tuff, then all the secondary minerals formed at 100°C, and the ambient rate is equal to 1/59 of the rate calculated using all the secondary minerals. This is because the temperature dependence of the feldspar dissolution rate, based on the Arrhenius relationship, is such that the rate at 96°C is 59 times the rate at 23°C (see the spreadsheet *Feldspar Dissolution Rate Calculations.xls* in Output DTN: SN0703PAEBSPCE.006).

The same type of analysis, calculating the ambient rate as a function of the length of time at elevated temperature, can be done for any temperature of formation, and the results, assuming secondary mineral formation temperatures of 60°C, 80°C, 100°C, and 180°C, are described and documented in spreadsheet *Uncertainty in WR interaction parameter.xls* (archived in Output DTN: SN0703PAEBSPCE.007). These calculations show that the ambient rate of feldspar dissolution is relatively insensitive to the thermal history of the tuff, with the range of possible values varying by only a few orders of magnitude. In order to further narrow the possible range, the information discussed above on the length of time spent at elevated temperatures is used. The ambient rate can also be directly related to the amount of feldspar dissolved (or secondary minerals formed) at elevated temperatures.

To estimate an uncertainty distribution on feldspar dissolution rate, consider the following (details of calculations in spreadsheet *Uncertainty in WR interaction parameter.xls* archived in Output DTN: SN0703PAEBSPCE.007):

(1) After emplacement, cooling to below boiling is unlikely to have taken more than a few thousand years (based on cooling rates from Wallace et al. 2003 [DIRS 178837], p. 109), and, even if secondary minerals formed at temperatures up to 180°C, the amount of minerals formed under conditions >100°C is likely to have been small.

(2) "Most" (e.g., interpreted to mean greater than 50%) secondary mineral formation occurred at elevated temperatures (40°C to 100°C) (Levy and O'Neil 1989 [DIRS 133364], p. 325).

(3) Elevated temperatures (>80°C) may have persisted, or have occurred intermittently, for up to three million years after emplacement of the tuff (Evans et al. 2005 [DIRS 178836]; Whelan et al. 2007 [DIRS 179305], Figure 8).

(4) Temperatures have been below 50°C for the last ~6.3 Ma, and below 35°C to 45°C for the last ~5.3 Ma (Wilson et al. 2003 [DIRS 163589], p. 1171). This is consistent with the model of Whelan et al. (2007 [DIRS 179305], Figure 8) as well.

Therefore, the rate calculated using the total abundance of secondary minerals (5.94×10^{-9} mol yr^{-1} kg $tuff^{-1}$) represents a mix of both ambient and higher temperature alteration. The ambient rate must be less than this value.

The maximum value for the likely range of possible ambient rates is defined by the ambient rate consistent with more than 50% of the minerals forming early, under elevated temperature conditions. This is approximately 3.14×10^{-9} mol yr^{-1} kg $tuff^{-1}$ (average of 50% values for 60°C, 80°C, 100°C curves; see Output DTN: SN0703PAEBSPCE.007, spreadsheet: *Uncertainty in WR interaction parameter.xls*, tab: "1c) timing of alteration," cell D422), more or less independent of the temperature or alteration.

Assuming that most of the alteration occurred between 40°C and 100°C, then the 100°C curve represents minimum values for the likely range of ambient dissolution rates. The unit cooled below 90°C by 9.7 Ma (Evans et al. 2005 [DIRS 178836], abstract); hence, the ambient dissolution rate value indicated by the 100°C curve at ~3 million years (12.8 Ma to 9.7 Ma) would be a minimum value. This is especially true if the thermal history of Whelan et al. (2007 [DIRS 179305], Figure 8) is correct, as it suggests that the tuff was actually much cooler during the interval from 12.8 Ma to 11.4 Ma, when Timber Mountain Group volcanism occurred. This value is 4.07×10^{-10} mol yr^{-1} kg $tuff^{-1}$.

Both of these values are assumed to be unlikely end-cases, and there is little information to justify choosing a specific most likely value between them. For these reasons, a Beta distribution (see Harr 1987 [DIRS 100580], Section 2.3) with a broad peak is chosen to represent the uncertainty in the ambient dissolution rate. The Beta distribution is calculated using the built-in EXCEL statistical function BETADIST, and the parameters are given in spreadsheet *Uncertainty in WR interaction parameter.xls* in Output DTN: SN0703PAEBSPCE.007.

When calculating the WRIP value, the mean value for the Beta distribution is used. This value, in the units used by the NFC model, is 1.14×10^{-15} moles L^{-1} sec^{-1} (Output DTN: SN0703PAEBSPCE.007, spreadsheet: *Uncertainty in WR interaction parameter.xls*). The uncertainty in the ambient alkali dissolution rate value scales linearly to uncertainty in the WRIP value, and is the largest contributor to uncertainty in the WRIP value.

6.12.2.2 Evaluating Uncertainty in the Activation Energy (E_a) for Feldspar Dissolution

The activation energy for feldspar dissolution does not affect the calculated ambient dissolution rate, but determines the temperature sensitivity of the reaction rate. The alkali feldspar E_a for dissolution was calculated from published values for "neutral" pH in the study by Blum and Stillings (1995 [DIRS 126590], Table 2) in the following manner: (AVE Albite E_a + AVE K-feldspar E_a)/2 at neutral pH, rounded to two significant digits = 49,000 J/mol, where AVE is the average. The values used, and the estimated uncertainties, are given in Output DTN: SN0703PAEBSPCE.007 (spreadsheet: *Uncertainty in WR interaction parameter.xls*, tab: "Ea for feldspar diss.").

The effect of uncertainty in the activation energy (E_a) for feldspar dissolution on the temperature sensitivity of the dissolution rate is small. The result is an uncertainty equivalent to a multiplier/divisor, for two standard deviations, of about two at the highest temperatures (96°C)

(see Output DTN: SN0703PAEBSPCE.007, spreadsheet: *Uncertainty in WR interaction parameter.xls*, tab: "E_a for feldspar diss."). It is unlikely that the error in the value for E_a adopted by the NFC model is that large because it is based on average measured values. A simulation, in which 5,000 values for the E_a were calculated assuming a normal distribution, shows that one standard deviation on the rate at 96°C is on the order of 40% of the rate, and only about 16% at 50°C (see Output DTN: SN0703PAEBSPCE.007, spreadsheet: *Uncertainty in WR interaction parameter.xls*, tab: "E_a for feldspar diss."). Even these values overestimate the error in the water–rock interaction parameter due to the uncertainty in E_a, as percolating waters will be exposed to a range of temperatures from ambient to boiling as they move downwards through the thermal field, and the maximum error, which occurs at 96°C, will be applicable for only a small part of the entire flow path. Given that the combined uncertainty in the feldspar dissolution rate due to uncertainties in mineral abundance and water:rock ratios is on the order of a factor of 3 to 4, the uncertainty in E_a, is considered insignificant, and not included in the uncertainty in the WRIP value.

6.12.2.3 Uncertainty Associated with the Plug Flow Implementation

To evaluate the effect of using a plug flow implementation to calculate transport times through the thermal profile, FEHM breakthrough curves for 1, 3, 10, 30, and 100 mm/yr were used to determine mean residence times. This analysis is documented in Section 6.3.3.2.4, and the data are summarized in spreadsheet *Transport time uncertainty.xls* archived in Output DTN: SN0703PAEBSPCE.007. The conclusions of the analysis are that assuming plug flow slightly under-estimates residence time in the NFC model (by a maximum of 15%), under-estimating the degree of water–rock interaction. The degree of under-estimation varies with the percolation flux. To correct for this, percolation fluxes used in the NFC model were adjusted slightly to generate transport times, assuming plug flow, that match the FEHM mean residence times. These "adjusted percolation fluxes" are used only internally to the NFC model; the WRIP lookup table is still entered using the unaltered percolation fluxes provided by TSPA. The FEHM simulations are archived in Output DTN: SN0703PAEBSPCE.007, and are presented in detail in Section 6.3.3.2.4.

After adjusting the percolation fluxes, the remaining uncertainty in residence times (and hence WRIP values), due to the spread in breakthrough times indicated by the FEHM simulations, was evaluated and found to be insignificant relative to the other model uncertainties presented in spreadsheet *Transport time uncertainty.xls* in Output DTN: SN0703PAEBSPCE.007). The uncertainty varies with many parameters, including percolation flux and time of seepage, but on the average, the change in the WRIP value due to the uncertainty in breakthrough time is only about 2.5% (1σ). Because this value is small relative to the effect of other uncertainties, and has a complex relationship to other model parameters, it is not included in the WRIP value. (See spreadsheet *Transport time uncertainty.xls* in Output DTN: SN0703PAEBSPCE.007 for details.)

6.12.2.4 Summary of WRIP Uncertainties

Three conclusions may be drawn from the analysis of uncertainty in the WRIP values:

- The uncertainty in the feldspar dissolution rate, due to uncertainties in secondary mineral abundance, rock hydrologic properties, and timing and temperature of alteration, is the largest uncertainty contributing to the WRIP value. The uncertainty in this parameter scales linearly to the WRIP value.

- The uncertainty in the WRIP value due to the activation energy (E_a) for feldspar dissolution is a function of temperature, and is small relative to the uncertainty in the feldspar dissolution rate. It is not incorporated into the net uncertainty in the WRIP that will be applied by TSPA.

- The model choice of plug flow relatively under-estimates transport times through the thermal gradient, potentially resulting in under-estimates in the WRIP value. This has been corrected for within the NFC model by the use of "adjusted percolation fluxes," internal to the model only. The spread in transport times indicated by the FEHM simulations results in a relatively small uncertainty in the WRIP value (on the average, less than 2.5%), and is a function of seepage time and percolation flux. It is not incorporated into the net uncertainty in the WRIP that will be applied by TSPA.

6.12.2.5 Combined Uncertainty in the WRIP

The combined uncertainty in the WRIP takes the form of a Beta distribution. The GoldSim beta distribution is implemented using the Beta distribution mean (μ) and standard deviation (σ), and the maximum (B) and minimum (A) values. The actual distribution was calculated in EXCEL, which uses a different form of the Beta distribution, also based on four parameters, α, β, A, and B, but the fitting parameters α and β do *not* correspond to μ and σ. The μ and σ values for the EXCEL Beta distribution were determined using the equations of Harr (1987 [DIRS 100580], Equations 2.3.2a and 2.3.2b), modified slightly to be consistent with the EXCEL form of the Beta distribution:

$$\mu = A + \frac{\alpha}{\alpha + \beta} \times (B - A) \qquad \text{(Eq. 6.12-1)}$$

$$\sigma = \sqrt{\frac{\alpha \times \beta}{(\alpha + \beta + 1) \times (\alpha + \beta)^2} \times (B - A)^2} \qquad \text{(Eq. 6.12-2)}$$

Hence, the uncertainty is passed to TSPA in the following way:

(1) The WRIP value (moles feldspar dissolved) is determined directly from the WRIP lookup tables. This value is the mean (μ) of the Beta distribution.

(2) A standard deviation (σ) of the Beta distribution is determined by μ * 0.4251.

(3) The maximum value (B) is equal to μ * 2.838.

(4) The minimum value (A) is equal to μ * 0.2039.

(5) A new WRIP value that includes the uncertainty is sampled from the Beta distribution defined using the above parameters.

In each realization, TSPA extracts the WRIP value from the WRIP lookup table and generates a new distribution at each time step. It implements the uncertainty in WRIP with self-correlation; that is, after sampling the WRIP beta distribution for the first time step, it samples the same probability value for the new distributions generated at each time step for the entire realization. The details of the derivation of the beta distribution can be found in Output DTN: SN0703PAEBSPCE.007 (spreadsheet: *Uncertainty in WR interaction parameter.xls,* tab: "summary 1)," cells AU20 through AU82).

6.12.3 Implementation of the IDPS and NFC Model Uncertainties in the Chemical Parameters of the P&CE Abstraction Models

IDPS uncertainty factors for the Cl, N, Cl:N, and *I* of in-drift water are used directly by the P&CE abstraction models and are given in Table 6.12-1. The uncertainty associated with Cl+N is calculated assuming linear combinations of the uncertainties on Cl and N provided by the IDPS model (SNL 2007 [DIRS 177411]) (see Table 6.12-1). These uncertainties apply between 20°C and 140°C and are defined as triangular distributions with the most likely uncertainty equal to ±0.0 with the maximum and minimum uncertainties defined in Table 6.12-1.

The uncertainty on pH adopted by the P&CE abstraction models is treated differently than in the IDPS over a portion of the relevant RH range (from 100% to 75%) (Table 6.12-2). See Section 6.12.3.1 for the re-evaluation of pH uncertainty.

Table 6.12-1. IDPS Uncertainty Factors for the Cl, N, Cl+N, Cl:N, and *I* of In-Drift Water

Parameter	Units	RH Range 100% to 85%	RH Range 85% to 65%	RH Range 65% to 40%	RH Range 40% to 20%	RH Range 20%to 0%
Cl	log molal	±0.0	±0.1	±0.4	±0.5	±0.7
N	log molal	±0.0	±0.2	±0.4	±0.5	±0.9
Cl:N	log mole ratio	±0.0	±0.2	±0.5	±0.5	±1.4
Cl+N*	log molal	±0.0	±0.22	±0.57	N/A	N/A
Ionic Strength, *I*	log molal	±0.1	N/A	N/A	N/A	N/A

Source: DTN: SN0611T0509206.007 [DIRS 179335], spreadsheet: *Estimated IDPS Uncertainties.xls*.

*Uncertainties calculated in this table assuming linear combinations of independent variables.

NOTE: N/A = not applicable. Data archived in Output DTN: SN0703PAEBSPCE.007, spreadsheet: *PCE_IDPS_Uncertainties.xls*.

Table 6.12-2. IDPS and NFC Uncertainty Factors for pH of In-Drift Water

Parameter	Units	RH Range 100% to 75%	RH Range* 75% to 65%	RH Range* 65% to 40%	RH Range* 40% to 20%	RH Range* 20% to 0%
pH	pH units	Discrete CDF	±1	±2	±2	±2

* DTN: SN0611T0509206.007 [DIRS 179335], spreadsheet: *Estimated IDPS Uncertainties.xls*. Discrete CDF is archived in Output DTN: SN0703PAEBSPCE.007, spreadsheet: *PCE_IDPS_Uncertainties.xls*.

Four values are extracted from the seepage dilution/evaporation lookup tables that are archived in Output DTN: SN0701PAEBSPCE.001: pH, *I*, Cl, and N. Among the uncertainties listed in Table 6.12-1, Cl, N, and Cl:N are assumed to be correlated (see discussion below). The uncertainties on pH, *I*, Cl, N and Cl:N are taken from DTN: SN0611T0509206.007 [DIRS 179335]. Prior to use by TSPA, these values are modified to incorporate model uncertainty (Table 6.12-1). The following steps are taken:

For pH and ionic strength: The pH value is taken directly from the lookup tables and is adjusted by the uncertainties reported in Table 6.12-1 using a triangular distribution for RH values below 75%. Between 100% to 75% RH , pH uncertainties are sampled from a discrete CDF archived in Output DTN: SN0703PAEBSPCE.007 (see discussion in Section 6.12.3.1). No uncertainty is associated with the ionic strength below 85% RH from the lookup tables because the ionic strength is not used by TSPA at these concentrations. Between 85% and 100% RH, the ionic strength is adjusted for uncertainty by applying a triangular distribution and the value in Table 6.12-1.

For Cl^-, NO_3^-, and Cl^-/NO_3^- ratio: The following steps should be taken to calculate the Cl, N, and Cl+N concentrations and Cl:N ratios. The P&CE abstraction models use the molal concentrations of Cl and N to represent Cl^- and NO_3^- concentrations.

1. TSPA will choose a P&CE potential seepage water chemistry lookup table from among the 396 archived in Output DTN: SN0701PAEBSPCE.001 (see description in Section 6.15.1) using a randomly selected group water type (1 through 4); a WRIP value (0, B, C,…L); a pCO_2 value of either 10^{-2}, 10^{-3}, or 10^{-4} bar; and a T_{wp} = 30°C, 70°C, or 100°C. The T_{wp}, and the independent variable, RH_{wp}, are provided by the MSTHM (SNL 2007 [DIRS 181383]). The data used to make the lookup table selection are archived in Output DTNs: SN0701PAEBSPCE.001, SN0701PAEBSPCE.002, and SN0703PAEBSPCE.006, and a detailed description of the calculations involved in lookup table selection are given in Section 6.15.1.

2. TSPA will evaluate for salt separation by comparing the RH_{wp} used to enter the lookup table selected in Step 1 to the salt separation RH found in the group water salt separation tables (e.g., *Gp1_Salt_separation_table.xls*) in Output DTN: SN0703PAEBSPCE.006. The RH of salt separation is used directly from the salt separation lookup tables for all group waters.

2.A. In the event of no salt separation:

a. Take the Cl+N concentrations from the lookup tables archived in Output DTN: SN0701PAEBSPCE.001.

b. Sample the [Cl+N] uncertainty using the appropriate RH range from Table 6.12-1 and archived in Output DTN: SN0703PAEBSPCE.007 by applying a triangular distribution.

c. Calculate ([Cl+N] + uncertainty) (x) obtained in Steps 2a and 2b.

d. Sample (Cl:N) (y) from discrete CDFs in Output DTN: SN0703PAEBSPCE.007. Uncertainty due to using a single pore water to represent a group of waters (e.g., the effect of binning potential starting pore waters chemically) is incorporated into the model by sampling the Cl^-/NO_3^- ratio (represented by Cl:N) for each starting water group from a discrete CDF for the starting water values.

e. Using x ([Cl+N] + uncertainty) and y (Cl:N) sampled from the CDFs to solve for [Cl] and [N], the calculated values will include uncertainty.

2.B. In the event of salt separation:

a. Once salt separation has occurred, the Cl:N CDFs no longer apply and Cl, Cl:N, and pH are taken directly from the lookup tables selected in Step 1 above. These values are valid at any RH below salt separation.

b. The model assumes that [Cl] is proportional to [Cl:N], and thus the uncertainties will also be correlated. Once TSPA samples the uncertainty on [Cl] using a triangular distribution with the end-points as shown in Table 6.12-1, an offset of the same sign (either positive or negative) will be applied to the [Cl:N].

c. The lookup tables can continue to be used until the RH rises in the drift, and exceeds the salt separation threshold. At that point, the lookup tables no longer apply and TSPA is instructed to assume that a Cl-rich brine can form. Because the process of salt-brine separation can not be explicitly modeled, the P&CE abstraction models do not attempt to provide the chemistry for the Cl-rich brines (see Figure 6.15-2 and Section 6.15.1 for discussion).

6.12.3.1 Reduction in pH Uncertainty

The IDPS model (SNL 2007 [DIRS 177411]) provides feeds to the P&CE model, which in turn provides water chemistries, including pH, for evaluating the occurrence of localized corrosion of the waste package outer barrier and the solubility of radionuclides in the invert. Included in the IDPS feeds are estimated model uncertainties in water compositional parameters, including the predicted pH. However, the IDPS uncertainty was developed by comparison of modeled data with pH values measured in several evaporation and mineral solubility experiments, and the process of measuring pH has significant error. This is especially true in concentrated brines,

where the development of an electrical potential across the electrode junction results in pH values which are increasingly erroneous with increasing ionic strength. In addition, standard pH electrodes are temperature-sensitive, and the appropriate corrections may not have been applied. Hence, much, perhaps most, of the pH uncertainty developed by the IDPS model may be a reflection of measurement error. This is likely to be an overestimate of the actual uncertainty in the predicted pH, as used in the P&CE and downstream models. As noted in the IDPS model report (SNL 2007 [DIRS 177411]), most geochemical systems have pH-sensitive components present, which can be used to either more accurately constrain the pH or to constrain the possible pH range. Hence, the predicted uncertainties are maximum values.

In addition, the form of the pH provided by the IDPS model and used by downstream models has changed since previous revisions of the model. The localized corrosion model is one of the most important downstream models, and it is based on an empirical fit to the pH, temperature, chloride concentration, and Cl^-/NO_3^- values of the solutions used in the corrosion experiments. In previous revisions of TSPA, the localized corrosion model was parameterized using measured pH values, and the IDPS model evaluated uncertainty based on the predicted "NBS pH." This is a value which represents neither the predicted concentration of the hydrogen ion, nor the activity of the hydrogen ion, but rather a value that should be most representative of a measured pH. However, the current localized corrosion model is parameterized using "Pitzer pH" values—values representing the predicted activity of the hydrogen ion in the solutions used in the corrosion experiments. All other downstream models are also parameterized using the Pitzer pH. Because Pitzer pH values and measured pH values are not equivalent, a comparison of Pitzer pH values to measured pH values, with their attendant errors, may not be a realistic estimation of the uncertainty in the predicted Pitzer pH values.

If measured pH values are not used, then how can the accuracy of the predicted Pitzer pH be evaluated? The error in predicted versus measured concentrations of pH-sensitive components may provide a more realistic measure of the uncertainty in pH. In systems of relevance to the P&CE model, one pH-sensitive solution parameter that is always present is total inorganic carbon concentration (TIC, or $[C]_{total}$), or the related parameters alkalinity, $[HCO_3^-]$, and $[CO_2^-]$.

In order to quantify the uncertainty in the Pitzer pH value, the sensitivity of the component used, $[C]_{total}$, to pH must be evaluated. This was done for five different solution compositions:

- 5 molal NaCl
- Group 1 representative water
- Group 3 representative water
- Group 1 representative water, evaporated to 75% RH
- Group 3 representative water, evaporated to 75% RH.

Each water was evaluated at 25°C and 100°C. In the first three cases, the waters were equilibrated in an EQ3 file at a pCO_2 of 10^{-3} bars, and an EQ3 pickup file was generated. For the unevaporated waters, the resulting EQ3 pickup files were appended to two EQ6 files and the waters were titrated to lower pH with HCl and to higher pH with NaOH, while holding the pCO_2 constant at 10^{-3} bars. The solid phases present were discarded after the initial step of reaction progress, to prevent them from buffering the liquid phase. For the evaporated waters, the EQ3 pickup files were appended to an EQ6 file, and the waters were evaporated to 75% RH.

The resulting EQ6 pickup file was then appended to EQ6 HCl and NaOH titration files and treated as above.

The results are shown in Figure 6.12-1. The titration curves show the classical behavior of carbonate systems. At low pH, there is little total carbon in solution, as the only aqueous species present is CO_2(aq) (or, H_2CO_3); the amount present is constant and is a direct function of temperature and pCO_2. Between approximately pH 5 and pH 4 in the evaporated pore-water solutions, the concentration in solution begins to increase, as HCO_3^- becomes increasingly abundant in solution. Over the near-neutral pH range (approximately 6 to 8), $\log[C]_{total}$ varies 1:1 with pH—that is, uncertainty in the value of $\log[C]_{total}$ corresponds to the same uncertainty in pH. Above pH 8, the slope begins to increase, as CO_3^{2-} becomes an increasingly important component of $[C]_{total}$. At some point, sodium carbonate begins to precipitate and the pH and carbonate concentration become invariant (not all of the titration curves illustrated in Figure 6.12-1 reached this point).

The evaporated Group 3 water follows the general trend, also displaying a slope of approximately 1. However, there are inflections in the NaOH titration curves; the slope changes for an interval of about one pH unit when hydromagnesite precipitates. After a short interval, the slope returns to 1.

The plots in Figure 6.12-1 illustrate that, over the interval from neutral to moderately basic pH, $[C]_{total}$ is sensitive to the pH, and in general, uncertainty in $\log[C]_{total}$ is a good estimate of uncertainty in pH. This is reasonable, as pH is a log-transformed value. It is important to note that although $[C]_{total}$ is not sensitive to pH in acidic solutions (and over an interval about 1 pH unit wide at neutral pH for evaporated Group 3 water), this does not indicate that the pH uncertainty is higher in these ranges. Rather, it merely means that $[C]_{total}$ is not adequately sensitive to evaluate the uncertainty in pH under these conditions.

The pH should exhibit the largest relative uncertainty in the near-neutral range, because at these values it does not contribute significantly to the charge balance of the solution, and is only loosely constrained by this requirement. At higher and lower pH values, the pH is "mass buffered" and relative uncertainty is less; hence, examination of $[C]_{total}$ uncertainty at neutral pH should provide a maximum, bounding relative uncertainty for all conditions.

To evaluate the uncertainty in $[C]_{total}$, the validation cases for the IDPS model were examined, and all cases for which measured data for $[C]_{total}$ or alkalinity in solution were available were summarized. In all, data from 11 different studies were examined, and 10 were used (138 data points). These validation studies are summarized in Table 6.12-3, and a short description is provided below. The actual data examined is provided in Table 6.12-4. Measured and calculated $[C]_{total}$ values were extracted from the IDPS validation simulations archived in DTN: MO0701EQ36IDPS.000 [DIRS 179290]. For a more complete description of these validation simulations, see the IDPS model report (SNL 2007 [DIRS 177411], Section 7).

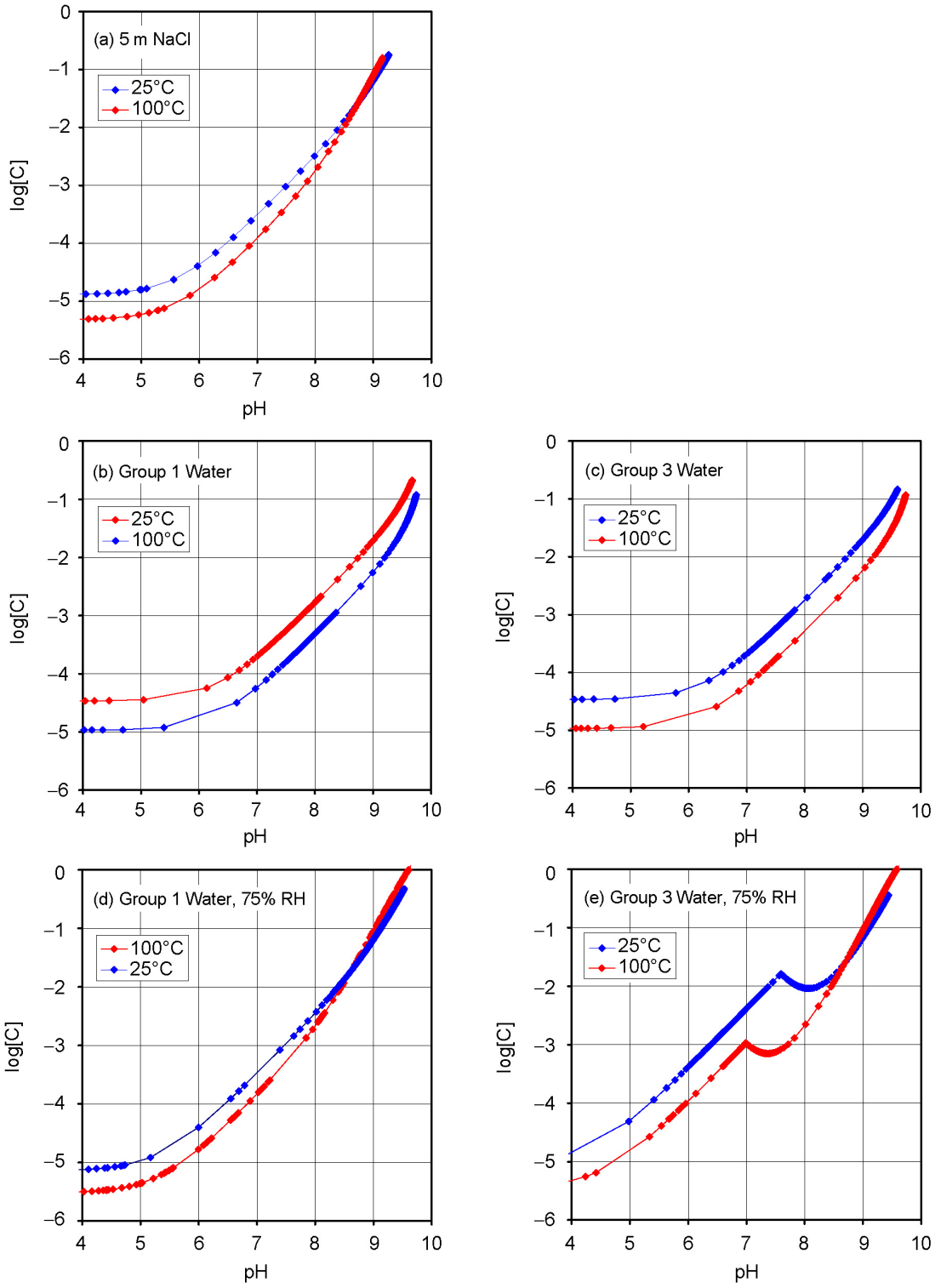

Source: Output DTN: SN0703PAEBSPCE.007, spreadsheet: *pH titration curves for various waters.xls*.

Figure 6.12-1. Change in [C] $_{total}$ with pH, Generated by Titrating HCl and NaOH into (a) 5 m NaCl, (b) Group 1 Representative Water, (c) Group 3 Representative Water, (d) Group 1 Water, Evaporated to 75% RH, and (e) Group 3 Water Evaporated to 75% RH

Table 6.12-3. List of IDPS Validation Studies Used to Evaluate Uncertainty in $[C]_{total}$

IDPS Validation Study	Number of Samples	Location (folder*file*)
See Section 4.1.16.2 for data qualification for intended use		
Evaporation of J13 Water LL991008104241.042 [DIRS 120489]	3	J13*j13n1pitpH.xls*
Evaporation of 100x Conc. J13 Water LL000202905924.117 [DIRS 144913]	2	100XJ13*j13b1 v3.xls*
Evaporation of Topopah Spring Tuff water at 75°C LL991008004241.041 [DIRS 120487]	1	Topopah*tspw3pitpH.xls*
IDPS DTN: MO0701EQ36IDPS.000 [DIRS 179290]		
Evaporation of Topopah Spring Tuff water at 95°C (SNL 2007 [DIRS 177411], Section 7.2.4)	16 (15 used)*	Topopah95*FEC[9/12/13/14]bsumPitpH r1.xls*
$CaCO_3$ solubility in Na-K-Ca-Mg-Cl-SO_4 solutions (SNL 2007 [DIRS 177411], Section 7.1.3.3.2)	15 (10 used)*	Ca-CO3-CO2\He&Morse*Calcite He and Morse r2.xls*
$CaCO_3$ solubility in KCl (SNL 2007 [DIRS 177411], Section 7.1.3.3.1)	18	Ca-CO3-CO2\Wolf*Calcite Wolf et al KCl r1.xls*
$CaCO_3$, $CaSO_4$ solubility in KCl (SNL 2007 [DIRS 177411], Section 7.1.3.3.1)	15	Ca-CO3-CO2\Wolf*Calcite Wolf et al KCl gyp r1.xls*
$CaCO_3$, $CaSO_4$ solubility in NaCl (SNL 2007 [DIRS 177411], Section 7.1.3.3.1)	18	Ca-CO3-CO2\Wolf*Calcite Wolf et al NaCl gyp r1.xls*
$CaCO_3$ solubility in $CaCl_2$ (SNL 2007 [DIRS 177411], Section 7.1.3.3.1)	31	Ca-CO3-CO2\Wolf*Calcite Wolf et al CaCl2 r1.xls*
$CaCO_3$ solubility in water (SNL 2007 [DIRS 177411], Section 7.1.3.2)	24	Ca-CO3-CO2\Linke*caco3-ev.xls*
CO_2 solubility in water at varying T, pCO_2 (SNL 2007 [DIRS 177411], Section 7.1.3.1)	42 (0 used)*	Ca-CO3-CO2\CO2*co2.xls*

* Some data were evaluated but not used in the final analysis. See text for discussion.

Table 6.12-4. Data Used to Evaluate Uncertainty in $[C]_{total}$

IDPS Validation Study	Temperature °C	Cl^- Measured (molal)	$\log([C]_{meas})$	$\log([C]_{model})$	Log[C] Difference
Evaporation of 100× Concentrated J13 water	90	2.06E-02	−1.17	−1.19	1.837E-02
	90	4.07E-01	−0.05	0.06	−1.035E-01
Evaporation of J13 water	85*	2.12E-04	−2.77	−2.91	1.356E-01
	85	2.39E-02	−1.15	−1.07	−8.187E-02
	85	1.36E-01	−0.39	−0.36	−3.250E-02
Evaporation of Topopah Spring Tuff water at 75°C	75*	2.20E-03	−3.58	−3.65	7.262E-02
Evaporation of Topopah Spring Tuff water at 95°C	95*	2.84E-03	−3.10	−3.90	8.021E-01
	95	3.04E-03	−3.51	−3.91	4.064E-01
	95	3.11E-03	−3.61	−3.92	3.075E-01
	95	3.68E-03	−3.94	−3.95	1.035E-02
	95	9.87E-03	−3.62	−4.05	4.288E-01

Table 6.12-4. Data Used to Evaluate Uncertainty in $[C]_{total}$ (Continued)

IDPS Validation Study	Temperature °C	Cl^- Measured (molal)	$\log([C]_{meas})$	$\log([C]_{model})$	Difference
Evaporation of Topopah Spring Tuff water at 95°C (continued)	95	9.80E-03	−3.80	−4.05	2.545E-01
	95	1.05E-01	−3.72	−4.09	3.720E-01
	95	1.06E+00	−3.99	−3.82	−1.682E-01
	95	1.09E+00	−3.71	−3.82	1.070E-01
	95	1.28E+00	−3.76	−3.81	5.001E-02
	95	1.46E+00	−3.78	−3.80	2.243E-02
	95	1.68E+00	−3.82	−3.79	−2.494E-02
	95	2.23E+00	−3.86	−3.82	−3.575E-02
	95	2.90E+00	−3.77	−3.93	1.594E-01
	95	4.40E+00	−3.81	−4.14	3.227E-01
	95	6.20E+00	−3.89	−4.29	3.985E-01
$CaCO_3$ solubility in Na-K-Ca-Mg-Cl-SO_4 solutions	0	1.14E+00	−3.01	−3.06	4.884E-02
	25	1.14E+00	−3.28	−3.33	5.044E-02
	50	1.14E+00	−3.43	−3.55	1.174E-01
	75	1.14E+00	−3.54	−3.74	2.010E-01
	100	1.14E+00	−3.62	−3.85	2.305E-01
	0	1.92E+00	−2.84	−2.71	−1.276E-01
	25	1.92E+00	−3.14	−2.99	−1.418E-01
	50	1.92E+00	−3.29	−3.20	−9.288E-02
	75	1.92E+00	−3.44	−3.37	−6.931E-02
	100	1.92E+00	−3.52	−3.49	−2.843E-02
$CaCO_3$ solubility in KCl	25	0.00E+00	−2.45	−2.47	1.681E-02
	25	1.00E-01	−2.30	−2.31	1.031E-02
	25	2.60E-01	−2.22	−2.25	3.114E-02
	25	7.60E-01	−2.13	−2.18	5.205E-02
	25	1.11E+00	−2.12	−2.17	5.089E-02
	25	1.72E+00	−2.11	−2.16	5.108E-02
	25	2.16E+00	−2.10	−2.17	6.401E-02
	25	2.33E+00	−2.11	−2.17	5.865E-02
	25	4.05E+00	−2.15	−2.21	6.167E-02
	25	4.81E+00	−2.18	−2.24	5.814E-02
	25	4.81E+00	−2.19	−2.24	4.823E-02
	60	2.30E-01	−2.52	−2.51	−9.866E-03
	60	4.50E-01	−2.51	−2.45	−5.520E-02
	60	1.04E+00	−2.40	−2.40	3.644E-03
	60	2.00E+00	−2.44	−2.39	−5.288E-02
	60	4.49E+00	−2.42	−2.44	2.121E-02
	60	5.14E+00	−2.49	−2.46	−3.138E-02
	60	5.89E+00	−2.50	−2.48	−1.995E-02

Table 6.12-4. Data Used to Evaluate Uncertainty in $[C]_{total}$ (Continued)

IDPS Validation Study	Temperature °C	Cl^- Measured (molal)	$\log([C]_{meas})$	$\log([C]_{model})$	Difference
$CaCO_3$, $CaSO_4$ solubility in NaCl	25	0.00E+00	−2.65	−2.47	−1.805E-01
	25	2.10E-01	−2.66	−2.65	−2.323E-03
	25	5.40E-01	−2.65	−2.64	−7.639E-03
	25	1.08E+00	−2.66	−2.66	−1.658E-03
	25	1.16E+00	−2.66	−2.66	2.029E-03
	25	2.12E+00	−2.69	−2.72	2.673E-02
	25	2.30E+00	−2.70	−2.73	2.971E-02
	25	3.60E+00	−2.81	−2.82	1.036E-02
	25	5.02E+00	−2.91	−2.91	−5.494E-03
	25	6.14E+00	−2.96	−2.96	4.268E-03
	60	0.00E+00	−3.04	−2.75	−2.877E-01
	60	0.00E+00	−3.07	−2.75	−3.123E-01
	60	2.00E-01	−3.00	−3.00	−1.598E-04
	60	5.10E-01	−3.01	−2.98	−3.115E-02
	60	1.03E+00	−3.06	−2.98	−7.156E-02
	60	2.08E+00	−3.13	−3.03	−1.007E-01
	60	4.00E+00	−3.17	−3.13	−4.002E-02
	60	5.05E+00	−3.23	−3.19	−4.178E-02
	60	6.33E+00	−3.26	−3.24	−1.642E-02
$CaCO_3$ solubility in $CaCl_2$	25	0.00E+00	−2.45	−2.47	1.924E-02
	25	2.00E-01	−2.88	−2.88	4.065E-03
	25	2.00E-01	−2.89	−2.88	−5.843E-03
	25	5.40E-01	−2.92	−2.92	4.207E-03
	25	6.40E-01	−2.95	−2.93	−2.554E-02
	25	1.06E+00	−2.99	−2.96	−3.150E-02
	25	2.32E+00	−3.08	−3.07	−4.087E-03
	25	2.74E+00	−3.09	−3.12	2.430E-02
	25	3.44E+00	−3.11	−3.20	8.721E-02
	25	4.78E+00	−3.20	−3.36	1.603E-01
	25	4.90E+00	−3.18	−3.38	1.960E-01
	25	6.08E+00	−3.26	−3.53	2.728E-01
	60	0.00E+00	−2.79	−2.76	−2.794E-02
	60	0.00E+00	−2.78	−2.76	−2.530E-02
	60	0.00E+00	−2.77	−2.76	−1.490E-02
	60	0.00E+00	−2.77	−2.76	−1.490E-02
	60	0.00E+00	−2.75	−2.76	7.635E-03
	60	4.00E-02	−3.16	−3.16	1.106E-03
	60	8.00E-02	−3.24	−3.21	−3.587E-02
	60	1.60E-01	−3.24	−3.24	−2.830E-03
	60	1.60E-01	−3.23	−3.24	1.215E-02

Table 6.12-4. Data Used to Evaluate Uncertainty in $[C]_{total}$ (Continued)

IDPS Validation Study	Temperature °C	Cl^- Measured (molal)	$\log([C]_{meas})$	$\log([C]_{model})$	Difference
$CaCO_3$ solubility in $CaCl_2$ (continued)	60	2.60E-01	−3.26	−3.26	−1.876E-03
	60	3.40E-01	−3.26	−3.27	5.412E-03
	60	8.40E-01	−3.30	−3.29	−1.232E-02
	60	8.60E-01	−3.30	−3.29	−1.147E-02
	60	1.20E+00	−3.29	−3.31	1.305E-02
	60	1.70E+00	−3.38	−3.34	−4.175E-02
	60	1.76E+00	−3.31	−3.34	2.922E-02
	60	3.60E+00	−3.34	−3.50	1.622E-01
	60	3.64E+00	−3.30	−3.50	2.025E-01
	60	5.52E+00	−3.33	−3.71	3.830E-01
$CaCO_3$, $CaSO_4$ solubility in KCl (suppressing syngenite and pentasalt)	25	0.00E+00	−2.63	−2.47	−1.692E-01
	25	3.00E-01	−2.63	−2.65	2.220E-02
	25	4.50E-01	−2.63	−2.65	1.368E-02
	25	1.36E+00	−2.64	−2.67	3.323E-02
	25	2.13E+00	−2.68	−2.71	3.171E-02
	25	3.05E+00	−2.69	−2.76	6.779E-02
	25	3.55E+00	−2.71	−2.79	7.660E-02
	25	4.80E+00	−2.79	−2.86	6.955E-02
	60	4.80E-01	−3.03	−2.98	−5.089E-02
	60	1.03E+00	−3.00	−2.98	−2.209E-02
	60	1.94E+00	−2.91	−3.00	8.716E-02
	60	3.06E+00	−3.00	−3.04	4.788E-02
	60	3.98E+00	−3.07	−3.08	1.774E-02
	60	4.63E+00	−3.02	−3.11	9.457E-02
	60	5.84E+00	−3.08	−3.17	9.123E-02
$CaCO_3$ solubility in water	0	0.00E+00	−2.15	−2.23	8.085E-02
	10	0.00E+00	−2.26	−2.31	4.659E-02
	20	0.00E+00	−2.37	−2.40	3.239E-02
	25	0.00E+00	−2.41	−2.43	2.278E-02
	30	0.00E+00	−2.45	−2.47	1.131E-02
	50	0.00E+00	−2.63	−2.61	−1.852E-02
	0	0.00E+00	−2.51	−2.61	9.114E-02
	10	0.00E+00	−2.62	−2.68	5.306E-02
	20	0.00E+00	−2.73	−2.76	3.333E-02
	25	0.00E+00	−2.77	−2.79	2.363E-02
	30	0.00E+00	−2.82	−2.83	1.207E-02
	50	0.00E+00	−2.99	−2.97	−1.968E-02
	0	0.00E+00	−2.85	−2.96	1.097E-01
	10	0.00E+00	−2.96	−3.03	6.950E-02
	20	0.00E+00	−3.07	−3.11	4.671E-02

Table 6.12-4. Data Used to Evaluate Uncertainty in $[C]_{total}$ (Continued)

IDPS Validation Study	Temperature °C	Cl^- Measured (molal)	$\log([C]_{meas})$	$\log([C]_{model})$	Difference
$CaCO_3$ solubility in water (continued)	25	0.00E+00	−3.11	−3.14	3.675E-02
	30	0.00E+00	−3.15	−3.18	2.489E-02
	50	0.00E+00	−3.33	−3.32	−8.855E-03
	0	0.00E+00	−3.02	−3.14	1.188E-01
	10	0.00E+00	−3.13	−3.21	7.841E-02
	20	0.00E+00	−3.23	−3.29	5.541E-02
	25	0.00E+00	−3.23	−3.32	8.652E-02
	30	0.00E+00	−3.32	−3.35	3.288E-02
	50	0.00E+00	−3.50	−3.49	−6.804E-03

Source: Output DTN: SN0703PAEBSPCE.007, spreadsheet: *Re-evaluation of pH uncertainty.xls.*

*Starting water composition.

6.12.3.1.1 Data Sets Examined

Eleven validation data sets were examined. Four are based on evaporation experiments; the other seven, equilibrium measurements of calcite or CO_2 solubility. These data are summarized in Output DTN: SN0703PAEBSPCE.007 (spreadsheet: *Re-evaluation of pH uncertainty.xls*).

Evaporation Experiments—Four groundwater/pore-water evaporation experiments have been carried out by Yucca Mountain Project (YMP) personnel (Table 6.12-3). Evaporation temperatures ranged from 75°C to 95°C, and these experiments are generally considered among the best available data for validation of the IDPS model, the intended use of which is to model evaporation in the repository drifts. However, with respect to $[C]_{total}$, these experiments may offer less useful data than for other components. Each starting water was based on an analyzed pore water, and represents a stable pore water at approximately 25°C, but at a pCO_2 slightly above atmospheric. When these waters are raised from ambient to 75°C to 95°C, they are highly out of equilibrium with respect to both calcite saturation and $[C]_{total}$ content. This is observed in three of the four evaporation data sets in Table 6.12-4 (the exception is the 100XJ13 data set). This degree of supersaturation with respect to CO_2 gas is not possible in the drift, where the temperature differential between the drift wall and the waste package is only a few degrees.

It is not clear that, once heating is initiated, equilibrium is rapidly reached with respect to CO_2 gas or calcite. The measured concentrations for most of the samples from the evaporation experiments consistently exceed the predicted values. If degassing occurs more rapidly than calcite precipitation, then the pH will rise, causing retention of carbonate, and may only slowly return to equilibrium as calcite precipitates. This may be the explanation for the elevated pH values observed early in the 85°C J-13 pore-water evaporation experiments (SNL 2007 [DIRS 177411], Figure 7-69).

Although these experiments may represent conditions of disequilibrium that are extreme with respect to what can develop in the drift, the data are conservatively retained in this uncertainty analysis, except for a single value. The error value for initial pore water for the 95°C Topopah Spring pore-water evaporation experiment is rejected. As just discussed, it represents a

comparison of the initial water composition at 25°C with a predicted equilibrium composition at 95°C, and a close match is not expected. Also, it is nearly twice the magnitude of the second largest error value, and is more than five standard deviations from the mean value for the data. If a normal distribution is assumed, it has a probability of occurrence of less than 2×10^{-6}; hence, even if it were a realistic value, including it in this distribution of 138 values would greatly over-weight it relative to its probability of occurrence.

Equilibrium Experiments—Seven data sets from equilibrium solubility experiments were examined (Table 6.12-3). Six evaluated calcite solubility in solutions ranging from pure water to concentrated brines. The seventh evaluated CO_2 solubility in pure water, and is not included in the analysis below. Although the $[C]_{total}$ concentrations were very well predicted in this experiment, the predicted pH values are 4 to 5, below the range where uncertainty in $[C]_{total}$ is a good analogue for pH uncertainty.

The six calcite solubility experiments include that of Linke (1958 [DIRS 166192], p. 539) in pure water; He and Morse (1993 [DIRS 162090]) in Na-K-Ca-Mg-Cl-SO_4 solutions (SNL 2007 [DIRS 177411], Section 7.1.3.3.2); and Wolf et al. (1989 [DIRS 177633], pp. 293 to 294) in KCl, with and without $CaSO_4$, in NaCl with $CaSO_4$, and in $CaCl_2$ (SNL 2007 [DIRS 177411], Section 7.1.3.3.1).

The Linke (1958 [DIRS 166192], p. 539) data and the IDPS simulations modeling were used with no modifications or omissions.

He and Morse (1993 [DIRS 162090], Table 3B) examined three solution compositions, and two of them, "Colby 12" and "Colby 18," including the IDPS simulations, were used with no modifications or omissions. The third data set, "Kennedy 1," was not used because the reported uncertainty in the $[C]_{total}$ measurement of 9×10^{-5} is as large as or larger than the reported concentrations of 6×10^{-5} to 11×10^{-5} molal (He and Morse 1993 [DIRS 162090], Table 3B; uncertainty in footnote).

All of the Wolf et al. (1989 [DIRS 177633], pp. 293 to 294) data were used, but in a few cases the IDPS simulations for the model data were modified. In the case of the solubility of calcite in $CaCl_2$ solutions, the IDPS EQ6 input files (files *Ca-CO3-CO2.zip*, Wolf*CaCCl25.6i*, and *CaCCl60.6i* in DTN: MO0701EQ36IDPS.000 [DIRS 179290]) were modified to provide a finer step size between $CaCl_2$ concentration steps to lessen the error associated with interpolating between the model output steps. The new files are archived in Output DTN: SN0703PAEBSPCE.007 (folder: \Files supporting re-evaluation of pH uncertainty\Calcite-CaCl2 reruns with smaller step size). In addition, for the system KCl-$CaSO_4$-$CaCO_3$, the IDPS simulation (DTN: MO0701EQ36IDPS.000 [DIRS 179290], files: *Ca-CO3-CO2.zip*, Wolf*CgyKCl25.6i*, and *CgyKCl60.6i*) was modified to suppress syngenite ($K_2Ca(SO_4)_2:H_2O$) and pentasalt ($K_2Ca_5(SO_4)_6:H_2O$). The new versions of these files are also archived in Output DTN: SN0703PAEBSPCE.007 (folder: \Files supporting re-evaluation of pH uncertainty\CaCO3-CaSO4-KCl system, syngenite, pentasalt suppressed). In the IDPS validation test cases, the mineral syngenite precipitated, and the comparisons between measured and predicted data are poor. As noted in the IDPS report, suppressing syngenite (and pentasalt, which saturates if syngenite is suppressed) to allow calcite and calcium sulfate (either gypsum or anhydrite, depending on the temperature) to be the solubility-controlling phases, results in a

much closer comparison of the model results to the independent data (Figure 6.12-2). However, because the IDPS model allows these phases to precipitate, they were not suppressed in the validation test cases used in the accompanying report (SNL 2007 [DIRS 177411]).

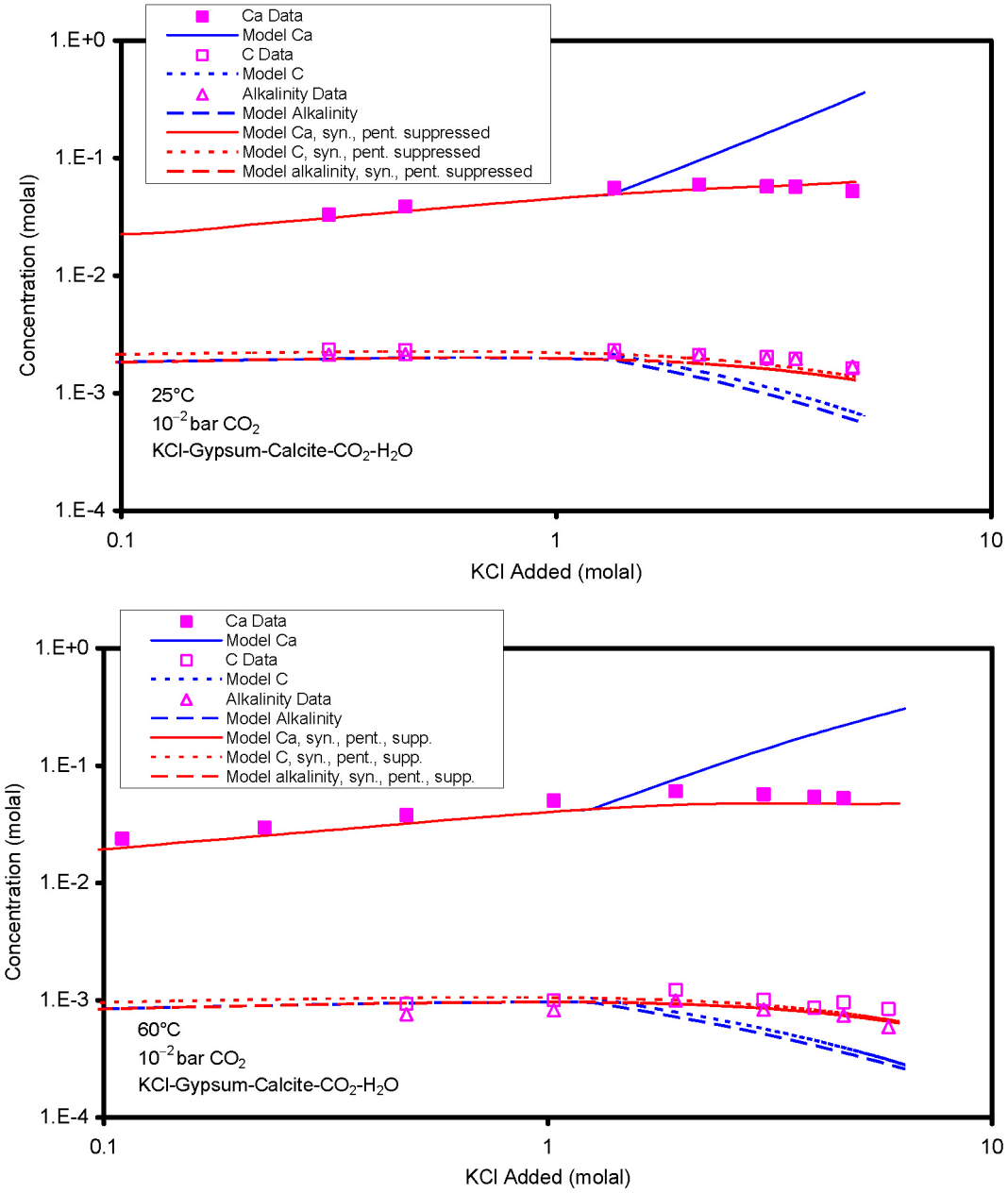

Source: Output DTN: SN0703PAEBSPCE.007, folder: \Files supporting re-evaluation of pH uncertainty\CaCO3-CaSO4-KCl system, syngenite, pentasalt suppressed.

NOTE: Fits are calculated both suppressing the minerals sy ngenite and pentasalt (red lines), and not suppressing these minerals (blue lines).

Figure 6.12-2. Measured and Modeled Data for Wolf et al. (1989 [DIRS 177633], pp. 293 to 294) $CaCO_3$-$CaSO_4$-KCl System, at 25°C and 60°C

The IDPS model was developed to model the composition of solutions as they evolve by evaporative concentration. Syngenite and pentasalt precipitate rapidly from solution under laboratory conditions, and occur in natural playa settings; hence, they are expected to precipitate under repository conditions, and are allowed to precipitate in the IDPS model. However, while the choice of mineral suppressions is part of the IDPS model, it is clear that allowing syngenite or pentasalt to precipitate when modeling these experiments is not appropriate for comparison of model results with the data from the test. The short duration of the test allows much smaller kinetic barriers to precipitation of specific minerals to override the attainment of the stable equilibrium assemblage and solution composition in a manner that does not necessarily apply to the longer time frames to be evaluated for the postclosure system. Assessing the conceptual uncertainty of whether these minerals will form or not in the drift environment requires some understanding of the magnitude of the kinetic barrier(s) and consideration of the relevant time frame. Phases that appear kinetically inhibited from precipitating in short-term studies may not manifest any effective inhibition at the longer time frames relevant to the system under consideration. If no additional data/observations/understanding of the kinetic aspects exist, then the conceptual uncertainty that results from the alternate choice of which phases are allowed/not allowed to precipitate in the model system should be addressed in another manner. For example, on the waste package surface, equilibrium with the drift atmosphere is appropriate because it has been shown in general that equilibration of gas-aqueous systems (particularly for CO_2) occurs very rapidly even at low temperatures, and the expected brines will persist for extended periods of time in the postclosure models. All other IDPS estimates of uncertainty in the output parameters (i.e., Cl, NO_3, pH, ionic strength) are based upon this approach, and the equilibrium assumption is consistent with the inclusion of syngenite and pentasalt in the geochemical system represented by the in-drift environment. However, because of the short term duration of the experiments by Wolf et al. (1989 [DIRS 177633], pp. 293 to 294), it is considered that the appropriate model data for the Wolf et al. $CaCO_3$-$CaSO_4$-KCl system are the data from the IDPS simulations with syngenite and pentasalt suppressed.

Independently determined measured values and IDPS model results for $[C]_{total}$ are compared in Figure 6.12-3. In general, the two sets of values match very well, except at low concentrations of $[C]_{total}$, which also correspond to the evaporation simulations. Mismatches are generally less than 0.1 log units, except at low concentrations of $[C]_{total}$, where mismatches for a few samples are as much as 0.4 log units.

Low concentrations of $[C]_{total}$ can correspond to a few different conditions, including either low pH or high temperature. To evaluate whether there is a correlation between these and the magnitude of the error in $[C]_{total}$, the error (the difference between measured and calculated values) is plotted against calculated pH in Figure 6.12-4a, and against temperature in Figure 6.12-4b. There is little apparent dependency on pH. There is some correlation with temperature, but the strongest factor seems to be whether the systems are evaporation or equilibrium systems.

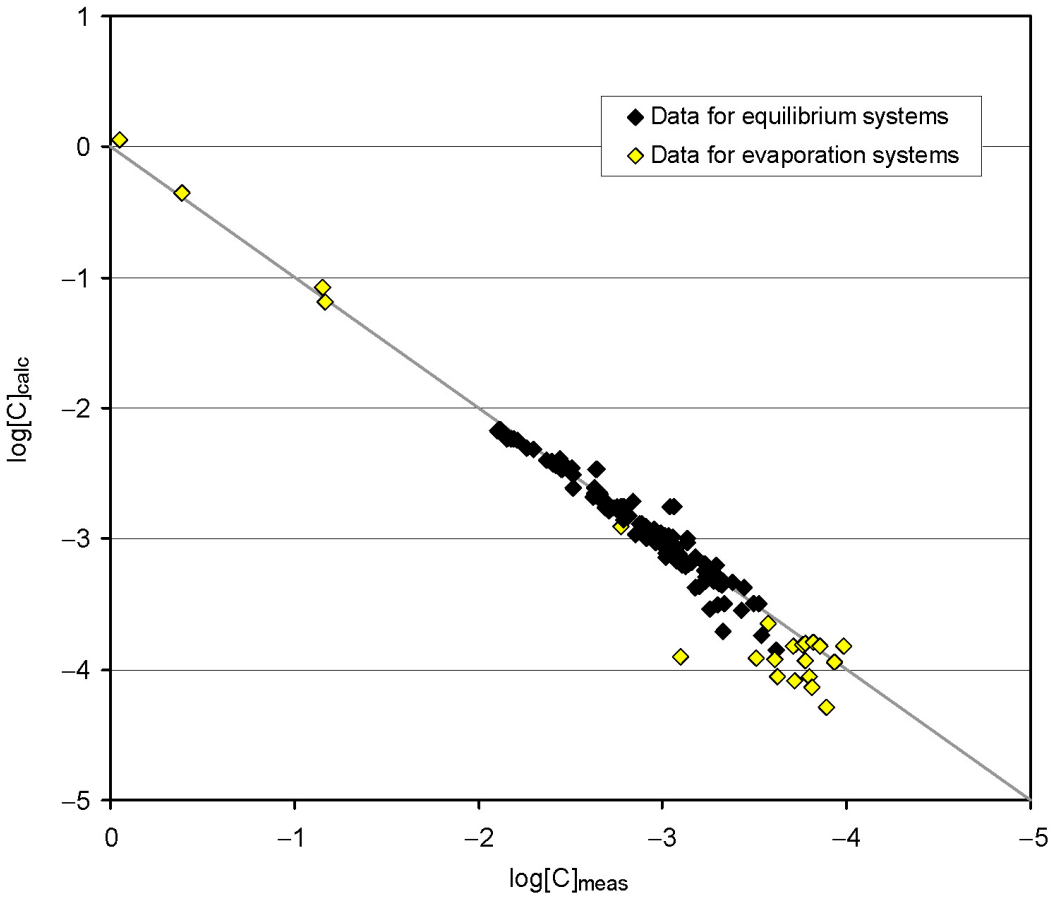

Source: Output DTN: SN0703PAEBSPCE.007, spreadsheet: *Re-evaluation of pH uncertainty.xls*, tab: "Summary charts."

NOTE: Measured and calculated values correlate very well, except at very low concentrations.

Figure 6.12-3. Plot of Measured and Calculated Total Carbon Values

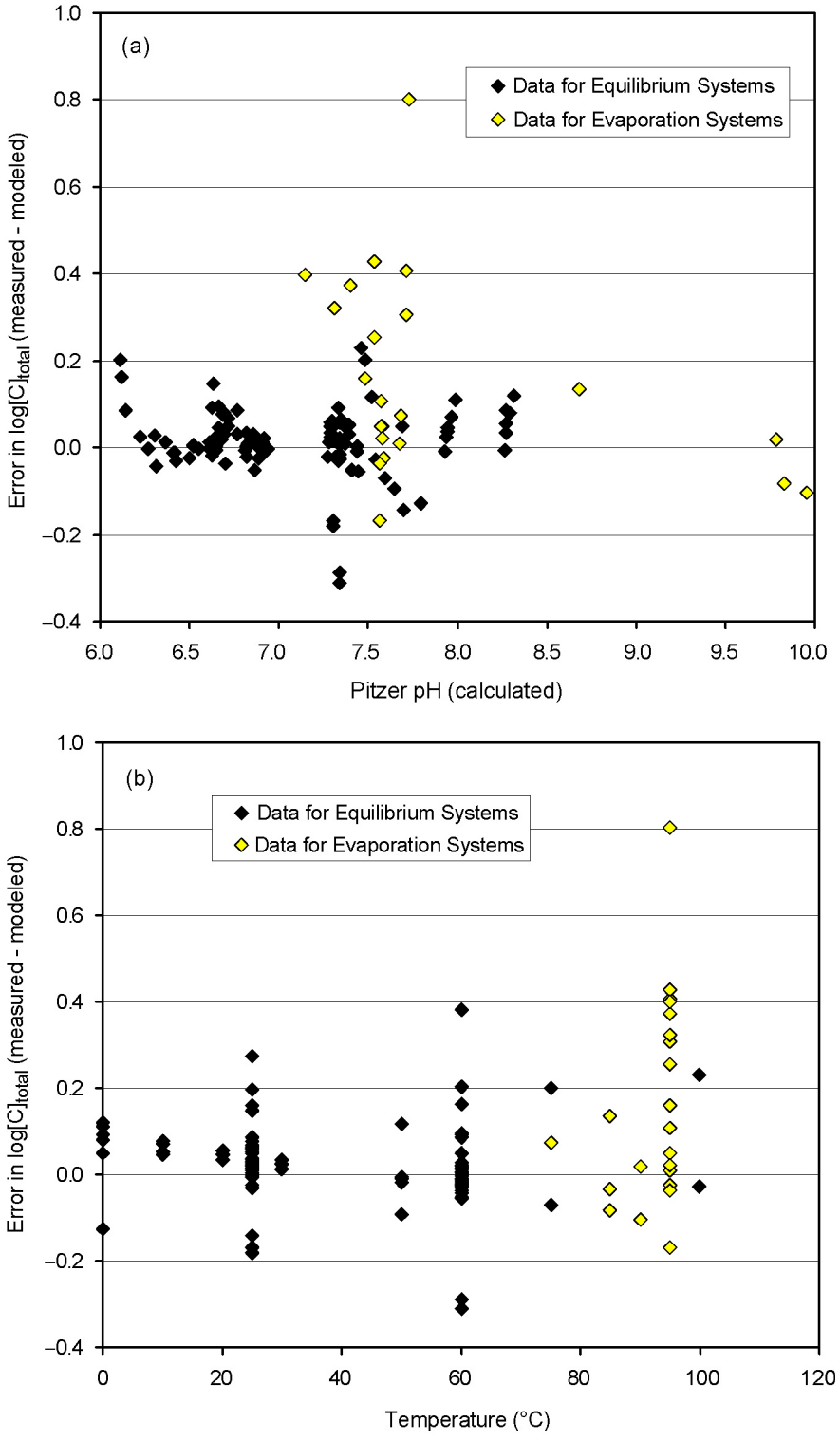

Source: Output DTN: SN0703PAEBSPCE.007, spreadsheet: *Re-evaluation of pH uncertainty.xls*, tab: "Summary charts."

Figure 6.12-4. Plot of Measured and Calculated Total Carbon Values: (a) Error in $[C]_{total}$ versus Calculated pH; (b) Error in $[C]_{total}$ versus Temperature

Another solution property that could affect $[C]_{total}$ would be ionic strength. To evaluate this, the error in $[C]_{total}$ was plotted against chloride concentration in Figure 6.12-5. There is no correlation with chloride concentration. The waters showing large uncertainties range from highly dilute—conditions where errors in the Pitzer model would have no effect because the Pitzer model reduces to a simpler activity model (Debye-Hückel)—to concentrated (up to 6 molal) brines, where the Pitzer interaction coefficients play a large role. This suggests that the uncertainty in $[C]_{total}$ may be largely due to experimental conditions or measurement error, and not be database-related. Specifically, the assumption of equilibrium may not hold in rapidly evaporating, higher temperature experimental systems.

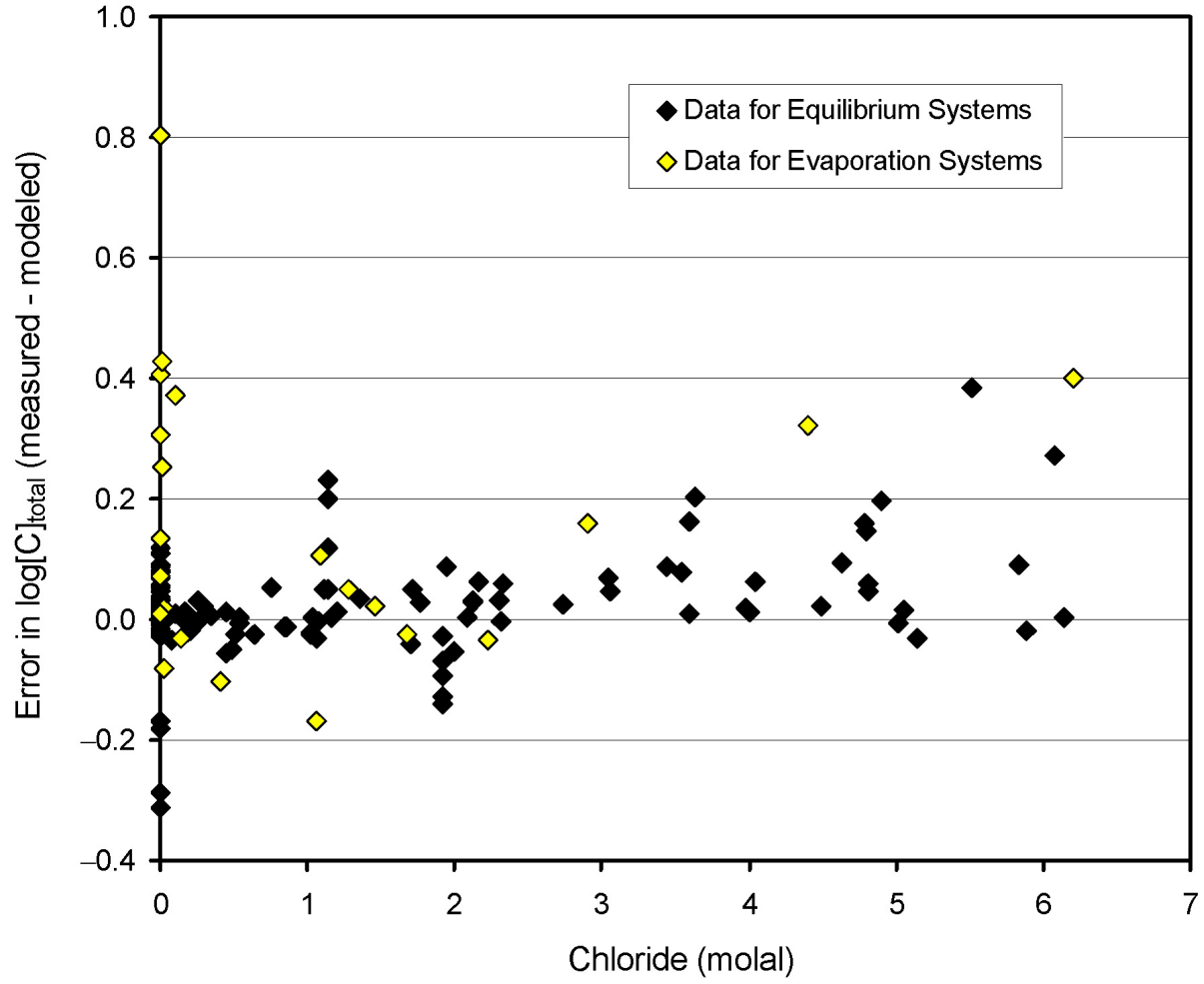

Source: Output DTN: SN0703PAEBSPCE.007, spreadsheet: *Re-evaluation of pH uncertainty.xls*, tab: "Summary charts."

Figure 6.12-5. Plot of Error in $[C]_{total}$ versus Chloride Concentration

6.12.3.1.2 Statistical Evaluation of Uncertainty in $[C]_{total}$ and, by Inference, pH

In this section, the uncertainty in $\log[C]_{total}$, and by inference, pH, is evaluated statistically. The entire data set of the error in $\log[C]_{total}$ ($\log[C]_{total\ measured} - \log[C]_{total\ modeled}$) is plotted as a histogram and a CDF in Figure 6.12-6. The majority of the data (approximately 80%) are distributed around a value slightly larger than zero, and fall within 0.1 log units of zero. A scatter of values occurs above and below this range, with higher values being somewhat more common, primarily because the measured values in the evaporative systems tend to significantly exceed the predicted values.

This data set is not amenable to fitting with any standard distribution; the central high-probability peak is too narrow, and extreme values cover too large a range. Normal, lognormal, triangular, beta, or gamma distributions either under-weight the extreme values or heavily over-weight the less extreme values, e.g., greatly overestimating the probability of difference values in the 0.1 to 0.2 range. Hence, the uncertainty is best characterized by sampling a discrete distribution of the values. This discrete distribution is archived in Output DTN: SN0703PAEBSPCE.007 (spreadsheet: *Re-evaluation of pH uncertainty.xls*, tab: "CDF of pH uncertainty").

While the number of systems considered is limited, it is proposed that, on the basis of this analysis, the uncertainty in pH can be reduced from the current value of ±1 units, for systems above approximately the RH of salt saturation (e.g., approximately 75%). The uncertainty is best described by use of a discrete distribution of the available data. There is clearly a dependence upon the type of experiment, with the non-equilibrium evaporation experiments generally yielding the greatest uncertainty. Because these data are included in the distribution, it is considered that this distribution is probably conservative, with a larger range, and more heavily weighted "tails" than is accurate for equilibrium systems.

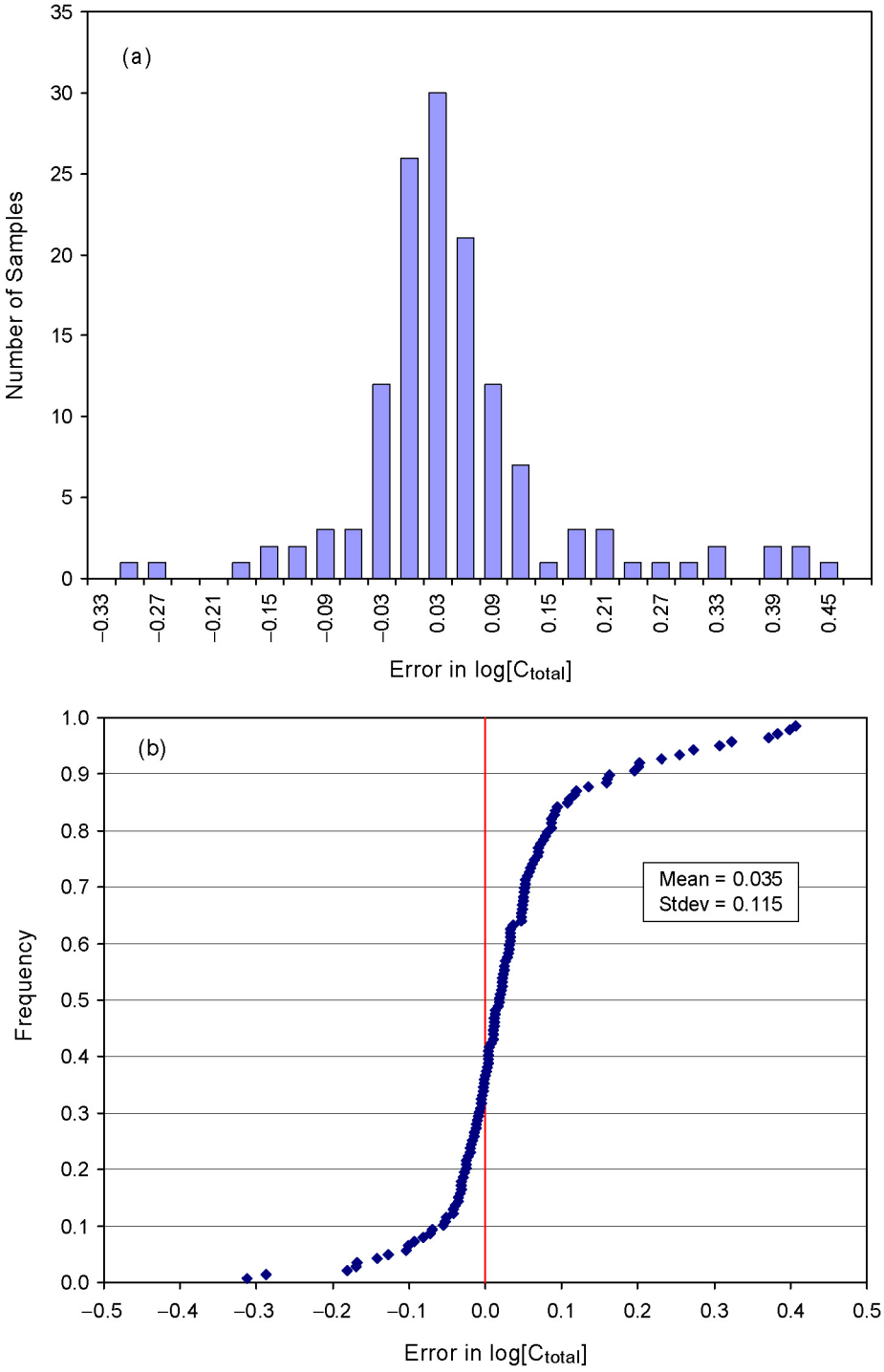

Source: Output DTN: SN0703PAEBSPCE.007, spreadsheet: *Re-evaluation of pH uncertainty.xls*, tab; "Summary charts."

NOTE: The error values form a distribution with a very narrow, high-probability peak, but with scattered higher and lower values. It is slightly offset towards positive values.

Figure 6.12-6. Histogram (a) and CDF (b) of Error in $[C]_{total}$

6.12.3.1.3 pH in Condensation

In pure condensation, the pH would be determined solely by the temperature and the pCO_2 of the system. Because the carbonate system is very well known and because thermodynamic behavior of aqueous species in highly dilute systems is very well constrained (e.g., activity coefficients are equal to 1), there would be very little pH uncertainty in such a system. However, TSPA treats condensation as very dilute pore water, which behaves differently than pure condensation. To evaluate how dilute a system has to be to exhibit the pure-water behavior, data were extracted from the EQ3/6 dilution files used in the construction of the dilution/evaporation tables in the P&CE abstraction (Output DTN: SN0701PAEBSPCE.001). In these tables, waters are diluted by a factor of 100; hence, the end-point RH varies with the initial ionic strength of the pore water. The results are shown for Group 1 and Group 3 waters with differing amounts of alkali feldspar titrated in, at three different temperatures, in Figures 6.12-7 and 6.12-8, respectively. For each case, the pH is plotted against RH; and it is clear that the pH values do converge with increasing dilution, although they do not completely coincide, as the degree of dilution is only a factor of 100 from the initial water compositions. The ionic strength for the most dilute waters ranges from 5×10^{-5} molal to 2×10^{-4} molal. In general, there is a trend for water compositions for each group to converge with dilution, until an activity of water of approximately 0.9999 is reached. After this point, the waters follow nearly parallel paths to higher dilution, converging only very slowly. Eventually, with greater degrees of dilution, the curves must converge; however, mass balance arguments (mass of percolating water intersecting the drift per meter vs. how much condensation can occur) suggest that higher degrees of dilution will not be reached in waters condensing on the drift walls or in the invert. Because the pH values only converge at very high RH values, it is inappropriate to assign no error to condensation pH values, unless the condensation is occurring on a surface with no pore-water contribution (e.g., the underside of the drip shield). Hence, the general uncertainty in pH described in the previous section applies to drift wall condensation.

Table 6.12-5 lists the results of equilibrating dilute water (actually, 10^{-12} molal NaCl solution), with pCO_2 values of 10^{-2}, 10^{-3}, and 10^{-4} bars, at temperatures of 30°C, 70°C, and 100°C. Also given is the ionic strength, which is equal to 10^{-pH} for the simple solutions. It is at these values of ionic strength, one to two orders of magnitude more dilute than the most dilute values in the P&CE dilution/evaporation tables (Output DTN: SN0701PAEBSPCE.001), that the diluted pore waters would converge to the same pH value at any given temperature and pCO_2. These correspond to RH values in the range from 0.99999 or higher. It is these pH values, without uncertainty, that should be used for condensation that forms in the absence of a pore-water contribution.

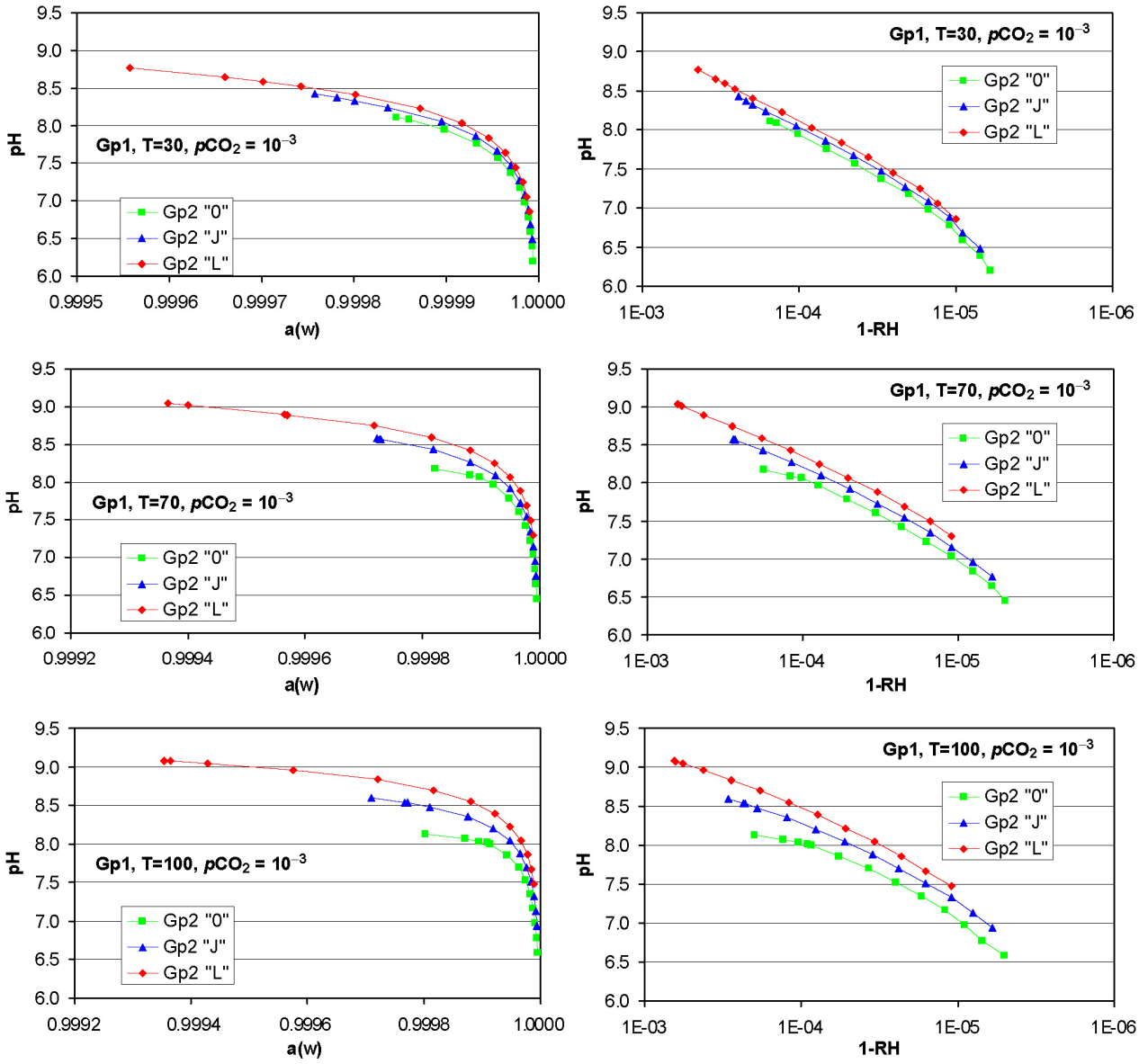

Source: Output DTN: SN0703PAEBSPCE.007, spreadsheet: *pH data from evap-dilution tables.xls.*

NOTES: "0" = no feldspar added; "J" = median amount of feldspar added; "L" = largest amount of feldspar added.

The labels on the x-axes correspond to activity of water (a(w)) and one minus the relative humidity (1−RH).

Figure 6.12-7. Group 1 Waters, with Varying Amounts of Alkali Feldspar Titrated into the Solution

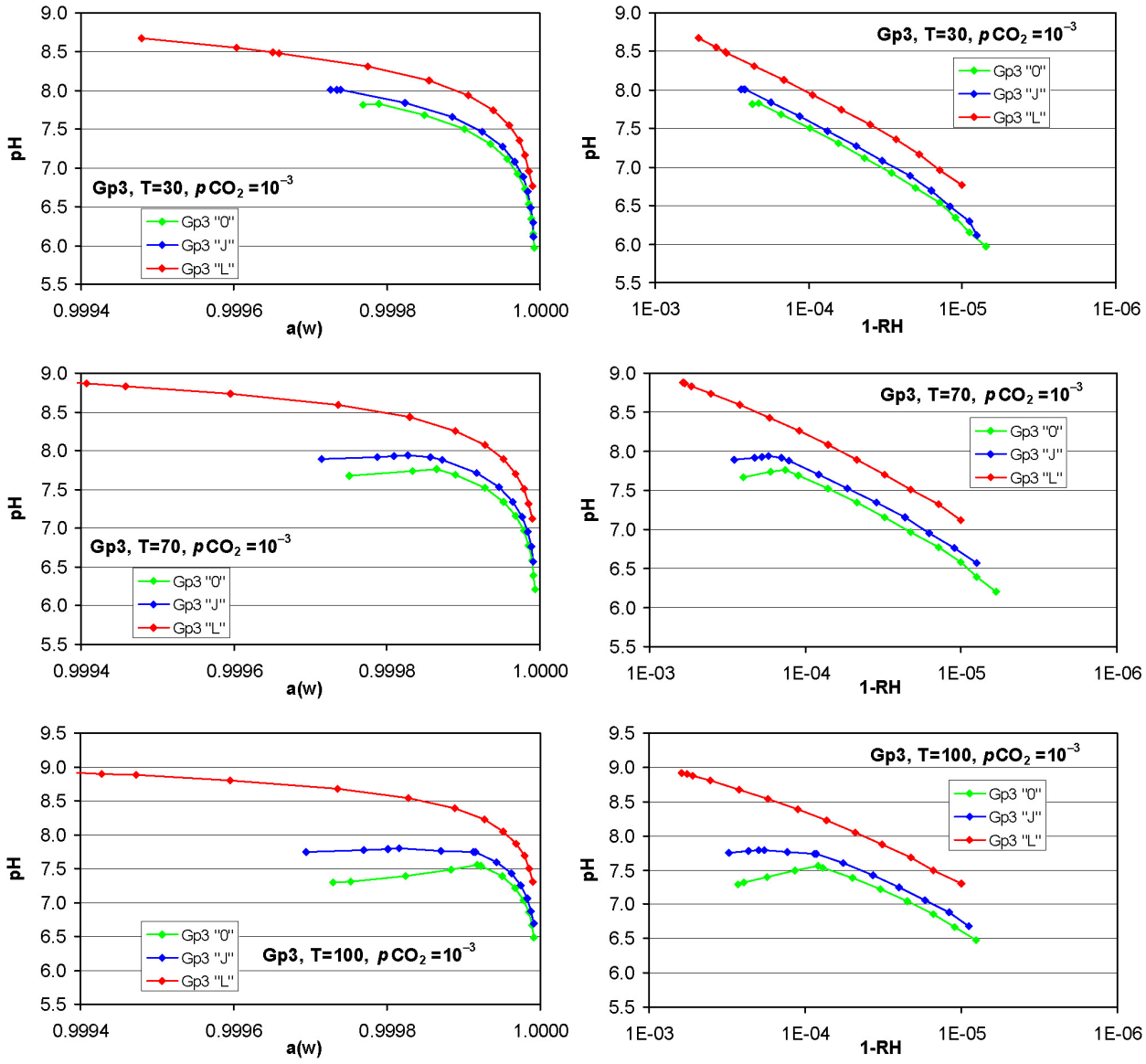

Source: Output DTN: SN0703PAEBSPCE.007, spreadsheet: *pH data from evap-dilution tables.xls.*

NOTES: "0" = no feldspar added; "J" = median amount of feldspar added; "L" = largest amount of feldspar added.
The labels on the x-axes correspond to activity of water (a(w)) and one minus the relative humidity (1−RH).

Figure 6.12-8. Group 3 Waters, with Varying Amounts of Alkali Feldspar Titrated into the Solution

Table 6.12-5. pH and Ionic Strength of "Dilute" Water at Various Temperatures and pCO_2 Values

Temperature (°C)	CO_2(g) Log Fugacity	a(w)	log(*I*)	Pitzer pH
30	−2	0.999990	−4.92	4.92
30	−3	0.999995	−5.42	5.42
30	−4	0.999996	−5.92	5.92
70	−2	0.999994	−5.06	5.06
70	−3	0.999997	−5.56	5.56
70	−4	0.999997	−6.02	6.02
100	−2	0.999995	−5.17	5.18
100	−3	0.999997	−5.65	5.65
100	−4	0.999997	−6.00	6.00

Source: Output DTN: SN0703PAEBSPCE.007, spreadsheet: *pH of condensation.xls*.

6.12.4 Factors Showing No Significant Impact on Water Chemistry

Several potential sources of perturbation to the predicted water chemistries contained within the lookup tables have been evaluated in sensitivity studies. These include:

- Steel corrosion and its interactions with seepage waters
- Lookup table extrapolation as a function of pCO_2
- Lookup table interpolation as a function of T and WRIP.

These studies show that variations due to these factors are well within the model uncertainty ranges and demonstrate that any additional errors caused by their exclusion from the lookup table calculations are subsumed by other modeling uncertainties.

6.12.4.1 Degradation of Stainless Steel in Ground Support Components

A range of possible sources of uncertainty in the steel–water interactions analysis were examined in Section 6.8. By increasing the amount of steel added to the waters, any uncertainty in the corrosion rates and surface areas was accounted for. Additional uncertainty may be due to limiting the evaluation to only two of the starting seepage water compositions. This is mitigated by selecting Group 1 and Group 3 water for comparison, as these are the two most chemically distinct seepage water compositions (see Section 6.6). Another source of uncertainty is the use of only two of the eleven WRIPs. The uncertainty is shown to be negligible by analyzing steel interactions with both a WRIP of zero and a moderate WRIP value for the two chosen water types. Only negligible differences in aqueous chemistry were observed leading to the conclusion that the impact of steel corrosion for all WRIPs may be safely ignored.

6.12.4.2 Extrapolating pCO_2 Values beyond Lookup Tables

As discussed in Section 6.15.1, extrapolation may be made when pCO_2 is outside the given range of the P&CE seepage dilution/evaporation lookup tables. A sensitivity study examined the range over which the lookup tables can be extrapolated and the details of the analysis and the results are reported in Section 7.2. The conclusion was that valid log linear extrapolation as a function

of pCO_2 can be performed to obtain values of pH, ionic strength, and chloride and nitrogen concentrations. Such an extrapolation both to high $pCO2$ (2×10^{-2} bar) and low $pCO2$ (10^{-5} bar) did not produce uncertainties beyond those assigned to the key chemical parameters utilized by TSPA-LA (pH, I, [Cl], [N]). At RH >85%, the IDPS report (SNL 2007 [DIRS 177411]) assigns zero uncertainty to the [Cl] and [N] values. The differences between the extrapolated and modeled values are non-zero (see Section 7.2). The calculated differences are negligible and will not increase the uncertainty associated with the TSPA implementation of the dilution/evaporation abstraction model.

6.12.4.3 Interpolating Values within the Lookup Tables

As discussed in Section 6.15.1, interpolation may be used by TSPA to obtain chemical parameters from the dilution/evaporation abstraction lookup tables. Interpolated values are compared with specific EQ6 simulations to ensure that the interpolation results adequately estimate the output from the IDPS process model (SNL 2007 [DIRS 177411]), within the bounds of the model uncertainty (from Table 6.12-1).

Section 7.2 documents a validation exercise that uses interpolation of two variables, pCO_2 and temperature, to assess the impact on uncertainty in TSPA implementation. The conclusion was that the P&CE seepage dilution/evaporation abstraction is a valid representation of evaporated seepage water compositions as calculated using EQ6 simulations to implement the IDPS process model, especially when propagation of the model uncertainty is included. Where the IDPS model uncertainty is nonzero, the abstraction model falls within those bounds and where the IDPS model uncertainty is zero, the differences are quantitatively insignificant and the validation criterion is met.

6.13 ENGINEERED BARRIER SYSTEM PHYSICAL AND CHEMICAL ENVIRONMENT

The engineered barrier system physical and chemical environment analyses focus on a quantitative description of pH, ionic strength (I), and major ionic and elemental compositions of waters in contact with the waste package, the drip shield, and the invert. The brines that form by evaporative concentration from the potential seepage water over time can potentially affect localized corrosion rates on the waste package and drip shield, and influence radionuclide mobility in the invert. Corrosion of the Alloy 22 may lead to release of radionuclides from the waste form. Elemental ratios such as Cl:N are important in assessing the potential for localized corrosion of the waste package in the EBS environment (SNL 2007 [DIRS 178519], Figure 6-1; SNL 2007 [DIRS 180778]). Acidic or alkaline pH values of water in the invert can enhance the solubility of radionuclides. The pH and ionic strength of water in the invert will impact the mobility of colloidal material transporting adsorbed radionuclides.

In addition, dust that accumulates on waste packages or drip shields during the operational and ventilation time periods may contain soluble salts, which will cause water condensation if the in-drift humidity is higher than the minimum deliquescent point of the salts. The resulting brine solutions and their significance to degradation of the waste package outer barrier are discussed in Section 6.10 and more thoroughly addressed in *Analysis of Dust Deliquescence for FEP Screening* (SNL 2007 [DIRS 181267]).

This section summarizes the results of the P&CE implementation of the NFC process model and the two abstraction models (dilution/evaporation and invert chemistry) described in this document, establishing the magnitude and range of chemical variables anticipated in the near field, and establishing the foundation for the TSPA-LA modeling approach for the EBS environment.

As described in Section 6.6, the analysis of more than 100 pore waters by the NFC model yielded 34 selected TSw compositions that, when further analyzed using principal component analysis, were reduced to four representative group waters. These four group waters form the basis for the NFC treatment of seepage water compositions (Table 4.1-3).

The NFC model is developed in Section 6.3.3 and provides water–rock interaction parameters (WRIPs), seepage water compositions, and a range of in-drift pCO_2 values. The WRIP values are calculated using rock mineral, thermal, and hydrologic properties taking into account the thermal perturbation due to waste emplacement and percolation fluxes over time. The seepage water compositions are generated by assuming saturation with SiO_2 (am) and calcite with varying alkali feldspar dissolved. A broad range of WRIP values are covered from zero to 1.47×10^{-2} moles of alkali feldspar added (Table 6.3-5). Maximum and minimum pCO_2 values are determined as described in Section 6.15.1. The NFC seepage water compositions and expected range of pCO_2 provide key inputs into the development of the P&CE dilution/evaporation and integrated invert chemistry abstraction models (Section 6.9).

Section 6.7 concludes that while oxygen may be consumed during the corrosion of low alloy steels in the invert, oxygen fugacity is not expected to drop below 10^{-9} bar due to these processes. The calculated pO_2 is discussed in terms of important redox couples in Section 6.7.1.6. The general conclusion of Section 6.7 is that conditions will remain oxidizing in the drift.

As calculated in Section 6.8, the quantifiable effects of steel corrosion on seepage water for the key chemical parameters provided to TSPA-LA by the P&CE are insignificant for relative humidities down to the eutectic composition. Based on these results which include an assessment of the uncertainty associated with corrosion parameters, it has been concluded that corrosion of the ground support and invert steels will not appreciably influence the composition of the seepage waters in the drift.

6.13.1 Engineered Barrier System Seepage Chemistry

Section 6.9 describes the development of the dilution/evaporation seepage abstraction model and the resulting lookup tables that represent the pH, *I*, and chemical compositions (Ca, Na, K, Mg, Al, F, S, Si, N, Cl, and C) of seepage and invert water. The P&CE instructs TSPA-LA to use the same lookup tables for seepage on the drip shield, waste package, and in the invert (Section 6.15.2). Further instructions are given such that invert water chemistries predicted by the P&CE are evaluated against compositions generated by the IPC abstraction (SNL 2007 [DIRS 180506]) to ensure that invert water compositions are selected to be conservative with respect to radionuclide mobility (see Table 6.15-1).

The results from the lookup tables are summarized as follows:

- Section 6.13.1.1 describes the NFC seepage water calculation limits and their utility to the construction of the lookup tables.

- Section 6.13.1.2 discusses what these lookup tables represent and the ranges of outputs associated with these tables.

6.13.1.1 Engineered Barrier System Seepage Chemistry Constraints

The NFC model seepage output may be calculated for any location in the drift by deriving a WRIP quantity associated with that location at a particular time step (described in detail in Section 6.3.3.2.6). In this manner, location-specific seepage water chemistry is generated by TSPA by randomly selecting a starting water, calculating a WRIP for the selected waste package location at a given time, obtaining temperature and relative humidity from the MSTHM report, and calculating and sampling within the range of pCO_2 values (see Section 6.15.1).

6.13.1.2 Engineered Barrier System Seepage Chemistry Equilibrium Response Surfaces

The seepage dilution/evaporation lookup tables developed and described in Section 6.9 provide discontinuous chemical equilibrium response curves. By interpolating and extrapolating among the various parameters (WRIP, T, pCO_2, RH) to calculate water chemistries, an equilibrium response surface becomes continuous for the range of in-drift environmental variables. From the lookup table values, key chemical parameters can be interpolated for water temperatures ranging from 30°C to 100°C, partial pressures of CO_2 from 10^{-4} to 10^{-2} bar, and relative humidity in the drift from 0% to 100% (Output DTN: SN0701PAEBSPCE.001) (see Section 7.2)

For each starting group water, there are 99 evaporation and 99 dilution simulations, one for each combination of temperature (40°C, 70°C, and 100°C), pCO_2 (10^{-4}, 10^{-3}, and 10^{-2} bar) and WRIP (0, B, C, D, E, F, G, H, I, J, L) (see Table 6.3-5). As each water composition evolves along the evaporative pathway, a series of changes occur associated with the concentration of aqueous species and subsequent precipitation of solid phases. A series of "chemical divides" may be encountered (see Section 6.3.2.2), resulting in a wide range of brine compositions depending on the initial water composition and the equilibrium temperature and pCO_2.

The combination of the 99 individual lookup tables (one evaporation and one dilution simulation for each) for each starting group water represents an equilibrium response surface for the chemistry in that group water, so they document the potential ranges of outputs for the ranges of inputs simulated. In the TSPA-LA simulations, the potential range of values is constrained to a single evolution path for each chemical variable by the choice of pCO_2, temperature, and WRIP. The predicted relative humidity will further constrain the possible value of each parameter to a narrow range.

6.13.2 Lookup Table Interpolation for Seepage

Aside from the general modeling uncertainty discussed in Section 6.12, this section considers the interpolation requirements associated with implementing the lookup tables within TSPA-LA. The lookup tables contain two types of parameters, independent and dependent. The

independent parameters are relative humidity, temperature, carbon dioxide pressure, and WRIP value. Values for these parameters are needed to determine the values of the dependent parameters, such as the pH, or the total concentration of a dissolved chemical component (chloride, for example).

The independent variables in the lookup tables (i.e., relative humidity, temperature, and pCO_2) have their own uncertainty in the TSPA-LA realizations. The uncertainties for temperature and relative humidity are defined outside the P&CE model and are not addressed here. As for pCO_2, a range of potential values is generated by the NFC model (see discussion in Sections 6.3.3.2.9 and 6.15.1). Lookup tables for the maximum pCO_2 values and the total carbon values used to derive the minimum pCO_2 values are archived in Output DTN: SN0701PAEBSPCE.002. Uncertainty is applied as a relative off-set within this range according to the TSPA implementation instructions in Section 6.15.1

The lookup tables provide direct results only for select combinations of independent variables. That is, they provide results at temperatures of 30°C, 70°C, and 100°C, pCO_2 of 10^{-2}, 10^{-3}, and 10^{-4} bar, and relative humidity at intervals up to 2%. Many humidity intervals are less than 2%. The TSPA-LA model is designed to interpolate and extrapolate dependent variable outputs for other combinations of these parameters (ranges described in Section 6.12 and defined in Output DTN: SN0703PAEBSPCE.007). By interpolating and extrapolating, the lookup tables provide a set of smooth and continuous equilibrium chemical response surfaces. Although some error may be introduced by interpolation and extrapolation, this error is negligible compared to model uncertainty and uncertainty in the predicted values of the independent variables (see Section 7.2 for confirmation).

6.13.3 Chemical Environments on the Drip Shield and Waste Package

For the waste package environment, the primary aqueous components of concern include Cl^-, and NO_3^-; these, along with pH and I, may affect corrosion of the waste package outer barrier. These parameters are discussed in terms of the major output of this model, i.e., the composition of in-drift evaporated seepage waters. For a detailed discussion of the chloride:nitrate ranges and treatment of uncertainty associated with determining the RH of salt separation, see Sections 6.12 and 6.15.

In-Drift Evaporated Seepage Waters—As shown in Tables 6.13-1 through 6.13-4, for waters from the four representative starting group waters, as WRIP increases so does their alkalinity. These tables show the evolution of the brines for all water types modeled by the P&CE as a function of RH. (Note: these brine evolution tables only present the maximum anion/cation pairs. For a more detailed examination of the end-point brine compositions, see Figures 6.13-1 to 6.13-4). Also shown is the endpoint relative humidity of the brines for each of the waters modeled. These data were hand-extracted from the 396 lookup tables in Output DTN: SN0701PAEBSPCE.001. If "N/A" appears in a box on the table, it indicates that the brine did not evolve to that point. The Group 1 water is dominantly Na-CO_3 brine at 98% RH. As dryout proceeds, Group 1 waters evolve to form Na-Cl, Na-NO_3 brines at low to moderate WRIP values and they become dominated by K as WRIP increases (Table 6.13-1). The Group 2 water is essentially Na-Cl at 98% RH until WRIP is at its maximum, L, when the 98% RH brines become Na-CO_3 dominant (Table 6.13-2). These brines evolve to form a variety of end-point

brines (see discussion to follow). Group 3 water form brines at 98% RH, similar to Group 2; however, the end-point brines are primarily Mg-Cl, Ca-Cl until moderate WRIP (Table 6.13-3). Under these conditions, the potential for aggressive localized corrosion exists. Above a WRIP of approximately E, K and Na chloride and nitrate brines dominate the end-point compositions. The Group 4 waters are similar to Group 2 and Group 3 in that they are Na-Cl brines at 98% RH until WRIP = L, where they form Na-CO_3 brines (Table 6.13-4). Up to a WRIP of G, the Group 4 waters tend to dry out to form Na-NO_3 brines. At higher WRIP Na and K chlorides dominate the end point brines.

For a more detailed examination of the dryout brine compositions, the relative percentage of each of the major cations and anions were plotted as a function of increasing WRIP (Figures 6.13-1 to 6.13-4). These data were extracted from the EQ3/6 evaporation output files in Output DTN: SN0701PAEBSPCE.001. Within each of the WRIP categories, the compositions were sorted by temperature, from low to high. The steps observed in these figures correspond to shifts in dryout brine composition as a function of temperature and pCO_2. The Group 1 waters are dominated by Na at low WRIP and become increasingly more K-rich as WRIP increases (Figure 6.13-1 upper). Nitrate dominates the anions at low WRIP and chlorides at moderate to high WRIP (Figure 6.13-1 lower). Only at the highest WRIP values do carbonate brines form. The Group 2 waters are predominantly Na-rich except for a few waters at low WRIP that are Ca-rich, and a few at the highest WRIP value that are K-rich (Figure 6.13-2 upper). The Group 2 waters form nitrate-rich (low WRIP) to chloride-rich (high WRIP) brines (Figure 6.13-2, lower panel). At the uppermost WRIP value a few of the waters form K-carbonate brines. The evaluation of the Group 3 end-point brine evolution is not as straightforward (Figure 6.13-3). Both Ca-Cl and Mg-Cl brines form at low to moderate WRIP values. As WRIP values exceed G, Na and K-rich brines can form (Figure 6.13-3, upper panel). Chloride is the dominant anion across the WRIP values, with an occasional nitrate-rich brine forming instead (Figure 6.13-3, lower panel). The Group 4 waters evolve to form Na-NO_3 to Na-Cl brines as WRIP increases (Figure 6.13-4). For this set of waters, K-Cl brines form at only the highest WRIP values. The end-point brine figures were generated by extracting data from the EQ3/6 output files at the last step. In some cases, this may not be the eutectic composition, if the simulation did not converge, or may include a turn-around in the activity of water. However, the general trends are preserved in these figures and the actual end-point compositions are archived in the lookup tables in the Output DTN: SN0701PAEBSPCE.001.

Table 6.13-1. Brine Evolution of Group 1 Waters

LUT Name	WRIP parameter (0, b-j, l)	Temp	pCO2	endpoint RH	98% RH brine	85% RH brine	65% RH brine	Endpoint brine
10p2t1.xls		100	1.00E-02	54.6739%	Na-CO3	Na-CO3	Na-Cl	Na-Cl
10p2t70.xls		70	1.00E-02	50.3601%	Na-CO3	Na-CO3	Na-Cl	Na-NO3
10p2t30.xls		30	1.00E-02	53.9228%	Na-CO3	Na-Cl	Na-Cl	Na-NO3
10p3t1.xls		100	1.00E-03	54.3497%	Na-Cl	Na-CO3	Na-Cl	Na-Cl
10p3t70.xls	0	70	1.00E-03	50.0020%	Na-CO3	Na-CO3	Na-Cl	Na-NO3
10p3t30.xls		30	1.00E-03	54.1287%	Na-CO3	Na-Cl	Na-Cl	Na-NO3
10p4t1.xls		100	1.00E-04	54.1020%	Na-Cl	Na-Cl	Na-Cl	Na-Cl
10p4t70.xls		70	1.00E-04	49.6950%	Na-Cl	Na-Cl	Na-Cl	Na-Cl
10p4t30.xls		30	1.00E-04	55.7319%	Na-CO3	Na-Cl	Na-Cl	Na-NO3
1bp2t1.xls		100	1.00E-02	54.4112%	Na-CO3	Na-CO3	Na-Cl	Na-Cl
1bp2t70.xls		70	1.00E-02	50.1209%	Na-CO3	Na-CO3	Na-Cl	Na-NO3
1bp2t30.xls		30	1.00E-02	53.9224%	Na-CO3	Na-Cl	Na-NO3	Na-NO3
1bp3t1.xls		100	1.00E-03	54.0209%	Na-CO3	Na-CO3	Na-Cl	Na-Cl
1bp3t70.xls	b	70	1.00E-03	49.6514%	Na-CO3	Na-CO3	Na-Cl	Na-NO3
1bp3t30.xls		30	1.00E-03	54.1291%	Na-CO3	Na-Cl	Na-Cl	Na-NO3
1bp4t1.xls		100	1.00E-04	53.7414%	Na-Cl	Na-Cl	Na-Cl	Na-Cl
1bp4t70.xls		70	1.00E-04	49.2853%	Na-Cl	Na-CO3	Na-Cl	Na-NO3
1bp4t30.xls		30	1.00E-04	55.7319%	Na-CO3	Na-Cl	Na-NO3	Na-NO3
1cp2t1.xls		100	1.00E-02	54.0598%	Na-CO3	Na-CO3	Na-Cl	Na-Cl
1cp2t70.xls		70	1.00E-02	49.7780%	Na-CO3	Na-CO3	Na-Cl	Na-NO3
1cp2t30.xls		30	1.00E-02	53.9221%	Na-CO3	Na-Cl	Na-Cl	Na-NO3
1cp3t1.xls		100	1.00E-03	53.5981%	Na-CO3	Na-CO3	Na-Cl	Na-Cl
1cp3t70.xls	c	70	1.00E-03	49.1979%	Na-CO3	Na-CO3	Na-Cl	Na-NO3
1cp3t30.xls		30	1.00E-03	54.1291%	Na-CO3	Na-Cl	Na-NO3	Na-NO3
1cp4t1.xls		100	1.00E-04	53.2874%	Na-Cl	Na-Cl	Na-Cl	Na-Cl
1cp4t70.xls		70	1.00E-04	48.7803%	Na-Cl	Na-CO3	Na-Cl	Na-NO3
1cp4t30.xls		30	1.00E-04	55.7319%	Na-CO3	Na-Cl	Na-Cl	Na-NO3
1dp2t1.xls		100	1.00E-02	53.2075%	Na-CO3	Na-CO3	Na-Cl	Na-Cl
1dp2t70.xls		70	1.00E-02	48.8778%	Na-CO3	Na-CO3	Na-Cl	Na-Cl
1dp2t30.xls		30	1.00E-02	53.9221%	Na-CO3	Na-Cl	Na-Cl	Na-NO3
1dp3t1.xls		100	1.00E-03	52.6058%	Na-CO3	Na-CO3	Na-Cl	Na-Cl
1dp3t70.xls	d	70	1.00E-03	48.0887%	Na-CO3	Na-CO3	Na-Cl	Na-Cl
1dp3t30.xls		30	1.00E-03	56.7947%	Na-CO3	Na-Cl	Na-Cl	Na-NO3
1dp4t1.xls		100	1.00E-04	52.2436%	Na-Cl	Na-CO3	Na-Cl	Na-Cl
1dp4t70.xls		70	1.00E-04	47.6127%	Na-CO3	Na-CO3	Na-Cl	Na-Cl
1dp4t30.xls		30	1.00E-04	63.2074%	Na-CO3	Na-Cl	Na-Cl	Na-Cl
1ep2t1.xls		100	1.00E-02	52.4099%	Na-CO3	Na-CO3	Na-Cl	Na-Cl
1ep2t70.xls		70	1.00E-02	49.3576%	Na-CO3	Na-CO3	Na-Cl	Na-Cl
1ep2t30.xls		30	1.00E-02	53.9221%	Na-CO3	Na-Cl	Na-Cl	Na-NO3
1ep3t1.xls		100	1.00E-03	51.7125%	Na-CO3	Na-CO3	Na-Cl	Na-Cl
1ep3t70.xls	e	70	1.00E-03	47.1104%	Na-CO3	Na-CO3	Na-Cl	Na-Cl
1ep3t30.xls		30	1.00E-03	59.8564%	Na-CO3	Na-Cl	Na-Cl	Na-NO3
1ep4t1.xls		100	1.00E-04	51.3321%	Na-Cl	Na-CO3	Na-Cl	Na-Cl
1ep4t70.xls		70	1.00E-04	47.4426%	Na-CO3	Na-CO3	Na-Cl	Na-Cl
1ep4t30.xls		30	1.00E-04	63.2074%	Na-CO3	Na-CO3	Na-Cl	Na-Cl

Table 6.13-1. Brine Evolution of Group 1 Waters (Continued)

LUT Name	WRIP parameter (0, b-j, l)	Temp	pCO2	endpoint RH	98% RH brine	85% RH brine	65% RH brine	Endpoint brine
1fp2t1.xls		100	1.00E-02	51.2971%	Na-Cl	Na-CO3	Na-Cl	Na-Cl
1fp2t70.xls		70	1.00E-02	50.4475%	Na-CO3	Na-CO3	Na-Cl	K-Cl
1fp2t30.xls		30	1.00E-02	53.9221%	Na-CO3	Na-Cl	Na-Cl	Na-NO3
1fp3t1.xls		100	1.00E-03	50.5516%	Na-CO3	Na-CO3	Na-Cl	Na-Cl
1fp3t70.xls	f	70	1.00E-03	48.0000%	Na-CO3	Na-CO3	Na-Cl	K-Cl
1fp3t30.xls		30	1.00E-03	62.6973%	Na-CO3	Na-Cl	Na-Cl	Na-Cl
1fp4t1.xls		100	1.00E-04	50.1602%	Na-Cl	Na-CO3	Na-Cl	Na-Cl
1fp4t70.xls		70	1.00E-04	47.9997%	Na-CO3	Na-CO3	Na-Cl	K-Cl
1fp4t30.xls		30	1.00E-04	63.2978%	Na-CO3	Na-CO3	Na-Cl	Na-Cl
1gp2t1.xls		100	1.00E-02	50.3809%	Na-CO3	Na-CO3	Na-Cl	K-Cl
1gp2t70.xls		70	1.00E-02	50.4428%	Na-CO3	Na-CO3	Na-Cl	K-Cl
1gp2t30.xls		30	1.00E-02	62.1340%	Na-CO3	Na-Cl	Na-Cl	Na-NO3
1gp3t1.xls		100	1.00E-03	49.7942%	Na-CO3	Na-CO3	Na-Cl	K-Cl
1gp3t70.xls	g	70	1.00E-03	48.0006%	Na-CO3	Na-CO3	Na-Cl	K-Cl
1gp3t30.xls		30	1.00E-03	62.6973%	Na-CO3	Na-Cl	Na-Cl	Na-Cl
1gp4t1.xls		100	1.00E-04	49.7310%	Na-CO3	Na-CO3	Na-Cl	K-Cl
1gp4t70.xls		70	1.00E-04	48.0002%	Na-CO3	Na-CO3	Na-Cl	K-Cl
1gp4t30.xls		30	1.00E-04	63.2978%	Na-CO3	Na-CO3	Na-Cl	Na-Cl
1hp2t1.xls		100	1.00E-02	52.0003%	Na-CO3	Na-CO3	K-Cl	K-Cl
1hp2t70.xls		70	1.00E-02	51.9997%	Na-CO3	Na-CO3	K-Cl	K-Cl
1hp2t30.xls		30	1.00E-02	62.1340%	Na-CO3	K-Cl	Na-Cl	Na-NO3
1hp3t1.xls		100	1.00E-03	50.6906%	Na-CO3	Na-CO3	K-Cl	K-Cl
1hp3t70.xls	h	70	1.00E-03	48.3575%	Na-CO3	Na-CO3	K-Cl	K-Cl
1hp3t30.xls		30	1.00E-03	62.6973%	Na-CO3	Na-Cl	Na-Cl	Na-Cl
1hp4t1.xls		100	1.00E-04	50.5014%	Na-CO3	Na-CO3	K-Cl	K-Cl
1hp4t70.xls		70	1.00E-04	48.3858%	Na-CO3	Na-CO3	K-Cl	K-Cl
1hp4t30.xls		30	1.00E-04	63.2978%	Na-CO3	Na-CO3	Na-Cl	Na-Cl
1ip2t1.xls		100	1.00E-02	52.7864%	Na-CO3	Na-CO3	K-Cl	K-Cl
1ip2t70.xls		70	1.00E-02	53.6259%	Na-CO3	Na-CO3	K-Cl	K-Cl
1ip2t30.xls		30	1.00E-02	62.8986%	Na-CO3	K-Cl	Na-Cl	Na-Cl
1ip3t1.xls		100	1.00E-03	53.1204%	Na-CO3	Na-CO3	K-Cl	K-Cl
1ip3t70.xls	i	70	1.00E-03	52.9094%	Na-CO3	Na-CO3	K-Cl	K-NO3
1ip3t30.xls		30	1.00E-03	68.8418%	Na-CO3	Na-CO3	N/A	Na-Cl
1ip4t1.xls		100	1.00E-04	55.1363%	Na-CO3	Na-CO3	K-Cl	K-Cl
1ip4t70.xls		70	1.00E-04	52.9234%	Na-CO3	Na-CO3	K-Cl	K-NO3
1ip4t30.xls		30	1.00E-04	69.2741%	Na-CO3	Na-CO3	N/A	K-Cl
1jp2t1.xls		100	1.00E-02	42.0003%	Na-CO3	Na-CO3	K-Cl	K-NO3
1jp2t70.xls		70	1.00E-02	53.6220%	Na-CO3	Na-CO3	K-Cl	K-NO3
1jp2t30.xls		30	1.00E-02	71.5685%	Na-CO3	K-Cl	N/A	K-CO3
1jp3t1.xls		100	1.00E-03	43.5055%	Na-CO3	Na-CO3	K-Cl	K-NO3
1jp3t70.xls	j	70	1.00E-03	48.0844%	Na-CO3	Na-CO3	K-Cl	K-CO3
1jp3t30.xls		30	1.00E-03	64.0457%	Na-CO3	Na-CO3	K-CO3	K-CO3
1jp4t1.xls		100	1.00E-04	55.1366%	Na-CO3	Na-CO3	K-Cl	K-Cl
1jp4t70.xls		70	1.00E-04	54.4724%	Na-CO3	Na-CO3	K-Cl	K-NO3
1jp4t30.xls		30	1.00E-04	51.8995%	Na-CO3	Na-CO3	K-CO3	K-CO3
1lp2t1.xls		100	1.00E-02	41.8830%	Na-CO3	Na-CO3	K-CO3	K-CO3
1lp2t70.xls		70	1.00E-02	53.6220%	Na-CO3	Na-CO3	K-CO3	K-CO3
1lp2t30.xls		30	1.00E-02	71.5685%	Na-CO3	K-CO3	N/A	K-CO3
1lp3t1.xls		100	1.00E-03	43.5052%	Na-CO3	Na-CO3	K-CO3	K-NO3
1lp3t70.xls	l	70	1.00E-03	48.0844%	Na-CO3	Na-CO3	K-CO3	K-CO3
1lp3t30.xls		30	1.00E-03	64.0457%	Na-CO3	Na-CO3	K-CO3	K-CO3
1lp4t1.xls		100	1.00E-04	50.9848%	Na-CO3	Na-CO3	K-Cl	K-NO3
1lp4t70.xls		70	1.00E-04	38.1266%	Na-CO3	Na-CO3	K-CO3	K-CO3
1lp4t30.xls		30	1.00E-04	51.9878%	Na-CO3	Na-CO3	K-CO3	K-CO3

Source: Output DTN: SN0701PAEBSPCE.001.

Table 6.13-2. Brine Evolution of Group 2 Water

LUT Name	WRIP parameter (0, b-j, l)	Temp	pCO2	endpoint RH	98% RH brine	85% RH brine	65% RH brine	Endpoint brine
20p2t1.xls		100	1.00E-02	51.8319%	Na-Cl	Na-Cl	Na-Cl	K-NO3
20p2t70.xls		70	1.00E-02	42.2200%	Na-Cl	Na-Cl	Na-Cl	Na-NO3
20p2t30.xls		30	1.00E-02	48.5901%	Na-Cl	Na-Cl	Na-NO3	Mg-NO3
20p3t1.xls		100	1.00E-03	51.8596%	Na-Cl	Na-Cl	Na-Cl	K-NO3
20p3t70.xls	0	70	1.00E-03	42.0922%	Na-Cl	Na-Cl	Na-Cl	Na-NO3
20p3t30.xls		30	1.00E-03	48.5602%	Na-Cl	Na-Cl	Na-NO3	Na-NO3
20p4t1.xls		100	1.00E-04	51.8650%	Na-Cl	Na-Cl	Na-Cl	K-NO3
20p4t70.xls		70	1.00E-04	42.1066%	Na-Cl	Na-Cl	Na-Cl	Na-NO3
20p4t30.xls		30	1.00E-04	42.2099%	Na-Cl	Na-Cl	Na-Cl	Ca-NO3
2bp2t1.xls		100	1.00E-02	45.9231%	Na-Cl	Na-Cl	Na-Cl	K-NO3
2bp2t70.xls		70	1.00E-02	42.8546%	Na-Cl	Na-Cl	Na-Cl	Na-NO3
2bp2t30.xls		30	1.00E-02	48.5663%	Na-Cl	Na-Cl	Na-Cl	Mg-NO3
2bp3t1.xls		100	1.00E-03	45.9335%	Na-Cl	Na-Cl	Na-Cl	K-NO3
2bp3t70.xls	b	70	1.00E-03	42.5404%	Na-Cl	Na-Cl	Na-Cl	Na-NO3
2bp3t30.xls		30	1.00E-03	45.7475%	Na-Cl	Na-Cl	Na-Cl	Ca-NO3
2bp4t1.xls		100	1.00E-04	45.9370%	Na-Cl	Na-Cl	Na-Cl	K-NO3
2bp4t70.xls		70	1.00E-04	42.5895%	Na-Cl	Na-Cl	Na-Cl	Na-NO3
2bp4t30.xls		30	1.00E-04	42.6394%	Na-Cl	Na-Cl	Na-Cl	Ca-NO3
2cp2t1.xls		100	1.00E-02	47.6173%	Na-Cl	Na-Cl	Na-Cl	Na-NO3
2cp2t70.xls		70	1.00E-02	42.7565%	Na-Cl	Na-Cl	Na-Cl	Na-NO3
2cp2t30.xls		30	1.00E-02	47.1730%	Na-Cl	Na-Cl	Na-Cl	Ca-NO3
2cp3t1.xls		100	1.00E-03	47.5998%	Na-Cl	Na-Cl	Na-Cl	Na-NO3
2cp3t70.xls	c	70	1.00E-03	42.6551%	Na-Cl	Na-Cl	Na-Cl	Na-NO3
2cp3t30.xls		30	1.00E-03	45.0614%	Na-Cl	Na-Cl	Na-Cl	Ca-NO3
2cp4t1.xls		100	1.00E-04	47.6170%	Na-Cl	Na-Cl	Na-Cl	Na-NO3
2cp4t70.xls		70	1.00E-04	42.6235%	Na-Cl	Na-Cl	Na-Cl	Na-NO3
2cp4t30.xls		30	1.00E-04	41.8463%	Na-Cl	Na-Cl	Na-Cl	Ca-NO3
2dp2t1.xls		100	1.00E-02	51.7331%	Na-Cl	Na-Cl	Na-Cl	Na-Cl
2dp2t70.xls		70	1.00E-02	44.2711%	Na-Cl	Na-Cl	Na-Cl	Na-NO3
2dp2t30.xls		30	1.00E-02	55.6610%	Na-Cl	Na-Cl	Na-Cl	Na-NO3
2dp3t1.xls		100	1.00E-03	51.7304%	Na-Cl	Na-Cl	Na-Cl	Na-Cl
2dp3t70.xls	d	70	1.00E-03	44.2582%	Na-Cl	Na-Cl	Na-Cl	Na-NO3
2dp3t30.xls		30	1.00E-03	55.6865%	Na-Cl	Na-Cl	Na-Cl	Na-NO3
2dp4t1.xls		100	1.00E-04	51.7284%	Na-Cl	Na-Cl	Na-Cl	Na-Cl
2dp4t70.xls		70	1.00E-04	44.2424%	Na-Cl	Na-Cl	Na-Cl	Na-NO3
2dp4t30.xls		30	1.00E-04	55.6880%	Na-Cl	Na-Cl	Na-Cl	Na-NO3
2ep2t1.xls		100	1.00E-02	52.9443%	Na-Cl	Na-Cl	Na-Cl	Na-Cl
2ep2t70.xls		70	1.00E-02	52.4414%	Na-Cl	Na-Cl	Na-Cl	Na-NO3
2ep2t30.xls		30	1.00E-02	55.6610%	Na-Cl	Na-Cl	Na-NO3	Na-NO3
2ep3t1.xls		100	1.00E-03	52.8825%	Na-Cl	Na-Cl	Na-Cl	Na-Cl
2ep3t70.xls	e	70	1.00E-03	52.4333%	Na-Cl	Na-Cl	Na-Cl	Na-NO3
2ep3t30.xls		30	1.00E-03	55.6865%	Na-Cl	Na-Cl	Na-NO3	Na-NO3
2ep4t1.xls		100	1.00E-04	52.8903%	Na-Cl	Na-Cl	Na-Cl	Na-Cl
2ep4t70.xls		70	1.00E-04	52.4250%	Na-Cl	Na-Cl	Na-Cl	Na-NO3
2ep4t30.xls		30	1.00E-04	55.6877%	Na-Cl	Na-Cl	Na-NO3	Na-NO3

Table 6.13-2. Brine Evolution of Group 2 Water (Continued)

LUT Name	WRIP parameter (0, b-j, l)	Temp	pCO2	endpoint RH	98% RH brine	85% RH brine	65% RH brine	Endpoint brine
2fp2t1.xls		100	1.00E-02	56.5735%	Na-Cl	Na-Cl	Na-Cl	Na-Cl
2fp2t70.xls		70	1.00E-02	52.9972%	Na-Cl	Na-Cl	Na-Cl	Na-NO3
2fp2t30.xls		30	1.00E-02	55.6608%	Na-Cl	Na-Cl	Na-NO3	Na-NO3
2fp3t1.xls		100	1.00E-03	56.5712%	Na-Cl	Na-Cl	Na-Cl	Na-Cl
2fp3t70.xls	f	70	1.00E-03	52.9861%	Na-Cl	Na-Cl	Na-Cl	Na-NO3
2fp3t30.xls		30	1.00E-03	55.6864%	Na-Cl	Na-Cl	Na-Cl	Na-NO3
2fp4t1.xls		100	1.00E-04	56.5680%	Na-Cl	Na-Cl	Na-Cl	Na-Cl
2fp4t70.xls		70	1.00E-04	52.9871%	Na-Cl	Na-Cl	Na-Cl	Na-NO3
2fp4t30.xls		30	1.00E-04	55.6880%	Na-Cl	Na-Cl	Na-NO3	Na-NO3
2gp2t1.xls		100	1.00E-02	56.4981%	Na-Cl	Na-Cl	Na-Cl	Na-Cl
2gp2t70.xls		70	1.00E-02	52.2936%	Na-Cl	Na-Cl	Na-Cl	Na-NO3
2gp2t30.xls		30	1.00E-02	63.8122%	Na-Cl	Na-Cl	Na-Cl	Na-NO3
2gp3t1.xls		100	1.00E-03	56.5000%	Na-Cl	Na-Cl	Na-Cl	Na-Cl
2gp3t70.xls	g	70	1.00E-03	52.2893%	Na-Cl	Na-Cl	Na-Cl	Na-NO3
2gp3t30.xls		30	1.00E-03	63.8199%	Na-Cl	Na-Cl	Na-Cl	Na-NO3
2gp4t1.xls		100	1.00E-04	56.5013%	Na-Cl	Na-Cl	Na-Cl	Na-Cl
2gp4t70.xls		70	1.00E-04	52.2839%	Na-Cl	Na-Cl	Na-Cl	Na-NO3
2gp4t30.xls		30	1.00E-04	63.8204%	Na-Cl	Na-Cl	Na-NO3	Na-NO3
2hp2t1.xls		100	1.00E-02	55.5012%	Na-Cl	Na-Cl	Na-Cl	Na-Cl
2hp2t70.xls		70	1.00E-02	54.1001%	Na-Cl	Na-Cl	Na-Cl	Na-Cl
2hp2t30.xls		30	1.00E-02	60.3479%	Na-Cl	Na-Cl	Na-NO3	Na-NO3
2hp3t1.xls		100	1.00E-03	55.5023%	Na-Cl	Na-Cl	Na-Cl	Na-Cl
2hp3t70.xls	h	70	1.00E-03	54.1020%	Na-Cl	Na-Cl	Na-Cl	Na-Cl
2hp3t30.xls		30	1.00E-03	60.3691%	Na-Cl	Na-Cl	Na-NO3	Na-NO3
2hp4t1.xls		100	1.00E-04	55.5025%	Na-Cl	Na-Cl	Na-Cl	Na-Cl
2hp4t70.xls		70	1.00E-04	54.1013%	Na-Cl	Na-Cl	Na-Cl	Na-Cl
2hp4t30.xls		30	1.00E-04	60.3733%	Na-Cl	Na-Cl	Na-NO3	Na-NO3
2ip2t1.xls		100	1.00E-02	72.0004%	Na-Cl	Na-Cl	N/A	Na-Cl
2ip2t70.xls		70	1.00E-02	61.6092%	Na-Cl	Na-Cl	Na-Cl	Na-Cl
2ip2t30.xls		30	1.00E-02	60.6966%	Na-Cl	Na-Cl	Na-Cl	Na-NO3
2ip3t1.xls		100	1.00E-03	72.0006%	Na-Cl	Na-Cl	N/A	Na-Cl
2ip3t70.xls	i	70	1.00E-03	61.7002%	Na-Cl	Na-Cl	Na-Cl	Na-Cl
2ip3t30.xls		30	1.00E-03	60.9578%	Na-Cl	Na-Cl	Na-Cl	Na-NO3
2ip4t1.xls		100	1.00E-04	71.9990%	Na-Cl	Na-Cl	N/A	Na-Cl
2ip4t70.xls		70	1.00E-04	61.7094%	Na-Cl	Na-Cl	Na-Cl	Na-Cl
2ip4t30.xls		30	1.00E-04	61.0001%	Na-Cl	Na-Cl	Na-Cl	Na-NO3
2jp2t1.xls		100	1.00E-02	58.7205%	Na-Cl	Na-Cl	Na-Cl	Na-Cl
2jp2t70.xls		70	1.00E-02	59.1603%	Na-Cl	Na-Cl	Na-Cl	Na-Cl
2jp2t30.xls		30	1.00E-02	60.6966%	Na-Cl	Na-Cl	Na-Cl	Na-NO3
2jp3t1.xls		100	1.00E-03	59.6561%	Na-Cl	Na-Cl	Na-Cl	Na-Cl
2jp3t70.xls	j	70	1.00E-03	61.6436%	Na-Cl	Na-Cl	Na-Cl	Na-Cl
2jp3t30.xls		30	1.00E-03	60.1251%	Na-Cl	Na-Cl	Na-Cl	Na-NO3
2jp4t1.xls		100	1.00E-04	59.1773%	Na-Cl	Na-Cl	Na-Cl	Na-Cl
2jp4t70.xls		70	1.00E-04	54.4724%	Na-CO3	Na-CO3	K-CO3	K-NO3
2jp4t30.xls		30	1.00E-04	60.8800%	Na-Cl	Na-Cl	Na-Cl	Na-NO3
2lp2t1.xls		100	1.00E-02	41.8830%	Na-CO3	Na-CO3	K-CO3	K-NO3
2lp2t70.xls		70	1.00E-02	53.6219%	Na-CO3	Na-CO3	K-CO3	K-NO3
2lp2t30.xls		30	1.00E-02	71.5685%	Na-CO3	K-Cl	N/A	K-CO3
2lp3t1.xls		100	1.00E-03	43.5053%	Na-CO3	Na-CO3	K-CO3	K-NO3
2lp3t70.xls	l	70	1.00E-03	48.0844%	Na-CO3	Na-CO3	K-CO3	K-CO3
2lp3t30.xls		30	1.00E-03	64.0457%	Na-CO3	Na-CO3	K-CO3	K-CO3
2lp4t1.xls		100	1.00E-04	55.1356%	Na-CO3	Na-CO3	K-Cl	K-Cl
2lp4t70.xls		70	1.00E-04	54.4723%	Na-CO3	Na-CO3	K-CO3	K-NO3
2lp4t30.xls		30	1.00E-04	51.8995%	Na-CO3	Na-CO3	K-CO3	K-CO3

Source: Output DTN: SN0701PAEBSPCE.001.

Table 6.13-3. Brine Evolution of Group 3 Water

LUT Name	WRIP parameter (0, b-j, l)	Temp	pCO2	endpoint RH	98% RH brine	85% RH brine	65% RH brine	Endpoint brine
30p2t1.xls		100	1.00E-02	38.2884%	Na-Cl	Na-Cl	Na-Cl	Mg-Cl
30p2t70.xls		70	1.00E-02	41.1663%	Na-Cl	Na-Cl	Na-Cl	Ca-Cl
30p2t30.xls		30	1.00E-02	45.9994%	Na-Cl	Na-Cl	Na-Cl	Mg-Cl
30p3t1.xls		100	1.00E-03	38.3096%	Na-Cl	Na-Cl	Na-Cl	Mg-Cl
30p3t70.xls	0	70	1.00E-03	39.5505%	Na-Cl	Na-Cl	Na-Cl	Ca-Cl
30p3t30.xls		30	1.00E-03	45.2649%	Na-Cl	Na-Cl	Na-Cl	Ca-Cl
30p4t1.xls		100	1.00E-04	38.3117%	Na-Cl	Na-Cl	Na-Cl	Mg-Cl
30p4t70.xls		70	1.00E-04	39.5578%	Na-Cl	Na-Cl	Na-Cl	Ca-Cl
30p4t30.xls		30	1.00E-04	35.2039%	Na-Cl	Na-Cl	Na-Cl	Ca-Cl
3bp2t1.xls		100	1.00E-02	38.2660%	Na-Cl	Na-Cl	Na-Cl	Mg-Cl
3bp2t70.xls		70	1.00E-02	41.0092%	Na-Cl	Na-Cl	Na-Cl	Mg-Cl
3bp2t30.xls		30	1.00E-02	40.0010%	Na-Cl	Na-Cl	Na-Cl	Mg-Cl
3bp3t1.xls		100	1.00E-03	38.2874%	Na-Cl	Na-Cl	Na-Cl	Mg-Cl
3bp3t70.xls	b	70	1.00E-03	40.1144%	Na-Cl	Na-Cl	Na-Cl	Ca-Cl
3bp3t30.xls		30	1.00E-03	44.0007%	Na-Cl	Na-Cl	Na-Cl	Ca-Cl
3bp4t1.xls		100	1.00E-04	38.2895%	Na-Cl	Na-Cl	Na-Cl	Mg-Cl
3bp4t70.xls		70	1.00E-04	40.1212%	Na-Cl	Na-Cl	Na-Cl	Ca-Cl
3bp4t30.xls		30	1.00E-04	38.8749%	Na-Cl	Na-Cl	Na-Cl	Ca-Cl
3cp2t1.xls		100	1.00E-02	38.0135%	Na-Cl	Na-Cl	Na-Cl	Mg-Cl
3cp2t70.xls		70	1.00E-02	40.9708%	Na-Cl	Na-Cl	Na-Cl	Ca-Cl
3cp2t30.xls		30	1.00E-02	40.0005%	Na-Cl	Na-Cl	Na-Cl	Mg-Cl
3cp3t1.xls		100	1.00E-03	38.0356%	Na-Cl	Na-Cl	Na-Cl	Mg-Cl
3cp3t70.xls	c	70	1.00E-03	40.7961%	Na-Cl	Na-Cl	Na-Cl	Ca-Cl
3cp3t30.xls		30	1.00E-03	44.0009%	Na-Cl	Na-Cl	Na-Cl	Ca-Cl
3cp4t1.xls		100	1.00E-04	38.0376%	Na-Cl	Na-Cl	Na-Cl	Mg-Cl
3cp4t70.xls		70	1.00E-04	40.8021%	Na-Cl	Na-Cl	Na-Cl	Ca-Cl
3cp4t30.xls		30	1.00E-04	42.5837%	Na-Cl	Na-Cl	Na-Cl	Ca-Cl
3dp2t1.xls		100	1.00E-02	33.6590%	Na-Cl	Na-Cl	Na-Cl	Mg-Cl
3dp2t70.xls		70	1.00E-02	42.1524%	Na-Cl	Na-Cl	Na-Cl	Ca-Cl
3dp2t30.xls		30	1.00E-02	50.0041%	Na-Cl	Na-Cl	Na-Cl	Mg-Cl
3dp3t1.xls		100	1.00E-03	33.6916%	Na-Cl	Na-Cl	Na-Cl	Mg-Cl
3dp3t70.xls	d	70	1.00E-03	42.2049%	Na-Cl	Na-Cl	Na-Cl	Ca-Cl
3dp3t30.xls		30	1.00E-03	44.9625%	Na-Cl	Na-Cl	Na-Cl	Ca-Cl
3dp4t1.xls		100	1.00E-04	46.0022%	Na-Cl	Na-Cl	Na-Cl	Mg-Cl
3dp4t70.xls		70	1.00E-04	42.2094%	Na-Cl	Na-Cl	Na-Cl	Ca-Cl
3dp4t30.xls		30	1.00E-04	48.1359%	Na-Cl	Na-Cl	Na-Cl	Ca-Cl
3ep2t1.xls		100	1.00E-02	33.6589%	Na-Cl	Na-Cl	Na-Cl	Mg-Cl
3ep2t70.xls		70	1.00E-02	41.4619%	Na-Cl	Na-Cl	Na-Cl	Mg-Cl
3ep2t30.xls		30	1.00E-02	50.0041%	Na-Cl	Na-Cl	Na-Cl	Mg-Cl
3ep3t1.xls		100	1.00E-03	33.6880%	Na-Cl	Na-Cl	Na-Cl	Mg-Cl
3ep3t70.xls	e	70	1.00E-03	41.5086%	Na-Cl	Na-Cl	Na-Cl	Mg-Cl
3ep3t30.xls		30	1.00E-03	45.3249%	Na-Cl	Na-Cl	Na-Cl	Ca-Cl
3ep4t1.xls		100	1.00E-04	33.6896%	Na-Cl	Na-Cl	Na-Cl	Mg-Cl
3ep4t70.xls		70	1.00E-04	41.5105%	Na-Cl	Na-Cl	Na-Cl	Mg-Cl
3ep4t30.xls		30	1.00E-04	42.8995%	Na-Cl	Na-Cl	Na-Cl	Ca-Cl

Table 6.13-3. Brine Evolution of Group 3 Water (Continued)

LUT Name	WRIP parameter (0, b-j, l)	Temp	pCO2	endpoint RH	98% RH brine	85% RH brine	65% RH brine	Endpoint brine
3fp2t1.xls		100	1.00E-02	38.4397%	Na-Cl	Na-Cl	Na-Cl	K-NO3
3fp2t70.xls		70	1.00E-02	50.0638%	Na-Cl	Na-Cl	Na-Cl	K-Cl
3fp2t30.xls		30	1.00E-02	50.5460%	Na-Cl	Na-Cl	Na-Cl	Mg-Cl
3fp3t1.xls		100	1.00E-03	38.3386%	Na-Cl	Na-Cl	Na-Cl	K-Cl
3fp3t70.xls	f	70	1.00E-03	50.0998%	Na-Cl	Na-Cl	K-Cl	K-Cl
3fp3t30.xls		30	1.00E-03	50.7871%	Na-Cl	Na-Cl	Na-Cl	Mg-Cl
3fp4t1.xls		100	1.00E-04	38.3294%	Na-Cl	Na-Cl	Na-Cl	K-NO3
3fp4t70.xls		70	1.00E-04	50.1043%	Na-Cl	Na-Cl	Na-Cl	K-Cl
3fp4t30.xls		30	1.00E-04	50.8109%	Na-Cl	Na-Cl	Na-Cl	Mg-Cl
3gp2t1.xls		100	1.00E-02	53.9999%	Na-Cl	Na-Cl	Na-Cl	K-Cl
3gp2t70.xls		70	1.00E-02	49.7476%	Na-Cl	Na-Cl	Na-Cl	K-Cl
3gp2t30.xls		30	1.00E-02	64.8245%	Na-Cl	Na-Cl	Na-Cl	Na-Cl
3gp3t1.xls		100	1.00E-03	53.9993%	Na-Cl	Na-Cl	Na-Cl	K-Cl
3gp3t70.xls	g	70	1.00E-03	49.7909%	Na-Cl	Na-Cl	Na-Cl	K-Cl
3gp3t30.xls		30	1.00E-03	64.8812%	Na-Cl	Na-Cl	Na-Cl	Na-Cl
3gp4t1.xls		100	1.00E-04	53.9990%	Na-Cl	Na-Cl	Na-Cl	K-Cl
3gp4t70.xls		70	1.00E-04	49.7960%	Na-Cl	Na-Cl	Na-Cl	K-Cl
3gp4t30.xls		30	1.00E-04	64.8868%	Na-Cl	Na-Cl	Na-Cl	Na-Cl
3hp2t1.xls		100	1.00E-02	53.9994%	Na-Cl	Na-Cl	Na-Cl	K-Cl
3hp2t70.xls		70	1.00E-02	55.5910%	Na-Cl	Na-Cl	Na-Cl	K-Cl
3hp2t30.xls		30	1.00E-02	65.1868%	Na-Cl	Na-Cl	Na-Cl	Na-Cl
3hp3t1.xls		100	1.00E-03	54.0003%	Na-Cl	Na-Cl	Na-Cl	K-Cl
3hp3t70.xls	h	70	1.00E-03	55.5924%	Na-Cl	Na-Cl	Na-Cl	K-Cl
3hp3t30.xls		30	1.00E-03	65.2386%	Na-Cl	Na-Cl	Na-Cl	Na-Cl
3hp4t1.xls		100	1.00E-04	54.0005%	Na-Cl	Na-Cl	Na-Cl	K-Cl
3hp4t70.xls		70	1.00E-04	60.0666%	Na-Cl	Na-Cl	Na-Cl	K-Cl
3hp4t30.xls		30	1.00E-04	65.2438%	Na-Cl	Na-Cl	Na-Cl	Na-Cl
3ip2t1.xls		100	1.00E-02	58.6237%	Na-Cl	Na-Cl	Na-Cl	K-Cl
3ip2t70.xls		70	1.00E-02	57.0495%	Na-Cl	Na-Cl	Na-Cl	K-Cl
3ip2t30.xls		30	1.00E-02	60.3480%	Na-Cl	Na-Cl	Na-NO3	Na-NO3
3ip3t1.xls		100	1.00E-03	58.6285%	Na-Cl	Na-Cl	Na-Cl	K-Cl
3ip3t70.xls	i	70	1.00E-03	57.0494%	Na-Cl	Na-Cl	Na-Cl	K-Cl
3ip3t30.xls		30	1.00E-03	60.3691%	Na-Cl	Na-Cl	Na-NO3	Na-NO3
3ip4t1.xls		100	1.00E-04	58.6279%	Na-Cl	Na-Cl	K-Cl	K-Cl
3ip4t70.xls		70	1.00E-04	57.0497%	Na-Cl	Na-Cl	Na-Cl	K-Cl
3ip4t30.xls		30	1.00E-04	60.3738%	Na-Cl	Na-Cl	Na-Cl	Na-NO3
3jp2t1.xls		100	1.00E-02	61.3285%	Na-Cl	Na-Cl	Na-Cl	Na-Cl
3jp2t70.xls		70	1.00E-02	61.0659%	Na-Cl	Na-Cl	Na-Cl	Na-Cl
3jp2t30.xls		30	1.00E-02	61.0188%	Na-Cl	Na-Cl	Na-Cl	Na-NO3
3jp3t1.xls		100	1.00E-03	61.3262%	Na-Cl	Na-Cl	Na-Cl	Na-Cl
3jp3t70.xls	j	70	1.00E-03	61.0660%	Na-Cl	Na-Cl	Na-Cl	Na-Cl
3jp3t30.xls		30	1.00E-03	61.0389%	Na-Cl	Na-Cl	Na-Cl	Na-NO3
3jp4t1.xls		100	1.00E-04	61.3248%	Na-Cl	Na-Cl	Na-Cl	Na-Cl
3jp4t70.xls		70	1.00E-04	61.0732%	Na-Cl	Na-Cl	Na-Cl	Na-Cl
3jp4t30.xls		30	1.00E-04	61.0447%	Na-Cl	Na-Cl	Na-Cl	Na-NO3
3lp2t1.xls		100	1.00E-02	41.8829%	Na-CO3	Na-CO3	K-Cl	K-NO3
3lp2t70.xls		70	1.00E-02	53.6218%	Na-CO3	Na-CO3	K-Cl	K-NO3
3lp2t30.xls		30	1.00E-02	61.8955%	Na-CO3	K-Cl	Na-Cl	Na-Cl
3lp3t1.xls		100	1.00E-03	43.5048%	Na-CO3	Na-CO3	K-Cl	K-NO3
3lp3t70.xls	l	70	1.00E-03	48.0813%	Na-CO3	Na-CO3	K-Cl	K-CO3
3lp3t30.xls		30	1.00E-03	63.2508%	Na-CO3	Na-CO3	Na-Cl	Na-Cl
3lp4t1.xls		100	1.00E-04	55.1342%	Na-Cl	Na-CO3	K-Cl	K-Cl
3lp4t70.xls		70	1.00E-04	54.4717%	Na-CO3	Na-CO3	K-Cl	K-NO3
3lp4t30.xls		30	1.00E-04	64.2332%	Na-CO3	Na-CO3	Na-Cl	Na-Cl

Source: Output DTN: SN0701PAEBSPCE.001.

Table 6.13-4. Brine Evolution of Group 4 Water

LUT Name	WRIP parameter (0, b-j, l)	Temp	pCO2	endpoint RH	98% RH brine	85% RH brine	65% RH brine	Endpoint brine
40p2t1.xls		100	1.00E-02	55.9368%	Na-Cl	Na-Cl	Na-Cl	Na-NO3
40p2t70.xls		70	1.00E-02	51.7688%	Na-Cl	Na-Cl	Na-Cl	Na-NO3
40p2t30.xls		30	1.00E-02	55.6610%	Na-Cl	Na-Cl	Na-NO3	Na-NO3
40p3t1.xls		100	1.00E-03	55.9381%	Na-Cl	Na-Cl	Na-Cl	Na-NO3
40p3t70.xls	0	70	1.00E-03	51.7610%	Na-Cl	Na-Cl	Na-NO3	Na-NO3
40p3t30.xls		30	1.00E-03	55.6865%	Na-Cl	Na-Cl	Na-NO3	Na-NO3
40p4t1.xls		100	1.00E-04	55.9388%	Na-Cl	Na-Cl	Na-Cl	Na-NO3
40p4t70.xls		70	1.00E-04	51.7603%	Na-Cl	Na-Cl	Na-Cl	Na-NO3
40p4t30.xls		30	1.00E-04	55.6880%	Na-Cl	Na-Cl	Na-NO3	Na-NO3
4bp2t1.xls		100	1.00E-02	55.9223%	Na-Cl	Na-Cl	Na-Cl	Na-NO3
4bp2t70.xls		70	1.00E-02	51.7638%	Na-Cl	Na-Cl	Na-NO3	Na-NO3
4bp2t30.xls		30	1.00E-02	55.6610%	Na-Cl	Na-Cl	Na-NO3	Na-NO3
4bp3t1.xls		100	1.00E-03	55.9247%	Na-Cl	Na-Cl	Na-Cl	Na-NO3
4bp3t70.xls	b	70	1.00E-03	51.7596%	Na-Cl	Na-Cl	Na-NO3	Na-NO3
4bp3t30.xls		30	1.00E-03	55.6864%	Na-Cl	Na-Cl	Na-NO3	Na-NO3
4bp4t1.xls		100	1.00E-04	55.9253%	Na-Cl	Na-Cl	Na-Cl	Na-NO3
4bp4t70.xls		70	1.00E-04	51.7528%	Na-Cl	Na-Cl	Na-Cl	Na-NO3
4bp4t30.xls		30	1.00E-04	55.6880%	Na-Cl	Na-Cl	Na-NO3	Na-NO3
4cp2t1.xls		100	1.00E-02	55.8955%	Na-Cl	Na-Cl	Na-Cl	Na-NO3
4cp2t70.xls		70	1.00E-02	51.7597%	Na-Cl	Na-Cl	Na-Cl	Na-NO3
4cp2t30.xls		30	1.00E-02	55.6610%	Na-Cl	Na-Cl	Na-NO3	Na-NO3
4cp3t1.xls		100	1.00E-03	55.8975%	Na-Cl	Na-Cl	Na-Cl	Na-NO3
4cp3t70.xls	c	70	1.00E-03	51.7692%	Na-Cl	Na-Cl	Na-NO3	Na-NO3
4cp3t30.xls		30	1.00E-03	55.6865%	Na-Cl	Na-Cl	Na-NO3	Na-NO3
4cp4t1.xls		100	1.00E-04	55.8998%	Na-Cl	Na-Cl	Na-Cl	Na-NO3
4cp4t70.xls		70	1.00E-04	51.7699%	Na-Cl	Na-Cl	Na-NO3	Na-NO3
4cp4t30.xls		30	1.00E-04	55.6880%	Na-Cl	Na-Cl	Na-NO3	Na-NO3
4dp2t1.xls		100	1.00E-02	55.8053%	Na-Cl	Na-Cl	Na-Cl	Na-NO3
4dp2t70.xls		70	1.00E-02	51.7967%	Na-Cl	Na-Cl	Na-Cl	Na-NO3
4dp2t30.xls		30	1.00E-02	55.6610%	Na-Cl	Na-Cl	Na-Cl	Na-NO3
4dp3t1.xls		100	1.00E-03	55.8090%	Na-Cl	Na-Cl	Na-Cl	Na-NO3
4dp3t70.xls	d	70	1.00E-03	51.8003%	Na-Cl	Na-Cl	Na-NO3	Na-NO3
4dp3t30.xls		30	1.00E-03	55.6865%	Na-Cl	Na-Cl	Na-NO3	Na-NO3
4dp4t1.xls		100	1.00E-04	55.8092%	Na-Cl	Na-Cl	Na-Cl	Na-NO3
4dp4t70.xls		70	1.00E-04	51.8015%	Na-Cl	Na-Cl	Na-NO3	Na-NO3
4dp4t30.xls		30	1.00E-04	55.6880%	Na-Cl	Na-Cl	Na-Cl	Na-NO3
4ep2t1.xls		100	1.00E-02	56.1883%	Na-Cl	Na-Cl	Na-Cl	Na-NO3
4ep2t70.xls		70	1.00E-02	51.8712%	Na-Cl	Na-Cl	Na-Cl	Na-NO3
4ep2t30.xls		30	1.00E-02	55.6610%	Na-Cl	Na-Cl	Na-NO3	Na-NO3
4ep3t1.xls		100	1.00E-03	56.1791%	Na-Cl	Na-Cl	Na-Cl	Na-NO3
4ep3t70.xls	e	70	1.00E-03	51.8671%	Na-Cl	Na-Cl	Na-Cl	Na-NO3
4ep3t30.xls		30	1.00E-03	55.6864%	Na-Cl	Na-Cl	Na-NO3	Na-NO3
4ep4t1.xls		100	1.00E-04	56.1779%	Na-Cl	Na-Cl	Na-Cl	Na-NO3
4ep4t70.xls		70	1.00E-04	51.8693%	Na-Cl	Na-Cl	Na-Cl	Na-NO3
4ep4t30.xls		30	1.00E-04	55.6880%	Na-Cl	Na-Cl	Na-NO3	Na-NO3

Table 6.13-4. Brine Evolution of Group 4 Water (Continued)

LUT Name	WRIP parameter (0, b-j, l)	Temp	pCO2	endpoint RH	98% RH brine	85% RH brine	65% RH brine	Endpoint brine
4fp2t1.xls		100	1.00E-02	56.7246%	Na-Cl	Na-Cl	Na-Cl	Na-NO3
4fp2t70.xls		70	1.00E-02	52.0294%	Na-Cl	Na-Cl	Na-Cl	Na-NO3
4fp2t30.xls		30	1.00E-02	55.6610%	Na-Cl	Na-Cl	Na-Cl	Na-NO3
4fp3t1.xls		100	1.00E-03	56.7252%	Na-Cl	Na-Cl	Na-Cl	Na-NO3
4fp3t70.xls	f	70	1.00E-03	52.0306%	Na-Cl	Na-Cl	Na-Cl	Na-NO3
4fp3t30.xls		30	1.00E-03	55.6865%	Na-Cl	Na-Cl	Na-Cl	Na-NO3
4fp4t1.xls		100	1.00E-04	56.7190%	Na-Cl	Na-Cl	Na-Cl	Na-NO3
4fp4t70.xls		70	1.00E-04	52.0346%	Na-Cl	Na-Cl	Na-Cl	Na-NO3
4fp4t30.xls		30	1.00E-04	55.6880%	Na-Cl	Na-Cl	Na-Cl	Na-NO3
4gp2t1.xls		100	1.00E-02	55.6951%	Na-Cl	Na-Cl	Na-Cl	Na-Cl
4gp2t70.xls		70	1.00E-02	51.3270%	Na-Cl	Na-Cl	Na-Cl	Na-NO3
4gp2t30.xls		30	1.00E-02	54.1053%	Na-Cl	Na-Cl	Na-NO3	Na-NO3
4gp3t1.xls		100	1.00E-03	55.6950%	Na-Cl	Na-Cl	Na-Cl	Na-Cl
4gp3t70.xls	g	70	1.00E-03	51.3940%	Na-Cl	Na-Cl	Na-Cl	Na-NO3
4gp3t30.xls		30	1.00E-03	54.1222%	Na-Cl	Na-Cl	Na-NO3	Na-NO3
4gp4t1.xls		100	1.00E-04	55.6558%	Na-Cl	Na-Cl	Na-Cl	Na-Cl
4gp4t70.xls		70	1.00E-04	51.3100%	Na-Cl	Na-Cl	Na-Cl	Na-NO3
4gp4t30.xls		30	1.00E-04	54.1255%	Na-Cl	Na-Cl	Na-Cl	Na-NO3
4hp2t1.xls		100	1.00E-02	60.8822%	Na-Cl	Na-Cl	Na-Cl	Na-Cl
4hp2t70.xls		70	1.00E-02	58.2682%	Na-Cl	Na-Cl	Na-Cl	Na-Cl
4hp2t30.xls		30	1.00E-02	60.3478%	Na-Cl	Na-Cl	Na-Cl	Na-NO3
4hp3t1.xls		100	1.00E-03	60.8848%	Na-Cl	Na-Cl	Na-Cl	Na-Cl
4hp3t70.xls	h	70	1.00E-03	58.2756%	Na-Cl	Na-Cl	Na-Cl	Na-Cl
4hp3t30.xls		30	1.00E-03	60.3689%	Na-Cl	Na-Cl	Na-Cl	Na-NO3
4hp4t1.xls		100	1.00E-04	60.8838%	Na-Cl	Na-Cl	Na-Cl	Na-Cl
4hp4t70.xls		70	1.00E-04	58.2745%	Na-Cl	Na-Cl	Na-Cl	Na-Cl
4hp4t30.xls		30	1.00E-04	60.3720%	Na-Cl	Na-Cl	Na-NO3	Na-NO3
4ip2t1.xls		100	1.00E-02	60.8062%	Na-Cl	Na-Cl	Na-Cl	Na-Cl
4ip2t70.xls		70	1.00E-02	58.6307%	Na-Cl	Na-Cl	Na-Cl	Na-Cl
4ip2t30.xls		30	1.00E-02	57.9993%	Na-Cl	Na-Cl	Na-Cl	Na-NO3
4ip3t1.xls		100	1.00E-03	60.8067%	Na-Cl	Na-Cl	Na-Cl	Na-Cl
4ip3t70.xls	i	70	1.00E-03	58.6242%	Na-Cl	Na-Cl	Na-Cl	Na-Cl
4ip3t30.xls		30	1.00E-03	57.9993%	Na-Cl	Na-Cl	Na-Cl	Na-NO3
4ip4t1.xls		100	1.00E-04	60.8070%	Na-Cl	Na-Cl	Na-Cl	Na-Cl
4ip4t70.xls		70	1.00E-04	58.6259%	Na-Cl	Na-Cl	Na-Cl	Na-Cl
4ip4t30.xls		30	1.00E-04	58.0000%	Na-Cl	Na-Cl	Na-Cl	Na-NO3
4jp2t1.xls		100	1.00E-02	58.2237%	Na-Cl	Na-Cl	Na-Cl	Na-Cl
4jp2t70.xls		70	1.00E-02	57.5079%	Na-Cl	Na-Cl	Na-Cl	Na-Cl
4jp2t30.xls		30	1.00E-02	62.0002%	Na-Cl	Na-Cl	Na-Cl	Na-NO3
4jp3t1.xls		100	1.00E-03	58.3931%	Na-Cl	Na-Cl	Na-Cl	Na-Cl
4jp3t70.xls	j	70	1.00E-03	57.3906%	Na-Cl	Na-Cl	Na-Cl	Na-Cl
4jp3t30.xls		30	1.00E-03	60.1250%	Na-Cl	Na-Cl	Na-Cl	Na-NO3
4jp4t1.xls		100	1.00E-04	58.3535%	Na-Cl	Na-Cl	Na-Cl	Na-Cl
4jp4t70.xls		70	1.00E-04	57.5022%	Na-Cl	Na-Cl	Na-Cl	Na-Cl
4jp4t30.xls		30	1.00E-04	60.8635%	Na-Cl	Na-Cl	Na-Cl	Na-NO3
4lp2t1.xls		100	1.00E-02	55.8043%	Na-CO3	Na-CO3	K-Cl	K-Cl
4lp2t70.xls		70	1.00E-02	56.8916%	Na-CO3	Na-CO3	K-Cl	K-Cl
4lp2t30.xls		30	1.00E-02	61.9297%	Na-CO3	Na-Cl	Na-Cl	Na-Cl
4lp3t1.xls		100	1.00E-03	56.0925%	Na-CO3	Na-CO3	K-Cl	K-Cl
4lp3t70.xls	l	70	1.00E-03	56.2216%	Na-CO3	Na-CO3	K-Cl	K-Cl
4lp3t30.xls		30	1.00E-03	63.1449%	Na-CO3	Na-CO3	Na-Cl	Na-Cl
4lp4t1.xls		100	1.00E-04	56.0809%	Na-Cl	Na-CO3	K-Cl	K-Cl
4lp4t70.xls		70	1.00E-04	61.0365%	Na-CO3	Na-CO3	K-Cl	K-Cl
4lp4t30.xls		30	1.00E-04	63.7998%	Na-CO3	Na-CO3	Na-Cl	Na-Cl

Source: Output DTN: SN0701PAEBSPCE.001.

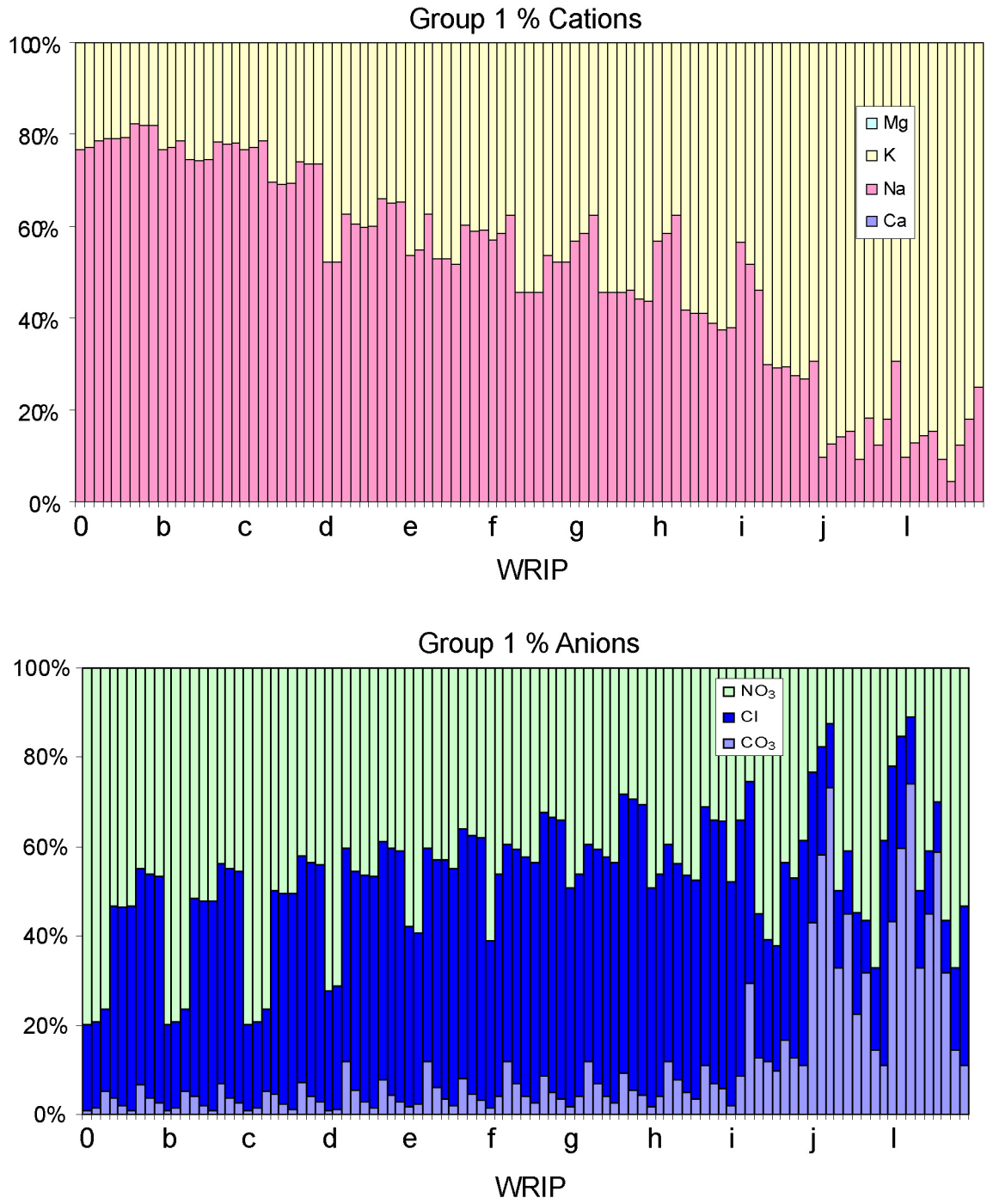

Source: Output DTN: SN0701PAEBSPCE.001.

Figure 6.13-1. Relative Proportions of the Major Cations (upper) and Anions (lower) That Comprise the End-Point Brine for Group 1 Waters

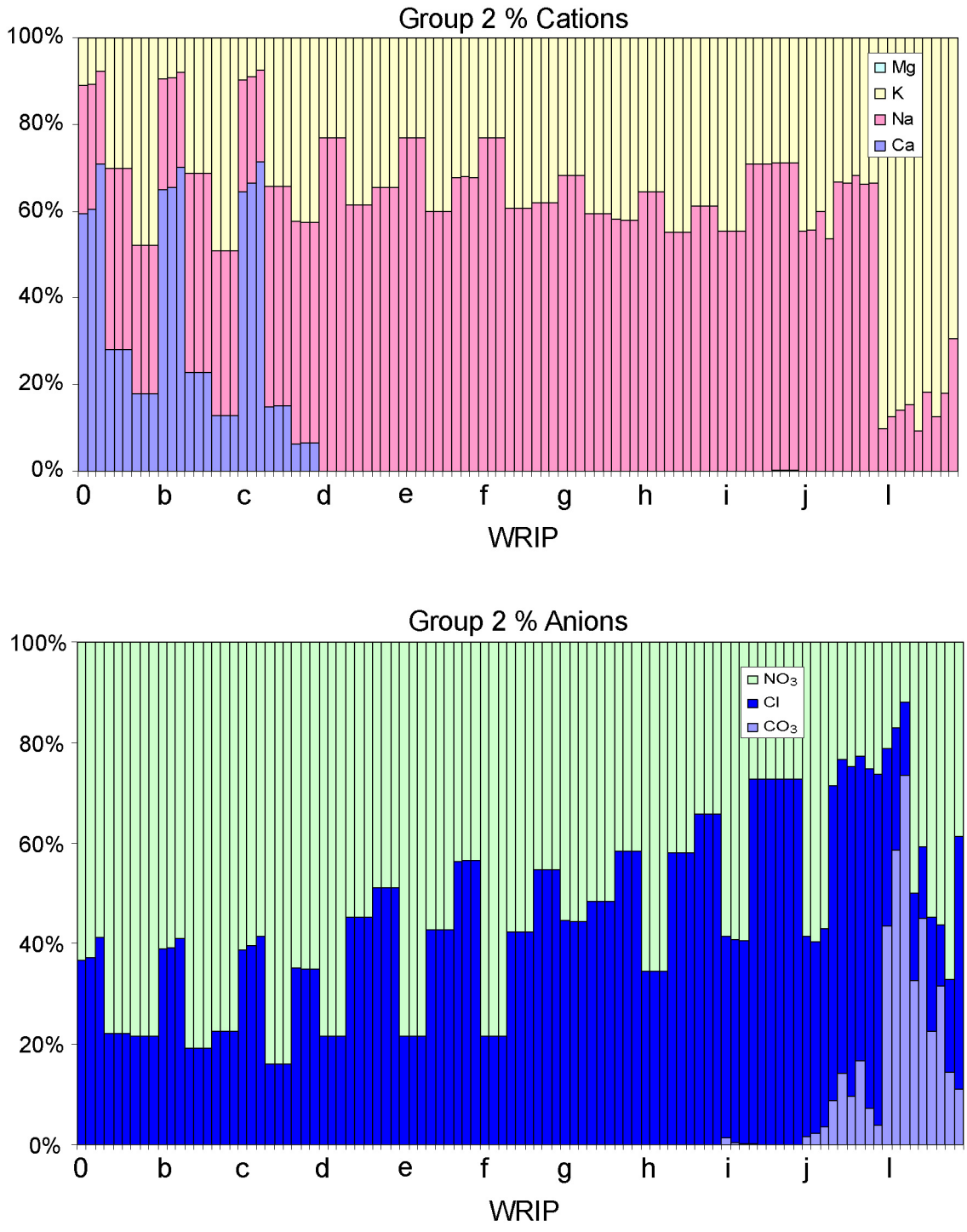

Source: Output DTN: SN0701PAEBSPCE.001.

Figure 6.13-2. Relative Proportions of the Major Cations (upper) and Anions (lower) That Comprise the End-Point Brine for Group 2 Waters

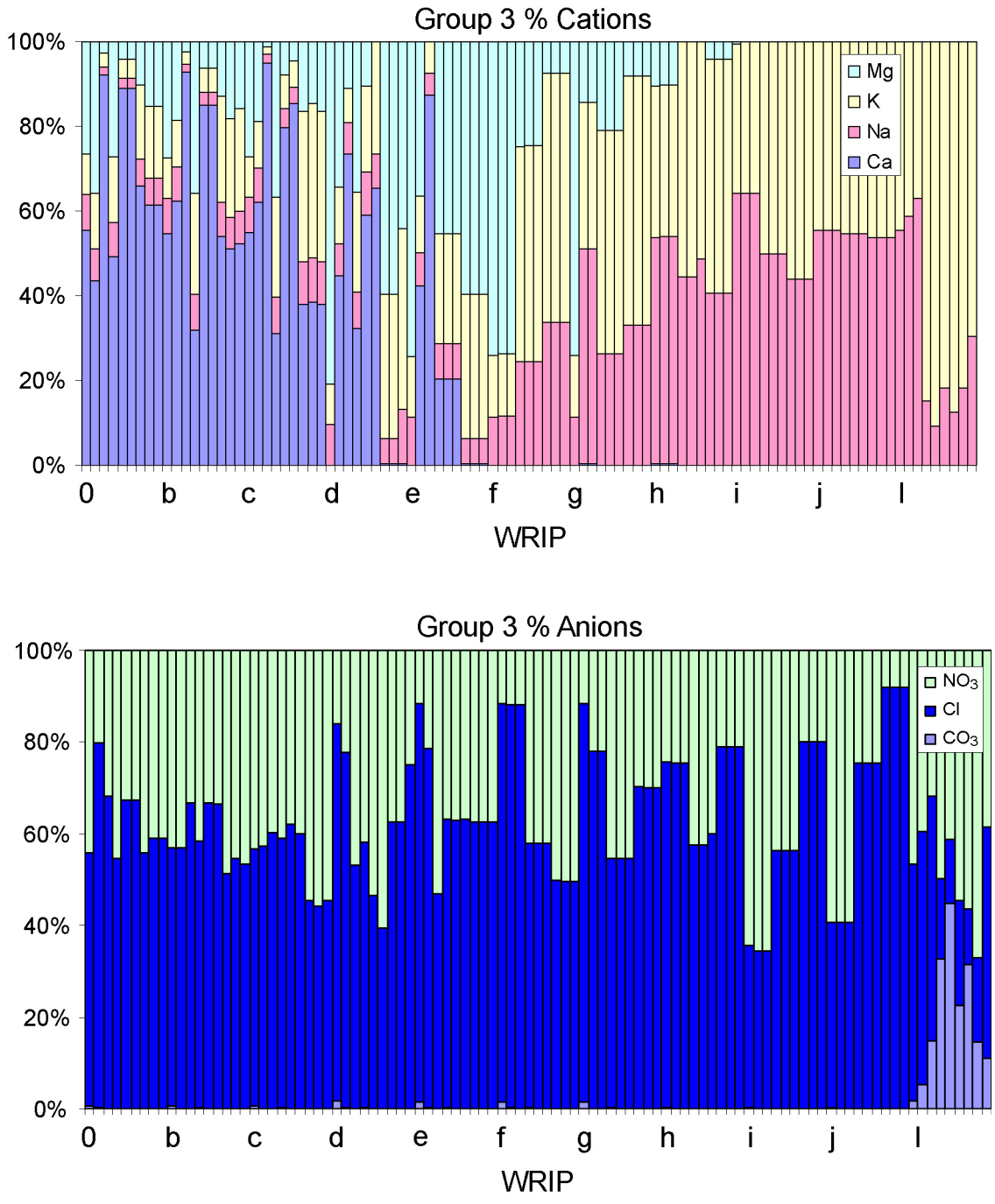

Source: Output DTN: SN0701PAEBSPCE.001.

Figure 6.13-3. Relative Proportions of the Major Cations (upper) and Anions (lower) That Comprise the End-Point Brine for Group 3 Waters

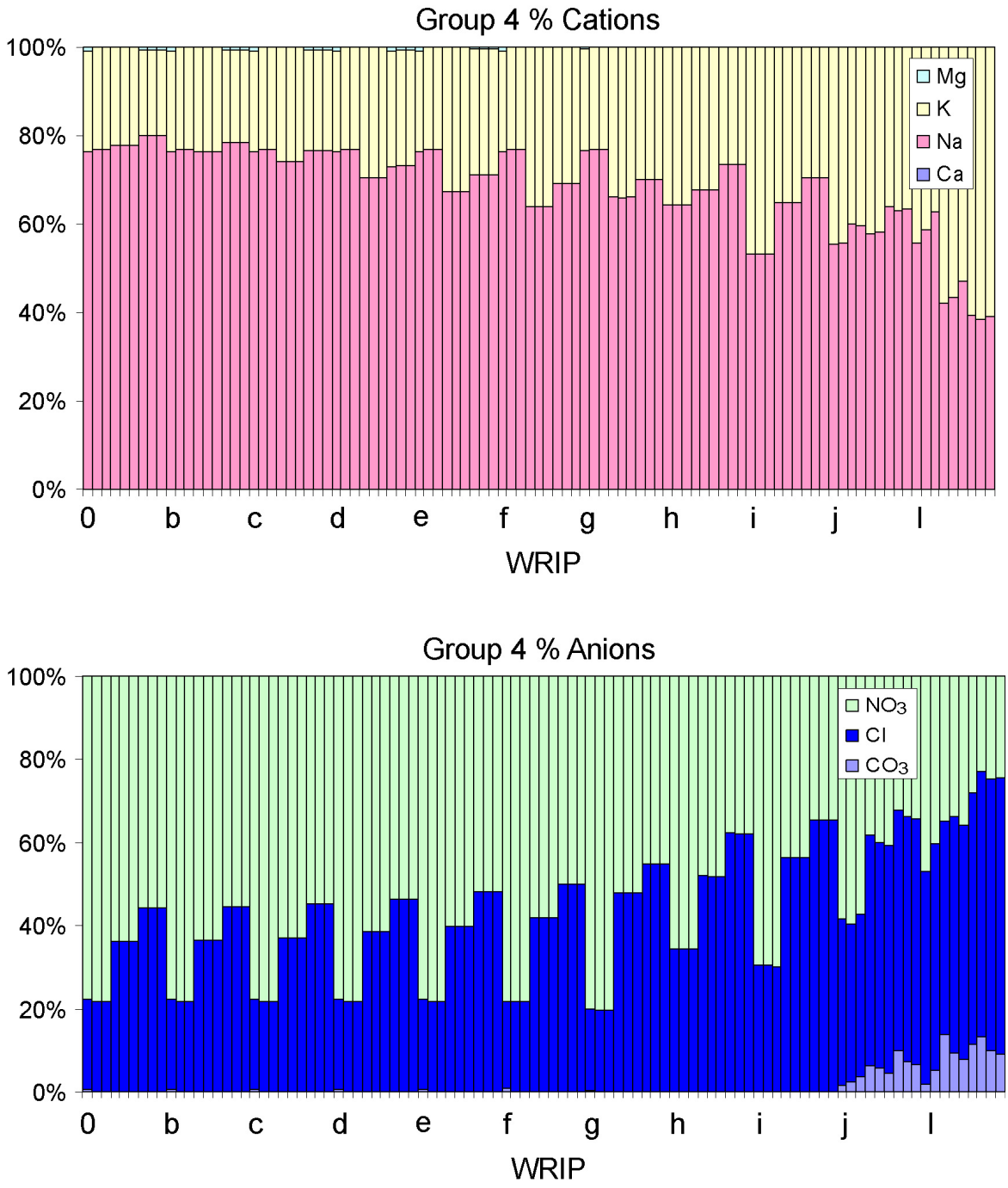

Source: Output DTN: SN0701PAEBSPCE.001.

Figure 6.13-4. Relative Proportions of the Major Cations (upper) and Anions (lower) That Comprise the End-Point Brine for Group 4 Waters

For an example of the variation in pH, Figures 6.13-5 to 6.13-8 show that the seepage pH range varies from group to group as a strong function, primarily of the WRIP, but also of relative humidity and pCO_2 and to a lesser extent temperature. The figures were generated by extracting pH data for the WRIP = 0 and the WRIP = J cases for each of the starting group waters. All three of the temperatures are shown, 30°C, 70°C, and 100°C, for two bounding *p*CO2 values, 10^{-2} and 10^{-4} bar (Output DTN: SN0701PAEBSPCE.001). The legend uses the nomenclature described for the lookup table results in Section 6.15.1. For completeness, the range of pH was also determined by examining the results from the lookup tables archived in the same DTN. For the initial seepage waters (i.e., before adding alkali feldspar), the pH values are highest when the T is lowest and the WRIP is high, and lowest when the T is highest and the WRIP is lowest (see trends in Figures 6.13-5 to 6.13-8). The range for each water is as follows: for Group 1, 7.2 to 9.7; for Group 2, 6.9 to 9.7; for Group 3, 6.9 to 9.6; and for Group 4, 7.0 to 9.5. Upon evaporating the seepage waters, the correlations among pH, pCO_2, T, and the WRIP value are not as straightforward (see Tables 6.13-1 to 6.13-4 for the dryout RH for each of the water types). However, it is possible to correlate the pH ranges to the WRIP values. For all the starting waters the highest WRIP values yield the highest pH values upon evaporating regardless of the dryout RH. For Groups 1, 2, and 4, the low end of the pH range corresponds to the lower WRIP values, while for Group 3 water the lowest pH values are associated with intermediate WRIP values. This is consistent with the observed formation of Mg-Cl brines shown in Figure 6.13-3. The pH ranges upon evaporation are as follows: for Group 1, 8.5 to 11.4; for Group 2, 5.5 to 11.1; for Group 3, 4.8 to 10.9; and for Group 4, 5.3 to 10.4.

Between 100% and 95% relative humidity in the drift, the ionic strength of the evaporating solutions exceeds 1 molal (read from the lookup tables archived in Output DTN: SN0701PAEBSPCE.001). At the lower relative humidity conditions, concentrations of well over 10 molal are possible. An examination of the water loss in the lookup tables shows that when the brines are very concentrated, the relative mass of water becomes extremely small. For example, when 1 kg of unevaporated seepage water is concentrated to an ionic strength of 10 or greater, the mass of remaining water becomes a gram or less. In some cases, the remaining brine is 10^{-4} grams or less. This indicates that the area affected by the corrosion capability of the brines reacting with the waste package or drip shield should decrease as evaporation increases due to the substantial reduction in evaporated seepage water mass. In addition, this small amount of fluid is only capable of holding a very small amount of dissolved waste package metal.

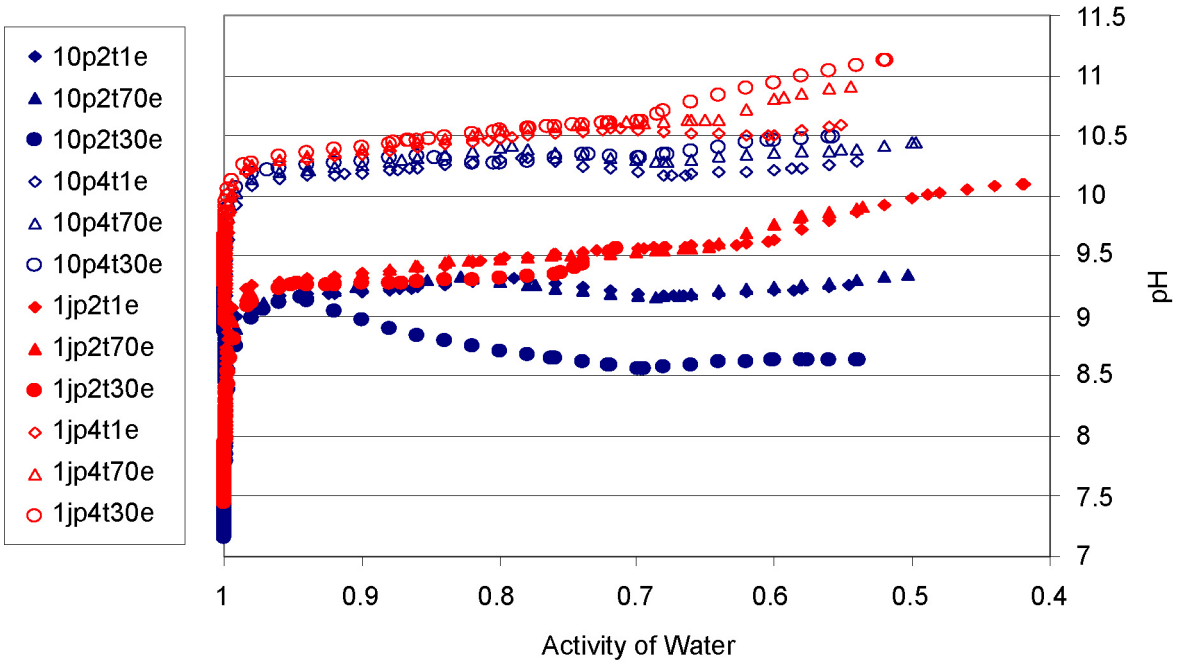

Source: Output DTN: SN0701PAEBSPCE.001.

Figure 6.13-5. pH Range for Group 1 Water from WRIP = 0 to WRIP = J, at $pCO_2 = 10^{-2}$ to 10^{-4} bar and at T = 30°C, 70°C, and 100°C

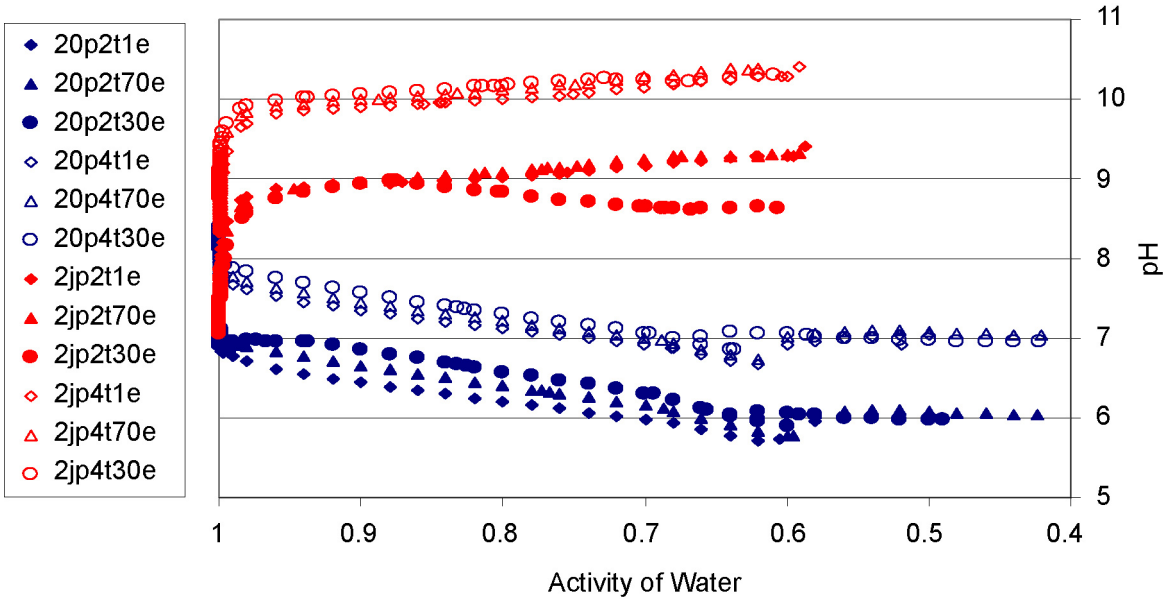

Source: Output DTN: SN0701PAEBSPCE.001.

Figure 6.13-6. pH Range for Group 2 Water from WRIP = 0 to WRIP = J, at $pCO_2 = 10^{-2}$ to 10^{-4} bar and at T = 30°C, 70°C, and 100°C

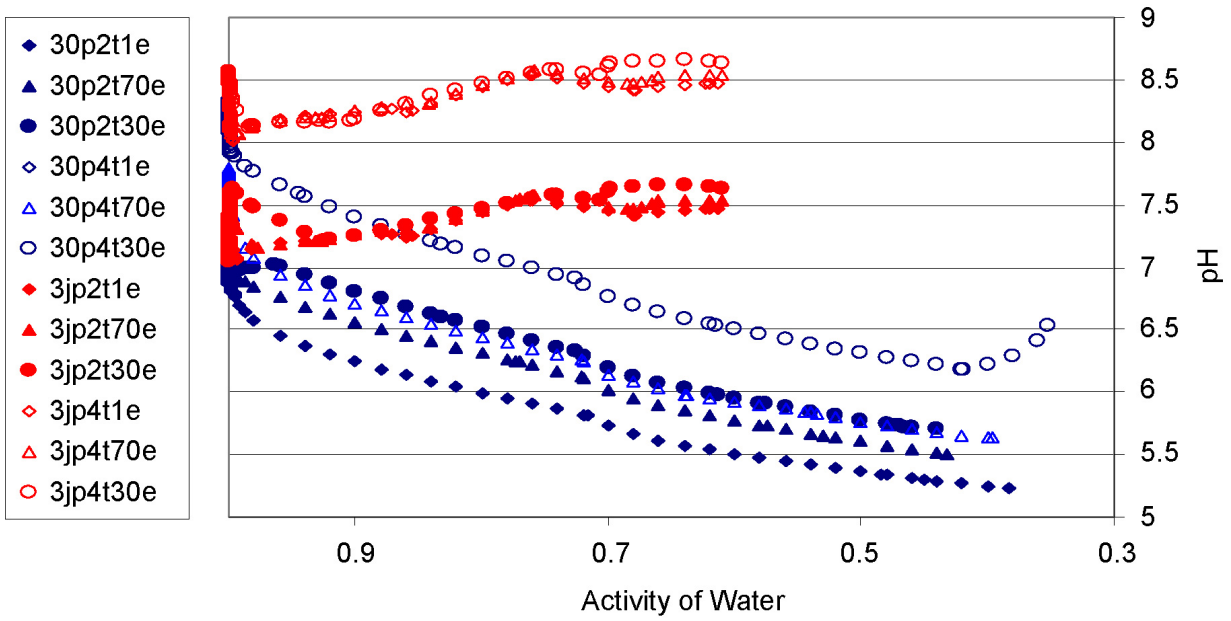

Source: Output DTN: SN0701PAEBSPCE.001.

Figure 6.13-7. pH Range for Group 3 Water from WRIP = 0 to WRIP = J, at $pCO_2 = 10^{-2}$ to 10^{-4} bar and at T = 30°C, 70°C, and 100°C

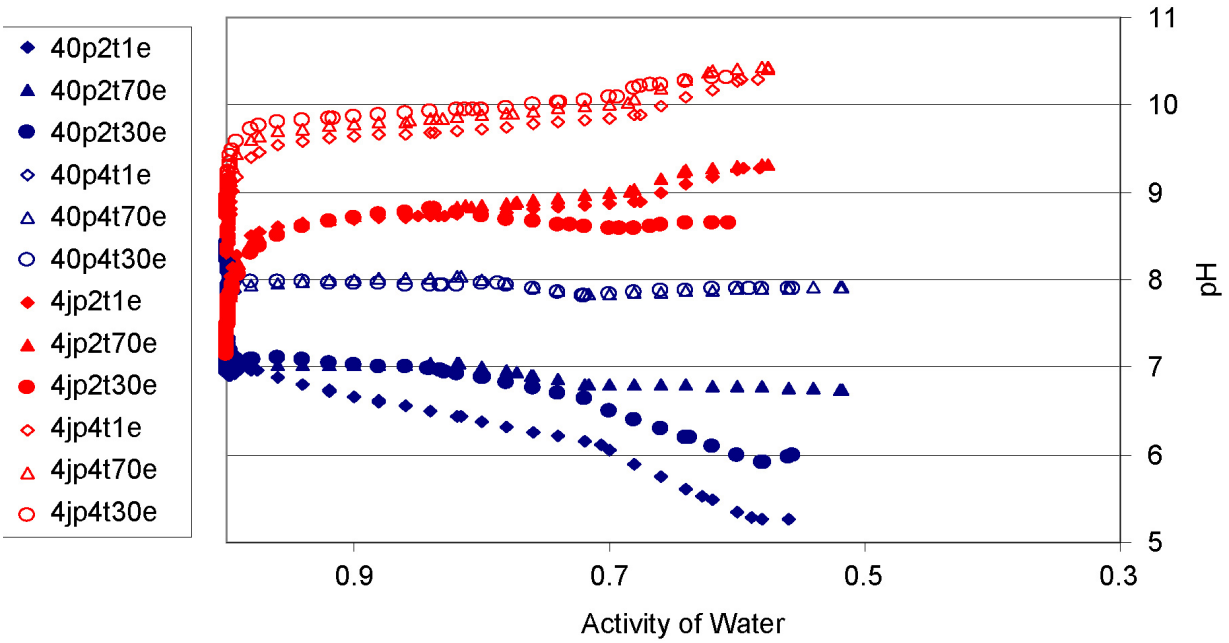

Source: Output DTN: SN0701PAEBSPCE.001.

Figure 6.13-8. pH Range for Group 4 Water from WRIP = 0 to WRIP = J, at $pCO_2 = 10^{-2}$ to 10^{-4} bar and at T = 30°C, 70°C, and 100°C

6.13.4 Chemical Environment in the Invert

The chemical environment in the invert is important for two key TSPA-LA parameters: radionuclide solubility and colloid stability. In general, the chemical parameters of interest are pH and ionic strength. All potential seepage chemistries discussed in the dilution/evaporation abstraction model with respect to waste package and drip shield impacts are possible in the invert, to establish the chemical environment in the invert, multiple sources of water must be considered. The P&CE integrated invert chemistry abstraction model instructs TSPA to perform a series of sensitivity calculations in order to establish that the selection of an appropriately conservative invert water chemistry by comparing outputs from the IPC report (SNL 2007 [DIRS 180506]) with P&CE outputs (see Table 6.15-1).

6.13.4.1 Chemistry of Waste Package Leakage

The compositions of water produced in the waste package by interactions of seepage or condensate water with waste package materials and waste is documented in the IPC report (SNL 2007 [DIRS 180506]), which provides data containing the parameters of interest. A review of Sections 6 and 8 of that report indicates that pH and ionic strengths through time are generally much different than those reported for the potential seepage water chemistries.

6.13.4.2 Evaporative Brine Precipitate Mineralogy and Chemical Divide Phenomena

Each lookup table developed in Section 6.9 has an associated precipitating mineral assemblage. Mineral precipitation as a function of relative humidity and degree of evaporative concentration is presented for each individual lookup table archived in Output DTN: SN0701PAEBSPCE.001. For the details of the precipitated mineral phases including the order of precipitation, see the lookup tables in that DTN. The dominant factor governing the minerals that precipitate and the order in which they form is the starting group water composition and the WRIP value (see Table 6.13-5). Implicit to the NFC model is the assumption of saturation with respect to calcite and amorphous silica. These phases are always present in equilibrium with the solutions. Table 6.13-5 reports the sequence of precipitation as a function of low, moderate, and high WRIP for the T = 70°C, $pCO_2 = 10^{-3}$ case. These data were hand extracted from the lookup table in Output DTN: SN0701PAEBSPCE.001. The same data for all 396 modeled waters are located in this DTN.

Table 6.13-5. Mineral Precipitation Sequence for Low (0), Moderate (F) and High (L) WRIP Values for Selected Group Water Types

Group	WRIP	Mineral Precipitation (in order)	Group	WRIP	Mineral Precipitation (in order)
1	0	1. Amorphous Antigorite 2. Celadonite 3. Fluorite* 4. Kogarkoite 5. Natrite 6. Halite 7. Thenardite*	3	0	1. Amorphous Antigorite 2. Stellerite* 3. Celadonite 4. Fluorite* 5. Anhydrite 6. Halite 7. Sellaite 8. Sylvite 9. Carnalite
1	F	1. Amorphous Antigorite 2. Celadonite 3. Fluorite* 4. Kogarkoite 5. Natrite 6. Halite 7. Sylvite	3	F	1. Amorphous Antigorite 2. Celadonite 3. Fluorite* 4. Anhydrite 5. Sellaite 6. Halite 7. Glauberite* 8. Pentasalt 9. Sylvite 10. Niter
1	L	1. Stellerite* 2. Phillipsite* 3. Celadonite 4. Natrite 5. Arcanite 6. Amorphous Antigorite 7. Fluorite 8. Sylvite 9. Niter	3	L	1. Stellerite* 2. Celadonite 3. Amorphous Antigorite 4. Arcanite 5. Natrite 6. Kogarkoite* 7. Sylvite 8. Fluorite 9. Villiaumite 10. Niter 11. Kalicinite
2	0	1. Amorphous Antigorite 2. Stellerite* 3. Celadonite* 4. Fluorite 5. Anhydrite 6. Halite 7. Niter	4	0	1. Amorphous Antigorite 2. Stellerite* 3. Celadonite 4. Fluorite 5. Anhydrite 6. Glauberite 7. Halite

Table 6.13-5. Mineral Precipitation Sequence for Low (0), Moderate (F) and High (L) WRIP Values for Selected Group Water Types (Continued)

Group	WRIP	Mineral Precipitation (in order)	Group	WRIP	Mineral Precipitation (in order)
2	F	1. Amorphous Antigorite 2. Celadonite 3. Fluorite 4. Anhydrite 5. Pentasalt 6. Glauberite 7. Halite	4	F	1. Amorphous Antigorite 2. Celadonite 3. Fluorite 4. Anhydrite 5. Glauberite 6. Halite
2	L	1. Stellerite* 2. Celadonite 3. Amorphous Antigorite 4. Arcanite 5. Natrite 6. Fluorite 7. Sylvite 8. Villiaumite 9. Kalicinite 10. Niter	4	L	1. Stellerite* 2. Celadonite 3. Amorphous Antigorite 4. Kogarkoite 5. Natrite 6. Arcanite 7. Sylvite

Source: Data were hand extracted from the lookup table in Output DTN: SN0701PAEBSPCE.001.

* Indicates that the mineral precipitated and then re-dissolved. Data correspond to T = 70°C and $pCO_2 = 10^{-3}$.

NOTE: For a description of these minerals, including their formulae, refer to Table 6.2-3.

6.13.5 Comparison to Corrosion Testing Chemistries

Initial corrosion testing environments can be related to three types of natural brines: calcium chloride, carbonate, and sulfate. Initial corrosion test studies focused on the carbonate type brine, based on reasoning that sodium carbonate type waters, as typified by J-13 well water from the saturated zone near Yucca Mountain, were the expected types of waters at the repository (Harrar et al. 1990 [DIRS 100814]). A later study (Rosenberg et al. 2001 [DIRS 154862]) showed that evaporative concentration of a water based on a reported analysis (Sonnenthal et al. 1998 [DIRS 118845]) of a pore water from Yucca Mountain resulted in a calcium chloride type brine. The types of aqueous solutions used for corrosion testing will be discussed in the context of the natural brines that follows.

Geochemical literature (e.g., Drever 1997 [DIRS 147480]) establishes the three types of brines that result from the evaporative concentration of dilute natural waters at the Earth's surface: (1) calcium chloride brine, (2) carbonate brine, and (3) sulfate brine. It is important to note that the compositions of brines are dependent on relative humidity, and the dominant ions in solution can and do change as a function of relative humidity. This classical treatment of groundwater evaporation does not include nitrate, which, with respect to the calcite and gypsum chemical divides, are indistinguishable. Thus, for the purposes of this classification, chloride- or nitrate-rich brines are treated similarly (e.g., Ca-nitrate brines are classified with Ca-chloride brines).

6.13.5.1 Corrosion Test Chemistries

Table 6.13-6 shows the composition of some of the solutions used for corrosion testing. These solutions were developed based on the evaporative concentration of carbonate-based water with a composition based on J-13 well water, which is saturated zone water near Yucca Mountain. The solutions represent various stages of evaporative concentration of this type of water. These aqueous solution compositions were concentrated to about 10 times (for SDW test solutions) to over 45,000 times (for simulated saturated water (SSW) and basic saturated water (BSW) test solutions) to simulate evaporative concentration of the water upon contacting the waste package or the drip shield. NaCl test solutions were also used where NaCl concentrations varied from 0.5 to 4.0 molar; $CaCl_2$ and $CaCl_2 + Ca(NO_3)_2$ test solutions were also used with $CaCl_2$ concentrations up to 9 molar.

In all cases, the NO_3^- component is the most soluble species and would dominate the solution composition at the deliquescent relative humidity or eutectic point of a mineral assemblage at elevated temperatures. It is not until the relative humidity is higher that Cl^- could become comparable to NO_3^-. This is discussed in more detail in Section 6.13.6, where it is related to the transport separation of halite.

Table 6.13-6. Target Composition of Standard Test Media Based on Evaporative Concentration of a Dilute Carbonate-Type Water

Ion	SDW (mg/L)	SCW (mg/L)	SAW (mg/L)	SSW* (mg/L)	BSW-12** (mg/L)
K^+	3.4×10^1	3.4×10^3	3.4×10^3	1.42×10^5	6.71×10^4
Na^+	4.09×10^2	4.09×10^4	3.769×10^4	4.87×10^5	1.057×10^5
Mg^{2+}	1	<1	1.00×10^3	0	0
Ca^{2+}	5×10^{-1}	<1	1.00×10^3	0	0
F^-	1.4×10^1	1.4×10^3	0	0	1.331×10^3
Cl^-	6.7×10^1	6.7×10^3	2.425×10^4	1.28×10^5	1.313×10^5
NO_3^-	6.4×10^1	6.4×10^3	2.30×10^4	1.313×10^6	1.395×10^5
SO_4^{2-}	1.67×10^2	1.67×10^4	3.86×10^4	0	1.392×10^4
HCO_3^-	9.47×10^2	7.0×10^4	0	0	0
Si	27 (60°C), 49 (90°C)	27 (60°C), 49 (90°C)	27 (60°C), 49 (90°C)	0	0
pH	9.8 to 10.2	9.8 to 10.2	2.7	5.5 to 7	12

Source: DTN: LL040803112251.117 [DIRS 171362].

* SSW values correspond to 100°C. **BSW-12 values rounded to ≈ 3 significant figures; these are only target compositions.

NOTE: The basis for the dilute carbonate water was J-13 well water, a saturated zone water near Yucca Mountain. The SDW, SCW, and BSW test solutions correspond to increasing evaporative concentration of the basis water. The SSW test solution contains only Cl^- and NO_3^- and corresponds to the scenario where the other anions have precipitated out of solution, that is, a very low relative humidity condition. The SAW test solution is a moderately acidic solution (hence, no carbonate because of its volatility) with an ionic strength similar to the SCW test solution. The SAW test solution also does not contain fluoride, which was excluded because of its high vapor pressure at the solution pH. pH is measured for actual solutions at room temperature.

6.13.5.2 In-Drift Brine Compared to Test Solutions

The potential compositions of evaporated seepage waters were discussed in Section 6.13.3. The following discussion relates those brine types to solution compositions used for corrosion testing by the Yucca Mountain Project.

As discussed in Section 6.3.3.1, in general, natural waters fall into three groups, defined on the basis the type of brine that forms upon evaporation of the waters. Those three groups are carbonate waters, sulfate waters, and calcium chloride waters. Characteristics of these waters are given below:

- Carbonate waters: Evolve towards higher pH, no significant Ca or Mg content; final compositions are Na-K-Cl-NO_3-CO_3-SO_4 brines.

- Sulfate waters: Evolve to neutral pH; no significant Ca or Mg; final compositions are Na-K-Cl-NO_3-SO_4 brines.

- Calcium chloride waters: Evolve towards lower pH, negligible fluoride, carbonate, sulfate; final compositions are Ca-[Mg]-Na-K-Cl-NO_3 brines.

Figures 6.13-1 to 6.13-4 summarize the range of brine compositions predicted to form within the repository by evaporation of seepage. As can be seen in these figures, classification of these waters is a function of the WRIP—the amount of feldspar dissolved. For low amounts of feldspar dissolved, Group 1 form carbonate brines, Group 4 form sulfate brines, and Group 2 and 3 waters form calcium chloride brines. With increasing amounts of feldspar dissolved, all the waters evolve into the carbonate-type brines. This is because feldspar dissolution and secondary mineral precipitation consumes Ca and Mg and raises the pH and bicarbonate concentrations.

In Table 6.13-7, the end-point brine composition and classification are given for each of the four P&CE starting waters, at three different WRIP values, corresponding to low, moderate, and high amounts of feldspar dissolved. In terms of the three stated natural brine types, the waters are classified dominantly as carbonate-type. As noted in Section 6.3.3.1, this categorization does not necessarily indicate that carbonate or bicarbonate is the dominant anion at end-point conditions. The composition of each group water as a function of WRIP, temperature, pCO_2, and relative humidity is given in the lookup tables discussed in Section 6.13.1.

Table 6.13-7. Evaporated Seepage Water and Corresponding Corrosion Test Solutions

Group Water	Dominant Constituents in Endpoint Brines	Brine Type	Corresponding Corrosion Test Solution
Group 1, low WRIP	Na-K-NO_3-Cl	Carbonate	SDW, SCW, BSW, SSW, NaCl
Group 1, moderate WRIP	Na-K-Cl-NO_3	Carbonate	SDW, SCW, BSW, SSW, NaCl
Group 1, high WRIP	K-Na-NO_3-CO_3-Cl	Carbonate	SDW, SCW, BSW, SSW, NaCl
Group 2, low WRIP	Ca-K-Na-NO_3-Cl	Calcium Chloride	$CaCl_2$; $CaCl_2$ + $Ca(NO_3)_2$, SSW, NaCl
Group 2, moderate WRIP	Na-K-NO_3-Cl	Sulfate	SAW, SSW, NaCl

Table 6.13-7. Evaporated Seepage Water and Corresponding Corrosion Test Solutions (Continued)

Group Water	Dominant Constituents in Endpoint Brines	Brine Type	Corresponding Corrosion Test Solution
Group 2, high WRIP	K-Na-NO_3-CO_3-Cl	Carbonate	SDW, SCW, BSW, SSW, NaCl
Group 3, low WRIP	Ca-Mg-Cl-NO_3	Calcium chloride	$CaCl_2$; $CaCl_2$ + $Ca(NO_3)_2$, SSW, NaCl
Group 3, moderate WRIP	Mg-K-Na-Cl-NO_3	Carbonate	SDW, SCW, BSW, SSW, NaCl
Group 3, high WRIP	K-Na-NO_3-Cl-CO_3	Carbonate	SDW, SCW, BSW, SSW, NaCl
Group 4, low WRIP	Na-K-NO_3-Cl	Sulfate	SAW, SSW, NaCl
Group 4, moderate WRIP	Na-K-NO_3-Cl	Sulfate	SAW, SSW, NaCl
Group 4, high WRIP	K-Na-Cl-NO_3-CO_3	Carbonate	SDW, SCW, BSW, SSW, NaCl

NOTE: See Figures 6.13-1 to 6.13-4. Cations, then anions, are listed in descending order of concentration.

6.13.5.3 Discussion of the Corrosion Test Solutions

In general, the water types that have been defined for surface waters are relevant to water chemistry in the repository. However, one major difference is expected: nitrate is a significant component of both pore waters and dust, and will comprise a large component of the brines because of the high solubility of nitrate minerals. With respect to the water types described above, nitrate behaves similarly to chloride.

Calcium Chloride Brines—Naturally occurring brines may have acidic to near-neutral pH and no significant bicarbonate, carbonate, fluoride, or sulfate content. These brines may contain other cations such as Na^+, K^+, and Mg^{2+}, and other anions such as NO_3^-. The endpoint of the evaporative concentration of this type of brine would contain Ca-Cl/NO_3 or a mixture of Ca/Mg-Cl/NO_3. Corrosion test solutions corresponding to calcium chloride-type brines include: calcium chloride, calcium chloride plus calcium nitrate, SSW (Table 6.13-6), and sodium chloride solutions. The SSW and sodium chloride test solutions represent the moderate relative humidity scenario where calcium is a minor component in the aqueous solution. Numerous electrochemical studies were performed in these test solutions. Thin film studies were also performed using these types of solutions on coupons of Alloy 22 using an environmental thermogravimetric analyzer.

Carbonate Brines—These brines are alkaline and do not contain significant calcium or magnesium. In the early stages of the evaporative concentration, calcium precipitates as carbonate minerals (calcite or aragonite). Magnesium precipitates as magnesium silicate. As shown in Table 6.13-7, carbonate-type brines are expected to comprise the largest fraction of those produced by seepage evaporation. Corrosion test solutions corresponding to carbonate-type brines include: SDW, SCW, BSW, and under certain circumstances, SSW and NaCl aqueous test solutions (Table 6.13-6). The SDW test solution is a dilute alkaline solution; solutions in this concentration range could be expected to form for high relative humidity (greater than 99%). The SCW test solution is a moderately concentrated alkaline solution; solutions in this concentration range could be expected to form for relative humidity in the range of 90% to 95%. The BSW test solution is a highly concentrated alkaline solution and could be expected under repository conditions where temperatures could be at its measured boiling point of nominally 112°C to 113°C, or where the relative humidity is nominally 70% to 75%.

Under conditions of low relative humidity, carbonate-type brines can be rich in Cl^--NO_3^- with low carbonate content—for example, Group 4 waters at moderate WRIP values (Figure 6.13-4). The SSW test solution has characteristics of this type of brine.

Sulfate Brines—These have near-neutral pH and no significant carbonate or calcium content. Calcium precipitates as carbonates and possibly sulfates. In addition, the brines typically have only a small amount of magnesium, though some surface brines have been observed to have high magnesium (Drever 1997 [DIRS 147480], Table 15-1, p. 333, brines 1 through 3). As with the other brine types, the dominant ions in sulfate brines vary with relative humidity. At low relative humidity, the solutions will be dominated by Cl^- and NO_3^- anions, with NO_3^- ions dominating at the lowest relative humidity. At moderate relative humidity (>70%), Cl^- ions may dominate. However, unlike the carbonate brines, these brines are expected to have near-neutral to slightly acidic pH. Significant amounts of dissolved carbonate and Ca^{2+} are not predicted until the relative humidity is greater than 85%.

The corrosion test solutions corresponding to sulfate-type brines include SAW, SSW, and sodium chloride. The SSW has characteristics of water at low relative humidity, where sulfate is not a major brine component. Sodium chloride test solutions simulate the scenario where Cl^- is the dominant anion under moderate relative humidity conditions. The SAW test solutions have characteristics of solutions in equilibrium with nominally 90% relative humidity.

6.13.6 Transport-Affected Salt Assemblages

The environment on the surface of the drip shield or waste package is subject to thermal-hydrologic conditions that may involve splashing. The surface may be covered with dust and debris on the surface, and may have dents or depressions caused by rockfall. In addition, crevices may form as stress corrosion cracks or where debris contacts the surface, and these may harbor stagnant liquid or immobilized solid phases. Over the long term, the surface of the drip shield and the waste package (depending on local seepage and possible drip shield damage) is subject to cumulative evaporation amounting to hundreds to thousands of liters per waste package.

Interaction of evaporated seepage water with the surfaces of the drip shields or exposed waste packages may produce mineral precipitates because the surface temperature is greater than that of the host rock, resulting in a lower local relative humidity. The most volumetrically important of these precipitates are calcite, anhydrite, and forms of silica. The effect of these processes on the chemical environment for corrosion is the possible accumulation of separated salts as well as inert products that affect hydraulics and chemical heterogeneity (Hall and Walton 2003 [DIRS 170586]). The effects of relatively inert scale (e.g., silica or calcite) are included in the measured data used to develop the corrosion models (SNL 2007 [DIRS 178519], Sections 1.2 and 6.4.4.2); however, the effects from separation of potentially aggressive species such as chloride are addressed explicitly in the P&CE seepage dilution/evaporation abstraction (Section 6.15).

Soluble salts containing chloride may precipitate along flow pathways if the temperature and humidity conditions (e.g., on the drip shield or waste package) are sufficiently different from the conditions at the drift wall. If transport of the residual liquid phase occurs, the chloride-bearing

precipitates are separated from the other chemical components of seepage, such as nitrate. The process could be enhanced by the presence of precipitates such as silica or calcite, which could cause ponding or channeling. Dents caused by rockfall or resulting from seismic shaking could cause similar effects on flow. Although this situation may be rare, it is incorporated in the seepage dilution/evaporation abstraction model used for TSPA in relation to the potential for localized corrosion of the waste package outer barrier. The drip shield titanium material is not susceptible to localized corrosion under in-drift environmental conditions (SNL 2007 [DIRS 180778], Section 6.3.3).

Chloride Salt Separation—The first chloride salt to precipitate during evaporation of the seepage waters is a function of the WRIP. As WRIP values increase, so does the K content in the waters. At low WRIP, halite (NaCl) precipitates first; as the WRIP value increases, sylvite (KCl) precipitates first. The range of relative humidity salt separation values depends upon WRIP, temperature, and pCO_2. The salt separation RH values may be used by TSPA-LA to implement this salt separation effect according to the instructions in Section 6.15.1. The RH of salt separation for all 396 modeled waters is archived in Output DTN: SN0703PAEBSPCE.006, and the treatment of uncertainty on this variable is documented in Section 6.12; related spreadsheets are archived in Output DTN: SN0703PAEBSPCE.007. (See discussion in Section 6.15.1.3.)

As noted earlier, the chloride:nitrate ratio impacts the likelihood of localized corrosion on the waste package outer barrier (Section 6.10). This is primarily due to the separation of nitrate-rich brines from precipitated Cl-bearing salts (see discussion in Section 6.15.1.3). As seepage evaporates, chloride and nitrate concentrate in solution. Because chloride and nitrate salts are highly soluble, these two species vary linearly with the degree of concentration and the relative humidity until a salt containing chloride or nitrate precipitates, generally between 60% and 75% relative humidity. At the point of salt precipitation, chloride concentrations vary from approximately 2 to approximately 8 molal. At higher degrees of evaporation, concentrations can increase to as high as 11 molal. The chloride:nitrate ratio of the evaporating solution remains constant until a chloride-containing or nitrate-containing salt precipitates. Chloride salts (halite or sylvite) nearly always precipitate first and the chloride:nitrate ratio decreases. In a few cases, a nitrate salt precipitates first and the chloride:nitrate ratio increases slightly; however, a chloride salt soon begins to precipitate, and the ratio drops. At highest degrees of evaporation, the chloride:nitrate ratio can increase again. The chloride:nitrate ratios throughout this report are quantified by the ratio of total Cl and total N in solution. The chloride:nitrate ratios as a function of the activity of water are plotted for each of the group waters utilized by the P&CE suite of models in Figures 6.13-9 to 6.13-12. The legend uses the nomenclature described for the lookup table results in Section 6.15.1. As the salt separation threshold is reached, chloride salts precipitate and the ratio of Cl to N decreases. This threshold RH value is a function of the starting water composition and the WRIP. There is also an influence on the salt separation RH of temperature and pCO_2. Each of the chloride:nitrate figures presents a representative set of results: for low (0) and high (J) WRIP, low (10^{-4}) and high (10^{-2}) pCO_2, and for all three temperatures (30°C, 70°C, 100°C) (Figures 6.13-9 to 6.13-12). It is noteworthy that for three out of the four group waters (1, 2, and 4), the chloride:nitrate values are relatively low: Group 1 = 2.5, Group 2 = 2.7, and Group 4 = 4.5. The Group 3 water has an initial chloride:nitrate ratio of approximately 22.

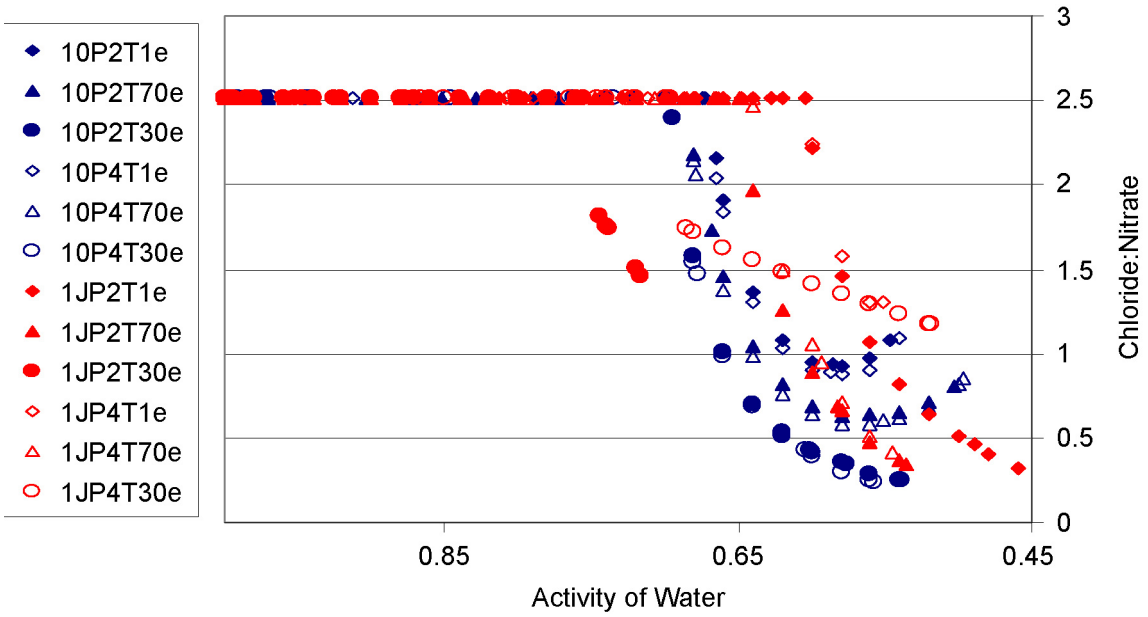

Source: Output DTN: SN0701PAEBSPCE.001.

Figure 6.13-9. Chloride:Nitrate Range for Group 1 Water from WRIP = 0 to WRIP = J, at $pCO_2 = 10^{-2}$ to 10^{-4} bar and at T = 30°C, 70°C, and 100°C

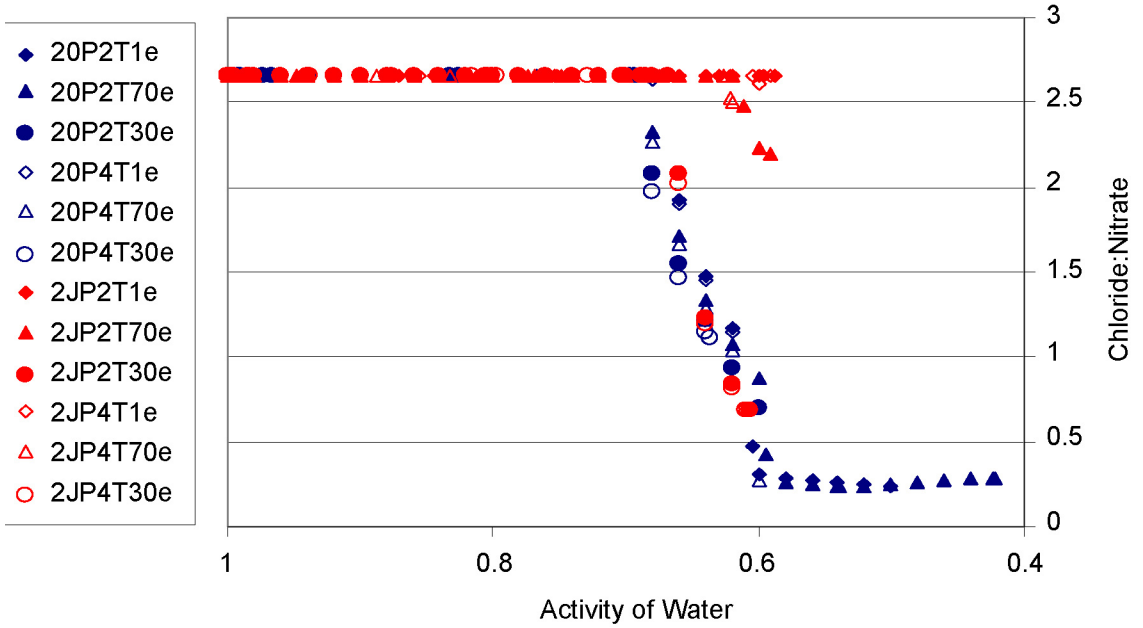

Source: Output DTN: SN0701PAEBSPCE.001.

Figure 6.13-10. Chloride:Nitrate Range for Group 2 Water from WRIP = 0 to WRIP = J, at $pCO_2 = 10^{-2}$ to 10^{-4} bar and at T = 30°C, 70°C, and 100°C

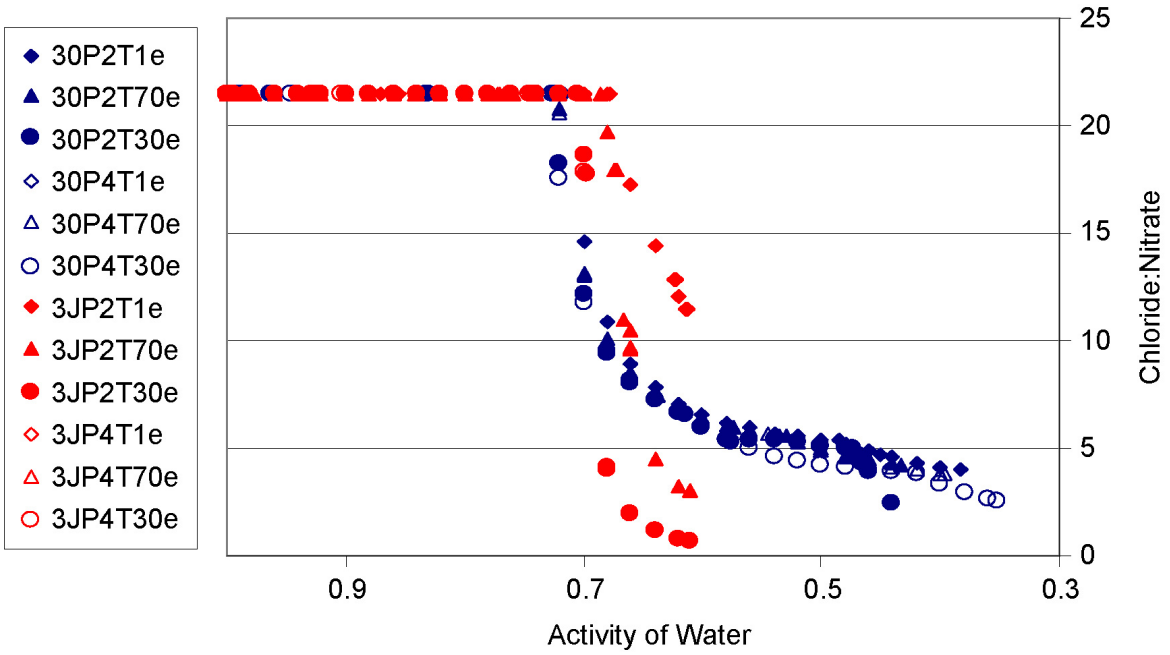

Source: Output DTN: SN0701PAEBSPCE.001.

Figure 6.13-11. Chloride:Nitrate Range for Group 3 Water from WRIP = 0 to WRIP = J, at $pCO_2 = 10^{-2}$ to 10^{-4} bar and at T = 30°C, 70°C, and 100°C

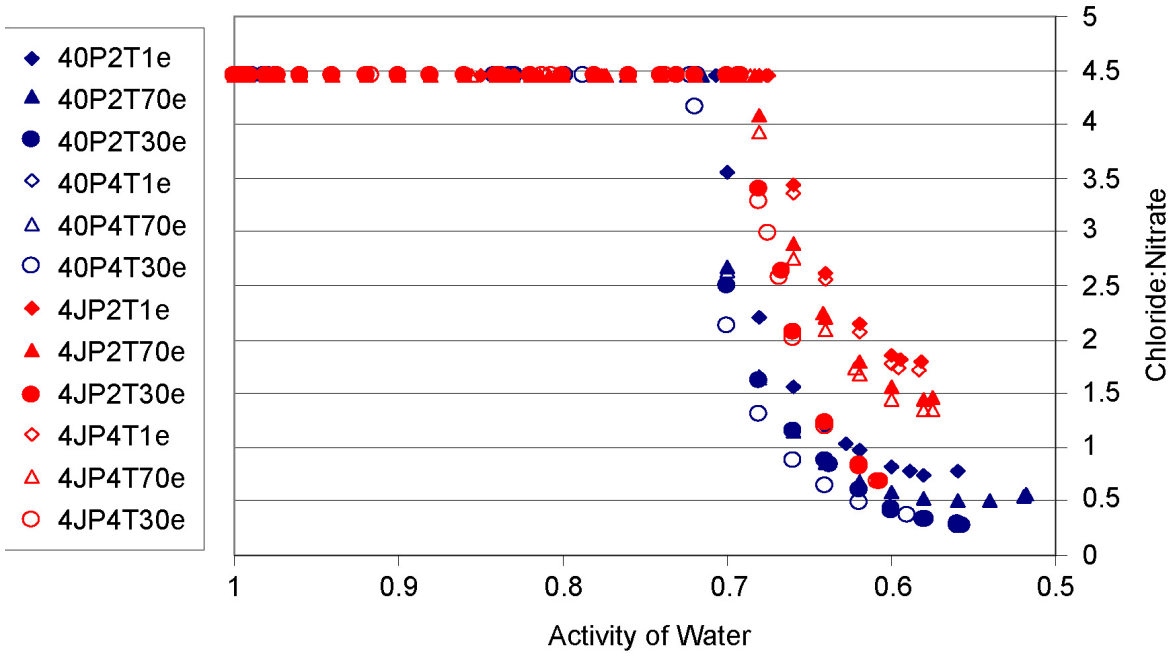

Source: Output DTN: SN0701PAEBSPCE.001.

Figure 6.13-12. Chloride:Nitrate Range for Group 4 Water from WRIP = 0 to WRIP = J, at $pCO_2 = 10^{-2}$ to 10^{-4} bar and at T = 30°C, 70°C, and 100°C

6.14 EVALUATION OF FEATURES, EVENTS, AND PROCESSES

As stipulated in *Technical Work Plan for: Revision of Model Reports for Near-Field and In-Drift Water Chemistry* (SNL 2007 [DIRS 179287], Table 4), this model report addresses the FEPs pertaining to near-field and in-drift water chemistry that are included through this report (i.e., included FEPs) for TSPA LA, as listed in Table 6.14-1. A deviation from the table of included FEPs presented in the TWP is discussed at the end of Section 1.0. Table 6.14-1 summarizes the FEPs that are relevant to this report in accordance with their assignment in the LA FEP list (DTN: MO0706SPAFEPLA.001 [DIRS 181613]). A brief description of the FEPs and the location within this report where they are addressed are also provided in Table 6.14-1. Additional details of these FEPs and their implementation in TSPA-LA is documented in the FEPs report (SNL 2007 [DIRS 179476]).

Table 6.14-1. Included Features, Events, and Processes Addressed in This Report

FEP Number	FEP Name	Description	Section(s) Where Addressed
2.1.08.06.0A	Capillary effects (wicking) in EBS	Capillary rise, or wicking, is a potential mechanism for water to move through the waste and EBS.	1, 6.9, 6.13.5, 6.15.2
2.1.08.07.0A	Unsaturated flow in the EBS	Unsaturated flow may occur along preferential pathways in the waste and EBS. Physical and chemical properties of the EBS and waste form, in both intact and degraded states, should be considered in evaluating pathways.	6.6, 6.9, 6.13
2.1.09.01.0A	Chemical characteristics of water in drifts	When flow in the drifts is reestablished following the peak thermal period, water may have chemical characteristics influenced by the near-field host rock and EBS. Specifically, the water chemistry (pH and dissolved species in the groundwater) may be affected by interactions with cementitious materials or steel used in the disposal region. These point-source contaminated waters may coalesce to form a larger volume of contaminated water. This altered groundwater is referred to as the carrier plume because dissolution and transport will occur in this altered chemical environment as contaminants move through the EBS, and down into the unsaturated zone.[a]	6.4, 6.6, 6.7, 6.8, 6.9, 6.12, 6.13
2.1.09.02.0A	Chemical interaction with corrosion products	Corrosion products produced during degradation of the waste form, metallic portions of the waste package, and metals in the drift (rock bolts, steel in invert, gantry rails) may affect the mobilization and transport of radionuclides. Corrosion products may facilitate sorption/desorption and coprecipitation/dissolution processes. Corrosion products may form a “rind” around the fuel that could (1) restrict the availability of water for dissolution of radionuclides or (2) inhibit advective or diffusive transport of water and radionuclides from the waste form to the EBS. Corrosion products also have the potential to retard the transport of radionuclides to the EBS. Finally, corrosion products may alter the local chemistry, possibly enhancing dissolution rates for specific waste forms, or altering radionuclide solubility.	6.7.1, 6.8
2.1.09.06.0B	Reduction-oxidation potential in drifts	The redox potential in the EBS influences the oxidation of the in-drift materials and the in-drift solubility of radionuclide species. Local variations in the in-drift redox potential can occur.	6.7.1
2.1.09.07.0B	Reaction kinetics in drifts	Chemical reactions, such as radionuclide dissolution/precipitation reactions and reactions controlling the reduction-oxidation state, may not be at equilibrium in the drifts.	6.5, 6.6, 6.7, 6.8, 6.9, 6.13
2.1.11.01.0A	Heat generation in EBS	Temperature in the waste and EBS will vary through time. Heat from radioactive decay will be the primary cause of temperature change, but other factors to be considered in determining the temperature history include the in situ geothermal gradient, thermal properties of the rock, EBS, and waste materials, hydrological effects, and the possibility of exothermic reactions. Considerations of the heat generated by radioactive decay should take different properties of different waste types, including DSNF, into account.	6.3, 6.9, 6.13

Table 6.14-1. Included Features, Events, and Processes Addressed in This Report (Continued)

FEP Number	FEP Name	Description	Section(s) Where Addressed
2.1.11.08.0A	Thermal effects on chemistry and microbial activity in the EBS	Temperature changes may affect chemical and microbial processes in the waste and EBS.	6.4, 6.7, 6.9
1.1.02.02.0A	Preclosure ventilation	The duration of preclosure ventilation acts together with waste package spacing (as per design) to control the extent of the boiling front (zone of reduced water content).	6.3
1.2.02.01.0A	Fractures	Groundwater flow in the Yucca Mountain region and transport of any released radionuclides may take place along fractures. The rate of flow and the extent of transport in fractures are influenced by characteristics such as orientation, aperture, asperity, fracture length, connectivity, and the nature of any linings or infills.	6.3
1.3.01.00.0A	Climate change	Climate change may affect the long-term performance of the repository. This includes the effects of long-term change in global climate (e.g., glacial/interglacial cycles) and shorter-term change in regional and local climate. Climate is typically characterized by temporal variations in precipitation and temperature.	6.3
1.4.01.01.0A	Climate modification increases recharge	Climate modification causes an increase in recharge in the Yucca Mountain region. Increased recharge might lead to increased flux through the repository, perched water, or water table rise.	6.3
2.1.08.01.0A	Water influx at the repository	An increase in the unsaturated water flux at the repository may affect thermal, hydrologic, chemical, and mechanical behavior of the system. Increases in flux could result from climate change, but the cause of the increase is not an essential part of the FEP.	6.3
2.2.03.01.0A	Stratigraphy	Stratigraphic information is necessary information for the performance assessment. This information should include identification of the relevant rock units, soils and alluvium, and their thickness, lateral extents, and relationships to each other. Major discontinuities should be identified.	4.1, 6.3
2.2.03.02.0A	Rock properties of host rock and other units	Physical properties such as porosity and permeability of the relevant rock units, soils, and alluvium are necessary for the performance assessment. Possible heterogeneities in these properties should be considered. Questions concerning events and processes that may cause these physical properties to change over time are considered in other FEPs	4.1, 6.3
2.2.07.08.0A	Fracture flow in the UZ	Fractures or other analogous channels may act as conduits for fluids to move into the subsurface to interact with the repository and as conduits for fluids to leave the vicinity of the repository and be conducted to the saturated zone. Water may flow through only a portion of the fracture network, including flow through a restricted portion of a given fracture plane.	6.3

Table 6.14-1. Included Features, Events, and Processes Addressed in This Report (Continued)

FEP Number	FEP Name	Description	Section(s) Where Addressed
2.2.07.09.0A	Matrix imbibition in the UZ	Water flowing in fractures or other channels in the unsaturated zone may be imbibed into the surrounding rock matrix. This may occur during steady flow, episodic flow, or into matrix pores that have been dried out during the thermal period.	6.3
2.2.07.11.0A	Resaturation of geosphere dry-out zone	Following the peak thermal period, water in the condensation cap may flow downward into the drifts. Influx of cooler water from above, such as might occur from episodic flow, may accelerate return flow from the condensation cap by lowering temperatures below the condensation point. Percolating groundwater will also contribute to resaturation of the dryout zone. Vapor flow, as distinct from liquid flow by capillary processes, may also contribute.	6.3
2.2.08.01.0B	Chemical characteristics of groundwater in the UZ	Chemistry and other characteristics of groundwater in the unsaturated zone may affect groundwater flow and radionuclide transport of dissolved and colloidal species. Groundwater chemistry and other characteristics, including temperature, pH, Eh, ionic strength, and major ionic concentrations, may vary spatially throughout the system as a result of different rock mineralogy.	4.1, 6.3, 6.6
2.2.08.12.0A	Chemistry of water flowing into the drift	Inflowing water chemistry may be used in analysis or modeling that requires initial water chemistry in the drift. Chemistry of water flowing into the drift is affected by initial water chemistry in the rock, mineral and gas composition in the rock, and thermal-hydrologic-chemical processes in the rock.	4.1, 6.3, 6.6
2.2.10.12.0A	Geosphere dry-out due to waste heat	Repository heat evaporates water from the unsaturated zone rocks near the drifts as the temperature exceeds the vaporization temperature. This zone of reduced water content (reduced saturation) migrates outward during the heating phase (about the first 1,000 years) and then migrates back to the waste packages as heat diffuses throughout the mountain and the radioactive sources decay. This FEP addresses the effects of dryout within the rocks.	6.3

[a] There is no defining limit as to what volume of contaminated water constitutes a plume.

FEP 2.1.08.07.0A, Unsaturated flow in the EBS, is considered as included in TSPA-LA from this report because this report contributes the chemistry resulting from differing flow pathways.

FEP 2.1.09.02.0A, Chemical interaction with corrosion products, is considered as included in TSPA-LA through the oxygen balance analysis, where in-drift gas composition calculations (Section 6.7.1) are used to evaluate oxygen consumption due to metal degradation in the drift. This determination sets the oxidizing environment used to generate the in-drift seepage chemistry. Additionally, the analysis of the effect of stainless steel ground support (Section 6.8) on seepage chemistry found it to be insignificant, so it was not considered further for the modeling of in-drift chemistry.

6.15 IMPLEMENTATION INSTRUCTIONS FOR THE TSPA-LA MODEL

This report develops, documents, and validates the NFC process model that, in turn, provides potential seepage water compositions, WRIPs, and a range of in-drift partial pressure of carbon dioxide (pCO_2) values. This report also develops two abstraction models: the seepage dilution/evaporation abstraction model and the integrated invert chemistry abstraction model. The seepage dilution/evaporation abstraction model quantifies the chemical parameters of interest (pH, *I*, [Cl], [N]) on the waste package surface as a function of relative humidity (RH) on the waste package surface (RH_{wp}). TSPA utilizes this abstraction model to evaluate the potential for localized corrosion of the waste package outer barrier (WPOB). The integrated invert chemistry abstraction model provides additional direction to TSPA for selecting the chemical parameters relevant to invert processes (pH and *I*) (see a detailed discussion in Section 6.15.2 and Table 6.15-1). In addition to the NFC process model, the IDPS process model (SNL 2007 [DIRS 177411]) provides the estimated uncertainties on the chemical parameters (pH, I, [Cl], [N]) as a function of in-drift RH (see Section 6.12.2 and Table 6.12-1).

This section describes how the seepage dilution/evaporation lookup tables, pCO_2 lookup tables, and uncertainty instructions developed in this report are to be implemented in TSPA-LA. This section provides roadmaps for implementation of the lookup tables developed in this report for the parameters of interest on the waste package surface and within the invert, during the development of the TSPA-LA model. Although the processes used to ascertain these parameters for the two locations are similar, the resulting chemical environments are different.

A general rule that applies to the seepage scenario discussed in the following subsection is that once a starting water is selected (i.e., Group 1, Group 2, Group 3, Group 4), and a WRIP identified, these two values must be used within TSPA to identify and select both the lookup tables required to calculate the range of pCO_2 gas (partial pressure of carbon dioxide) and the appropriate seepage dilution/evaporation lookup table. These lookup tables must be selected using the same starting water and WRIP value.

The appropriate WRIP value is selected from the WRIP lookup table by TSPA. The WRIP values are tabulated as a function of the thermal measure (a location-specific measure of the thermal history, generated by summing the time when the drift wall drops below boiling in years and the maximum drift wall temperature in degrees Celsius), the percolation flux, and time. The thermal measure and percolation flux will be outputs of the MSTHM report (SNL 2007 [DIRS 181383]).

6.15.1 Implementation of P&CE Chemistry on Waste Package Surfaces: Seepage Dilution/Evaporation Abstraction Model

TSPA-LA implements the lookup tables for chemistry on the waste package surface when seepage is directly dripping onto the drip shields and waste packages. This scenario is modeled in TSPA-LA by using the roadmap given in Figure 6.15-1 and described further here.

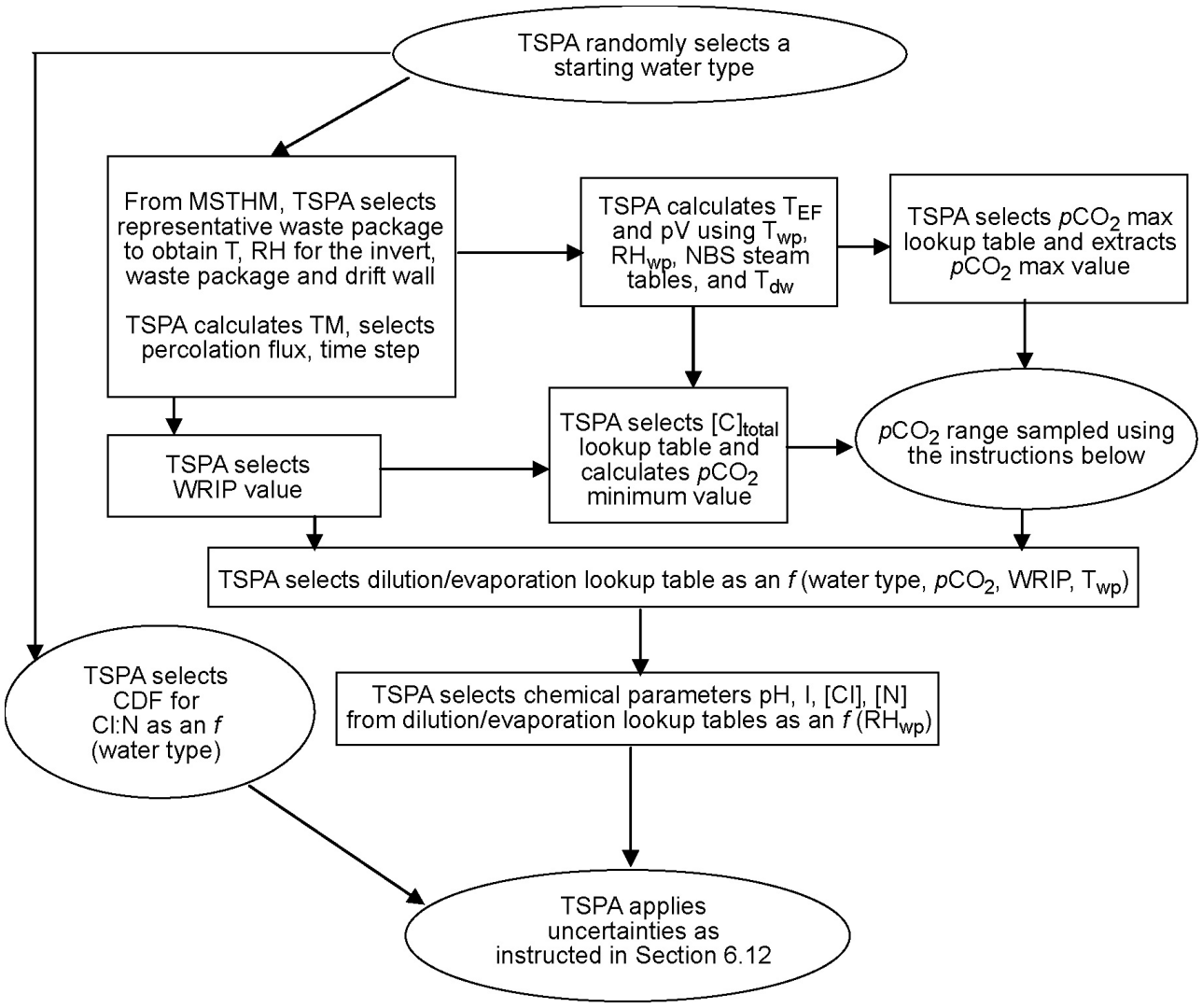

NOTE: The subscripts "wp," and "EF" denote the waste package, and the evaporation front, respectively.

Figure 6.15-1. Roadmap for TSPA-LA Implementation of P&CE Chemistry on the Waste Package Outer Barrier Using the Seepage Dilution/Evaporation Abstraction Model

Two parameters are used to select both the lookup tables used by TSPA to calculate the range of appropriate pCO_2 values and the set of diluted/evaporated water chemistry lookup tables. These are the starting water type (Groups 1 through 4) and the WRIP. For each TSPA-LA Monte Carlo realization, the starting water (Group 1, Group 2, Group 3, or Group 4) is randomly selected. All four of these waters have an equal probability of selection for any given realization. Therefore,

the probability of any given water being selected is 25%. The WRIP value is determined using parameters such as T and RH available from the MSTHM (SNL 2007 [DIRS 181383]) for various relevant locations (see Figure 6.15-1 and discussion below).

In addition to the starting water, a second parameter, ΔpCO_2, is also determined at the beginning of each TSPA realization. This parameter is sampled uniformly between −1 and 1. The NFC process model provides a range of possible pCO_2 values, from a maximum to a minimum, and the ΔpCO_2 value represents the relative offset within that range. If the offset is positive, then the offset is carried through time as a constant fraction multiplied by the maximum pCO_2 value. This preserves the pCO_2 trend (i.e., the offset curve will parallel the maximum pCO_2 trend) (Figure 6.15-2). Likewise, if the ΔpCO_2 is negative, then the offset is propagated through time as a constant fraction multiplied by the minimum pCO_2 value in order to preserve the pCO_2 behavior over time. The ΔpCO_2 is treated as a stochastic (epistemic) uncertainty, and sampled only once per realization.

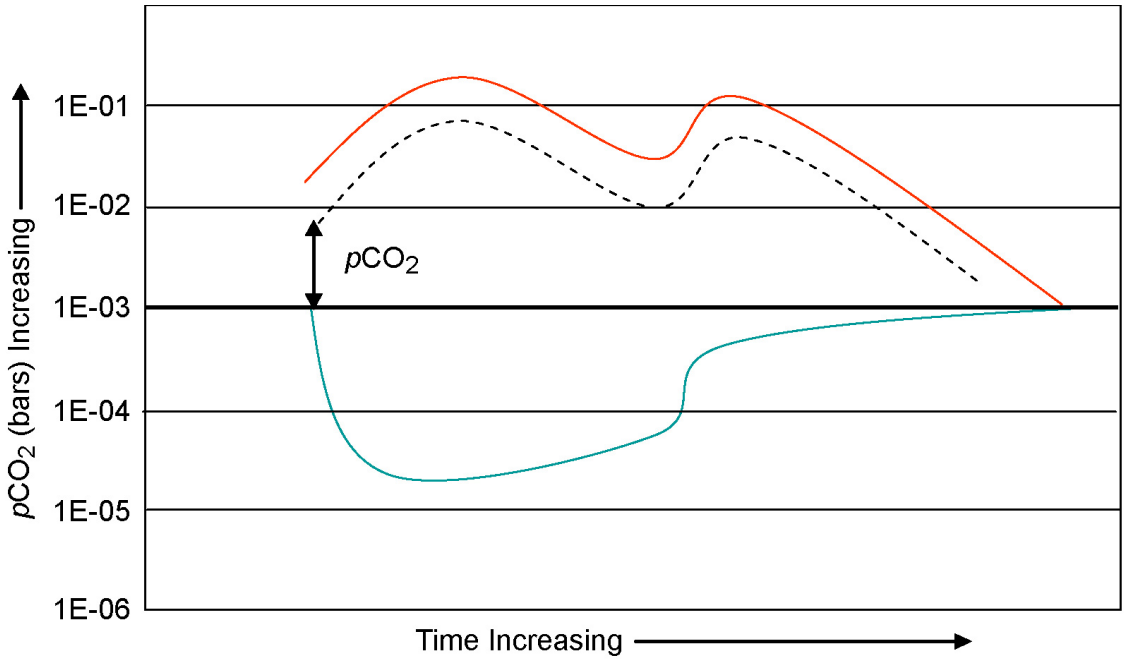

NOTE: The upper line in red represents the maximum pCO_2 time history while the lower blue line represents the pCO_2 minimum. See discussion below for how these values are calculated in the NFC model. The dotted black line is the sampled offset curve. In this example, the ΔpCO_2 is positive and the offset curve retains the shape of the maximum curve over time. Refer to Figure 7.1-12 for an actual calculated example.

Figure 6.15-2. Schematic Illustration of the pCO_2 Range Calculated by the NFC Model and the Relative Offset (ΔpCO_2)

The WRIP lookup table provides the value of the water–rock interaction parameter over the history of the repository, at any given repository location and percolation flux. Once a starting water is selected, an appropriate, location-specific set of WRIP time history maps is identified for the waste package of interest by calculating the thermal measure (sum of the time when drift wall drops below boiling in years and the maximum drift wall temperature in degrees Celsius) for the package from the MSTHM (SNL 2007 [DIRS 181383]) outputs and selecting the closest

value from the WRIP map. Because these parameters are also provided for the case where the drift wall has collapsed, the implementation is also valid for that case. For a collapsed drift, the intact drift wall is farther away from the waste package and, thus, is cooler. The temperature associated with the initial intact drift wall would be approximately mid-way through the rubble. The NFC implementation described in this section considers that seepage onto the drip shield or the waste package surface can only occur once the evaporation front intersects the drift wall at approximately 96°C. The only part of the flow path not captured is then the portion through the rubble from the drift wall to the 96°C isotherm. There are 336 different thermal measures in the WRIP map, covering the expected span of repository conditions. For each thermal measure, twenty sets of time histories are given, each representing a different set of four percolation fluxes, corresponding to the four climate states—"present day," "monsoonal," "glacial transition," and "post-10K." The applicable WRIP value at any given time step is chosen by interpolating between the percolation flux sets using the value of the percolation flux at the time and location of interest from the MSTHM (SNL 2007 [DIRS 181383]). The WRIP lookup table is archived in Output DTN: SN0703PAEBSPCE.006. For a detailed description of the uncertainty treatment in the WRIP value, see Section 6.12.2.5.

The starting water identity and WRIP value are used to select the lookup tables used to calculate the relevant pCO_2 range. The lookup tables are unique to each starting water and provide the maximum pCO_2 as a function of temperature (archived in Output DTN: SN0701PAEBSPCE.002). However, the temperature to be used to enter the table is not the drift wall temperature (T_{dw}); it is the temperature at the evaporation front (T_{EF}). This is either (1) 96°C, if the drift wall temperature is greater than 96°C; or (2) the temperature for which the vapor pressure in the drift (pV) represents pSAT (the saturation vapor pressure of water). The in-drift pV is calculated by TSPA from the temperature and the RH on the surface of the waste package, T_{wp} and RH_{wp}, respectively, from the MSTHM (SNL 2007 [DIRS 181383]) using the following relationship:

$$RH_{wp} = pV/(p\text{SAT at } T_{wp}) \quad \text{(Eq. 6.15-1)}$$

$$pV = (p\text{SAT at } T_{wp}) \times RH_{wp} \quad \text{(Eq. 6.15-2)}$$

The temperature at which pV is equal to pSAT is T_{EF} and is determined by interpolation between pSAT values as a function of T_{wp} in the NBS steam tables (Haar et al. 1984 [DIRS 105175]; data for the relevant temperature range are provided to TSPA in Output DTN: SN0703PAEBSPCE.006). Over the long term, T_{EF} will converge to the drift wall temperature. Once T_{EF} is determined (either 96°C or the temperature at which pV represents pSAT), the lookup tables provide the maximum value of pCO_2. For temperatures below 23°C, the set of values at 23°C is used.

A summary of TSPA implementation instructions for determining maximum in-drift pCO_2 values is presented below:

Use the starting water and WRIP to determine the appropriate pCO_2 lookup table to use.

If the drift wall temperature (T_{dw}) is > 96°C, then use the 96°C pCO_2 values.

If T_{dw} is < 96°C, then use the temperature at the evaporation front (T_{EF}). Calculate T_{EF} in the following manner:

1. Obtain the temperature and RH for the waste package surface (T_{wp} and RH_{wp}, respectively) from the MSTHM (SNL 2007 [DIRS 181383]).

2. Calculate pV using Equation 6.15-2 above and set pSAT (at T_{EF}) = pV.

3. Determine T_{EF} by interpolating between pSAT values in the NBS steam table data (Haar et al. 1984 [DIRS 105175]; provided to TSPA in Output DTN: SN0703PAEBSPCE.006).

4. Use T_{EF} to enter the lookup table selected in Step 1 above to extract the maximum $p\mathrm{CO_2}$ value.

The minimum $p\mathrm{CO_2}$ in the drift is calculated assuming that the gas phase in the rock is at ambient $p\mathrm{CO_2}$ (10^{-3} bars), and that this gas phase diffuses into the drift and is diluted by water vapor released by boiling or evaporation of water at the dryout front. This is a bounding assumption because it implies that gas phase transport through the mountain is very rapid, such that there is no significant perturbation in the ambient gas phase $p\mathrm{CO_2}$ due to the thermal pulse.

If the pV in the drift is less than 0.0281 bar, which is pSAT at 23°C (Haar et al. 1984 [DIRS 105175]; provided to TSPA in Output DTN: SN0703PAEBSPCE.006), then no dilution of the ambient gas phase is assumed, and the minimum in-drift $p\mathrm{CO_2}$ is assumed to be the ambient value of 10^{-3} bars. Otherwise, the degree of dilution (DD) of the in-rock gas phase by water vapor is calculated to be:

$$\mathrm{DD} = [1 - (0.0281 \text{ bar}/0.89 \text{ bar})]/[1 - (p\mathrm{V} \text{ bar}/0.89 \text{ bar})] \qquad \text{(Eq. 6.15-3)}$$

and the mole fraction of added water vapor (F_{H2O}) is:

$$F_{H2O} = 1 - (1/\mathrm{DD}) \qquad \text{(Eq. 6.15-4)}$$

Also required is the concentration of carbon in the water, assuming equilibrium with a $p\mathrm{CO_2}$ of 10^{-3} bars. In general, approximately half of the total inorganic carbon is degassed upon evaporation (Section 6.3.1.4.8). This value is obtained from the total inorganic carbon lookup tables, for each of the starting waters (archived in Output DTN: SN0701PAEBSPCE.002) using the T_{EF} and the appropriate WRIP value determined earlier. Finally, the minimum $p\mathrm{CO_2}$ in the drift can be calculated:

$$\text{Minimum } p\mathrm{CO_2} \text{ bar} = p\mathrm{CO_2}_{\text{ ambient}} \text{ bar}/\mathrm{DD} + (F_{H2O} \times (\tfrac{1}{2}\,[\mathrm{C}]_{\text{total}} \text{ mol (kg• } \mathrm{H_2O})^{-1} / 55.5084 \text{ mol (kg• } \mathrm{H_2O})^{-1})) \times 0.89 \text{ bar} \qquad \text{(Eq. 6.15-5)}$$

where the value 55.5084 represents the moles of water in 1 kg of water, and the $[\mathrm{C}]_{\text{total}}$ values are in moles/kg $\mathrm{H_2O}$.

A summary of TSPA implementation instructions for determining minimum in-drift pCO_2 values is presented below:

1. Use the starting water and WRIP to determine the appropriate lookup table to use.

2. If the vapor pressure in the drift is ≤ 0.0281, then set the minimum pCO_2 value equal to 10^{-3} bar.

3. If pV is > 0.0281 bar, then calculate the minimum pCO_2 in the following manner:

    a. Calculate the DD using pV and Equation 6.15-3 above.

    b. Calculate the mole fraction of added water vapor (F_{H2O}) using Equation 6.15-4 above.

    c. Calculate the minimum in-drift pCO_2 using Equation 6.15-5 above and an ambient $pCO_2 = 10^{-3}$ bar, the DD and F_{H2O} calculated in Steps 3a and 3b. The dissolved total inorganic carbon concentration is taken from the lookup table selected in Step 1.

The pCO_2 lookup tables and the total inorganic carbon lookup tables that are used to calculate the minimum and maximum pCO_2 are archived in Output DTN: SN0701PAEBSPCE.002. The WRIP history map table and the pCO_2 lookup tables are unique to the particular starting water type. The relevant set of diluted/evaporated seepage water lookup tables is selected using the same starting water, WRIP value, and the calculated pCO_2 that is finally determined by applying the offset, ΔpCO_2, as described below.

Once the pCO_2 range is determined for the time step of interest, the ΔpCO_2 value sampled at the beginning of the realization is applied. As described earlier, the value is the relative offset from the ambient value (10^{-3} bar) to the sampled value, shifted in a direction towards the maximum pCO_2 values if the ΔpCO_2 is positive, and shifted in a direction towards the minimum value if the ΔpCO_2 value is negative (see Figure 6.15-2).

Once the starting water, WRIP value, pCO_2, and T_{wp} provided by the MSTHM (SNL 2007 [DIRS 181383]) are obtained, the appropriate lookup tables may be identified and used for determining diluted/evaporated seepage water compositions.

The relative humidity at the waste package surface (RH_{wp}) is used to access the appropriate row of the combined dilution/evaporation lookup tables to retrieve the chemical parameters of interest (pH, *I,* [Cl], [N]). The pH reported in the lookup tables corresponds to the Pitzer pH, and pH as used through this report refers to the Pitzer pH unless explicitly stated otherwise. The P&CE seepage dilution/evaporation abstraction model instructs TSPA to use total molal chlorine, [Cl], and total molal nitrogen, [N], for their evaluation of chloride and nitrate. This is consistent with the use of these parameters in other Yucca Mountain Project analysis/model reports. In this report, the dilution and evaporation data are combined into continuous lookup tables for each of the group waters (Groups 1 through 4), at three pCO_2 values (10^{-2}, 10^{-3}, and 10^{-4} bar), at three temperatures (30°C, 70°C, and 100°C), and for eleven different discrete WRIP

values (0 through L) (see Table 6.3-5). These Excel files are archived in Output DTN: SN0701PAEBSPCE.001, which contains the 396 lookup tables.

The lookup table file title nomenclature is ?*P#T%.xls where:

"?" is the one-digit starting water type number (1, 2, 3, 4).

"*" is 0, B, C,…L representing varying values of the WRIP (quantities of alkali feldspar added to the water).

"#" is 2, 3, 4 and designates the pCO_2 (P) equal to 10^{-2}, 10^{-3}, or 10^{-4} bar, respectively.

"%" is 30, 70, or 1 for temperature (T) equal to 30°C, 70°C, or 100°C, respectively.

For example, the lookup table titled "1DP2T30.xls" contains the chemical parameters for a Group 1 water type with the "D" quantity of alkali feldspar added, at a $pCO_2 = 10^{-2}$ bar and at a temperature of 30°C. In these dilution/evaporation lookup tables, the values for pCO_2 are in bar and the numbers 2, 3, and 4 after the "P" in the table titles merely indicate whether the simulations archived in the tables were conducted at 0.01, 0.001, and 0.0001 bar, respectively.

The independent variable in the lookup tables is relative humidity. To select the appropriate chemistry from a selected lookup table, TSPA will interpolate between rows representing relative humidities that bound the waste package surface relative humidity. When selecting chemical parameters that fall between lookup tables, the parameters should be estimated using linear interpolation on temperature and log linear for pCO_2 parameters. Chemistry values will be extrapolated for pH, I, Cl^-, and NO_3^- if the pCO_2 exceeds the range of 10^{-4} to 10^{-2} bar, established in the lookup tables. TSPA is instructed to use linear extrapolations for pH, I, [Cl] and [N] up to 2×10^{-2} and down to 1×10^{-5} bar pCO_2. A sensitivity analyses documented in Section 7.2 established that this range of pCO_2 represents an acceptable extrapolation range for potential seepage water chemistries. For temperatures above 100°C and below 30°C, extrapolation should not be used and lookup table values at 100°C or 30°C should be used, respectively. If the relative humidity is greater than the highest value in the lookup tables, use the highest value; if the relative humidity is lower than the lowest value in the lookup tables, use the lowest value. Implementation of uncertainty on any parameter should be done in accordance with the instructions found in Section 6.12.

6.15.1.1 Nonconvergence

The EQ3/6 numerical simulations used to produce the seepage lookup tables did not always converge on the eutectic point associated with the deliquescence or dryout relative humidity value for very low water-to-solute ratios (at low relative humidity values). An appropriate method to deal with this limitation is to specify that aqueous conditions exist at all times when seepage is occurring, regardless of the in-drift relative humidity. This implementation is also consistent with experimental work performed at Lawrence Livermore National Laboratories on salt deliquescence/dryout points, which indicated that a salt assemblage likely to be relevant to concentrated seepage would not be expected to dryout under any postclosure repository-relevant conditions (DTN: LL040901831032.008 [DIRS 173659], spreadsheet: *Boiling_temperatures_Rlc_1.doc*, Figure 3). For TSPA-LA, the selection of chemical parameters below the lowest

relative humidity in the lookup tables can be done as described in next paragraph, because NO_3^- (represented by total [N]) is conserved relative to Cl^- (represented by total [Cl]) at low relative humidity due to the presence of the halite/sylvite chemical divide (where chloride salts are precipitating prior to nitrate salts). Therefore, nitrate concentrations climb relative to Cl^- ion at these lower relative humidity values (i.e., the chloride to nitrate ratio decreases). In addition, several of the EQ3/6 simulations of Group 3 water resulted in activities of water that began increasing near the dryout point, an indication of nonconvergence in the simulation. In the event that the activity of water showed an increase near dryout (a modeling limitation and physically un-real), the data in the dilution/evaporation lookup tables were truncated at that point.

6.15.1.2 Implementation at or below the Lowest Relative Humidity Point for Seepage

When seepage is predicted to occur, aqueous conditions are assumed to be present regardless of RH. If the RH value used to enter the table falls below the last RH point in the particular seepage lookup table, then the composition for the last value is used.

6.15.1.3 Salt Separation

If the relative humidity on a waste package undergoing seepage should fall below a threshold relative humidity value for each lookup table, chloride salts (halite or sylvite) will precipitate. Once a salt has precipitated, the remaining nitrate-rich brine, or some fraction of it, can advect off of the waste package, or at least away from the precipitated salts, and hence be physically separated from the precipitated salts. Because the brine is chemically different from the bulk brine-salt geochemical system, brine-salt separation changes the bulk composition of the system represented by the precipitated salts and whatever brine is retained by them. In general, because the removed brine is nitrate-rich relative to the bulk system (chloride salts have precipitated), the remaining salt-brine system is more chloride-rich. A schematic representation of the conceptual process of brine-salt separation is shown in Figure 6.15-3. The evaporative pathway is shown in red; the dilution pathway followed when the RH rises, in blue. An initial seepage water has composition X. When the RH is lowered and condition X^1 is reached, a chloride salt precipitates. The evaporating liquid phase follows the liquid line of descent toward point C, the eutectic composition. At some point, a physical separation of the precipitated salt and some of the brine occurs (X^2); the brine left in contact with the salt assemblage may continue to evaporate along the liquid line of descent and concentrate. As the RH in the drift begins to rise, the brine absorbs water and evolves back up the curve, retracing its path to X^1; however, with a further increase in RH, the dilution path diverges from the original evaporation path. It continues to follow the liquid line of descent to some point X^3, at which point all chloride salts are dissolved and the brine evolves off of the line towards X^4. The seepage dilution/evaporation lookup tables can be used to predict water chemistry throughout the evaporation pathway, and along the dilution pathway until the RH rises again to point X^1; beyond this point, TSPA must assume a Cl-rich brine will form. These threshold relative humidity values at which salt precipitation occurs (point X^1) are tabulated in Output DTN: SN0703PAEBSPCE.006. The specific steps required to ensure that Cl and N concentrations are calculated and uncertainties appropriately incorporated are outlined in Section 6.12.

In a few rare cases, a nitrate salt precipitates first (i.e., initial composition X to the right of the eutectic point “C” in Figure 6.15-3). These cases cannot result in a brine with a chloride:nitrate

ratio higher than that of the eutectic composition, but, because the actual composition of the brines that could form due to brine-salt separation cannot be predicted accurately, they are conservatively treated in the same manner as the other water compositions.

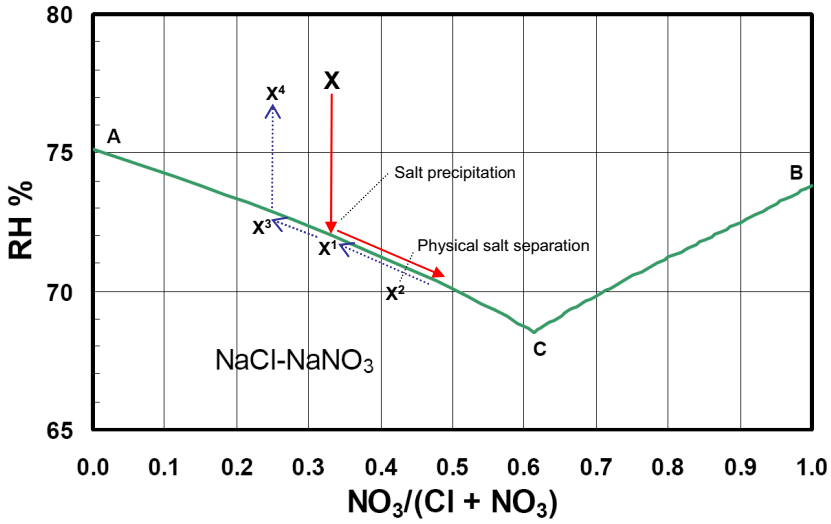

NOTE: See text for details.

Figure 6.15-3. Schematic Representation of the Conceptual Process of Salt Precipitation and Separation

6.15.2 Implementation of P&CE Integrated Invert Chemistry Abstraction Model

One of the intended uses of the integrated invert chemistry abstraction model generated by this report is to predict the chemical parameters such as pH and ionic strength, *I,* in the invert that likely control solubility and colloidal stability of radionuclides. The occurrence of invert pore water ranges from capillary condensation in the smallest pores (no-seepage case) to seepage (0.01 to >1,000 kg/yr per waste package). The pore-water composition therefore ranges from highly evolved with long residence time, to unevaporated seepage. More dilute compositions in the invert are possible from drift wall and drip shield condensation. The invert pore-water composition is important for TSPA only when there are *diffusive* releases from the waste package. Advective transport through the waste package will have a strong influence on the aqueous composition along radionuclide or colloid transport pathways through the invert.

Drift-wall condensation as represented in TSPA originates above the drip shield and follows the same path as seepage through the engineered barrier system. Drift wall condensation may occur separately or in conjunction with seepage. The composition of drift wall condensation can range between very dilute (e.g., dilute solution of silica and bicarbonate) and more concentrated (i.e., like seepage). For conditions when drift wall condensation occurs with or without seepage, a reasonable upper bound approximation is used to represent the maximum attainable state of dilution. To calculate this dilution maximum, solutions were equilibrated with calcite, amorphous silica, over a range of temperatures (30°C to 100°C) and pCO_2 (10^{-4} to 10^{-2}) (Section 6.9.4). The maximum equilibrium relative humidity for all examined conditions was 99.994% for the T = 30°C, $pCO_2 = 10^{-4}$ bar case (see Table 6.9-1). Equilibrium RH limits are

provided to TSPA for each of the nine combinations of T and pCO_2 used by the P&CE dilution/evaporation abstraction model as described in Section 6.9.4.

Drip shield condensation will be excluded in TSPA-LA, including the performance margin analysis. Low-consequence exclusion arguments will include: (1) condensate is benign to waste package localized corrosion (see SNL 2007 [DIRS 177407], Section 6.3.3.3); and (2) models for general corrosion of the WPOB and drip shield do not depend on the presence of condensate or its composition. Additional justification is provided in the FEP screening justification (DTN: MO0706SPAFEPLA.001 [DIRS 181613]) and will be supplemented in *In-Drift Natural Convection and Condensation* (SNL 2007 [DIRS 181648]).

Nominal and seismic scenario treatment will be identical with respect to the chemistry of seepage, drift wall condensation, and drip shield condensation. For the igneous intrusion scenario, all affected waste package locations experience seepage. Drift wall condensation is nil because the drift wall is no longer accessible to the gas phase. Drip shield condensation is possible but can be neglected as a source of water for transport because the drip shields are failed and seepage is applied at all affected locations.

An integrated technical description of the composition for waters originating as seepage as they occur inside the waste package and in the invert is highly desirable. The recommended approach involves assessing both the outputs of this report (Output DTNs: SN0701PAEBSPCE.001 and SN0701PAEBSPCE.002) and the water chemistries provided by the IPC abstraction (DTN: SN0702PAIPC1CA.001 [DIRS 180451]).

A summary of the recommended approach is described below and presented in Table 6.15-1.

6.15.2.1 Relative Humidity Constraints on Invert Pore-Water Composition

This section identifies specific measures to be implemented in TSPA to ensure integration between values of relative humidity (RH) in the invert as calculated from thermal-hydrology models (i.e., the multiscale model; SNL 2007 [DIRS 181383]) and the activity of water in aqueous solutions at high RH. The hydrologic properties of the invert and host rock allow RH to approach unity (e.g., >99.99%) during cooldown, whereas constraints on the chemistry of aqueous solutions require dilution to achieve such high RH.

The measures to be implemented in TSPA prevent unrealistic over-dilution of the solution compositions in response to high RH values generated by the MSTHM. The rationale for these measures includes: (1) the UZ contains limited water available for dilution, and (2) even the most dilute waters present in the repository near field will have some dissolved solids including CO_2, silica, and calcite, which lower the water activity (i.e., equilibrium RH) slightly from 100%.

For all invert conditions, compare the RH in the invert from the MSTHM (SNL 2007 [DIRS 181383]) to the RH boundary corresponding to the local temperature and pCO_2 (Output DTN: SN0706PAEBSPCE.016, spreadsheet: *Invert_RH_Boundary.xls*). TSPA is instructed to use linear interpolation on T and then on log pCO_2 to calculate the RH boundary associated with the local conditions. Then choose the water composition associated with the lower value of RH (dilution of seepage by condensation in the invert will not cause the equilibrium RH to exceed

the RH boundary). If the RH boundary is a smaller value than the extant RH, then use the composition associated with the boundary case for invert pore water. If the extant RH is smaller, then re-enter and interpolate the lookup tables using this RH, and the extant temperature and pCO_2, to obtain the equilibrated seepage water composition.

Invert transport is implemented for three scenarios:

a. **In the event of seepage**: Apply the RH test described above, and the lookup tables determined using the WRIP value for the seepage.

b. **In the event of drift-wall condensation, no seepage:** Apply the RH test described above. The composition of drift-wall condensate is represented by the "immature" waters in the lookup tables, with the minimum WRIP value (i.e., WRIP = 0). The lookup tables for this WRIP value are entered by interpolating the RH boundary provided in Output DTN: SN0706PAEBSPCE.016 (spreadsheet: *Invert_RH_Boundary.xls*).

c. **In the event of no-seepage, no-condensation**: Apply the RH test described above. Water vapor condenses in the invert during cooldown, re-dissolving the soluble residue of pore waters precipitated when the tuff particles were desiccated. In addition, there may be a tiny flux of pore water from the host rock into the invert. The composition of such pore waters is represented by seepage, equilibrated to the local temperature, pCO_2, and RH.

The treatment of seepage in the invert is conservative in the sense that the volumetric flow rate is unaltered by evaporation, whereas the composition is equilibrated to the extant temperature, pCO_2, and RH. During the thermal period while the RH is significantly less than 100%, the result of the seepage treatment in TSPA is to produce more concentrated chemistries with higher or lower pH than unevaporated conditions, depending on which of the four starting pore waters is selected. Seepage composition in the invert is used in representing radionuclide transport in the invert, for the case of diffusion dominated releases from the waste package.

Radionuclides that are released by diffusion from waste packages, and then entrained in seepage flow in the invert, can be transported as dissolved or colloidal species, or precipitated if solubility limits are exceeded. Transport is likely if dilution occurs; however, precipitation or colloidal destabilization could occur in some circumstances, such that equilibration of seepage to the extant conditions would be non-conservative with respect to transport. The effects of assuming IPC chemistry in the invert for advective releases from the waste package, and of equilibrating seepage composition to the extant environmental conditions, as represented in Table 6.15-1, can be further investigated using sensitivity studies in the TSPA model, such as: (1) comparing invert radionuclide mass-release rates using evaporated seepage compositions instead of IPC compositions; and (2) comparing mass-release rates using unevaporated seepage compositions instead of IPC compositions.

Table 6.15-1. Summary of Chemistry for Seepage and Condensation

	Seepage		No Seepage	
	Drift Wall Condensation	**No Drift Wall Condensation**	**Drift Wall Condensation**	**No Drift Wall Condensation**
Seismic/Nominal				
WPOB; Drip Shield Intact [a]	Dry air or humidity environment only.			
WPOB; Drip Shield Failed [b]	Use seepage composition equilibrated to T, RH, pCO_2 of WPOB.			
IPC; Drip Shield Intact [c] (Waste Package Failed)	$[F^-] = 0$; use chemistry for no-seepage case.			
IPC; Drip Shield Failed [d] (Waste Package Failed)	$[F^-] \leq$ Fmax; use chemistry for seepage case if $Q_4 \geq 0.1$ L/yr; otherwise, no-seepage chemistry.		$[F^-] = 0$; use chemistry for seepage case if $Q_4 \geq 0.1$ L/yr; otherwise, no-seepage chemistry.	$[F^-] = 0$; use chemistry for no-seepage case.
Invert; Drip Shield Intact [e] (Waste Package Failed)	Use seepage composition equilibrated to T, RH, pCO_2 of invert. (Sensitivity #1a and #1b)			
Invert; Drip Shield Failed [f] (Waste Package Failed)	Use IPC (seepage-based) to represent advective transport. (Sensitivity #2)			

Table 6.15-1. Summary of Chemistry for Seepage and Condensation (Continued)

	Seepage		No Seepage	
	Drift Wall Condensation	**No Drift Wall Condensation**	**Drift Wall Condensation**	**No Drift Wall Condensation**
Igneous Intrusion				
IPC; Drip Shield Failed [g] (Waste Package Failed)		Use basalt water without modification for environment; choose from alternatives in IPC documentation.		
Invert; Drip Shield Failed [h] (Waste Package Failed)		Use IPC selected above.		

[a] For waste package conditions under intact drip shields, dust deliquescence/localized corrosion is excluded. General corrosion of the waste package and drip shield underside is not compositionally dependent.

[b] Drip shield failure may occur by stress corrosion cracking, or larger breaches from general corrosion or rupture. Regardless of the mode of drip shield failure, if seepage or drift wall condensation occurs then they dominate the WPOB corrosion environment.

[c] [F^-] constraint is used by *Dissolved Concentration Limits of Elements with Radioactive Isotopes* (SNL 2007 [DIRS 177418]), and incorporated in the solubility uncertainty function used in TSPA.

[d] [F^-] constraint is used by *Dissolved Concentration Limits of Elements with Radioactive Isotopes* (SNL 2007 [DIRS 177418]), and incorporated in the solubility uncertainty function used in TSPA. Fmax is the maximum [F^-].

[e] With the drip shield intact, releases from failed waste packages can occur by diffusion only.

[f] Drip shield failure may occur by stress corrosion cracking, or larger breaches from general corrosion or rupture. Advection through the waste package controls the invert water chemistry, except for the no-seepage (no-condensation) case. In the latter case, invert moisture accumulates by capillary condensation, with composition represented by "young" formation water equilibrated to T, RH, and pCO_2.

[g] Sensitivity studies documented in the IPC abstraction (DTN: SN0702PAIPC1CA.001 [DIRS 180451]), using three representative basalt water compositions, show no impact on in-package chemistry.

[h] Following approach for seismic/nominal, use the IPC abstraction (DTN: SN0702PAIPC1CA.001 [DIRS 180451]) to represent radionuclide transport in the invert.

NOTES: T = temperature; Q_4 = the liquid flux into the waste package as defined in the IPC abstraction (DTN: SN0702PAIPC1CA.001 [DIRS 180451]).

The condition specified in the first column corresponds to the implementation specified in the second column and applies in like colored boxes. The white boxes indicate a stand-alone implementation corresponding to row and column header conditions.

INTENTIONALLY LEFT BLANK